

Studies on the assembly and architecture of the *Drosophila* active zone scaffold

Inaugural-Dissertation

to obtain the academic degree
Doctor rerum naturalium (Dr. rer. nat.)

submitted to the Department of Biology, Chemistry, Pharmacy
of Freie Universität Berlin

by

Jan Heiner Driller

2018

This work was carried out in the period of June 2013 to October 2018 under the supervision of Prof. Dr. Markus C. Wahl at the Institute of Chemistry and Biochemistry, Freie Universität Berlin, Germany.

First Reviewer: Prof. Dr. Markus C. Wahl
Structural Biochemistry
Institute of Chemistry and Biochemistry
Freie Universität Berlin
Takustraße 6
14195 Berlin, Germany

Second Reviewer: Prof. Dr. Stephan J. Sigrist
Genetics
Institute of Biology
Freie Universität Berlin
Takustraße 6
14195 Berlin, Germany

Date of defense: 15.01.2019

Table of contents

Abstract	1
Zusammenfassung	3
List of publications	5
1. Introduction	7
1.1. Chemical Synapse and the synaptic vesicle cycle	7
1.2. Active zone morphology	9
1.3. The active zone scaffold	10
1.3.1. Bruchpilot and ELKS family	11
1.3.2. RIM-binding protein	12
1.3.3. Rab3 interacting molecule (RIM)	13
1.3.4. (M)Unc13	13
1.3.5. Syd-1 and Liprin α	14
1.3.6. Ca ²⁺ channels	14
1.3.7. Piccolo and Bassoon	15
1.3.8. Rab proteins	15
1.4. Transport of active zone proteins	17
1.4.1. Serine arginine protein kinase at cytological position 79D (SRPK79D)	19
2. Aims	21
3. Results and Discussion	22
3.1. Interaction network of the Drosophila active zone scaffold	22
3.2. Bruchpilot	24
3.2.1. Interaction network of Bruchpilot	25
3.2.2. BRP N-terminal phosphorylation by SRPK79D	27
3.2.3. Central dimerization domain in Bruchpilot	31
3.2.4. Bruchpilot tethers synaptic vesicles at the C-terminus	32
3.3. RIM-binding protein	34
3.3.1. Interaction network of RIM-binding protein	34
3.3.2. N-terminal domain of RIM-binding protein	35
3.3.3. SH3 domains of RIM-binding protein	37
3.3.4. The three central FN-III domains of RIM-BP	40
3.4. Spinophilin and Syd-1 interact with the Neurexin-1 C-terminus	43
3.5. Unc13 isoforms A and B within the active zone scaffold	46

Table of contents

4. Outlook	48
4.1. Bruchpilot	49
4.2. RIM-binding protein	50
5. Appendix: Yeast-two hybrid	51
References	52
Abbreviations	61
List of Figures and Tables	62
Acknowledgment	63

Abstract

Presynaptic membranes are covered by protein scaffolds that are formed from few conserved families of extended proteins: ELKS/Bruchpilot family, RIM-BP, (M)Unc13, Liprin- α , Syd-1 and the RIM-superfamily including the mammalian proteins Piccolo, Bassoon. These scaffolds regulate the docking and priming of synaptic vesicles at the active zones (AZ) and thus control information transfer. Scaffold components must be safely transported along the axon before being integrated into the scaffold upon their arrival at active zone membranes. In an “early” assembly the scaffold proteins Syd-1 and Liprin- α predefine the synaptic vesicle release sites together with Neurexin and recruit the “late” scaffold components, particularly Bruchpilot and RIM-BP, to assemble the mature AZ scaffold. Neither the structural rules, by which these AZ scaffolds are transported and assembled, nor how the scaffolds exactly support AZ functions are presently well understood. In *Drosophila*, the integrity of the active zone scaffold depends particularly on the large core scaffold proteins Bruchpilot and RIM-BP.

During my PhD work, I conducted a comprehensive yeast-two hybrid (Y2H) analysis that covered 135 constructs of 35 known AZ proteins. The protein-protein interaction network generated from these data provide a profound basis on interacting domains/regions within the AZ scaffold. Based on the Y2H results, I identified specific serine residues in the N-terminus of Bruchpilot as a substrate of the SRPK79D kinase. *In vivo* analysis of site specific mutations by the Sigrist group confirmed that phosphorylation of these serine residues acts as a master switch in the transport of the “late” scaffold components Bruchpilot, RIM-BP and Unc13A. Furthermore, the Y2H approach provides evidence on the interaction of the major scaffold proteins Bruchpilot and RIM-BP and explains the isoform specific co-localization of Unc13A to the “late” scaffold while Unc13B co-localize with the “early” scaffold.

I characterized important domains and interactions of the large scaffold protein RIM-BP at a molecular level by solving corresponding crystal structures. The C-terminal SH3-II and SH3-III domains in RIM-BP bind several PXXP motifs in other AZ proteins while no interactions were identified for SH3-I. SH3-II and SH3-III binding to the transport adaptor Aplip1 is several fold stronger compared to other interactions and is of utmost

Abstract

importance for the transport of the “late” scaffold components. The crystal structure of the central FN-III array in RIM-BP suggests a potential hinge region or a preformed binding site by the three FN-III domains.

Furthermore, I crystallized and characterized the binding of Spinophilin and the “early” scaffold component Syd-1 to the transmembrane protein NrX-1. The interaction of Spinophilin and Syd-1 with NrX-1 regulates the assembly and proper localization of the mature AZ scaffold at the synaptic terminal.

Zusammenfassung

Präsynaptische Membranen beinhalten ein Gerüst aus Proteinen, die sich aus wenigen konservierten Familien von langen Proteinen zusammensetzen: ELKS/Bruchpilot-Familie, RIM-BP, (M)Unc13, Liprin- α , Syd-1 sowie der, RIM-Superfamilie mit den säugetierspezifischen Proteinen Piccolo und Bassoon. Diese Gerüstproteine regeln das Andocken und Vorbereiten von synaptischen Vesikeln an den aktiven Zonen der Plasmamembran und steuern so den Informationsfluss. Um bei Ankunft an der präsynaptischen Membran in das AZ-Gerüst integriert zu werden, müssen diese Proteine entlang des Axons transportiert werden. In einem „frühen“ Assemblierungsschritt definieren die Gerüstproteine Syd-1 und Liprin- α zusammen mit Neurexin die Regionen für das neue AZ-Gerüst und rekrutieren anschließend die „späten“ Gerüstproteine, insbesondere Bruchpilot und RIM-BP, um ein funktionsfähiges AZ-Gerüst zu assemblieren. Weder die molekularen Mechanismen, nach denen diese AZ-Gerüste transportiert und integriert werden, noch die genaue Funktionsweise der AZ-Gerüste sind derzeit gut verstanden. In *Drosophila* hängt die Integrität des AZ-Gerüsts besonders von den großen Proteinen Bruchpilot und RIM-BP ab.

Während meiner Doktorarbeit führte ich umfassende Hefe-zwei-Hybrid-Analysen (Y2H) von über 135 Konstrukte aus 35 bekannten AZ Proteinen durch. Das aus diesen Daten generierte Protein-Protein-Interaktionsnetzwerk liefert eine fundierte Grundlage für weitere Studien über interagierende Domänen/Regionen innerhalb des AZ-Gerüsts. Basierend auf den Y2H-Ergebnissen identifizierte ich spezifische Serinreste im N-Terminus von Bruchpilot als Substrat der SRPK79D-Kinaseaktivität. Die AG Sigrist führte spezifische Mutationen in BRP ein und konnte so diese Phosphorylierungen als Hauptschalter beim Transport der "späten" Gerüstkomponenten Bruchpilot, RIM-BP und Unc13A. Darüber hinaus liefert der Y2H-Ansatz Hinweise auf die Interaktion der großen Gerüstproteine Bruchpilot und RIM-BP und erklärt die isoform-spezifische Co-Lokalisierung von Unc13A zum „späten“ Gerüst, während Unc13B mit dem „frühen“ Gerüst co-lokalisiert.

Ich charakterisierte wichtige Domänen und Wechselwirkungen des großen Gerüstproteins RIM-BP auf molekularer Ebene durch das Lösen entsprechender Kristallstrukturen. Die C-terminalen SH3-II und SH3-III Domänen in RIM-BP binden an

Zusammenfassung

mehrere PXXP-Motive in anderen AZ-Proteinen, während für die SH3-I Domäne keine Wechselwirkungen identifiziert wurden. Die Bindung von SH3-II und SH3-III an den Transportadapter Aplip1 ist im Vergleich zu anderen Wechselwirkungen um ein Vielfaches stärker und ist für den Transport der "späten" Gerüstbauteile von größter Bedeutung. Die Kristallstruktur der drei zentralen FN-III-Domänen in RIM-BP zeigt eine mögliche Bindungsstelle zwischen FN-III(1) und FN-III(2) sowie einen möglichen Schanierbereich zwischen FN-III(2) und FN-III(3) vermuten lässt.

Darüber hinaus kristallisierte und charakterisierte ich die Bindung von Spinophilin sowie der "frühen" Gerüstkomponente Syd-1 an das Transmembranprotein NrX-1, wodurch der Aufbau und die korrekte Lokalisierung des reifen AZ-Gerüsts am synaptischen Terminal geregelt wird.

List of publications

- I. Lardong, J. A., J. H. Driller, H. Depner, C. Weise, A. Petzoldt, M. C. Wahl, S. J. Sigrist and B. Loll (2015). "Structures of *Drosophila melanogaster* Rab2 and Rab3 bound to GMPPNP" *Acta Crystallogr F Struct Biol Commun* 71(Pt 1): 34-40., [10.1107/S2053230X1402617X](https://doi.org/10.1107/S2053230X1402617X)

JHD designed expression constructs and planned experiments.

- II. Siebert, M., M. A. Bohme, J. H. Driller, H. Babikir, M. M. Mampell, U. Rey, N. Ramesh, T. Matkovic, N. Holton, S. Reddy-Alla, F. Gottfert, D. Kamin, C. Quentin, S. Klinedinst, T. F. Andlauer, S. W. Hell, C. A. Collins, M. C. Wahl, B. Loll and S. J. Sigrist (2015). "A high affinity RIM-binding protein/Aplip1 interaction prevents the formation of ectopic axonal active zones" *Elife* 4., [10.7554/eLife.06935](https://doi.org/10.7554/eLife.06935)

JHD expressed, purified RIM-BP SH3 II and III and crystallized the SH3 domains together with peptides derived from *Cacophony* and *Aplip1*, collected X-ray diffraction data, solved and built the structures and wrote parts of the manuscript.

- III. Muhammad, K., S. Reddy-Alla, J. H. Driller, D. Schreiner, U. Rey, M. A. Bohme, C. Hollmann, N. Ramesh, H. Depner, J. Lutzkendorf, T. Matkovic, T. Gotz, D. D. Bergeron, J. Schmoranzler, F. Goettfert, M. Holt, M. C. Wahl, S. W. Hell, P. Scheiffele, A. M. Walter, B. Loll and S. J. Sigrist (2015). "Presynaptic spinophilin tunes neurexin signalling to control active zone architecture and function" *Nat Commun* 6: 8362., [10.1038/ncomms9362](https://doi.org/10.1038/ncomms9362)

JHD cloned, expressed and purified all *in vitro* constructs, performed pulldown and ITC experiments, crystallized, solved and build the structure of the SPN-Nrx-1 complex, collected X-ray diffraction data and wrote parts of the manuscript.

List of publications

- IV. Bohme, M. A., C. Beis, S. Reddy-Alla, E. Reynolds, M. M. Mampell, A. T. Grasskamp, J. Lutzkendorf, D. D. Bergeron, J. H. Driller, H. Babikir, F. Gottfert, I. M. Robinson, C. J. O'Kane, S. W. Hell, M. C. Wahl, U. Stelzl, B. Loll, A. M. Walter and S. J. Sigrist (2016). "Active zone scaffolds differentially accumulate Unc13 isoforms to tune Ca(2+) channel-vesicle coupling" Nat Neurosci 19(10): 1311-1320., [10.1038/nn.4364](https://doi.org/10.1038/nn.4364)

JHD cloned constructs, performed Yeast-Two Hybrid experiments and analyzed the data.

- V. Driller, J. H., Lützkendorf, J., Depner, H., Siebert, M., Kuropka, B., Weise, C., Petzoldt, A. G., Lehmann, M., Stelzl, U., Zahedi, R., Sickmann, A., Freund, C., Sigrist, S. J., Wahl, M. C. "Phosphorylation of the Bruchpilot N-terminus by SRPK79D controls axonal transport of active zone building blocks" J. Cell Sci., *in revision*

JHD designed experiments; cloned constructs and performed Yeast-Two Hybrid experiments and analyzed the data. JHD expressed and purified *in vitro* constructs of SRPKs and ELKS family members, performed analytical SEC, peptide SPOT assay and phosphorylation assays, analyzed mass spectrometry data, prepared figures and wrote the manuscript

Publications not included in this thesis:

Gerth F., Jaepel M., Sticht J., Schmitt X. J., Benno Kuropka B., Driller J. H., Loll B., Wahl M. C., Pagel K., Haucke V., Freund C., "Exon inclusion enhances conformational plasticity and modulates autoinhibition in the SH3A domain of intersectin 1" Structure, *in revision*

1. Introduction

The human brain is the most complex part of the human body. It is the major component of the **central nervous system (CNS)** which allows control and fast communication through the body and can be found in all vertebrates. The CNS is primarily composed of two cell types: neurons and glial cells. Over 100 billion neurons or nerve cells can be found in the brain, their main function is to receive and transmit information (Bartheld et al., 2016). The communication between cells happens at specialized junctional structures called **synapses** (from the Greek *synapsis*, meaning conjunction). Two types of synapses can be found: chemical synapses and electrical synapses. At electrical synapses the pre- and postsynaptic cells are connected by gap junctions and are thereby able to pass an electric current from one cell to the other. The nerve cells within the CNS mainly communicate via chemical synapses, where an electrical signal (**action potential, AP**) is converted into a chemical signal to overcome the synaptic cleft between the cells. (Waites et al., 2005)

1.1. Chemical Synapse and the synaptic vesicle cycle

The presynapse of a chemical synapse (Figure 1) clusters **synaptic vesicles (SVs)** of roughly 40 nm size, that store 1500-2000 **neurotransmitter (NT)** molecules within their spherical membrane (Haucke et al., 2011). NTs can fulfil either excitatory (e.g. acetylcholine, glutamate) or inhibitory (e.g. GABA, Glycine) functions in signal transduction. SVs filled with NTs are stored in a recycling pool of vesicles, for NTs release these SVs have to undergo docking and priming at specialized sites called **active zones (AZs)** located in close proximity to the **voltage-gated Ca^{2+} channels (VGCCs)** (Couteaux and Pecot-Dechavassine, 1970). Primed SVs at the presynaptic plasma membrane build up a **readily-releasable pool (RRP)** of vesicles, a state where SVs can be released immediately (Haucke et al., 2011). The fusion of synaptic vesicles is mediated mainly by **SNARE proteins (soluble NSF attachment receptor proteins)** and **SM proteins (Sec1/Munc18-like proteins)** (Südhof, 2013). Upon the arrival of an action potential presynaptic plasma membranes depolarize which opens the VGCCs. The Ca^{2+} influx triggers the fusion of the primed SVs

with the presynaptic plasma membrane and thereby releasing the NTs into the synaptic cleft (exocytosis) (Figure 1). Binding of the NTs to specialized postsynaptic receptors triggers an ongoing signal cascade. The postsynaptic site, reacting to the signal, is organized by an electron-dense scaffold, the **postsynaptic density (PSD)**. This process of exocytosis has to occur in less than a millisecond. To ensure fast signal transduction tight coupling and close proximity of SV release site to VGCCs and the postsynaptic receptor fields is indispensable. (Südhof, 2013, Südhof, 2004). Since synaptic transmission requires a constantly filled pool of vesicles, SV endocytosis takes place in the periphery of the AZ (periaxial zone) to recycle SV membranes. After vesicle endocytosis, SVs are refilled with NTs and are clustered in the recycling pool.

At the large **neuromuscular junctions (NMJ)**, sites where neurons contact muscle fibers *via* chemical synapses, thousands of SVs, AZs and PSDs ensure that muscle contraction occurs precisely (Ackermann et al., 2015).

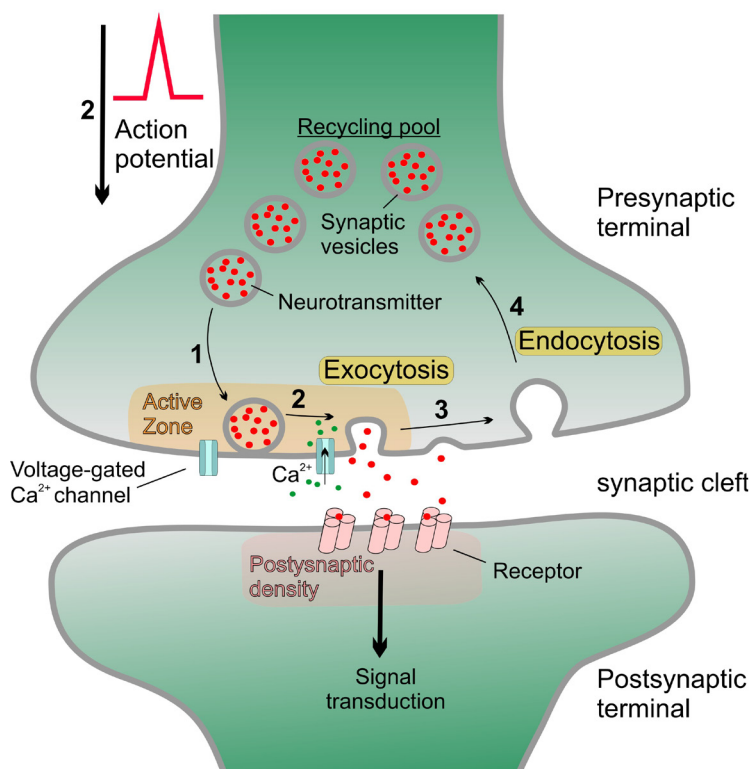


Figure 1 The Chemical Synapse

The protein scaffold at the active zone (AZ) is responsible for the docking and priming of synaptic vesicles (SVs) **(1)** from the recycling pool of SVs. This constitutes a readily releasable pool (RRP) of SVs bound to the presynaptic plasma membrane. AZ scaffolds localize next to voltage-gated Ca²⁺ channels (VGCCs) to ensure fast response on the influx of Ca²⁺-ions triggered by an arriving action potential (AP). Influx of Ca²⁺-ions triggers exocytosis by mediating the fusion of SVs with the presynaptic plasma membrane **(2)**. Subsequent release of the neurotransmitter into the synaptic cleft activates postsynaptic receptors within the postsynaptic density and propagates the signal further. After exocytosis the release site is cleared to dock and prime new SVs and to enable endocytosis in the periphery of the AZs **(3)**. After endocytosis SVs are filled with neurotransmitters and are clustered in the recycling pool of synaptic vesicles **(4)**.

After exocytosis the release site is cleared to dock and prime new SVs and to enable endocytosis in the periphery of the AZs **(3)**. After endocytosis SVs are filled with neurotransmitters and are clustered in the recycling pool of synaptic vesicles **(4)**.

1.2. Active zone morphology

AZs were first described in 1970 by Cousteaux and Pecot-Dechavassine as the presynaptic sites where SVs fuse with the plasma membrane (Cousteaux and Pecot-Dechavassine, 1970). Electron micrographs of AZs from different neurons and organisms revealed conserved localization, function and size, although their shape can differ immensely (Figure 2). At the NMJ of *Drosophila melanogaster* AZs have an elaborated electron-dense projection, called T-bar, tethering SVs to the release sites. In vertebrates AZs structures differ from a prominent structure called synaptic ribbon in sensory synapses to less complex structures in central synapses (Figure 2) (Ackermann et al., 2015). These electron-dense projections of a set of large multi-domain proteins are also referred to as the cytomatrix of the active zone (CAZ).

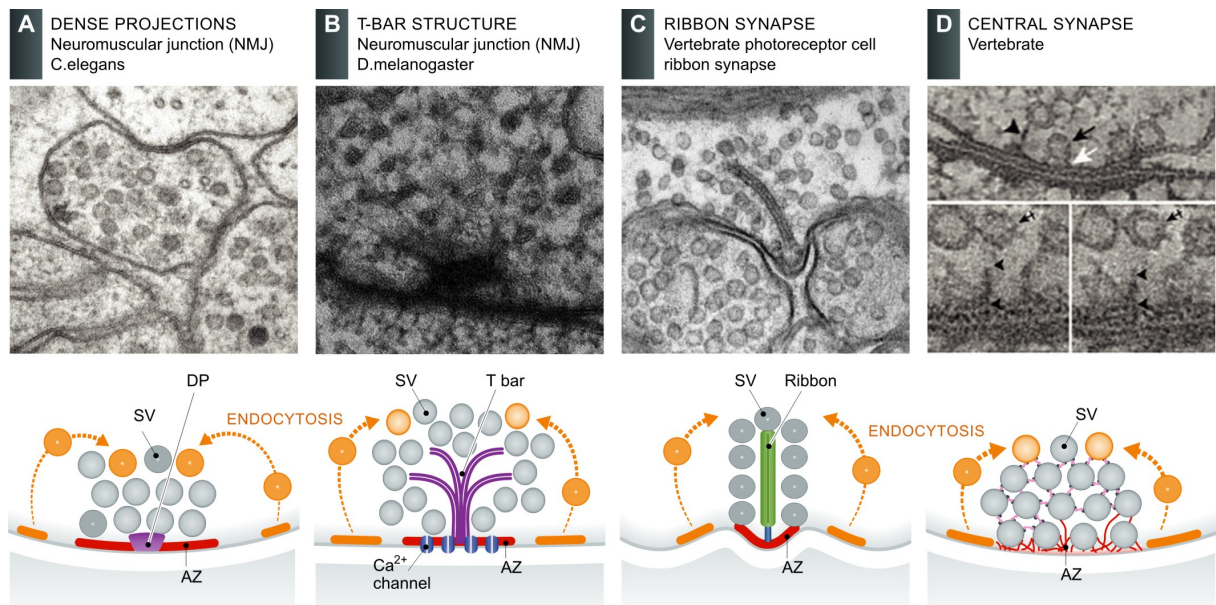


Figure 2 Morphology of active zones

The morphology of AZs can be divided into two distinct groups; those with elaborate electron-dense projections and those with less prominent dense projections, here shown by the electron micrographs and a corresponding schematic drawing. **(A)** The AZ scaffold from the *Caenorhabditis elegans* NMJ are quite simple, with small electron-dense projections on the surface of plasma membrane. **(B)** The AZ scaffold at the NMJ of *Drosophila melanogaster* has a more elaborated shape, called T-bar (from the side view of the electron micrographs). These ring-like structures are located on top of the Ca^{2+} -channels. **(C)** The AZ scaffold in vertebrate photoreceptor cell ribbon synapse is characterized by a specialized organelle, the synaptic ribbon, which tethers the SVs near the AZ. **(D)** AZ scaffold of vertebrate central synapses is less complex and exhibits fine filamentous projections that connect SVs up to 100 nm from the plasma membrane. Adapted and modified from (Ackermann et al., 2015)

1.3. The active zone scaffold

Although the shape of AZs in electron micrographs can differ immensely, their function in SV guidance to the release sites is retained. Over the years a conserved set of major AZ proteins has been identified, namely ELKS/Bruchpilot (BRP) family, Rab3-interacting molecule (RIM), RIM-binding protein (RIM-BP), (M)Unc13, Liprin- α , Syd-1 and the vertebrate specific proteins Piccolo and Bassoon (Figure 3) (Gundelfinger et al., 2015, Sudhof, 2012, Ackermann et al., 2015, Walter et al., 2018, Petzoldt and Sigrist, 2014).

An important factor for the AZ scaffold is redundancy. Single knockouts in mammals of the main scaffolding proteins RIM, RIM-BP and ELKS/BRP leads to impairments of the scaffold but only a combination of ELKS/BRP and RIM knockouts (Wang et al., 2016) or RIM and RIM-BP knockouts (Acuna et al., 2016) disrupts the AZ scaffold. The AZ scaffold in *Drosophila* is less complex than in vertebrates and the deletion of BRP (Wagh et al., 2006) or RIM-BP (Liu et al., 2011) already leads to a disruption of the characteristic T-bar.

In a process that is still not completely resolved the scaffold tethers vesicles by large scaffold proteins. Direct binding of SVs to the AZ scaffold is also mediated by Rab proteins, small GTPases on the surface of SVs, that work as organizers of intracellular membrane trafficking and membrane architecture (Kiral et al., 2018).

Finally, the fusion of SVs with the presynaptic plasma membrane is carried out by SNARE proteins, (M)Unc18, (M)Unc13 and the Ca²⁺ sensor Synaptotagmin (Figure 3). The SNARE complex assembles from Synaptobrevin/VAMP of the SVs and Syntaxin-1 and SNAP-25 of the presynaptic plasma membrane. (M)Unc18 binds to the SNARE *via* Syntaxin-1 and is an essential protein for NT release. (Burkhardt et al., 2008, Verhage et al., 2000). The SNARE complex forms a highly stable four helical bundle, that can generate a force onto the two membranes by forming a “trans”-SNARE complex. This force brings the SV membrane in close proximity to the presynaptic plasma membrane which destabilizes their hydrophobic bilayer and opens a fusion pore (Sudhof and Rizo, 2011, Jahn and Fasshauer, 2012).

The release sites are closely located next to the PSD only separated by the synaptic cleft to ensure fast binding of released NT to the postsynaptic receptors (Figure 3).

Presynaptic and postsynaptic scaffold assembly is regulated by the interaction of the two transmembrane proteins Neurexin-1 and Neuroligin-1 (Sudhof, 2008).

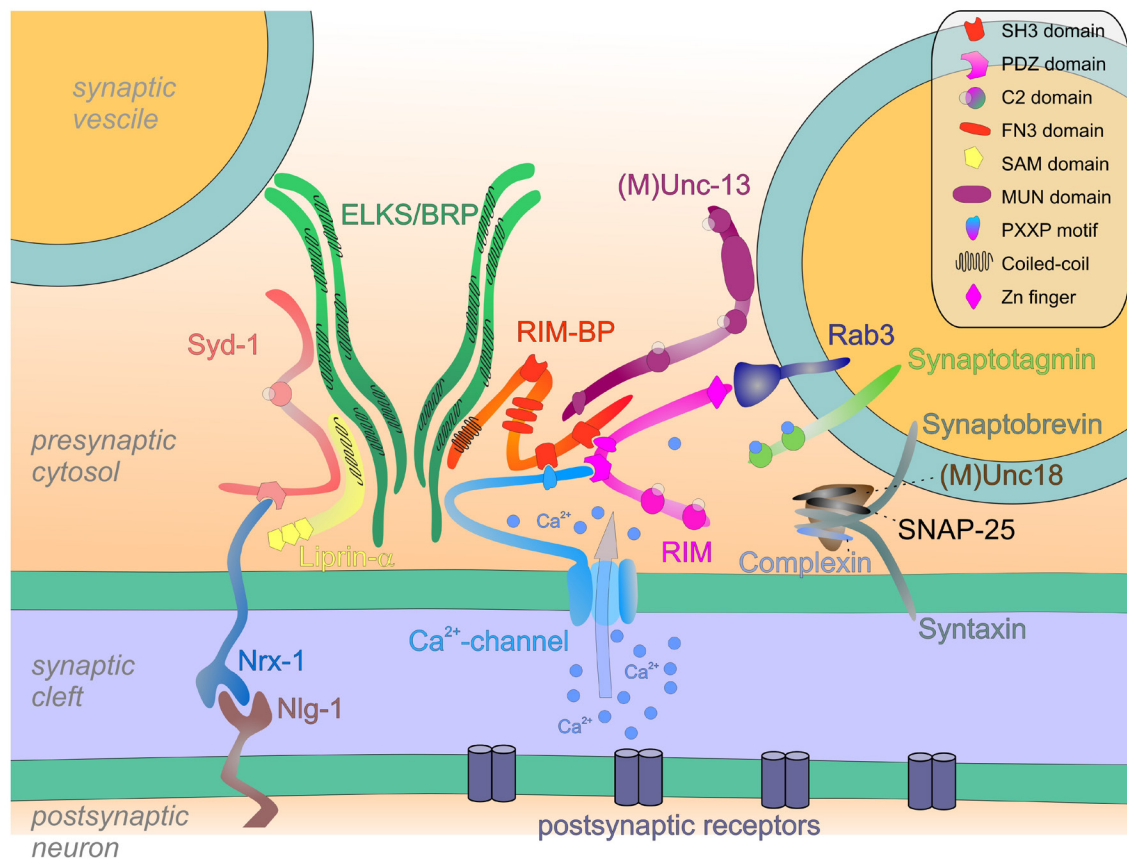


Figure 3 The synaptic active zone scaffold

The schematic drawing shows the major components of the *Drosophila* AZ scaffold, important domains/regions and their interactions are highlighted (see legend). Syd-1, Liprin-α are early assembly factors that coordinate localization of the AZ and the PSD *via* a Neurexin-1 (Nrx-1) and Neuroligin-1 (Nlg-1). The major scaffolding proteins ELKS/BRP, RIM and RIM-BP control the docking and priming of synaptic vesicles (SVs) and control the localization of Ca²⁺-channels to the SV release machinery. The influx of Ca²⁺-ions triggers the release of primed SVs *via* the complex of fusion proteins (Synaptotagmin, (M)Unc13, (M)Unc18, SNAP-25, complexin, syntaxin and synaptobrevin).

1.3.1. Bruchpilot and ELKS family

The name of the ELKS family originates from its major amino acid content (rich of glutamic acid **E**, leucine **L**, lysine **K** and serine **S**), other names like Rab6IP2 (Rab6 interacting protein 2), CAST (**C**ytomatrix at the active zone **A**ssociated **S**tructural protein) or ERC (**E**LKS/**R**ab6IP2/**C**AST), are used occasionally. The mammalian genome encodes for

two very similar ELKS proteins, ELKS1 and ELKS2, of roughly 1000 amino acid residues in length and several shorter transcript variants (Sudhof, 2012). Human ELKS shares approximately 99% protein sequence identity with the corresponding mouse and rat homologs (Wang et al., 2002). *Caenorhabditis elegans* only expresses one protein, highly homologous to the mammalian proteins. ELKS proteins lack a clear domain architecture, instead they contain long stretches of α -helical coiled-coil regions. Several interactions within the AZ scaffold have been addressed to ELKS proteins: RIM, Ca^{2+} -channels, (M)Unc13, Liprin α , Bassoon and Piccolo (Wang et al., 2002, Ohtsuka et al., 2002, Chen et al., 2011, Ko et al., 2003, Takao-Rikitsu et al., 2004, Kawabe et al., 2017). *Drosophila* expresses an ELKS fusion protein called Bruchpilot (BRP), consisting of a N-terminal ELKS related region and a C-terminal plectin related domain, exclusively present in insects. BRP is present with two major isoforms at the AZ, BRP-190 (isoform G, 206 kDa 1786 amino acid residues) and BRP-170 (isoform I; 160kDa, 1397 amino acid residues) (Matkovic et al., 2013), with the shorter BRP-170 isoform lacking the first 320 N-terminal residues of the longer BRP-190 isoform. In contrast to ELKS proteins in mammals (tom Dieck et al., 2012), BRP is an essential scaffold for AZ assembly. It clusters Ca^{2+} - channels and forms the characteristic T-bar structure of *Drosophila* AZs by its elongated structure (Kittel et al., 2006, Fouquet et al., 2009). When BRP lacks the very last 17 residues, vesicle tethering to the T-bar structure is nearly completely abolished (Hallermann et al., 2010). Interestingly, the whole C-terminus of BRP is not conserved and cannot be found in mammalian ELKS proteins. It may therefore fulfil tasks of the mammalian Piccolo and Bassoon, that have no direct homologs in *Drosophila* (Wagh et al., 2006).

1.3.2. RIM-binding protein

RIM-BP are conserved multi-domain scaffold proteins connecting several major AZ proteins *via* direct or indirect interactions (Kaeser, 2011). Mammals express three *rim-bp* genes, whereas there is only a single gene in *Drosophila*. They all contain three central fibronectin 3 (FN-III) domains and three Src-homology 3 (SH3) domains. One SH3 domain resides in front of the FN-III domains and two at the C-terminal region. Folded domains are intersected by non-conserved, mostly predicted unstructured regions. RIM-BP acts as an interaction hub within the AZ scaffold bringing several proteins in close proximity. The

SH3 domains can bind to different partners like RIM (Wang et al., 2000) and Ca²⁺-channels (Liu et al., 2011), all containing a typical PXXP binding motif. For the FN3 domains big potassium (BK) channels have been identified as binding partners in mammals recently (Sclip et al., 2018). For the intervening, unstructured regions in RIM-BP no binding partners have been identified so far. In *Drosophila* Rim-BP is essential for AZ scaffold integrity (Liu et al., 2011), whereas in the mammalian system a double mutant of RIM-BP and RIM is needed to interfere with the integrity of the scaffold (Acuna et al., 2016).

1.3.3. Rab3 interacting molecule (RIM)

Rab3 interacting molecule (RIM) proteins function as a central interaction hub within the AZ scaffold (Acuna et al., 2016). Mammals contain four genes, while *C. elegans* and *Drosophila* contain only one. It contains four folded domains for interactions with other proteins and a PXXP motif (X stands for any amino acid) for interaction with the SH3 domains of RIM-BP. The N-terminal zinc-finger interacts with (M)Unc13, important for vesicle priming by disrupting the (M)Unc13 homodimer (Lu et al., 2006, Deng et al., 2011). The Zn-finger is flanked by binding regions for Rab3 and Rab27 that are located on SVs. A central PDZ domain mediates binding to ELKS and importantly to Ca-channel, which is important for their recruitment to AZs (Kaeser et al., 2011). The function of the two C2 domains in the C-terminus of RIM stays elusive, although some interactions have been proposed (Coppola et al., 2001, Schoch et al., 2002, Kaeser, 2011).

1.3.4. (M)Unc13

(Mammalian) **Un**coordinated13 ((M)Unc13) proteins are essential for NT release and priming of SVs, furthermore they have several functions for the RRP of vesicles (Augustin et al., 1999, Varoqueaux et al., 2002, Basu et al., 2005, Walter et al., 2018). While mammals have five (M)Unc13 genes, the *Drosophila* genome only encodes for one. (M)Unc13s are large multi-domain proteins of around 200 kDa in mammals and over 300 kDa in *Drosophila*. (M)Unc13 shares a conserved C-terminal region in all isoforms and homologs, containing several folded domains; a Ca²⁺-phospholipid binding C2 domain (C2B), a MUN domain and a C-terminal non Ca²⁺ binding C2 domain (C2C). The N-terminal

region differs between the isoforms and homologs, giving rise to some large predicted unstructured regions but can also contain folded domains like a C2A domain, a Calmodulin (CaM) binding domain, and a phorbol ester/diacylglycerol binding C1 domain. (M)Unc13 is regulated by RIM which binds to the C2A domain with its zinc-finger domain to disrupt the C2A homodimer and thereby activating (M)Unc13s priming function *via* the MUN domain (Deng et al., 2011, Dulubova et al., 2005, Lu et al., 2006, Xu et al., 2017).

1.3.5. Syd-1 and Liprin α

Synapse-defective (Syd)1 and Liprin α are early scaffolding proteins, that were found to precede the later AZ proteins like BRP, RIM-BP and (M)Unc13A by hours (Fouquet et al., 2009). Liprin- α contains a long predicted coiled-coil region at the N-terminus and three sterile alpha motif (SAM) domains. The coiled-coil region forms homodimers (Taru and Jin, 2011) and binds to several other AZ proteins, like ELKS (Dai et al., 2006) or RIM (Schoch et al., 2002). The SAM domains bind Liprin- β , CASK and LAR-type receptor phosphotyrosine phosphatases (Serra-Pages et al., 1995, Olsen et al., 2005). Syd-1 in *Drosophila* contains three folded domains, a PDZ domain, a C2 domain and a Rho-GAP domain, separated by long predicted unstructured regions. In *drosophila* Syd-1 PDZ domain is important for Neurexin-1 binding and by this synchronizing AZ and PSD assembly (Li et al., 2007, Oswald et al., 2012). In mammalian only a distant ortholog of Syd-1, mSYD1A, has been identified yet, lacking the invertebrates typical PDZ domain. In mSYD1A an intrinsically disordered region was found to interact with several AZ proteins and by this stimulating presynaptic differentiation (Wentzel et al., 2013).

1.3.6. Ca²⁺ channels

VGCC are very important to the release machinery. Upon the arrival of an AP they open and increase cytoplasmic Ca²⁺-ion concentration which triggers NT release by SV exocytosis within 100 nm around the channel (Südhof, 2013, Eggermann et al., 2011). Of the three different subclasses only the second, P/Q-(Ca_v2.1), N-(Ca_v2.2) and R-(Ca_v2.3), have been found to localize at AZ sites (Südhof, 2013), the Ca_v2.1 channels are thereby found to be predominant Ca_v2 channel to mediate NT release. The *Drosophila* homolog of

this $\text{Ca}_v2.1$ channel is Cacophony. Ca^{2+} channels get recruited to the AZ sites by the RIM/RIM-BP complex, a core scaffold within the AZ and by this linking the Ca^{2+} channels to SVs and release machinery (Acuna et al., 2015, Acuna et al., 2016). RIM directly bind Ca^{2+} channels via their PDZ domain (Kaesler et al., 2011) as well as RIM-BPs bind them *via* their SH3 domains by conserved PXXP motifs (Hibino et al., 2002). Furthermore, the ELKS/BRP family also has been found to control $\text{Ca}_v2.1$ channel abundance at AZs in mammals (Dong et al., 2018) and *Drosophila* (Kittel et al., 2006). The identified binding sites of AZ proteins to Ca^{2+} channels all lay within its cytosolic, unstructured C-terminus. These redundant interactions thereby ensure proper localization of the VGCC, since Ca^{2+} influx, triggered by an AP, is indispensable for SV release.

1.3.7. Piccolo and Bassoon

Piccolo and Bassoon are huge elongated proteins, each over 400 kDa, containing multiple domains. They fulfil their main function in guiding SV from the backfield of the synapse to the AZ. These proteins are not essential for the AZ scaffold but loss of both proteins causes a disruption of vesicle clustering (Gundelfinger et al., 2015, Mukherjee et al., 2010). For transport Piccolo and Bassoon seem to undergo pre-assembly and get co-transported with ELKS on Piccolo-Bassoon-ELKS/CAST transport vesicles (PTVs) to the synaptic membranes (Maas et al., 2012). Piccolo and Bassoon have been long thought to be vertebrate specific proteins, however, distant related proteins in *Drosophila*, Bruchpilot (Wagh et al., 2006) and Fife, have been identified to similar functions (Bruckner et al., 2012, Bruckner et al., 2017).

1.3.8. Rab proteins

Rab proteins are small monomeric GTPases and belong to the larger class of the Ras superfamily. They are key organizers of intracellular membrane trafficking and membrane organization (Kiral et al 2018). Crucial for their precise regulation and organization are the interactions with their effector proteins. Known effectors range over coat proteins (COP or clathrins), motor proteins (kinesins dyneins), and tethering complexes (EEA1, Golgins) up to SNAREs (Grosshans et al., 2006). They function as molecular switches and cycle

Introduction

between a GTP-bound active state and a GDP-bound inactive state. Three Rab proteins have been identified in binding to AZ proteins so far: Rab3 as well as Rab27 bind to the RIM α -helices surrounding the zinc-finger domain (Fukuda, 2003) and Rab6 binds and recruits the mammalian ELKS proteins to Golgi membranes (Monier et al., 2002). Of these three Rabs only Rab3 has been shown to effect the AZ scaffold, by enabling long-term plasticity via its RIM interaction (Tsetsenis et al., 2011).

1.4. Transport of active zone proteins

Exact transport and integration of AZ components to specific sites is an important factor for scaffold assembly and synaptic plasticity. This is not only important for *de novo* assembly but also for turnover of AZ proteins and their adaptation. One key adaptive response of the synapse is structural plasticity, allowing synaptic sites to be added or remodeled in order to change their functional properties (Van Vactor and Sigrist, 2017).

In *C. elegans* AZ components and SVs undergo extensive co-transport through the axon (Wu et al., 2013). In mammals AZ components are co-transported through the axon by presumably “preformed complexes” on Golgi derived vesicles called **Piccolo-Bassoon Transport Vesicles (PTVs)** and **synaptic vesicle protein transport vesicles (STVs)** (Figure 4) (Zhai et al., 2001, Shapira et al., 2003, Bury and Sabo, 2016, Maas et al., 2012). ELKS/Cast requires Piccolo and Bassoon to leave the Golgi with PTVs while STVs can carry a diverse set of AZ proteins (Bury and Sabo, 2016). Other proteins like RIM associates with these vesicles in a post-Golgi compartment. (M)Unc13 leaves the Golgi on (M)Unc13 transport vesicles, but can be found on PTVs at distal axons suggesting also further maturation steps to form common AZ precursor vesicles (Shapira et al., 2003, Maas et al., 2012, Bury and Sabo, 2016). After the formation of transport vesicles, they have to tether to motor proteins to be transported along microtubules through the axon (Figure 4). Microtubules (MT) are oriented with their minus end towards the soma and the plus end towards the distal axon. The Kinesin superfamily transports packages towards the plus end (anterograde) while the Dynein superfamily towards the minus end (retrograde) (Hirokawa et al., 2010). The transport vesicles can attach to these motor proteins through linker proteins. PTVs are primarily linked to the KIF5B motor protein by syntabulin while other transport vesicles are bound *via* Syd-2/Liprin α to KIF1A/UNC-104 kinesin motor (Cai et al., 2007, Wagner et al., 2009). The underlying molecular mechanisms controlling associated transport as well as the signaling determining the stop and clustering of AZ proteins remains largely elusive (Torres and Inestrosa, 2018).

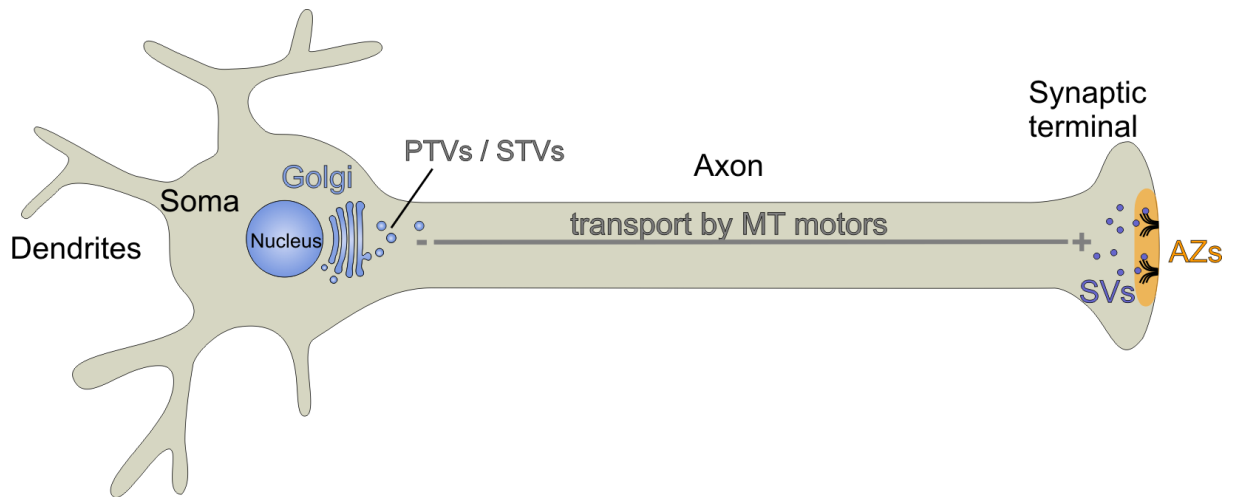


Figure 4 Axonal transport of AZ precursors

Presynaptic proteins are packaged into Golgi derived **Piccolo-Bassoon Transport Vesicles (PTVs)** or **synaptic vesicle protein transport vesicles (STVs)** to be transported along axonal microtubules (MT). Transport occurs via kinesin or dynein microtubule motors, that can be attached directly or indirectly via a linking protein to the PTVs or STVs. Since axonal MTs are oriented with their plus end towards the synaptic terminals, kinesin motors are suggested to transport newly synthesized protein from the soma. In a still enigmatic step these transported packages are integrated into maturing or newly forming AZ scaffolds.

One theoretical model proposed for the trapping of AZ proteins is the 'Q' assembly hypothesis, where proteins undergo a prion-like concentration-dependent conversion, mediated by domains rich of glutamine and asparagine. Thereby adopting a conformation that stimulates their own aggregation and aggregation of other proteins (Fernandez et al., 2010).

Premature aggregation of AZ proteins has been described for *Drosophila* as well as for *C. elegans*. In *C. elegans* the small protein Arl-8 promotes the axonal transport of synaptic cargo vesicles and prevents their accumulation (Klassen et al., 2010). In *Drosophila* two independent studies showed that the serine arginine protein kinase at cytological position 79D (SRPK79D) prevents axonal aggregation of BRP (Johnson et al., 2009, Nieratschker et al., 2009).

1.4.1. Serine arginine protein kinase at cytological position 79D (SRPK79D)

SRPKs belong to the family of serine-threonine kinases. They can recognize and phosphorylate specific serine residues within serine-arginine rich motifs, so called RS-domains (Gui et al., 1994). So far three members of SRPK (Gui et al., 1994); SRPK1, SRPK2 (Wang et al., 1998) and SRPK3 (Nakagawa et al., 2005), have been identified in mammals. At least one orthologue of this family has been identified in yeast, *C. elegans* and *Drosophila*. This kinase family is best studied in phosphorylation of SR proteins, containing RS-domains, which are involved in pre-mRNA splicing and other gene regulatory processes (Lin and Fu, 2007, Zhou and Fu, 2013).

Structurally, SRPKs comprise the canonical N- and C-terminal lobes of Ser/Thr protein kinases. In SRPKs these regions are intervened by an intrinsically disordered region of up to 200 residues (Ghosh and Adams, 2011). At the N-terminus a shorter region of predicted intrinsic disorder precedes the N-terminal lobe (Figure 5). While the N- and C-lobes are highly conserved, the disordered regions show no conservation and can differ immense between protein isoforms. SRPKs have been shown to engage their substrate *via* a docking groove at the C-lobe, while the active site of the kinase lays on the N-lobe (Ngo et al., 2005).

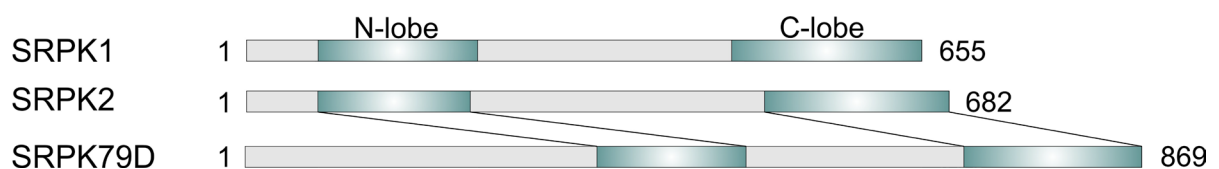


Figure 5 SRPK family

The SRPK family members share a highly conserved split kinase domain consisting of an N- and C-terminal lobe sharing 70-80% protein sequence identity. The lobes are separated by a non-conserved region of predicted intrinsic disorder of up to 200 residues. The SRPK79D harbors a significantly longer N-terminal region of predicted intrinsic disorder compared to its mammalian homologs.

SRPKs can employ different modes of operation depending on the nature of the substrate proteins; processive, semiprocessive and distributive. Lengthy SR can be efficiently phosphorylated by binding of the docking groove to the substrate and a

Introduction

subsequent funneling of the substrate, in a C- to N-terminal direction through the active site. Targets with shorter SR repeats are phosphorylated in a distributive mechanism, where docking groove binding can be dispensable. Substrates with shorter and longer SR repeats can be phosphorylated by a combination of both mechanisms, a semiprocessive mechanism (Lukasiewicz et al., 2007, Ghosh and Adams, 2011, Aubol et al., 2013).

SRPK79D is the only SRPK family member that has been identified in *Drosophila* so far. Two independent studies reported the axonal aggregation of BRP upon the loss of its kinase activity. A specific N-terminus of the SRPK79D-PC and -PF isoform is required for proper localization to the AZ (Johnson et al., 2009, Nieratschker et al., 2009).

2. Aims

The project of this thesis is embedded into the collaborative research center 958, dealing with the scaffolding of membranes. In a shared project with the Sigrist group an overall goal is to elucidate the architecture of the *Drosophila* AZ scaffold mainly organized by BRP and RIM-BP. We addressed this question by a combination of *in vivo* genetics with state of the art microscopy and the *in vitro* analyses of interactions and X-ray structures.

In my thesis, I aimed to:

- I. Uncover unknown protein-protein interactions within the scaffold by using a high throughput yeast-two hybrid approach and generate an interaction network.
- II. Characterize the functional regions of BRP and new interactions identified by the yeast-two hybrid approach.
- III. Biochemically and structurally characterize the RIM-BP domains.
- IV. Study the PDZ domain interaction of Spinophilin and Syd-1 with the Neurexin-1 C-terminus.

3. Results and Discussion

3.1. Interaction network of the *Drosophila* active zone scaffold

A major part of this thesis was spent on a large Yeast-Two-Hybrid (Y2H) screen in the lab of Ulrich Stelzl at the MPI for Molecular Genetics. This Y2H approach was part of a collaborative project shared between the Sigrist group and the Wahl group, parts of the experiments were conducted by Janine Lützkendorf and Eva Michael. By using Ulrich Stelzl's high throughput Y2H approach (Worseck et al., 2012) we intended to identify several **protein-protein interactions (PPIs)** within the *Drosophila* AZ scaffold. To gain knowledge not only of PPI but also on regions or specific domains contributing to the binding, proteins were dissected in overlapping constructs of known domains, functional regions or predicted structural regions.

I generated a first set of 96 constructs from 10 different major AZ proteins, each construct was cloned in two "bait" and two "prey" vectors and performed Y2H experiments (see 5). In a second round Janine Lützkendorf and Eva Michael (Sigrist group) generated another set of constructs from other AZ proteins and screened them against my initial matrix and their newly cloned proteins. Known interactions like the Neurexin-1 interaction with the PDZ domain of Spinophilin and the RIM-BP SH3 interaction with the RIM and the Cacophony PXXP motifs were used as positive controls in our experiments. In total 135 constructs of more than 35 AZ proteins were analyzed. The results of all screenings were analyzed to obtain a final PPI network of the tested proteins. In total 268520 mated yeasts were analyzed for growth on selective media, corresponding to 86310 different construct constellations.

The final list contained 893 putative PPI between the different constructs in our Y2H screen, covering 182 interactions between the full-length proteins (Figure 6). Because of the large number of screened constructs from each protein we were able to identify specific binding regions of less than 200 residues length. Many of these Y2H interactions correspond to hitherto unknown putative interactions, while others had been reported earlier.

Parts of these results were already validated by other methods and were incorporated in two publications (see 3.2.2, 3.5). The interaction network contains many more putative interactions that must be evaluated and validated in further studies.

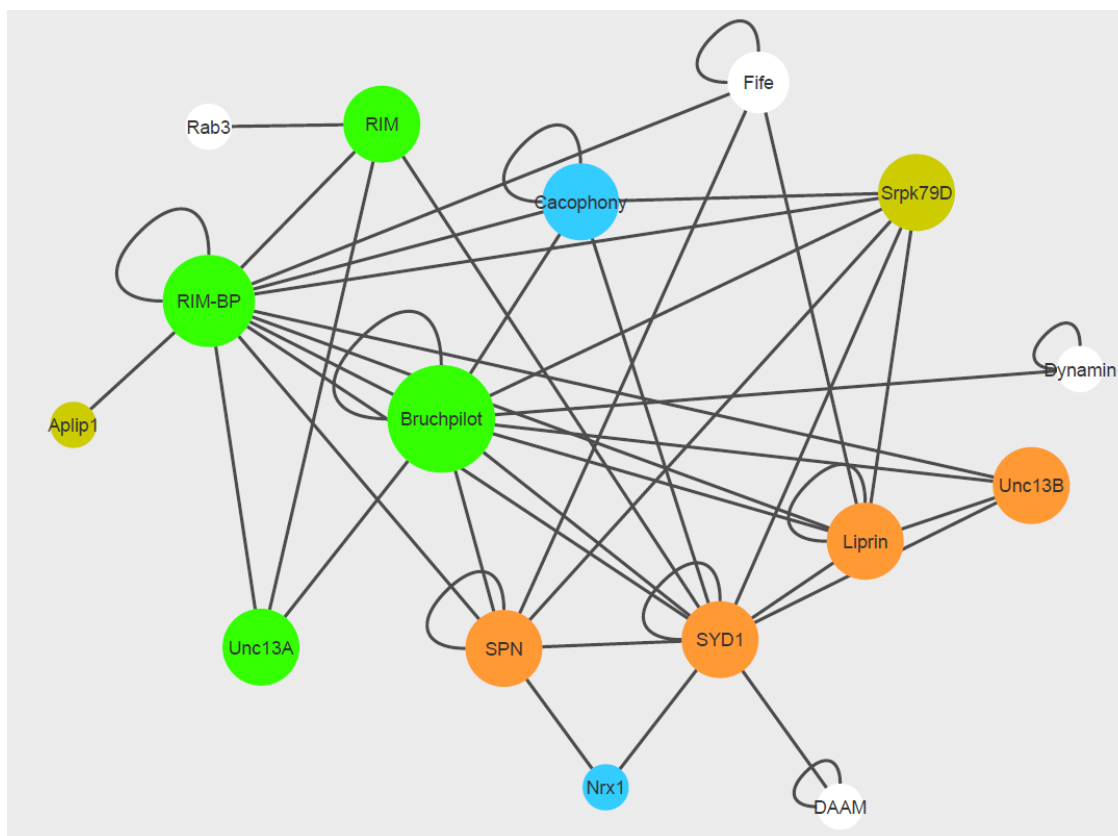


Figure 6 Y2H interaction network of the *Drosophila* active zone

The interaction network of the *Drosophila* AZ was generated based on the PPI identified in the Y2H approach. Interactions of the proteins can correspond to interactions of several constructs. Putative interactions are indicated connections, homodimerization by loops. Early scaffold proteins are shown in orange, the later scaffold proteins in green. Membrane proteins are shown in blue, known transport effectors in olive and other proteins in white. Graphical illustration of the interactions was generated by using Cytoscape (Shannon et al., 2003).

3.2. Bruchpilot

Bruchpilot (BRP) is the major AZ scaffold protein that shapes the electron dense T-bar structure in *Drosophila* synapses. While the N-terminus is located at the plasma membrane, next to the Ca²⁺-channels, the C-terminus expands nearly 70 nm (Fouquet et al., 2009) into the cytosol to tether synaptic vesicles (Hallermann et al., 2010). This extended shape is presumably formed by long stretches of coiled-coil regions (Figure 7). BRP is lacking known folded domains, but was divided by the Sigrist group into four overlapping regions of certain functions: D1 is responsible for anchoring of BRP at the membrane, D2 is probably involved in PPI and is needed for crucial BRP localization to the AZ scaffold, D3 is facilitating homodimerization of BRP and D4 is tethering synaptic vesicles to the scaffold (Fouquet et al., 2009) (unpublished Sigrist group data)

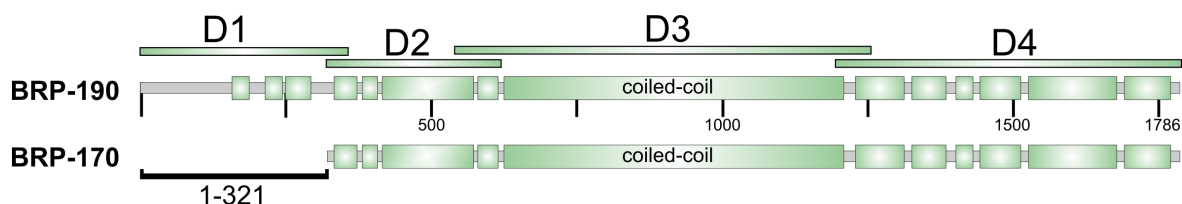


Figure 7 The Bruchpilot isoforms BRP-190 and BRP-170

Overview of the predicted BRP protein domain structure of the BRP-190 (isoform G) and the BRP-170 (isoform I) isoforms. Except for the N-terminus of the BRP-190 isoform, which is predicted to be intrinsically unstructured (grey), the BRP secondary structure is predicted to consist exclusively of α -helices that form continuous coiled-coil stretches (green) interrupted by short loop regions.

BRP-190 full length protein cannot be expressed in *E. coli*, but I achieved to express it in insect cells. Purification of the full length BRP-190 isoform was conducted using different affinity tags at the N-terminus and the C-terminus. Highest yields and purity were obtained by using a C-terminal Strep-tag, but most protein was lost during affinity chromatography as it did not properly bind to the column. The same was observed when using other affinity tags such as GST or poly-His. BRP-190 samples were prone to severe degradation, regardless of the use of protease inhibitors. Two prominent degradation bands were identified by mass spectrometry as a N-terminal fragment (75 kDa) and a C-terminal fragment (140 kDa) from the full length protein. BRP-190 samples did not bind to anion or cation exchange chromatography resin and did not elute as single peaks from

size exclusion chromatography (SEC), but rather eluted in a broad peak at the void volume, indicating strong aggregation. In collaboration with the Max-Planck Institute for Molecular Genetics we tested purified BRP-190 samples in electron microscopy negative stains, showing protein aggregation rather than elongated BRP-190 molecules. BRP co-expression in insect cells with major AZ proteins like RIM-BP, Syd-1, SRPK79D, Liprin- α did not improve the stability of BRP. Consequently, several shorter fragments of BRP were cloned and expressed. BRP fragments lacking the first 152 N-terminal residues were solubly expressed in *E. coli*, but also showed severe degradation and aggregation. The generated expression constructs of BRP in insect cells enabled Janine Lützkendorf (Sigrist group) to identify specific cysteine residues in the BRP N-terminus being posttranslational modified by palmitoylation. Analysis of cysteine to alanine mutations *in vivo* revealed an influence on Liprin- α binding to BRP and the reduction of BRP levels at AZs (Lützkendorf, 2018).

A major challenge in purifying BRP is probably the homodimerization/multimerization of its coiled-coil regions and the strong degradation during purification, resulting in very inhomogeneous/aggregated samples, observed during purification. The average number of BRP molecules at AZs is estimated to be approximately 140 (Ehmann et al., 2014). The mechanism by which BRP molecules homodimerize remains elusive. In our Y2H experiments we identified several regions involved in BRP-BRP interactions. Knowledge of this mechanism would allow the introduction of residue exchanges interfering with the homodimerization that could help in the generation of homogeneous samples.

3.2.1. Interaction network of Bruchpilot

Our Y2H approach of *Drosophila* AZ proteins revealed several interactions of BRP with other AZ proteins (Figure 8). Most of the interactions take place in the N-terminal D1 and D2 regions of BRP. Interactions for Syd-1 (Owald et al., 2010) and Cacophony (Fouquet et al., 2009) with BRP have been shown earlier, although we are now able to define a smaller minimal interacting region (Figure 8). Further *in vitro* validation failed due to the insolubility of C-terminal Cacophony constructs and severe degradation or low expression levels of Syd-1 constructs. The interaction for Liprin- α has been only shown for the

mammalian proteins so far (Ko et al., 2003). Putative new interactions of BRP were identified with RIM-BP, SRPK79D and Spinophilin (Spn) as well as homodimerization of a long coiled-coil region (D2-D4). Putative interactions with a rather low score were found for Unc13A, Unc13B, Fife and Dynamin. No interactions were found between BRP and RIM which has been described for the mammalian homologs (Wang et al., 2002).

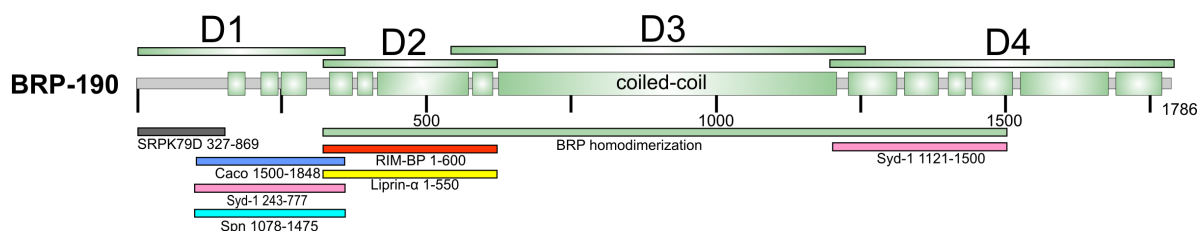


Figure 8 Domain architecture of BRP-190 isoform with mapped Y2H interactions

Schematic view of BRP-190 shown in green with its coiled-coil or functional regions (D1-D4) (Fouquet et al., 2009). Interaction regions with other AZ proteins, identified in our Y2H screen, are mapped BRP, showing only interactions that were identified with at least two different constructs.: SRPK (dark grey), Cacophony (blue), Syd-1 (pink) and Spinophilin (Spn) in the BRP D1 region; RIM-BP (red), Liprin- α (yellow) in D2 and another Syd-1 binding at the D4 region. BRP (green) homodimerization can be found between different constructs from D2 till D4.

All interactions of BRP lay within the predicted coiled-coil regions, except for the interaction with SRPK79D. Interestingly, the parts of the proteins that interact with BRP are also predicted to be mainly unstructured or contain coiled-coil regions. Coiled-coil regions are known to cause homo- or heterodimerization (Mason and Arndt, 2004) and would thereby provide an easy way to mediate several PPI with the AZ interaction network. The region in BRP to which the SRPK79D kinase domain (N- & C-lobe) is binding, has been mapped to the first 152 residues and will be discussed in a separate section (see 3.2.2). The found interaction of RIM-BP's N-terminus with BRP will be discussed in the RIM-BP section of this thesis (see 3.3.1).

3.2.2. BRP N-terminal phosphorylation by SRPK79D

This section refers to the following publication:

Driller, J. H., Lützkendorf, J., Depner, H., Siebert, M., Kuroopka, B., Weise, C., Petzoldt, A. G., Lehmann, M., Stelzl, U., Zahedi, R., Sickmann, A., Freund, C., Sigrist, S. J., Wahl, M. C. “Phosphorylation of the Bruchpilot N-terminus by SRPK79D controls axonal transport of active zone building blocks” *J. Cell Sci., in revision*

Previous studies suggest, that SRPK79D prevents the axonal aggregation of BRP during axonal transport (Johnson et al., 2009, Nieratschker et al., 2009). In our recent study on the transport effector Aplip1 the Sigrist group could show that these SRPK79D dependent aggregates not only contain BRP but also RIM-BP (Siebert et al., 2015). Our Y2H results on the BRP interaction with SRPK79D indicated for the first time a direct interaction between these two proteins. In order to study the underlying mechanisms of this phenotype observed in *Drosophila* axons we combined *in vitro* methods with *in vivo* studies.

We verified the Y2H interaction of BRP-190¹⁻¹⁵² with SRPK79D^{core} (SRPK79³²⁷⁻⁸⁶⁹) *in vitro* with purified proteins in analytical SEC (Figure 9A). To test whether this interaction resides within the docking groove of SRPK79D, we mutated four conserved residues (SRPK79D^{CoreΔDock}) which have been described to disrupt the substrate binding at the C-lobe docking groove in SRPKs (Lukasiewicz et al., 2007). Indeed, the interaction of SRPK79D and BRP was abolished by these mutations (Figure 9B). To identify binding sites of SRPK79D in the BRP-190¹⁻¹⁵² construct, a peptide SPOT array was conducted. Specifically, three arginine rich motifs appeared to be the potential binding site. These motifs fit well to a proposed binding sequence (RXX(X)RXX(X)R, three basic residues separated by two to three residues) by the Ghosh lab (Lukasiewicz et al., 2007). We identified the BRP-190 N-terminus as a substrate of SRPK79D by using a radioactive phosphorylation assay. BRP¹⁻¹⁵² as well as BRP-190 were phosphorylated, while BRP-190^{Δ1-152} was not phosphorylated (Figure 9C). The docking groove mutant showed a similar activity as the SRPK79D^{core} construct in this phosphorylation assay. Phosphorylation of BRP abolished the interaction with SRPK79D^{core} in analytical SEC. This phosphorylation dependent interaction is probably due to electric repulsion of the acidic docking groove with the attached phosphates (Ghosh and Adams, 2011).

correlated well with the phosphorylation sites identified in immunoprecipitated BRP from *in vivo* samples (Figure 10).

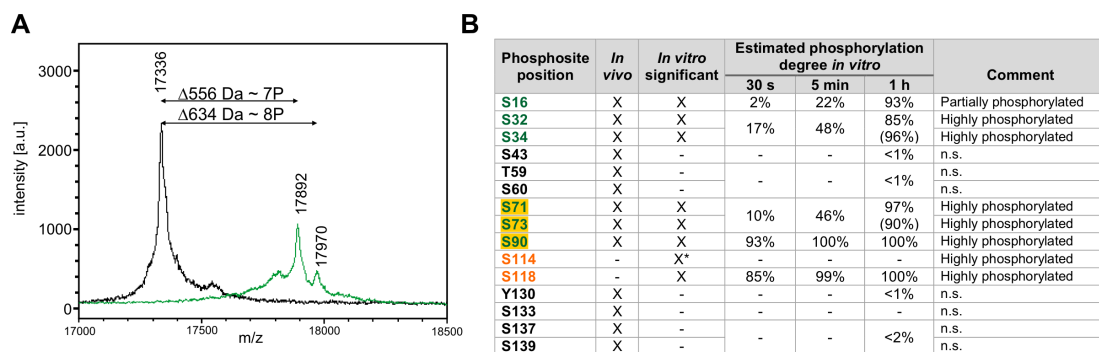


Figure 10 Identification of phosphorylation sites in BRP

(A) MALDI-TOF analysis of untreated BRP-190¹⁻¹⁵² (black) and BRP-190¹⁻¹⁵² phosphorylated by SRPK79D^{Core} (green) indicates 7-8 phosphorylation sites. BRP-190¹⁻¹⁵² $M_{\text{theoretical}} = 17340$ Da. **(B)** *In vitro* and *in vivo* phosphorylation sites within the BRP-190 N-terminus identified by mass spectrometric analysis. Phosphorylation sites on yellow background were found to pheno-copy *srpk79D* mutants *in vivo*. The degree of phosphorylation was estimated from comparing MS peak intensities of unphosphorylated and phosphorylated peptides, in brackets indicated the estimation for the double phosphorylated peptide. Phosphorylation sites with an estimated degree of less than 5% where considered as not significant (n.s.) *in vitro*.

Protein sequence analysis of the mammalian BRP homolog Cast revealed strict conservation of the BRP-190 serine sites S71, S73 and S90 while the other sites are only partially conserved. By generating a triple, non phosphorylatable serine to alanine mutation, the Sigrist group was able to show that this variant results in a phenotype similar to the described SRPK79D mutant phenotype (Figure 11). Characterization of these axonal aggregates by confocal microscopy, stimulated emission depletion light microscopy (STED) and electron microscopy (EM) identified the same morphology and protein content (BRP and RIM-BP) of these aggregates. Furthermore, the Sigrist group identified Unc13A as another protein within these aggregates, suggesting axonal co-transport of BRP/RIM-BP/Unc13A as a central building for integration in mature AZ scaffolds.

In order to prove that the phosphorylation-binding relationship between members of the ELKS family and SRPK family follows a conserved mechanism, binding and phosphorylation of mammalian homologs Cast1 and Cast2 by the SRPK79D homologs

SRPK1 and SRPK2 was tested *in vitro*. Indeed, Cast1 and Cast2 are phosphorylated by SRPK1 and SRPK2.

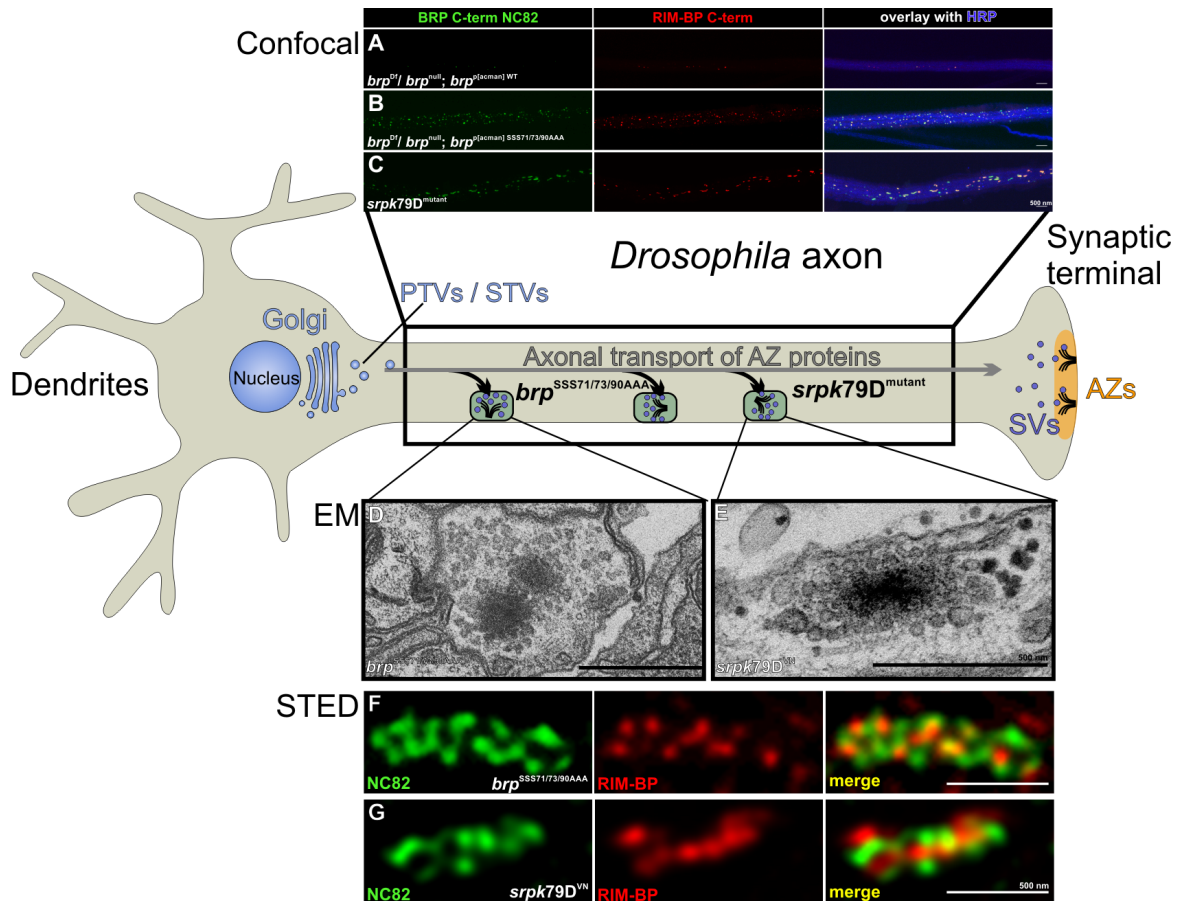


Figure 11 Characterization of the axonal aggregates

Immunofluorescence images of the indicated genotypes. **(A)** The control (*brp^{rescue}*) shows only few, isolated and small BRP and RIM-BP spots per individual axon area, compared to BRP and RIM-BP of a *brp^{SSS71/73/90AAA}* phospho-destructive mutant **(B)** and *srpk79D^{VN}* mutant **(C)** and in a *brp^{null}* mutant (*brp^{Δ6.1}/brp^{Df(2R)69}*) background. **(D, E)** Electron micrographs showing a large, electron-dense, ectopic super-assembly of AZ structures in axons of *srpk79D* mutants **(D)** and *brp^{SSS71/73/90AAA}* mutants **(E)**. Scale bars – 500 nm. **(F, G)** Immunofluorescence images of nerve bundles of the indicated genotypes with the indicated antibodies, of the *brp^{SSS71/73/90AAA}* phosphorylation mutant **(F)** and the *srpk79D^{VN}* mutant **(G)** in a *brp^{null}* mutant (*brp^{Δ6.1}/brp^{Df(2R)69}*) background. Confocal, STED as well as electron microscopy (EM) data were obtained by the Sigrist group.

3.2.3. Central dimerization domain in Bruchpilot

BRP is the major scaffold protein of the *Drosophila* T-bar structure and is important for the tethering of SVs to the CAZ. Since no domains have been identified in BRP so far, we used the bioinformatics tools of the Swiss institute for bioinformatics (Pagni et al., 2004) to look for protein or domain patterns, motifs or functional sites within BRP that could be relevant within the AZ scaffold. Within the PROSITE database (Sigrist et al., 2010) the search revealed a pattern for a BAR domain profile with a low probability within the D3 region of BRP (799-1123 amino acid residues, Figure 8). BAR domains are comprised of dimeric α -helical coiled-coils, binding negatively charged phospholipids to induce or stabilize membrane curvature (Daumke et al., 2014).

BRP constructs comprising the putative BAR domain (BRP⁷⁹⁰⁻¹¹²⁹, BRP⁸⁰³⁻¹¹¹⁶) form dimers in solution (Figure 12A), as shown by multiangle light scattering (MALS) and tend to build up oligomers at higher protein concentrations. In an initial crystallization attempt, BRP⁷⁹⁰⁻¹¹²⁹ was concentrated to 15 mg/ml and screened against various conditions by using the sitting drop vapor diffusion method. Needle-bundle crystals were obtained in a condition containing 0.2 M calciumacetate, 0.1 M imidazole and 10 % PEG8000 (w/v) (Figure 12B) but did not diffract. Construct optimization by limited proteolysis followed by N-terminal sequencing and reductive methylation of lysine residues did not improve crystal quality. Different cryo-protectants as well as dehydration of the crystals in the drop were tested but did not result in diffracting crystals. The Sigrist group tested the putative BAR domain in membrane binding/ curvature assays but could not observe any effect on membrane architecture. Therefore, it is not entirely clear whether this coiled-coil region really comprises a BAR domain or whether it only contains a dimerization motif similar to those in BAR domains. Furthermore, our Y2H results indicate homodimerization of BRP over a long stretch of its sequence (Figure 8) indicating multiple coiled-coil dimerization regions within its elongated structure. The purpose of multi dimerization regions in BRP might be an increase in redundancy to dimerize.

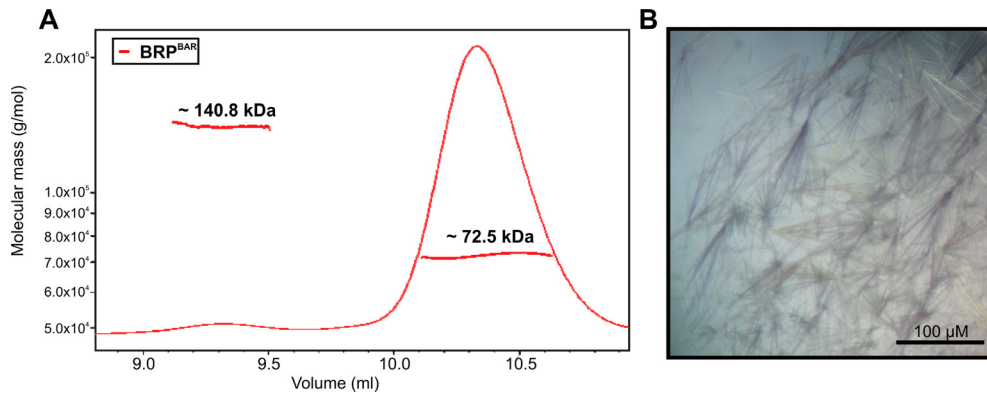


Figure 12 Central dimerization region in Bruchpilot

(A) Multi angle light scattering (MALS) of the putative BAR domain in BRP showing a clear dimeric state (72,5 kDa), with a small fraction generating a dimer of a dimer (140.8 kDa). **(B)** Crystals of the putative BAR domain.

3.2.4. Bruchpilot tethers synaptic vesicles at the C-terminus

This section refers to the following publication:

Lardong, J. A., J. H. Driller, H. Depner, C. Weise, A. Petzoldt, M. C. Wahl, S. J. Sigrist and B. Loll (2015). "Structures of *Drosophila melanogaster* Rab2 and Rab3 bound to GMPPNP" *Acta Crystallogr F Struct Biol Commun* 71(Pt 1): 34-40.

Results in this part were obtained by Jennifer Lardong during her master thesis under my supervision.

The very last 17 residues of BRP are important for the tethering of SVs to the CAZ (Hallermann et al., 2010). The underlying mechanism of this SV tethering by BRP still remains unclear. Microscopy data suggested Rab proteins, especially Rab6 and Rab8, as a linker between SVs and the scaffold protein BRP (unpublished Sigrist group data).

The proteins Rab2, Rab3, Rab6 and Rab8 were tested for binding to the last 50 or 200 amino acid residues of BRP. They were tested either in their inactivated state, GDP bound, or their activated state, GTP bound. Moreover, a constitutive active mutant (Der et al., 1986, Prive et al., 1992) was generated by mutating a conserved glutamine in the switch II region to leucine. No binding was observed between Rabs and the BRP C-terminus *in vitro*. These results are also in accordance to our Y2H results that were performed later on. The published Rab3 RIM interaction was used as a positive control, while the only

other putative interactions were identified between Rab3 and Liprin- α and Rab8 and Fife, but with a much weaker score than the Rab3 RIM interaction. BRP was not among the found Rab interactions, although it was part of the screen with several construct, nor did BRP show any PPI at its very C-terminus.

In addition we solved the crystal structures of Rab2 and Rab3 in their constitutive active form at 2.1 Å and 1.5 Å, respectively (Figure 13).

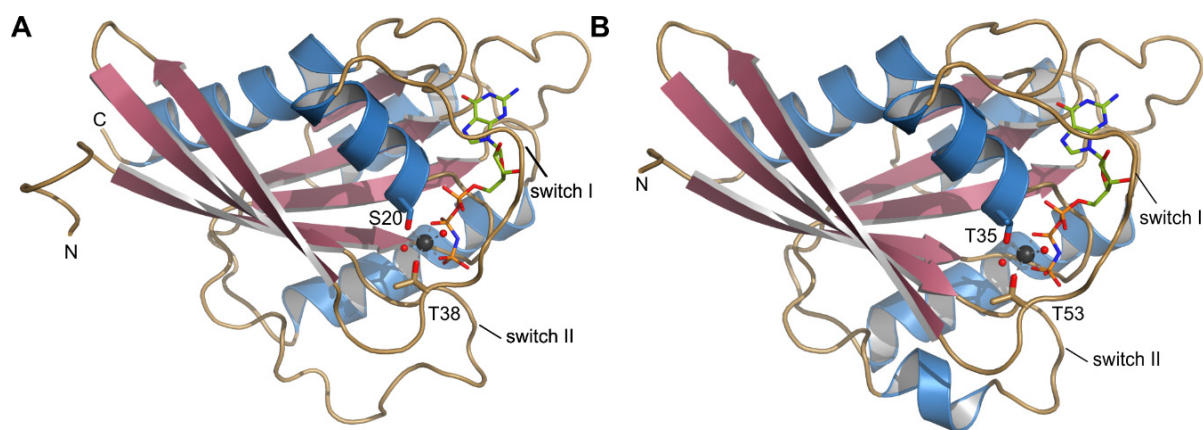


Figure 13 Structure of Rab2 and Rab3

Structures of dmRab2Q65L (**A**) and dmRab3Q80L (**B**) drawn in cartoon representation. α -Helices are colored blue, β -strands salmon and connecting loop regions brown. The bound GMPPNP is shown in stick representation, as are the Mg^{2+} -coordinating residues. The octahedrally coordinated Mg^{2+} is depicted as a black sphere and coordinating water molecules as red spheres. Grey dashed lines indicate the coordination sphere of Mg^{2+} .

3.3. RIM-binding protein

The large multi-domain protein RIM-BP is one of the major scaffolding proteins in the CAZ. It binds directly or indirectly to nearly all other AZ proteins and Ca²⁺-channels. Its function within the AZ scaffold is largely redundant to RIM (Acuna et al., 2016) which it also binds via its SH3 domains. In contrast to mammals (Acuna et al., 2016), RIM-BP proteins in *Drosophila* are necessary for the structural integrity of the AZ scaffold (Liu et al., 2011).

In *Drosophila* RIM-BP is a protein of nearly 2000 amino acid residues that is predicted to contain large intrinsically unstructured regions at the N- and C-terminus and in the linking regions of the conserved SH3 and FNIII domains (Figure 14). We are able to express this large protein in insect cells. In our attempts to purify this protein we observed strong degradation of this protein during purification. In order to study RIM-BP interactions and RIM-BP domains *in vitro*, the protein was dissected into its known stable domains.

3.3.1. Interaction network of RIM-binding protein

This section refers to a manuscript that is currently in preparation with me as a shared first author.

Our Y2H approach contained in total 30 constructs of this large multi-domain protein, covering its known domains and its predicted unstructured regions in overlapping constructs of different size. Our Y2H results validate published interactions with the Ca²⁺-channel (Cacophony) (Liu et al., 2011) and RIM (Wang et al., 2000) by the SH3-II and SH3-III at the C-terminus of RIM-BP.

We also observed a strong interaction of SH3II and SH3III to APP-like protein interacting protein 1 (Aplip1), a transport adaptor for the RIM-BP and BRP co-transport, identified by our collaborators at the Sigrist lab earlier. The interactions of the SH3-II and SH3-III to Aplip1, RIM and Cacophony were further characterized biochemically and structurally (see 3.3.3) (Siebert et al., 2015). Our screen revealed new interactions of the SH3 domains to Unc13A (see 3.5) (Bohme et al., 2016) and Fife (Figure 14).

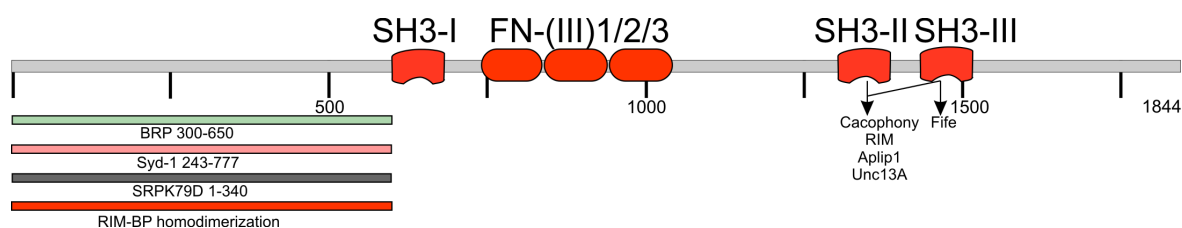


Figure 14 Domain architecture of RIM-BP with mapped Y2H interactions

RIM-BP is a multi-domain protein of over 200 kDa in size. RIM-BP exhibits six folded domains (red), three SH3 domains and an array of three FN-(III) domains, while the rest of the protein is predicted to be mainly unstructured (grey). The long N-terminus region interacts with BRP (green), Syd-1 (pink) and SRPK79D (dark grey). No interactions were identified for SH3-I and the FN-(III) domains. While both SH3-II/III interact with PXXP motifs in Cacophony, RIM, Aplip1 and Unc13A, only SH3-III shows binding to Fife.

Very interesting, putative PPI were also mapped to of RIM-BP predicted disordered regions: BRP (minimal construct BRP³⁰⁰⁻⁶⁵⁰), Syd-1 (minimal construct Syd-1²⁴³⁻⁷⁷⁷) and SRPK79D (SRPK79D¹⁻³⁴⁰) showed binding to a construct comprising the first 600 amino acid residues of RIM-BP. The same RIM-BP construct seemed to homodimerize in our Y2H approach. Binding of RIM-BP to BRP would fit well in the picture of the overall AZ scaffold organization since these proteins co-localize at the scaffold and are transported together (Figure 14). The Y2H interaction of the SRPK79D N-terminus to RIM-BP might explain the localization to the BRP/ RIM-BP transport vesicles, since the SRPK79D N-terminus has already been shown to influence its localization (Johnson et al., 2009).

3.3.2. N-terminal domain of RIM-binding protein

This section refers to a manuscript that is currently in preparation with me as a shared first author.

The N-terminus of *Drosophila* RIM-BP preceding the first SH3 domain (Figure 14) contains nearly 600 amino acid residues, while in mammalian RIM-BP this N-terminal part differs immensely between different isoforms. Bioinformatic analysis of the amino acid sequence identified a hitherto uncharacterized domain at the N-terminus of RIM-BP. Longer isoforms of the mammalian RIM-BP also contain a predicted α -helical region. The predicted domain comprises the very N-terminus to residue 254 (NTD) and is predicted to

be α -helical. Circular dichroisms (CD) spectroscopy identified a predominant α -helical content of the NTD (Figure 15). The defined melting point of 50 °C indicates that the NTD constructs adopt a stable fold. After heating the NTD to 95 °C, a CD spectrum was measured again to determine the NTD's secondary structure composition. The recorded CD spectrum is indistinguishable to the first one, indicating that folding and refolding are reversible.

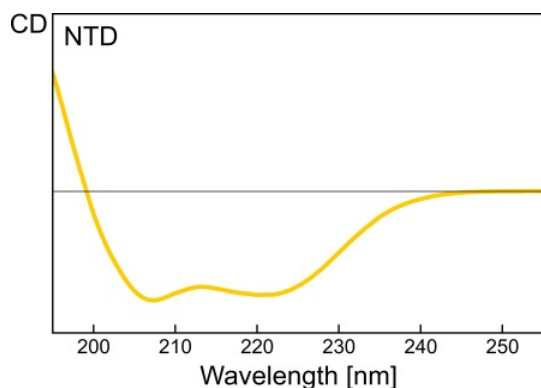


Figure 15 Circular Dichroisms spectroscopy of the RIM-BP NTD

The circular Dichroisms (CD) spectrum of the N-terminal domain (NTD) of RIM-BP shows a clear α -helical content.

Analysis of the amino acid sequence reveals several ER/K motifs within the NTD, especially in the first 150 amino acids. ER/K motifs can stabilize single α -helices (Swanson and Sivaramakrishnan, 2014), these stabilized α -helices can help to mediate interactions (Ulrich et al., 2016). So far Y2H interactions with the RIM-BP N-terminus were not validated by other methods, since RIM-BP¹⁻⁶⁰⁰ from insect cells shows severe degradation during purification. The Sigrist group analyzed N-terminal deletions of RIM-BP in their fly models. While the deletion of the first 250 amino acids showed no severe phenotype, a construct lacking the amino acids 151-600 (RIM-BP ^{Δ 150-600}) showed a strong effect on the recruitment of SVs, which has been also shown for the BRP C-terminus (Hallermann et al., 2010). In STED microscopy, RIM-BP N-terminus co-localize with the vertical structure of BRP and the overall scaffold appeared atypical in RIM-BP ^{Δ 150-600} mutants. Recent mass spectrometry cross-linking data from the Sigrist group verified the interaction of BRP and RIM-BP within the identified NTD region of RIM-BP.

3.3.3. SH3 domains of RIM-binding protein

This section refers to the following publication:

Siebert, M., M. A. Bohme, J. H. Driller, H. Babikir, M. M. Mampell, U. Rey, N. Ramesh, T. Matkovic, N. Holton, S. Reddy-Alla, F. Gottfert, D. Kamin, C. Quentin, S. Klinedinst, T. F. Andlauer, S. W. Hell, C. A. Collins, M. C. Wahl, B. Loll and S. J. Sigrist (2015). "A high affinity RIM-binding protein/Aplip1 interaction prevents the formation of ectopic axonal active zones" *Elife* 4.

SH3 domains are common PPI domains that can bind to PXXP motifs (X stands for any amino acid) in different orientations within their hydrophobic binding pocket (Lim et al., 1994). Interestingly all published interactions for the SH3 domains of *Drosophila* RIM-BP were confirmed for SH3-II and SH3-III. Our Y2H approach revealed similar results, while we identified several binding partners for SH3-II and SH3-III, no interaction was observed for SH3-I. While SH3-II and SH3-III share around 50% protein sequence identity, SH3-I shows only 32% and 37% protein sequence identity to SH3-II and SH3-III. A sequence alignment reveals an insertion of five amino acids at the SH3-I domain compared to SH3-II and SH3-III (Figure 16).

Our collaborators at the Sigrist group identified a new interaction for SH3II and SH3III by an earlier Y2H approach; Aplip1. The transport adaptor protein Aplip1 is a known linker of motor proteins to SV during axonal transport (Koushika, 2008). *In vivo* interference with the interaction showed protein aggregation of RIM-BP and BRP during axonal transport; a similar phenotype as already described for the SRPK79D mutant or our BRP^{SSS71/73/90AAA} phosphorylation defective mutant (see 3.2.2) (Johnson et al., 2009, Nieratschker et al., 2009). While Aplip1 interaction is necessary for axonal transport, interactions of the SH3 domains with RIM and Cacophony (Ca²⁺-channel) are dispensable for AZ integration of RIM-BP. Since only the SH3/ Aplip1 interaction seems to be necessary *in vivo*, the question arose if there are measurable differences between these interactions.

To compare the thermodynamics of the binding event between the SH3 domain and its known synaptic ligands, isothermal titration calorimetry (ITC) measurements were performed. Constructs of SH3-I, SH3-II, SH3-III and SH3-II+III were tested against peptides deriving from RIM, Cacophony and Aplip1 (Figure 16A). The binding of the SH3-II and

SH3-III domains to Aplip1 were several folds stronger compared to the peptides derived from Cacophony or RIM. The SH3-II+III binding of Aplip1 showed a co-operative binding with nanomolar affinity, while this was not seen for the other peptides (Figure 16 A).

X-ray structures of SH3-II bound to the Aplip1 and the Cacophony (Figure 16B, C) derived peptides as well as the structure of SH3-III bound to the Cacophony (Figure 16D) derived peptide, revealed the important residues involved in peptide binding. All three structures show mainly hydrophobic interactions between the peptide and the hydrophobic SH3 binding pocket. Interestingly, nearly all the residues involved in the formation of hydrogen bonds to the peptides are conserved between SH3-II and SH3-III, while SH3-I shows nearly no sequence conservation at these positions (Figure 16E). This might indicate why SH3-I does not bind to the same PXXP motifs as the second or third SH3 domains of RIM-BP. Its function within RIM-BP still needs to be further investigated.

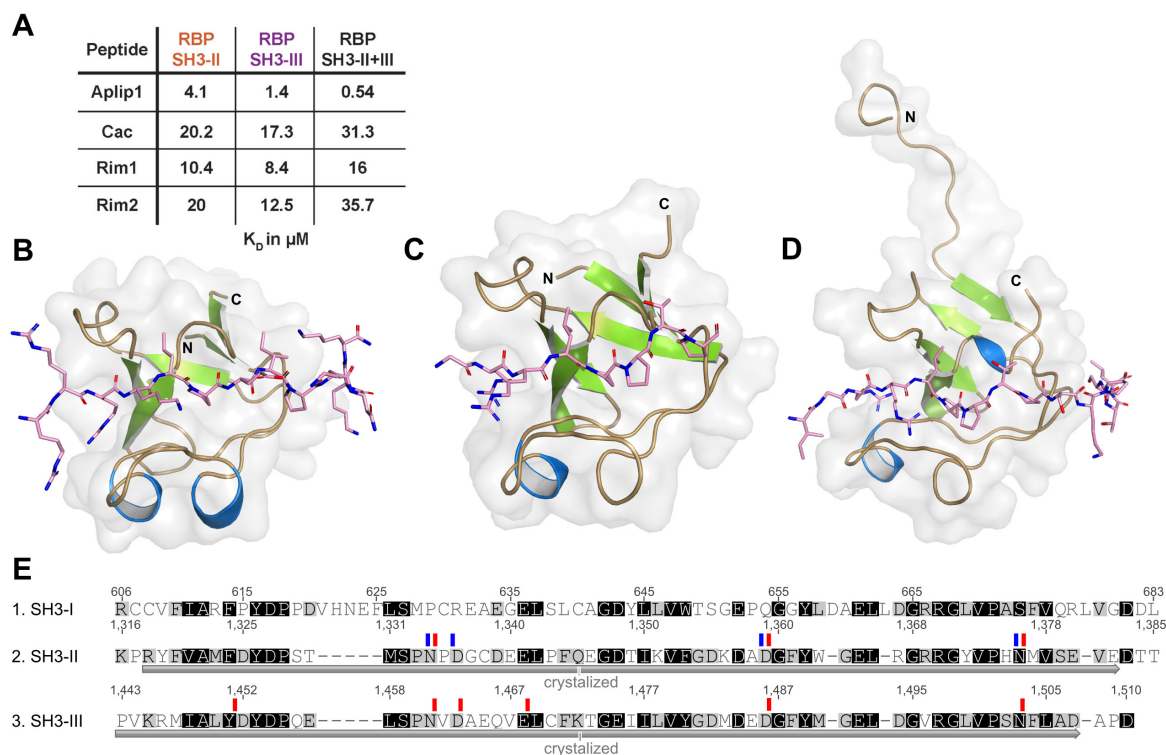


Figure 16 Characterization of SH3-II and SH3-III binding to Aplip1, Cacophony and RIM

(A) In ITC measurements Aplip1 shows the strongest interaction with SH3-II and SH3-III of RIM-BP compared to Cacophony (Cac) and RIM peptides. The strongest affinity (lowest KD) was identified between Aplip1 and the RBP SH3-II+III domain. **(B-D)** Crystal structures of SH3-II bound to an Aplip1 **(B)** and a Cacophony **(C)** derived peptide and SH3-III bound to a Cacophony **(D)** derived peptide. SH3 domains are shown in gray surface representation with the respective protein in cartoon representation. The bound peptides are drawn in stick representation **(E)** Protein sequence alignment of the RIM-BP SH3 domains. SH3-II and SH3-III share the highest identity (52%) while SH3-I only shares 32-37% sequence identity. SH3 residue sidechains involved in hydrogen bonds (≤ 3.3 Å) with the peptides are marked with rectangles, Aplip1 in blue and Cacophony in red.

3.3.4. The three central FN-III domains of RIM-BP

This section refers to a manuscript that is currently in preparation with me as a shared first author.

The central part of RIM-BP comprises an array of three FN-III domains. FN-III domains are found in many different proteins, including proteins of the extracellular matrix, cell surface receptors (Schwarzbauer and DeSimone, 2011), muscle proteins (Meyer and Wright, 2013) and enzymes (Pena et al., 2009). FN-III domains can serve as PPI elements, as seen for the ninth and tenth FN-III domain in human fibronectin (Leahy et al., 1996). Recently, the three FN-III domains in RIM-BP have been implicated in binding of the RCK domains at the C-terminus of BK-channels (Sclip et al., 2018).

The crystal structure of the three FN-III domains of RIM-BP was solved at 2.45 Å resolution by multiple anomalous diffraction using selenomethionine-labeled protein. The asymmetric unit contains two polypeptide chains, in which residues 745-838, 843-945 and 946-1042 form the three FN-III domains (Figure 17A). In both copies of the protein FN-III(1) and FN-III(2) interact mainly via a short β -sheet formed by the β -strand G of FN-III(1) and the BC loop of FN-III(2) (Figure 17B). In contrast, FN-III(3) is more loosely appended to FN-III(2). In molecule 'B' the FN-III(3) interacts with its BC loop to the linker regions of FN-III(2) and FN-III(3) via hydrogen bonds of R974 to the amide group of T944 and a main chain/ main chain interaction of T978 and G946 (Figure 17C). In molecule 'A' the BC loop lacks electron density, indicating a flexible conformation. C854 of the FN-III(2) AB loop seems to stabilize the linker region in the first molecule by a hydrogen bond to the amide group of T944, while in molecule 'A' it adopts a different conformation and is not involved in hydrogen bonding the linker region.

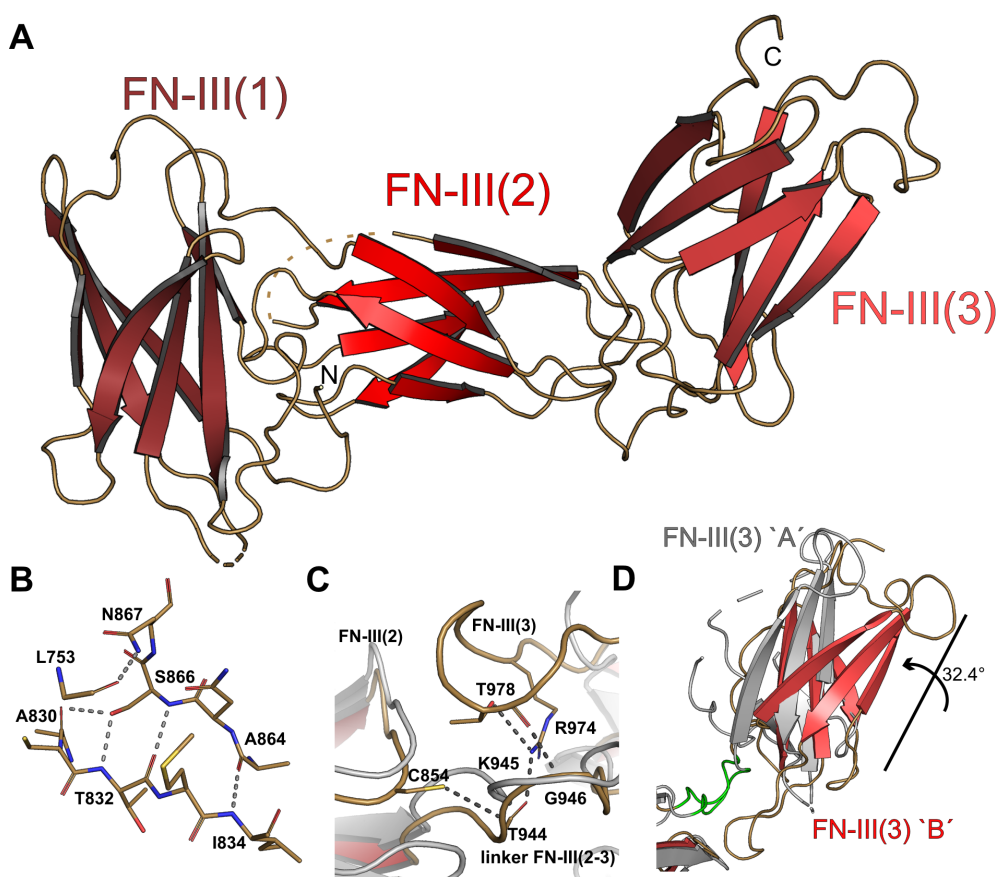


Figure 17 Structure of the three FN-III domains in RIM-BP

(A) A structural cartoon representation of molecule 'B' of the three FN-III domains in RIM-BP. Linker regions are colored in sand, β -strands in red and not modeled linker regions are indicated by dashed lines. (B) Stick representation of the short β -sheet formed between FN-III(1) β -strand G (A830, T832 and I834) and FN-III(2) BC loop (S864, S866 and N867). Grey dashed lines indicate potential hydrogen, bonds with a distance cut-off of $\leq 3.3\text{\AA}$. (C) Linker region of FN-III(2-3) in molecule 'B' (red, sand) and molecule 'A' (light grey) when aligning both molecules on FN-III(1-2). Stick representation of sidechains involved in potential hydrogen bonds, grey dashed lines indicate potential hydrogen, bonds with a distance cut-off of $\leq 3.3\text{\AA}$. (D) Alignment of molecules 'B' and 'A' on the fixed FN-III(1-2) region reveals movement of FN-III(3) domain. Flexible linker (green) as well as the rotation of the domain were calculated by the DynDom server (Christopher and Steven, 2016).

The differences in the FN-III(2)-FN-III(3) contacts of the two polypeptide chains leads to different orientations of the FN-III(3) domain relative to FN-III(1-2) in the two molecules (Figure 17D). Analysis of the FN-III(3) movement by the DynDom server (Christopher and Steven, 2016) showed a rotation of FN-III(3) of 32.4° and a translation of -1.3 Å between molecule 'A' and molecule 'B' together with a bending of the residues within the FN-III(2)-FN-III(3) linker region (Figure 17D).

Most of the published arrays of FN-III regions adopt an arrangement with no or minor direct contacts between the FN-III domains like in fibronectin (Leahy et al., 1996). The limited conformation flexibility of the FN-III(1-2) module suggests that this region could provide a rigid spacer or a pre-formed binding site for a ligand. In the extracellular domain of gp130 FN-III domains (D4 and D5) adopt a rather similar arrangement with a rigid interface. This allows the domains to adopt a C-shape and thus allowing signaling without major conformational changes upon ligand binding (Xu et al., 2010). In contrast, the flexible apposition of FN-III(2) and FN-III(3) indicates that this region represent a hinge-like element within RIM-BP.

Some FN-III regions have been also shown to homodimerize (Carr et al., 2001, Leppanen et al., 2017). This is not observed for the three FN-III domains in RIM-BP. MALS revealed a clearly monomeric state ($M_{\text{theoretical}}$: 32466 Da, M_n : 32610±107 Da) in agreement with structure analysis of the PISA server (Krissinel and Henrick, 2007).

3.4. Spinophilin and Syd-1 interact with the Neurexin-1 C-terminus

This section refers to the following publication:

Muhammad, K., S. Reddy-Alla, J. H. Driller, D. Schreiner, U. Rey, M. A. Bohme, C. Hollmann, N. Ramesh, H. Depner, J. Lutzkendorf, T. Matkovic, T. Gotz, D. D. Bergeron, J. Schmoranzer, F. Goettfert, M. Holt, M. C. Wahl, S. W. Hell, P. Scheiffele, A. M. Walter, B. Loll and S. J. Sigrist (2015). "Presynaptic spinophilin tunes neurexin signalling to control active zone architecture and function" *Nat Commun* 6: 8362.

Together with the Sigrist group, I reported several mechanisms for the mature AZ proteins to be transported through the axon (see 3.2.2, 3.3.3) to be subsequently integrated into the AZ scaffolds at presynaptic terminals. Previous to the integration of the "late" scaffold, an early assembly step has to occur to define and prepare the specific sites for AZ scaffold assembly. The Liprin- α /Syd-1 "early" complex has been shown to precede the BRP/RBP/Unc13 complex by hours (Fouquet et al., 2009, Oswald et al., 2010). Syd-1 was found to initiate AZ assembly by clustering Nr x -1, a transmembrane protein at the presynaptic membrane (Oswald et al., 2012). Nr x -1 furthermore interacts with adhesion molecule Nlg1, which in a PSD95 mediated interaction decreases mobility of GluA2-containing AMPA-type glutamate receptors. This interaction is conserved within Nlg1 and the *Drosophila* protein Discs large (Dlg), to promote accumulation of postsynaptic glutamate receptors at early time points (Banovic et al., 2010). This trans-synaptic crosstalk enables cooperative assembly of pre- and postsynaptic scaffolds, to ensure proper signal transduction by bringing newly formed AZs in close proximity with the PSD.

The Sigrist group identified the conserved scaffold protein Spinophilin (Spn) to fine tune AZ assembly, mediated by Syd-1. In absence of Spn, Syd-1 promotes excessive seeding of new AZ scaffolds. While Spn promotes mobility to Nr x -1 and thereby limits Nr x -1/Nlg1 signaling, Syd-1 immobilizes Nr x -1. These antagonistic effects on Nr x -1 are transmitted via PDZ domain binding, present in Spn as well as in Syd-1.

I characterized the interactions of the PDZ domains from Syd-1 and Spn with the Nr x -1 C-terminus *in vitro*. *In vivo* observations on the Nr x -1/Spn interaction in *Drosophila*, as

well as putative Y2H interactions were verified in pulldown experiments using *in vitro* purified protein samples. The interactions were further analyzed by ITC to compare the binding affinities of Spn and Syd-1 on the Nr_x-1 C-terminus. A peptide comprising the last ten residues of Nr_x-1 was bound 10-fold stronger by Syd-1 PDZ (5 μ M) than by Spn PDZ (50 μ M). These data support the proposed model where Spn binding to Nr_x-1 promotes mobility to Nr_x-1 and the stronger binding of Syd-1 immobilizes Nr_x-1 at a certain point to initiate mature AZ assembly. Pulldowns with the mammalian homolog of Spn, Neurabin-II, and the mammalian Neurexin-1 identified a conserved binding at the Nr_x-1 C-terminus.

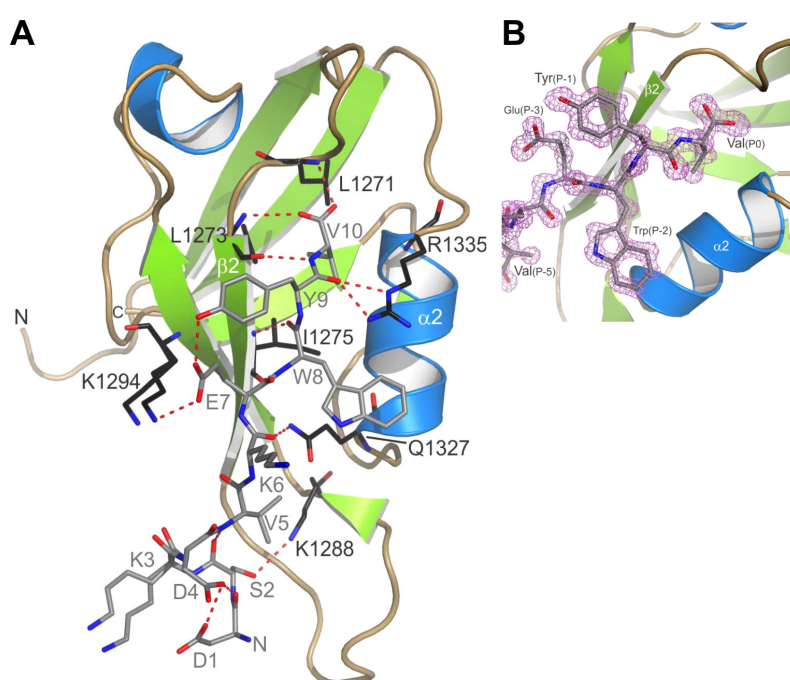


Figure 18 Characterization of the Spn-PDZ interaction with Nr_x-1

(A) A structural representation of the Spn-PDZ interacting with the Nr_x-1 C-term peptide. The C-terminal Nr_x-1 peptide is shown in grey using a stick representation. Residues on Spn-PDZ that interact with the Nr_x-1 peptide are highlighted in black. Red dashed lines indicate potential hydrogen bonds with a distance cut-off of $\leq 3.3\text{\AA}$. **(B)** mFoDFc simulated annealing omit map shown as violet mesh contoured at 3.0σ around the bound peptide. For calculation of the electron density map the Nr_x-1 peptide had been omitted.

The crystal structure of the *Drosophila* Spn PDZ domain in complex with the peptide comprising the ten C-terminal residues of Nr_x-1 was solved at 1.2 \AA resolution (Figure 18A, B). The PDZ domain of Spn shares the canonical fold of PDZ domains, comprising six

β -strands and two α -helices. The peptide binds in an anti-parallel mode and only the last five residues of Nr x -1 are involved in PDZ domain binding. Amino acid residues involved in interactions are highly conserved (Figure 19A). Mapping the sequence conservation on the surface of our structure shows very high sequence identity in the binding pocket as well as in the bound peptide (Figure 19B). Together with our pulldown experiments these results strongly indicate a conserved mechanism for the Spn/Nrx-1 interaction in mammals.

We were also able to obtain crystals of Syd-1/Nrx-1 C-terminus that diffracted to 2.1 Å resolution but unfortunately data bad quality from high anisotropy we were not able to solve the structure (unpublished data).

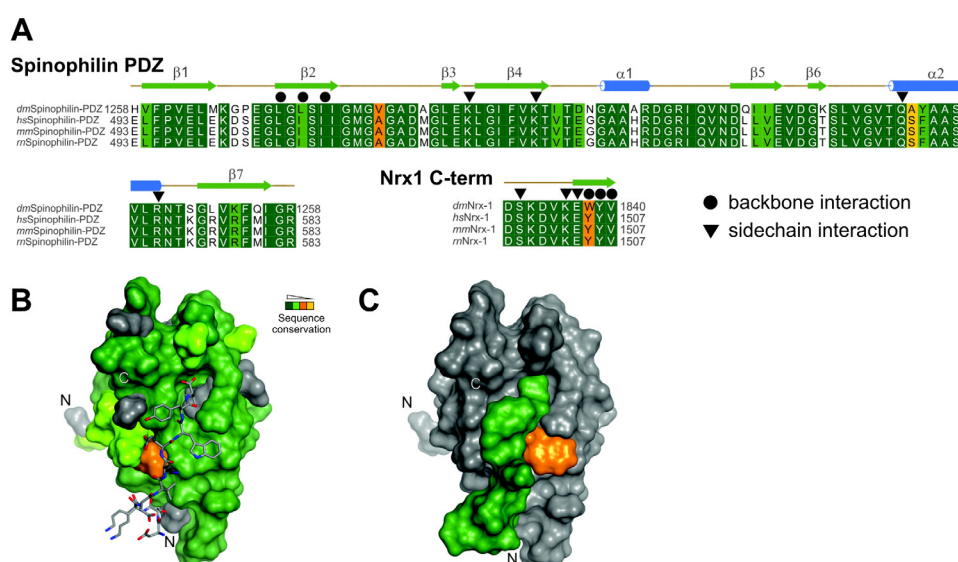


Figure 19 Conservation of the Spn-PDZ domain and the Nr x -1 C-terminus

(A) Alignment of PDZ domains from *Drosophila melanogaster* Spinophilin (*dm*Spinophilin), *Homo sapiens* Spinophilin (*hs*Spinophilin), *Mus musculus* Spinophilin (*mm*Spinophilin), and *Rattus norvegicus* Spinophilin (*rn*Spinophilin). Secondary structure elements are indicated on top of the sequences. Filled circles indicate residues involved in *dm*Spinophilin protein backbone to peptide backbone interactions and triangles describe residues involved in side chain interactions. Alignment of the last ten C-terminal amino acid residues of *Drosophila melanogaster* Neurexin-1 (*dm*Nrx-1), *Homo sapiens* Neurexin-1 (*hs*Nrx-1), *Mus musculus* Neurexin-1 (*mm*Nrx-1), and *Rattus norvegicus* Neurexin-1 (*rn*Nrx-1). **(B)** Sequence conservation is mapped on the surface of the crystal structure of *dm*Spinophilin-PDZ. The bound *dm*Neurexin-1 peptide is shown in stick representation. Secondary structure elements are indicated on top of the sequences. Filled circles indicate residues involved in *dm*Spinophilin protein backbone to peptide backbone interactions and triangles describe residues involved in side chain interactions. **(C)** Sequence conservation is mapped on the surface of the bound *dm*Neurexin-1 peptide. *dm*Spinophilin-PDZ is shown as gray surface.

3.5. Unc13 isoforms A and B within the active zone scaffold

This section refers to the following publication:

Bohme, M. A., C. Beis, S. Reddy-Alla, E. Reynolds, M. M. Mampell, A. T. Grasskamp, J. Lutzkendorf, D. D. Bergeron, J. H. Driller, H. Babikir, F. Gottfert, I. M. Robinson, C. J. O'Kane, S. W. Hell, M. C. Wahl, U. Stelzl, B. Loll, A. M. Walter and S. J. Sigrist (2016). "Active zone scaffolds differentially accumulate Unc13 isoforms to tune Ca(2+) channel-vesicle coupling" *Nat Neurosci* 19(10): 1311-1320.

M(Unc)13 proteins are essential for the AZ fusion machinery of SVs with established functions in SV docking and priming and NT release (Walter et al., 2018). Our collaborators in the Sigrist group identified two major isoforms of Unc13 in *Drosophila*, Unc13A and Unc13B. Both isoforms share the same C-terminal region, covering all important domains for their conserved functions in SV exocytosis (Walter et al., 2018). Each isoform comprises a unique N-terminus of nearly 2000 amino acid residues, lacking known domains and showing the profile of predicted unstructured regions. Unc13B is recruited by the "early" scaffolding protein Liprin- α and Syd-1, while Unc13A is recruited at a later stage together with the main scaffolding proteins BRP and RIM-BP. The studies on the phosphorylation dependent aggregation of BRP in the axons revealed, that proteins of the "late" scaffold most likely are co-transported, presumably as a pre-complex, to be integrated into the mature AZ scaffold (see 3.2.2). Characterization of the two isoforms by the Sigrist group showed that Unc13A localizes closer to the center of AZ scaffolds than Unc13B. Loss of Unc13A resulted in dramatically (~90%) reduced synaptic transmission and strong reduction (~50%) in SV docking, implying it to dock SV in close proximity to the AZ for exocytosis. Since both isoforms only differ in their N-terminal region must be involved in the localization to the "early" or "late" scaffolds.

Our PPI network, generated by Y2H experiments, provides evidence for the direct interaction of the N-terminal regions to specific proteins of the "early" or "late" scaffold (Table 1). We identified several strong interactions of the Unc13A specific N-terminus with BRP, RIM and the SH3 II and SH3III domains of RIM-BP, all proteins of the "late" scaffold (Table 1). Point mutants in the PXXP motif bound by the SH3 domains of RIM-BP showed no binding in Y2H experiments. *In vivo* mutation of PXXP motif although did not have

major impact on Unc13A localization, demonstrating again the importance of redundant interactions to preserve function in case of single failures. The Unc13B specific N-terminus only interacted reproducibly with a protein of the "early" scaffold, Liprin- α (Table 1).

Table 1 Yeast-two hybrid results for Unc13 isoforms

	BRP	RIM-BP	RIM	Liprin-α
Unc13A¹⁻⁶⁰⁶	++ (1201-1490)	++ (SH3II/III)	++ (1-500)	
Unc13B⁶⁰⁰⁻¹³²²				++ (1-267)
Unc13B¹²⁰⁰⁻¹⁹⁴⁴				++ (1-267)

* only Y2H interactions are shown with a reproducibility over 66% and were identified with at least two different vector combinations

4. Outlook

My Y2H studies on the network of the *Drosophila* AZ scaffold provide a robust basis for further studies on the importance of certain regions and interactions with other proteins. Many of these interactions have been observed before but lack biochemical and structural characterization while many others have not been described yet and need to be verified by other methods. During my studies I started working on biochemical and structural characterization of interactions and generated many expression constructs that can be used for further *in vitro* studies of the putative Y2H interactions. Further validation is currently done in the Sigrist group by MS crosslinking of immunoprecipitated AZ proteins from *in vivo* samples.

Y2H screens are an established tool to screen for binary PPI but can give no information on interactions that depend on other interaction. Therefore, it remains elusive how these interactions contribute to the scaffold in presence of the other proteins. The SH3 domains in RIM-BP or the D1/D2 region in BRP for example can bind to three or four different proteins within the AZ scaffold. AZ scaffolds however also show a high degree of redundancy in interactions as well as many possible weaker or transient interactions between coiled-coil or unstructured regions. Together with the problems in the expression of large scaffold proteins this makes *in vitro* studies of the huge AZ challenging. It is highly questionable if it is possible to assemble large complexes suitable for structural studies, due to inhomogeneity and flexibility.

To overcome these experimental limitations, we started a collaboration with the group of Cecilia Clementi (Rice University) to combine our data on the AZ scaffold in an integrative modeling approach (Ward et al., 2013, Webb et al., 2018). Based on the Y2H interaction network one can then implement further data, like MS crosslinking data, to refine this model.

Structural studies of the overall scaffold may also benefit from recent advantages in the field of cryo-electron microscopy (cryoEM), that contributed tremendously to the deeper understanding of large macromolecular structures (Cheng, 2018). While it is still necessary to purify homogeneous protein samples for high resolution structures, cryo-electron tomography (cryoET) can already visualize structures within their native

environment (Beck and Baumeister, 2016). With this technique native complexes in isolated synaptosomes can be studied to generate low resolution structures, which can be used to refine models derived from an integrative modeling approach. A fixed state of the flexible AZ scaffold would be of advantage for cryoET as it is then possible to average multiple images of identical conformations. The BRP^{nude} mutant reported previously (Hallermann et al., 2010) could be of interest since it is not able to tether SVs and thus may represent a defined state without intermediate SV bound states of the scaffold.

4.1. Bruchpilot

The central scaffold protein BRP in the *Drosophila* AZ still remains enigmatic in its elongated structure although a significant progress in the identification of possible binding partners was made. One can think of several ways to study this protein further. I generated shorter constructs of BRP covering nearly the entire protein sequence. These constructs may be used in the biochemical and structural characterization of BRP's coiled-coil regions and their specific interactions.

For visualization of BRP samples rotary shadowing electron microscopy, a technique suitable for thin elongated samples (Sherratt et al., 2009) might be also more suitable than the tested negative stains. This technique has also been used to visualize elongated EEA1, a protein tethering vesicles to the endosomal membrane (Murray et al., 2016). EEA1 adopts an elongated state on the endosomal membrane to tether vesicles, upon Rab5 binding it undergoes an entropic collapse to guide the vesicles towards the membrane. A similar model might be also possible for the AZ scaffold and SVs. While our studies could not identify a direct binding of Rabs to BRP our Y2H screen identified an interesting interaction of Rab8 to Fife. This interaction might provide a linker of the AZs to SVs and explain the effects of Fife on neurotransmitter release (Bruckner et al., 2017).

In order to be transported BRP is phosphorylated by SRPK79D, which potentially brings BRP in a more stable state. To mimic this phosphorylated BRP, I generated a phosphor-mimetic construct, replacing phosphorylated serine residues at the N-terminus

by aspartate residues. This may mimic the transport stable state of BRP but still might need stabilizing binding partners.

The studies of BRP also revealed a significant influence of **post-translational modification** (PTMs); N-terminal phosphorylation prevents axonal aggregation during transport (see 3.2.2) while dephosphorylation may be necessary for integration into the mature scaffold at synaptic terminals. Another PTM of BRP was identified by Janine Lützkendorf (Sigrist group), palmitoylation. Palmitoylation seems to influence Liprin- α /BRP binding (Lutzkendorf, 2018) and may help to anchor BRP to the plasma membrane. The role of PTMs for the AZ scaffold and their function is presently poorly understood but the ELKS family seems to be highly regulated by PTMs. The mammalian ELKS family member Cast is specifically phosphorylated to control the release probability of SVs (Mochida et al., 2016).

4.2. RIM-binding protein

The domains and its functions of RIM-BP have been extensively studied and characterized *in vitro*. While the SH3 domains II and III contribute to several interactions the function of the first SH3 domain is still enigmatic.

A recently identified interaction of the central FN-III array in RIM-BP with BK-channels provides an interesting target for further structural studies of this interaction (Sclip et al., 2018). In contrast to many other interactions within the AZ scaffold, the interaction originates from stable domains. Since this interaction was only found in the mammalian proteins it needs to be validated for *Drosophila* proteins. Available structures of the mammalian RCK domains of BK-channels (Wu et al., 2010, Yuan et al., 2011), might help in designing constructs for the expression of the RCK domains of the *Drosophila* homolog Slowpoke.

5. Appendix: Yeast-two hybrid

In our Y2H experiments, proteins are coupled to two parts of the galactose-gene transcription factor (GAL4). One is coupled to a DNA-binding domain (BD) recognizing an upstream activating sequence while the other to an activating domain (AD) able to activate transcription by binding RNA polymerase. If desired proteins interact with each the AD and is brought in close proximity to the DB and thus activates transcription of a reporter gene, allowing the yeast to grow on a selective media. Proteins fused to the BD are called “baits” while the one coupled to the AD are called “preys”. Since concentration has a huge influence on interactions, low expression vectors were used for all “preys” and “baits”. In total four different vectors were used, two for the “baits” (pBTM116-D9, pBTMcc24-DM) and two for the “preys” (pACT4-DM and pGAD426-D3, that was replaced in the second screen by pCBDU-JW) giving rise to unique fusion proteins either containing a N-terminal or a C-terminal BD or AD fusion. After transformation in yeast and removal of auto-active “baits” all remaining “baits” were tested against a “prey-matrix” in 384-well format. The prey matrix comprised the unique construct two times from independent transformations and only if both unique constructs showed growth with the respective bait it was counted as putative PPI. All baits that showed at least one putative PPI by yeast growth on selective media were tested again using another clone from an independent transformation with the “prey-matrix”. By this each protein construct was tested at least eight times (two times for each of the four vectors) against all the constructs in our screen.

Interactions that were only found twice or less were omitted from evaluation, due to the lack of reproducibility. For each PPI the “count” represents how often this specific interaction was found in our experiments. The strength of the interaction within our screen is rated by a score for each PPI, representing the reproducibility in our experiments (counts divided by the total number this PPI was tested). Further information about the orientation (bait-prey; BP or prey-bait, PB), if the interaction came with different vectors combinations from one orientation (BP2V/PB2V) or even with both orientation (*vice versa*) were listed to evaluate each interaction. Dimerization of a specific construct is indicated by DM.

References

- ACKERMANN, F., WAITES, C. L. & GARNER, C. C. 2015. Presynaptic active zones in invertebrates and vertebrates. *EMBO Rep*, 16, 923-38.
- ACUNA, C., LIU, X., GONZALEZ, A. & SUDHOF, T. C. 2015. RIM-BPs Mediate Tight Coupling of Action Potentials to Ca(2+)-Triggered Neurotransmitter Release. *Neuron*, 87, 1234-1247.
- ACUNA, C., LIU, X. & SUDHOF, T. C. 2016. How to Make an Active Zone: Unexpected Universal Functional Redundancy between RIMs and RIM-BPs. *Neuron*, 91, 792-807.
- AUBOL, B. E., JAMROS, M. A., MCGLONE, M. L. & ADAMS, J. A. 2013. Splicing kinase SRPK1 conforms to the landscape of its SR protein substrate. *Biochemistry*, 52, 7595-605.
- AUGUSTIN, I., ROSENMUND, C., SUDHOF, T. C. & BROSE, N. 1999. Munc13-1 is essential for fusion competence of glutamatergic synaptic vesicles. *Nature*, 400, 457-61.
- BANOVIC, D., KHORRAMSHAHI, O., OWALD, D., WICHMANN, C., RIEDT, T., FOUQUET, W., TIAN, R., SIGRIST, S. J. & ABERLE, H. 2010. Drosophila Neuroligin 1 Promotes Growth and Postsynaptic Differentiation at Glutamatergic Neuromuscular Junctions. *Neuron*, 66, 724-738.
- BARTHELD, C. S., BAHNEY, J. & HERCULANO-HOUZEL, S. 2016. The search for true numbers of neurons and glial cells in the human brain: A review of 150 years of cell counting. *Journal of Comparative Neurology*, 524, 3865-3895.
- BASU, J., SHEN, N., DULUBOVA, I., LU, J., GUAN, R., GURYEV, O., GRISHIN, N. V., ROSENMUND, C. & RIZO, J. 2005. A minimal domain responsible for Munc13 activity. *Nat Struct Mol Biol*, 12, 1017-8.
- BECK, M. & BAUMEISTER, W. 2016. Cryo-Electron Tomography: Can it Reveal the Molecular Sociology of Cells in Atomic Detail? *Trends Cell Biol*, 26, 825-837.
- BOHME, M. A., BEIS, C., REDDY-ALLA, S., REYNOLDS, E., MAMPELL, M. M., GRASSKAMP, A. T., LUTZKENDORF, J., BERGERON, D. D., DRILLER, J. H., BABIKIR, H., GOTTFERT, F., ROBINSON, I. M., O'KANE, C. J., HELL, S. W., WAHL, M. C., STELZL, U., LOLL, B., WALTER, A. M. & SIGRIST, S. J. 2016. Active zone scaffolds differentially accumulate Unc13 isoforms to tune Ca(2+) channel-vesicle coupling. *Nat Neurosci*, 19, 1311-20.
- BRUCKNER, J. J., GRATZ, S. J., SLIND, J. K., GESKE, R. R., CUMMINGS, A. M., GALINDO, S. E., DONOHUE, L. K. & O'CONNOR-GILES, K. M. 2012. Fife, a Drosophila Piccolo-RIM homolog, promotes active zone organization and neurotransmitter release. *J Neurosci*, 32, 17048-58.
- BRUCKNER, J. J., ZHAN, H., GRATZ, S. J., RAO, M., UKKEN, F., ZILBERG, G. & O'CONNOR-GILES, K. M. 2017. Fife organizes synaptic vesicles and calcium channels for high-probability neurotransmitter release. *J Cell Biol*, 216, 231-246.
- BURKHARDT, P., HATTENDORF, D. A., WEIS, W. I. & FASSHAUER, D. 2008. Munc18a controls SNARE assembly through its interaction with the syntaxin N-peptide. *The EMBO Journal*, 27, 923-933.
- BURY, L. A. D. & SABO, S. L. 2016. Building a Terminal: Mechanisms of Presynaptic Development in the CNS. *The Neuroscientist*, 22, 372-391.

References

- CAI, Q., PAN, P.-Y. & SHENG, Z.-H. 2007. Syntabulin–Kinesin-1 Family Member 5B-Mediated Axonal Transport Contributes to Activity-Dependent Presynaptic Assembly. *The Journal of Neuroscience*, 27, 7284-7296.
- CARR, P. D., GUSTIN, S. E., CHURCH, A. P., MURPHY, J. M., FORD, S. C., MANN, D. A., WOLTRING, D. M., WALKER, I., OLLIS, D. L. & YOUNG, I. G. 2001. Structure of the complete extracellular domain of the common beta subunit of the human GM-CSF, IL-3, and IL-5 receptors reveals a novel dimer configuration. *Cell*, 104, 291-300.
- CHEN, J., BILLINGS, S. E. & NISHIMUNE, H. 2011. Calcium channels link the muscle-derived synapse organizer laminin beta2 to Bassoon and CAST/Erc2 to organize presynaptic active zones. *J Neurosci*, 31, 512-25.
- CHENG, Y. 2018. Single-particle cryo-EM—How did it get here and where will it go. *Science*, 361, 876-880.
- CHRISTOPHER, G. & STEVEN, H. 2016. The DynDom3D Webserver for the Analysis of Domain Movements in Multimeric Proteins. *Journal of Computational Biology*, 23, 21-26.
- COPPOLA, T., MAGNIN-LUTHI, S., PERRET-MENOUD, V., GATTESCO, S., SCHIAVO, G. & REGAZZI, R. 2001. Direct interaction of the Rab3 effector RIM with Ca²⁺ channels, SNAP-25, and synaptotagmin. *J Biol Chem*, 276, 32756-62.
- COUTEAUX, R. & PECOT-DECHAVASSINE, M. 1970. [Synaptic vesicles and pouches at the level of "active zones" of the neuromuscular junction]. *C R Acad Sci Hebd Seances Acad Sci D*, 271, 2346-9.
- DAI, Y., TARU, H., DEKEN, S. L., GRILL, B., ACKLEY, B., NONET, M. L. & JIN, Y. 2006. SYD-2 Liprin-alpha organizes presynaptic active zone formation through ELKS. *Nat Neurosci*, 9, 1479-87.
- DAUMKE, O., ROUX, A. & HAUCKE, V. 2014. BAR Domain Scaffolds in Dynamin-Mediated Membrane Fission. *Cell*, 156, 882-892.
- DENG, L., KAESER, P. S., XU, W. & SUDHOF, T. C. 2011. RIM proteins activate vesicle priming by reversing autoinhibitory homodimerization of Munc13. *Neuron*, 69, 317-31.
- DER, C. J., FINKEL, T. & COOPER, G. M. 1986. Biological and biochemical properties of human rasH genes mutated at codon 61. *Cell*, 44, 167-76.
- DONG, W., RADULOVIC, T., GORAL, R. O., THOMAS, C., SUAREZ MONTESINOS, M., GUERRERO-GIVEN, D., HAGIWARA, A., PUTZKE, T., HIDA, Y., ABE, M., SAKIMURA, K., KAMASAWA, N., OHTSUKA, T. & YOUNG, S. M. 2018. CAST/ELKS Proteins Control Voltage-Gated Ca²⁺ Channel Density and Synaptic Release Probability at a Mammalian Central Synapse. *Cell Reports*, 24, 284-293.e6.
- DULUBOVA, I., LOU, X., LU, J., HURYEVA, I., ALAM, A., SCHNEGGENBURGER, R., SUDHOF, T. C. & RIZO, J. 2005. A Munc13/RIM/Rab3 tripartite complex: from priming to plasticity? *EMBO J*, 24, 2839-50.
- EGGERMANN, E., BUCURENCIU, I., GOSWAMI, S. P. & JONAS, P. 2011. Nanodomain coupling between Ca²⁺(+) channels and sensors of exocytosis at fast mammalian synapses. *Nat Rev Neurosci*, 13, 7-21.
- EHMANN, N., VAN DE LINDE, S., ALON, A., LJASCHENKO, D., KEUNG, X. Z., HOLM, T., RINGS, A., DIANTONIO, A., HALLERMANN, S., ASHERY, U., HECKMANN, M., SAUER, M. & KITTEL, R. J. 2014. Quantitative super-resolution imaging of Bruchpilot distinguishes active zone states. *Nat Commun*, 5, 4650.

References

- FERNANDEZ, F., TORRES, V. & ZAMORANO, P. 2010. An evolutionarily conserved mechanism for presynaptic trapping. *Cell Mol Life Sci*, 67, 1751-4.
- FOUQUET, W., OWALD, D., WICHMANN, C., MERTEL, S., DEPNER, H., DYBA, M., HALLERMANN, S., KITTEL, R. J., EIMER, S. & SIGRIST, S. J. 2009. Maturation of active zone assembly by *Drosophila* Bruchpilot. *J Cell Biol*, 186, 129-45.
- FUKUDA, M. 2003. Distinct Rab binding specificity of Rim1, Rim2, rabphilin, and Noc2. Identification of a critical determinant of Rab3A/Rab27A recognition by Rim2. *J Biol Chem*, 278, 15373-80.
- GHOSH, G. & ADAMS, J. A. 2011. Phosphorylation mechanism and structure of serine-arginine protein kinases. *FEBS J*, 278, 587-97.
- GROSSHANS, B. L., ORTIZ, D. & NOVICK, P. 2006. Rabs and their effectors: achieving specificity in membrane traffic. *Proc Natl Acad Sci U S A*, 103, 11821-7.
- GUI, J. F., LANE, W. S. & FU, X. D. 1994. A serine kinase regulates intracellular localization of splicing factors in the cell cycle. *Nature*, 369, 678-82.
- GUNDELFINGER, E. D., REISSNER, C. & GARNER, C. C. 2015. Role of Bassoon and Piccolo in Assembly and Molecular Organization of the Active Zone. *Front Synaptic Neurosci*, 7, 19.
- HALLERMANN, S., KITTEL, R. J., WICHMANN, C., WEYHERSMULLER, A., FOUQUET, W., MERTEL, S., OWALD, D., EIMER, S., DEPNER, H., SCHWARZEL, M., SIGRIST, S. J. & HECKMANN, M. 2010. Naked dense bodies provoke depression. *J Neurosci*, 30, 14340-5.
- HAUCKE, V., NEHER, E. & SIGRIST, S. J. 2011. Protein scaffolds in the coupling of synaptic exocytosis and endocytosis. *Nat Rev Neurosci*, 12, 127-38.
- HIBINO, H., PIRONKOVA, R., ONWUMERE, O., VOLOGODSKAIA, M., HUDSPETH, A. J. & LESAGE, F. 2002. RIM binding proteins (RBPs) couple Rab3-interacting molecules (RIMs) to voltage-gated Ca(2+) channels. *Neuron*, 34, 411-23.
- HIROKAWA, N., NIWA, S. & TANAKA, Y. 2010. Molecular motors in neurons: transport mechanisms and roles in brain function, development, and disease. *Neuron*, 68, 610-38.
- JAHN, R. & FASSHAUER, D. 2012. Molecular machines governing exocytosis of synaptic vesicles. *Nature*, 490, 201-7.
- JOHNSON, E. L., 3RD, FETTER, R. D. & DAVIS, G. W. 2009. Negative regulation of active zone assembly by a newly identified SR protein kinase. *PLoS Biol*, 7, e1000193.
- KAESER, P. S. 2011. Pushing synaptic vesicles over the RIM. *Cell Logist*, 1, 106-110.
- KAESER, P. S., DENG, L., WANG, Y., DULUBOVA, I., LIU, X., RIZO, J. & SUDHOF, T. C. 2011. RIM proteins tether Ca²⁺ channels to presynaptic active zones via a direct PDZ-domain interaction. *Cell*, 144, 282-95.
- KAWABE, H., MITKOVSKI, M., KAESER, P. S., HIRRLINGER, J., OPAZO, F., NESTVOGEL, D., KALLA, S., FEJTOVA, A., VERRIER, S. E., BUNGERS, S. R., COOPER, B. H., VAROQUEAUX, F., WANG, Y., NEHRING, R. B., GUNDELFINGER, E. D., ROSENMUND, C., RIZZOLI, S. O., SUDHOF, T. C., RHEE, J. S. & BROSE, N. 2017. ELKS1 localizes the synaptic vesicle priming protein bMunc13-2 to a specific subset of active zones. *J Cell Biol*, 216, 1143-1161.
- KIRAL, F. R., KOHRS, F. E., JIN, E. J. & HIESINGER, P. R. 2018. Rab GTPases and Membrane Trafficking in Neurodegeneration. *Curr Biol*, 28, R471-r486.
- KITTEL, R. J., WICHMANN, C., RASSE, T. M., FOUQUET, W., SCHMIDT, M., SCHMID, A., WAGH, D. A., PAWLU, C., KELLNER, R. R., WILLIG, K. I., HELL, S. W., BUCHNER, E.,

References

- HECKMANN, M. & SIGRIST, S. J. 2006. Bruchpilot promotes active zone assembly, Ca²⁺ channel clustering, and vesicle release. *Science*, 312, 1051-4.
- KLASSEN, M. P., WU, Y. E., MAEDER, C. I., NAKAE, I., CUEVA, J. G., LEHRMAN, E. K., TADA, M., GENGYO-ANDO, K., WANG, G. J., GOODMAN, M., MITANI, S., KONTANI, K., KATADA, T. & SHEN, K. 2010. An Arf-like Small G Protein, ARL-8, Promotes the Axonal Transport of Presynaptic Cargoes by Suppressing Vesicle Aggregation. *Neuron*, 66, 710-723.
- KO, J., NA, M., KIM, S., LEE, J. R. & KIM, E. 2003. Interaction of the ERC family of RIM-binding proteins with the liprin-alpha family of multidomain proteins. *J Biol Chem*, 278, 42377-85.
- KOUSHIKA, S. P. 2008. "JIP"ing along the axon: the complex roles of JIPs in axonal transport. *Bioessays*, 30, 10-4.
- KRISSINEL, E. & HENRICK, K. 2007. Inference of macromolecular assemblies from crystalline state. *J Mol Biol*, 372, 774-97.
- LEAHY, D. J., AUKHIL, I. & ERICKSON, H. P. 1996. 2.0 Å Crystal Structure of a Four-Domain Segment of Human Fibronectin Encompassing the RGD Loop and Synergy Region. *Cell*, 84, 155-164.
- LEPPANEN, V. M., SAHARINEN, P. & ALITALO, K. 2017. Structural basis of Tie2 activation and Tie2/Tie1 heterodimerization. *Proc Natl Acad Sci U S A*, 114, 4376-4381.
- LI, J., ASHLEY, J., BUDNIK, V. & BHAT, M. A. 2007. Crucial role of Drosophila neurexin in proper active zone apposition to postsynaptic densities, synaptic growth, and synaptic transmission. *Neuron*, 55, 741-55.
- LIM, W. A., RICHARDS, F. M. & FOX, R. O. 1994. Structural determinants of peptide-binding orientation and of sequence specificity in SH3 domains. *Nature*, 372, 375-379.
- LIN, S. & FU, X. D. 2007. SR proteins and related factors in alternative splicing. *Adv Exp Med Biol*, 623, 107-22.
- LIU, K. S., SIEBERT, M., MERTEL, S., KNOCHE, E., WEGENER, S., WICHMANN, C., MATKOVIC, T., MUHAMMAD, K., DEPNER, H., METTKE, C., BUCKERS, J., HELL, S. W., MULLER, M., DAVIS, G. W., SCHMITZ, D. & SIGRIST, S. J. 2011. RIM-binding protein, a central part of the active zone, is essential for neurotransmitter release. *Science*, 334, 1565-9.
- LU, J., MACHIUS, M., DULUBOVA, I., DAI, H., SUDHOF, T. C., TOMCHICK, D. R. & RIZO, J. 2006. Structural basis for a Munc13-1 homodimer to Munc13-1/RIM heterodimer switch. *PLoS Biol*, 4, e192.
- LUKASIEWICZ, R., NOLEN, B., ADAMS, J. A. & GHOSH, G. 2007. The RGG domain of Npl3p recruits Sky1p through docking interactions. *J Mol Biol*, 367, 249-61.
- LUTZKENDORF, J. 2018. *Synaptic Targeting, Transport and Modulation of Drosophila Active Zone Components*. PhD thesis, Freie Universität Berlin.
- MAAS, C., TORRES, V. I., ALTROCK, W. D., LEAL-ORTIZ, S., WAGH, D., TERRY-LORENZO, R. T., FEJTOVA, A., GUNDELFINGER, E. D., ZIV, N. E. & GARNER, C. C. 2012. Formation of Golgi-Derived Active Zone Precursor Vesicles. *The Journal of Neuroscience*, 32, 11095-11108.
- MASON, J. M. & ARNDT, K. M. 2004. Coiled Coil Domains: Stability, Specificity, and Biological Implications. *ChemBioChem*, 5, 170-176.
- MATKOVIC, T., SIEBERT, M., KNOCHE, E., DEPNER, H., MERTEL, S., OWALD, D., SCHMIDT, M., THOMAS, U., SICKMANN, A., KAMIN, D., HELL, S. W., BURGER, J., HOLLMANN, C., MIELKE, T., WICHMANN, C. & SIGRIST, S. J. 2013. The Bruchpilot cytomatrix

References

- determines the size of the readily releasable pool of synaptic vesicles. *J Cell Biol*, 202, 667-83.
- MEYER, L. C. & WRIGHT, N. T. 2013. Structure of giant muscle proteins. *Front Physiol*, 4, 368.
- MOCHIDA, S., HIDA, Y., TANIFUJI, S., HAGIWARA, A., HAMADA, S., ABE, M., MA, H., YASUMURA, M., KITAJIMA, I., SAKIMURA, K. & OHTSUKA, T. 2016. SAD-B Phosphorylation of CAST Controls Active Zone Vesicle Recycling for Synaptic Depression. *Cell Rep*, 16, 2901-2913.
- MONIER, S., JOLLIVET, F., JANOUEIX-LEROSEY, I., JOHANNES, L. & GOUD, B. 2002. Characterization of novel Rab6-interacting proteins involved in endosome-to-TGN transport. *Traffic*, 3, 289-97.
- MUKHERJEE, K., YANG, X., GERBER, S. H., KWON, H. B., HO, A., CASTILLO, P. E., LIU, X. & SUDHOF, T. C. 2010. Piccolo and bassoon maintain synaptic vesicle clustering without directly participating in vesicle exocytosis. *Proc Natl Acad Sci U S A*, 107, 6504-9.
- MURRAY, D. H., JAHNEL, M., LAUER, J., AVELLANEDA, M. J., BROUILLY, N., CEZANNE, A., MORALES-NAVARRETE, H., PERINI, E. D., FERGUSON, C., LUPAS, A. N., KALAIIDZIDIS, Y., PARTON, R. G., GRILL, S. W. & ZERIAL, M. 2016. An endosomal tether undergoes an entropic collapse to bring vesicles together. *Nature*, 537, 107-111.
- NAKAGAWA, O., ARNOLD, M., NAKAGAWA, M., HAMADA, H., SHELTON, J. M., KUSANO, H., HARRIS, T. M., CHILDS, G., CAMPBELL, K. P., RICHARDSON, J. A., NISHINO, I. & OLSON, E. N. 2005. Centronuclear myopathy in mice lacking a novel muscle-specific protein kinase transcriptionally regulated by MEF2. *Genes Dev*, 19, 2066-77.
- NGO, J. C., CHAKRABARTI, S., DING, J. H., VELAZQUEZ-DONES, A., NOLEN, B., AUBOL, B. E., ADAMS, J. A., FU, X. D. & GHOSH, G. 2005. Interplay between SRPK and Clk/Sty kinases in phosphorylation of the splicing factor ASF/SF2 is regulated by a docking motif in ASF/SF2. *Mol Cell*, 20, 77-89.
- NIERATSCHKER, V., SCHUBERT, A., JAUCH, M., BOCK, N., BUCHER, D., DIPPACHER, S., KROHNE, G., ASAN, E., BUCHNER, S. & BUCHNER, E. 2009. Bruchpilot in ribbon-like axonal agglomerates, behavioral defects, and early death in SRPK79D kinase mutants of *Drosophila*. *PLoS Genet*, 5, e1000700.
- OHTSUKA, T., TAKAO-RIKITSU, E., INOUE, E., INOUE, M., TAKEUCHI, M., MATSUBARA, K., DEGUCHI-TAWARADA, M., SATOH, K., MORIMOTO, K., NAKANISHI, H. & TAKAI, Y. 2002. Cast: a novel protein of the cytomatrix at the active zone of synapses that forms a ternary complex with RIM1 and munc13-1. *J Cell Biol*, 158, 577-90.
- OLSEN, O., MOORE, K. A., FUKATA, M., KAZUTA, T., TRINIDAD, J. C., KAUER, F. W., STREULI, M., MISAWA, H., BURLINGAME, A. L., NICOLL, R. A. & BREDDT, D. S. 2005. Neurotransmitter release regulated by a MALS-liprin-alpha presynaptic complex. *J Cell Biol*, 170, 1127-34.
- OWALD, D., FOUQUET, W., SCHMIDT, M., WICHMANN, C., MERTEL, S., DEPNER, H., CHRISTIANSEN, F., ZUBE, C., QUENTIN, C., KORNER, J., URLAUB, H., MECHTLER, K. & SIGRIST, S. J. 2010. A Syd-1 homologue regulates pre- and postsynaptic maturation in *Drosophila*. *J Cell Biol*, 188, 565-79.
- OWALD, D., KHORRAMSHAHI, O., GUPTA, V. K., BANOVIC, D., DEPNER, H., FOUQUET, W., WICHMANN, C., MERTEL, S., EIMER, S., REYNOLDS, E., HOLT, M., ABERLE, H. &

References

- SIGRIST, S. J. 2012. Cooperation of Syd-1 with Neurexin synchronizes pre- with postsynaptic assembly. *Nat Neurosci*, 15, 1219-26.
- PAGNI, M., IOANNIDIS, V., CERUTTI, L., ZAHN-ZABAL, M., JONGENEEL, C. V. & FALQUET, L. 2004. MyHits: a new interactive resource for protein annotation and domain identification. *Nucleic Acids Research*, 32, W332-W335.
- PENA, V., JOVIN, S. M., FABRIZIO, P., ORLOWSKI, J., BUJNICKI, J. M., LÜHRMANN, R. & WAHL, M. C. 2009. Common Design Principles in the Spliceosomal RNA Helicase Brr2 and in the Hel308 DNA Helicase. *Molecular Cell*, 35, 454-466.
- PETZOLDT, A. G. & SIGRIST, S. J. 2014. Synaptogenesis. *Curr Biol*, 24, R1076-80.
- PRIVE, G. G., MILBURN, M. V., TONG, L., DE VOS, A. M., YAMAIZUMI, Z., NISHIMURA, S. & KIM, S. H. 1992. X-ray crystal structures of transforming p21 ras mutants suggest a transition-state stabilization mechanism for GTP hydrolysis. *Proc Natl Acad Sci U S A*, 89, 3649-53.
- SCHOCH, S., CASTILLO, P. E., JO, T., MUKHERJEE, K., GEPPERT, M., WANG, Y., SCHMITZ, F., MALENKA, R. C. & SUDHOF, T. C. 2002. RIM1alpha forms a protein scaffold for regulating neurotransmitter release at the active zone. *Nature*, 415, 321-6.
- SCHWARZBAUER, J. E. & DESIMONE, D. W. 2011. Fibronectins, their fibrillogenesis, and in vivo functions. *Cold Spring Harb Perspect Biol*, 3.
- SCLIP, A., ACUNA, C., LUO, F. & SUDHOF, T. C. 2018. RIM-binding proteins recruit BK-channels to presynaptic release sites adjacent to voltage-gated Ca(2+)-channels. *EMBO J*.
- SERRA-PAGES, C., KEDERSHA, N. L., FAZIKAS, L., MEDLEY, Q., DEBANT, A. & STREULI, M. 1995. The LAR transmembrane protein tyrosine phosphatase and a coiled-coil LAR-interacting protein co-localize at focal adhesions. *EMBO J*, 14, 2827-38.
- SHANNON, P., MARKIEL, A., OZIER, O., BALIGA, N. S., WANG, J. T., RAMAGE, D., AMIN, N., SCHWIKOWSKI, B. & IDEKER, T. 2003. Cytoscape: a software environment for integrated models of biomolecular interaction networks. *Genome Res*, 13, 2498-504.
- SHAPIRA, M., ZHAI, R. G., DRESBACH, T., BRESLER, T., TORRES, V. I., GUNDELFINGER, E. D., ZIV, N. E. & GARNER, C. C. 2003. Unitary assembly of presynaptic active zones from Piccolo-Bassoon transport vesicles. *Neuron*, 38, 237-52.
- SHERRATT, M. J., MEADOWS, R. S., GRAHAM, H. K., KIELTY, C. M. & HOLMES, D. F. 2009. ECM macromolecules: rotary shadowing and transmission electron microscopy. *Methods Mol Biol*, 522, 175-81.
- SIEBERT, M., BOHME, M. A., DRILLER, J. H., BABIKIR, H., MAMPELL, M. M., REY, U., RAMESH, N., MATKOVIC, T., HOLTON, N., REDDY-ALLA, S., GOTTFERT, F., KAMIN, D., QUENTIN, C., KLINEDINST, S., ANDLAUER, T. F., HELL, S. W., COLLINS, C. A., WAHL, M. C., LOLL, B. & SIGRIST, S. J. 2015. A high affinity RIM-binding protein/Aplip1 interaction prevents the formation of ectopic axonal active zones. *Elife*, 4.
- SIGRIST, C. J., CERUTTI, L., DE CASTRO, E., LANGENDIJK-GENEVAUX, P. S., BULLIARD, V., BAIROCH, A. & HULO, N. 2010. PROSITE, a protein domain database for functional characterization and annotation. *Nucleic Acids Res*, 38, D161-6.
- SUDHOF, T. C. 2004. The synaptic vesicle cycle. *Annu Rev Neurosci*, 27, 509-47.
- SUDHOF, T. C. 2008. Neuroligins and neurexins link synaptic function to cognitive disease. *Nature*, 455, 903-11.
- SUDHOF, T. C. 2012. The presynaptic active zone. *Neuron*, 75, 11-25.

References

- SUDHOF, T. C. & RIZO, J. 2011. Synaptic vesicle exocytosis. *Cold Spring Harb Perspect Biol*, 3.
- SWANSON, C. J. & SIVARAMAKRISHNAN, S. 2014. Harnessing the unique structural properties of isolated alpha-helices. *J Biol Chem*, 289, 25460-7.
- SÜDHOF, THOMAS C. 2013. Neurotransmitter Release: The Last Millisecond in the Life of a Synaptic Vesicle. *Neuron*, 80, 675-690.
- TAKAO-RIKITSU, E., MOCHIDA, S., INOUE, E., DEGUCHI-TAWARADA, M., INOUE, M., OHTSUKA, T. & TAKAI, Y. 2004. Physical and functional interaction of the active zone proteins, CAST, RIM1, and Bassoon, in neurotransmitter release. *J Cell Biol*, 164, 301-11.
- TARU, H. & JIN, Y. 2011. The Liprin homology domain is essential for the homomeric interaction of SYD-2/Liprin-alpha protein in presynaptic assembly. *J Neurosci*, 31, 16261-8.
- TOM DIECK, S., SPECHT, D., STRENZKE, N., HIDA, Y., KRISHNAMOORTHY, V., SCHMIDT, K. F., INOUE, E., ISHIZAKI, H., TANAKA-OKAMOTO, M., MIYOSHI, J., HAGIWARA, A., BRANDSTATTER, J. H., LOWEL, S., GOLLISCH, T., OHTSUKA, T. & MOSER, T. 2012. Deletion of the presynaptic scaffold CAST reduces active zone size in rod photoreceptors and impairs visual processing. *J Neurosci*, 32, 12192-203.
- TORRES, V. I. & INESTROSA, N. C. 2018. Vertebrate Presynaptic Active Zone Assembly: a Role Accomplished by Diverse Molecular and Cellular Mechanisms. *Mol Neurobiol*, 55, 4513-4528.
- TSETSENIS, T., YOUNTS, T. J., CHIU, C. Q., KAESER, P. S., CASTILLO, P. E. & SUDHOF, T. C. 2011. Rab3B protein is required for long-term depression of hippocampal inhibitory synapses and for normal reversal learning. *Proc Natl Acad Sci U S A*, 108, 14300-5.
- ULRICH, A. K. C., SEEGER, M., SCHUTZE, T., BARTLICK, N. & WAHL, M. C. 2016. Scaffolding in the Spliceosome via Single alpha Helices. *Structure*, 24, 1972-1983.
- VAN VACTOR, D. & SIGRIST, S. J. 2017. Presynaptic morphogenesis, active zone organization and structural plasticity in *Drosophila*. *Curr Opin Neurobiol*, 43, 119-129.
- VAROQUEAUX, F., SIGLER, A., RHEE, J. S., BROSE, N., ENK, C., REIM, K. & ROSENMUND, C. 2002. Total arrest of spontaneous and evoked synaptic transmission but normal synaptogenesis in the absence of Munc13-mediated vesicle priming. *Proc Natl Acad Sci U S A*, 99, 9037-42.
- VERHAGE, M., MAIA, A. S., PLOMP, J. J., BRUSSAARD, A. B., HEEROMA, J. H., VERMEER, H., TOONEN, R. F., HAMMER, R. E., VAN DEN , T. K., BERG, MISSLER, M., GEUZE, H. J. & SÜDHOF, T. C. 2000. Synaptic Assembly of the Brain in the Absence of Neurotransmitter Secretion. *Science*, 287, 864-869.
- WAGH, D. A., RASSE, T. M., ASAN, E., HOFBAUER, A., SCHWENKERT, I., DURRBECK, H., BUCHNER, S., DABAUVALLE, M. C., SCHMIDT, M., QIN, G., WICHMANN, C., KITTEL, R., SIGRIST, S. J. & BUCHNER, E. 2006. Bruchpilot, a protein with homology to ELKS/CAST, is required for structural integrity and function of synaptic active zones in *Drosophila*. *Neuron*, 49, 833-44.
- WAGNER, O. I., ESPOSITO, A., KOHLER, B., CHEN, C. W., SHEN, C. P., WU, G. H., BUTKEVICH, E., MANDALAPU, S., WENZEL, D., WOUTERS, F. S. & KLOPFENSTEIN, D. R. 2009. Synaptic scaffolding protein SYD-2 clusters and activates kinesin-3 UNC-104 in *C. elegans*. *Proc Natl Acad Sci U S A*, 106, 19605-10.

References

- WAITES, C. L., CRAIG, A. M. & GARNER, C. C. 2005. Mechanisms of vertebrate synaptogenesis. *Annu Rev Neurosci*, 28, 251-74.
- WALTER, A. M., BOHME, M. A. & SIGRIST, S. J. 2018. Vesicle release site organization at synaptic active zones. *Neurosci Res*, 127, 3-13.
- WANG, H. Y., LIN, W., DYCK, J. A., YEAKLEY, J. M., SONGYANG, Z., CANTLEY, L. C. & FU, X. D. 1998. SRPK2: a differentially expressed SR protein-specific kinase involved in mediating the interaction and localization of pre-mRNA splicing factors in mammalian cells. *J Cell Biol*, 140, 737-50.
- WANG, S. S. H., HELD, R. G., WONG, M. Y., LIU, C. L., KARAKHANYAN, A. & KAESER, P. S. 2016. Fusion Competent Synaptic Vesicles Persist upon Active Zone Disruption and Loss of Vesicle Docking. *Neuron*, 91, 777-791.
- WANG, Y., LIU, X., BIEDERER, T. & SUDHOF, T. C. 2002. A family of RIM-binding proteins regulated by alternative splicing: Implications for the genesis of synaptic active zones. *Proc Natl Acad Sci U S A*, 99, 14464-9.
- WANG, Y., SUGITA, S. & SUDHOF, T. C. 2000. The RIM/NIM family of neuronal C2 domain proteins. Interactions with Rab3 and a new class of Src homology 3 domain proteins. *J Biol Chem*, 275, 20033-44.
- WARD, A. B., SALI, A. & WILSON, I. A. 2013. Biochemistry. Integrative structural biology. *Science*, 339, 913-5.
- WEBB, B., VISWANATH, S., BONOMI, M., PELLARIN, R., GREENBERG, C. H., SALTZBERG, D. & SALI, A. 2018. Integrative structure modeling with the Integrative Modeling Platform. *Protein Science*, 27, 245-258.
- WENTZEL, C., SOMMER, J. E., NAIR, R., STIEFVATER, A., SIBARITA, J. B. & SCHEIFFELE, P. 2013. mSYD1A, a mammalian synapse-defective-1 protein, regulates synaptogenic signaling and vesicle docking. *Neuron*, 78, 1012-23.
- WORSECK, J. M., GROSSMANN, A., WEIMANN, M., HEGELE, A. & STELZL, U. 2012. A stringent yeast two-hybrid matrix screening approach for protein-protein interaction discovery. *Methods Mol Biol*, 812, 63-87.
- WU, Y., YANG, Y., YE, S. & JIANG, Y. 2010. Structure of the gating ring from the human large-conductance Ca(2+)-gated K(+) channel. *Nature*, 466, 393-7.
- WU, YE E., HUO, L., MAEDER, CELINE I., FENG, W. & SHEN, K. 2013. The Balance between Capture and Dissociation of Presynaptic Proteins Controls the Spatial Distribution of Synapses. *Neuron*, 78, 994-1011.
- XU, J., CAMACHO, M., XU, Y., ESSER, V., LIU, X., TRIMBUCH, T., PAN, Y.-Z., MA, C., TOMCHICK, D. R., ROSENMUND, C. & RIZO, J. 2017. Mechanistic insights into neurotransmitter release and presynaptic plasticity from the crystal structure of Munc13-1 C1C2BMUN. *eLife*, 6, e22567.
- XU, Y., KERSHAW, N. J., LUO, C. S., SOO, P., POCOCK, M. J., CZABOTAR, P. E., HILTON, D. J., NICOLA, N. A., GARRETT, T. P. & ZHANG, J. G. 2010. Crystal structure of the entire ectodomain of gp130: insights into the molecular assembly of the tall cytokine receptor complexes. *J Biol Chem*, 285, 21214-8.
- YUAN, P., LEONETTI, M. D., HSIUNG, Y. & MACKINNON, R. 2011. Open structure of the Ca²⁺ gating ring in the high-conductance Ca²⁺-activated K⁺ channel. *Nature*, 481, 94.
- ZHAI, R. G., VARDINON-FRIEDMAN, H., CASES-LANGHOFF, C., BECKER, B., GUNDELFINGER, E. D., ZIV, N. E. & GARNER, C. C. 2001. Assembling the Presynaptic Active Zone: A Characterization of an Active Zone Precursor Vesicle. *Neuron*, 29, 131-143.

References

ZHOU, Z. & FU, X. D. 2013. Regulation of splicing by SR proteins and SR protein-specific kinases. *Chromosoma*, 122, 191-207.

Abbreviations

(M)Unc13	(mammalian)uncoordinated-13
AP	action potential
AZ	active zone
BRP	Bruchpilot
<i>C. elegans</i>	<i>Caenorhabditis elegans</i>
CAZ	cytomatrix at the active zone
CD	circular dichroism
CNS	central nervous system
<i>E. coli</i>	<i>Escherichia coli</i>
kDa	kilodalton
LC-ESI-MS	liquid chromatography electrospray ionization mass spectrometry
MALDI-TOF-MS	matrix-assisted laser desorption/ionization time-of-flight mass spectrometry
MALS	multiangle light scattering
MT	microtubule
NMJ	neuromuscular junction
NT	neurotransmitter
PPI	protein-protein interaction
PSD	postsynaptic density
RIM	Rab3 interacting molecule
RIM-BP	Rim-binding protein
RRP	readily releasable pool
SDS-PAGE	sodium dodecyl sulfate polyacrylamid gel electrophoresis
SEC	size-exclusion chromatography
SRPK79D	serine arginine protein kinase at cytological position 79D
SV	synaptic vesicle
Syd-1	synapse defective 1
VGCC	voltage gated calcium channel

List of Figures and Tables

Figure 1 The Chemical Synapse.....	8
Figure 2 Morphology of active zones.....	9
Figure 3 The synaptic active zone scaffold	11
Figure 4 Axonal transport of AZ precursors.....	18
Figure 5 SRPK family.....	19
Figure 6 Y2H interaction network of the <i>Drosophila</i> active zone.....	23
Figure 7 The Bruchpilot isoforms BRP-190 and BRP-170	24
Figure 8 Domain architecture of BRP-190 isoform with mapped Y2H interactions.....	26
Figure 9 Bruchpilot binding and phosphorylation by SRPK79D.....	28
Figure 10 Identification of phosphorylation sites in BRP	29
Figure 11 Characterization of the axonal aggregates.....	30
Figure 12 Central dimerization region in Bruchpilot	32
Figure 13 Structure of Rab2 and Rab3.....	33
Figure 14 Domain architecture of RIM-BP with mapped Y2H interactions.....	35
Figure 15 Circular Dichroisms spectroscopy of the RIM-BP NTD	36
Figure 16 Characterization of SH3-II and SH3-III binding to Aplip1, Cacophony and RIM.....	39
Figure 17 Structure of the three FN-III domains in RIM-BP.....	41
Figure 18 Characterization of the Spn-PDZ interaction with NrX-1	44
Figure 19 Conservation of the Spn-PDZ domain and the NrX-1 C-terminus.....	45
Table 1 Yeast-two hybrid results for Unc13 isoforms	47

Acknowledgment

First of all, I would like to thank Prof. Dr. Markus Wahl for giving me the opportunity to work on this project and for his support and great ideas on the project. I would also like to thank Prof. Dr. Stephan Sigrist for the pleasant collaboration on the AZ project, for all the productive meetings and for providing the scientific background on the topic.

I enjoyed the time I spent in the AG Wahl and I would like to thank all the people for providing such a nice working atmosphere, many fruitful discussions and all the support during that time. Especially I would like to thank Dr. Bernhard Loll for teaching me a lot on crystallography and for his supervision, constant support and for reviewing my thesis. Special thanks also to Nicole Holton for all her support on the project and Steffi Habibi for starting this project. I would like to thank Jennifer Lardong, Dr. Eva Absmeier, Dr. Jan Wollenhaupt, Francesca De Bortoli and the students that worked with me on this project. Thanks also to Claudia Alings, Clemens Langner, Karin Hesse and Carsten Jakob for keeping everything running in the lab. During my time in the AG Wahl I was very happy to meet my wife, Ronja Driller, and I would like to give huge thanks and a big kiss to her for all support and critical reviewing of my thesis.

I would also like to thank all my collaborators in the AG Sigrist especially Dr. Janine Lützkendorf, Dr. Harald Depner and Dr. Astrid Petzold. Thanks also to Prof. Dr. Ulrich Stelzl for letting me work in his lab and for all his help on analyzing the Y2H data.

Big thanks to my collaborators in the mass spectrometry facility Dr. Christoph Weise and Dr. Benno Kuroпка and to my collaborators on projects not related to this thesis, Prof. Dr. Christian Freund and Dr. Fabian Gerth.

Last but not least, I would like to thank my family and friends for all their support and for cheering me up during my PhD.

Publication I

Lardong, J. A., J. H. Driller, H. Depner, C. Weise, A. Petzoldt, M. C. Wahl, S. J. Sigrist and B. Loll
(2015). "Structures of *Drosophila melanogaster* Rab2 and Rab3 bound to GMPPNP" *Acta
Crystallogr F Struct Biol Commun* 71(Pt 1): 34-40.

Acta Crystallographica Section F

**Structural Biology
Communications**

ISSN 2053-230X

Structures of *Drosophila melanogaster* Rab2 and Rab3 bound to GMPPNP

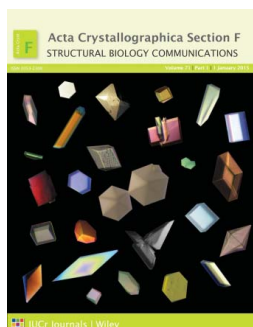
Jennifer A. Lardong, Jan H. Driller, Harald Depner, Christoph Weise, Astrid Petzoldt, Markus C. Wahl, Stephan J. Sigrist and Bernhard Loll

Acta Cryst. (2015). F71, 34–40

Copyright © International Union of Crystallography

Author(s) of this paper may load this reprint on their own web site or institutional repository provided that this cover page is retained. Republication of this article or its storage in electronic databases other than as specified above is not permitted without prior permission in writing from the IUCr.

For further information see <http://journals.iucr.org/services/authorrights.html>



Acta Crystallographica Section F: Structural Biology Communications is a rapid all-electronic journal, which provides a home for short communications on the crystallization and structure of biological macromolecules. Structures determined through structural genomics initiatives or from iterative studies such as those used in the pharmaceutical industry are particularly welcomed. Articles are available online when ready, making publication as fast as possible, and include unlimited free colour illustrations, movies and other enhancements. The editorial process is completely electronic with respect to deposition, submission, refereeing and publication.

Crystallography Journals **Online** is available from journals.iucr.org

Jennifer A. Lardong,^a Jan H. Driller,^a Harald Depner,^{b,c} Christoph Weise,^d Astrid Petzoldt,^{b,c} Markus C. Wahl,^a Stephan J. Sigrist^{b,c,*} and Bernhard Loll^{a,*}

^aInstitut für Chemie und Biochemie Abteilung Strukturbiochemie, Freie Universität Berlin, Takustrasse 6, 15195 Berlin, Germany,

^bBiologie Abteilung Genetik, Freie Universität Berlin, Takustrasse 6, 15195 Berlin, Germany,

^cNeuroCure Cluster of Excellence, Charité Universitätsmedizin Berlin, Virchowweg 6, 10117 Berlin, Germany, and ^dInstitut für Chemie und Biochemie, BioSupraMol Core Facility, Freie Universität Berlin, Thielallee 63, 15195 Berlin, Germany

Correspondence e-mail: stephan.sigrist@fu-berlin.de, loll@chemie.fu-berlin.de

Received 13 October 2014
Accepted 28 November 2014

PDB references: Rab3, 4rkf; Rab2, 4rke

Structures of *Drosophila melanogaster* Rab2 and Rab3 bound to GMPPNP

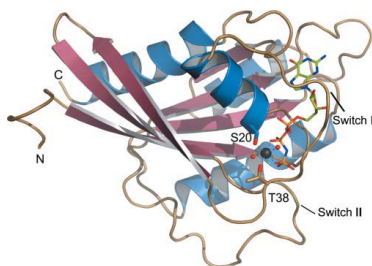
Rab GTPases belong to the large family of Ras proteins. They act as key regulators of membrane organization and intracellular trafficking. Functionally, they act as switches. In the active GTP-bound form they can bind to effector proteins to facilitate the delivery of transport vesicles. Upon stimulation, the GTP is hydrolyzed and the Rab proteins undergo conformational changes in their switch regions. This study focuses on Rab2 and Rab3 from *Drosophila melanogaster*. Whereas Rab2 is involved in vesicle transport between the Golgi and the endoplasmic reticulum, Rab3 is a key player in exocytosis, and in the synapse it is involved in the assembly of the presynaptic active zone. Here, high-resolution crystal structures of Rab2 and Rab3 in complex with GMPPNP and Mg²⁺ are presented. In the structure of Rab3 a modified cysteine residue is observed with an enigmatic electron density attached to its thiol function.

1. Introduction

Rab proteins are small monomeric GTP-binding proteins (GTPases) which constitute the largest branch of the Ras superfamily (Pereira-Leal & Seabra, 2000). They are evolutionarily conserved, with 55–75% identity between orthologues from yeast to mammals. More than 70 different Rab proteins are encoded in the *Homo sapiens* genome (Zerial & McBride, 2001; Bhui & Roy, 2014), 11 in *Saccharomyces cerevisiae* (Lazar *et al.*, 1997), 29 in *Caenorhabditis elegans* (Pereira-Leal & Seabra, 2000), 57 in *Arabidopsis thaliana* (Vernoud *et al.*, 2003) and about 33 in *Drosophila melanogaster* (Chan *et al.*, 2011). Rab GTPases act as key regulators of membrane organization and intracellular trafficking in all eukaryotic cells (Pfeffer, 1994; Zerial & McBride, 2001; Stenmark, 2009; Bhui & Roy, 2014), and as such take part in vesicle formation, motility, tethering and fusion of the vesicles with their target membrane (Zerial & McBride, 2001; Pfeffer, 2007). These functions are carried out by a diverse collection of effector molecules, which are recruited by specific Rab proteins, owing to their role as molecular switches. Thus, Rab proteins regulate their particular pathways by interacting with various effector proteins.

In their function as molecular switches, Rab proteins undergo two alternate conformational transitions upon binding to either GDP or GTP. Firstly, the protein is activated by a guanine-exchange factor (GEF), which exchanges GDP for GTP. In the GTP-bound active form, each Rab can interact with a different set of proteins (effectors) to facilitate the delivery of transport vesicles to different acceptor membranes (Molendijk *et al.*, 2004). While in this conformation, Rabs can associate with their target membrane and interact with their effectors to recruit them to specific subcellular compartments or to activate them. Upon stimulation by GTPase-activating proteins (GAPs) the GTP is hydrolyzed, releasing an inorganic phosphate group, and the now inactive Rab returns to the cytosol. Owing to the identical mechanisms of effector binding and nucleotide exchange and hydrolysis, Rabs share a conserved and well characterized fold with most of the small GTPase family members.

The tertiary structure is composed of a six-stranded β -sheet surrounded by α -helices. Extensive analyses of other GTPases have defined two regions, termed switches I and II, located near the phosphate region of the bound guanine nucleotide (Dumas *et al.*, 1999; Ostermeier & Brunger, 1999). These regions undergo dramatic



© 2015 International Union of Crystallography
All rights reserved © 2015 International Union of

Table 1
Macromolecule-production information.

	<i>dmRab2</i> ^{O65L}	<i>dmRab3</i> ^{O80L}
Source organism	<i>D. melanogaster</i>	<i>D. melanogaster</i>
DNA source	cDNA	cDNA
Forward primer	ACCATGGGATGCTCTACGGTACTTG	TATACCATGGGCATGGCGAGTGGCG
Reverse primer	TATAGTCGACTCACTGGATCTTCTCGTAAATC	TATAGTCGACTCACTGGACATCTTATCG
Expression vector	pET-MBP	pET-MBP
Expression host	<i>E. coli</i>	<i>E. coli</i>
Complete amino-acid sequence of the construct produced†	GAMSYAYLFKYIIIGDGTGVGKSCLLQLQFTDKRFQPVHDLTIGVEFGARMITIDGKQ- IKLQIWDTAGLEAFRSITRSYYRGAAGALLVYDITRRETFNHLTTWLEDARQHS- NSNMVIMLIGNKSDLRSREVKKEGEAFAREHGLVFMETSARTAAANVEEAFIN- TAKEIYEKIQ	GAMASGGDPKWQKDAADQNFDFYMKLLIIGNSSVKGTSFLFRYADDSFTSAFVSTV- GIDFKVKTVFRHDKRVKQLQIWDTAGLERVRTITATAYRGAMGFILMYDVTNEDS- FNSVQDWTQIKTYSWDNAQVILVGNKCDMEDQRVISFERGRQLADQLGVEFFE- TSAKENVNVKAVFERLVDIICDKMSE

† The remaining tag sequence after TEV cleavage is underlined.

Table 2
Crystallization.

	<i>dmRab2</i> ^{O65L}	<i>dmRab3</i> ^{O80L}
Method	Sitting-drop vapour diffusion	Sitting-drop vapour diffusion
Plate type	Cryschem plate	Cryschem plate
Temperature (K)	291	291
Protein concentration (mg ml ⁻¹)	50	40
Buffer composition of protein solution	200 mM NaCl, 20 mM HEPES pH 7.5, 5 mM magnesium acetate, 2 mM DTT, 2% (v/v) glycerol	200 mM NaCl, 20 mM HEPES pH 7.5, 5 mM magnesium acetate, 2 mM DTT, 2% (v/v) glycerol
Composition of reservoir solution	34% (v/v) polyethylene glycol (PEG) 400, 200 mM sodium acetate pH 4.6	28% (v/v) PEG 200, 5% (w/v) PEG 3000, 100 mM MES buffer pH 6.0
Volume and ratio of drop	1:1	1:1
Volume of reservoir (µl)	600	600

conformational changes on nucleotide exchange and are involved in protein–protein interactions; hence, they account for the nucleotide-dependency of most GTPase interactions (Bhuin & Roy, 2014; Sprang, 1997). In the GDP-bound form these regions are highly disordered and thus inactive. They only become ordered upon GTP binding and then expose a triad of hydrophobic amino acids to the surface of the protein. This triad, together with other residues of the switch I and switch II regions, is crucial for the interaction of the Rabs with their respective effector proteins, and this is thought to define the specificity of Rabs for their different effector partners (Merithew *et al.*, 2001; Eathiraj *et al.*, 2005; Burguete *et al.*, 2008).

Rab2 has been identified as a specific regulator of vesicle transport between the Golgi and the endoplasmic reticulum (Liu & Storrer, 2012; Stenmark, 2009) with several known effector proteins, including GM130 and golgin-45 (Short *et al.*, 2001). For instance, Rab2 is able to promote the recruitment of COP I vesicles by binding to its effector PKC 1/λ (Tisdale, 2000). Furthermore, Tisdale and Balch showed that the amino-terminus of Rab2 might be involved in the maturation of pre-Golgi intermediates (Tisdale & Balch, 1996).

Rab3 is one of the most investigated Rab GTPases in the context of neuronal functions. It has been identified as a specific regulator in the exocytosis of secretory granules, including synaptic vesicles and vesicles, from the trans-Golgi-network to apico-lateral membranes (Stenmark, 2009; Bhuin & Roy, 2014). There are several known effector proteins of Rab3, including RIM, which plays a role in synaptic vesicle trafficking (Wang *et al.*, 1997). In *Drosophila* Rab3 seems to have a different function at the synapse: not synaptic vesicle trafficking but rather the trafficking of membrane/cargo for assembly of the presynaptic active-zone cytomatrix (Graf *et al.*, 2009).

2. Materials and methods

2.1. Macromolecule production

The cDNAs for full-length *D. melanogaster* Rab2 (*dmRab2*) and Rab3 (*dmRab3*) were purchased from the *Drosophila* Genomics

Resource Center. The Rab2 and Rab3 genes were amplified by polymerase chain reaction and cloned into the pET-MBP vector using *NcoI* and *SalI* restriction sites (Table 1). The resulting constructs comprise an N-terminal MBP tag followed by a *Tobacco etch virus* (TEV) protease cleavage site followed by the N-terminal GTPase domain of *dmRab2* (amino acids 1–172) and *dmRab3* (amino acids 1–188), respectively. These construct boundaries were chosen based on bioinformatic analysis of deposited GTPase structures in the Protein Data Bank. Furthermore, the conserved glutamine (*dmRab2* Gln65 and *dmRab3* Gln80) located in the switch II region and involved in transition-state stabilization (Privé *et al.*, 1992; Der *et al.*, 1986) was mutated to a leucine. Rab mutants were prepared by site-directed mutagenesis according to the manufacturer’s protocol (EURX ‘Site-directed mutagenesis’). The correctness of the DNA sequences was confirmed by DNA sequencing.

2.2. Protein expression and purification

Protein expression was conducted using chemically competent *Escherichia coli* Rosetta cells. The cells were grown in autoinduction ZY medium (Studier, 2005) with kanamycin and chloramphenicol for 4 h at 37°C. The temperature was then decreased to 18°C and the cells were grown overnight. The cells were harvested by centrifugation and the cell pellet was resuspended in resuspension buffer [200 mM NaCl, 20 mM HEPES pH 7.5, 5 mM magnesium acetate, 2 mM DTT, 2% (v/v) glycerol, 10 mg l⁻¹ lysozyme, 5 mg l⁻¹ DNase I] and subsequently lysed by sonication for 15 min. The lysate was centrifuged at 56 000g for 45 min to pellet the cell debris. The supernatant was applied to affinity chromatography using a column packed with 20 ml amylose resin (NEB). The average incubation time was 1 h. Two washing steps were then performed using 50 ml washing buffer [200 mM NaCl, 20 mM HEPES pH 7.5, 5 mM magnesium acetate, 2 mM DTT, 2% (v/v) glycerol] for each step. For elution, the amylose resin was incubated with 20 ml washing buffer supplemented with 20 mM maltose for 15 min. The MBP tag of the truncated *dmRab* constructs was cleaved off using TEV protease (1 mg ml⁻¹)

Table 3
Data collection and processing.

Values in parentheses are for the highest resolution shell.

	<i>dmRab2</i> ^{O65L} -GMPPNP	<i>dmRab3</i> ^{O80L} -GMPPNP
Diffraction source	BESSY 14.3	BESSY 14.3
Wavelength (Å)	0.895	0.895
Temperature (K)	100	100
Detector	Rayonix MX-225	Rayonix MX-225
Crystal-to-detector distance (mm)	230	145
Rotation range per image (°)	1.0	0.5
Total rotation range (°)	100	110
Exposure time per image (s)	5.2	12
Space group	<i>P</i> 3 ₁ 21	<i>P</i> 2 ₁ 2 ₁ 2 ₁
<i>a</i> , <i>b</i> , <i>c</i> (Å)	81.4, 81.4, 53.1	37.2, 80.5, 123.9
α , β , γ (°)	90.0, 90.0, 120.0	90.0, 90.0, 90.0
Mosaicity (°)	0.2	0.1
Resolution (Å)	50.00–2.00 (2.12–2.00)	50.00–1.50 (1.54–1.50)
Total No. of reflections	70633	222056
No. of unique reflections	13981 (2209)	60482 (4425)
Completeness (%)	99.8 (99.2)	99.9 (100.0)
Multiplicity	5.0 (5.0)	3.7 (3.7)
$\langle I/\sigma(I) \rangle$	7.9 (1.8)	12.9 (2.6)
$R_{\text{meas}}^{\dagger}$	0.216 (0.989)	0.082 (0.616)
$CC_{1/2}^{\ddagger}$	99.0 (72.4)	99.8 (75.0)
Wilson <i>B</i> (Å ²)	25.7	19.7

$\dagger R_{\text{meas}} = \sum_{hkl} |N(hkl) - \langle N(hkl) \rangle| / \sum_{hkl} N(hkl)$, where $\langle N(hkl) \rangle$ is the mean intensity of symmetry-equivalent reflections and $N(hkl)$ is the redundancy. \ddagger The high-resolution cutoff was estimated using $CC_{1/2}$.

in the presence of 100 μM guanosine 5'-(β,γ -imido)triphosphate (GMPPNP; Jena Bioscience). The protease was added to the eluted protein at a molar ratio of 1:25 and the reaction was incubated at 4°C overnight. TEV-cleaved constructs were purified using a Superdex 75 26/60 column (GE Healthcare). The protein-containing fractions were pooled and concentrated using a 10 kDa molecular-weight cutoff concentrator (Millipore). The progress of protein purification was monitored by SDS-PAGE. Protein concentrations were determined by UV absorption with extinction coefficients $\epsilon(\text{Rab2}) = 21\,430\text{ l mol}^{-1}\text{ cm}^{-1}$ and $\epsilon(\text{Rab3}) = 32\,430\text{ l mol}^{-1}\text{ cm}^{-1}$, respectively.

2.3. Crystallization

For crystallization experiments, *dmRab2*^{O65L} was concentrated to 50 mg ml⁻¹ and *dmRab3*^{O80L} to 40 mg ml⁻¹ and they were incubated with equimolar concentrations of GMPPNP (Jena Bioscience) prior to crystallization. Crystals were obtained by the sitting-drop vapour-diffusion method at 291 K with drops consisting of 1 μl reservoir solution and 1 μl protein solution (Table 2). No additional cryoprotection was necessary for flash-cooling the crystals in liquid nitrogen.

2.4. Data collection and indexing, structure determination and refinement

Synchrotron diffraction data were collected on beamline 14.3 of the MX Joint Berlin laboratory at BESSY, Berlin, Germany. X-ray data collection was performed at 100 K. Diffraction data were indexed and processed with *XDS* (Kabsch, 2010; Table 3).

2.5. Structure solution and refinement

The structure of *dmRab3*^{O80L} was solved by molecular replacement using *Phaser* (McCoy *et al.*, 2007) with the known structure of Rab3A from *Rattus norvegicus* (*rnRab3A*; PDB entry 3rab) as a search model (Dumas *et al.*, 1999). The structure of *dmRab2*^{O65L} was solved by molecular replacement using our initially solved structure of *dmRab3*^{O80L}. For the calculation of the free *R* factor, a randomly generated set of 5% of the reflections from the diffraction data sets was used and was excluded from the refinement. The structures were

Table 4
Structure solution and refinement.

Values in parentheses are for the highest resolution shell.

	<i>dmRab2</i> ^{O65L} -GMPPNP	<i>dmRab3</i> ^{O80L} -GMPPNP
Resolution range (Å)	42.4–2.0	38.3–1.5
Completeness (%)	99.8	99.7
No. of reflections, working set	132267	57442
No. of reflections, test set	699	3025
Final $R_{\text{work}}^{\dagger}$	0.167 (0.237)	0.157 (0.206)
Final $R_{\text{free}}^{\ddagger}$	0.224 (0.313)	0.194 (0.237)
No. of non H-atoms		
Protein	1412	2964
Mg ²⁺	1	2
GMPPNP	32	64
PEG	21	43
Water	113	378
Total	1579	3451
R.m.s. deviation		
Bond lengths (Å)	0.008	0.010
Bond angles (°)	1.10	1.26
Average <i>B</i> factors (Å ²)		
Protein	22.5	16.5
Mg ²⁺	19.6	9.1
GMPPNP	19.7	9.1
PEG	28.3	26.2
Water	28.4	28.7
Ramachandran plot§		
Outliers (%)	0	0
Favoured (%)	97.0	98.4

$\dagger R_{\text{work}} = \sum_{hkl} ||F_{\text{obs}}| - |F_{\text{calc}}|| / \sum_{hkl} |F_{\text{obs}}|$. $\ddagger R_{\text{free}}$ is the same as R_{cryst} but calculated using 5% of the data, which were excluded from refinement. \S As calculated by *MolProbity*.

initially refined by applying a simulated-annealing protocol and in later refinement cycles by maximum-likelihood restrained refinement using *PHENIX* (Adams *et al.*, 2010; Afonine *et al.*, 2012). Model building and water picking was performed with *Coot* (Emsley *et al.*, 2010). The model quality was evaluated with *MolProbity* (Chen *et al.*, 2010) and *PROCHECK* (Laskowski *et al.*, 1993). Secondary-structure elements were assigned with *DSSP* (Kabsch & Sander, 1983). Final refinement statistics are given in Table 4. Figures were prepared using *PyMOL* (DeLano, 2002). The atomic coordinates and structure-factor amplitudes have been deposited in the Protein Data Bank under accession codes 4rke (*dmRab2*^{O65L}) and 4rkf (*dmRab3*^{O80L}).

2.6. Mass spectrometry

Protein masses were analyzed by matrix-assisted laser desorption/ionization–time of flight mass spectrometry (MALDI-TOF MS) using an Ultraflex-II TOF/TOF instrument (Bruker Daltonics, Bremen, Germany) equipped with a 200 Hz solid-state Smart beam laser. The mass spectrometer was operated in the positive linear mode. MS spectra were acquired over an *m/z* range of 5000–25 000 and data were analyzed using the *FlexAnalysis* 2.4 software provided with the instrument. The mass accuracy was estimated to be $\pm 1\%$ in the relevant mass range. Sinapinic acid was used as the matrix and samples were spotted using the dried-droplet technique undiluted and in a 1:5 dilution with 33% acetonitrile/0.1% trifluoroacetic acid.

3. Results

3.1. Expression, crystallization and structure determination

We prepared expression constructs of Rab2 and Rab3 from *D. melanogaster* comprising only the GTPase domain. In addition, we mutated the catalytically important glutamine to leucine, locking both *dmRab2* and *dmRab3* into the activated GTP-bound state (Der *et al.*, 1986; Privé *et al.*, 1992). To unravel the architecture of

dmRab2^{O65L} and *dmRab3*^{O80L}, we overexpressed both proteins in *E. coli* and subsequently purified and crystallized them. We could collect high-resolution data sets to 2.0 Å resolution for *dmRab2*^{O65L} and to 1.5 Å resolution for *dmRab3*^{O80L}. Whereas the *dmRab3*^{O80L} crystals were indexed in space group *P*₂₁₂₁, the *dmRab2*^{O65L} crystals belonged to space group *P*₃₁₂₁ (Tables 3 and 4). Both structures were solved by molecular replacement, locating two *dmRab3*^{O80L} molecules and one *dmRab2*^{O65L} molecule in the asymmetric unit. The structure of *dmRab2*^{O65L} was refined to *R*_{work} = 0.167 and *R*_{free} = 0.224 and that of *dmRab3*^{O80L} to *R*_{work} = 0.157 and *R*_{free} = 0.194 with excellent geometry. Data collection and refinement statistics are given in Tables 3 and 4. The electron density maps for both proteins were well defined; therefore, the model of *dmRab3*^{O80L} could be built except for the 15 N-terminal and the two C-terminal amino acids of the construct. In addition, the structure of *dmRab2*^{O65L} could also be completely modelled, including four amino acids of the N-terminal linker region that remained after TEV cleavage. The initial *2mF*_o - *DF*_c and *mF*_o - *DF*_c electron density maps clearly revealed the localization of GMPPNP and Mg²⁺ (Fig. 2). Moreover, we

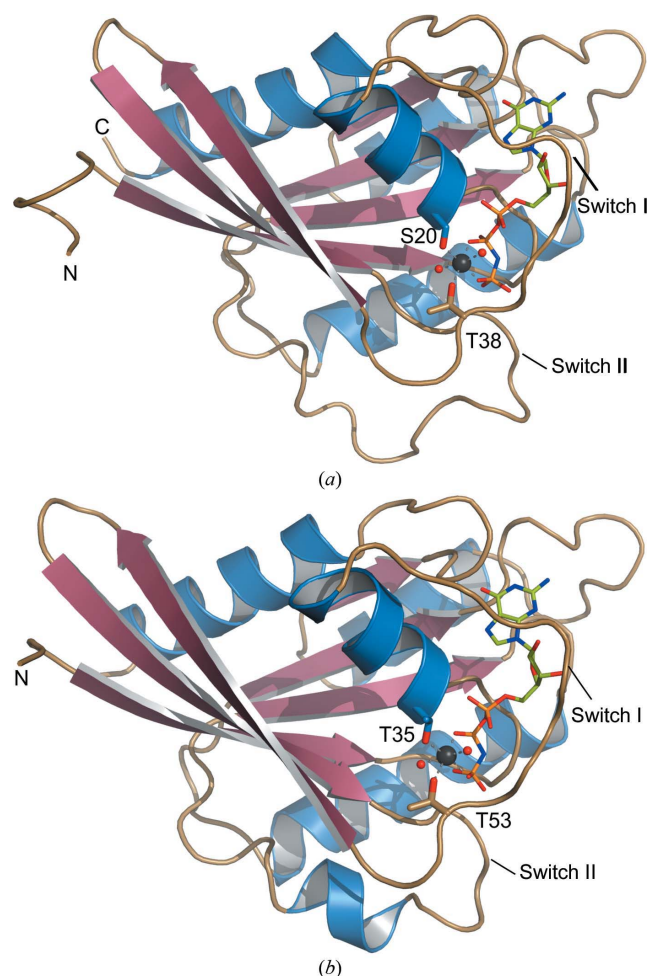


Figure 1
Structures of *dmRab2*^{O65L} and *dmRab3*^{O80L} drawn in cartoon representation. α -Helices are coloured blue, β -strands salmon and connecting loop regions brown. The bound GMPPNP is shown in stick representation, as are the Mg²⁺-coordinating residues. The octahedrally coordinated Mg²⁺ is depicted as a black sphere and coordinating water molecules as red spheres. Grey dashed lines indicate the coordination sphere of Mg²⁺. (a) Structure of *dmRab2*^{O65L}; (b) structure of *dmRab3*^{O80L}.

Table 5

Hydrogen-bonding interactions of GMPPNP in complex with *dmRab2*^{O65L} and *dmRab3*^{O80L}.

Distances ≤ 3.2 Å are given. Canonical interactions of the α - and β -phosphates of GMPPNP with the protein backbone of the P-loops are not listed.

GMPPNP		<i>dmRab2</i> ^{O65L}	Distance (Å)	<i>dmRab3</i> ^{O80L}	Distance (Å)
Guanine base	O6	Ala150 N	2.9	Ala165 N	2.9
	N1	Asp122 OD1	2.8	Asp137 OD1	2.8
	N2	Asp122 OD2	2.8	Asp137 OD2	2.9
	N7	Asn119 ND2	3.1	Asn134 ND2	3.2
Ribose	O2'	Gln32 O	2.8	Thr47 O	2.9
	O2'	Pro33 O	2.8		
	O3'	Pro33 O	3.2	Ser48 O	2.7
γ -Phosphate	O1G	Gly64 N	2.8	Gly79 N	2.8
	O2G	Thr38 N	3.0	Thr53 N	2.8
	O2G	Thr38 OG2	2.7	Thr53 OG2	2.9
	O3G	Thr15 OG2	2.6	Ser30 OG	2.7
	O3G	His35 NE2	2.9	Ser52 OG	2.6

observed electron density in a horseshoe shape that we could interpret as PEG fragments originating from the crystallization cocktail.

3.2. Overall structure

Both proteins are monomeric based on an interface analysis with the PISA server (Krissinel & Henrick, 2007) and in agreement with our experimental size-exclusion chromatography. *dmRab2*^{O65L} and *dmRab3*^{O80L} adopt the classical fold of the Rab family of GTP-binding proteins, with one β -sheet that is composed of six β -strands surrounded by five α -helices (Fig. 1). *dmRab2* and *dmRab3* share 33% sequence identity and 52% similarity. The overall folds are related to the Ras superfamily (Tong *et al.*, 1989; Pai *et al.*, 1989). *dmRab2*^{O65L} and *dmRab3*^{O80L} are practically indistinguishable, with a root-mean-square deviation (r.m.s.d.) of 0.8 Å for 157 pairs of C α atoms. *dmRab2* shares 65% sequence identity and *dmRab3* shares 73% sequence identity with *mRab3A*. The reported structure of *mRab3A* in a GMPPNP-bound form (PDB entry 3rab) superimposes with *dmRab2*^{O65L} and *dmRab3*^{O80L} with an r.m.s.d. of 0.6 Å for 169 pairs of C α atoms. In both structures the switch I and II regions are very well defined (Sprang, 1997; Kjeldgaard *et al.*, 1996) and are involved in a hydrogen-bonding network to stabilize the bound nucleotide and coordinate the Mg²⁺ cation (Fig. 1).

3.3. Nucleotide-binding site of *dmRab2*^{O65L}

The guanine function of GMPPNP bound to *dmRab2*^{O65L} is involved in hydrogen bonding to Ala150, Asp122 and Asn119. The hydroxyl functions are in contact with Gln32 and Pro33 (Table 5). The α - and β -phosphate are stabilized by interactions with the Walker A motif or P-loop (Saraste *et al.*, 1990; Walker *et al.*, 1982). This motif in *dmRab2*^{O65L} is ¹³GDTDVDKS²⁰, with the catalytic Walker A lysine at position Lys19. The switch II region of exocytic Rab GTPase is highly conserved and is found within the region ⁶⁰WDTAGLEAFRSITRSYYRGA⁷⁹ in *dmRab2*^{O65L} (Fig. 1a). The γ -phosphate interacts with Thr15, His35 and Thr38 as well as Gly64 (Table 5). The Mg²⁺ ion is octahedrally coordinated by the hydroxyl functions of Ser20 and Thr38 of *dmRab2*^{O65L}, the β - and γ -phosphate groups of GMPPNP and two water molecules (Fig. 1a and Table 5). The latter two water molecules are embedded in a dense hydrogen-bonding network including Asp36, Thr38, Asp61, Thr62 and the phosphate functions of GMPPNP.

3.4. Nucleotide-binding site of *dmRab3*^{O80L}

The GMPPNP bound to *dmRab3*^{O80L} establishes similar interactions with the protein as described above for *dmRab2*^{O65L}. The

guanine base is hydrogen-bonded to Ala165, Asp137 and Asn134, and the hydroxyls of the ribose moiety are hydrogen-bonded to Ser48 and Thr47 (Table 5). The Walker A motif is established by the motif ²⁸GNSSVGKT³⁵, with the conserved Walker A lysine being Lys34. The side chains of *dmRab2* Lys19 and *dmRab3* Lys34 point to and interact with the O atoms of the β - and γ -phosphates of the bound GMPPNP and hence adopt the so-called ‘conventional’ conformation (Dikfidan *et al.*, 2014). The switch II region of *dmRab3*^{Q80L} comprises the sequence ⁷⁵WDTAGLERTITTTAYRGA⁹⁴ (Fig. 1*b*) and is shorter by two amino-acid residues compared with *dmRab2*^{Q65L}. This difference is reflected in an α -helix within the switch II region in the structure of *dmRab3*^{Q80L}. Switches I and II as well as the inter-switch regions are important in effector protein binding (Ostermeier & Brunger, 1999; Dumas *et al.*, 1999). In the GTP-bound state these regions are well ordered and expose a hydrophobic aromatic triad of residues to the protein surface. In concert with other residues, these residues are believed to define the specificity of different Rabs for different effector molecules (Merithew *et al.*, 2001). The triad is conserved in both *dmRab2*^{Q65L} and *dmRab3*^{Q80L}: Phe43, Trp60 and Tyr75 in *dmRab2*^{Q65L} and Phe58, Trp75 and Tyr90 in *dmRab3*^{Q80L}. All residues are solvent-exposed, with one exception, *dmRab2*^{Q65L} Tyr75, the side chain of which points towards the protein. The γ -phosphate of GMPPNP is hydrogen-bonded to Gly79, Thr53, Ser30 and Ser32 (Table 5). In the *dmRab3*^{Q80L} structure two threonine residues, Thr35 and Thr53, are involved in Mg²⁺ coordination as well as the γ -phosphate groups of GMPPNP and two water molecules (Figs. 1*b* and 2). The latter two water molecules are hydrogen-bonded to Thr35, Asp76, Thr77, Val51 and Thr53.

3.5. Modified cysteine in *dmRab3*^{Q80L}

The free thiol function of cysteine allows a large variety of modifications. Many post-translational modifications such as phosphorylation, *S*-nitrosylation, *S*-glutathionylation, sulfhydration, sulenylation, sulfinic acids, sulfonic acid polyprenylation and sulfenyl-amides are known (Walsh *et al.*, 2005; Chung *et al.*, 2013). On

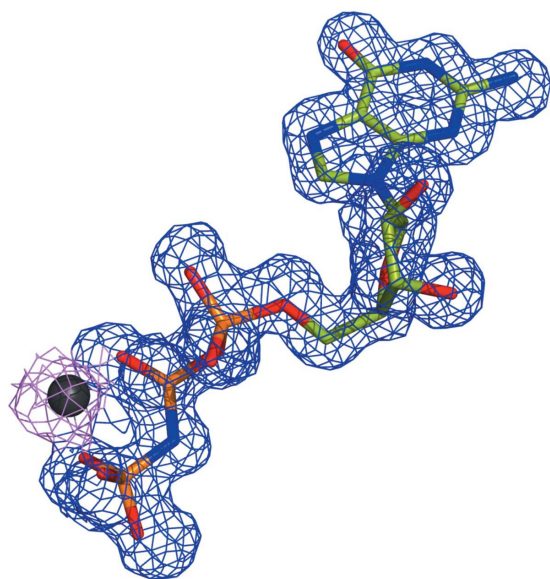


Figure 2
Nucleotide-binding site of *dmRab3*^{Q80L}. $2mF_o - DF_c$ simulated-annealing OMIT map contoured at 1σ shown as a blue mesh for the omitted GMPPNP and in violet for the Mg²⁺ ion. The GMPPNP is shown in stick representation and the Mg²⁺ ion is shown as black sphere.

the other hand, the thiol function is extensively exploited in the context of *in vitro* protein modifications such as fluorescent tagging, paramagnetic spin labelling and many more diverse applications. In the initially calculated electron-density maps we could observe additional electron density attached to Cys183 that resides on the very C-terminal α -helix of *dmRab3*^{Q80L}. The electron density has an approximately twofold rotational symmetry and has a planar shape (Fig. 3). The volume of the electron density is large enough to accommodate six atoms. The unknown electron density is located in a hydrophobic pocket on the surface of the protein formed by the side chains of Tyr20, Phe22, His66, Lys68, Val70 and Met186. The plane of the electron density is parallel to the phenolic ring of Tyr20 (Fig. 3), tentatively establishing a π -interaction with the unknown cysteine modification. Even though DTT was present in our purification buffers, the planarity and symmetry of the electron density rules out a mixed disulfide with DTT. To shed light on the modification, we performed MALDI-TOF MS of the *dmRab3*^{Q80L} protein prior to crystallization. The experimental molecular weight of 21 925 Da is in reasonable agreement with the calculated theoretical mass of

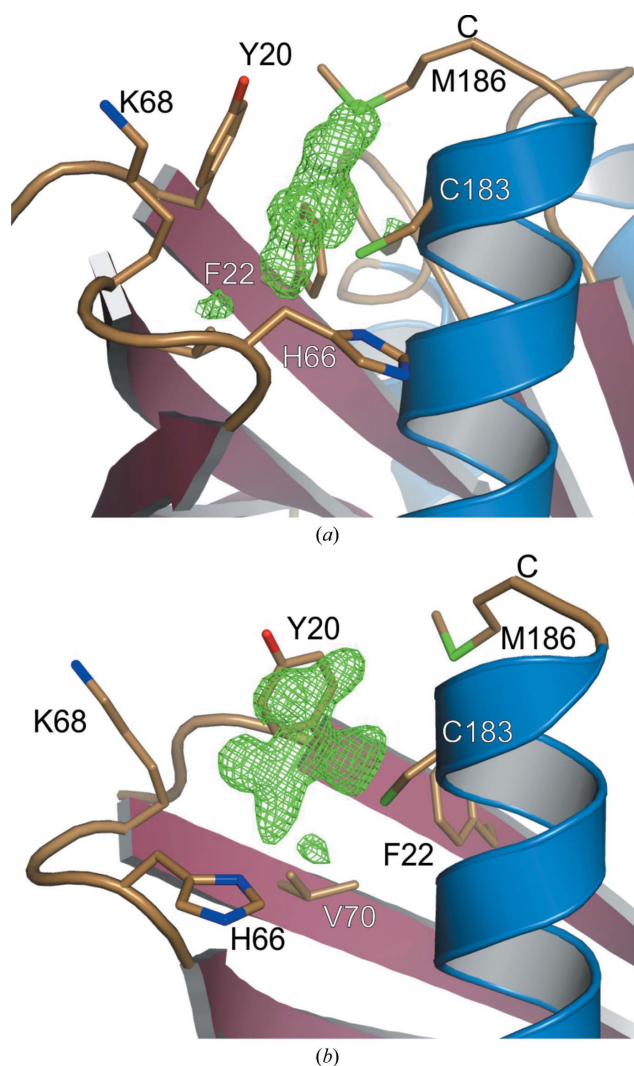


Figure 3
Protein surroundings of Cys183 in *dmRab3*^{Q80L}. (a) $mF_o - DF_c$ electron-density map contoured at 3σ shown as a green mesh. Difference electron density with a planar shape is attached to the S atom of Cys183. (b) The view in (a) rotated by 45° .

21 939 Da. This raised the question of the point in time at which the modification is made. Hence, we washed and dissolved *dmRab3*^{O80L} crystals in water and subjected them to MALDI-TOF MS. We could now see a mass difference of 135 Da compared with the theoretical mass of the protein. Consequently, the thiol modification must take place during the crystallization process. Next, we intended to identify the atom establishing the thiol linkage. We therefore collected a highly redundant, anomalous diffraction data set at 1.7 Å wavelength. We could detect the positions of most of the sulfur atoms of cysteine and methionine amino-acid side chains in the anomalous difference electron density, but no anomalous difference electron density for the atom covalently attached to the thiol of Cys183. It is tempting to speculate about the origin of the modification. Since the modification seems to be nearly complete for Cys183, the only source could be the crystallization cocktail. We can merely speculate that a degradation product of the precipitant PEG 200 might have caused the modification.

4. Discussion

We have determined the crystal structures of constitutively active *dmRab2*^{O65L} and *dmRab3*^{O80L} variants with bound Mg²⁺ and the nonhydrolysable GTP analogue GMPPNP to atomic resolution. Our structures provide information on the residues involved in Mg²⁺ coordination and interaction with GMPPNP. In the crystal structure of *dmRab3*^{O80L} we detected a covalently attached modification at Cys183. The latter modification remains enigmatic and hence has not been modelled in the crystal structure of *dmRab3*^{O80L}.

Our structure of *dmRab2*^{O65L} represents the first crystal structure of a Rab2 protein in the 'GTP'-bound active state and allows comparison with the structure of *mRab2A* (PDB entry 1z0a; Eathiraj *et al.*, 2005) in the GDP-bound state. In the structure of *mRab2A*-GDP the switch I region adopts different conformations in the four copies within the asymmetric unit. In three copies (chains A, B and D) the switch I region is not defined in the electron-density maps and hence is lacking from the model, whereas in one copy (chain C) the entire switch I region could be modelled but with truncated side chains, indicating increased flexibility. *dmRab2*^{O65L} and *mRab2A* share 94% identity and the structures superimpose with an r.m.s.d. of 1.7 Å for 165 pairs of C^α atoms of chain C, whereas for chain A, which lacks residues Pro33–His35, the r.m.s.d. is 1.4 Å for 166 pairs of C^α atoms. The different conformations are likely to be influenced by crystal packing. Major structural differences between *dmRab2*^{O65L} and *mRab2A* are observed in the switch I and II regions (Fig. 4*a*). In the structure of *dmRab2*^{O65L} presented here the switch I region is well defined in the electron density and establishes the expected interactions with the hydroxyl functions of the ribose and the γ-phosphate of the GMPPNP nucleotide (Table 5). Even though the switch I region of *dmRab2*^{O65L} is involved in crystal packing, our structure strongly suggests that the switch I region adopts the conformation of the active state of *dmRab2*. The switch II region undergoes a more drastic conformational change (Fig. 4*a*). By this conformational change it establishes contact with the γ-phosphate of the GMPPNP (Table 5). Again, the observed conformation of the switch II region could be potentially involved in crystal contacts.

dmRab2 and *dmRab3* share 33% sequence identity and the structures of the proteins are nearly identical, with an r.m.s.d. of 0.8 Å for 157 pairs of C^α atoms (Fig. 4*b*). Whereas the conformation of the switch I region of both proteins is very similar, the conformation of the switch II region is altered. In *dmRab3*^{O80L} we observe a α-helix of six residues in length from Arg84 to Ala89 (Fig. 1*b*). In the structure

of *dmRab2*^{O65L} the switch II region adopts a random-coil conformation. Since the switch region is involved in crystal contacts in both structures, we cannot fully exclude a possible influence on their conformation. These observed alterations, especially within the switch II regions, hint at the capability of *dmRab2* and *dmRab3* to bind to different effector proteins.

A potential interaction partner of Rab3A is Bruchpilot, since upon loss of Rab3 Bruchpilot is dramatically reduced (Graf *et al.*, 2009). Bruchpilot acts as one of the main scaffolding proteins that decorate the intracellular face of the active zone in *Drosophila* where synaptic vesicles fuse with the membrane (Haucke *et al.*, 2011; Kittel *et al.*, 2006; Liu *et al.*, 2011). Bruchpilot is critical for the structural integrity and functionality of the active zone. Graf and coworkers showed that the Rab3 GTPase is essential for correct assembly of the active zone in *Drosophila* (Graf *et al.*, 2009). Owing to their described properties and function in vesicular transport, the question arose of whether Rab GTPases might interact with active zone proteins in synaptic vesicle tethering. In future experiments, we would like to shed light

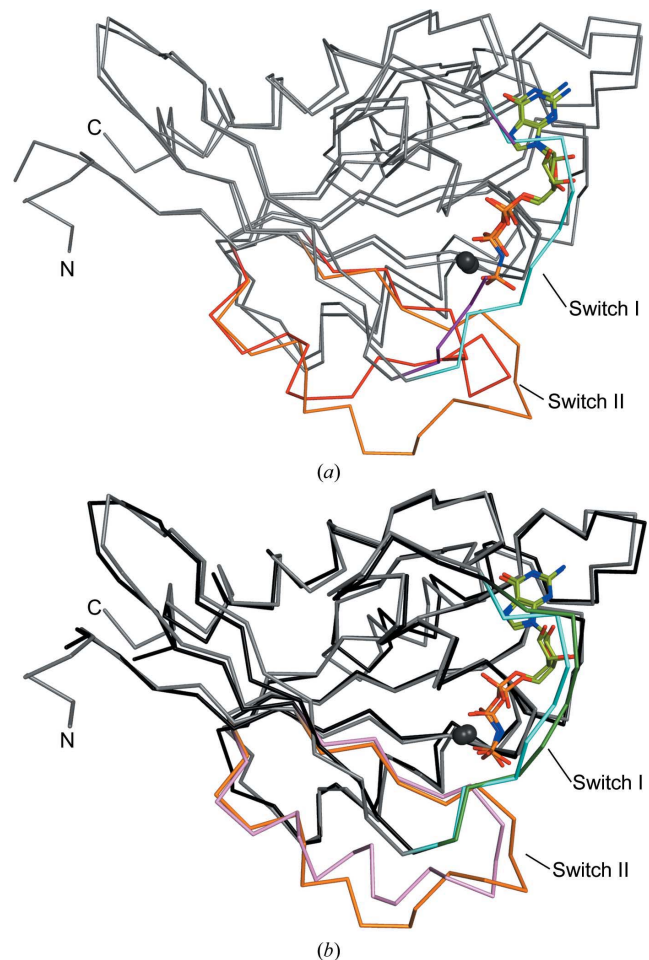


Figure 4
Superposition of different Rab structures shown in ribbon presentation. (a) Superposition of *mRab2A* (PDB entry 1z0a, chain A) bound to GDP and *dmRab2* bound to GMPPNP. The switch I and switch II regions of *mRab2A*-GDP are coloured purple and orange, respectively, whereas the switch I and switch II regions of *dmRab2A*-GMPPNP are coloured light blue and red, respectively. (b) Superposition of *dmRab2A* (grey ribbon) and *dmRab3A* (black ribbon) both in the GMPPNP-bound state. The switch regions of *dmRab2A* are coloured as in (a). The switch I and switch II regions of *dmRab3A* are coloured green and pink, respectively.

on these possible interactions by using our Rab GTPase constructs in pull-down experiments.

All authors are grateful to the Deutsche Forschungsgemeinschaft for grants SFB958/A3, A6 and Z3. We accessed the beamlines of BESSY II (Berliner Elektronenspeicherring-Gesellschaft für Synchrotronstrahlung II storage ring, Berlin, Germany) via the Joint Berlin MX-Laboratory sponsored by the Helmholtz Zentrum Berlin für Materialien und Energie, the Freie Universität Berlin, the Humboldt-Universität zu Berlin, the Max-Delbrück Centrum and the Leibniz-Institut für Molekulare Pharmakologie.

References

- Adams, P. D. *et al.* (2010). *Acta Cryst.* **D66**, 213–221.
- Afonine, P. V., Grosse-Kunstleve, R. W., Echols, N., Headd, J. J., Moriarty, N. W., Mustyakimov, M., Terwilliger, T. C., Urzhumtsev, A., Zwart, P. H. & Adams, P. D. (2012). *Acta Cryst.* **D68**, 352–367.
- Bhuni, T. & Roy, J. K. (2014). *Exp. Cell Res.* **328**, 1–19.
- Burgute, A. S., Fenn, T. D., Brunger, A. T. & Pfeffer, S. R. (2008). *Cell*, **132**, 286–298.
- Chan, C.-C., Scoggin, S., Wang, D., Cherry, S., Dembo, T., Greenberg, B., Jin, E. J., Kuey, C., Lopez, A., Mehta, S. Q., Perkins, T. J., Brankatschk, M., Rothenfluh, A., Buszczak, M. & Hiesinger, P. R. (2011). *Curr. Biol.* **21**, 1704–1715.
- Chen, V. B., Arendall, W. B., Headd, J. J., Keedy, D. A., Immormino, R. M., Kapral, G. J., Murray, L. W., Richardson, J. S. & Richardson, D. C. (2010). *Acta Cryst.* **D66**, 12–21.
- Chung, H. S., Wang, S.-B., Venkatraman, V., Murray, C. I. & Van Eyk, J. E. (2013). *Circ. Res.* **112**, 382–392.
- DeLano, W. (2002). *PyMOL*. <http://www.pymol.org>.
- Der, C. J., Finkel, T. & Cooper, G. M. (1986). *Cell*, **44**, 167–176.
- Dikfidan, A., Loll, B., Zeymer, C., Magler, I., Clausen, T. & Meinhart, A. (2014). *Mol. Cell*, **54**, 975–986.
- Dumas, J. J., Zhu, Z., Connolly, J. L. & Lambright, D. G. (1999). *Structure*, **7**, 413–423.
- Eathiraj, S., Pan, X., Ritacco, C. & Lambright, D. G. (2005). *Nature (London)*, **436**, 415–419.
- Emsley, P., Lohkamp, B., Scott, W. G. & Cowtan, K. (2010). *Acta Cryst.* **D66**, 486–501.
- Graf, E. R., Daniels, R. W., Burgess, R. W., Schwarz, T. L. & DiAntonio, A. (2009). *Neuron*, **64**, 663–677.
- Hauke, V., Neher, E. & Sigrist, S. J. (2011). *Nature Rev. Neurosci.* **12**, 127–138.
- Kabsch, W. (2010). *Acta Cryst.* **D66**, 125–132.
- Kabsch, W. & Sander, C. (1983). *Biopolymers*, **22**, 2577–2637.
- Kittel, R. J., Wichmann, C., Rasse, T. M., Fouquet, W., Schmidt, M., Schmid, A., Wagh, D. A., Pawlu, C., Kellner, R. R., Willig, K. I., Hell, S. W., Buchner, E., Heckmann, M. & Sigrist, S. J. (2006). *Science*, **312**, 1051–1054.
- Kjeldgaard, M., Nyborg, J. & Clark, B. F. (1996). *FASEB J.* **10**, 1347–1368.
- Krissinel, E. & Henrick, K. (2007). *J. Mol. Biol.* **372**, 774–797.
- Laskowski, R. A., MacArthur, M. W., Moss, D. S. & Thornton, J. M. (1993). *J. Appl. Cryst.* **26**, 283–291.
- Lazar, T., Götte, M. & Gallwitz, D. (1997). *Trends Biochem. Sci.* **22**, 468–472.
- Liu, K. S. Y. *et al.* (2011). *Science*, **334**, 1565–1569.
- Liu, S. & Storrie, B. (2012). *Cell. Mol. Life Sci.* **69**, 4093–4106.
- McCoy, A. J., Grosse-Kunstleve, R. W., Adams, P. D., Winn, M. D., Storoni, L. C. & Read, R. J. (2007). *J. Appl. Cryst.* **40**, 658–674.
- Merithew, E., Hatherly, S., Dumas, J. J., Lawe, D. C., Heller-Harrison, R. & Lambright, D. G. (2001). *J. Biol. Chem.* **276**, 13982–13988.
- Molendijk, A. J., Ruperti, B. & Palme, K. (2004). *Curr. Opin. Plant Biol.* **7**, 694–700.
- Ostermeier, C. & Brunger, A. T. (1999). *Cell*, **96**, 363–374.
- Pai, E. F., Kabsch, W., Kregel, U., Holmes, K. C., John, J. & Wittinghofer, A. (1989). *Nature (London)*, **341**, 209–214.
- Pereira-Leal, J. B. & Seabra, M. C. (2000). *J. Mol. Biol.* **301**, 1077–1087.
- Pfeffer, S. R. (1994). *Curr. Opin. Cell Biol.* **6**, 522–526.
- Pfeffer, S. R. (2007). *Annu. Rev. Biochem.* **76**, 629–645.
- Privé, G. G., Milburn, M. V., Tong, L., de Vos, A. M., Yamaizumi, Z., Nishimura, S. & Kim, S.-H. (1992). *Proc. Natl Acad. Sci. USA*, **89**, 3649–3653.
- Saraste, M., Sibbald, P. R. & Wittinghofer, A. (1990). *Trends Biochem. Sci.* **15**, 430–434.
- Short, B., Preisinger, C., Körner, R., Kopajtich, R., Byron, O. & Barr, F. A. (2001). *J. Cell Biol.* **155**, 877–883.
- Sprang, S. R. (1997). *Curr. Opin. Struct. Biol.* **7**, 849–856.
- Stenmark, H. (2009). *Nature Rev. Mol. Cell Biol.* **10**, 513–525.
- Studier, F. W. (2005). *Protein Expr. Purif.* **41**, 207–234.
- Tisdale, E. J. (2000). *Traffic*, **1**, 702–712.
- Tisdale, E. J. & Balch, W. E. (1996). *J. Biol. Chem.* **271**, 29372–29379.
- Tong, L., Milburn, M. V., de Vos, A. M. & Kim, S.-H. (1989). *Science*, **245**, 244.
- Vernoud, V., Horton, A. C., Yang, Z. & Nielsen, E. (2003). *Plant Physiol.* **131**, 1191–1208.
- Walker, J. E., Saraste, M., Runswick, M. J. & Gay, N. J. (1982). *EMBO J.* **1**, 945–951.
- Walsh, C. T., Garneau-Tsodikova, S. & Gatto, G. J. (2005). *Angew. Chem. Int. Ed.* **44**, 7342–7372.
- Wang, Y., Okamoto, M., Schmitz, F., Hofmann, K. & Südhof, T. C. (1997). *Nature (London)*, **388**, 593–598.
- Zerial, M. & McBride, H. (2001). *Nature Rev. Mol. Cell Biol.* **2**, 107–117.

Publication II

Siebert, M., M. A. Bohme, J. H. Driller, H. Babikir, M. M. Mampell, U. Rey, N. Ramesh, T. Matkovic, N. Holton, S. Reddy-Alla, F. Gottfert, D. Kamin, C. Quentin, S. Klinedinst, T. F. Andlauer, S. W. Hell, C. A. Collins, M. C. Wahl, B. Loll and S. J. Sigrist (2015). "A high affinity RIM-binding protein/Aplip1 interaction prevents the formation of ectopic axonal active zones" *Elife* 4.

A high affinity RIM-binding protein/Aplip1 interaction prevents the formation of ectopic axonal active zones

Matthias Siebert^{1†}, Mathias A Böhme^{1,2†}, Jan H Driller³, Husam Babikir¹, Malou M Mampell¹, Ulises Rey^{1,4}, Niraja Ramesh¹, Tanja Matkovic¹, Nicole Holton³, Suneel Reddy-Alla¹, Fabian Göttfert⁵, Dirk Kamin⁵, Christine Quentin¹, Susan Klinedinst⁶, Till FM Andlauer¹, Stefan W Hell⁵, Catherine A Collins⁶, Markus C Wahl³, Bernhard Loll³, Stephan J Sigrist^{1,2*}

¹Institute for Biology/Genetics, Freie Universität Berlin, Berlin, Germany; ²NeuroCure, Charité-Universitätsmedizin Berlin, Berlin, Germany; ³Institute of Chemistry and Biochemistry/Structural Biochemistry, Freie Universität Berlin, Berlin, Germany; ⁴Department of Theory and Bio-Systems, Max Planck Institute of Colloids and Interfaces, Potsdam, Germany; ⁵Department of Nanobiophotonics, Max Planck Institute for Biophysical Chemistry, Göttingen, Germany; ⁶Department of Molecular Cellular and Developmental Biology, University of Michigan, Ann Arbor, United States

Abstract Synaptic vesicles (SVs) fuse at active zones (AZs) covered by a protein scaffold, at *Drosophila* synapses comprised of ELKS family member Bruchpilot (BRP) and RIM-binding protein (RBP). We here demonstrate axonal co-transport of BRP and RBP using intravital live imaging, with both proteins co-accumulating in axonal aggregates of several transport mutants. RBP, via its C-terminal Src-homology 3 (SH3) domains, binds Aplip1/JIP1, a transport adaptor involved in kinesin-dependent SV transport. We show in atomic detail that RBP C-terminal SH3 domains bind a proline-rich (PxxP) motif of Aplip1/JIP1 with submicromolar affinity. Pointmutating this PxxP motif provoked formation of ectopic AZ-like structures at axonal membranes. Direct interactions between AZ proteins and transport adaptors seem to provide complex avidity and shield synaptic interaction surfaces of pre-assembled scaffold protein transport complexes, thus, favouring physiological synaptic AZ assembly over premature assembly at axonal membranes.

DOI: [10.7554/eLife.06935.001](https://doi.org/10.7554/eLife.06935.001)

*For correspondence: stephan.sigrist@fu-berlin.de

[†]These authors contributed equally to this work

Competing interests: The authors declare that no competing interests exist.


Funding: See page 26

Received: 09 February 2015

Accepted: 24 July 2015

Published: 14 August 2015

Reviewing editor: Mani Ramaswami, Trinity College Dublin, Ireland

 Copyright Siebert et al. This article is distributed under the terms of the [Creative Commons Attribution License](https://creativecommons.org/licenses/by/4.0/), which permits unrestricted use and redistribution provided that the original author and source are credited.

Introduction

The primary function of the presynaptic active zone (AZ) is to regulate the release of neurotransmitter-filled synaptic vesicles (SVs) in response to action potentials entering the synaptic bouton (*Südhof, 2012*). Before AZ scaffold components (e.g., ELKS family protein Bruchpilot: BRP, Rab3-interacting molecule (RIM)-binding protein: RBP) are integrated into synapses, however, they have to be transported down the often very long axons. AZ scaffold proteins are characterized by strings of interaction motifs (particularly coiled coil motifs) contributing to the avidity and tenacity of synaptic scaffolds (*Tsuriel et al., 2009*). Therefore they might be considered as ‘sticky cargos’ whose association status has to be precisely controlled during transport. Long-range axonal transport is conducted along polarised microtubules, using kinesin-family motor proteins for anterograde and dyneins for retrograde transport (reviewed in *Maeder et al., 2014*). Kinesin-1 family motor kinesin heavy chain (KHC, also known as KIF5; *Sato-Yoshitake et al., 1992; Hurd and Saxton, 1996; Takamori et al., 2006*) and Unc-104/Imac/KIF1 (*Hall and Hedgecock, 1991; Pack-Chung et al., 2007*) have been

eLife digest To pass on information, the neurons that make up the nervous system connect at structures known as synapses. Chemical messengers called neurotransmitters are released from one neuron, and travel across the synapse to trigger a response in the neighbouring cell. The formation of new synapses plays an important role in learning and memory, but many aspects of this process are not well understood.

In a specific region of the synapse called the active zone, a scaffold of proteins helps to release the neurotransmitters. These proteins are made in the cell body of the neuron, and are then transported to the end of the long, thin axons that protrude from the cell body. This presents a challenge for the cell, because the components of the active zone scaffold must be correctly targeted to the synapse at the end of the axon, ensuring the active zone scaffold assembles only at its proper location.

Siebert, Böhme et al. studied how some of the proteins that are found in the active zone scaffold of the fruit fly *Drosophila* are transported along axons. Labelling the proteins with fluorescent markers allowed their movement to be examined under a microscope in living *Drosophila* larvae. The results showed that two of the proteins—known as BRP and RBP—are transported along the axons together. Further investigation revealed that a transport adaptor protein called Aplip1, which binds to RBP, is required for this movement. Siebert, Böhme et al. established the structure of the part of RBP where this interaction occurs, and found that mutating this region causes premature active zone scaffold assembly in the axonal part of the neuron. The interaction between RBP and Aplip1 is very strong, and this helps to prevent the scaffold assembling before it has reached the correct part of the neuron. Exactly how the transport adaptor and active zone protein are separated once they reach their final destination (the synapse) remains to be discovered.

DOI: [10.7554/eLife.06935.002](https://doi.org/10.7554/eLife.06935.002)

implicated in the transport of SVs, in conjunction with regulators of this process, such as Syd-1 (Hallam et al., 2002), Syd-2/Liprin- α (Serra-Pagès et al., 1998; Zhen and Jin, 1999; Miller et al., 2005; Stryker and Johnson, 2007; Wagner et al., 2009), RSY-1 (Patel and Shen, 2009), or ARL-8 (Klassen et al., 2010; Wu et al., 2013). In *Caenorhabditis elegans*, SV and AZ scaffold proteins exhibit extensive co-transport and undergo frequent pauses, with immobile phases promoting cargo dissociation and assembly (Wu et al., 2013). Long axons, typical for *Drosophila* or mammals, pose high demands for the ‘processivity’ of axonal AZ scaffold component transport. The molecular mechanisms, which provide this processivity and thus block premature assembly processes remain speculative, but might also be relevant in the context of axonal transport deficits of neurodegenerative scenarios (Millecamps and Julien, 2013). In addition, we know little concerning the composition of cargos destined for synaptic AZs.

The electron-dense AZ cytomatrix (T-bar) at the *Drosophila* neuromuscular junction (NMJ) is among others composed of oligomers of BRP and RBP (Kittel et al., 2006; Fouquet et al., 2009; Liu et al., 2011a; Ehmman et al., 2014). We report here that BRP and RBP, but no other tested AZ components, are co-transported in discrete transport complexes along the axon. Via a screen for RBP interaction partners, we identified the APP-like protein interacting protein 1 (Aplip1), an adaptor protein previously implicated in SV transport. Further analysis by X-ray crystallography and calorimetry showed that the second and third Src homology 3 (SH3) domain of RBP bind a specific N-terminal proline-rich (PxxP) motif of Aplip1/JIP1 with more than 10-fold higher affinity than RBP binds its synaptic ligands (Ca²⁺channels/RIM) by their cognate PxxP motifs. The integrity of this motif was essential to protect axons from forming ectopic axonal synapses, which were observed in *aplip1* mutant axons by electron microscopy (EM) and super-resolution light microscopy.

In summary, we characterize a mechanism of axonal AZ protein transport through a high affinity interaction between preassembled, stoichiometric scaffold protein complexes and the transport adaptor Aplip1. This high affinity interaction is needed to allow for effective axonal transport and to protect from premature AZ assembly processes.

Results

The molecular basis of how axonal protein transport is coupled to AZ assembly remains largely unexplored. We hypothesized that BRP might be co-transported with further AZ scaffold proteins, as

transport of preformed complexes of AZ material has been suggested previously (Zhai *et al.*, 2001; Shapira *et al.*, 2003; Maas *et al.*, 2012).

RBP co-clusters with BRP in axonal aggregates of SR kinase mutants

Firstly, we chose a previously characterized mutant of a serine–arginine (SR) protein kinase at location 79D (*srpk79D*). The SRPK79D protein is a member of the serine–arginine protein kinase family previously shown to be involved in mRNA splicing and processing (Wang *et al.*, 1998). Mutants of *srpk79D* form dramatic BRP aggregates in the axoplasm, while its endogenous substrates remain elusive (Johnson *et al.*, 2009; Nieratschker *et al.*, 2009). The axonal aggregations here served as a sensitive background to screen for proteins that co-accumulate together with BRP in the axon, and therefore indicate a joint transport mechanism.

In order to visualise the aggregates forming within axons of *srpk79D* mutant larvae, we stained with antibodies (Abs) directed against the BRP C- and N-terminus (Figure 1A, as control), and further probed for the presence of additional AZ proteins, such as Liprin- α (Figure 1B) and Syd-1 (Figure 1C), which interact with BRP at the AZ (Owald *et al.*, 2010, 2012) and the small GTPase Rab3 that was previously shown to regulate the distribution of presynaptic components at AZs (Figure 1D; Graf *et al.*, 2009). However, none of these AZ proteins showed co-accumulation with BRP in the aggregates (B as also described in Johnson *et al.*, 2009). Staining with anti-RBP Abs (Liu *et al.*, 2011a), by contrast, revealed strong co-localization of BRP and RBP in the axonal aggregates (Figure 1E). Quantification of BRP and RBP co-localization in two different *srpk79D* mutant null alleles (*atc* from Johnson *et al.*, 2009; *vn* from Nieratschker *et al.*, 2009) confirmed the impression that the axonal RBP/BRP signals were of identical size (Figure 1F; mean area of axonal spots, BRP^{C-term} $0.3797 \pm 0.03694 \mu\text{m}^2$ in *srpk79D*^{ATC}, $0.3259 \pm 0.02212 \mu\text{m}^2$ in *srpk79D*^{vn}; RBP^{C-term} $0.3892 \pm 0.02097 \mu\text{m}^2$ in *srpk79D*^{ATC}, $0.3696 \pm 0.01645 \mu\text{m}^2$ in *srpk79D*^{vn}; $n = 8$ nerves; mean \pm SEM), and that BRP and RBP nearly always co-localized in these aggregates (Figure 1G; BRP^{C-term} co-localizing with RBP^{C-term} $93.26\% \pm 2.172$ in *srpk79D*^{ATC}, $95.85\% \pm 1.302$ in *srpk79D*^{vn}; RBP^{C-term} co-localizing with BRP^{C-term} $95.7\% \pm 0.9713$ in *srpk79D*^{ATC}, $94.24\% \pm 1.162$ in *srpk79D*^{vn}; $n = 8$ nerves; mean \pm SEM).

Thus, RBP was the only AZ protein that robustly co-accumulates with BRP in *srpk79D* mutant axonal aggregates. To further explore the distribution of BRP and RBP in these aggregates we used stimulated emission depletion (STED) light microscopy at a resolution of about 50 nm (Hell, 2007). Two-colour STED microscopy revealed a tight and stoichiometric association of BRP and RBP in the floating axonal aggregates of *srpk79D* mutants (Figure 1H), reminiscent of EM images showing T-bar super assemblies in these axons (Figure 1H; Johnson *et al.*, 2009; Nieratschker *et al.*, 2009). In fact, the relative distribution of RBP vs BRP^{C-term} was very reminiscent of the organisation at mature, synaptic AZs (Liu *et al.*, 2011a). The tight association of BRP and RBP in these ectopic aggregates further suggested a co-transport of both AZ components. Indeed, we could identify axonal BRP spots co-positive for RBP (Figure 1I, arrows) in wild type (WT) larvae as well. Compared to *srpk79D* mutant axons, WT BRP/RBP co-positive aggregates were present at a lower frequency and displayed a \sim four times smaller average diameter in control axons (Figure 1F; mean area of axonal spots, BRP^{C-term} $0.06895 \pm 0.01 \mu\text{m}^2$ in WT; RBP^{C-term} spots: 0.09184 ± 0.0133 in WT; $n = 8$ nerves; mean \pm SEM).

BRP and RBP are co-transported in axons together with Aplip1

We observed active anterograde and retrograde transport of the BRP (GFP-labelled)/RBP (cherry-labelled) co-positive spots when using intravital imaging of axons of intact larvae (Rasse *et al.*, 2005) (Figure 2A; Video 1). Thus, as our data strongly suggested that BRP and RBP are co-transported, we searched for adaptor proteins coupling them to axonal motors.

RBP, via its second and third SH3 domain, is known to bind synaptic ligands such as Ca²⁺ channels and RIM (Liu *et al.*, 2011a). Both the SH3 domains and the cognate PxxP motifs of the synaptic ligands are highly conserved between mammals and *Drosophila* (Liu *et al.*, 2011a; Südhof, 2012; Davydova *et al.*, 2014). However, in order to identify novel RBP interaction partners which might be relevant in the context of axonal transport, we performed a large-scale yeast two-hybrid (Y2H) screen using a construct consisting of the second and third SH3 domains of *Drosophila* RBP as bait (also shown in Figure 3A). As expected, several clones representing RIM and the Ca²⁺ channel α 1-subunit Cacophony (Cac) were isolated (not shown). In addition, the screen recovered 14 independent fragments of Aplip1, including a full length cDNA clone (Figure 2B). Aplip1 is the *Drosophila* homolog

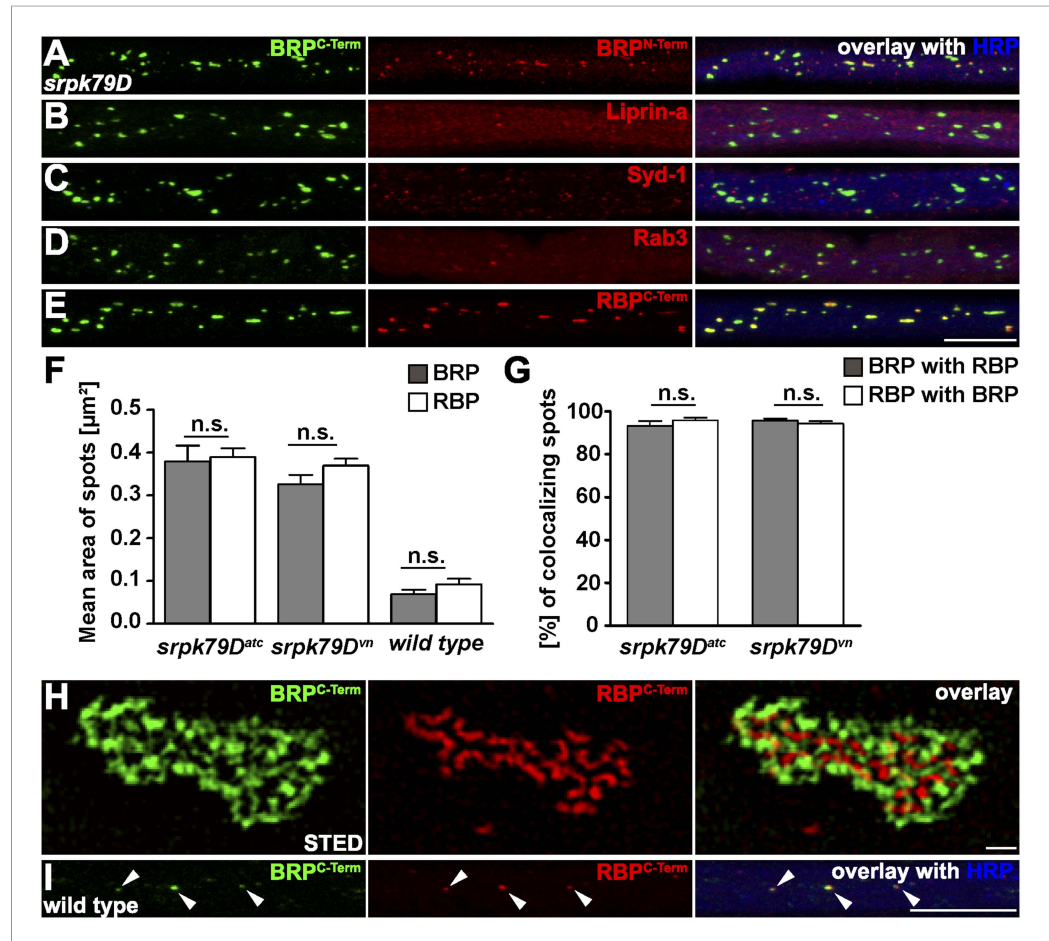


Figure 1. Co-accumulation of Bruchpilot (BRP) and RIM-binding protein (RBP) in *srpk79D* axonal aggregates. (A–E, I) Nerve bundles of segments A1–A3 from third instar larvae of the genotypes indicated labeled with the antibodies (Abs) indicated. (A–E, H) BRP accumulated in axonal aggregates of *srpk79D* mutants. (B–D) Liprin- α (B), Syd-1 (C), and Rab3 (D), did not co-localize with axonal BRP spots. (E) By contrast, RBP invariably co-localized with BRP in these axonal aggregates. (F) Quantification of mean area of axonal BRP and RBP spots in wild type (WT) and *srpk79D* mutants. BRP^{C-term} spots: $0.3797 \pm 0.03694 \mu\text{m}^2$ in *srpk79D^{ATC}*, $0.3259 \pm 0.02212 \mu\text{m}^2$ in *srpk79D^{VN}*, $0.06895 \pm 0.01 \mu\text{m}^2$ in WT; RBP^{C-term} spots: $0.3892 \pm 0.02097 \mu\text{m}^2$ in *srpk79D^{ATC}*, $0.3696 \pm 0.01645 \mu\text{m}^2$ in *srpk79D^{VN}*, 0.09184 ± 0.0133 in WT; n = 8 nerves each; all panels show mean values and errors bars representing SEM; ns, not significant, $p > 0.05$, Mann–Whitney U test. (G) Quantification for BRP co-localization with RBP and vice versa in *srpk79D* mutants. BRP^{C-term} co-localizing with RBP^{C-term}: $93.26\% \pm 2.172$ in *srpk79D^{ATC}*, $95.85\% \pm 1.302$ in *srpk79D^{VN}*; RBP^{C-term} co-localizing with BRP^{C-term}: $95.7\% \pm 0.9713$ in *srpk79D^{ATC}*, $94.24\% \pm 1.162$ in *srpk79D^{VN}*; n = 8 nerves each; all panels show mean values and errors bars representing SEM; ns, not significant, $p > 0.05$, Mann–Whitney U test. (H) Two-colour stimulated emission depletion (STED) images of axonal aggregates in *srpk79D* mutants revealed that RBP^{C-term} label localized to the inside of the axonal aggregates and was surrounded by BRP^{C-term} label. (I) BRP and RBP also co-localized in axonal spots of WT animals (arrow heads show co-localization of BRP and RBP in the axon). Scale bars: (A–E, I) 10 μm ; (H) 200 nm.

DOI: 10.7554/eLife.06935.003

of c-Jun N-terminal kinase (JNK)-interacting protein 1 (JIP1), a scaffolding protein that has been shown to bind kinesin light chain (KLC; Verhey et al., 2001), Alzheimer's amyloid precursor protein (APP; Taru et al., 2002), JNK pathway kinases (Horiuchi et al., 2005, 2007) and the autophagosome adaptor LC3 (Fu et al., 2014). If Aplip1 was mediating the axonal transport of RBP, moving spots co-positive for both RBP and Aplip1 should be expected. In fact, we robustly observed co-transport of RBP^{cherry} and Aplip1^{GFP} spots in both anterograde (Figure 2C, arrowhead; Video 2) and retrograde (not shown) direction at a frequency consistent with the low frequency of single Aplip1^{GFP} moving particles (not shown). Furthermore, we observed BRP-short^{straw} co-transport with Aplip1^{GFP} (Figure 2D;

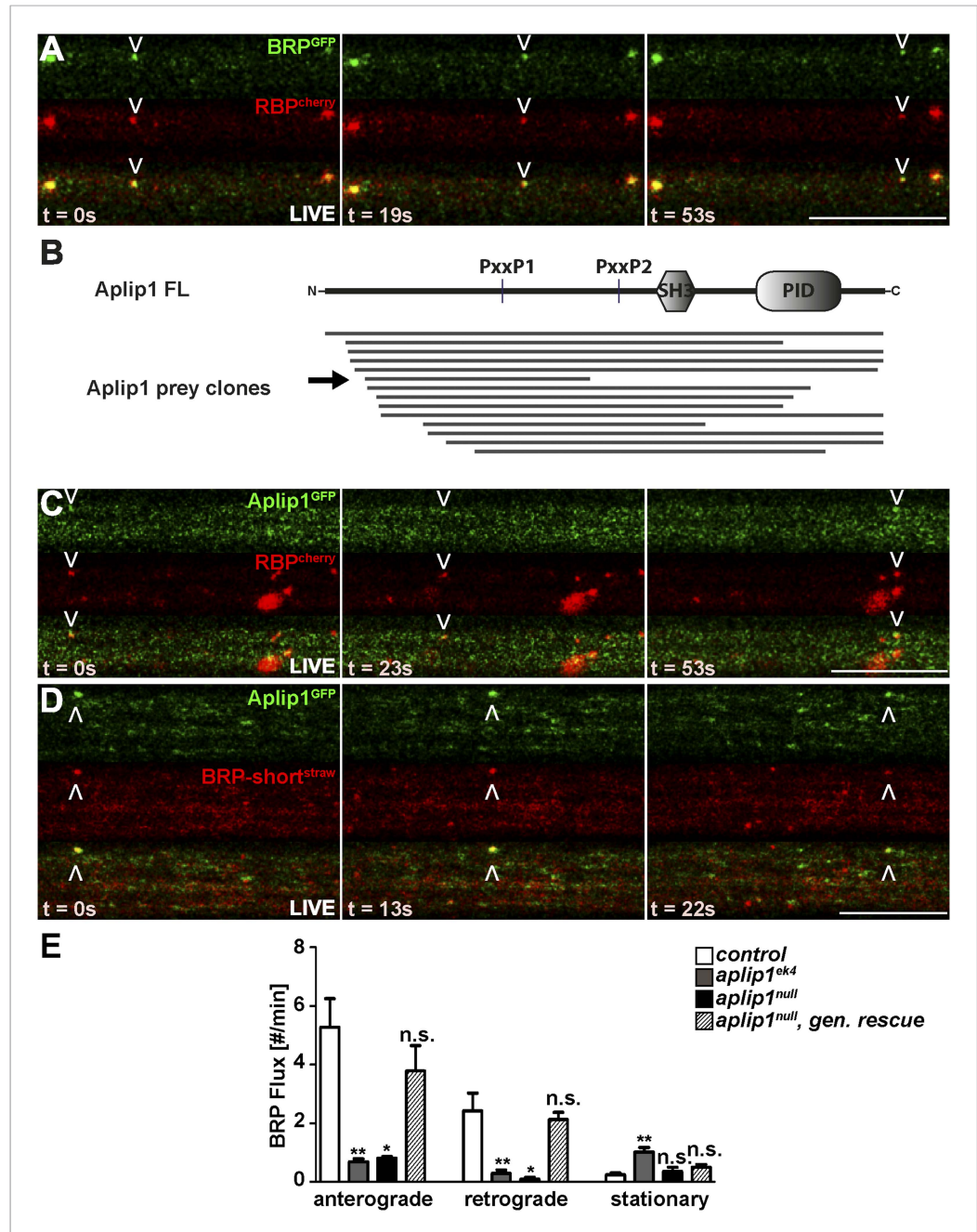


Figure 2. Live imaging of anterograde co-transport between BRP, RBP and APP-like protein interacting protein 1 (Aplip1). (A) Live imaging in intact third instar larvae showed anterograde co-transport of BRP^{GFP} and RBP^{cherry}. See also, **Video 1**. (B) Schematic representation of Aplip1 domain structure containing two PxxP motifs, one Src-homology 3 (SH3) domain and one C-terminal phosphotyrosine interaction domain (PID) (FL = full-length). Lines represent Aplip1 prey fragments recovered in RBP SH3-II+III bait yeast-two-hybrid (Y2H) screen. Arrow indicates one single clone that contained only the first of the two Aplip1-PxxP motifs. (C, D) Live imaging in intact third instar larvae showed anterograde co-transport of Aplip1^{GFP} and RBP^{cherry} (C), as well as Aplip1^{GFP} and BRP-short^{straw} (D). Scale bars: (A, C, D) 10 μm. See also, **Videos 2, 3**. (E) Quantification of live imaging of BRP-short^{straw} flux (spots passing through an axonal cross-section per minute) within the genetic backgrounds indicated. Anterograde and retrograde BRP-short^{straw} flux was severely impaired in *aplip1^{ek4}* and *aplip1^{null}* mutant background, which was rescued when a genomic rescue construct for Aplip1 was introduced into the *aplip1^{null}* mutant background. BRP-short^{straw} flux per min, control (n = 14 nerves): anterograde: 5.267 ± 0.975, retrograde: 2.423 ± 0.604, stationary: 0.241 ± 0.071; *aplip1^{ek4}* (n = 28 nerves): anterograde: 0.687 ± 0.098, retrograde: 0.284 ± 0.125, stationary: 1.023 ± 0.145; *aplip1^{null}*

Figure 2. continued on next page

Figure 2. Continued

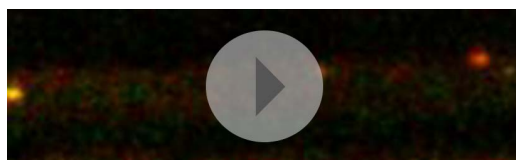
(n = 11 nerves): anterograde: 0.808 ± 0.051 , retrograde: 0.085 ± 0.064 , stationary: 0.354 ± 0.148 ; *aplip1^{null}, gen rescue* (n = 26 nerves): anterograde: 3.783 ± 0.861 , retrograde: 2.123 ± 0.239 , stationary: 0.505 ± 0.084 . All panels show mean values and errors bars representing SEM. * $p \leq 0.05$; ** $p \leq 0.01$; *** $p \leq 0.001$; ns, not significant, $p > 0.05$, Mann–Whitney U test.

DOI: [10.7554/eLife.06935.004](https://doi.org/10.7554/eLife.06935.004)

Video 3, as expected with similarly low frequencies as observed for RBP/Aplip1 co-transport (not shown), further pointing towards a co-transport of RBP and BRP in conjunction with Aplip1. We used the live imaging assay to investigate BRP transport in different *aplip1* mutants to directly address whether removal of Aplip1 affects AZ scaffold protein transport. The *aplip1^{null}* allele completely and specifically removes the *aplip1* gene and was generated by P-element excision (Klinedinst et al., 2013). By comparison, the *aplip1^{ek4}* allele contains a point mutation in the C-terminal kinesin binding domain of Aplip1 that was shown to almost completely abolish the ability of Aplip1 to bind to KLC (Horiuchi et al., 2005). Anterograde and retrograde transport of BRP was drastically reduced compared to controls in both *aplip1* mutant alleles (Figure 2E). Through the introduction of a genomic (gen.) construct of Aplip1 into the *aplip1^{null}* mutant background (*aplip1^{null}, gen. rescue*), however, BRP flux (spots passing through an axonal cross-section in a given time) could be restored to WT level (Figure 2E). Quantification showed that retrograde transport in the *aplip1^{null}* mutant situation was somewhat more affected (27× less compared to control) than anterograde transport (7× less). Both directions appeared equally affected (about 8× less compared to controls) in the kinesin-binding defective *aplip1^{ek4}* mutant. It is noteworthy that the transport of SV cargo in the same mutant was reduced equally in both directions, whereas transport of mitochondria is only impaired in the retrograde direction (Horiuchi et al., 2005).

RBP binds the transport adaptor Aplip1 via a high affinity PxxP-SH3 interaction

As our Y2H screen used the SH3-II and -III domains of RBP as bait (Figure 3A), PxxP motifs are expected to mediate the interaction with Aplip1. In fact, Aplip1 contains two PxxP motifs which were both present in most of the prey clones recovered in the Y2H screen, except for one single clone that contained only the first more N-terminal motif (Figure 2B, arrow). Using a semi-quantitative liquid Y2H assay and a set of Aplip1 constructs containing only either the first or the second PxxP motif (Figure 3B), we mapped the interaction between RBP and Aplip1 to the first of the two candidate PxxP motifs present in all clones isolated (Figure 2B). The second and third SH3 domain of RBP bound to this motif with comparable strength when measured with a semi-quantitative liquid Y2H assay (Figure 3C; mean β -Gal4 units for: Aplip1-PxxP1/RBP SH3-II: 24.3 ± 6.6 ; Aplip1-PxxP1/RBPSH3-III: 29.1 ± 7.4 ; n = 3 independent experiments; mean \pm SEM). No binding was observed between the second and third SH3 domains of RBP and Aplip1-PxxP2 (Figure 3C; mean β -Gal4 units for: Aplip1-PxxP2/RBP SH3-II: 0.2 ± 0.0 ; Aplip1-PxxP2/RBPSH3-III: 0.2 ± 0.1 ; n = 3 independent experiments; mean \pm SEM). When mutating either the PxxP1 motif of Aplip1 (P156 \rightarrow A; P159 \rightarrow A, giving rise to AxxA1) or introducing mutations known to interfere with PxxP ligand binding into the



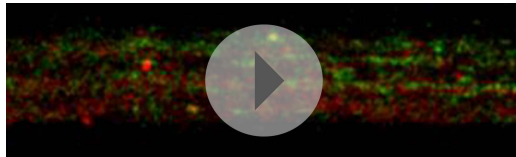
Video 1. Anterograde co-transport of BRP^{GFP} and RBP^{cherry}. Live imaging in intact third instar larvae showed anterograde co-transport of BRP^{GFP} and RBP^{cherry}. Video was captured at 0.6 s per frame and played back at 7x real time.

DOI: [10.7554/eLife.06935.005](https://doi.org/10.7554/eLife.06935.005)



Video 2. Anterograde co-transport of Aplip1^{GFP} and RBP^{cherry}. Live imaging in intact third instar larvae showed anterograde co-transport of Aplip1^{GFP} and RBP^{cherry}. Video was captured at 0.6 s per frame and played back at 7x real time.

DOI: [10.7554/eLife.06935.012](https://doi.org/10.7554/eLife.06935.012)



Video 3. Anterograde co-transport of Aplip1^{GFP} and BRP-short^{straw}. Live imaging in intact third instar larvae showed anterograde co-transport of Aplip1^{GFP} and BRP-short^{straw}. Video was captured at 0.414 s per frame and played back at 5x real time.

DOI: [10.7554/eLife.06935.013](https://doi.org/10.7554/eLife.06935.013)

domains (II+III) (see also **Figure 3A**). Whereas we could not detect any binding of the Aplip1 peptides to RBP SH3-I, we could determine K_D constants for the single SH3-II, SH3-III and the tandem SH3-II+III (**Figure 3D**; **Figure 3—figure supplement 1**) domains of RBP. Both SH3-II and SH3-III single domains showed a binding affinity to Aplip1 peptides several fold stronger compared to either Cac, RIM1 or RIM2 (**Figure 3D**; **Figure 3—figure supplements 2–4**). However, the affinity of the Aplip1 peptides to the SH3-II+III domain was the highest observed which is indicative of co-operativity between both domains in peptide binding that could increase the local concentrations of Aplip1 at RBP binding pockets (BPs).

Finally, in order to get a deeper atomic insight into the structural basis of the binding of RBP towards Aplip1 in comparison to its synaptic ligands, we crystallized the *Drosophila* RBP SH3-II domain together with both an Aplip1 (**Figure 3E**; **Tables 1, 2, 3**) and a Cac peptide (**Figure 3F**; **Tables 1, 3, 4**), and RBP SH3-III with a Cac peptide (**Figure 3—figure supplement 5**; **Tables 1, 3**). *Drosophila* RBP SH3-II and -III share 49.2% sequence identity and adopt the canonical fold of SH3 domains (**Figure 3E,F**; **Figure 3—figure supplement 5**). Both domains superimpose with a root mean deviation of 0.8 Å for 64 pairs of C α -atoms. Both peptides sequences harbor the canonical class I interaction motif +x Ψ PxxP (+, positively charged; x, any amino acid; Ψ hydrophobic amino acid, see **Figure 3D** for sequence) and are bound into the respective SH3 domain in ‘plus’ direction. We observed the classical poly-proline helix that allows for mainly hydrophobic protein-peptide interaction in all three structures. We detected the same hydrogen pattern between the protein side chains and peptide backbone in the structure of SH3-II with Aplip1 and Cac. The major difference is the side chain orientation of R1687 of Cac that π -stacks with its guanidinium function with Y1372, except for one copy, where it forms a salt-bridge to E1341. The equivalent residue to R1687 of Cac is R153 of the Aplip1 peptide, which forms, by contrast, a bidentate salt-bridge to D1336 (**Table 3**). A second major difference is induced by the two consecutive proline residues in the Cac peptide. Consequently, the peptide has a more polyproline type II conformation that brings T1692 closer to the protein surface and allows P1693 to deeper point in a hydrophobic pocket of the SH3-II domain. Whereas the C-terminal portion of the Aplip1 peptide is folded in a short 3_{10} helix, the N-terminus of the Aplip1 peptide adopts a random coil conformation with hydrophobic interactions to the surface of SH3-II. The Cac-derived peptide bound to SH3-III is fully defined in the electron density. However, the peptide main chain interaction with the SH3 domains is conserved. The side chain orientation of Cac R1687 is again different if bound to SH3-II or SH3-III. In complex with SH3-III, R1687 forms a bidentate hydrogen bond to SH3-III D1463 and E1648. A π -stacking interaction is not possible since Y1372 of SH3-II is replaced by SH3-III L1499. The central PxxP motifs of Aplip1 superimpose well in both structures if bound to SH3-II and SH3-III. Towards its C-terminus, the Aplip1-PxxP1 peptide adopts a slightly different random coil conformation compared to the structure when bound to SH3-II caused by two additional hydrogen bonds from T1692 and K1695 to the SH3-II domain (**Table 3**).

The Aplip1-PxxP1 motif is needed for effective axonal RBP/BRP transport

Consistent with the idea that Aplip1 is mediating RBP transport, we found axonal aggregates consisting of both RBP and BRP in the *aplip1*^{ek4}, as well as the *aplip1*^{null} allele (**Figure 4B,C**). This ectopic

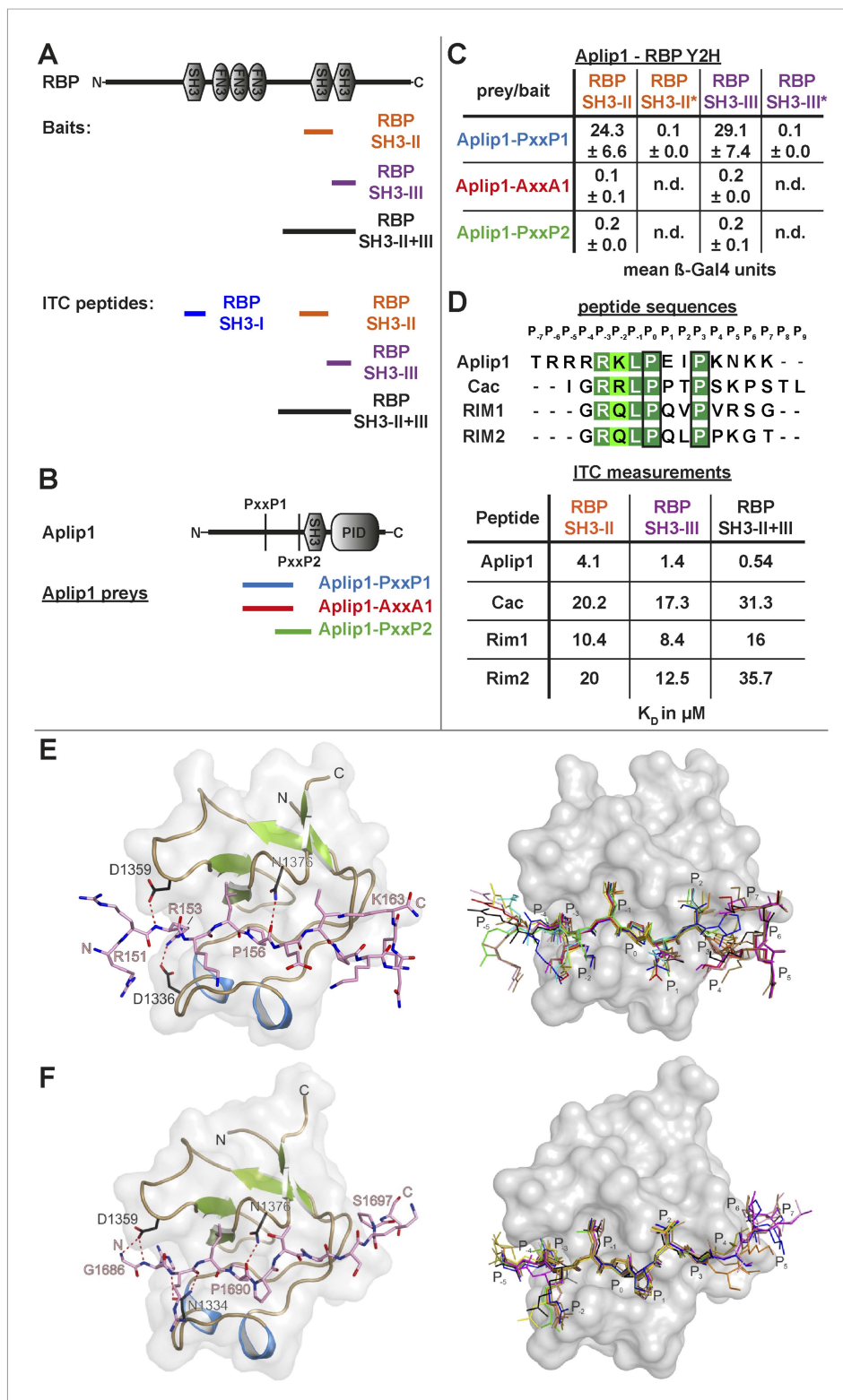


Figure 3. Aplip1 binds RBP using a high-affinity PxxP1-SH3 interaction. **(A)** Schematic representation of RBP domain structure containing three SH3 domains (I-III from the N-terminus) and three Fibronectin 3 (FN3) domains. The corresponding fragments used in the large scale Y2H screen (SH3-II+III) and used as bait (SH3-II and SH3-III) in the Y2H assay **(C)** against different Aplip1 prey constructs **(B)** are indicated. Different isothermal titration calorimetry *Figure 3. continued on next page*

Figure 3. Continued

(ITC) peptides (SH3-I, SH3-II, SH3-III and SH3-II+III) used for ITC measurements (D) are also shown. (B) Schematic representation of Aplip1 domain structure entailing two PxxP motifs, one SH3 and one C-terminal PID. Different preys (Aplip1-PxxP1, -AxxA1 and -PxxP2) used in Y2H assay (C) are indicated. (C) Liquid Y2H assay of individual Aplip1 prey fragments against different RBP baits. Aplip1-PxxP1 interacted with both the single SH3-II and -III domains of RBP. Mutating this first PxxP motif (Aplip1-AxxA1) construct abolished the binding. Aplip1-PxxP2 showed no interaction to RBP SH3 domains. Constructs with point-mutated RBP SH3 domains (SH3-II*, SH3-III*) abolished the binding to Aplip1-PxxP1. (D) Peptide sequences used for ITC measurements. Aplip1 showed the strongest interaction with RBP compared with Cacophony (Cac), RIM1 and RIM2, with the strongest affinity (lowest K_D) between Aplip1 and the RBP SH3-II+III domain. (E, F) Crystal structure of Aplip1-peptide (E; see also, 3D for peptide sequence) and of Cac-peptide (F; see also, **Figure 3D** for peptide sequence) bound to RBP SH3-II. The SH3 domain is shown in gray surface representation with (left) and without (right) the respective protein in cartoon representation. The bound peptides are drawn in stick representation. Hydrogen bonds ≤ 3.3 Å are indicated by red dashes. In the right panel, several peptide SH3-II complexes as observed in the asymmetric unit are superimposed and shown in different colors. See also, **Tables 1–4**.

DOI: [10.7554/eLife.06935.006](https://doi.org/10.7554/eLife.06935.006)

The following figure supplements are available for figure 3:

Figure supplement 1. ITC measurements for Aplip1 and RBP SH3 domains.

DOI: [10.7554/eLife.06935.007](https://doi.org/10.7554/eLife.06935.007)

Figure supplement 2. ITC measurements for Cac and RBP SH3 domains.

DOI: [10.7554/eLife.06935.008](https://doi.org/10.7554/eLife.06935.008)

Figure supplement 3. ITC measurements for RIM1 and RBP SH3 domains.

DOI: [10.7554/eLife.06935.009](https://doi.org/10.7554/eLife.06935.009)

Figure supplement 4. ITC measurements for RIM2 and RBP SH3 domains.

DOI: [10.7554/eLife.06935.010](https://doi.org/10.7554/eLife.06935.010)

Figure supplement 5. Crystal structure of Cac-peptide bound to RBP SH3-III domain.

DOI: [10.7554/eLife.06935.011](https://doi.org/10.7554/eLife.06935.011)

RBP/BRP accumulation was rescued after introducing a genomic construct of Aplip1 into the *aplip1^{null}* mutant background (*aplip1^{null}*, gen. rescue; **Figure 4D**). Pan-neuronal expression of an Aplip1 cDNA equally rescued the axonal RBP/BRP accumulations (**Figure 4I**, quantification in K, L). Importantly, however, the expression of an Aplip-AxxA1 cDNA construct (integrated at the same chromosomal integration site as the control construct; expression and axonal presence confirmed with a newly generated Aplip1 Ab; not shown) could no longer rescue the RBP/BRP accumulation phenotype (**Figure 4J**, quantification in **Figure 4K,L**). Thus, we conclude that Aplip1 is involved in the transport of RBP/BRP to the AZ, whereby its functionality in this context largely depends on the integrity of its N-terminal PxxP1 motif.

Aplip1 promotes BRP transport in absence of RBP

As indicated above, BRP accumulated in the axons of *aplip1* mutants as well. Thus, BRP could be transported through Aplip1 via binding to RBP, other yet undetected co-transported AZ proteins, or BRP could bind Aplip1 independently of RBP. We therefore created *aplip1/rbp* and *aplip1/brp* double mutants to investigate the functional relation of RBP and BRP with regard to Aplip1-dependent transport. While removing BRP in *srpk79D* mutants also abolished the axonal RBP spots (**Figure 5—figure supplement 1D**), removing BRP in *aplip1* mutants had no apparent effect on axonal RBP accumulations (**Figure 5B**; control in **Figure 5A**). On the other hand, genetic elimination of RBP did not interfere with the accumulation of BRP in *aplip1* mutant axons (**Figure 5E**; controls in **Figure 5C,D**). Thus, BRP transport also ‘suffers’ from the absence of the Aplip1 adaptor when RBP is removed in parallel. Hence, Aplip1 promotes BRP transport even in the absence of RBP. To address a putative molecular basis of this relationship, we performed a Y2H assay to test for direct interaction between five different BRP constructs and a full length Aplip1 construct (see **Figure 3B** for domain structure). Despite these efforts, robust interactions between Aplip1 and BRP fragments could not be detected (data not shown). Nonetheless, both RBP but also BRP were easily detected in anti-GFP immunoprecipitations (IPs) from a synaptic membrane preparation (**Figure 5F**; **Figure 5—figure supplement 2**) derived from *Drosophila*

Table 1. Data collection and refinement statistics
Data collection

Structure	RBP SH3-II	RBP SH3-II	RBP SH3-III
	Aplip1	Cac	Cac
PDB entry	4Z88	4Z89	4Z8A
Space group	C2	P2 ₁	I222
Wavelength (Å)	0.91841	0.91841	0.91841
Unit cell			
a; b; c (Å)	108.3; 62.4; 163.6	58.3; 122.2; 68.5	52.1; 54.3; 73.6
α; β; γ (°)	90.0; 90.3; 90.0	90.0; 113.2; 90.0	90.0; 90.0; 90.0
Resolution (Å)*	50.00–2.09 (2.19–2.09)	50.00–2.64 (2.74–2.64)	50.00–1.75 (1.86–1.75)
Unique reflections	64,269 (7760)	25,229 (2591)	10,690 (1579)
Completeness*	98.9 (92.4)	96.9 (95.0)	98.7 (92.6)
<I/σ(I)>*	7.7 (2.6)	8.0 (2.1)	14.2 (2.2)
R _{meas} [*] , †	0.127 (0.533)	0.157 (0.726)	0.127 (0.663)
CC _{1/2} [*]	99.1 (68.0)	98.9 (81.2)	99.7 (76.5)
Redundancy*	3.7 (3.7)	3.5 (3.2)	5.6 (3.1)
Refinement			
Non-hydrogen atoms	7564	6239	850
R _{work} [*] , ‡	0.210 (0.314)	0.255 (0.367)	0.159 (0.233)
R _{free} [*] , §	0.236 (0.396)	0.312 (0.490)	0.208 (0.332)
Average B-factor (Å ²)	40.8	52.10	18.8
No. of complexes	24	10	1
Protein residues	6484/41.0	663/51.1	74/17.6
Peptide residues	861/42.7	92/63.6	15/15.9
Buffer molecules	11/40.2	1/46.3	–
Water molecules	57/29.6	134/30.3	110/28.6
r.m.s.d.#			
bond length (Å)	0.007	0.005	0.010
bond angles (°)	1.224	1.140	1.210
Ramachandran outliers (%)	0.1	0.56	0
Ramachandran favoured (%)	98.4	98.0	100

*values in parentheses refer to the highest resolution shell.

† $R_{meas} = \sum_h [n/(n-1)]^{1/2} \sum_i |I_h - I_{h,i}| / \sum_h \sum_i I_{h,i}$ where I_h is the mean intensity of symmetry-equivalent reflections and n is the redundancy.

‡ $R_{work} = \sum_h |F_o - F_c| / \sum F_o$ (working set, no σ cut-off applied).

§ R_{free} is the same as R_{work} , but calculated on 5% of the data excluded from refinement.

#Root-mean-square deviation (r.m.s.d.) from target geometries.

CC, coiled coil.

DOI: [10.7554/eLife.06935.014](https://doi.org/10.7554/eLife.06935.014)

head extracts of pan-neuronal driven Aplip1-GFP cDNA construct (Depner et al., 2014). Of note, within axons of *rbp^{null}* mutant larvae, ectopic BRP accumulations could not be observed (not shown). Thus, we provide evidence for an RBP-independent but Aplip1-dependent transport component for BRP, whose mechanistic details have still to be deciphered. Taken together, our results imply that though BRP and RBP are co-transported in the WT situation, their Aplip1-dependent transport can be genetically uncoupled.

Table 2. Completeness of the model for RBP SH3-II and bound Aplip1 peptide

RBP SH3-II	Range	Aplip1	Range
chain A	1318–1382	chain M	153–163
chain B	*1318–1382	chain N	155–159
chain C	*1318–1381	chain O	154–163
chain D	*1318–1382	chain P	153–159
chain E	1319–1381	chain Q	151–163
chain F	*1318–1380	chain R	153–159
chain G	*1318–1381	chain S	151–163
chain H	*1318–1382	chain T	152–156
chain I	*1318–1382	chain U	152–163
chain J	*1318–1381	chain V	152–158
chain K	*1318–1381	chain W	152–163
chain L	*1318–1381	chain X	152–158

Completeness of the model given for the 12 complexes of RBP SH3-II bound to the Aplip1 peptide ¹⁴⁹TRRRRKLPEIPKNKK¹⁶³. Superscript 'x' indicates additional N-terminal residues of RBP SH3-II originating from the linker region between the protease cleavage site and the N-terminus.

DOI: [10.7554/eLife.06935.015](https://doi.org/10.7554/eLife.06935.015)

RBP and BRP form ectopic AZs at the axonal plasma membrane of *aplip1* mutants

The BRP flux in axons of *aplip1* mutants was severely diminished, but not completely abolished (**Figure 2E**). At the same time, AZ localization of both BRP and RBP at synaptic terminals of *aplip1* mutants was still observed in both *aplip1* alleles (not shown), although slightly reduced (not shown). This indicates that alternative transport mechanisms and adaptors exist which operate in parallel to Aplip1, as the synaptic phenotype is relatively weak. In fact, axonal accumulations of BRP have already been described for Acyl-CoA long-chain Synthetase (*Acsl*, *Liu et al., 2011b*) as well as for Unc-51 (*Atg1*) mutants (*Wairkar et al., 2009*). In our experiments, we found RBP to invariably co-cluster with BRP in the mutants mentioned (**Figure 6B,C**; control in **Figure 6A**), and equally in mutants of the *Drosophila* β -amyloid protein precursor-like (*Appl*; *Torroja et al., 1999a, 1999b*; **Figure 6D**) and Unc-76 (*Gindhart et al., 2003*; **Figure 6E**). The fact that RBP and BRP tightly co-accumulated in axonal aggregates of all these transport mutants strengthens the probability that BRP is always co-transported with RBP.

To gain a deeper insight into the substructure of the BRP/RBP accumulations in *aplip1* mutant axons, we again used two-colour STED microscopy. In contrast to the *srpk79D* aggregates, however, STED images of axonal BRP/RBP accumulations were reminiscent of mature synaptic AZs (*Liu et al., 2011a*), with BRP^{C-term} signal surrounding the RBP signal, which, in turn, is oriented closer towards the axonal plasma membrane (**Figure 7A**, arrow head; plasma membrane indicated by dashed line). Interestingly, in contrast to the floating T-bar super-aggregates in *srpk79D* mutants (*Johnson et al., 2009*; *Nieratschker et al., 2009*), these axonal BRP spots in *aplip1* mutants were positive for Syd-1 (compare **Figures 1C, 7B**). Intriguingly, floating T-bars have been observed in synaptic boutons in *syd-1* mutants (*Owald et al., 2010*). Together, this is suggestive of a role of Syd-1 in the membrane-anchoring of AZ proteins.

Furthermore, we asked whether BRP/RBP aggregates identified in *aplip1* mutants represent ectopic AZs forming at the axonal plasma membrane. In fact, EM analysis easily revealed T-bar structures, typical for synaptic terminals (**Figure 7C**, arrow heads, magnification in E), at axonal plasma membranes of *aplip1* mutants (**Figure 7D**, arrow heads, magnification in F), but never in controls (not shown). We found these ectopic axonal T-bars surrounded by SV profiles (**Figure 7D**, arrows), very similar to 'normally positioned' T-bars at the presynaptic terminal (**Figure 7C**, arrows). Consistently, the SV marker Synaptotagmin-1 (*Syt-1*) was found to be associated with BRP/RBP accumulations in *aplip1*^{null} mutants (**Figure 7H**, quantification in **Figure 7K**). This phenotype could be rescued by the expression of an Aplip1 WT cDNA construct (**Figure 7I**, quantification in **Figure 7K**) but not by the expression of the Aplip1-AxxA1 construct (**Figure 7J**; quantification in **Figure 7K**). Thus, a point-like interaction surface of Aplip1 which binds RBP with high affinity is important to block a whole sequence of assembly events at the axonal plasma membrane, including AZ scaffold ('T-bar') formation and the accumulation of SVs.

To further support the importance of adaptor protein—cargo interaction in blocking ectopic AZ assembly we downregulated the expression of motor proteins. This also leads to transport defects and ectopic axonal AZ protein accumulations but in principle leaving the adaptor protein—cargo interaction intact. Interestingly, motoneuronal driven *Imac-RNAi* led to only few axonal BRP/RBP accumulations although with no preference concerning their direction in relation to the axonal plasma membrane (**Figure 7—figure supplement 1B**; arrow heads).

Table 3. Hydrogen bonding interaction

Aplip1	SH3-II	Distance
Arg153 ^N	Asp1359 ^{OD2}	2.4
Arg153 ^{NH2}	Asp1336 ^{OD1}	3.0
Arg153 ^{NH2}	Asp1336 ^{OD2}	2.6
Lys154 ^N	Asn1334 ^{OD1}	2.9
Lys154 ^O	Asn1334 ^{ND2}	3.0
Pro156 ^O	Asn1376 ^{ND2}	2.8
Cac	SH3-II	Distance
Gly1686 ^N	Asp1359 ^{OD2}	2.7
Arg1687 ^N	Asp1359 ^{OD2}	2.8
Arg1688 ^N	Asn1334 ^{OD1}	3.0
Arg1688 ^O	Asn1334 ^{ND2}	2.9
Pro1690 ^O	Asn1376 ^{ND2}	2.8
Cac	SH3-III	Distance
Arg1687 ^{NH1}	Asp1463 ^{OD1}	2.9
Arg1687 ^{NH1}	Glu1488 ^{OE2}	3.0
Arg1687 ^{NH2}	Glu1488 ^{OE2}	3.1
Arg1688 ^N	Asn1461 ^{OD1}	2.8
Arg1688 ^O	Asn1461 ^{ND2}	3.0
Pro1690 ^O	Asn1376 ^{ND2}	2.9
Thr1692 ^{OG}	Asn1376 ^{ND2}	2.9
Lys1695 ^O	Tyr1451 ^{OH}	2.8
Ser1697 ^{OG}	Leu1450 ^O	2.7

Hydrogen bonding interaction of RBP SH3-II with Aplip1 and Cac, as well as RBP SH3-III in complex with Cac. Distance ≤ 3.2 Å are given in Å.

DOI: [10.7554/eLife.06935.016](https://doi.org/10.7554/eLife.06935.016)

their 'safe' arrival at the synaptic terminal remains to be addressed. We find here that the AZ scaffold protein RBP binds the transport adaptor Aplip1 using a 'classic' PxxP/SH3 interaction. Notably, the same RBP SH3 domain (II and III) interaction surfaces are used for binding the synaptic AZ ligands of RBP, that is, RIM and the voltage gated Ca²⁺ channel (Wang et al., 2002; Kaeser et al., 2011; Liu et al., 2011a; Davydova et al., 2014), though with clearly lower affinity than for Aplip1. A point mutation which disrupts the Aplip1-RBP interaction provoked a 'premature' capture of RBP and the co-transported BRP at the axonal membrane, thus forming ectopic but, concerning T-bar shape and BRP/RBP arrangement, WT-like AZ scaffolds. The Aplip1 orthologue Jip1 has been shown to homo-dimerize via interaction of its SH3 domain (Kristensen et al., 2006). Thus, the multiplicity of interactions, with Aplip1 dimers binding to two SH3 domains of RBP as well as to KLC, might form transport complexes of sufficient avidity to ensure tight adaptor-cargo interaction and prevent premature capture of the scaffold components.

Our intravital imaging experiments showed that within axons RBP and BRP are co-transport in shared complexes together with Aplip1, whereas we, despite efforts, were unable to detect any co-transport of other AZ scaffold components, that is, Syd-1 or Liprin- α with BRP/RBP (not shown). In addition, STED analysis of axonal aggregates in *srpk79D* mutants showed BRP/RBP in stoichiometric amounts, but also failed to detect other AZ scaffold components. Moreover, BRP and RBP co-aggregated in the axoplasm of several other transport mutants we tested (*acsl*, *unc-51*, *appl*, *unc-76*), consistent with both proteins entering synaptic AZ assembly from a common transport complex. Of note, during AZ assembly at the NMJ, BRP incorporation is invariably delayed compared to the 'early assembly' phase which is driven by the accumulation of Syd-1/Liprin- α scaffolds (Fouquet et al., 2009;

In contrast motoneuronal driven KHC-RNAi showed prominent axonal aggregates consistent of BRP/RBP but most of the time showing an irregular, elongated shape (Figure 7—figure supplement 1C; arrow heads). As mentioned above, proper T-bars were identified in *aplip1* mutant axons with ease. In contrast, systematic EM analysis of *khc* mutant axons revealed just one electron dense material that showed a T-bar-like appearance (Figure 7—figure supplement 1D; arrow head, magnifications in E, F) but never in control (ctrl) or motoneuronal driven *lmac-RNAi*.

In summary, we find that the SH3-II and -III interaction surface of RBP serves as a multi-functional platform for differential protein interaction with either other AZ components or the transport adaptor and therefore, motor-cargo linkage. Thus, interaction surfaces of RBP/BRP 'cargo complexes' might be shielded and blocked from undergoing premature assembly by interactions with transport adaptors, while genetically induced loss of these adaptors might provoke premature AZ assembly.

Discussion

Large multi-domain scaffold proteins such as BRP/RBP are ultimately destined to form stable scaffolds, characterized by remarkable tenacity and a low turnover, likely due to stabilization by multiple homo- and heterotypic interactions simultaneously (Sigrist and Schmitz, 2011). How these large and 'sticky' AZ scaffold components engage into axonal transport processes to ensure

Table 4. Completeness of the model for RBP SH3-II and bound Cac peptide

RBP SH3-II	Range	Cac	Range
chain A	1318–1381	chain a	1686–1697
chain B	*1318–1381	chain b	1686–1695
chain C	*1318–1382	chain c	1686–1697
chain D	*1318–1381	chain d	1686–1697
chain E	1318–1382	chain e	1685–1694
chain F	*1318–1382	chain f	1685–1693
chain G	*1318–1382	chain g	1686–1693
chain H	1318–1381	chain h	1686–1693
chain I	*1318–1381	chain i	1686–1693
chain J	*1318–1382	chain j	1686–1697

Completeness of the model given for the six complexes of RBP SH3-II and the bound Cac peptide ¹⁶⁸⁵IGRRLLPPTPSKPSTL¹⁶⁹⁹. Superscript 'x' indicates additional N-terminal residues of RBP SH3-II originating from the linker region between the protease cleavage site and the N-terminus.

DOI: [10.7554/eLife.06935.017](https://doi.org/10.7554/eLife.06935.017)

and by the lack of genetic or biochemical options for specifically interfering with their transport or final incorporation into AZs.

Despite efforts we were not able to detect a direct interaction of Aplip1 and BRP although their common transport can be uncoupled from the presence of RBP. One possible explanation could be a direct interaction of Aplip1 to other AZ proteins that are co-transported together with BRP and RBP. It is interesting that the very C-terminus of BRP is essential for SV clustering around the BRP-based AZ cytomatrix (Hallerman et al., 2010). Thus, it is tempting to speculate that adaptor/transport complex binding might block premature AZ protein/SV interactions before AZ assembly, but further analysis will have to await more atomic details as we could gain for the RBP::Aplip1 interaction.

The down-regulation of the motor protein KHC also provoked severe axonal co-accumulations of BRP and RBP but per se should leave the adaptor protein-AZ cargo interaction intact. In contrast to *aplip1*, the axonal aggregations in *khc* mutants adapted irregular shapes most of the time, likely not representing T-bar-like structures. Thus, our data suggest a mechanistic difference when comparing the consequences between eliminating adaptor cargo interactions with a direct impairment of motor functions. Still, we cannot exclude that trafficking of AZ complexes naturally antagonizes their ability to assemble into T-bars.

The idea that proteins/molecules are held in an inactive state till they reach their final target has been observed in many other cell types. For example, in the context of local translation control, mRNAs are shielded or hidden in messenger ribonucleoprotein particles during transport so that they are withheld from cellular processing events such as translation and degradation. Shielding is thought to operate through proteins that bind to the mRNA and alter its conformation while at the correct time or place the masking protein is influenced by a signal that alleviates its shielding effect (Spirin, 1996; Johnstone and Lasko, 2001). As another example, hydrolytic enzymes, for example, lysosomes, are transported as proteolytically inactive precursors that become matured by proteolytic processing only within late endosomes or lysosomes (Ishidoh and Kominami, 2002). Particularly relevant in the context of AZ proteins involved in exocytosis, the H_{abc} domain of Syntaxin-1 folds back on the central helix of the SNARE motif to generate a closed and inactive conformation which might prevent the interaction of Syntaxin-1 with other AZ proteins during diffusion (Dulubova et al., 1999; Ribbault et al., 2011).

Previously, genetic analysis of *C. elegans* axons forming *en passant* synapses suggested a tight balance between capture and dissociation of protein transport complexes to ensure proper positioning of presynaptic AZs. In this study, overexpression of the kinesin motor Unc-104/KIF1A

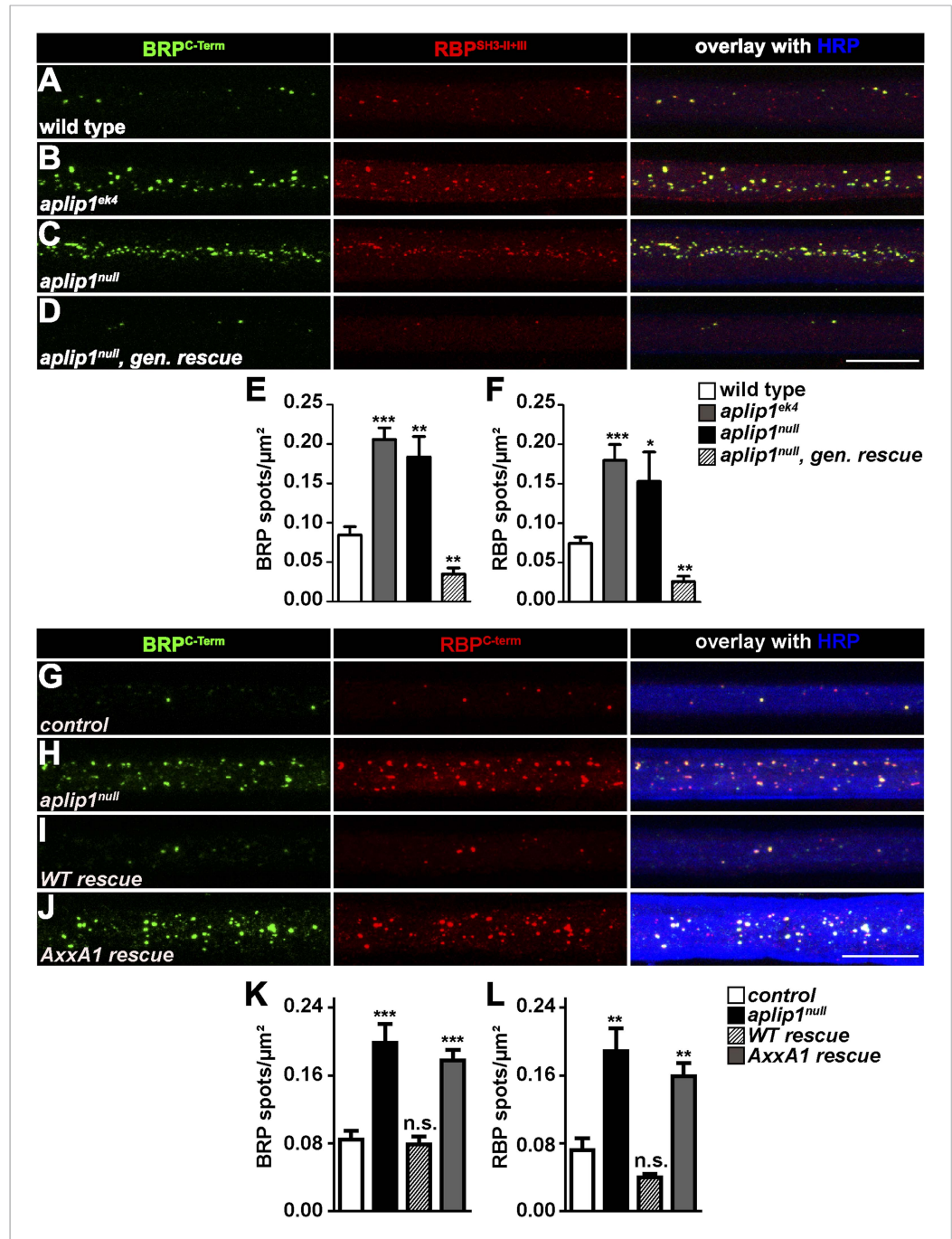


Figure 4. Aplip1-PXXP1 motif is needed for its function as RBP/BRP transport adaptor. (A–D) Nerve bundles of segments A1–A3 from third instar larvae of the genotypes indicated labeled with the Abs indicated. (E, F) Quantification of BRP/RBP spot numbers. BRP spots per μm^2 : WT (n = 8 nerves): 0.084 ± 0.010 ; *aplip1^{ek4}* (n = 9 nerves): 0.205 ± 0.025 ; *aplip1^{null}* (n = 8 nerves): 0.183 ± 0.025 ; *aplip1^{null}, gen. rescue* (n = 8 nerves): 0.034 ± 0.007 ; RBP spots per μm^2 , WT (n = 8 nerves): 0.074 ± 0.007 ; *aplip1^{ek4}* (n = 9 nerves): 0.180 ± 0.019 ; *aplip1^{null}* (n = 8 nerves): 0.153 ± 0.037 ; *aplip1^{null}, gen. rescue* (n = 8 nerves): 0.025 ± 0.006 . All panels show mean values and errors bars representing SEM. * $p \leq 0.05$; ** $p \leq 0.01$; *** $p \leq 0.001$; ns, not significant, $p > 0.05$, Mann–Whitney U test. (G–J) Nerve bundles of segment A1–A3 from third instar larvae of the genotypes indicated labeled with the Abs indicated. BRP and RBP co-localized in control animals and accumulated in a co-localizing fashion in axons of *aplip1^{null}* mutant animals. Re-expression of an Aplip1-WT cDNA construct in the *aplip1^{null}* background rescued the phenotype, while re-expression of an AxxA1 construct did not. Figure 4. continued on next page

Figure 4. Continued

(K, L) Quantification of the number of BRP/RBP spots per μm^2 axon. BRP spots per μm^2 , control (n = 12 nerves): 0.084 ± 0.010 ; *aplip1^{null}* (n = 16 nerves): 0.198 ± 0.022 ; *WT rescue* (n = 14 nerves): 0.078 ± 0.009 ; *AxxA1 rescue* (n = 14 nerves): 0.177 ± 0.012 ; RBP spots per μm^2 , control (n = 12 nerves): 0.071 ± 0.013 ; *aplip1^{null}* (n = 16 nerves): 0.188 ± 0.026 ; *WT rescue* (n = 14 nerves): 0.039 ± 0.004 ; *AxxA1 rescue* (n = 14 nerves): 0.158 ± 0.015 . All panels show mean values and errors bars representing SEM. * $p \leq 0.05$; ** $p \leq 0.01$; *** $p \leq 0.001$; ns, not significant, $p > 0.05$, Mann-Whitney U test. Scale bar: (A–D, G–J) 10 μm .

DOI: 10.7554/eLife.06935.018

reduced the capture rate and could suppress the premature axonal accumulations of AZ/SV proteins in mutants of the small, ARF-family G-protein *Arl-8*. Interestingly, large axonal accumulations in *arl-8* mutants displayed a particularly high capture rate (Klassen et al., 2010; Wu et al., 2013). Similarly, both *aplip1* alleles exhibited enlarged axonal BRP/RBP accumulations. Thus, the capture/dissociation balance for AZ components might be shifted towards ‘capture’ in these mutants, consistent with the ectopic axonal T-bar formation. It is tempting to speculate that loss of *Aplip1*-dependent scaffolding and/or kinesin binding provokes the exposure of critical ‘sticky’ patches of scaffold components such as RBP and BRP. Such opening of interaction surfaces might increase ‘premature’ interactions of cargo proteins actually destined for AZ assembly, thus increase overall size of the cargo complexes by oligomerization between AZ proteins and, finally, promote premature capture and ultimately ectopic AZ-like assembly. On the other hand, the need for the system to unload the AZ cargo at places of physiological assembly (i.e., presynaptic AZ) might pose a limit to the ‘wrapping’ of AZ components and ask for a fine-tuned capture/dissociation balance.

Several mechanisms for motor/cargo separation such as (i) conformational changes induced by guanosine-5'-triphosphate hydrolysis, (ii) posttranslational modification as de/phosphorylation, or (iii) acetylation affecting motor-tubulin affinity, have been suggested for cargo unloading (Hirokawa et al., 2010). Notably, *Aplip1* also functions as a scaffold for JNK pathway kinases, whose activity causes motor-cargo dissociation. JNK probably converges with a mitogen-activated protein kinase (MAPK) cascade (MAPK kinase kinase Wallenda phosphorylating MAPK kinase Hemipterous) in the phosphorylation of *Aplip1*, thereby dissociating *Aplip1* from KLC. Thus, JNK signaling, co-ordinated by the *Aplip1* scaffold, provides an attractive candidate mechanism for local unloading of SVs (Horiuchi et al., 2007) and, as shown here, AZ cargo at synaptic boutons. Our study further emphasises the role of the *Aplip1* adaptor, whose direct scaffolding role through binding AZ proteins might well be integrated with upstream controls via JNK and MAP kinases. Intravital imaging in combination with genetics of newly assembling NMJ synapses should be ideally suited to further dissect the obviously delicate interplay between local cues mediating capturing and axonal transport with motor-cargo dissociation.

Materials and methods

Genetics

Fly strains were reared under standard laboratory conditions (Sigrist et al., 2003) on semi-defined medium (Bloomington recipe). For all experiments both male and female larvae were used for analysis. The following genotypes were used: WT: +/+ (*w1118*). *srpk79D*: *srpk79D^{atc}/srpk79D^{atc}* (unless otherwise noted). *srpk79D^{vn}*: *srpk79D^{vn}/srpk79D^{vn}*. *srpk79D^{atc}*: *srpk79D^{atc}/srpk79D^{atc}*. *brp^{Df}/+*; *srpk79D*: *Df(2R)BSC29/+*; *srpk79D^{atc}/srpk79D^{atc}*. *brp^{null}/brp^{Df}*; *srpk79D*: *brp^{G9}/Df(2R)BSC29*; *srpk79D^{atc}/srpk79D^{atc}*. *rbp^{Df}/+*; *srpk79D*: *Df(3R)S2.01/+*; *srpk79D^{atc}/srpk79D^{atc}*. *rbp^{null}/rbp^{Df}*; *srpk79D*: *rbp^{STOP1}/Df(3R)S201*; *srpk79D^{atc}/srpk79D^{atc}*. *aplip1^{ek4}*: *aplip1^{ek4}/aplip1^{ek4}*. *aplip1^{null}*: *aplip1^{ex213}/aplip1^{ex213}*. *aplip1*, *gen.rescue*: *aplip1^{gen.rescue(ex213)}/aplip1^{gen.rescue(ex213)}*. *Aplip1* cDNA rescue: control: *elav/+*; *aplip1^{ex213}/+*. *aplip1^{null}*: *elav/+*; *aplip1^{ex213}/aplip1^{ex213}*. *WT rescue*: *elav/+*; *UAS-Aplip1-WT/+*; *aplip1^{ex213}/aplip1^{ex213}*. *AxxA1 rescue*: *elav/+*; *UAS-Aplip1-AxxA1/+*; *aplip1^{ex213}/aplip1^{ex213}*. *brp^{Df}/+*; *aplip1^{ek4}*: *Df(2R)BSC29/+*; *aplip1^{ek4}/aplip1^{ek4}*. *brp^{null}/brp^{Df}*; *aplip1^{ek4}*. *brp^{G9}/Df(2R)BSC29*; *aplip1^{ek4}/aplip1^{ek4}*. *Ok6>+*: *OK6-Gal4/+*. *OK6>Aplip1-RNAi*; *rbp^{Df}/+*: *OK6-Gal4/UAS-aplip1-RNAi*; *Df(3R)S2.01/+*. *OK6>Aplip1-RNAi*; *rbp^{null}/rbp^{Df}*: *OK6-Gal4/UAS-aplip1-RNAi*; *rbp^{STOP1}/Df(3R)S201*. *acsl*: *acsl^{J05847}/acsl¹*. *unc51 (atg-1)*: *atg^{1ey07351}/Df(3L)BSC10*. *appl*: *appl^{BG0264}/appl^{Df(1)y7-518}*. *unc-76*: *unc-76^{G0158}/y*. *Aplip1^{GFP},BRP-short^{straw}*: *OK6-Gal4/UAS-BRP-short^{straw};UAS-Aplip1^{GFP}/+*. *Aplip1^{GFP},RBP^{cherry}*: *OK6-Gal4/OK6-Gal4;UAS-Aplip1^{GFP}/UAS-Aplip1^{GFP}*

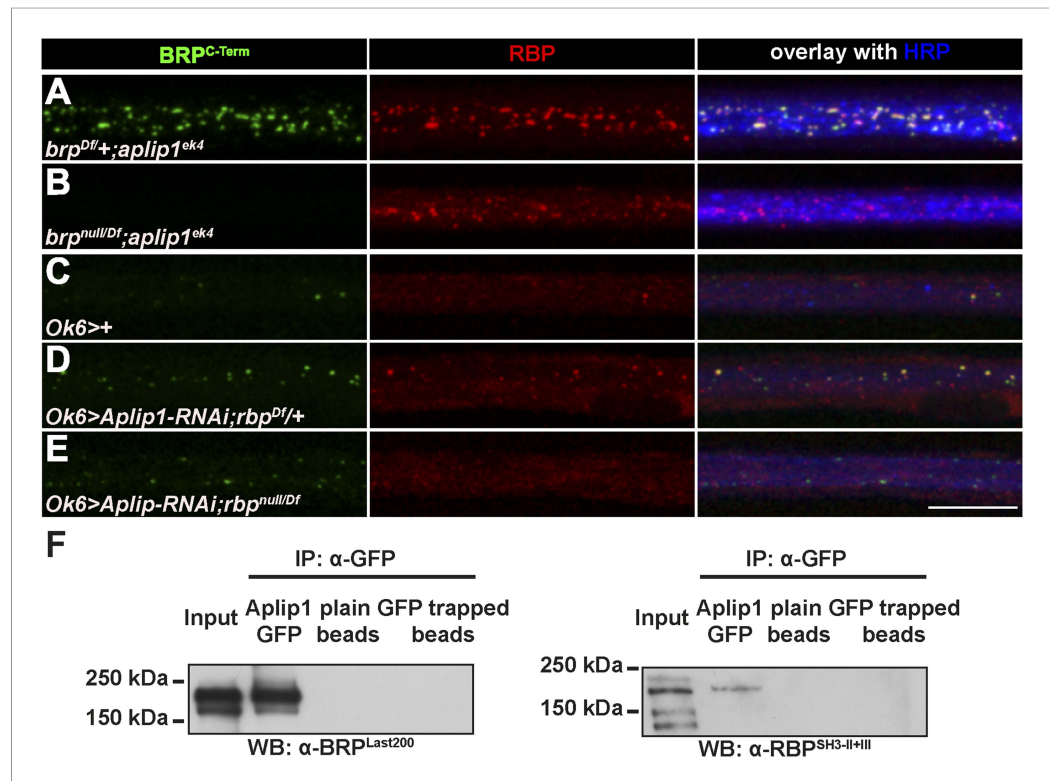


Figure 5. Aplip1 promotes BRP transport in absence of RBP. (A–E) Nerve bundles of segments A1–A3 from third instar larvae of the genotypes indicated labeled with the Abs indicated. (A) Removing one copy of BRP in *aplip1^{ek4}* mutants had no apparent effect on axonal RBP accumulation. (B) RBP still accumulates in *brp^{null}; aplip1^{ek4}* double mutants. (C, D) Driver control and removing one copy of RBP in motoneuronal driven Aplip1-RNAi had no apparent effect on axonal BRP accumulation. (E) BRP still accumulates in *rbp^{null}; aplip1* double mutants Scale bar: (A–E) 10 μ m. (F) Immunoprecipitation (IP) of Aplip1^{GFP} with anti-GFP Ab from Drosophila active zone (AZ) protein-enriched fraction was followed by Western blot (WB) analysis using anti-BRP^{Last200} and anti-RBP^{SH3-II+III}. Both BRP and RBP could be detected in Aplip1^{GFP} IPs, but are absent in controls (plain beads; GFP trapped beads). (For whole WBs, see **Figure 5—figure supplement 2**).

DOI: [10.7554/eLife.06935.019](https://doi.org/10.7554/eLife.06935.019)

The following figure supplements are available for figure 5:

Figure supplement 1. Accumulation of BRP in *srpk79D* mutant axons is unaffected by removing RBP.

DOI: [10.7554/eLife.06935.020](https://doi.org/10.7554/eLife.06935.020)

Figure supplement 2. IP of Aplip1^{GFP} with anti-GFP (Full blot).

DOI: [10.7554/eLife.06935.021](https://doi.org/10.7554/eLife.06935.021)

were crossed to upstream activator sequence (UAS)-RBP^{cherry}/UAS-RBP^{cherry}. BRP^{GFP}, RBP^{cherry}: OK6-Gal4/OK6-Gal4; genomicBRP^{GFP}/genomicBRP^{GFP} were crossed to UAS-RBP^{cherry}/UAS-RBP^{cherry}. Live imaging BRP-short^{straw} in *aplip1* mutant backgrounds (**Figure 2E**): ctrl: OK6-Gal4/UAS-BRP-short^{straw}. *aplip1^{ek4}*: OK6-Gal4/UAS-BRP-short^{straw}; *aplip1^{ek4}/aplip1^{ek4}*. *aplip1^{null}*: OK6-Gal4/UAS-BRP-short^{straw}; *aplip1^{ex213}/aplip1^{ex213}*. *aplip1^{gen.rescue}*: OK6-Gal4/UAS-BRP-short^{straw}; *aplip1^{gen.rescue(ex213)}/aplip1^{gen.rescue(ex213)}*. *Ok6/+; UAS-KHC-RNAi*. *Ok6/+; UAS-Imac-RNAi*.

Stocks were obtained from: *brp⁶⁹* (Kittel et al., 2006), *Df(3R)S2.01* and *rbp^{STOP1}* (Liu et al., 2011a), *aplip1^{ex213}* and *aplip1^{gen.rescue(ex213)}* gift from Catherine Collins (Klinedinst et al., 2013), *srpk79D^{atc}* (Johnson et al., 2009), *srpk79D^{vn}* (Nieratschker et al., 2009), UAS-Aplip1^{GFP} (Horiuchi et al., 2005), UAS-BRP-short^{straw} (Schmid et al., 2008) and genomic BRP^{GFP} (Matkovic et al., 2013). The *aplip1^{ek4}*, *Df(2R)BSC29*, *acs1⁰⁵⁸⁴⁷*, *acs1¹*, *atg1^{ey07351}*, *appl^{BG0264}*, *appl^{Df(1)yT7-518}*, *Df(3L)BSC10*, *unc-76^{G0158}* lines were provided by the Bloomington Drosophila Stock Center. UAS-Aplip1-RNAi, UAS-Imac-RNAi and UAS-KHC-RNAi from VDRC.

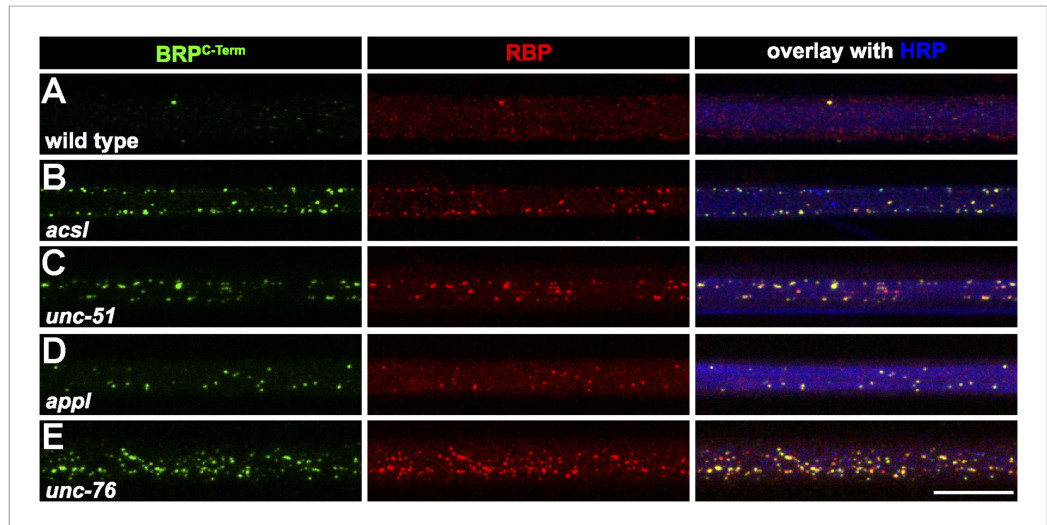


Figure 6. Several known transport adaptor mutants showed axonal BRP and RBP co-accumulations. (A–E) Nerve bundles of segment A1–A3 from third instar larvae of the genotypes indicated labeled with the Abs indicated. BRP and RBP accumulated in a co-localizing manner in axons of WT (A), *acsl* (B), *unc-51* (*atg-1*; C), *appl* (D) and *unc-76* (E). Scale bar: 10 μ m.

DOI: [10.7554/eLife.06935.022](https://doi.org/10.7554/eLife.06935.022)

Generation of RBP^{cherry} cDNA construct

RBP cDNA was assembled based on exon annotation sequence of RBP-PF isoform from flybase. cDNA clones, AT04807; RH38268 and a gene synthesis fragment from MWG eurofins GMBH, Germany, containing 1–1131 bp of RBP-PF isoform were used to assemble the cDNA. All the fragments were cloned into a modified pENTR4 cloning vector described in *Fouquet et al. (2009)*. The final pENTR4 construct contains 5499 bp RBP cDNA was recombined with pTW-Cherry gateway *Drosophila* transgenic vector. Transgenic flies were generated at Bestgene Inc., CA, USA and insertion was confirmed by genotyping.

Generation of Aplip-WT1 and Aplip1-AxxA1 construct

To generate the cDNA of Aplip1 (with WT or mutated first PXXP motif), the full length cDNA clone of Aplip1 was kindly obtained from HYBRIGENICS Services, France and used as a template for cloning full length Aplip1 into pENTR/D-Topo (Invitrogen, Germany) using the following primers:

Aplip1-FL-FW 5'-CACCATGGCCGACAGCGAATTCGAGGAGTT-3'

Aplip1-FL-REV 5'-TCGGCGCGCCACCCTTCTACTCAATGTAG-3'

Through Gateway reaction, the construct was shuttled into GAL4/UAS vector and sent for injection at BestGene Inc., CA, USA. Point mutations were introduced into the constructs via mutated primers with the 'Quick Change II Site-Directed Mutagenesis Kit' from Stratagene, CA, USA. This induced a change of the prolines of PxxP1 (155-PEIP-160) into alanines (155-AEIA-160) after mutagenesis. Following primers were used:

Forward 5' CGTCGTCGCAAGTTGGCGGAAATAGCGAAAAACAAGAAATCT 3'

Reverse 5' AGATTTCTTGTTCGCTATTTCCGCCAACTTGCGACGACG 3'

Generation of peptides for crystallography

For crystallography constructs comprising either the RBP SH3-II (residue 1318–1382) or SH3-III (residue 1441–1507) domain of RBP were amplified by PCR and cloned into the pGEX-6P1 vector using *EcoRI* and *XhoI* restriction sites.

The following primers were used:

SH3II_for 5'-CAGAATTCGCTATTTTGTGGCCATGTTTC-3'

SH3II_rev 5'-TACTCGAGTCACTCCACCTCGGAGACCAT-3'

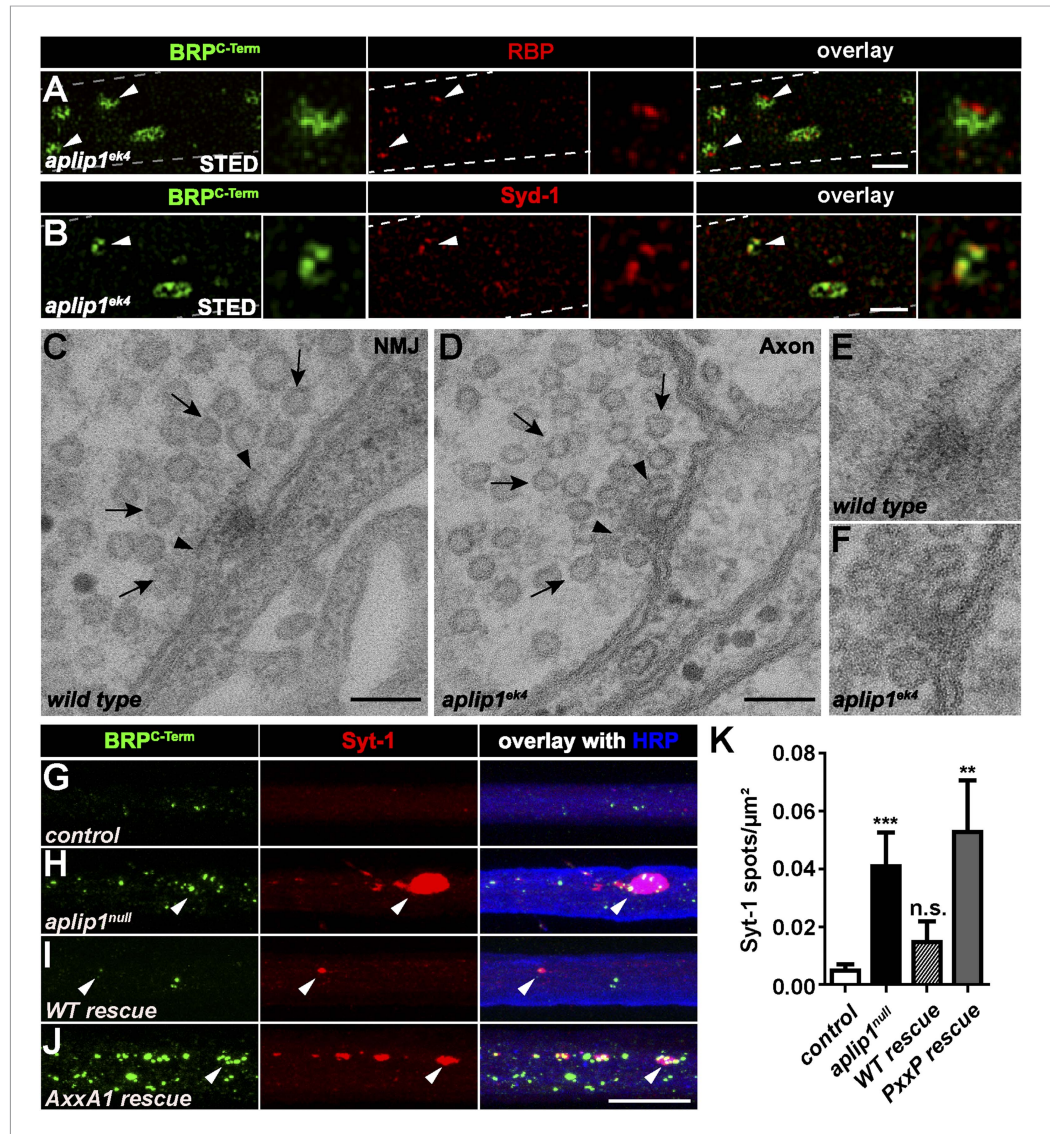


Figure 7. Ectopic AZ scaffold and synaptic vesicle (SV) accumulation in *aplip1* mutant axons. **(A)** Two-colour STED images of axonal aggregates in *aplip1^{ek4}* mutants revealed that the structures observed (arrow heads) have identical BRP and RBP arrangement, as recently observed at presynaptic AZs (Liu et al., 2011a). Right panels display magnifications of single axonal AZ. Dashed lines indicate axonal plasma membrane. **(B)** Two-colour STED images of axonal aggregates in *aplip1^{ek4}* mutants revealed that the structures observed (arrow head) have identical BRP and Syd-1 arrangement as observed at immature presynaptic AZs (Owald et al., 2010). Right panels display magnifications of single axonal AZ. Dashed lines indicate axonal plasma membrane. **(C)** Terminal T-bar (arrow heads) surrounded by SVs (arrows) taken from electron micrographs of WT third instar larvae after conventional embedding. **(D)** Ectopic axonal T-bar (arrow heads) taken from electron micrographs from *aplip1^{ek4}* mutant third instar larvae after conventional embedding. SVs accumulate around the ectopic T-bar (arrows). **(E)** Magnification of **(C)**. **(F)** Magnification of **(D)**. **(G–J)** Nerve bundles of segment A1–A3 from third instar larvae of the genotypes indicated labeled with the Abs indicated. Syt-1 accumulates at a subset of axonal BRP aggregations in *aplip1^{null}* and *AxxA1 rescue* (**H, J**) larvae, but not in control and WT rescue larvae (**G, I**). **(K)** Quantification of the number of Syt-1 spots per μm² axon. control (n = 12 nerves): 0.004 ± 0.002; *aplip1^{null}* (n = 16 nerves): 0.040 ± 0.011; WT rescue (n = 13 nerves): 0.014 ± 0.007; *AxxA1 rescue* (n = 13 nerves): 0.052 ± 0.017. All panels show mean values and errors bars representing SEM. *p ≤ 0.05; **p ≤ 0.01; ***p ≤ 0.001; ns, not significant, p > 0.05, Mann–Whitney U test. Scale bars: **(A, B)** 500 nm; **(C, D)** 100 nm; **(G, J)** 10 μm. DOI: 10.7554/eLife.06935.023

The following figure supplement is available for figure 7:

Figure supplement 1. Ectopic AZ protein accumulations in motoneuronal driven *Imac*- and *KHC*-RNAi axons. DOI: 10.7554/eLife.06935.024

SH3III_for 5'-CAGAATTC AACATGCCCGTGAAGCGAATG-3'
 SH3III_rev 5'-TACTCGAGTCAGTCCGCCAGGAAGTTAGA-3'

The resulting constructs comprise an N-terminal GST-tag that is followed by a PreScission cleavage site and the respective SH3 domain. Correctness of the DNA sequences was confirmed by DNA sequencing.

Yeast two-Hybrid

The Yeast two-Hybrid screen for RBP interaction partners was carried out in collaboration with HYBRIGENICS Services, France using the LexA system (pB27 with bait; pP6 vector with prey) against the HYBRIGENICS *Drosophila melanogaster* head (adult) library. The vector maps of the bait and prey vectors are confidential (protected under material transfer agreement).

The plasmids (pP6 and pB27) encode tryptophan (Trp) and leucine (Leu) biosynthesis genes, and were successfully double transformed into the TATA strain lacking genes for synthesis of Leu and Trp which can be followed by positive growth in LT media. Reporter genes for the protein-protein interaction are HIS3, which can be later detected by growth on plates lacking histidin, as well as lacZ which allows the detection of interaction in a more quantitative fashion with a β -galactosidase assay. To transform the yeast cells with the pP6 and pB27 vector respectively the LiAc/single strand DNA/PEG technique was used (Gietz and Schiestl, 2007).

The RBP constructs for Y2H were cloned into pB27 bait vector. The RBP cDNA clone AT04807 (*Drosophila* Genomics Resource Centre, IN, USA) was used as a template for PCR reaction. For amplification the following primers were used:

5'-CAGAATTCGGTCAACCGGGACAACCGGGG-3'
 5'-TAACTAGTTCAGTCGGGCGCGTCCGCCAGGA-3'

Protein sequence of the bait fragment

RBP SH3-II+III (length: 209 AA; Orientation C-term free [N-LexA-bait-C])
 GQPGQPGQMPGAQKKPRYFVAMFDYDPSTMSPNPDGCDEELPFQEGDTIKVFGDKDADGFYWGELRG
 RRGYVPHNMVSEVEDTTASMTAGGQMPGQMPGQMGQGVGVGGTAQVMPGQGAPOQSMRNV
 RDRWGDYANMPVKRMIALYDYPQELSPNVDAEQVELCFKTGEIILVYGDMEDEDFYMGELDGVRGLVP
 SNFLADAPD

Liquid Y2H β -Galactosidase assay

The assay was carried out as described in JH Miller 'Experiments in Molecular Genetics' 1972 Cold Spring Harbor Laboratories pages 352–355.

The RBP constructs for Y2H were cloned into pB27 bait vector. The RBP cDNA clone AT04807 (*Drosophila* Genomics Resource Centre) was used as a template for PCR reaction. For amplification the following primers were used:

RBP SH3-II
 5'-CAGAATTCGGTCAACCGGGACAACCGGGG-3'
 5'-TAACTAGTTCAGTCCTCCACCTCGGAGACC-3'

Giving rise to the following sequence

PGQPGQPGQMPGAQKKPRYFVAMFDYDPSTMSPNPDGCDEELPFQEGDTIKVFGDKDADGFYWGELR
 GRRGYVPHNMVSEVED

RBP SH3-III
 5'-CAGAATTCATGCCCGTGAAGCGAATG-3'
 5'-TAACTAGTTCAGTCGGGCGCGTCCGCCAGGA-3'

Giving rise to the following sequence

MPVKRMIALYDYPQELSPNVDAEQVELCFKTGEIILVYGDMEDEDFYMGELDGVRGLVPSNFLADAPD

RBP SH3-II+III
 5'-CAGAATTCGGTCAACCGGGACAACCGGGG-3'
 5'-TAACTAGTTCAGTCGGGCGCGTCCGCCAGGA-3'

Giving rise to the following sequence

GQPGQPGQMPGAQKKPRYFVAMFDYDPSTMSPNPDGCDEELPFQEGDTIKVFGDKDADGFYWGELRG
RRGYVPHNMVSEVEDTTASMTAGGQMPGQMPGQMGQGVGGTAQVMPGQGAPOQSMRNVS
RDRWGDYANMPVKRMIALYDYDPOELSPNVDAEQVELCFKTGEIILVYGDMDDEDGFYMGELDGVRGLVPS
NFLADAPD

By applying the site-directed mutagenesis strategy, different constructs were designed for RBP using mutated primers. Mutagenesis was carried out by Dr Martin Meixner (SMB. GmbH, Germany,). The following point mutations were used:

RBP SH3-II*: Prolin₁₃₇₃ → Leucin

Giving rise to the following sequence

PGQPGQPGQMPGAQKKPRYFVAMFDYDPSTMSPNPDGCDEELPFQEGDTIKVFGDKDADGFYWGELR
GRRGYVLHNMVSEVED

RBP SH3-III*: Prolin₁₅₀₀ → Leucin

Giving rise to the following sequence

MPVKRMIALYDYDPOELSPNVDAEQVELCFKTGEIILVYGDMDDEDGFYMGELDGVRGLVLSNFLADAPD

The Aplip1 prey fragment only containing the first PXXP was generated from the full length fragment via PCR using the primers

Aplip first PXXP FW 5'-CGTACTCCATGGCTGAGGACGATGAGCTGGGCGA-3'

Aplip first PXXP REV 5'-CTGACTACTAGTTGGAGTCCTCGTCCATCAAGTA-3'

Giving rise to the following sequence

Aplip1-PXXP1 (length: 139 AA)

EDDELGDGLKVTLSDDGSLDTNDSFNHRHPLNHQDAIGGFLGMDTSGLGGNSAPVTIGASTDLLAPNT
AATRRRRLPEIPKKNKSSILHLLGGSNFGSLADEFRNGGGGGIPPAVRSGQORSFSLKCGYLMDDEDS

The Aplip1 prey fragment only containing the second PXXP was generated from the full length fragment via PCR using the primers

Aplip second PXXP FW 5'-CGTACTCCATGGCTCTTCTAGGTGGCTCCAACCTT-3'

Aplip second PXXP REV 5'-CTGACTACTAGTTCTGGCCAAAGGGCACGC-3'

Giving rise to the following sequence

Aplip1-PXXP2 (length: 100 AA)

LLGGSNFGSLADEFRNGGGGGIPPAVRSGQORSFSLKCGYLMDDESSPDSERMOSLGDVDSGHSTAHS
PNDFKSMSPQITSPVSQSPFPFPGGVPFGQ

The Aplip1 prey fragment only containing the mutated first PXXP motif (AxxA) (see also Generation of Aplip-WT1 and Aplip1-AxxA1 construct) was generated from the full length fragment via PCR using the primers:

Forward 5' CGTCGTCGCAAGTTGGCGGAAATAGCGAAAAACAAGAAATCT 3'

Reverse 5' AGATTTCTTGTTTTTCGCTATTTCCGCCAACTTGCGACGACG 3'

Giving rise to the following peptide sequence

Aplip1-AXXA1 (length: 139 AA)

EDDELGDGLKVTLSDDGSLDTNDSFNHRHPLNHQDAIGGFLGMDTSGLGGNSAPVTIGASTDLLAPNT
AATRRRRLAEIAKKNKSSILHLLGGSNFGSLADEFRNGGGGGIPPAVRSGQORSFSLKCGYLMDDEDS

The BRP constructs for Y2H were cloned into pB27 bait vector. Yeast two-hybrid constructs for BRP were obtained by PCR using the corresponding cDNA as template (modified from *Wagh et al., 2006*).

To generate BRP prey fragments the following primers were used:

Forward 5' CAGCGGCCGCTCCAGTAACTAGCTCTGG 3'

Reverse 5' TAACTAGTTTATATGTGCCGCTGGTAGTC 3'

Giving rise to the following peptide sequence

BRP-D1 (length: 359 AA)

PVTSSGVRSPGRVRRQLQELPTVDRSPSRDYGAPRGSPLAMGSPYYRDMDEPTSPAGAGHHRSRASRPPM
 AHAMDYPRTRYQSLDRGGLVDPHDREFIPIREPRDRSRDRSLERGLYLEDELYGRSARQSPSAMGGYNTG
 MGPTSDRAYLGDLOHQNTDLORELGNLKRELELTNQKLGSSMHSIKTFWSPELKKERAPRKEESAKYSLIN
 DQLKLLSTENQKQAMLVROLEEEELRLMRQPNLEMROQMEAIYAENDHLQREISILRETVKDLECRVETQK
 QTLIARDESIIKLEMLQAKGMGKEEERQMFQMQQAMAQKQLDEFRLQRRDQEIILAMAAMKMLEE
 QHQDYQRHI

Forward 5' CAGCGGCCGCGATGTTCCAGCAGATGC 3'

Reverse 5' TAACTAGTTTACTGTGTGACTCTCAGCTCGGC 3'

Giving rise to the following peptide sequence

BRP-D2 (length: 339 AA)

MFQQMQAMAQKQLDEFRLQRRDQEIILAMAAMKMLEEQHQDYQRHIAVLKESLCAKEEHYNMLQTD
 VEEMRARLEEKNRLIEKKTQGTLOTVOERNRLTSELTELKDHMDIKDRKISVLQRKINLEDLLKEKDNQVDM
 ARARLSAMQAHSSSEGALTSLEEAIKDKEKQMAQLRDQRDRAEHEKOEERDLHEREVADYKIKLRAAESE
 VEKLOTRPERAVTERERLEIKLEASQSELGKSKELEKATCEMGRSSADWESTKQRTARLEENERLKHDLER
 SQNVQKLMFETGKISTTFGRITMTTSQELDRAQERADKASAE LRRTQAE LRVTQ

Forward 5' CAGAATTCGAGCGGGCCGACAAGGC 3'

Reverse 5' TAACTAGTTCACATTTGCGCCTTCTC 3'

Giving rise to the following peptide sequence

BRP-D3 (length: 636 AA)

ERADKASAE LRRTQAE LRVTQSDAERAREEAAAALQEKLEKSQGEVYRLKAKLENAOGEQESLRQLEKQAO
 SGVSRIHADRDRAFSEVEKIKEEMERTQATLGKSQLOHEKLNQSLDKAQNEVDHLQDKLDKACTENRRLV
 LEKEKLTYYDYNLQSQDLKALGQAARMQKERETLSLDTDRIREKLEKTQVQLGRIQKERDQFSDELETLKER
 SESAQTLMLKAARDREAMQTDLEVLKERYEKSHAIQKQKQMERDDAVTEVEILKEKLDKALYASQKLIIDEK
 DTSNKEFEKMLEKYDRAQNEIYRQSRCDTAEADRARLEVEAERSGLAASKAREDLRKLQDESTRLQEQACD
 RAALQLSRAKCECEDNARSELEHSRDRFDKLDQDIRRAQGEKEHFQSELERVYELERAHAAQTKASASVEA
 AKEEAAHYAVELEKMRDRYEKSQVELRKLQDQDTDFGRETRRLKEENERLREKLDKTLMELETIRGKSQYESE
 SFEKYKDKYEKIEMEVQNMESKLHETSLOLELSKGEVAKMLANQEQORSELERAHIEREKARDKHEKLLKEV
 DRLRLQSSVSPGDPVRASTSSSSALSAGERQEI DRLRDRLEKALQSRDATELEAGRLAKELEKAQM

Forward 5' CAGCGGCCGCCCTGCAACAGTCCTCGG 3'

Reverse 5' TAACTAGTTTACAACCTCTGTGACCAG 3'

Giving rise to the following peptide sequence

BRP-D4 N-term (length: 348 AA)

LQSSVSPGDPVRASTSSSSALSAGERQEI DRLRDRLEKALQSRDATELEAGRLAKELEKAQMHLAKQOEN
 TESTRIEFERMGAE LGR LHDRLEKAEAEERALRQANRSGGAGAAPHQLEKHVQKLESDVKQLAMEREQL
 VLQLEKSQEILMNFQKELQNAEAELOKTRREENRKLNRNGHQVPPVAAPPAGPSPAEFQAMQKEIQTLOQK
 LQESERALQAAGPQQAQAAAAAGASREEIEQWRKVIEQEKSRADMADKAAQEMHKRIQLMDQHIKQD
 HAQMOKMQQQMQQQQQAQAVQQAQQQQAAGAGGADPKELEKVRGELQAACTERDRFQQ
 QLELLVTEL

Forward 5' CAGAATTCAGAGCAAGATGTCCAAC 3'

Reverse 5' TAACTAGTTTAGAAAAAGCTCTTCAA 3'

Giving rise to the following peptide sequence

BRP-D4 C-term (length: 227 AA)

SKMSNQEQAKQLQTAQQQVQQLQQQVQQLQQQMQQLOQAASAGAGATDVQRQOLEQQQKQLE
 EVRKQIDNQAKATEGERKIIDEQRKQIDAKRKDIEEKEKMAEFDVQLRKRKEQMDQLEKSLQTQGGGAA
 AAGELNKKLMDTQRQLEACVKELQNTKEEHKKAATETERLLQLVQMSQEEQNAKEKTIMDLQQALKIAQ
 AKVKQAQTQQQQQQDAGPAGFLKSFF

IP

IP of *elav-Gal4/+;UAS-Aplip1^{GFP/+}* was performed as described in *Depner et al. (2014)*. In brief, the experiment was performed as following, 500 μ l adult fly heads were mechanically homogenized in 500 μ l lysis buffer (50 mM Tris pH 8.0, 150 mM KCl, 1 mM MgCl₂, 1 mM EGTA, 10% glycerol containing protease inhibitor cocktail [Roche, Germany]). 0.4% Sodium deoxycholate was added, and the lysate was incubated on ice for 30 min. The lysate was diluted 1:1 with sodiumdeoxycholat-free lysis buffer, then 1% Triton X-100 was added and lysate was kept on the wheel at 4°C for 30 min. After centrifugation for 15 min at 16,000 \times g, the supernatant was used in IPs with GFP-Trap-A beads and blocked agarose beads as binding control (Chromotek, Germany). After incubation overnight at 4°C, beads were washed in buffer without detergent and glycerol. Proteins were eluted from the beads with SDS sample buffer. Afterward, the SDS-PAGE samples were subjected to Western blot (WB).

SDS-PAGE and Tris-Acetate gel electrophoresis

The gel electrophoresis for both SDS-PAGE and Tris-acetate gels was conducted according to the standard protocols (*Laemmli, 1970; Schägger, 2006*). Colloidal Coomassie blue stain was used to detect proteins based on manufacture protocol (Carl-Roth, Germany and Invitrogen). For BRP, RBP and Aplip1, standard SDS-PAGE gels (6–12%) were used to separate the target protein.

WB analysis

Following the separation by gel electrophoresis, the proteins were transferred into a nitrocellulose membrane by wet transfer procedure using cold transfer buffer (25 mM Tris, pH 8.0, 150 mM glycine, 20% methanol). For visualization of proteins, the membrane was stained using Ponceau-S staining solution (Sigma–Aldrich, MO, USA). 5% milk powder in phosphate buffered saline (PBS) was used for blocking of the membrane. Following the blocking, the membrane was incubated with the primary Abs guinea pig BRP^{Last200} (1:5000, Ullrich et al., in submission) and rabbit RBP^{SH3-II+III} (1:1000, *Depner et al., 2014*) at 4°C for overnight. After several washing steps, the membrane was incubated with horseradish peroxidase (HRP) conjugated secondary Abs (Dianova, Germany). For detection, an enhanced chemoluminescence substrate (GE Healthcare, United Kingdom) was used and the X-ray film (GE Healthcare) development was carried manually.

Immunostaining

Larval filets were dissected and stained as described previously (*Owald et al., 2010*). The following primary Abs were used: rabbit BRP^{N-term} (1:500; *Qin et al., 2005*); rabbit Liprin- α (1:500; *Fouquet et al., 2009*); rabbit Syd-1 (1:500; *Owald et al., 2010*); rabbit Rab3 (1:500; *Graf et al., 2009*); rabbit RBP^{C-term}, rabbit RBP^{SH3-II+III} (1:500; *Depner et al., 2014*); rabbit Syt1-CL1 (1:1000; gift from N Reist [*Mackler et al., 2002*], Colorado State University, CO, USA); mouse GFP (3E6) (1:500, Life Technologies, Germany), mouse Nc82 = anti-BRP^{C-term} (1:100, Developmental Studies Hybridoma Bank, University of Iowa, Iowa City, IA, USA). Except for staining against Ca^{GFP}, where larvae were fixed for 5 min with ice-cold methanol, all fixations were performed for 10 min with 4% paraformaldehyde in 0.1 mM PBS. Secondary Abs for standard immunostainings were used in the following concentrations: goat anti-HRP-Cy5 (1:250, Jackson ImmunoResearch, PA, USA); goat anti-rabbit Cy3 (1:500, Life Technologies); goat anti-mouse Alexa-Fluor-488 (1:500, Life Technologies). Larvae were mounted in vectashield (Vector labs, United Kingdom). Secondary Abs for STED were used in the following concentrations: For **Figures 1H, 7A**: goat anti-mouse Atto594 (1:250); goat anti-rabbit Atto594 (1:250); goat anti-mouse Atto647N (1:100), goat anti-rabbit Atto647N (1:100) (ATTO-TEC, Germany). For **Figure 7B**: goat anti-mouse Atto590 (1:100); goat anti-rabbit star635 1:100 (Atto590 [ATTO-TEC] and star635 [Abberior, Germany]) coupled to respective IgGs (Dianova, Germany). For **Figure 7—figure supplement 1A–C**: goat anti-mouse Alexa-Fluor-488 (1:500, Life Technologies) and goat anti-rabbit Alexa-Fluor-532 (1:500, Life Technologies) was used. For STED imaging larvae were mounted in Mowiol (Max-Planck Institut for Biophysical Chemistry, Group of Stefan Hell) or Prolong Gold antifade reagent (Life Technologies; **Figure 7—figure supplement 1A–C**).

Image acquisition, processing and analysis

Confocal microscopy was performed with a Leica TCS SP5 (all except for **Figure 4G–J** and **Figure 7G–J**) or a Leica SP8 (**Figure 4G–J** and **Figure 7G–J**) confocal microscope (Leica Microsystems, Germany).

STED microscopy was performed with a custom-built STED-microscope (see below). Images of fixed and live samples were acquired at room temperature. Confocal imaging of axons was done using a z step of 0.25 μm . The following objective was used: 63 \times 1.4 NA oil immersion for NMJ confocal imaging. All confocal images were acquired using the LCS AF software (Leica, Germany). Images from fixed samples were taken from third instar larval nerve bundles (segments A1–A3). Images for figures were processed with ImageJ software to enhance brightness using the brightness/contrast function. If necessary images were smoothed (0.5–1 pixel Sigma radius) using the Gaussian blur function.

Quantifications of axonal spot number and size were performed following an adjusted manual ([Andlauer and Sigrist, 2012](#)), briefly as follows. The signal of a HRP-Cy5 Ab was used as template for a mask, restricting the quantified area to the shape of the axon/nerve bundles. The original confocal stacks were converted to maximal projections and after background subtraction, a mask of the axonal area was created by applying a certain threshold to remove the irrelevant lower intensity pixels. The segmentation of single spots was done semi-automatically via the command 'Find Maxima' and by hand with the pencil tool and a line thickness of 1 pixel. To remove high frequency noise a Gaussian blur filter (0.5 pixel Sigma radius) was applied. The processed picture was then transformed into a binary mask using the same lower threshold value as in the first step. This binary mask was then projected onto the original unmodified image using the 'min' operation from the ImageJ image calculator. The axonal spots of the resulting images were counted with the help of the 'analyze particle' function with a lower threshold set to 1. The spot density was obtained by normalizing the total number of analyzed particles to the axonal area measured via HRP. Colocalization of RBP/BRP spots ([Figure 1G](#)) was counted manually.

Data were analyzed using the Mann–Whitney U test for linear independent data groups. Means are annotated \pm SEM. Asterisks are used to denote significance: * $p < 0.05$; ** $p < 0.01$; *** $p < 0.001$; n.s. (not significant), $p > 0.05$.

STED microscopy

For [Figures 1H, 7A](#) two-colour STED images were recorded with a custom-built STED microscope which combines two pairs of excitation and STED laser beams all derived from a single supercontinuum laser source ([Bückers et al., 2011](#)). For [Figure 7B](#) STED microscopy was performed as previously described in [Li et al. \(2014\)](#). Here, two-colour STED images were recorded on a custom-built STED-microscope ([Göttfert et al., 2013](#)), which combines two pairs of excitation laser beams of 595 nm and 640 nm wavelength with one STED fiber laser beam at 775 nm. All STED images were acquired using Imspector Software (Max Planck Innovation GmbH). STED images were processed using a linear deconvolution function integrated into Imspector Software (Max Planck Innovation GmbH, Germany). Regularization parameters ranged from $1e^{-09}$ to $1e^{-10}$. The point spread function (PSF) for deconvolution was generated by using a 2D Lorentz function with its half-width and half-length fitted to the half-width and half-length of each individual image. For [Figure 7—figure supplement 1](#), STED microscopy was performed with a Leica TCS SP5 time gated STED microscope equipped with a 100 \times 1.4 NA objective using the LCS AF software (Leica) for image acquisition. Alexa-Fluor-488 and Alexa-Fluor-532 were excited using a pulsed white light laser at 488 and 545 nm, respectively. STED was achieved with a continuous STED laser at 592 nm. In gSTED mode time gated detection started at 1.2 ns–6 ns for Alexa488 while for Alexa532 gating time was set to 2.3 ns–6 ns. Raw gSTED images were deconvolved using the built-in algorithm of the LAS AF software (Signal intensity; regularisation parameter 0.05). The PSF was generated using a 2D Lorentz function with the full-width half maximum set to 60 nm. Images for figures were processed with ImageJ software to remove obvious background, enhance brightness/contrast and smoothed (1 pixel Sigma radius) using the Gaussian blur function.

Live imaging and analysis

Live imaging was performed as previously described ([Füger et al., 2007](#)). Briefly, third instar larvae were put into a live imaging chamber and anaesthetized with 10–20 short pulses of a desflurane-air mixture until the heartbeat completely stopped. For assessing axonal transport, axons immediately after exiting the ventral nerve cord were imaged for 10 min using timelapse confocal microscopy. The flux was determined by manually counting the number of moving spots (unidirectional for >3

frames) passing a virtual line in the middle of the nerve bundle. Mean flux was calculated by pooling results from at least three independent larvae and at least six nerves. If little or no flux was observed, additional nerves were imaged to avoid any bias from selecting specific nerves.

ITC

ITC experiments were performed at 25°C on an iTC200 microcalorimeter (Malvern Instruments Ltd., United Kingdom). The same peptides were employed as used for the co-crystallization experiments (see below). Lyophilized peptides were resuspended in the final buffer of the proteins (10 mM Tris-HCl pH 7.4, 100 mM NaCl). RBP SH3-II and SH3-III were both provided at a concentration of 150 µM, RBP SH3-II+III was provided at 78 µM. The proteins were titrated with 16 injections of 2.5 µl of either Aplip1, Cac, RIM1 or RIM2 peptide at a concentration of 2 mM with 2-min intervals. The released heat was obtained by integrating the calorimetric output curves. Binding parameters were calculated using the Origin5 software using the 'One Set of Sites' curve fitting model provided by the software.

The following peptides were used

RBP SH3-I

RFPYDPPEEAEGELSLCAGDYLLVWTSGEPOGGYLDAAELLDGRRGLVPASFVQRLVG

RBP SH3-II

RYFVAMFDYDPSTMSPNPDGCDEELPFQEGDTIKVFGDKDADGFYWGELRGRRGYVPHNMVSEVE

RBP SH3-III

KRMIALYDYDPOELSPNVDAEQVELCFKTEIILVYGDMDDEDGFYMGELDGVRGLVPSNFLAD

RBP SH3-II+III

RYFVAMFDYDPSTMSPNPDGCDEELPFQEGDTIKVFGDKDADGFYWGELRGRRGYVPHNMVSEVEDTT
ASMTAGGQMPGQMPGQMGQGGVGGTAQVMPGQGAQHSMRNVSRDRWGDYANMPVKRM
IALYDYDPOELSPNVDAEQVELCFKTEIILVYGDMDDEDGFYMGELDGVRGLVPSNFLAD

Aplip-PxxP1: TRRRRKLPEIPKNNK

Cac: IGRRLPPTPSKPSTL

RIM1: GRQLPQVPVRS

RIM2: GRQLPQLPPKGT

Protein expression and purification for crystallization

Protein expression was conducted using chemically competent *Escherichia coli* BL21-CodonPlus-RIL cells. The cells were grown in autoinduction ZY-medium (Studier, 2005) with ampicillin and chloramphenicol for 4 hr at 37°C. Afterwards, the temperature was decreased to 18°C, and the cells were grown overnight. The cells were harvested by centrifugation at 8,000×g for 6 min. The cell pellet was resuspended in resuspension buffer (40 mM Tris/HCl pH 7.5 at RT, 250 mM NaCl, 1 mM DTT, 10 mg/l lysozyme and 5 mg/l DNase I) and subsequently lysed by sonification for 20 min. The lysate was centrifuged at 56,000×g for 45 min to pellet the cell debris. The supernatant was applied for affinity chromatography using 10 ml glutathione sepharose 4B (GE Healthcare). Hereafter, two washing steps were performed using 80 ml washing buffer (20 mM Tris/HCl pH 7.5 at RT, 250 mM NaCl, 1 mM DTT) for each step. The GST-tag of the respective SH3 domain was cleaved off on the beads using PreScission protease (1 mg/ml). Therefore 40 ml washing buffer with PreScission protease in a molar ratio of 1:30 to the maximum loading capacity of the glutathione sepharose were incubated with the beads at 4°C while gently rotating overnight. The PreScission-cleaved constructs were purified using a Superdex 75 26/60 column (GE Healthcare). The protein containing fractions were pooled and concentrated using a 3 kDa molecular weight cut-off concentrator (Millipore, Germany). Protein concentrations were determined by UV-absorption.

Crystallization and crystal cooling

For crystallization experiment the RBP SH3-II was concentrated to 56 mg/ml and the RBP SH3-III to 62 mg/ml. The same peptides as for ITC measurements were used and synthesized at the Leibniz Institute for Molecular Pharmacology with N-terminal acetylation and C-terminal amidation. The

unsolubilized peptides were mixed in a fivefold molar excess with the protein solution and incubated for 2 hr on ice. Insoluble peptide was removed by centrifugation (16,000×g for 1 min) prior to crystallization experiments. All crystallization experiments were carried out at 291 K in a sitting drop setup. Crystals of RBP SH3-II bound to the Aplip1 peptide were obtained over a reservoir solution composed of 2.2–2.6 M ammonium sulfate, 0.1 M bicine with final pH 9. For cryoprotection, the crystals were transferred to a reservoir solution supplemented with 25% (vol/vol) glycerol. Crystals of RBP SH3-II bound to Cac were obtained over a reservoir solution of 0.2 M Ca(Ac)₂, 0.1 M MES pH 6.0, and 20% (wt/vol) polyethyleneglycol (PEG) 8000. For cryoprotection, the crystals were transferred to a reservoir solution supplemented with 15% (vol/vol) PEG 400. Crystals of RBP SH3-III bound to the Cac peptide appeared over a reservoir solution of 0.2 M Li₂SO₄, 0.1 M MES pH 6.5, and 30% (vol/vol) PEG 400. After cryoprotection the crystals were flash-cooled in liquid nitrogen.

Diffraction data collection and analysis as well as structure determination

Synchrotron diffraction data were collected at the beamline 14.2 of the MX Joint Berlin laboratory at BESSY (Berlin, Germany). X-ray data collection was performed at 100 K. Diffraction data were processed with the XDS package (Kabsch, 2010). The diffraction data of RBP SH3-II/Aplip1-PxxP1 were initially indexed in *P*622. Cumulative intensity distribution analysis as well as calculation of the moment of the observed intensity/amplitude distribution performed with PHENIX.XTRIAGE and POINTLESS (Evans, 2011) indicated an unusual intensity distribution, likely caused by twinning. For determination of the correct space group, the diffraction data were processed in *P*1. Subsequently, the structure was solved by molecular replacement with the program PHASER (McCoy et al., 2007). We used the NMR structure of the SH3-II domain of human RBP (PDB entry 2CSQ) as search model and could locate 24 copies of the SH3 domain. Next the diffraction data and the coordinates of our molecular replacement were analysed by the program ZANUDA (Lebedev and Isupov, 2014) revealing that sixfold is in fact broken and *C*2 is the true symmetry, with sixfold twinning with the six twin operators: $h, h, l; h, -k, -l; 1/2h - 3/2k, -1/2h - 1/2k, -k; -1/2h + 3/2k, 1/2h + 1/2k, -l; -1/2h - 3/2k, -1/2h + 1/2k, -l$ and $1/2h + 3/2k, 1/2h - 1/2k, -l$. In total we could locate in the asymmetric unit 12 copies of RBP SH3-II bound to Aplip1-PxxP1. The crystals of RBP SH3-II and SH3-III bound to the Cac peptide have *P*2₁ and *I*222 symmetry, respectively. Analyses of the diffraction data of the complex of RBP SH3-II and Cac revealed one pseudo-merohedral twin operator ($h, -k, -h - l$), that was later included in the refinement protocol. The structures of RBP SH3-II and SH3-III each bound to the Cac derived peptide were solved by molecular replacement with our previously determined structure of RBP SH3-II. The asymmetric unit of RBP SH3-II bound to Cac contains 10 complexes and of RBP SH3-III bound to Cac one complex, respectively.

Refinement and validation

The refined molecular replacement solution clearly revealed the presence of the bound Aplip1-PxxP1 peptide in $2mFo - DFc$ and $mFo - DFc$ electron density maps. For refinement, a set of 4.7% of R_{free} reflections was generated in *P*622 and then expanded to *C*2 to insure equal distribution of the R_{free} reflections in all six twin domains. For calculation of the free R-factor of the other two data sets, a randomly generated set of 5% of the reflections from the diffraction data set was used and excluded from the refinement. The structure was manually built in COOT (Emsley et al., 2010) and refined in REFMAC 5.8.0073 (Murshudov et al., 2011) with intensity based twin refinement. In final stages TLS refinement was applied with every protein and peptide chain as single TLS group. The structures with bound Cac peptide were refined with PHENIX.REFINE (Adams et al., 2010; Afonine et al., 2012). Water molecules were picked with COOT and manually inspected. All structures were evaluated with MOLPROBITY (Chen et al., 2010) and PROCHECK (Laskowski et al., 1993). Figures were drawn with PYMOL (DeLano, 2002).

EM

Conventional embedding was performed as described previously (Fouquet et al., 2009).

Statistics

Data were analyzed using the Mann–Whitney rank sum test for linear independent data groups (Prism; GraphPad Software, Inc.). Means are annotated ± SEM. Asterisks are used to denote significance (**p* < 0.05; ***p* < 0.01; ****p* < 0.005; not significant, *p* > 0.05).

Acknowledgements

This work was supported by grants from the Deutsche Forschungsgemeinschaft to SJS (Exc 257, TP A3/SFB 958, TP B9/SFB665) and JHD, MCW, BL, SJS (TP A6/SFB 958). MS was supported by a Ph.D. fellowship from the Max Delbrück Center for Molecular Medicine and a Boehringer Ingelheim Fonds Ph.D. fellowship. MB was supported by a Ph.D. fellowship from the graduate school GRK 1123 funded by the DFG. UR was supported by the International Max Planck Research School (IMPRS) on Multiscale Bio-Systems. We are grateful to Noreen Reist for generously contributing antibodies. We would like to thank Janine Lützkendorf (SFB958) for help with genetic analysis, Madeleine Brünner and Anastasia Stawrakakis for excellent technical assistance and Astrid Petzoldt for comments on the manuscript. We thank Thorsten Mielke for help with electron microscopy. We are grateful to G Bourenkov for discussion on the unusual twinning phenomenon. We accessed beamlines of the BESSY II (Berliner Elektronenspeicherring-Gesellschaft für Synchrotronstrahlung II) storage ring (Berlin, Germany) via the Joint Berlin MX-Laboratory sponsored by the Helmholtz Zentrum Berlin für Materialien und Energie, the Freie Universität Berlin, the Humboldt-Universität zu Berlin, the Max-Delbrück Centrum, and the Leibniz-Institut für Molekulare Pharmakologie. We thank C Weise SFB958/Z3 for mass spectrometric analysis.

Additional information

Funding

Funder	Grant reference	Author
Deutsche Forschungsgemeinschaft (DFG)	SFB958/A3	Markus C Wahl, Bernhard Loll, Stephan J Sigrist
Deutsche Forschungsgemeinschaft (DFG)	SFB665/B9	Stephan J Sigrist
Deutsche Forschungsgemeinschaft (DFG)	Graduate Student Fellowship, GRK 1123	Mathias A Böhme
Deutsche Forschungsgemeinschaft (DFG)	SFB958/Z3	Markus C Wahl, Bernhard Loll
Deutsche Forschungsgemeinschaft (DFG)	SFB958/A6	Markus C Wahl, Bernhard Loll, Stephan J Sigrist
Max-Planck-Gesellschaft	International Max Planck Research School	Ulises Rey

The funders had no role in study design, data collection and interpretation, or the decision to submit the work for publication.

Author contributions

MS, MAB, BL, Conception and design, Acquisition of data, Analysis and interpretation of data, Drafting or revising the article; JHD, Conception and design, Acquisition of data, Analysis and interpretation of data; HB, MMM, UR, NR, TM, NH, SR-A, FG, DK, CQ, TFMA, SWH, Acquisition of data, Analysis and interpretation of data; SK, Acquisition of data, Contributed unpublished essential data or reagents; CAC, Conception and design, Contributed unpublished essential data or reagents; MCW, Conception and design, Drafting or revising the article; SJS, Conception and design, Analysis and interpretation of data, Drafting or revising the article

Author ORCIDs

Matthias Siebert,  <http://orcid.org/0000-0002-1739-5825>
 Mathias A Böhme,  <http://orcid.org/0000-0002-0947-9172>
 Niraja Ramesh,  <http://orcid.org/0000-0002-2867-7131>
 Till FM Andlauer,  <http://orcid.org/0000-0002-2917-5889>
 Bernhard Loll,  <http://orcid.org/0000-0001-7928-4488>

References

- Adams PD, Afonine PV, Bunkoczi G, Chen VB, Davis IW, Echols N, Headd JJ, Hung LW, Kapral GJ, Grosse-Kunstleve RW. 2010. PHENIX: a comprehensive Python-based system for macromolecular structure solution. *Acta Crystallographica. Section D, Biological Crystallography* **66**:213–221. doi: [10.1107/S0907444909052925](https://doi.org/10.1107/S0907444909052925).
- Afonine PV, Grosse-Kunstleve RW, Echols N, Headd JJ, Moriarty NW, Mustyakimov M, Terwilliger TC, Urzhumtsev A, Zwart PH, Adams PD. 2012. Towards automated crystallographic structure refinement with phenix.refine. *Acta Crystallographica. Section D, Biological Crystallography* **68**:352–367. doi: [10.1107/S0907444912001308](https://doi.org/10.1107/S0907444912001308).
- Ahmari SE, Buchanan J, Smith SJ. 2000. Assembly of presynaptic active zones from cytoplasmic transport packets. *Nature Neuroscience* **3**:445–451. doi: [10.1038/74814](https://doi.org/10.1038/74814).
- Andlauer TF, Sigrist SJ. 2012. Quantitative analysis of *Drosophila* larval neuromuscular junction morphology. *Cold Spring Harbor Protocols* **2012**:490–493. doi: [10.1101/pdb.prot068601](https://doi.org/10.1101/pdb.prot068601).
- Bury L, Sabo S. 2011. Coordinated trafficking of synaptic vesicle and active zone proteins prior to synapse formation. *Neural Development* **6**:24. doi: [10.1186/1749-8104-6-24](https://doi.org/10.1186/1749-8104-6-24).
- Bückers J, Wildanger D, Vicidomini G, Kastrop L, Hell SW. 2011. Simultaneous multi-lifetime multi-color STED imaging for colocalization analyses. *Optics Express* **19**:3130–3143. doi: [10.1364/OE.19.003130](https://doi.org/10.1364/OE.19.003130).
- Cai Q, Pan PY, Sheng ZH. 2007. Syntabulin-kinesin-1 family member 5B-mediated axonal transport contributes to activity-dependent presynaptic assembly. *The Journal of Neuroscience* **27**:7284–7296. doi: [10.1523/JNEUROSCI.0731-07.2007](https://doi.org/10.1523/JNEUROSCI.0731-07.2007).
- Chen VB, Arendall WB III, Headd JJ, Keedy DA, Immormino RM, Kapral GJ, Murray LW, Richardson JS, Richardson DC. 2010. MolProbity: all-atom structure validation for macromolecular crystallography. *Acta Crystallographica. Section D, Biological Crystallography* **66**:12–21. doi: [10.1107/S0907444909042073](https://doi.org/10.1107/S0907444909042073).
- Davydova D, Marini C, King C, Klueva J, Bischof F, Romorini S, Montenegro-Venegas C, Heine M, Schneider R, Schröder MS, Altmann WD, Henneberger C, Rusakov DA, Gundelfinger ED, Fejtova A. 2014. Bassoon specifically controls presynaptic P/Q-type Ca(2+) channels via RIM-binding protein. *Neuron* **82**:181–194. doi: [10.1016/j.neuron.2014.02.012](https://doi.org/10.1016/j.neuron.2014.02.012).
- DeLano WL. 2002. The PyMOL Molecular Graphics System on World Wide Web. <http://www.pymol.org>.
- Depner H, Lützkendorf J, Babkir HA, Sigrist SJ, Holt MG. 2014. Differential centrifugation-based biochemical fractionation of the *Drosophila* adult CNS. *Nature Protocols* **9**:2796–2808. doi: [10.1038/nprot.2014.192](https://doi.org/10.1038/nprot.2014.192).
- Dulubova I, Sugita S, Hill S, Hosaka M, Fernandez I, Südhof TC, Rizo J. 1999. A conformational switch in syntaxin during exocytosis: role of munc18. *The EMBO Journal* **18**:4372–4382. doi: [10.1093/emboj/18.16.4372](https://doi.org/10.1093/emboj/18.16.4372).
- Ehmann N, van de Linde S, Alon A, Ljaschenko D, Keung XZ, Holm T, Rings A, DiAntonio A, Hallermann S, Ashery U, Heckmann M, Sauer M, Kittel RJ. 2014. Quantitative super-resolution imaging of Bruchpilot distinguishes active zone states. *Nature Communications* **5**:4650. doi: [10.1038/ncomms5650](https://doi.org/10.1038/ncomms5650).
- Emsley P, Lohkamp B, Scott WG, Cowtan K. 2010. Features and development of Coot. *Acta Crystallographica. Section D, Biological Crystallography* **66**:486–501. doi: [10.1107/S0907444910007493](https://doi.org/10.1107/S0907444910007493).
- Evans PR. 2011. An introduction to data reduction: space-group determination, scaling and intensity statistics. *Acta Crystallographica. Section D, Biological Crystallography* **67**:282–292. doi: [10.1107/S090744491003982X](https://doi.org/10.1107/S090744491003982X).
- Fejtova A, Davydova D, Bischof F, Lazarevic V, Altmann WD, Romorini S, Schone C, Zuschratter W, Kreutz MR, Garner CC, Ziv NE, Gundelfinger ED. 2009. Dynein light chain regulates axonal trafficking and synaptic levels of Bassoon. *The Journal of Cell Biology* **185**:341–355. doi: [10.1083/jcb.200807155](https://doi.org/10.1083/jcb.200807155).
- Fouquet W, Oswald D, Wichmann C, Mertel S, Depner H, Dyba M, Hallermann S, Kittel RJ, Eimer S, Sigrist SJ. 2009. Maturation of active zone assembly by *Drosophila* Bruchpilot. *The Journal of Cell Biology* **186**:129–145. doi: [10.1083/jcb.200812150](https://doi.org/10.1083/jcb.200812150).
- Fu MM, Holzbaur EL. 2013. JIP1 regulates the directionality of APP axonal transport by coordinating kinesin and dynein motors. *The Journal of Cell Biology* **202**:495–508. doi: [10.1083/jcb.201302078](https://doi.org/10.1083/jcb.201302078).
- Fu MM, Nirschl JJ, Holzbaur EL. 2014. LC3 binding to the scaffolding protein JIP1 regulates processive dynein-driven transport of autophagosomes. *Developmental Cell* **29**:577–590. doi: [10.1016/j.devcel.2014.04.015](https://doi.org/10.1016/j.devcel.2014.04.015).
- Füger P, Behrends LB, Mertel S, Sigrist SJ, Rasse TM. 2007. Live imaging of synapse development and measuring protein dynamics using two-color fluorescence recovery after photo-bleaching at *Drosophila* synapses. *Nature Protocols* **2**:3285–3298. doi: [10.1038/nprot.2007.472](https://doi.org/10.1038/nprot.2007.472).
- Gindhart JG, Chen J, Faulkner M, Gandhi R, Doerner K, Wisniewski T, Nandlstadt A. 2003. The kinesin-associated protein UNC-76 is required for axonal transport in the *Drosophila* nervous system. *Molecular Biology of the Cell* **14**:3356–3365. doi: [10.1091/mbc.E02-12-0800](https://doi.org/10.1091/mbc.E02-12-0800).
- Gietz DR, Schiestl RH. 2007. High-efficiency yeast transformation using the LiAc/SS carrier DNA/PEG method. *Nature Protocols* **2**:31–34. doi: [10.1038/nprot.2007.13](https://doi.org/10.1038/nprot.2007.13).
- Göttfert F, Wurm CA, Mueller V, Berning S, Cordes VC, Honigsmann A, Hell SW. 2013. Coaligned dual-channel STED nanoscopy and molecular diffusion analysis at 20 nm resolution. *Biophysical Journal* **105**:L01–L03. doi: [10.1016/j.bpj.2013.05.029](https://doi.org/10.1016/j.bpj.2013.05.029).
- Graf ER, Daniels RW, Burgess RW, Schwarz TL, DiAntonio A. 2009. Rab3 dynamically controls protein composition at active zones. *Neuron* **64**:663–677. doi: [10.1016/j.neuron.2009.11.002](https://doi.org/10.1016/j.neuron.2009.11.002).
- Hall DH, Hedgecock EM. 1991. Kinesin-related gene unc-104 is required for axonal transport of synaptic vesicles in *C. elegans*. *Cell* **65**:837–847. doi: [10.1016/0092-8674\(91\)90391-B](https://doi.org/10.1016/0092-8674(91)90391-B).
- Hallam SJ, Goncharov A, McEwen J, Baran R, Jin Y. 2002. SYD-1, a presynaptic protein with PDZ, C2 and rhoGAP-like domains, specifies axon identity in *C. elegans*. *Nature Neuroscience* **5**:1137–1146. doi: [10.1038/nn959](https://doi.org/10.1038/nn959).
- Hallermann S, Kittel RJ, Wichmann C, Weyhersmüller A, Fouquet W, Mertel S, Oswald D, Eimer S, Depner H, Schwarzel M, Sigrist SJ, Heckmann M. 2010. Naked dense bodies provoke depression. *The Journal of Neuroscience* **30**:14340–14345. doi: [10.1523/JNEUROSCI.2495-10.2010](https://doi.org/10.1523/JNEUROSCI.2495-10.2010).

- Hell SW. 2007. Far-field optical nanoscopy. *Science* **316**:1153–1158. doi: [10.1126/science.1137395](https://doi.org/10.1126/science.1137395).
- Hirokawa N, Niwa S, Tanaka Y. 2010. Molecular motors in neurons: transport mechanisms and roles in brain function, development, and disease. *Neuron* **68**:610–638. doi: [10.1016/j.neuron.2010.09.039](https://doi.org/10.1016/j.neuron.2010.09.039).
- Hoang B, Chiba A. 2001. Single-cell analysis of *Drosophila* larval neuromuscular synapses. *Developmental Biology* **229**:55–70. doi: [10.1006/dbio.2000.9983](https://doi.org/10.1006/dbio.2000.9983).
- Horiuchi D, Barkus RV, Pilling AD, Gassman A, Saxton WM. 2005. APLIP1, a kinesin binding JIP-1/JNK scaffold protein, influences the axonal transport of both vesicles and mitochondria in *Drosophila*. *Current Biology* **15**: 2137–2141.
- Horiuchi D, Collins CA, Bhat P, Barkus RV, DiAntonio A, Saxton WM. 2007. Control of a kinesin-cargo linkage mechanism by JNK pathway kinases. *Current Biology* **17**:1313–1317. doi: [10.1016/j.cub.2007.06.062](https://doi.org/10.1016/j.cub.2007.06.062).
- Hurd DD, Saxton WM. 1996. Kinesin mutations cause motor neuron disease phenotypes by disrupting fast axonal transport in *Drosophila*. *Genetics* **144**:1075–1085.
- Ishidoh K, Kominami E. 2002. Processing and activation of lysosomal proteinases. *Biological Chemistry* **383**: 1827–1831. doi: [10.1515/BC.2002.206](https://doi.org/10.1515/BC.2002.206).
- Johnson EL III, Fetter ED, Davis GW. 2009. Negative regulation of active zone assembly by a newly identified SR protein kinase. *PLOS Biology* **7**:e1000193. doi: [10.1371/journal.pbio.1000193](https://doi.org/10.1371/journal.pbio.1000193).
- Johnstone O, Lasko P. 2001. Translational regulation and RNA localization in *Drosophila* Oocytes and embryos. *Annual Review of Genetics* **35**:365–406. doi: [10.1146/annurev.genet.35.102401.090756](https://doi.org/10.1146/annurev.genet.35.102401.090756).
- Kabsch W. 2010. XDS. *Acta Crystallographica. Section D, Biological Crystallography* **66**:125–132. doi: [10.1107/S0907444909047337](https://doi.org/10.1107/S0907444909047337).
- Kaesler PS, Deng L, Wang Y, Dulubova I, Liu X, Rizo J, Südhof TC. 2011. RIM proteins tether Ca²⁺ channels to presynaptic active zones via a direct PDZ-domain interaction. *Cell* **144**:282–295. doi: [10.1016/j.cell.2010.12.029](https://doi.org/10.1016/j.cell.2010.12.029).
- Kim MD, Wen Y, Jan YN. 2009. Patterning and organization of motor neuron dendrites in the *Drosophila* larva. *Developmental Biology* **336**:213–221. doi: [10.1016/j.ydbio.2009.09.041](https://doi.org/10.1016/j.ydbio.2009.09.041).
- Kittel RJ, Wichmann C, Rasse TM, Fouquet W, Schmidt M, Schmid A, Wagh DA, Pawlu C, Kellner RR, Willig KI, Hell SW, Buchner E, Heckmann M, Sigrist SJ. 2006. Bruchpilot promotes active zone assembly, Ca²⁺ channel clustering, and vesicle release. *Science* **312**:1051–1054. doi: [10.1126/science.1126308](https://doi.org/10.1126/science.1126308).
- Klassen MP, Wu YE, Maeder CI, Nakae I, Cueva JG, Lehrman EK, Tada M, Gengyo-Ando K, Wang GJ, Goodman M, Mitani S, Kontani K, Katada T, Shen K. 2010. An Arf-like small G protein, ARL-8, promotes the axonal transport of presynaptic cargoes by suppressing vesicle aggregation. *Neuron* **66**:710–723. doi: [10.1016/j.neuron.2010.04.033](https://doi.org/10.1016/j.neuron.2010.04.033).
- Klinedinst S, Wang X, Xiong X, Haeflner JM, Collins CA. 2013. Independent pathways downstream of the Wnd/DLK MAPKKK regulate synaptic structure, axonal transport, and injury signaling. *The Journal of Neuroscience* **33**: 12764–12778. doi: [10.1523/JNEUROSCI.5160-12.2013](https://doi.org/10.1523/JNEUROSCI.5160-12.2013).
- Kristensen O, Guenat S, Dar I, Allaman-Pillet N, Abderrahmani A, Ferdaoussi M, Roduit R, Maurer F, Beckmann JS, Kastrop JS, Gajhede M, Bonny C. 2006. A unique set of SH3-SH3 interactions controls IB1 homodimerization. *The EMBO Journal* **25**:785–797. doi: [10.1038/sj.emboj.7600982](https://doi.org/10.1038/sj.emboj.7600982).
- Laemmli UK. 1970. Cleavage of structural proteins during the assembly of the head of bacteriophage T4. *Nature* **227**:680–685. doi: [10.1038/227680a0](https://doi.org/10.1038/227680a0).
- Laskowski RA, MacArthur MW, Moss DS, Thornton JM. 1993. PROCHECK: a program to check the stereochemical quality of protein structures. *Journal of Applied Crystallography* **26**:283–291. doi: [10.1107/S0021889892009944](https://doi.org/10.1107/S0021889892009944).
- Landgraf M, Bossing T, Technau GM, Bate M. 1997. The origin, location, and projections of the embryonic abdominal motoneurons of *Drosophila*. *The Journal of Neuroscience* **17**:9642–9655.
- Lebedev AA, Isupov MN. 2014. Space-group and origin ambiguity in macromolecular structures with pseudo-symmetry and its treatment with the program Zanuda. *Acta Crystallographica. Section D, Biological Crystallography* **70**:2430–2443. doi: [10.1107/S1399004714014795](https://doi.org/10.1107/S1399004714014795).
- Li L, Tian X, Zhu M, Bulgari D, Böhme MA, Goettfert F, Wichmann C, Sigrist SJ, Levitan ES, Wu C. 2014. *Drosophila* Syd-1, Liprin-a, and Protein Phosphatase 2A B' Subunit Wrd Function in a Linear Pathway to Prevent Ectopic Accumulation of Synaptic Materials in Distal Axons. *The Journal of Neuroscience* **34**:8474–8487. doi: [10.1523/JNEUROSCI.0409-14.2014](https://doi.org/10.1523/JNEUROSCI.0409-14.2014).
- Liu KS, Siebert M, Mertel S, Knoche E, Wegener S, Wichmann C, Matkovic T, Muhammad K, Depner H, Mettke C, Buckers J, Hell SW, Müller M, Davis GW, Schmitz D, Sigrist SJ. 2011a. RIM-binding protein, a central part of the active zone, is essential for neurotransmitter release. *Science* **334**:1565–1569. doi: [10.1126/science.1212991](https://doi.org/10.1126/science.1212991).
- Liu Z, Huang Y, Zhang Y, Chen D, Zhang YQ. 2011b. *Drosophila* Acyl-CoA synthetase long-chain family member 4 regulates axonal transport of synaptic vesicles and is required for synaptic development and transmission. *The Journal of Neuroscience* **31**:2052–2063. doi: [10.1523/JNEUROSCI.3278-10.2011](https://doi.org/10.1523/JNEUROSCI.3278-10.2011).
- Maas C, Torres VI, Altmann WD, Leal-Ortiz S, Wagh D, Terry-Lorenzo RT, Fejtova A, Gundelfinger ED, Ziv NE, Garner CC. 2012. Formation of golgi-derived active zone precursor vesicles. *The Journal of Neuroscience* **32**: 11095–11108. doi: [10.1523/JNEUROSCI.0195-12.2012](https://doi.org/10.1523/JNEUROSCI.0195-12.2012).
- Maeder CI, Shen K, Hoogenraad CC. 2014. Axon and dendritic trafficking. *Current Opinion in Neurobiology* **27**: 165–170. doi: [10.1016/j.conb.2014.03.015](https://doi.org/10.1016/j.conb.2014.03.015).
- Mackler JM, Drummond JA, Loewen CA, Robinson IM, Reist NE. 2002. The C2B Ca²⁺-binding motif of synaptotagmin is required for synaptic transmission in vivo. *Nature* **418**:340–344. doi: [10.1038/nature00846](https://doi.org/10.1038/nature00846).
- Matkovic T, Siebert M, Knoche E, Depner H, Mertel S, Oswald D, Schmidt M, Thomas U, Sickmann A, Kamin D, Hell SW, Bürger J, Hollmann C, Mielke T, Wichmann C, Sigrist SJ. 2013. The Bruchpilot cytomatrix determines the size of the readily releasable pool of synaptic vesicles. *The Journal of Cell Biology* **202**:667–683. doi: [10.1083/jcb.201301072](https://doi.org/10.1083/jcb.201301072).

- McCoy AJ**, Grosse-Kunstleve RW, Adams PD, Winn MD, Storoni LC, Read RJ. 2007. Phaser crystallographic software. *Journal of Applied Crystallography* **40**:658–674. doi: [10.1107/S0021889807021206](https://doi.org/10.1107/S0021889807021206).
- Millecamps S**, Julien JP. 2013. Axonal transport deficits and neurodegenerative diseases. *Nature Reviews Neuroscience* **14**:161–176. doi: [10.1038/nrn3380](https://doi.org/10.1038/nrn3380).
- Miller KE**, DeProto J, Kaufmann N, Patel BN, Duckworth A, Van Vactor D. 2005. Direct observation demonstrates that Liprin-alpha is required for trafficking of synaptic vesicles. *Current Biology* **15**:684–689. doi: [10.1016/j.cub.2005.02.061](https://doi.org/10.1016/j.cub.2005.02.061).
- Murshudov GN**, Skubak P, Lebedev AA, Pannu NS, Steiner RA, Nicholls RA, Winn MD, Long F, Vagin AA. 2011. REFMAC5 for the refinement of macromolecular crystal structures. *Acta Crystallographica. Section D, Biological Crystallography* **67**:355–367. doi: [10.1107/S0907444911001314](https://doi.org/10.1107/S0907444911001314).
- Nieratschker V**, Schubert A, Jauch M, Bock N, Bucher D, Dippacher S, Krohne G, Asan E, Buchner S, Buchner E. 2009. Bruchpilot in ribbon-like axonal agglomerates, behavioral defects, and early death in SRPK79D kinase mutants of *Drosophila*. *PLOS Genetics* **5**:e1000700. doi: [10.1371/journal.pgen.1000700](https://doi.org/10.1371/journal.pgen.1000700).
- Owald D**, Fouquet W, Schmidt M, Wichmann C, Mertel S, Depner H, Christiansen F, Zube C, Quentin C, Körner J, Urlaub H, Mechtler K, Sigrist SJ. 2010. A Syd-1 homologue regulates pre- and postsynaptic maturation in *Drosophila*. *The Journal of Cell Biology* **188**:565–579. doi: [10.1083/jcb.200908055](https://doi.org/10.1083/jcb.200908055).
- Owald D**, Khorramshahi O, Gupta VK, Banovic D, Depner H, Fouquet W, Wichmann C, Mertel S, Eimer S, Reynolds E, Holt M, Aberle H, Sigrist SJ. 2012. Cooperation of Syd-1 with Neuexin synchronizes pre- with postsynaptic assembly. *Nature Neuroscience* **15**:1219–1226. doi: [10.1038/nn.3183](https://doi.org/10.1038/nn.3183).
- Pack-Chung E**, Kurshan PT, Dickman DK, Schwarz TL. 2007. A *Drosophila* kinesin required for synaptic bouton formation and synaptic vesicle transport. *Nature Neuroscience* **10**:980–989. doi: [10.1038/nn1936](https://doi.org/10.1038/nn1936).
- Patel MR**, Shen K. 2009. RSY-1 is a local inhibitor of presynaptic assembly in *C. elegans*. *Science* **323**:1500–1503. doi: [10.1126/science.1169025](https://doi.org/10.1126/science.1169025).
- Prokop A**. 2006. Organization of the efferent system and structure of neuromuscular junctions in *Drosophila*. *International Review of Neurobiology* **75**:71–90. doi: [10.1016/S0074-7742\(06\)75004-8](https://doi.org/10.1016/S0074-7742(06)75004-8).
- Qin G**, Schwarz T, Kittel RJ, Schmid A, Rasse TM, Kappei D, Ponimaskin E, Heckmann M, Sigrist SJ. 2005. Four different subunits are essential for expressing the synaptic glutamate receptor at neuromuscular junctions of *Drosophila*. *The Journal of Neuroscience* **25**:3209–3218. doi: [10.1523/JNEUROSCI.4194-04.2005](https://doi.org/10.1523/JNEUROSCI.4194-04.2005).
- Rasse TM**, Fouquet W, Schmid A, Kittel RJ, Mertel S, Sigrist CB, Schmidt M, Guzman A, Merino C, Qin G, Quentin C, Madeo FF, Heckmann M, Sigrist SJ. 2005. Glutamate receptor dynamics organizing synapse formation in vivo. *Nature Neuroscience* **8**:898–905. doi: [10.1038/nn1484](https://doi.org/10.1038/nn1484).
- Ribrault C**, Reingruber J, Petkovic M, Galli T, Ziv NE, Holcman D, Triller A. 2011. Syntaxin1A lateral diffusion reveals transient and local SNARE interactions. *The Journal of Neuroscience* **31**:17590–17602. doi: [10.1523/JNEUROSCI.4065-11.2011](https://doi.org/10.1523/JNEUROSCI.4065-11.2011).
- Sato-Yoshitake R**, Yorifuji H, Inagaki M, Hirokawa N. 1992. The phosphorylation of kinesin regulates its binding to synaptic vesicles. *The Journal of Biological Chemistry* **267**:23930–23936.
- Schägger H**. 2006. Tricine-sds-page. *Nature Protocols* **1**:16–22. doi: [10.1038/nprot.2006.4](https://doi.org/10.1038/nprot.2006.4).
- Schmid A**, Chiba A, Doe CQ. 1999. Clonal analysis of *Drosophila* embryonic neuroblasts: neural cell types, axon projections and muscle targets. *Development* **126**:4653–4689.
- Schmid A**, Hallermann S, Kittel RJ, Khorramshahi O, Frölich AM, Quentin C, Rasse TM, Mertel S, Heckmann M, Sigrist SJ. 2008. Activity-dependent site-specific changes of glutamate receptor composition in vivo. *Nature Neuroscience* **11**:659–666. doi: [10.1038/nn.2122](https://doi.org/10.1038/nn.2122).
- Serra-Pagès C**, Medley QG, Tang M, Hart A, Streuli M. 1998. Liprins, a family of LAR transmembrane protein-tyrosine phosphatase-interacting proteins. *The Journal of Biological Chemistry* **273**:15611–15620. doi: [10.1074/jbc.273.25.15611](https://doi.org/10.1074/jbc.273.25.15611).
- Shapira M**, Zhai RG, Dresbach T, Bresler T, Torres VI, Gundelfinger ED, Ziv NE, Garner CC. 2003. Unitary assembly of presynaptic active zones from Piccolo-Bassoon transport vesicles. *Neuron* **38**:237–252. doi: [10.1016/S0896-6273\(03\)00207-1](https://doi.org/10.1016/S0896-6273(03)00207-1).
- Sigrist SJ**, Reiff DF, Thiel PR, Steinert JR, Schuster CM. 2003. Experience-dependent strengthening of *Drosophila* neuromuscular junctions. *The Journal of Neuroscience* **23**:6546–6556.
- Sigrist SJ**, Schmitz D. 2011. Structural and functional plasticity of the cytoplasmic active zone. *Current Opinion in Neurobiology* **21**:144–150. doi: [10.1016/j.conb.2010.08.012](https://doi.org/10.1016/j.conb.2010.08.012).
- Sink H**, Whittington PM. 1991. Location and connectivity of abdominal motoneurons in the embryo and larva of *Drosophila melanogaster*. *Journal of Neurobiology* **22**:298–311. doi: [10.1002/neu.480220309](https://doi.org/10.1002/neu.480220309).
- Spirin A**. 1996. Masked and translatable messenger ribonucleoproteins in higher eukaryotes. In: Hershey JW, Mathews MB, Sonenberg N, editors. *Translational control*. Cold Spring Harbor, NY: Cold Spring Harbor Laboratory Press. p. 319–334.
- Stryker E**, Johnson KG. 2007. LAR, liprin alpha and the regulation of active zone morphogenesis. *Journal of Cell Science* **120**:3723–3728. doi: [10.1242/jcs.03491](https://doi.org/10.1242/jcs.03491).
- Studier FW**. 2005. Protein production by auto-induction in high density shaking cultures. *Protein Expression and Purification* **41**:207–234. doi: [10.1016/j.pep.2005.01.016](https://doi.org/10.1016/j.pep.2005.01.016).
- Südhof TC**. 2012. The presynaptic active zone. *Neuron* **75**:11–25. doi: [10.1016/j.neuron.2012.06.012](https://doi.org/10.1016/j.neuron.2012.06.012).
- Takamori S**, Holt M, Stenius K, Lemke EA, Grønborg M, Riedel D, Urlaub H, Schenck S, Brügger B, Ringler P, Müller SA, Rammner B, Gräter F, Hub JS, De Groot BL, Mieskes G, Moriyama Y, Klingauf J, Grubmüller H, Heuser J, Wieland F, Jahn R. 2006. Molecular anatomy of a trafficking organelle. *Cell* **127**:831–846. doi: [10.1016/j.cell.2006.10.030](https://doi.org/10.1016/j.cell.2006.10.030).
- Tao-Cheng JH**. 2007. Ultrastructural localization of active zone and synaptic vesicle proteins in a preassembled multi-vesicle transport aggregate. *Neuroscience* **150**:575–584. doi: [10.1016/j.neuroscience.2007.09.031](https://doi.org/10.1016/j.neuroscience.2007.09.031).

- Taru H**, Kirino Y, Suzuki T. 2002. Differential roles of JIP scaffold proteins in the modulation of amyloid precursor protein metabolism. *The Journal of Biological Chemistry* **277**:27567–27574. doi: [10.1074/jbc.M203713200](https://doi.org/10.1074/jbc.M203713200).
- Torroja L**, Chu H, Kotovsky I, White K. 1999a. Neuronal overexpression of APPL, the *Drosophila* homologue of the amyloid precursor protein (APP), disrupts axonal transport. *Current Biology* **9**:489–492. doi: [10.1016/S0960-9822\(99\)80215-2](https://doi.org/10.1016/S0960-9822(99)80215-2).
- Torroja L**, Packard M, Gorczyca M, White K, Budnik V. 1999b. The *Drosophila* beta-amyloid precursor protein homolog promotes synapse differentiation at the neuromuscular junction. *The Journal of Neuroscience* **19**:7793–7803.
- Tsuriel S**, Fisher A, Wittenmayer N, Dresbach T, Garner CC, Ziv NE. 2009. Exchange and redistribution dynamics of the cytoskeleton of the active zone molecule bassoon. *The Journal of Neuroscience* **29**:351–358. doi: [10.1523/JNEUROSCI.4777-08.2009](https://doi.org/10.1523/JNEUROSCI.4777-08.2009).
- Verhey KJ**, Meyer D, Deehan R, Blenis J, Schnapp BJ, Rapoport TA, Margolis B. 2001. Cargo of kinesin identified as JIP scaffolding proteins and associated signaling molecules. *The Journal of Cell Biology* **152**:959–970. doi: [10.1083/jcb.152.5.959](https://doi.org/10.1083/jcb.152.5.959).
- Wagh DA**, Rasse TM, Asan E, Hofbauer A, Schwenkert I, Dürrbeck H, Buchner S, Dabauvalle MC, Schmidt M, Qin G, Wichmann C, Kittel R, Sigrist SJ, Buchner E. 2006. Bruchpilot, a protein with homology to ELKS/CAST, is required for structural integrity and function of synaptic active zones in *Drosophila*. *Neuron* **49**:833–844. doi: [10.1016/j.neuron.2006.02.008](https://doi.org/10.1016/j.neuron.2006.02.008).
- Wagner OI**, Esposito A, Kohler B, Chen CW, Shen CP, Wu GH, Butkevich E, Mandalapu S, Wenzel D, Wouters FS, Klopfenstein DR. 2009. Synaptic scaffolding protein SYD-2 clusters and activates kinesin-3 UNC-104 in *C. elegans*. *Proceedings of the National Academy of Sciences of USA* **106**:19605–19610. doi: [10.1073/pnas.0902949106](https://doi.org/10.1073/pnas.0902949106).
- Wairkar YP**, Toda H, Mochizuki H, Furukubo-Tokunaga K, Tomoda T, DiAntonio A. 2009. Unc-51 controls active zone density and protein composition by downregulating ERK signaling. *The Journal of Neuroscience* **29**:517–528. doi: [10.1523/JNEUROSCI.3848-08.2009](https://doi.org/10.1523/JNEUROSCI.3848-08.2009).
- Wang H**, Lin W, Dyck JA, Yeakley JM, Songyang Z, Cantley LC, Fu XD. 1998. SRPK2: a differentially expressed SR protein-specific kinase involved in mediating the interaction and localization of pre-mRNA splicing factors in mammalian cells. *The Journal of Cell Biology* **23**:737–750. doi: [10.1083/jcb.140.4.737](https://doi.org/10.1083/jcb.140.4.737).
- Wang Y**, Liu X, Biederer T, Südhof TC. 2002. A family of RIM-binding proteins regulated by alternative splicing: Implications for the genesis of synaptic active zones. *Proceedings of the National Academy of Sciences of USA* **99**:14464–14469. doi: [10.1073/pnas.182532999](https://doi.org/10.1073/pnas.182532999).
- Wu YE**, Huo L, Maeder CI, Feng W, Shen K. 2013. The balance between capture and dissociation of presynaptic proteins controls the spatial distribution of synapses. *Neuron* **78**:994–1011. doi: [10.1016/j.neuron.2013.04.035](https://doi.org/10.1016/j.neuron.2013.04.035).
- Zhai RG**, Vardinon-Friedman H, Cases-Langhoff C, Becker B, Gundelfinger ED, Ziv NE, Garner CC. 2001. Assembling the presynaptic active zone: a characterization of an active zone precursor vesicle. *Neuron* **29**:131–143. doi: [10.1016/S0896-6273\(01\)00185-4](https://doi.org/10.1016/S0896-6273(01)00185-4).
- Zhen M**, Jin Y. 1999. The liprin protein SYD-2 regulates the differentiation of presynaptic termini in *C. elegans*. *Nature* **401**:371–375. doi: [10.1038/43886](https://doi.org/10.1038/43886).

Figures and figure supplements

A high affinity RIM-binding protein/Aplip1 interaction prevents the formation of ectopic axonal active zones

Matthias Siebert, et al.

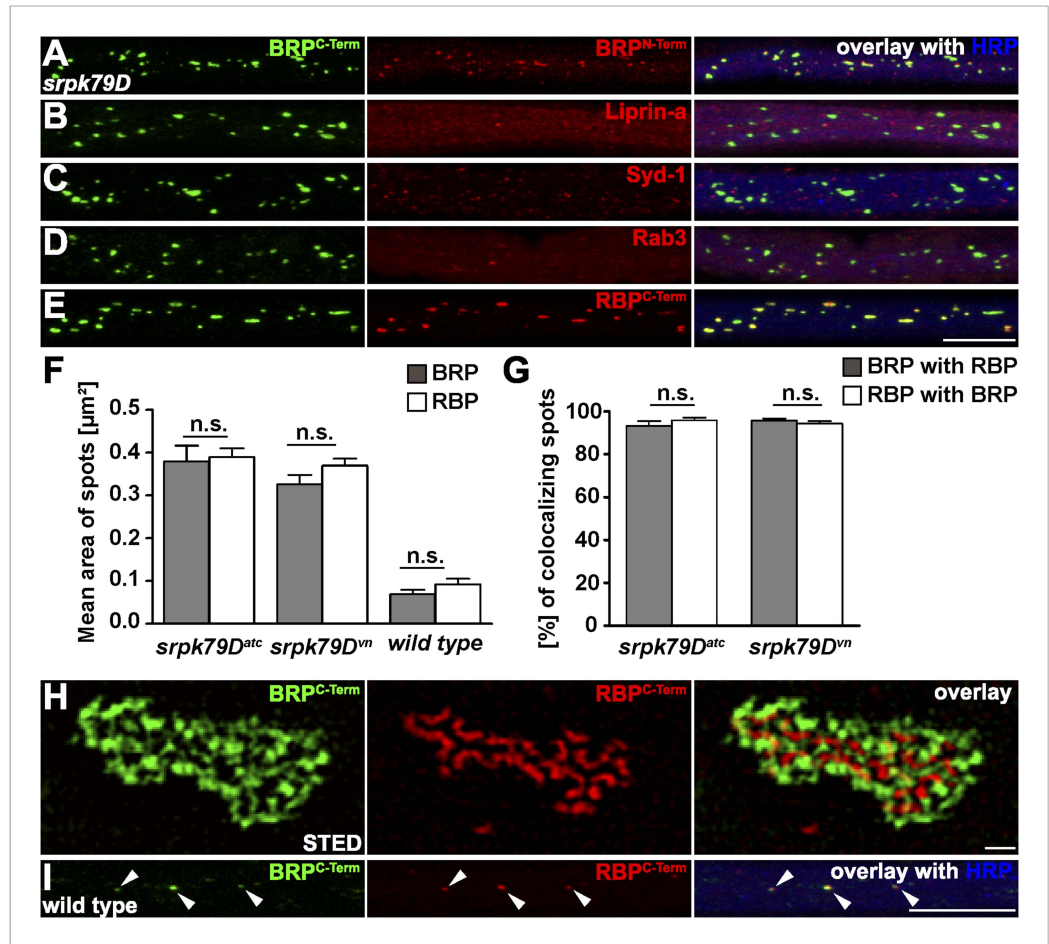


Figure 1. Co-accumulation of Bruchpilot (BRP) and RIM-binding protein (RBP) in *srpk79D* axonal aggregates. (A–E, I) Nerve bundles of segments A1–A3 from third instar larvae of the genotypes indicated labeled with the antibodies (Abs) indicated. (A–E, H) BRP accumulated in axonal aggregates of *srpk79D* mutants. (B–D) Liprin- α (B), Syd-1 (C), and Rab3 (D), did not co-localize with axonal BRP spots. (E) By contrast, RBP invariably co-localized with BRP in these axonal aggregates. (F) Quantification of mean area of axonal BRP and RBP spots in wild type (WT) and *srpk79D* mutants. BRP^{C-term} spots: $0.3797 \pm 0.03694 \mu\text{m}^2$ in *srpk79D^{ATC}*, $0.3259 \pm 0.02212 \mu\text{m}^2$ in *srpk79D^{vn}*, $0.06895 \pm 0.01 \mu\text{m}^2$ in WT; RBP^{C-term} spots: $0.3892 \pm 0.02097 \mu\text{m}^2$ in *srpk79D^{ATC}*, $0.3696 \pm 0.01645 \mu\text{m}^2$ in *srpk79D^{vn}*, 0.09184 ± 0.0133 in WT; $n = 8$ nerves each; all panels show mean values and errors bars representing SEM; ns, not significant, $p > 0.05$, Mann–Whitney U test. (G) Quantification for BRP co-localization with RBP and vice versa in *srpk79D* mutants. BRP^{C-term} co-localizing with RBP^{C-term}: $93.26\% \pm 2.172$ in *srpk79D^{ATC}*, $95.85\% \pm 1.302$ in *srpk79D^{vn}*; RBP^{C-term} co-localizing with BRP^{C-term}: $95.7\% \pm 0.9713$ in *srpk79D^{ATC}*, $94.24\% \pm 1.162$ in *srpk79D^{vn}*; $n = 8$ nerves each; all panels show mean values and errors bars representing SEM; ns, not significant, $p > 0.05$, Mann–Whitney U test. (H) Two-colour stimulated emission depletion (STED) images of axonal aggregates in *srpk79D* mutants revealed that RBP^{C-term} label localized to the inside of the axonal aggregates and was surrounded by BRP^{C-term} label. (I) BRP and RBP also co-localized in axonal spots of WT animals (arrow heads show co-localization of BRP and RBP in the axon). Scale bars: (A–E, I) 10 μm ; (H) 200 nm.

DOI: 10.7554/eLife.06935.003

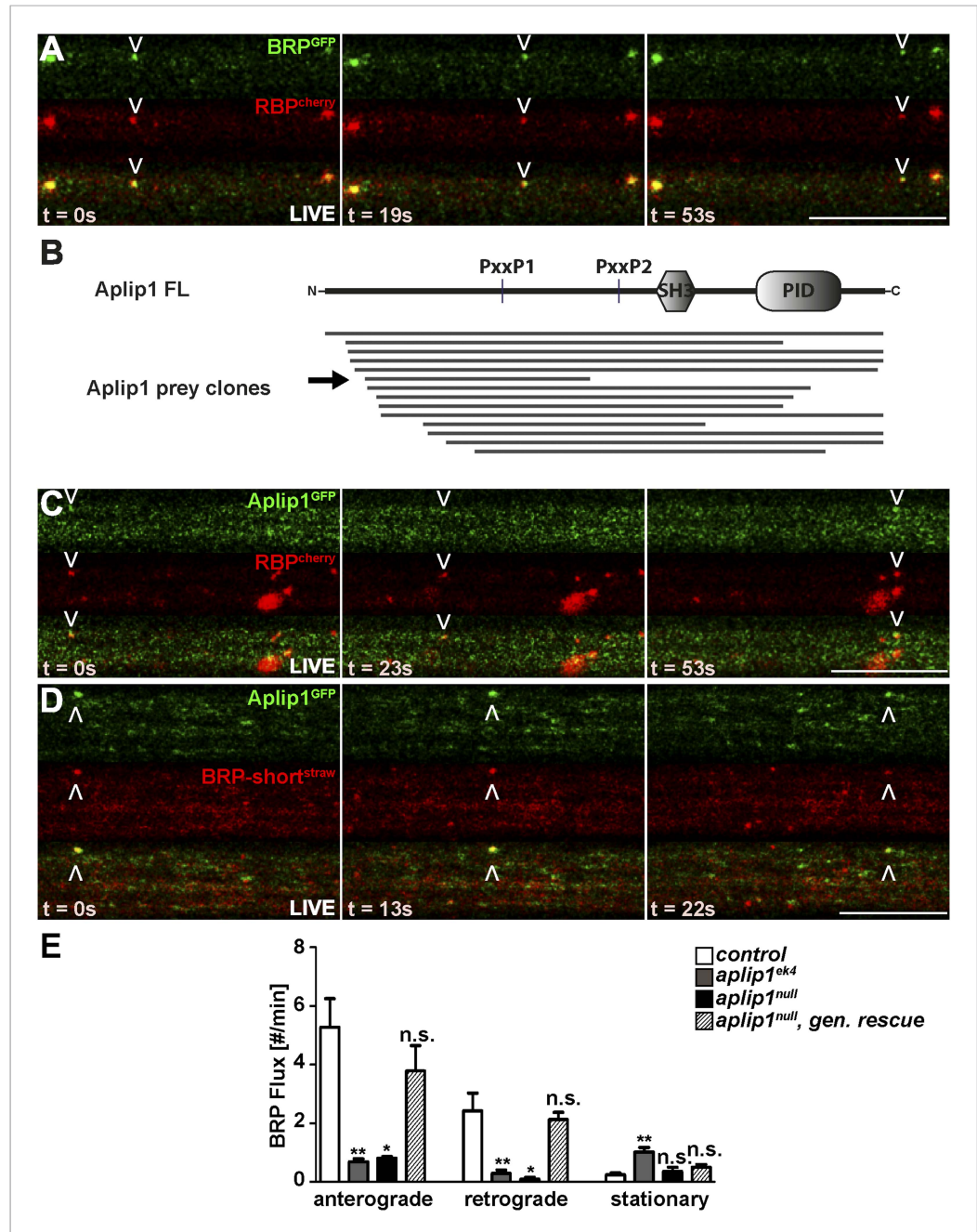


Figure 2. Live imaging of anterograde co-transport between BRP, RBP and APP-like protein interacting protein 1 (Aplip1). **(A)** Live imaging in intact third instar larvae showed anterograde co-transport of BRP^{GFP} and RBP^{cherry}. See also, **Video 1**. **(B)** Schematic representation of Aplip1 domain structure containing two PxxP motifs, one Src-homology 3 (SH3) domain and one C-terminal phosphotyrosine interaction domain (PID) (FL = full-length). Lines represent Aplip1 prey fragments recovered in RBP SH3-II+III bait yeast-two-hybrid (Y2H) screen. Arrow indicates one single clone that contained only the first of the two Aplip1-PxxP motifs. **(C, D)** Live imaging in intact third instar larvae showed anterograde co-transport of Aplip1^{GFP} and RBP^{cherry} **(C)**, as well as Aplip1^{GFP} and BRP-short^{straw} **(D)**. Scale bars: **(A, C, D)** 10 μ m. See also, **Videos 2, 3**. **(E)** Quantification of live imaging of BRP-short^{straw} flux (spots passing through an axonal cross-section per minute) within the genetic backgrounds indicated. Anterograde and retrograde BRP-short^{straw} flux was severely impaired in *aplip1^{ek4}* and *aplip1^{null}* mutant background, which was rescued when a genomic rescue construct for Aplip1 was introduced into the *aplip1^{null}* mutant background. BRP-short^{straw} flux per min, control (n = 14 nerves): anterograde: 5.267 ± 0.975 , retrograde: 2.423 ± 0.604 , stationary: 0.241 ± 0.071 ; *Figure 2. continued on next page*

Figure 2. Continued

aplip1^{ek4} (n = 28 nerves): anterograde: 0.687 ± 0.098 , retrograde: 0.284 ± 0.125 , stationary: 1.023 ± 0.145 ; *aplip1^{null}* (n = 11 nerves): anterograde: 0.808 ± 0.051 , retrograde: 0.085 ± 0.064 , stationary: 0.354 ± 0.148 ; *aplip1^{null}, gen rescue* (n = 26 nerves): anterograde: 3.783 ± 0.861 , retrograde: 2.123 ± 0.239 , stationary: 0.505 ± 0.084 . All panels show mean values and errors bars representing SEM. * $p \leq 0.05$; ** $p \leq 0.01$; *** $p \leq 0.001$; ns, not significant, $p > 0.05$, Mann–Whitney U test.
DOI: [10.7554/eLife.06935.004](https://doi.org/10.7554/eLife.06935.004)

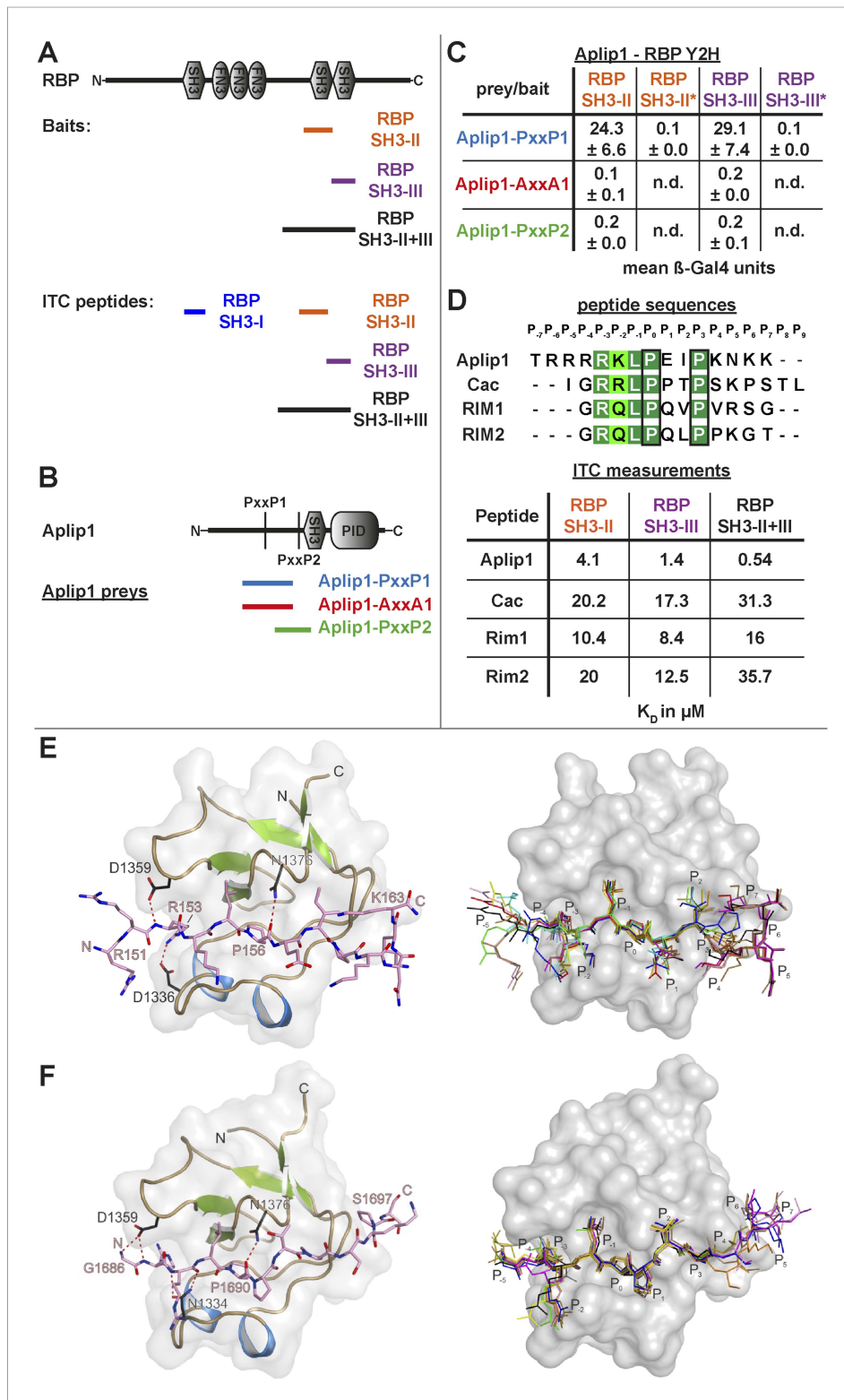


Figure 3. Aplip1 binds RBP using a high-affinity PxxP1-SH3 interaction. **(A)** Schematic representation of RBP domain structure containing three SH3 domains (I-III from the N-terminus) and three Fibronectin 3 (FN3) domains. The corresponding fragments used in the large scale Y2H screen (SH3-II+III) and used as bait (SH3-II and SH3-III) in the Y2H assay **(C)** against different Aplip1 prey constructs **(B)** are indicated. Different isothermal titration calorimetry *Figure 3. continued on next page*

Figure 3. Continued

(ITC) peptides (SH3-I, SH3-II, SH3-III and SH3-II+III) used for ITC measurements (**D**) are also shown. (**B**) Schematic representation of Aplip1 domain structure entailing two PxxP motifs, one SH3 and one C-terminal PID. Different preys (Aplip1-PxxP1, -AxxA1 and -PxxP2) used in Y2H assay (**C**) are indicated. (**C**) Liquid Y2H assay of individual Aplip1 prey fragments against different RBP baits. Aplip1-PxxP1 interacted with both the single SH3-II and -III domains of RBP. Mutating this first PxxP motif (Aplip1-AxxA1) construct abolished the binding. Aplip1-PxxP2 showed no interaction to RBP SH3 domains. Constructs with point-mutated RBP SH3 domains (SH3-II*, SH3-III*) abolished the binding to Aplip1-PxxP1. (**D**) Peptide sequences used for ITC measurements. Aplip1 showed the strongest interaction with RBP compared with Cacophony (Cac), RIM1 and RIM2, with the strongest affinity (lowest K_D) between Aplip1 and the RBP SH3-II+III domain. (**E, F**) Crystal structure of Aplip1-peptide (**E**; see also, 3D for peptide sequence) and of Cac-peptide (**F**; see also, **Figure 3D** for peptide sequence) bound to RBP SH3-II. The SH3 domain is shown in gray surface representation with (left) and without (right) the respective protein in cartoon representation. The bound peptides are drawn in stick representation. Hydrogen bonds ≤ 3.3 Å are indicated by red dashes. In the right panel, several peptide SH3-II complexes as observed in the asymmetric unit are superimposed and shown in different colors. See also, **Tables 1–4**.

DOI: [10.7554/eLife.06935.006](https://doi.org/10.7554/eLife.06935.006)

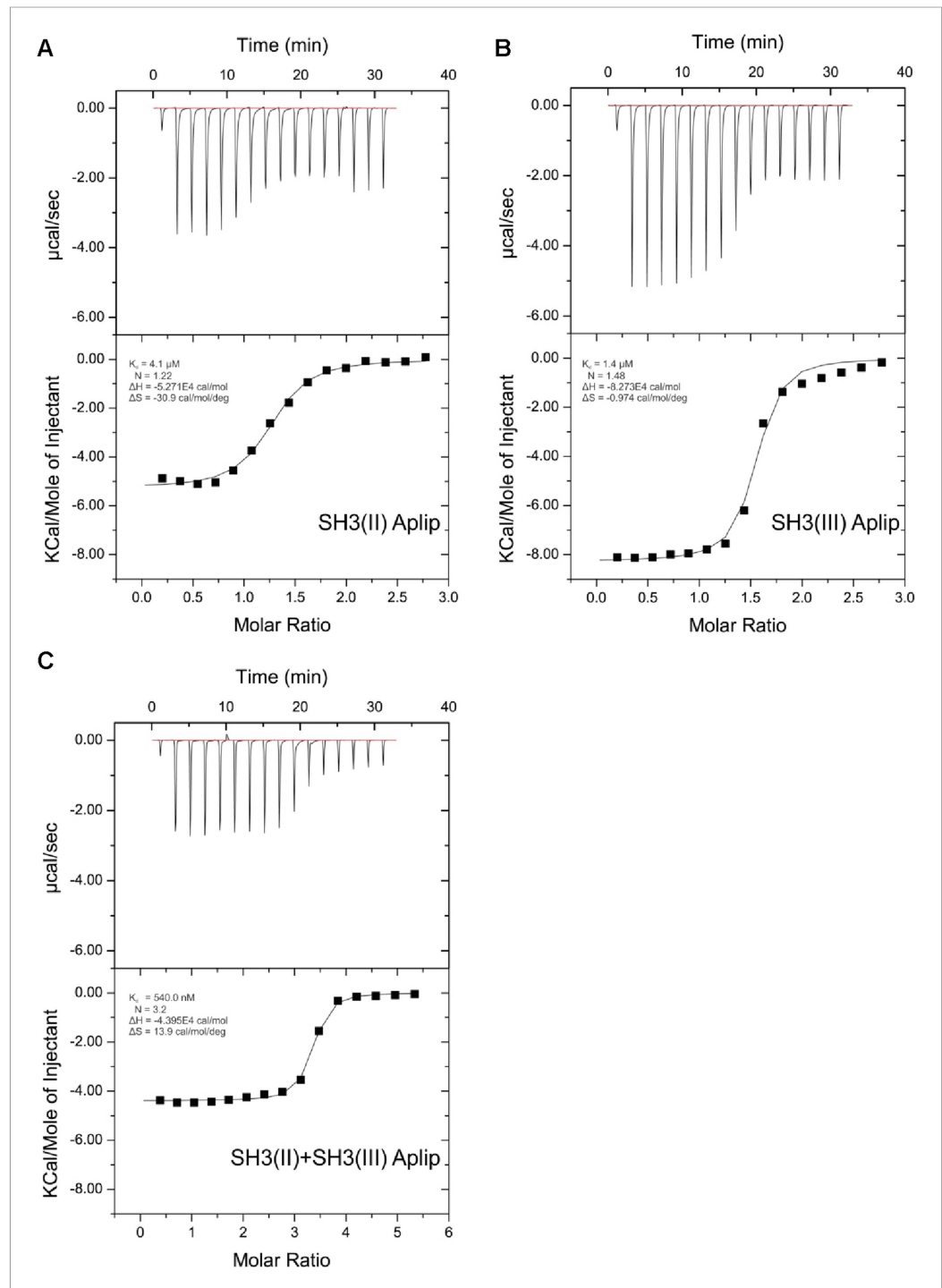


Figure 3—figure supplement 1. ITC measurements for Aplip1 and RBP SH3 domains. Quantification of protein-peptide interactions by ITC. Both the raw data and the data integrated are shown. Data were fitted based on the 'One Set of Sites' model. **(A)** Titration of RBP-BP SH3-II and the Aplip1 peptide. **(B)** Titration of RBP-BP SH3-III and the Aplip1 peptide. **(C)** Titration of RBP-BP SH3-II+SH3-III and the Aplip1 peptide.

DOI: [10.7554/eLife.06935.007](https://doi.org/10.7554/eLife.06935.007)

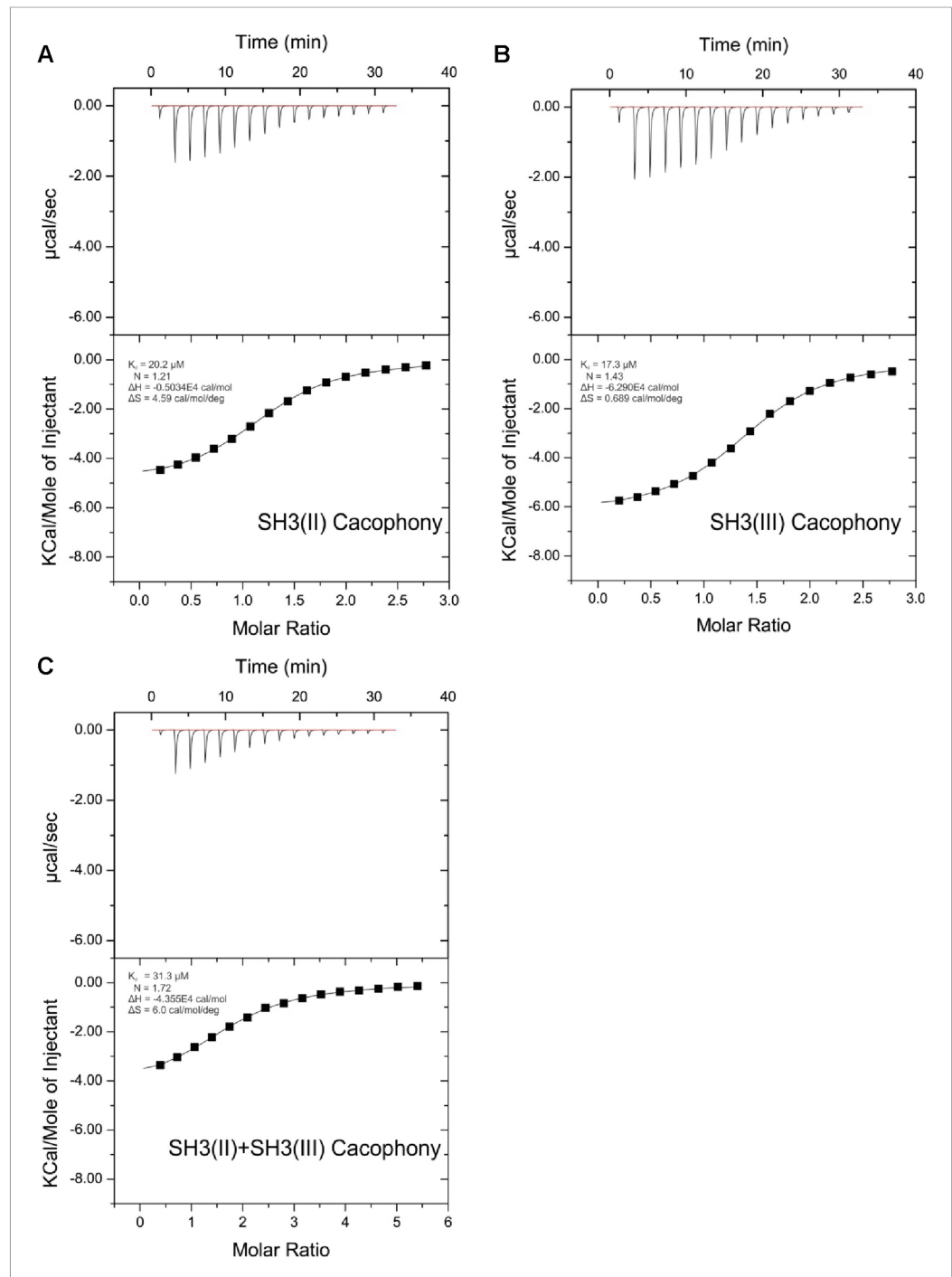


Figure 3—figure supplement 2. ITC measurements for Cac and RBP SH3 domains. Quantification of protein-peptide interactions by ITC. Both the raw data and the data integrated are shown. Data were fitted based on the ‘One Set of Sites’ model. **(A)** Titration of RBP-BP SH3-II and the Cac peptide. **(B)** Titration of RBP-BP SH3-III and the Cac peptide. **(C)** Titration of RBP-BP SH3-II+SH3-III and the Cac peptide.

DOI: [10.7554/eLife.06935.008](https://doi.org/10.7554/eLife.06935.008)

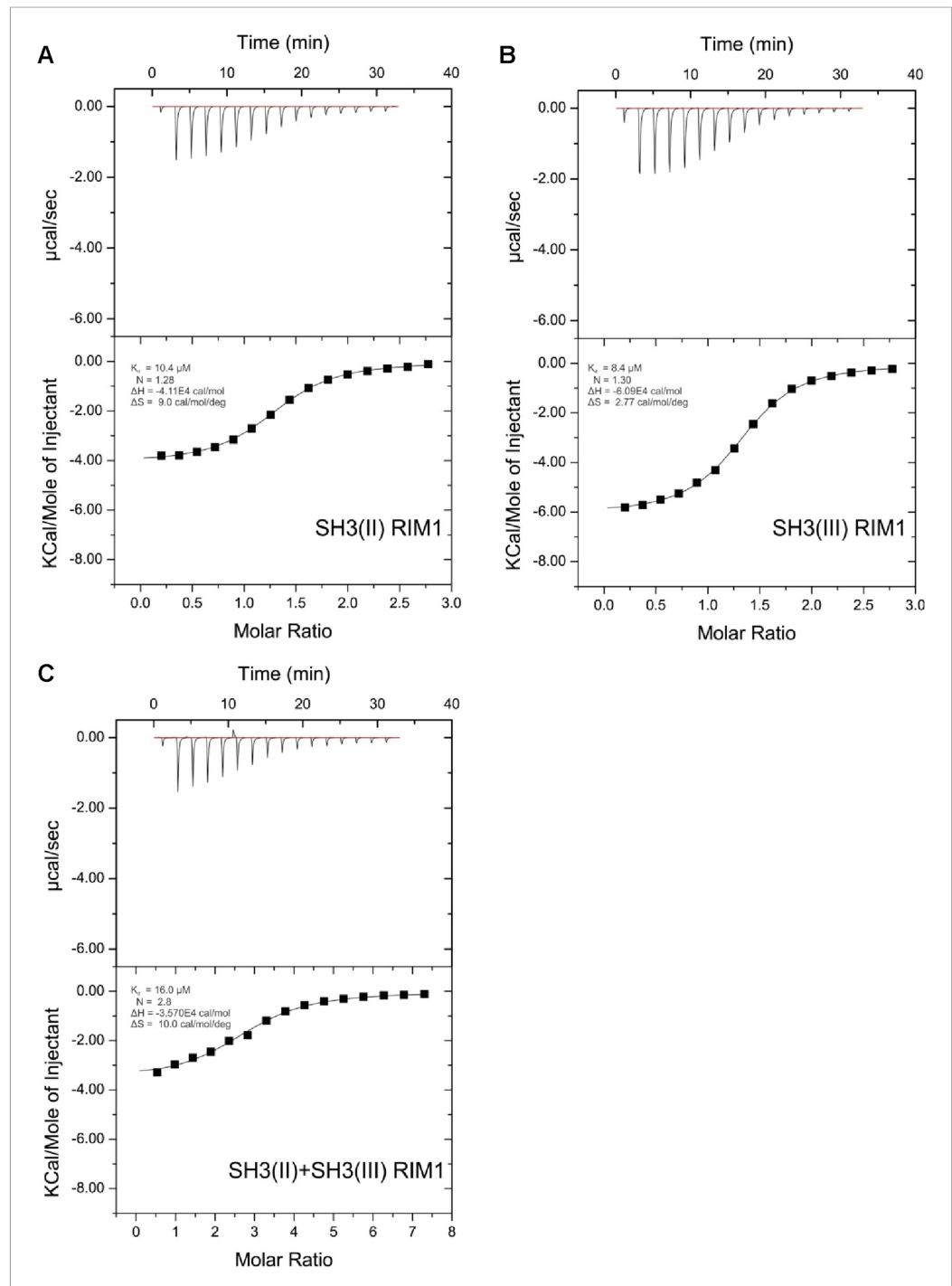


Figure 3—figure supplement 3. ITC measurements for RIM1 and RBP SH3 domains. Quantification of protein-peptide interactions by ITC. Both the raw data and the data integrated are shown. Data were fitted based on the 'One Set of Sites' model. (A) Titration of RBP-BP SH3-II and the RIM1 peptide. (B) Titration of RBP-BP SH3-III and the RIM1 peptide. (C) Titration of RBP-BP SH3-II+SH3-III and the RIM1.

DOI: [10.7554/eLife.06935.009](https://doi.org/10.7554/eLife.06935.009)

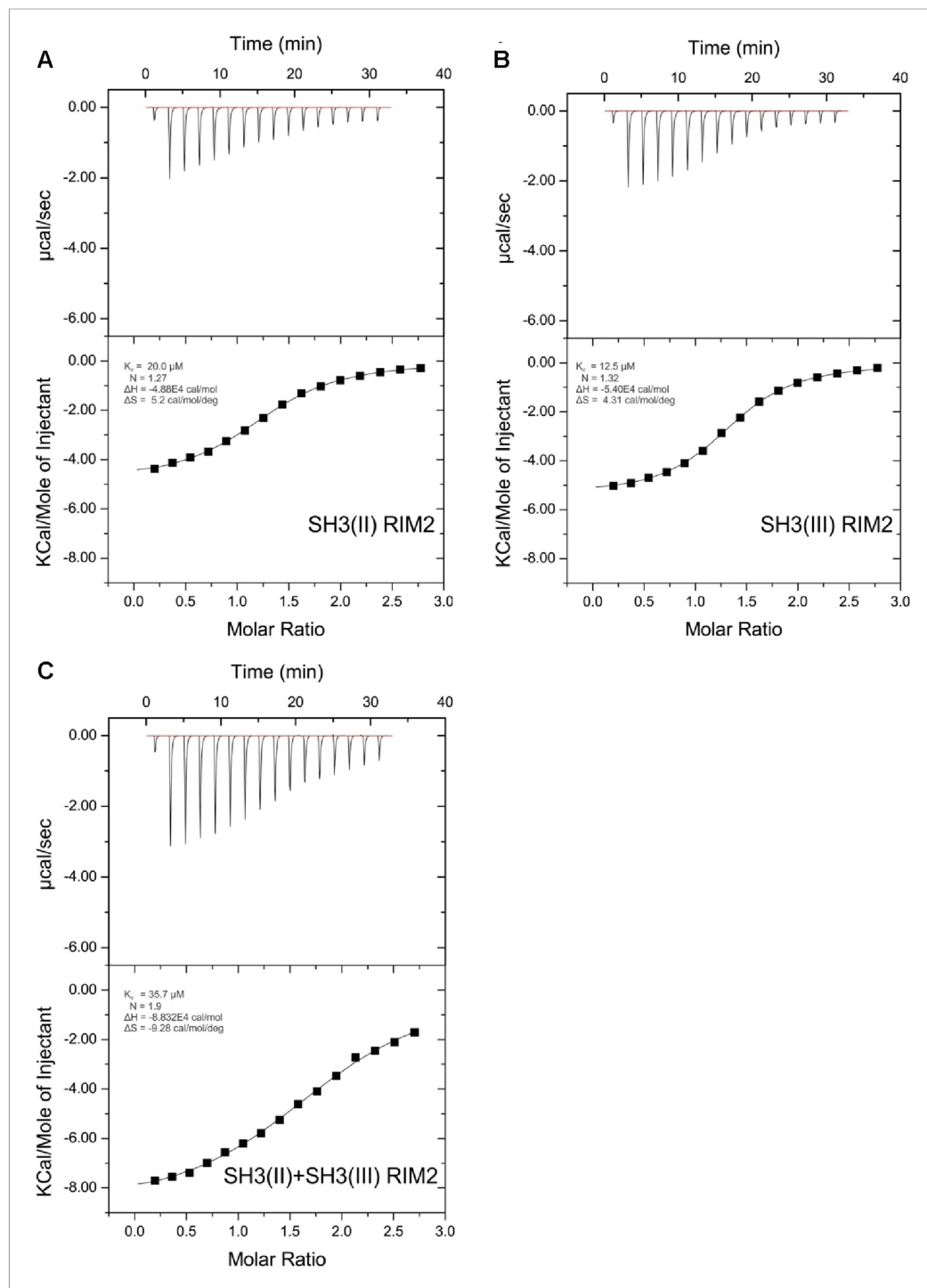


Figure 3—figure supplement 4. ITC measurements for RIM2 and RBP SH3 domains. Quantification of protein-peptide interactions by ITC. Both the raw data and the data integrated are shown. Data were fitted based on the 'One Set of Sites' model. **(A)** Titration of RBP-BP SH3-II and the RIM2 peptide. **(B)** Titration of RBP-BP SH3-III and the RIM2 peptide. **(C)** Titration of RBP-BP SH3-II+SH3-III and the RIM2.

DOI: [10.7554/eLife.06935.010](https://doi.org/10.7554/eLife.06935.010)

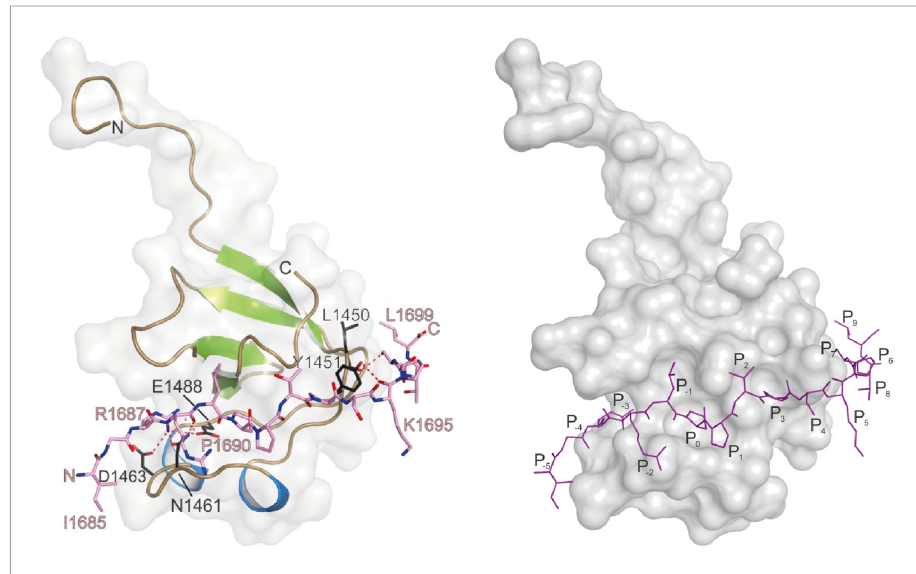


Figure 3—figure supplement 5. Crystal structure of Cac-peptide bound to RBP SH3-III domain. The SH3 domain is shown in gray surface representation, with (left) and without (right) the respective protein in cartoon representation. The bound peptides are drawn in stick representation. Hydrogen bonds ≤ 3.3 Å are indicated by red dashes.

DOI: [10.7554/eLife.06935.011](https://doi.org/10.7554/eLife.06935.011)

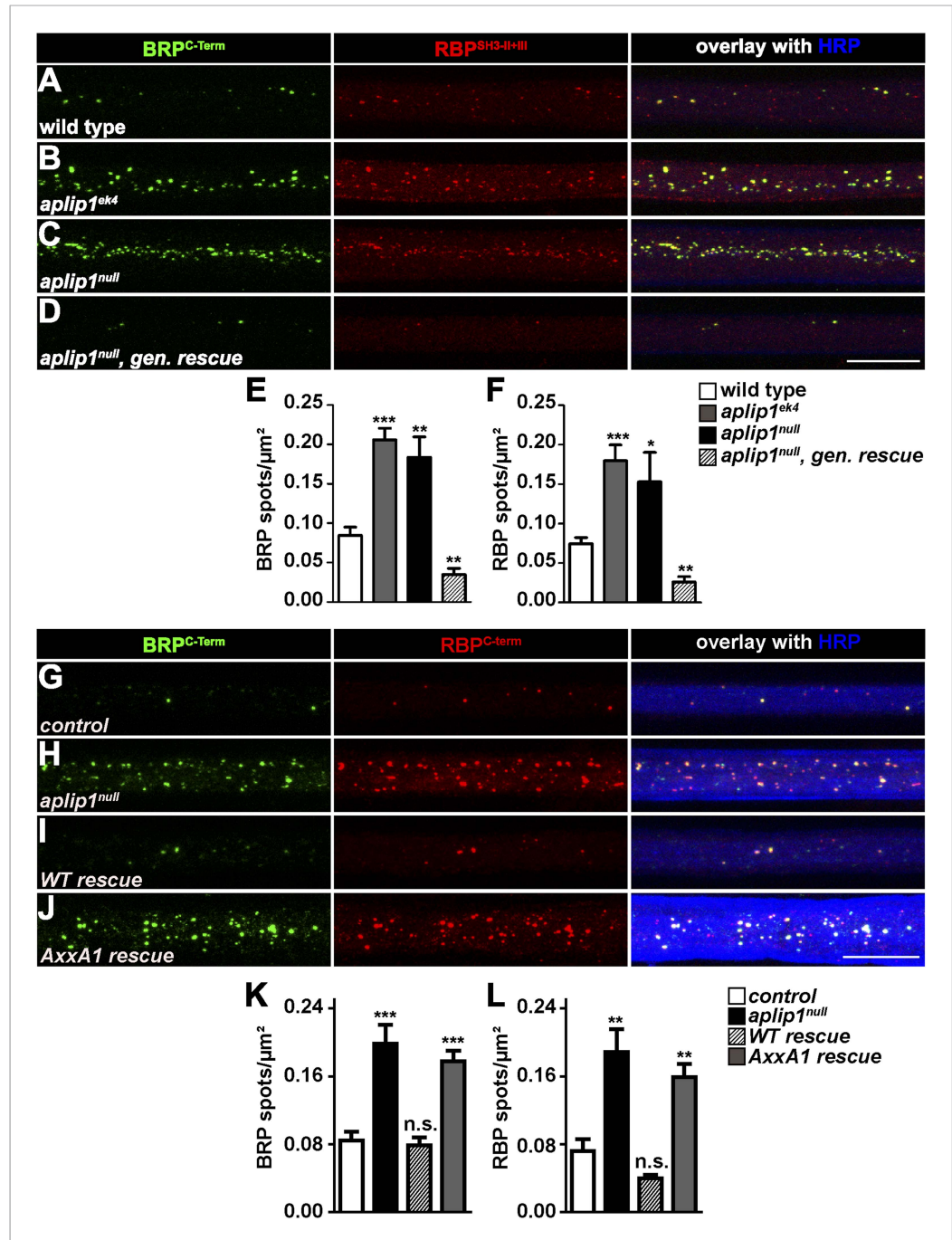


Figure 4. APLIP1-PXXP1 motif is needed for its function as RBP/BRP transport adaptor. (A–D) Nerve bundles of segments A1–A3 from third instar larvae of the genotypes indicated labeled with the Abs indicated. (E, F) Quantification of BRP/RBP spot numbers. BRP spots per μm^2 : WT (n = 8 nerves): 0.084 ± 0.010 ; *aplip1^{ek4}* (n = 9 nerves): 0.205 ± 0.025 ; *aplip1^{null}* (n = 8 nerves): 0.183 ± 0.025 ; *aplip1^{null}, gen. rescue* (n = 8 nerves): 0.034 ± 0.007 ; RBP spots per μm^2 , WT (n = 8 nerves): 0.074 ± 0.007 ; *aplip1^{ek4}* (n = 9 nerves): 0.180 ± 0.019 ; *aplip1^{null}* (n = 8 nerves): 0.153 ± 0.037 ; *aplip1^{null}, gen. rescue* (n = 8 nerves): 0.025 ± 0.006 . All panels show mean values and errors bars representing SEM. * $p \leq 0.05$; ** $p \leq 0.01$; *** $p \leq 0.001$; ns, not significant, $p > 0.05$, Mann–Whitney U test. (G–J) Nerve bundles of segment A1–A3 from third instar larvae of the genotypes indicated labeled with the Abs indicated. BRP and RBP co-localized in control animals and accumulated in a co-localizing fashion in axons of *aplip1^{null}* mutant animals. Re-expression of an APLIP1-WT cDNA construct in the *aplip1^{null}* background rescued the phenotype, while re-expression of an AxxA1 construct did not. Figure 4. continued on next page

Figure 4. Continued

(K, L) Quantification of the number of BRP/RBP spots per μm^2 axon. BRP spots per μm^2 , control (n = 12 nerves): 0.084 ± 0.010 ; *aplip1^{null}* (n = 16 nerves): 0.198 ± 0.022 ; *WT rescue* (n = 14 nerves): 0.078 ± 0.009 ; *AxxA1 rescue* (n = 14 nerves): 0.177 ± 0.012 ; RBP spots per μm^2 , control (n = 12 nerves): 0.071 ± 0.013 ; *aplip1^{null}* (n = 16 nerves): 0.188 ± 0.026 ; *WT rescue* (n = 14 nerves): 0.039 ± 0.004 ; *AxxA1 rescue* (n = 14 nerves): 0.158 ± 0.015 . All panels show mean values and errors bars representing SEM. * $p \leq 0.05$; ** $p \leq 0.01$; *** $p \leq 0.001$; ns, not significant, $p > 0.05$, Mann–Whitney U test. Scale bar: (A–D, G–J) 10 μm .
DOI: 10.7554/eLife.06935.018

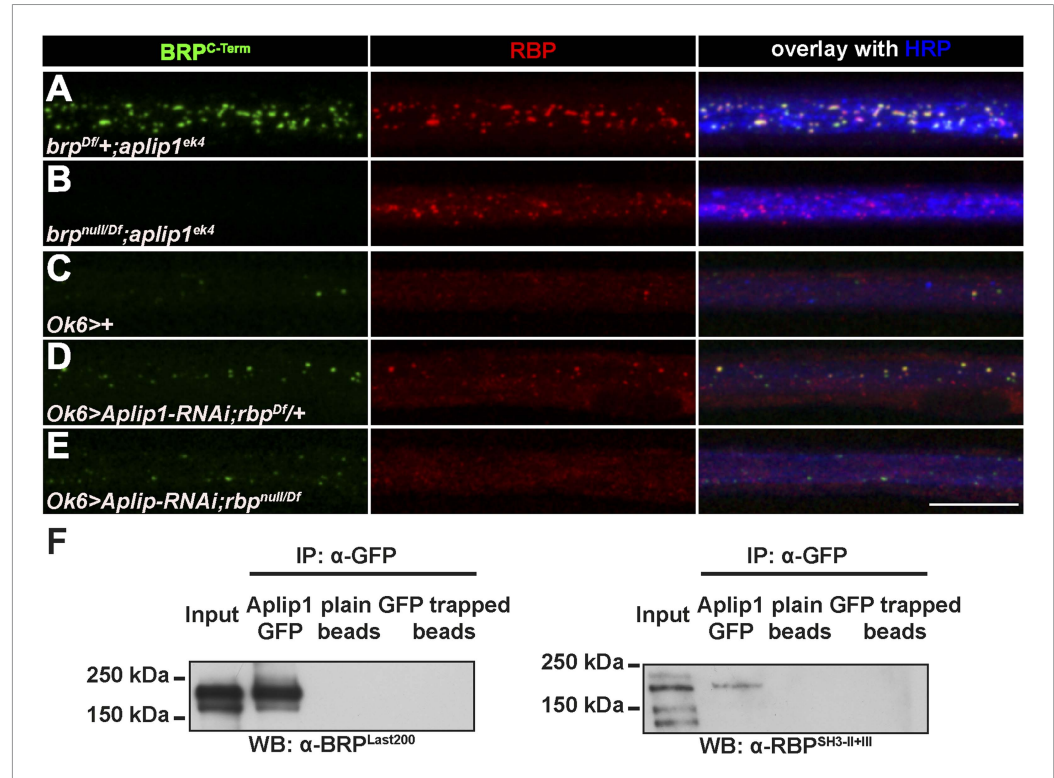


Figure 5. Aplip1 promotes BRP transport in absence of RBP. (A–E) Nerve bundles of segments A1–A3 from third instar larvae of the genotypes indicated labeled with the Abs indicated. (A) Removing one copy of BRP in *aplip1^{ek4}* mutants had no apparent effect on axonal RBP accumulation. (B) RBP still accumulates in *brp^{null};aplip1^{ek4}* double mutants. (C, D) Driver control and removing one copy of RBP in motoneuronal driven Aplip1-RNAi had no apparent effect on axonal BRP accumulation. (E) BRP still accumulates in *rbp^{null};aplip1^{ek4}* double mutants. Scale bar: (A–E) 10 μm . (F) Immunoprecipitation (IP) of Aplip1^{GFP} with anti-GFP Ab from *Drosophila* active zone (AZ) protein-enriched fraction was followed by Western blot (WB) analysis using anti-BRP^{Last200} and anti-RBP^{SH3-II+III}. Both BRP and RBP could be detected in Aplip1^{GFP} IPs, but are absent in controls (plain beads; GFP trapped beads). (For whole WBs, see Figure 5—figure supplement 2).
DOI: 10.7554/eLife.06935.019

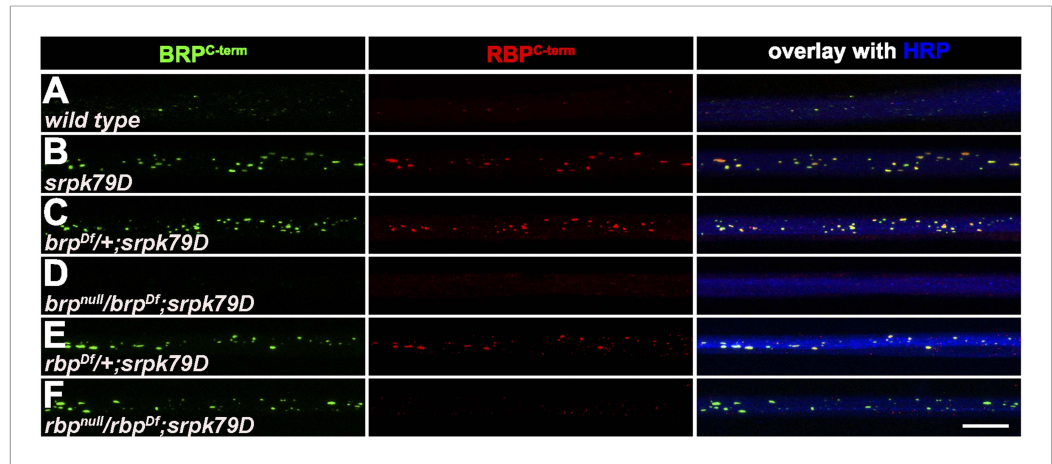


Figure 5—figure supplement 1. Accumulation of BRP in *srpk79D* mutant axons is unaffected by removing RBP. (A–F) Nerves of segments A1–A3 from third instar larvae of the genotypes indicated labeled with the Abs indicated. Removing BRP in *srpk79D* mutants (D) also abolished axonal RBP spots, while removing RBP in *srpk79D* mutants did not affect BRP accumulations (F).
DOI: [10.7554/eLife.06935.020](https://doi.org/10.7554/eLife.06935.020)

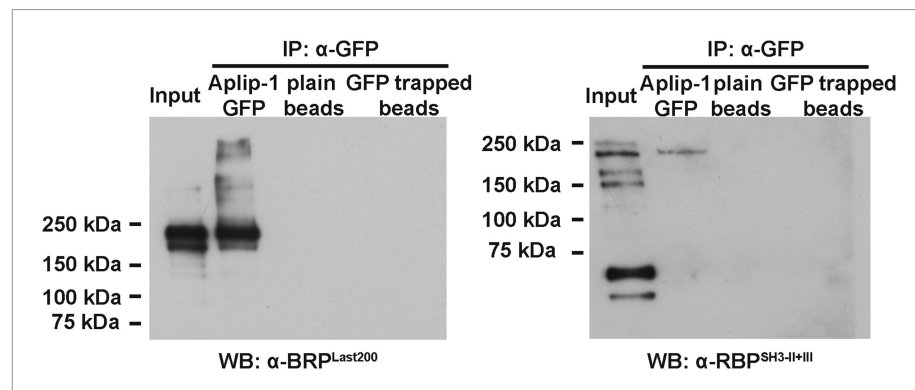


Figure 5—figure supplement 2. IP of APLIP1^{GFP} with anti-GFP (Full blot). Full blot IP of APLIP1^{GFP} with anti-GFP from Drosophila AZ protein-enriched fraction was followed by WB analysis using anti-BRP^{Last200} and anti-RBP^{SH3-II+III} Abs.
DOI: [10.7554/eLife.06935.021](https://doi.org/10.7554/eLife.06935.021)

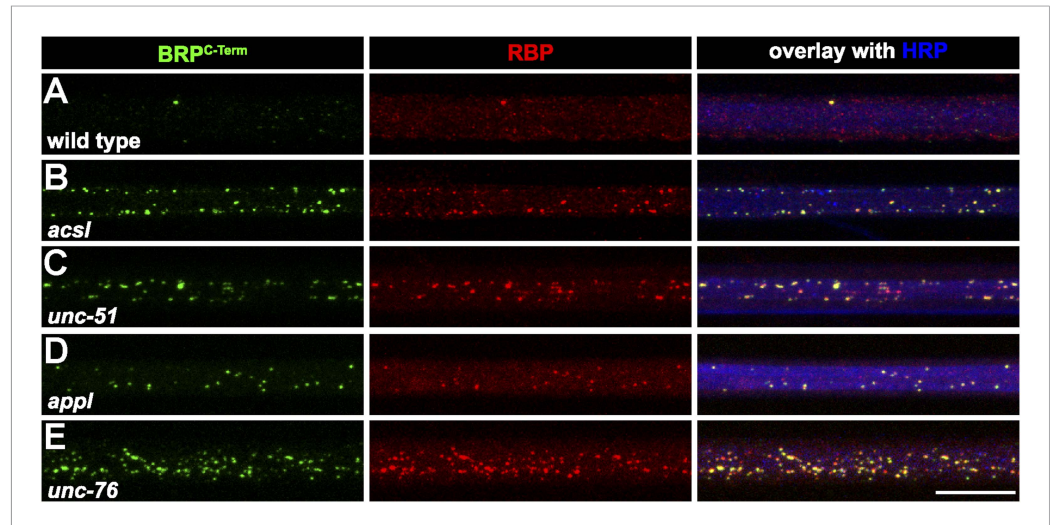


Figure 6. Several known transport adaptor mutants showed axonal BRP and RBP co-accumulations. (A–E) Nerve bundles of segment A1–A3 from third instar larvae of the genotypes indicated labeled with the Abs indicated. BRP and RBP accumulated in a co-localizing manner in axons of WT (A), *acsl* (B), *unc-51* (*atg-1*; C), *appl* (D) and *unc-76* (E). Scale bar: 10 μ m.

DOI: [10.7554/eLife.06935.022](https://doi.org/10.7554/eLife.06935.022)

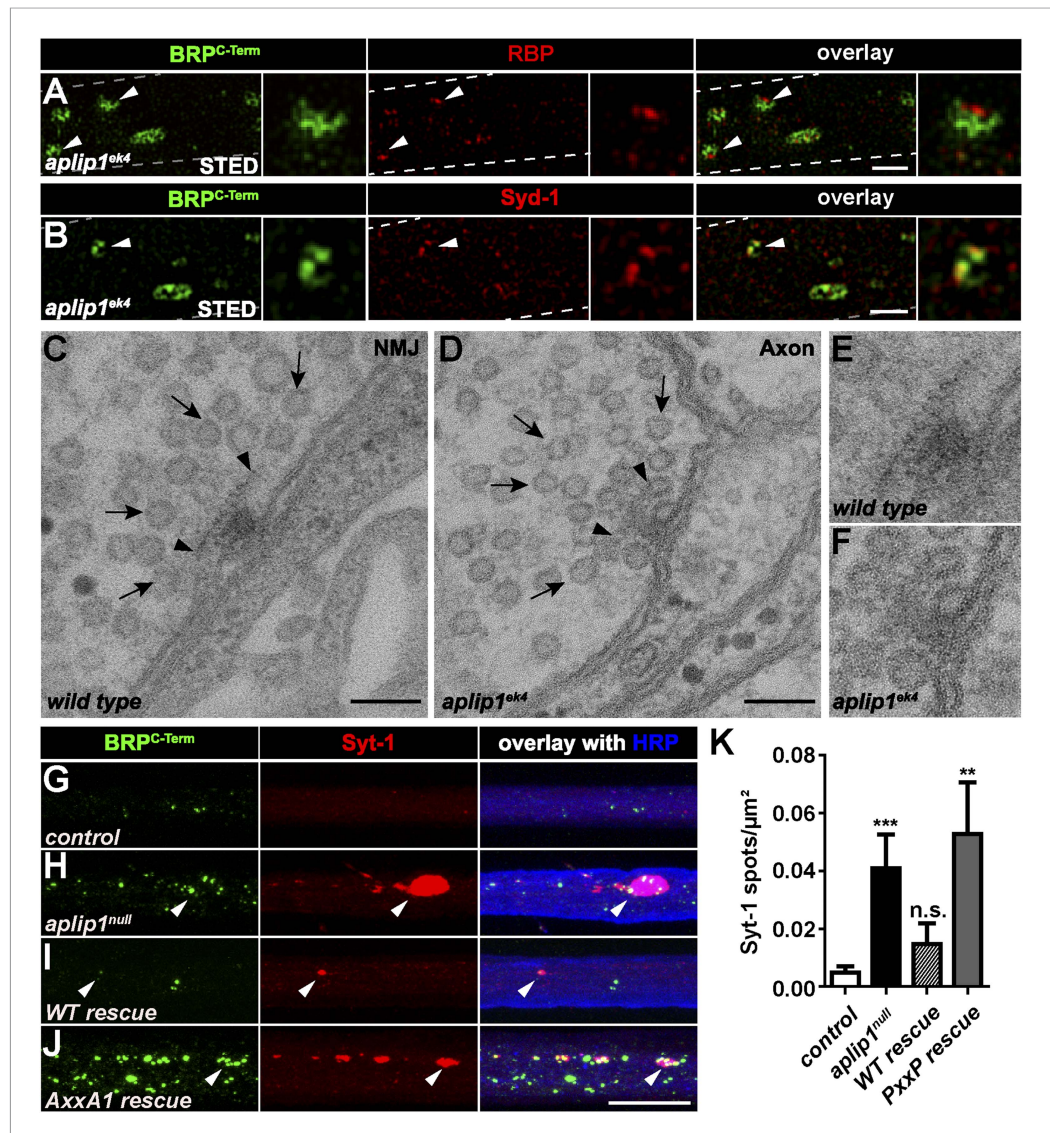


Figure 7. Ectopic AZ scaffold and synaptic vesicle (SV) accumulation in *aplip1* mutant axons. **(A)** Two-colour STED images of axonal aggregates in *aplip1^{ek4}* mutants revealed that the structures observed (arrow heads) have identical BRP and RBP arrangement, as recently observed at presynaptic AZs (Liu et al., 2011a). Right panels display magnifications of single axonal AZ. Dashed lines indicate axonal plasma membrane. **(B)** Two-colour STED images of axonal aggregates in *aplip1^{ek4}* mutants revealed that the structures observed (arrow head) have identical BRP and Syd-1 arrangement as observed at immature presynaptic AZs (Owald et al., 2010). Right panels display magnifications of single axonal AZ. Dashed lines indicate axonal plasma membrane. **(C)** Terminal T-bar (arrow heads) surrounded by SVs (arrows) taken from electron micrographs of WT third instar larvae after conventional embedding. **(D)** Ectopic axonal T-bar (arrow heads) taken from electron micrographs from *aplip1^{ek4}* mutant third instar larvae after conventional embedding. SVs accumulate around the ectopic T-bar (arrows). **(E)** Magnification of **(C)**. **(F)** Magnification of **(D)**. **(G–J)** Nerve bundles of segment A1–A3 from third instar larvae of the genotypes indicated labeled with the Abs indicated. Syt-1 accumulates at a subset of axonal BRP aggregations in *aplip1^{null}* and *AxxA1* rescue (**H, J**) larvae, but not in control and WT rescue larvae (**G, I**). **(K)** Quantification of the number of Syt-1 spots per μm² axon. control (n = 12 nerves): 0.004 ± 0.002; *aplip1^{null}* (n = 16 nerves): 0.040 ± 0.011; WT rescue (n = 13 nerves): 0.014 ± 0.007; *AxxA1* rescue (n = 13 nerves): 0.052 ± 0.017. All panels show mean values and errors bars representing SEM. *p ≤ 0.05; **p ≤ 0.01; ***p ≤ 0.001; ns, not significant, p > 0.05, Mann–Whitney U test. Scale bars: **(A, B)** 500 nm; **(C, D)** 100 nm; **(G, J)** 10 μm. DOI: 10.7554/eLife.06935.023

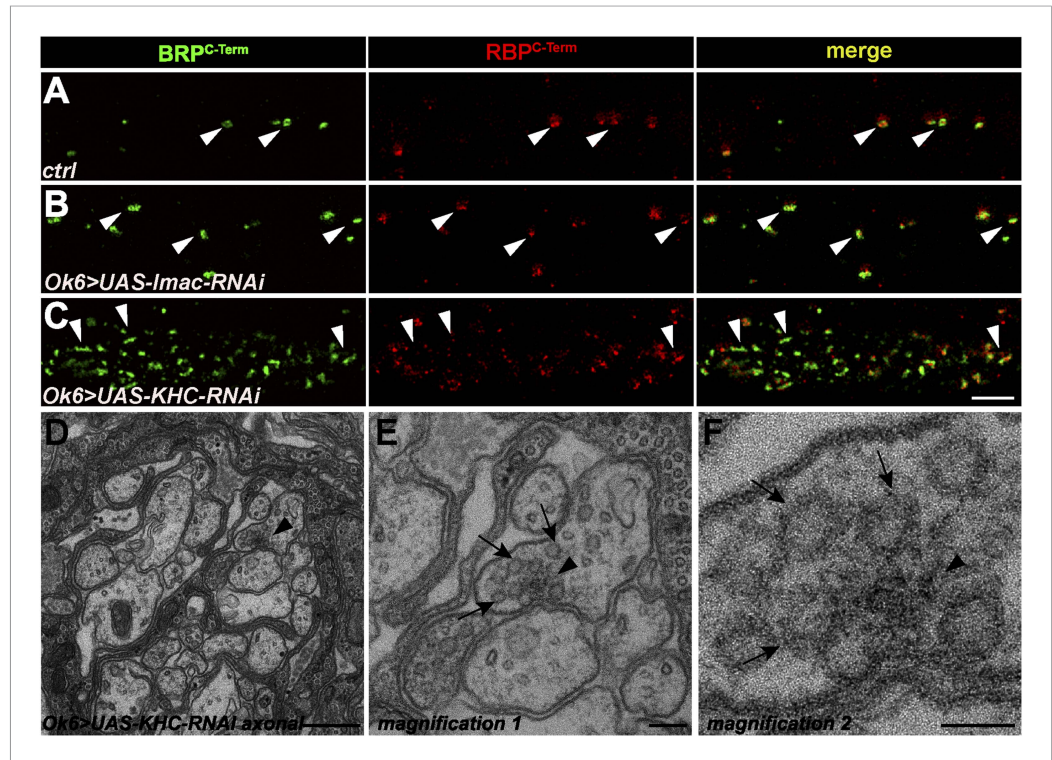


Figure 7—figure supplement 1. Ectopic AZ protein accumulations in motoneuronal driven *Imac-* and *KHC-RNAi* axons. (A, B) Two-colour STED images of axonal aggregates in *ctrl* and *Ok6::UAS-Imac-RNAi* revealed that BRP and RBP co-accumulate in both genotypes but, in contrast to *aplip1* mutants, show no preference concerning orientation towards the axonal plasma membrane (arrow heads). (C) Two-colour STED images of axonal aggregates in *Ok6::UAS-KHC-RNAi* revealed that the BRP-RBP accumulations observed in this genotype mostly show irregular shapes (arrow heads) with diverse orientations in the axon. (D) The only ectopic axonal electron dense formation (arrow head) found in electron micrographs in *Ok6::UAS-KHC-RNAi* third instar larvae after conventional embedding. (E, F) Magnification of (D). SVs (arrows) accumulate around the ectopic electron-dense structure (arrow head) but are also accumulating all along the axon. Scale bars: (A–C) 1.5 μ m; (D) 200 nm; (E) 100 nm; (F) 50 nm.

DOI: [10.7554/eLife.06935.024](https://doi.org/10.7554/eLife.06935.024)

Publication III

Muhammad, K., S. Reddy-Alla, J. H. Driller, D. Schreiner, U. Rey, M. A. Bohme, C. Hollmann, N. Ramesh, H. Depner, J. Lutzkendorf, T. Matkovic, T. Gotz, D. D. Bergeron, J. Schmoranzer, F. Goettfert, M. Holt, M. C. Wahl, S. W. Hell, P. Scheiffele, A. M. Walter, B. Loll and S. J. Sigrist (2015). "Presynaptic spinophilin tunes neurexin signalling to control active zone architecture and function" *Nat Commun* 6: 8362.

ARTICLE

Received 23 Mar 2015 | Accepted 13 Aug 2015 | Published 16 Oct 2015

DOI: 10.1038/ncomms9362

OPEN

Presynaptic spinophilin tunes neurexin signalling to control active zone architecture and function

Karzan Muhammad^{1,2,†}, Suneel Reddy-Alla^{1,2}, Jan H. Driller³, Dietmar Schreiner⁴, Ulises Rey², Mathias A. Böhme², Christina Hollmann², Niraja Ramesh¹, Harald Depner^{1,2}, Janine Lützkendorf², Tanja Matkovic^{1,2}, Torsten Götz^{1,2}, Dominique D. Bergeron², Jan Schmoranzner^{3,5}, Fabian Goettfert⁶, Mathew Holt⁷, Markus C. Wahl³, Stefan W. Hell⁶, Peter Scheiffele⁴, Alexander M. Walter^{2,5}, Bernhard Loll³ & Stephan J. Sigris^{1,2}

Assembly and maturation of synapses at the *Drosophila* neuromuscular junction (NMJ) depend on trans-synaptic neurexin/neuroigin signalling, which is promoted by the scaffolding protein Syd-1 binding to neurexin. Here we report that the scaffold protein spinophilin binds to the C-terminal portion of neurexin and is needed to limit neurexin/neuroigin signalling by acting antagonistic to Syd-1. Loss of presynaptic spinophilin results in the formation of excess, but atypically small active zones. Neuroigin-1/neurexin-1/Syd-1 levels are increased at *spinophilin* mutant NMJs, and removal of single copies of the *neurexin-1*, *Syd-1* or *neuroigin-1* genes suppresses the spinophilin-active zone phenotype. Evoked transmission is strongly reduced at *spinophilin* terminals, owing to a severely reduced release probability at individual active zones. We conclude that presynaptic spinophilin fine-tunes neurexin/neuroigin signalling to control active zone number and functionality, thereby optimizing them for action potential-induced exocytosis.

¹ Freie Universität Berlin, Institute for Biology/Genetics, Takustrasse 6, Berlin 14195, Germany. ² NeuroCure, Charité, Charitéplatz 1, Berlin 10117, Germany. ³ Freie Universität Berlin, Institut für Chemie und Biochemie /Strukturbiochemie, Takustrasse 6, Berlin D-14195, Germany. ⁴ Biozentrum, University of Basel, Klingelbergstrasse 50-70, Basel 4056, Switzerland. ⁵ Leibniz Institut für Molekulare Pharmakologie, Robert-Roessle-Strasse 10, Berlin 13125, Germany. ⁶ Department of NanoBiophotonics, Max Planck Institute for Biophysical Chemistry, Am Fassberg 11, Göttingen 37077, Germany. ⁷ VIB Center for the Biology of Disease, Herestraat 49, Leuven 3000, Belgium. † Present address: Max Planck Institute for Brain Research, Neocortical Circuits Lab, Max-von-Laue-Str. 4, 60438 Frankfurt, Germany. Correspondence and requests for materials should be addressed to S.J.S (email: stephan.sigris@fu-berlin.de).

Chemical synapses release synaptic vesicles (SVs) at specialized presynaptic membranes, so-called active zones (AZs), which are characterized by electron-dense structures, reflecting the presence of extended molecular protein scaffolds. These AZ scaffolds confer stability and facilitate SV release¹. Importantly, at individual AZs, scaffold size is found to scale with the propensity to engage in action potential-evoked release^{2–4}. An evolutionarily conserved set of large multi-domain proteins operating as major building blocks for these scaffolds has been identified over the last years: Syd-2/Liprin- α , RIM, RIM-binding-protein (RBP) and ELKS family proteins (of which the *Drosophila* homologue is called Bruchpilot (BRP))^{1,5–7}. However, how presynaptic scaffold assembly and maturation are controlled and coupled spatiotemporally to the postsynaptic assembly of neurotransmitter receptors remains largely unknown, although trans-synaptic signalling via Neurexin-1 (Nrx-1)–Neuroigin-1 (Nlg1) adhesion molecules is a strong candidate for a conserved ‘master module’ in this context, based on Nrx-Nlg signalling promoting synaptogenesis *in vitro*, synapses of rodents^{8,9}, *Caenorhabditis elegans*¹⁰ and *Drosophila*^{11–16}. With respect to scaffolding proteins, Syd-1 was found to promote synapse assembly in *C. elegans*⁵, *Drosophila*¹⁷ and rodents¹⁸. In *Drosophila*, the Syd-1-PDZ domain binds the Nrx-1 C terminus and couples pre- with postsynaptic maturation at nascent synapses of glutamatergic neuromuscular junctions (NMJs) in *Drosophila* larvae. Syd-1 cooperates with Nrx-1/Nlg1 to stabilize newly formed AZ scaffolds, allowing them to overcome a ‘threshold’ for synapse formation¹³. Additional factors tuning scaffold assembly, however, remain to be identified. We show here that the conserved scaffold protein spinophilin (Spn) is able to fine-tune Nrx-1 function by binding the Nrx-1 C terminus with micromolar affinity via its PDZ domain. In the absence of presynaptic Spn, ‘excessive seeding’ of new AZs occurred over the entire NMJ due to elevated Nrx-1/Nlg1 signalling. Apart from structural changes, we show that Spn plays an important role in neurotransmission since it is essential to establish proper SV release probability, resulting in a changed ratio of spontaneous versus evoked release at *Spn* NMJ terminals.

Results

Presynaptic Spn restricts the AZ number. Glutamatergic NMJs of *Drosophila* larvae continuously expand to meet the requirements of the growing muscle fibres by adding new release sites (or synapses) to their structure^{19,20}. These synapses are characterized by a single presynaptic AZ opposed by a single postsynaptic density (PSD) composed of glutamate receptors (GluRs). AZ formation is initiated by both Syd-1 and Liprin- α clusters and finalized by the incorporation of BRP²¹. Here we used the *Drosophila* NMJ model system to search for factors restricting the number of BRP scaffolds. To this end, a set of proteins and their known binding partners, which we previously detected in immunoprecipitation experiments against BRP²², were suppressed by RNA interference (RNAi) restricted to presynaptic motor neurons. RNAi-induced presynaptic knockdown of the only *Drosophila* homologue of the Neurabin/Spn family caused an increase of AZ numbers at the NMJ (Fig. 1a; Supplementary Fig. 1a–e). Simultaneously, the total area of postsynaptic GluRs increased (Supplementary Fig. 1b–e).

Motivated by this result, we generated a *Spn* null allele using Flippase-mediated trans-deletion of FRT sites with two transposon lines flanking the *spn* locus, resulting in a complete deletion of the Spn-encoding sequence (*spn* ^{Δ 3.1}) (Fig. 1b). Genomic PCR²³ was used to validate the elimination of the entire *spn* locus. Animals died in pupal stages when we put the *spn* ^{Δ 3.1} chromosome in trans to a large deficiency (*spn* ^{Δ 3.1}/*dfBSc116*,

from hereafter *Spn*). Neurabin/Spn family proteins in rodents are strongly expressed in postsynaptic spines^{24,25} and are also found in presynaptic compartments^{26,27}. Our presynaptic Spn knockdown clearly affected AZ scaffold formation, pointing towards a presynaptic role for Spn at *Drosophila* NMJs. To validate this hypothesis, and to determine Spn localization, we raised a polyclonal antibody against a fusion protein from the Spn N-terminal region (Anti-Spn^{Nterm}, Fig. 1a; green bar). The Spn antibody robustly stained wild-type NMJs, but the signal was lost in *Spn* mutant larvae (Fig. 1c,d). Staining was restored after crossing in a genomic Spn rescue construct (Pac(*Spn*¹)), proving the specificity of the NMJ Spn antibody signal (Fig. 1e). To characterize the localization of endogenous Spn in pre- versus postsynaptic compartments, we expressed the Spn-RNAi transgene in either the pre- or postsynaptic compartment of the NMJ using specific Gal4-driver lines. Motoneuron-driven presynaptic RNAi left the anti-Spn staining intact at the bouton periphery, but removed the staining within the *horseradish peroxidase* (HRP) signal, which outlines the neuronal membrane (Fig. 1f). Muscle-driven postsynaptic RNAi made the Spn staining surrounding the boutons vanish. However, the signal inside the presynaptic boutons (Fig. 1g) remained unchanged. When a GFP-Spn fusion construct was co-expressed with the AZ marker BRP-D3^{Straw} within the motoneurons²¹, presynaptic Spn formed discrete clusters, often found adjacent to BRP-labelled AZ scaffolds (Fig. 1g,h). This pattern was very similar to the residual endogenous Spn staining found remaining after the expression of RNAi in the postsynaptic muscle (Fig. 1g). Thus, Spn localizes to both pre- and postsynaptic compartments at larval NMJs. Presynaptic Spn localizes close to presynaptic AZ scaffolds.

Subsequently, we analysed the role of Spn in synaptic organization at developing NMJs, using the null allele (*Spn*) we created (Fig. 1b). Detailed analysis of *Spn* NMJs revealed that AZ scaffold densities increased. Postsynaptic GluR (GluRIID) labelling²⁸ was also strikingly increased (Fig. 2a,b). We expressed two different but overlapping genomic pacman transgenes²⁹ containing the full *spn* locus (Pac(*Spn*^{1&2}); Fig. 1b) in the null allele mutant background to prove the specificity of the *Spn* null phenotype. Both genomic constructs fully rescued adult viability and, importantly, the NMJ phenotypes of *Spn*. In addition, deletion of a stretch encoding the Spn open reading frame within the genomic construct of Pac(*Spn*²), named Pac(*Spn*^{*}), abolished rescue activity (data not shown). We further tested a semi-lethal transposon insertion within the *spn* locus (Mi(Mic)Spn^{Mi06873}), which we found to significantly reduce anti-Spn staining. The latter mutant showed NMJ phenotypes similar, but somewhat weaker, than those observed in *Spn* null larvae (Supplementary Fig. 2a–e). Taken together, we show that loss of Spn affects the synaptic structure of the NMJ. We quantified relevant structural parameters using BRP/GluRIID/HRP co-stainings to further characterize this phenotype (Fig. 2d–g). Average NMJ size (visualized via HRP) was not significantly changed in the *Spn* null background. Similarly, but more pronounced than in the RNAi experiments, the densities of presynaptic AZs (BRP cluster numbers normalized to synaptic HRP area) were significantly increased in *Spn* when compared with controls (Fig. 2d,e). We re-expressed the protein using a neuronal driver line *elav(x)-C155-gal4* in the *Spn* null background to test whether this was due to a loss of presynaptic Spn. Indeed, presynaptic expression of Spn complementary DNA (cDNA) effectively re-established normal AZ densities (Fig. 2c–e). By contrast, postsynaptic (that is, muscle) expression of Spn in the null background appeared to have no effect (data not shown). Moreover, the postsynaptic phenotype of increased GluR fields was reverted towards normal levels on presynaptic Spn expression (Fig. 2f). Thus, presynaptic

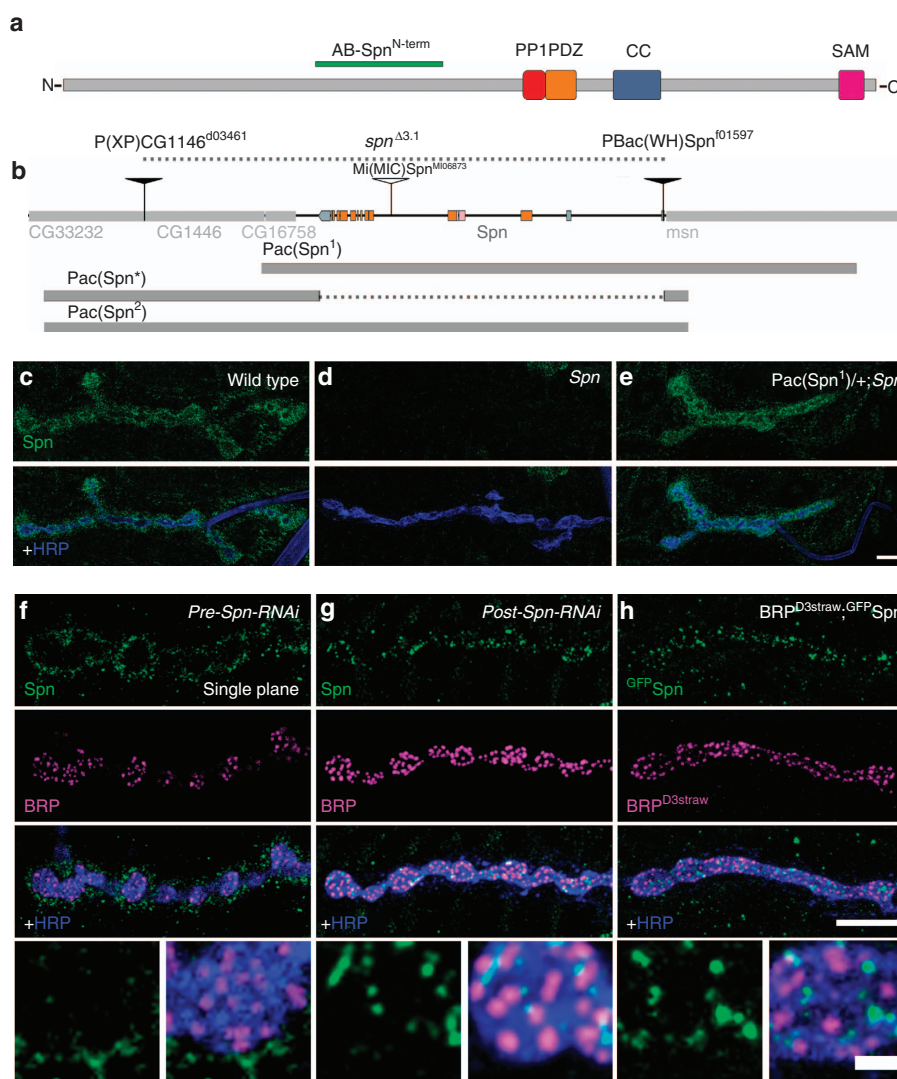


Figure 1 | Characterization of the *Drosophila spn* locus. (a) Domain structure of Spn: protein phosphatase 1 (PP1) binding motif, PDZ domain, coiled coil (CC) domain and sterile alpha motif (SAM) domain. (b) Organization of the *spn* locus. Transposon lines used in the generation of *Spn* mutants, positions covered by the Pacman constructs indicated on a genomic map of *Spn*. (c) Immunostaining with Spn antibody (green) and HRP antibody (blue) at control NMJs, (d) at *Spn* null NMJs (e) and *Spn* null NMJs with a genomic rescue construct. (f) Presynaptic knockdown of Spn leaves the HRP boundaries devoid of Spn protein. (g) Postsynaptic knockdown of Spn using a muscle driver line reveals discrete clusters of Spn within the presynaptic terminals. (h) Presynaptic co-labelling of ^{GFP}Spn together and BRP D3^{strawberry} using a motor neuron driver. Scale bars, 10 μm; 2 μm in magnified images.

Spn restricts both the dimensions of the PSD, as well as the number of juxtaposed presynaptic BRP scaffolds. The BRP scaffold is tightly associated with Ca²⁺ channels and RBP, another structural component of the AZ scaffold³⁰. Numbers of Ca²⁺ channel clusters and RBP clusters were also increased at *Spn* terminals (Supplementary Fig. 3a–f). By contrast, cysteine string protein, a SV protein, appeared unchanged when compared with controls (Supplementary Fig. 3d–h). Taken together, these data show that *Spn* terminals have a specific increase in the number of AZ scaffolds.

AZ scaffolds lacking Spn remain small. Confocal images suggested that individual presynaptic AZ scaffolds, as identified by their BRP spots, were atypically small at *Spn* terminals. However, confocal resolution (~250 nm) is not sufficient to reliably quantify AZ scaffold size. Thus, we turned to stimulated emission

depletion (STED) microscopy operating with ≈45 nm lateral resolution^{21,31} to visualize AZ scaffolds in their planar orientation (Fig. 3a–c). Analysing the longest peak-to-peak axes through individual AZs revealed that the diameters of BRP AZ scaffolds were substantially reduced in *Spn* mutants, while presynaptic Spn re-expression restored normal AZ size (Fig. 3a–e).

In summary, a larger number of smaller presynaptic AZ scaffolds are forming in the absence of presynaptic Spn. Electron microscopic (EM) analysis consistently revealed smaller but otherwise normal T-bars (Fig. 3f,h, arrowheads; Supplementary Fig. 4a–e). In some cases, two of these small T-bars converged (juxtaposed) into one common large postsynaptic compartment, identified by a region in which pre- and postsynaptic membranes were tightly apposed (Fig. 3g).

GluRs at wild-type NMJ synapses localize at postsynaptic membranes opposed to presynaptic AZs. As mentioned above

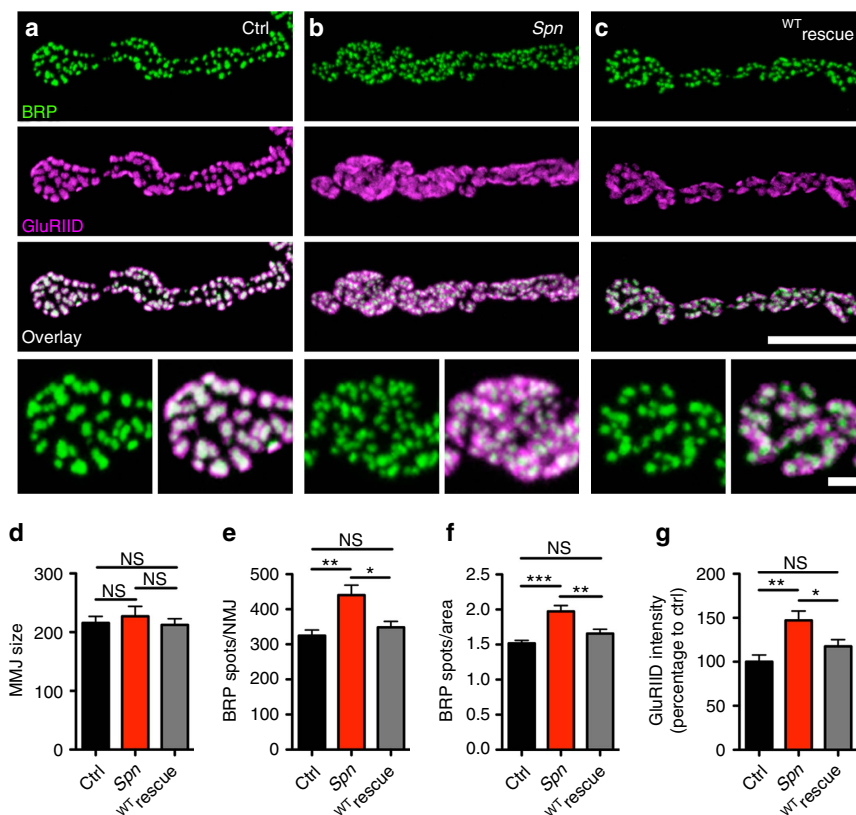


Figure 2 | Presynaptic *Spn* limits NMJ AZ numbers. (a–c) Projected confocal stacks of NMJs (muscle 4), labelled against BRP (BRP^{Nc82}, green) and GluRIID (magenta). (d) NMJ sizes measured using HRP labelling. (e) Numbers of AZ scaffolds per NMJ measured using BRP^{Nc82} labelling (Ctrl: 324.8 ± 16.29 , $n = 14$; *Spn*: 440.5 ± 28.4 , $n = 13$; neuronal ^{WT}*Spn* cDNA expression (^{WT}*rescue*): 348.4 ± 17.45 , $n = 14$; Ctrl versus *Spn* $P < 0.01$, ($U = 25$); Ctrl versus ^{WT}*rescue*: $P > 0.05$, ($U = 79$); *Spn* versus ^{WT}*rescue*: $P < 0.05$, ($U = 38$)). (f) AZ scaffold densities (spots per μm^2): ^{WT}*Spn* cDNA expression (Ctrl: 1.5 ± 0.04 , $n = 14$; *Spn*: 1.97 ± 0.08 , $n = 13$; ^{WT}*rescue*: 1.65 ± 0.6 , $n = 14$; Ctrl versus *Spn* $P < 0.001$, ($U = 13$); Ctrl versus ^{WT}*Spn* *rescue*: $P > 0.05$; ($U = 57$); *Spn* versus ^{WT}*rescue*: $P < 0.01$, ($U = 36$)). (g) Integrated GluRIID intensity is higher in *Spn* (Ctrl: 100 ± 7.6 , $n = 14$; *Spn*: 147.1 ± 10.74 , $n = 13$; ^{WT}*rescue*: 117.6 ± 7.6 , $n = 14$; Ctrl versus *Spn*: $P < 0.01$, ($U = 31$); Ctrl versus ^{WT}*rescue*: $P > 0.05$, ($U = 65$); *Spn* versus ^{WT}*rescue*: $P < 0.05$, ($U = 53$). All tests are Mann-Whitney *U*-test, values are mean \pm s.e.m., NS, not significant; * $P \leq 0.05$; ** $P \leq 0.01$; *** $P \leq 0.001$. Scale bar, 10 or 1.5 μm in magnified images.

(Fig. 2), individual GluR clusters were atypically enlarged in *Spn*. As details of the GluR organization may not be resolved by standard confocal imaging, we used three-dimensional structured illumination microscopy (3D SIM) with an isotropic resolution of $\approx 120 \text{ nm}$ ³². This provides a significant improvement in optical resolution along the *z*-axis, while STED only increases the *x*–*y* resolution. Therefore, SIM allowed us to resolve the 3D organization of GluR fields relative to the AZs. Consistent with the EM analysis, *Spn* NMJs showed extended, often continuous receptor fields, juxtaposed to several small AZs, with a clear increase in the area of the postsynaptic compartment labelled with GluRs (Fig. 3i–l).

Increased *Nrx-1* signalling mediates the *Spn* phenotype. PSDs of *Drosophila* NMJs contain two subtypes of GluR complexes, distinguished by the incorporation of either receptor subunit GluRIIA or GluRIIB²⁸. Immature wild-type PSDs contain more GluRIIA than IIB, while GluRIIB incorporation occurs during subsequent PSD maturation, revealed by *in vivo* imaging³³. We recently discovered that *Nlg1*, *Nrx-1* and *Syd-1* mutants share a specific deficit in the incorporation of GluRIIA receptors into the PSD driving ‘early’ PSD growth¹³. In contrast, here we observed a threefold increase of GluRIIA intensity at *Spn* terminals, probably

responsible for the overgrowth of the postsynaptic GluR fields, while GluRIIB levels remained unchanged (Supplementary Fig. 5a–e). Thus, lack of *Spn* apparently results in an opposite phenotype to *Nrx-1* signalling pathway mutants (*Nrx-1*, *Nlg1*, *Syd-1*), which show fewer but larger and often mis-shapen AZ scaffolds^{13,15,16}. To further investigate a possible antagonistic relationship between *Spn* and *Nrx-1/Nlg1*, we investigated whether *Nrx-1* levels were changed at *Spn* terminals, using an antibody detecting endogenous *Nrx-1* (ref. 15). We observed a significant increase in the levels of *Nrx-1* (measured either as the total integrated fluorescence from the anti-*Nrx-1* label, or total area of *Nrx-1* clusters normalized to synaptic HRP area; Fig. 4a–d). We next asked whether this increase in *Nrx-1* could promote *Nrx-1* signalling. To test this, we first evaluated the levels of *Nlg1* and *Syd-1* in *Spn* mutants. We found that the level of both proteins increased at *Spn* NMJs (Fig. 4e–h; Supplementary Fig. 6a–g). However, Fasciclin-II (another cell adhesion molecule unrelated to the *Nrx-1/Nlg1* signalling pathway³⁴) was unchanged (Supplementary Fig. 7a,b). Next, to confirm that *Nrx-1* signalling is directly responsible for the generation of more AZs at *Spn* terminals, a single copy of the *nrx-1* gene (allele *Nrx-1241*; ref. 15) was removed from the *Spn* background. This manipulation in wild type background had no detectable effect on NMJ and AZ organization (ref. 15; data not shown). Strikingly,

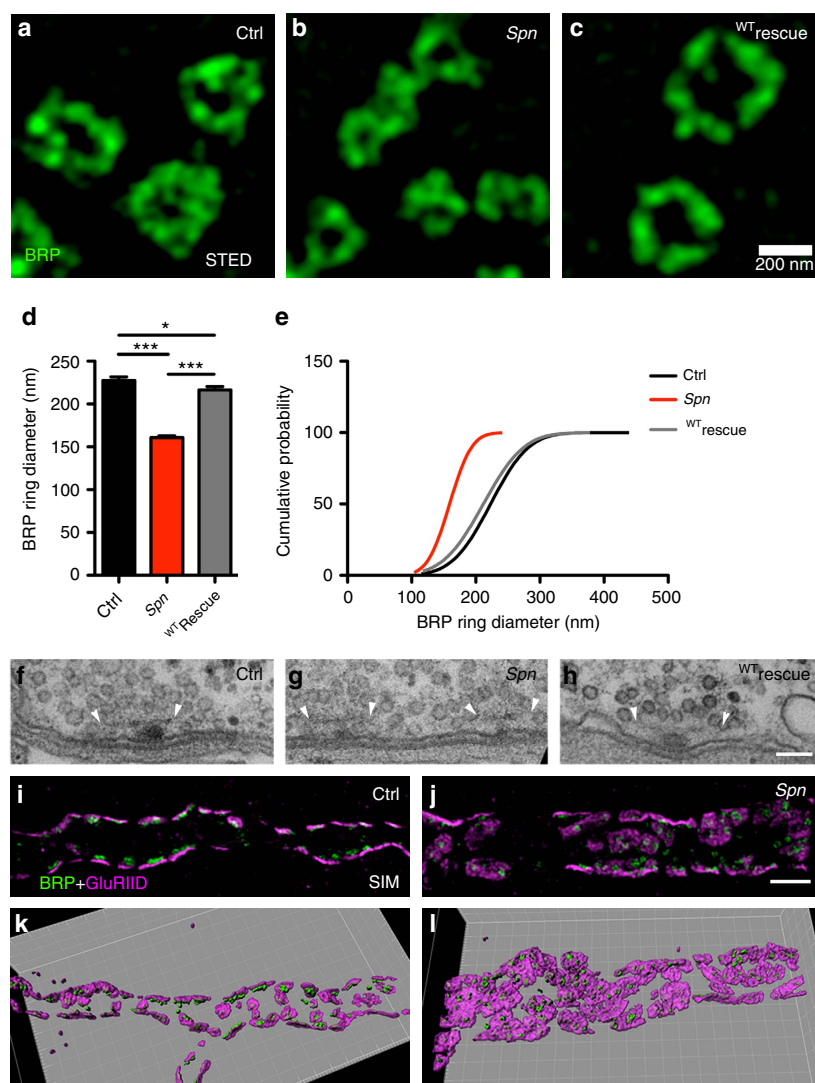


Figure 3 | Ultrastructural analyses of *Spn*NMJ synapses. (a-c) STED-derived BRP rings are atypically small in *Spn* terminals. (d,e) Quantification of BRP ring diameters. Control: 227.5 ± 4 nm, $n = 168$; *Spn*: 160.8 ± 2 nm, $n = 178$; WT_{rescue} : 216.3 ± 3.9 nm, $n = 156$; Kruskal-Wallis test with Dunn's multiple comparison test ($K = 186$). $*P \leq 0.05$; $**P \leq 0.01$; $***P \leq 0.001$. Error bars: mean \pm s.e.m. (f,h) Electron microscopy of presynaptic electron-dense projections (T-bars) of (f) control boutons, (g) *Spn* boutons with more, but smaller T-bars; the *Spn* phenotype which can be rescued by presynaptic re-expression of *Spn* (h). Arrowheads indicate the edges of T-bars platforms. (i,j) Structured Illumination (SIM) analysis of WT and *Spn* NMJs. Co-labelling of GluRIID and BRP^{Nc82} for wild-type (i) and *Spn* (j) NMJs show excessive accumulations of GluRs at *Spn* NMJs with arrays of small BRP scaffolds converging on enlarged GluR fields. (k,l) 3D rendering of SIM images shown above. Scale bars: STED, 200 nm; EM, 100 nm; SIM, 2 μ m.

AZ numbers were reduced to wild type levels after removing a single *nrx-1* gene copy from the *Spn* background (Fig. 4i-l). The AZ assembly and maturation mediated by Nr x -1 depends on both muscle expressed (postsynaptic) Nlg1 (refs 11,35) and presynaptic Syd-1. In fact, removing a single *nlg1* gene copy in *Spn* null background (*nlg*^{2,3}; ref. 11) suppressed the *Spn* phenotype (Fig. 4m-p). Furthermore, removing a single gene copy of *syd-1* also suppressed the *Spn* phenotype (Fig. 4q-t). We went on to analyse the functional relationship between *Spn* and Syd-1; both are presynaptically expressed scaffold proteins containing a PDZ domain.

Antagonism of *Spn* and Syd-1 for Nr x -mediated synapse assembly. We previously found that Nr x -1 levels are decreased in *Syd-1* mutants, but stabilized on re-expression of Syd-1.

Moreover, previous fluorescence recovery after photobleaching (FRAP) analysis showed elevated mobility of Nr x -1^{GFP} in a *Syd-1* mutant background¹³. As Nr x -1 and Syd-1 clusters in *Spn* were upregulated (Fig. 4a-d; Supplementary Fig. 6a-g), we asked whether it was possible that the motility of Nr x -1 was altered in *Spn* mutants by performing FRAP experiments on Nr x -1^{GFP}. We found a delayed recovery and, thus, reduced motility of Nr x -1 in the *Spn* null background (Supplementary Fig. 6i-l). At the same time, lack of *Drosophila* CASK (Caki), another scaffolding protein that binds to the Nr x -1 C terminus^{36,37}, did not show any noticeable effect on Nr x -1 motility (Supplementary Fig. 6). Moreover, the recovery of Syd-1^{GFP} clusters appeared to be unchanged at *Spn* terminals (even though the cluster density was increased) (Supplementary Fig. 6i-k). Thus, *Spn*-mediated Nr x -1 motility is apparently not connected to altered Syd-1 motility.

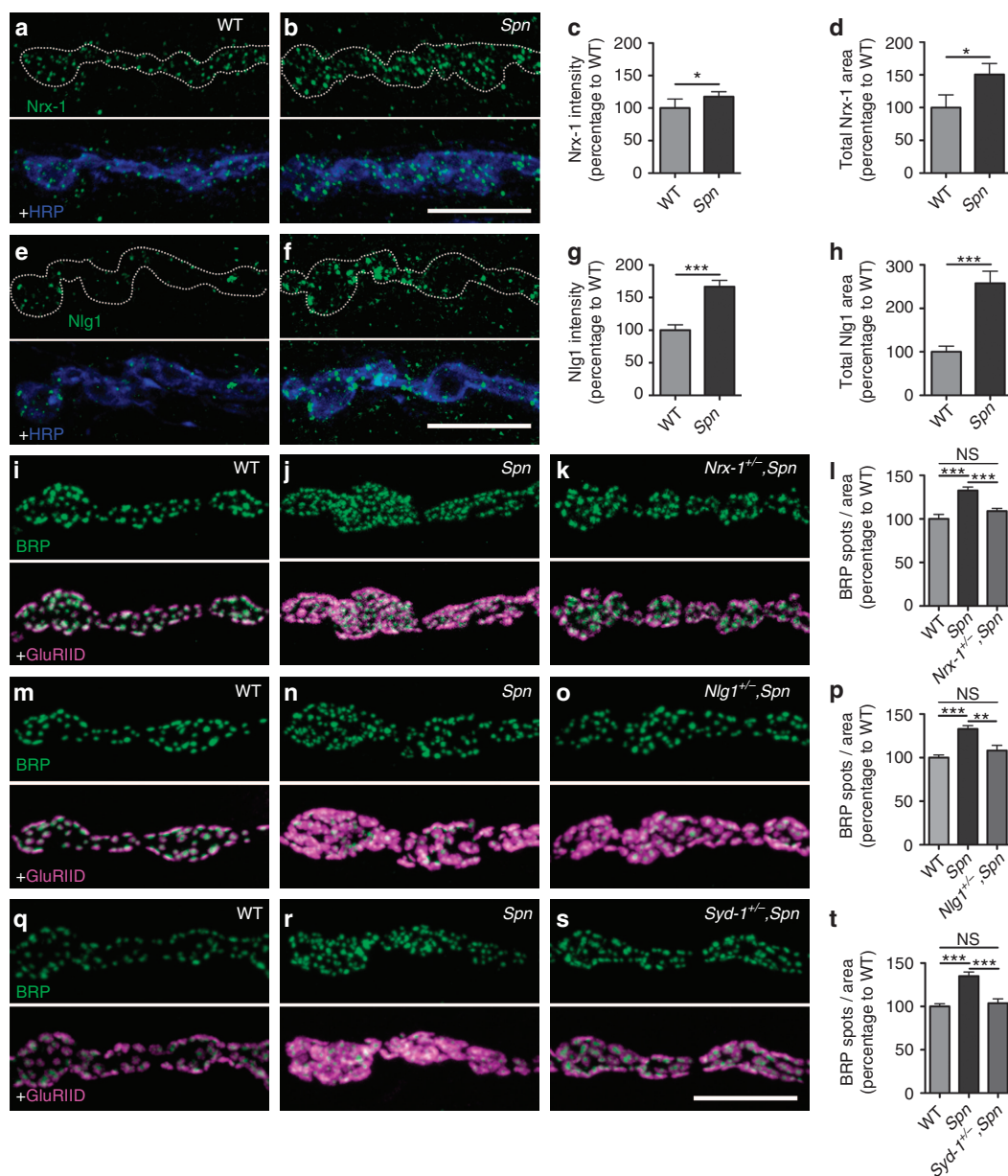


Figure 4 | *Spn* regulates trans-synaptic signalling. All mutant tests Mann-Whitney *U*-test, values are mean \pm s.e.m., NS, not significant; * $P \leq 0.05$; ** $P \leq 0.01$; *** $P \leq 0.001$. (a-d) Upregulation of Nr1 levels at *Spn* mutant NMJs. (a,b) Muscle 4 NMJs of wild-type and *Spn* larvae immunostained for Nr1. (c,d) Quantification of Nr1 signals. Total Nr1 covered area (a.u.): wild type 100 ± 19.63 , $n = 19$; *Spn* 150.7 ± 16.6 , $n = 19$; wild type versus *Spn* $P < 0.05$, ($U = 92$); Nr1 intensity (a.u.): wild type 100 ± 14.12 , $n = 19$; *Spn* 117.5 ± 7.6 , $n = 19$; wild type versus *Spn* $P < 0.05$, $U = 108$. (e-h) Upregulation of Nlg1 levels at *Spn* NMJs. (e,f) Wild type and *Spn* larvae immunostained for Nlg1. (g,h) Quantifications of Nlg1 signals. Total Nlg1 covered area (a.u.): wild type 100 ± 13.21 , $n = 19$; *Spn* 257 ± 27 , $n = 19$; wild type versus *Spn* $P < 0.001$, ($U = 42$). Nlg1 intensities (a.u.): wild type 100 ± 8.3 , $n = 19$; *Spn* 166.7 ± 9.8 , $n = 19$; wild type versus *Spn* $P < 0.001$, ($U = 33$). (i-t) Genetic interaction analysis of *Spn* phenotypes. (i-l) Genetic suppression of *Spn* phenotypes by Nr1. (i-k) NMJs immunostained for BRP^{Nc82} and GluRIID. (l) Quantification of BRP spot densities at NMJs. Wild type 100 ± 5 , $n = 11$; *Spn* 132.7 ± 3.8 , $n = 12$; *Nrx-1²⁴¹/+*, *Spn*: 108.9 ± 3.1 ; wild type versus *Spn* $P < 0.001$, ($U = 10$); wild type versus *Nrx-1²⁴¹/+*, *Spn* $P > 0.05$, ($U = 50$); *Spn* versus *Nrx-1²⁴¹/+*, *Spn* $P < 0.001$, ($U = 17$). (m-p) Genetic suppression of *Spn* phenotype by Nlg1; (p) Quantification of BRP spot densities. Wild type 100 ± 3.1 , $n = 10$; *Spn* 132.9 ± 3.7 , $n = 11$; *Nlg1^{2.3}/+*, *Spn* 108.1 ± 6 ; wild type versus *Spn* $P < 0.001$, ($U = 3$); wild type versus *Nlg1^{2.3}/+*, *Spn* $P > 0.05$, ($U = 37$); *Spn* versus *Nlg1^{2.3}/+*, *Spn* $P < 0.01$, ($U = 20$). (q-t) Genetic suppression by Syd-1. (t) wild type: 100 ± 3 , $n = 10$; *Spn*: 135.1 ± 4.6 , $n = 13$; *Syd-1^{3.4}/+*, *Spn*: 103.7 ± 5 ; wild type versus *Spn* $P < 0.001$; ($U = 4$). Wild type versus *Syd-1^{3.4}/+*, *Spn* $P > 0.05$; ($U = 57$). *Spn* versus *Syd-1^{3.4}/+*, *Spn* $P < 0.001$; ($U = 21$). Scale bars, 10 μ m.

We further investigated whether, as suggested by the Nr1 FRAP data, Syd-1 and *Spn* would operate in a competitive manner. Consequently, we revisited our previous finding that overexpression of Syd-1 within motoneurons results in

co-expressed Nr1^{GFP} being recruited into AZs¹³. However, when *Spn* was also co-overexpressed with Nr1^{GFP} and mStrawberrySyd-1, both the Nr1^{GFP} level and mStrawberrySyd-1 level at AZs dropped (Nr1^{GFP} intensity in wild-type background:

1.0 ± 0.06 , $n = 20$; $Nrx1^{GFP}$ intensity in the presence of overexpressed Spn: 0.8 ± 0.04 , $n = 19$; $P < 0.01$; Mann–Whitney t -test ($U = 113$). $mStraw^{Syd-1}$ intensity in wild-type background: 1.0 ± 0.04 , $n = 20$; $mStraw^{Syd-1}$ intensity in the presence of Spn: 0.76 ± 0.05 ; $P < 0.01$; Mann–Whitney t -test ($U = 75$). Thus, Spn gain-of-function might influence $Nrx-1$, antagonistic to the Spn loss-of-function phenotype (Fig. 4b; Supplementary Fig. 6a–g). In fact, AZ sizes on Spn overexpression were slightly (but significantly) increased over controls (Ctrl: 222 ± 3 , $n = 108$; GFP^{Spn} : 246 ± 4.5 , $n = 160$; ctrl versus GFP^{Spn} OE $P < 0.001$; Student's t -test).

The Spn-PDZ domain interacts with $Nrx-1$ C terminus. We performed immunoprecipitation experiments from *Drosophila*

head extracts²², using antibodies against $Nrx-1$ (refs 13,15), to test whether Spn and $Nrx-1$ might be part of a common complex. Western blot analysis with the anti-Spn antibody specifically detected bands in the range of ~ 200 kDa, validating the specificity of our custom-made anti-Spn antibodies (Fig. 5a; upper panel). Using $Nrx-1$ antibodies, which robustly immunoprecipitated $Nrx-1$ (Fig. 5a; middle panel), Spn could be co-immunoprecipitated, but was absent in negative controls which used an irrelevant IgG (Fig. 5a; lower panel). We performed a yeast two-hybrid (Y2H) analysis using a C-terminal fragment of $Nrx-1$ to screen against different fragments of Spn to investigate a direct $Nrx-1$ /Spn interaction (Fig. 5b,c). As a control, we included a Syd-1 fragment, which we had previously shown to interact with $Nrx-1$ (ref. 13). Semiquantitative Y2H analysis uncovered a strong and specific interaction between the cytosolic part of $Nrx-1$

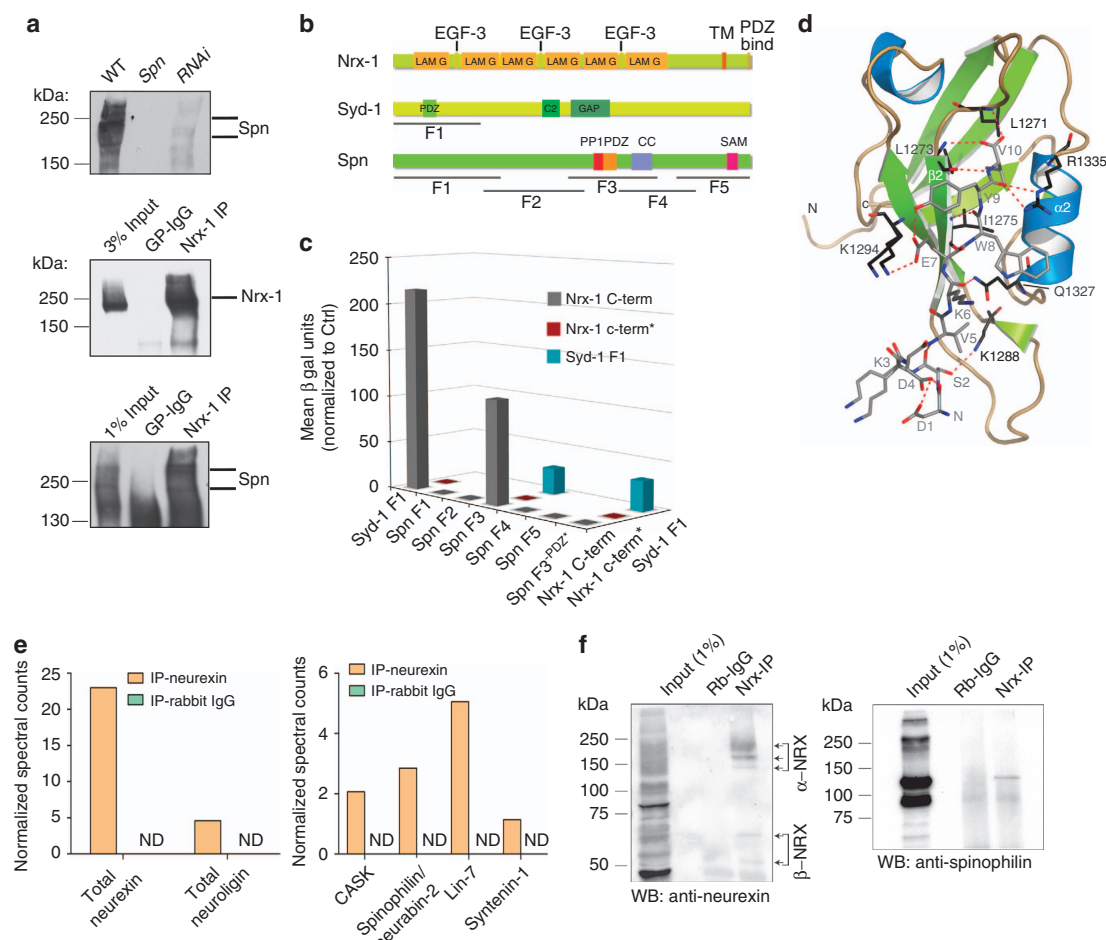


Figure 5 | Spn interacts directly with the $Nrx-1$ C-term. (a) Western blot analysis of larval head extracts from wild type, Spn and pan-neuronal $elav(x)-c155-gal4$ driven Spn -RNAi show the specificity of our custom anti- Spn^{Nterm} antibody. Immunoblot of $Nrx-1$ immunoprecipitate (IP) from *Drosophila* head fractionation enriched for AZ proteins (Methods). Spn can be detected using a $Nrx-1$ Co-immunoprecipitation (co-IP), but is absent when a control immunoglobulin G is used (IgG). (b) Domain structures of $Nrx-1$, $Syd-1$ and Spn . $Nrx-1$ possesses extracellular laminin G (LAM G) and epidermal growth factor (EGF)-3 domains, as well as a PDZ binding motif at the C terminus. $Syd-1$ comprises an N-terminally located PDZ domain, a C2 domain and a putative RhoGAP domain. Spn domain structure and the boundaries of fragments used in Y2H experiments (F1–F5) (Supplementary Fig. 7). (c) Quantitative liquid Y2H assay for binding of individual Spn fragments (and $Syd-1$ F1) with the $Nrx-1$ C terminus. Fragment 3, containing the PDZ domain, binds strongly to the $Nrx-1$ C-term. Binding is fully abolished when a point mutation is introduced into the ligand-binding site of the Spn -PDZ domain, or when the last five amino acid residues of the $Nrx-1$ C-term ($Nrx-1$ c-term*) are deleted. (d) A structural representation of the Spn -PDZ interacting with the $Nrx-1$ C-term peptide. The C-terminal Nrx peptide is shown in grey using a stick representation. Residues on Spn -PDZ that interact with the Nrx peptide are highlighted in black. Red dashed lines indicate potential hydrogen bonds with a distance cut-off of $\leq 3.3 \text{ \AA}$. (e) Mass-spectrometric analysis of protein complexes immunoprecipitated from mouse whole brain homogenate using $Nrx-1$ antibody. (f) Western blot analysis showing the Nrx antibody effectively co-IPs Spn (see Supplementary Fig. 12).

(hereafter termed Nr_x-1 C-term) and a 500 amino acid region of Spn containing the PDZ domain (Spn-F3) (Spn-F3 × Nr_x-1 C-term in Fig. 5c). The fact that the overlapping constructs F2 and F4 (Fig. 5b) did not show any interaction narrowed down the possible interacting stretch to a region comprising only the PP1 and the PDZ domains. These domains are present in all Spn family members and are highly conserved between fly, worm and rodent (Supplementary Fig. 8a). The Nr_x-1 C-term/Spn-F3 interaction was eliminated after deleting the last five amino acids of the Nr_x-1 C terminus. In addition, introduction of a point mutation³⁸ in the Spn-PDZ domain (in the ligand-binding pocket) which abolishes ligand binding, also abolished the interaction (Fig. 5c). Thus, the very C-terminal PDZ-binding motif of Nr_x-1 interacts directly with PDZ domains found in both Spn and Syd-1. To characterize the binding of Nr_x-1 C-term to the Spn-PDZ domain at atomic resolution, we turned to X-ray crystallography. We solved the structure of PDZ domain containing residues 1,258–1,347 of Spn in complex with the last 10 C-terminal residues of Nr_x-1 (at 1.2 Å resolution) (Fig. 5d; Supplementary Fig. 8; Supplementary Table 1). The Spn-PDZ domain shares the characteristic canonical fold of PDZ domains, which is composed of six β-strands and two α-helices³⁹. According to its specificity for C-terminal peptides, Spn-PDZ is a class II PDZ domain, recognizing the signature motif X-Ψ-X-Ψ (X, unspecified; and Ψ, hydrophobic amino acid residue). We found the peptide-binding groove to be flanked by a β-strand (β2) and an α-helix (α2). The Nr_x-1 peptide binds in an anti-parallel mode, with main chain/main chain hydrogen bonding to β2 of the Spn-PDZ. The carboxylate of the Nr_x-1 peptide is hydrogen bonded to backbone amides of L1271 and L1273 in Spn-PDZ (Fig. 5d; Supplementary Table 2). Further interactions are established with the side chains of Spn-PDZ residues residing on β4 and α2 (Fig. 5d). In addition, we observed an inter-peptide interaction that might be important for stabilizing the peptide conformation. We investigated the binding thermodynamics of the Nr_x-1 C-term peptide to the PDZ domains of Spn or Syd-1 using isothermal calorimetry (ITC). The Syd-1-PDZ domain showed higher affinity binding (K_d 5 μM) than the Spn-PDZ domain (50 μM) (Supplementary Fig. 8e,f). Both Spn-PDZ domains and Nr_x-1 C-termini are highly conserved between *Drosophila* and rodents (Supplementary Fig. 8a,c). In fact, an *in vitro* pull-down experiment effectively precipitated both the *Drosophila* Spn-PDZ and rat Spn-PDZ using the respective Nr_x-1 peptides (Supplementary Fig. 9a). To validate an *in vivo* interaction between Spn and Nr_xs in rodents, we performed co-immunoprecipitation experiments from mouse whole brain lysates using a newly generated affinity-purified pan-Nr_x antibody (Supplementary Fig. 9b). We analysed the co-immunoprecipitated proteins by mass spectrometry. Nlg, Spn and several additional synaptic PDZ-domain-containing proteins known to interact with Nr_xs could be detected in the Nr_x immunoprecipitates, but not in precipitations with control IgGs (Fig. 5e). The presence of Spn/Nr_x complexes was further confirmed by western blotting of the precipitates (Fig. 5f). Thus, we find that Spn/Nr_x interactions show evolutionary conservation fully consistent with their shared sequence conservation.

PDZ domain ligand binding of Spn controls AZ structure and function. If binding of the Spn-PDZ domain to Nr_x-1 was, in fact, functionally relevant, introducing the point mutation^{13,38} that interferes with Nr_x-1 binding *in vitro* should compromise Spn function *in vivo*. Indeed, expression of the Spn cDNA containing the relevant point mutation (PDZ*Spn) no longer rescued the structural presynaptic AZ phenotype of *Spn* mutants.

As expected, expression of wild-type cDNA (WTSpn; Fig. 2c) rescued the phenotype (Fig. 6a–e). Thus, interfering with ligand binding to the Spn-PDZ domain renders the protein incapable of limiting AZ numbers.

Finally, we investigated the physiological consequences of presynaptic Spn loss. We performed two-electrode voltage-clamp recordings (TEVC) to assay SV release. We observed a clear increase in the frequency of spontaneous SV release from *Spn* terminals, which dropped to normal rates when normal (WTSpn) was re-expressed in the presynaptic motoneuron (Fig. 6f,i). However, on expression of PDZ*Spn under identical conditions, the frequencies of spontaneous release events remained high (Fig. 6f,i). The amplitudes of single spontaneous release events were significantly larger at *Spn* terminals (Fig. 6j), potentially reflecting the larger postsynaptic GluRIIA receptor fields described above (Fig. 2b; Supplementary Fig. 5; Fig. 3i–l). In contrast, release evoked by single action potentials was clearly decreased at *Spn* NMJs (Fig. 6g,k). Loss of Spn also altered synaptic short-term plasticity, in response to stimulation with a pair of action potentials (at 10- or 30-ms intervals). Here *Spn* NMJs displayed abnormal facilitation (Fig. 6h,m,n). Both defects were rescued by the presynaptic expression of WTSpn, while expression of the PDZ*Spn again did not rescue. Altogether, these results suggest that Spn is not only responsible for the functional distribution of presynaptic AZ scaffolds but also plays an important role in SV release, and that the reduced evoked responses were not due to decreased postsynaptic sensitivity. In addition, a higher number of presynaptic AZs, as observed in *Spn* terminals, is in line with an increased number of spontaneous release events detected. However, the fact that evoked release is lowered is unexpected, raising the question of whether the additional AZs observed in *Spn* are sub-optimal for evoked release, but can maintain spontaneous release. To answer this question, we went on to investigate the function of Spn at the single AZ level.

Spinophilin optimizes evoked release at single synapses. The TEVC recordings sample release events over the whole NMJ of the respective muscle, but do not allow for the analysis of individual AZs. To investigate the latter, we used a recently developed assay employing post-synaptically expressed GCaMP to characterize the spatial and temporal dynamics of exocytotic events^{2,3,40}. We imaged GCaMP responses to spontaneous exocytosis for 100 s (see Supplementary Movies 1 and 2 for examples) and, subsequently GCaMP response to action potential stimulation (35 action potentials given at 0.2 Hz, see Supplementary Movies 3 and 4 for examples). After recordings, larvae were fixed, stained against BRP and visualized using confocal microscopy. Alignment of these confocal images to the live movies (Supplementary Fig. 10; see methods for further details) allowed us to map activity at individual AZs (Fig. 7). Strikingly, spontaneous activity per AZ was not changed at *Spn* NMJs, suggesting that the net increase of spontaneous events observed in TEVC experiments is, indeed, due to an increase in synapse number rather than in their individual release rates (Fig. 7a,c). By contrast, the probability of evoked exocytosis was drastically reduced (Fig. 7b,d). However, the individual evoked GCaMP signals were indistinguishable between *Spn* and control NMJs (Fig. 7d). Consistent with our TEVC results, we found that loss of Spn changed the partitioning of AZs between these two discrete release modes: the fraction of AZs dedicated to evoked release was significantly reduced in *Spn* (Fig. 7e). Therefore, we conclude that even though *Spn*-deficient synapses participate in both modes of SV release, Spn is essential for establishing correct synaptic release probability, in agreement with the altered short-term plasticity we observed in our TEVC experiments (Fig. 6k–n).

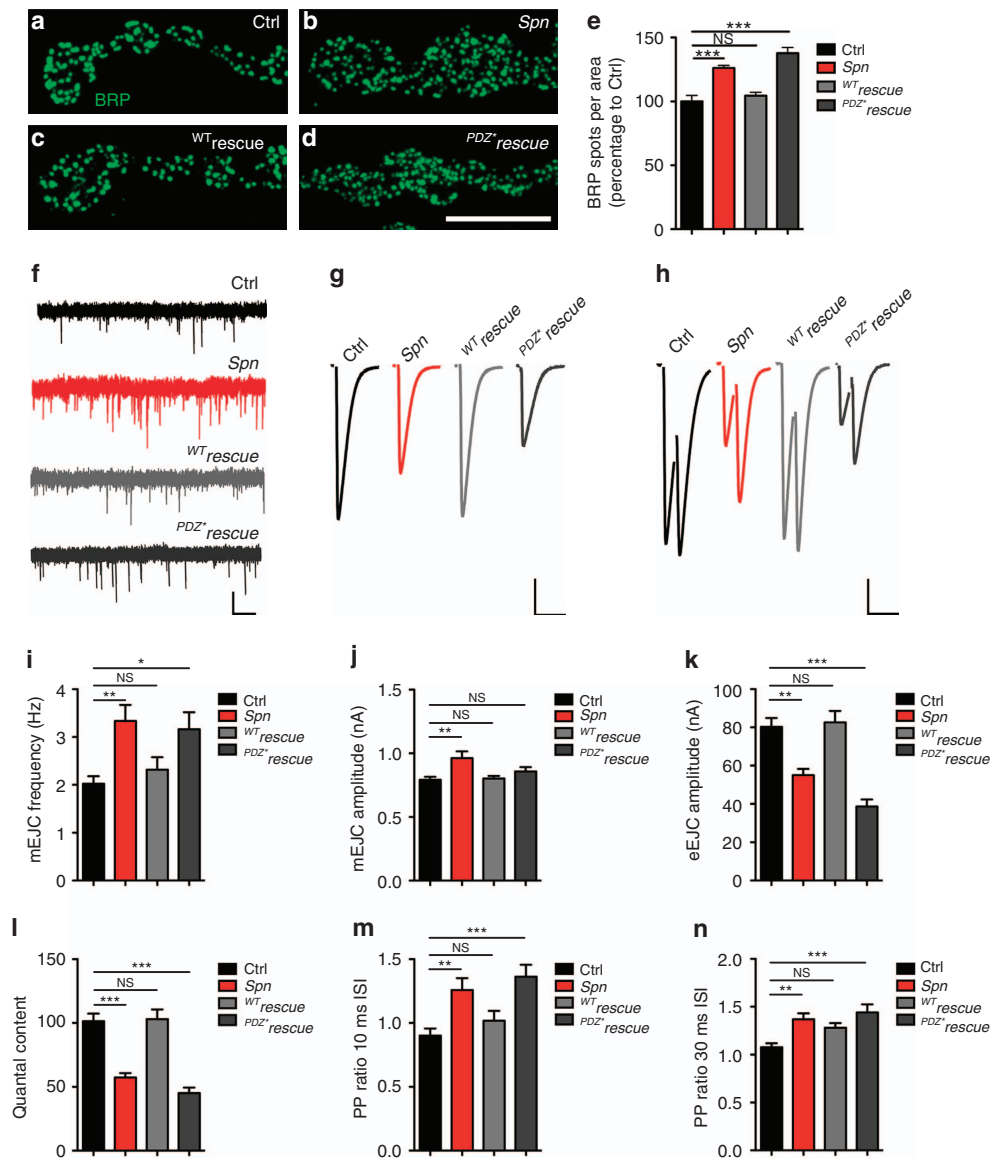


Figure 6 | Electrophysiological characterization of *Spn* NMJs. (a-d) BRP^{Nc82} labelling in indicated genotypes. (e) Quantification of BRP spot densities in a-d. Ctrl: 100 ± 4.6, n = 6; *Spn*: 126.1 ± 2.08, n = 8; ^{WT}rescue: 104.5 ± 2.6, n = 8; ^{PDZ}rescue: 137.8 ± 4.45, n = 7. Ctrl versus *Spn* P < 0.001, (U = 2). *Spn* versus ^{WT}rescue P < 0.001, (U = 0.0). ^{WT}rescue versus ^{PDZ}rescue P < 0.001, (U = 0). (f) Representative mEJCs traces. (g) Representative eEJCs traces. (h) Paired-pulse measurements with inter stimulus interval (ISI) of 10 ms; (i) Quantification of mEJC frequencies (Ctrl: 2.02 ± 0.16, n = 28; *Spn*: 3.33 ± 0.34, n = 15, P < 0.01; ^{WT}rescue: 2.32 ± 0.26, n = 16, P > 0.05; ^{PDZ}rescue: 3.16 ± 0.36, n = 16, P < 0.05. (j) Quantification of mEJC amplitudes (Ctrl: -0.78 ± 0.03 nA, n = 28; *Spn*: -0.96 ± 0.05 nA, n = 15, P < 0.01; ^{WT}rescue: -0.80 ± 0.02 nA, n = 16, P > 0.05; ^{PDZ}rescue: -0.86 ± 0.03 nA, n = 15, P > 0.05). (k) Quantification of eEJC amplitudes (Ctrl: -80.23 ± 4.66 nA, n = 28; *Spn*: -55.00 ± 3.29 nA, n = 24, P < 0.01; ^{WT}rescue: -82.58 ± 6.0 nA, n = 18, P > 0.05; ^{PDZ}rescue: -38.66 ± 3.67, n = 18, P < 0.01). (l) Quantification of quantal content (Ctrl: 101.4 ± 5.89, n = 28; *Spn*: 57.20 ± 3.42, n = 24, P < 0.001; ^{WT}rescue: 103.0 ± 7.53, n = 18, P > 0.05; ^{PDZ}rescue: 45.13 ± 4.29, n = 18, P < 0.001). (m) Quantification of the pair pulse ratio with an ISI of 10 ms. (Ctrl: 0.90 ± 0.05, n = 28; *Spn*: 1.26 ± 0.09, n = 22; P < 0.01; ^{WT}rescue: 1.01 ± 0.08, n = 18, P > 0.05; ^{PDZ}rescue: 1.36 ± 0.05, n = 18, P < 0.001). (n) Quantification of the paired-pulse ratio with a 30 ms ISI (Ctrl: 1.08 ± 0.04, n = 28; *Spn*: 1.37 ± 0.06, n = 21, P < 0.01; ^{WT}rescue: 1.28 ± 0.05, n = 18, P > 0.05; ^{PDZ}rescue: 1.44 ± 0.08, n = 17, P < 0.001). Statistics: one-way analysis of variance with Tukey's multiple comparison post test. All panels show mean ± s.e.m., NS, not significant; *P ≤ 0.05; **P ≤ 0.01; ***P ≤ 0.001. Scale bars: a-d, 10 μm; f, 1 nA/1s; g,h, 20 nA/20 ms.

It was found recently that release probability at individual AZs correlated with the local levels of BRP^{2,40} which, as mentioned above, is reduced at *Spn* synapses (Fig. 3). Is the decrease in release probability at *Spn* synapses due to a reduction in their BRP levels? To address this question, we investigated the relationship between synaptic BRP and the number of release

events evoked at single AZs². We found that release probability was indeed positively correlated with BRP levels (Fig. 7f). Furthermore, the average number of release events evoked at *Spn* synapses also (but somewhat weaker) correlated with BRP level. However, as this relationship differed from that observed in control animals we can rule out the possibility

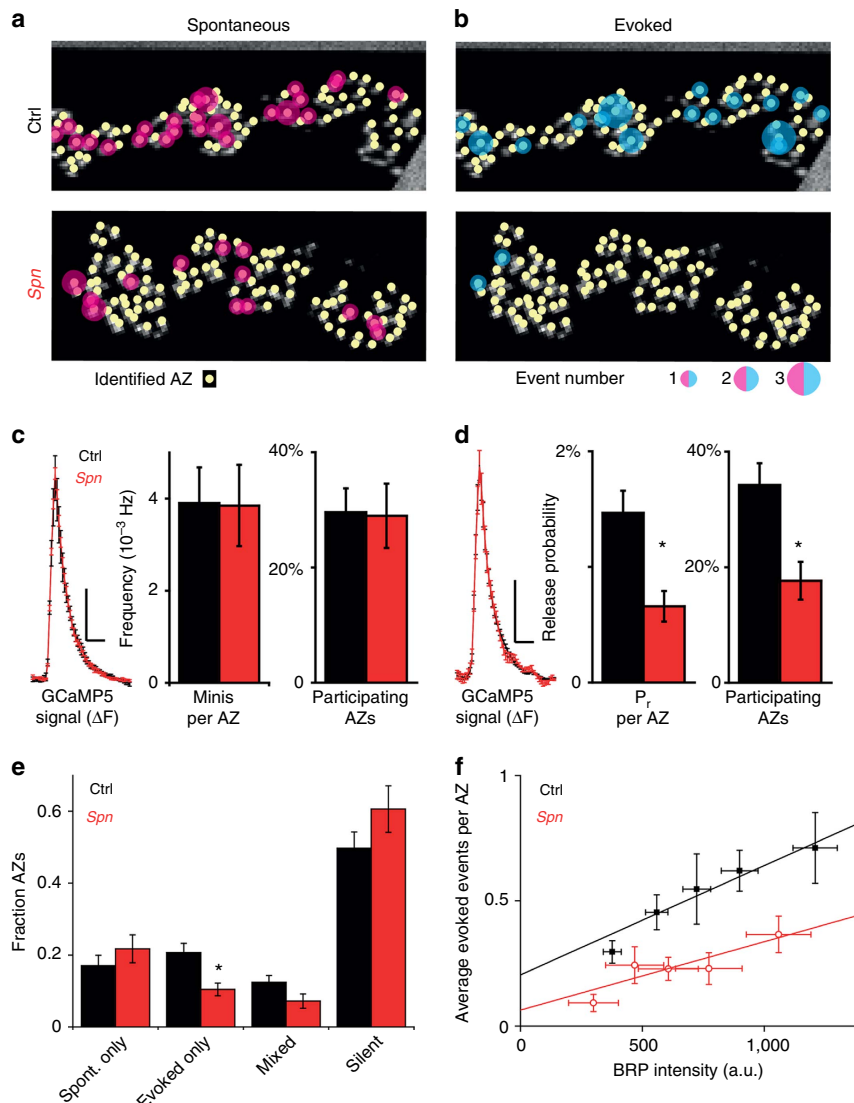


Figure 7 | Individual *Spn*AZs show normal spontaneous release, but lower probabilities for action potential-induced (evoked) release. (a,b) Synaptic activity at control and *Spn* NMJs was first imaged for 100 s without stimulation. Subsequently, exocytosis was stimulated by 35 action potentials at 0.2 Hz. Images are montages of NMJ confocal scans showing staining for BRP^{Nc82}. Spontaneous and evoked activities indicated by magenta and cyan circles, sizes reflect the number of events per AZ. (c) Local average postsynaptic GCaMP5 signals at *Spn* and control AZs in response to spontaneous release events (left traces). Frequencies of spontaneous ('mini') events per AZ in *Spn* and controls very similar (centre bar graph), as is the fraction of AZs participating at least once in spontaneous activity (right bar graph). (d) Evoked release causes similar postsynaptic GCaMP5 signals at individual *Spn* and control AZs (left traces). The probability that an AZ shows release in response to a single action potential (p_r) significantly reduced in *Spn* compared with controls (centre bar graph). The fraction of AZs responding at least once to stimulation also significantly reduced in *Spn* mutants AZs (right bar graph). (e) Categorization of AZs based on their activity pattern: (1) AZs exclusively active during spontaneous release (spont. only), (2) AZs exclusively responsive to AP-stimulation (evoked only), (3) AZs releasing both modes at least once (mixed) or (4) AZs not responding (silent). The fraction of 'evoked only' AZs was significantly reduced at *Spn* NMJs. (f) Reduced p_r at *Spn* AZs is not secondary to lower BRP levels. AZs were binned with regard to their local BRP intensity and the average number of evoked events was plotted against the average BRP intensities (Supplementary Information File). Evoked events per AZ were correlated to local BRP levels in controls (black data points: experimental data, black line: linear fit, reduced $r^2 = 0.92$) and, to a lesser extent, at *Spn* AZs (red data points: experimental data, red line: linear fit, reduced $r^2 = 0.69$). Loss of *Spn* reduced evoked release more than expected by a mere reduction of BRP and both dependencies were best fit by different lines (F-test, $P < 0.05$). Values are mean \pm s.e.m. Vertical/horizontal scale bars in c,d: 100 a.u./200 ms. Number of animals (n): Control: $n = 5$, *Spn*: $n = 4$. * $P < 0.05$ in Mann-Whitney U -test.

that the effect is mediated solely through BRP reduction. Thus, we conclude that *Spn* is not only important for controlling synapse number and size, but also for optimizing action-potential-induced exocytosis by enhancing release probability at individual AZs.

Discussion

The trans-synaptic dialogue between *Nrx-1* and *Nlg1* aids in the initial assembly, specification and maturation of synapses, and is a key component in the modification of neuronal networks^{12,41,42}. Regulatory factors and processes that fine-tune

and coordinate *Nrx-1/Nlg1* signalling during synapse assembly process are currently under investigation. Our data indicate that *Drosophila* Spn-like protein acts presynaptically to attenuate *Nrx-1/Nlg1* signalling and protects from excessive seeding of new AZ scaffolds at the NMJ. In *Spn* mutants, excessive AZs suffered from insufficient evoked release, which may be partly explained by their reduced size, and partly by a genuine functional role of Spn (potentially mediated via *Nrx-1* binding).

In mice, loss of Spn (Neurabin II), one of the two Neurabin protein families present in mammals, was reported to provoke a developmental increase in synapse numbers⁴³. While Spinophilin was found to be expressed both pre- and post-synaptically^{26,27}, its function, so far, has only been analysed in the context of postsynaptic spines^{43–46}. Given the conserved Spn/*Nrx-1* interaction we report (Fig. 5), Spn family proteins might execute a generic function in controlling *Nrx-1/Nlg1*-dependent signalling during synapse assembly. We consistently find that Spn counteracts another multi-domain synaptic regulator, Syd-1, in the control of *Nrx-1/Nlg1* signalling. Previous genetic work in *C. elegans* identified roles of Syd-1 epistatic to Syd-2/*Liprin- α* in synaptogenesis^{5,47}. Syd-1 also operates epistatic to Syd-2/*Liprin- α* at *Drosophila* NMJs^{17,48}. Syd-1 immobilizes *Nrx-1* (ref. 13), positioning *Nlg1* at juxtaposed postsynaptic sites, where it is needed for efficient incorporation of GluR complexes. Intravital imaging suggested an early checkpoint for synapse assembly, involving Syd-1, *Nrx-1/Nlg1* signalling and oligomerization of *Liprin- α* in the formation of an early nucleation lattice^{49,50}, which is followed later by ELKS/BRP-dependent scaffolding events^{21,51} (our model in Fig. 8, upper panel). As Spn promotes the diffusional motility of *Nrx-1* over the terminal surface and limits *Nrx-1/Nlg1* signalling, and as its phenotype is reversed by loss of a single gene copy of *nrx-1*, *nlg1* or *syd-1*, Spn displays all the features of a ‘negative’ element mounting, which effectively sets the threshold for AZ assembly. As suggested by our FRAP experiments (Supplementary Fig. 6), Spn might withdraw a population of *Nrx-1* from the early assembly process, establishing an assembly threshold that ensures a ‘typical’ AZ design and

associated postsynaptic compartments (Fig. 8). As a negative regulatory element, Spn might allow tuning of presynaptic AZ scaffold size and function (see below).

The *C. elegans* Spn homologue NAB-1 (*NeurABin1*) was previously shown to bind Syd-1 in cell culture recruitment assays⁵². We found consistent evidence for Syd-1/*Nrx-1*/Spn tripartite complexes in salivary gland experiments (Supplementary Fig. 11). Moreover, the PDZ domain containing regions of Spn and Syd-1 interacted in Y2H experiments (Fig. 5c). It would be interesting to dissect whether the interaction of Spn/Syd-1 plays a role in controlling the access of *Nrx-1* to one or both factors. For *C. elegans* HSN synapses, a previous study⁵² showed that loss of NAB-1 results in a deficit of synaptic markers, such as Syd-1 and Syd-2/*Liprin- α* , while NAB-1 binding to F-actin was also found to be important for synapse assembly. Though at first glance rather contradictory to the results we describe in this study, differences might result from Chia *et al.* studying synapse assembly executed over a short time window, when partner cells meet for the first time⁵². In contrast, we used a model (*Drosophila* larval NMJs) where an already functional neuronal terminal adds novel AZs^{17,21}. Despite our efforts, we were unable to demonstrate a role of F-actin in the assembly of AZs of late larval *Drosophila* NMJs. F-actin patches might be particularly important to establish the first synaptic contacts between partner cells. Both the study by Chia *et al.* and this study, however, point clearly towards important regulatory roles of Spn family members in the presynaptic control of synapse assembly.

Further, we describe a novel interaction between the Spn-PDZ domain and the intracellular C-term of *Nrx-1* at the atomic level. Interestingly, we found that all functions of Spn reported in this study, structural as well as functional, were strictly dependent on the ligand-binding integrity of this PDZ domain. It is noteworthy that the Spn-PDZ domain binds other ligands as well, for example, Kalirin-7 and p70^{S6K} (refs 53–55), and further elucidation of its role as a signal ‘integrator’ in synapse plasticity should be interesting. The fact that *Nrx-1* levels were increased at *Spn* NMJs and, most importantly, that genetic removal of a single

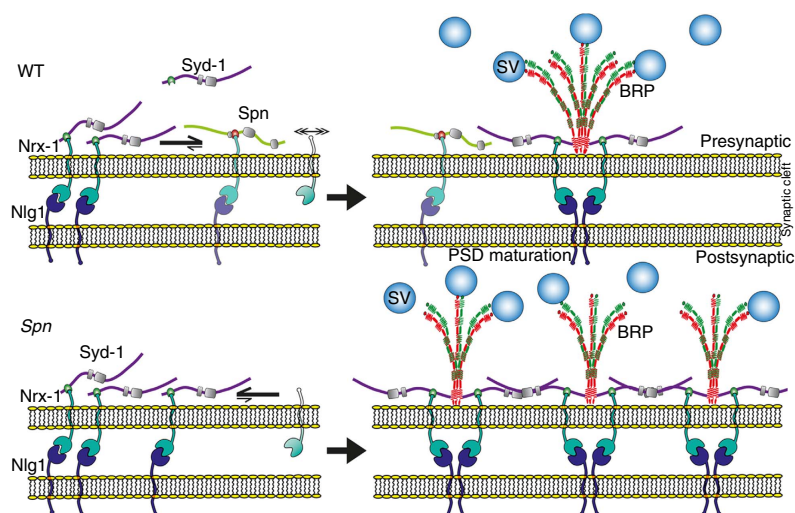


Figure 8 | Model describing the role of Spn in controlling the synaptogenic activity of *Nrx-1* at *Drosophila* NMJs. Spn acts antagonistically to Syd-1. In wild-type animals (upper panel), *Nrx-1* interacts with postsynaptic *Nlg1*, as well as with either Syd-1 or Spn via PDZ domain-mediated interactions. In this way, trans-synaptic contact with *Nlg1* can also steer postsynaptic assembly. The presence of Spn reduces the amount of *Nrx-1* available for Syd-1 binding and, consequently, controls the number of AZs, by keeping the availability of critical proteins (BRP) below an assembly threshold. In addition, *Nlg1*-mediated postsynaptic assembly is also affected (not shown). In the absence of Spn (lower panel), *Nrx-1* is less mobile and more efficiently recruited into complexes by Syd-1, resulting in the formation of excessive presynaptic AZ scaffolds.

nrx-1 gene copy effectively suppressed the *Spn* AZ phenotype, indicates an important role of the *Spn*/*Nrx-1* interaction in this context. Affinity of *Spn*-PDZ of the *Nrx-1* C-term was somewhat lower than that of the *Syd-1*-PDZ, both in ITC and Y2H experiments (Fig. 5c). Nonetheless, overexpression of *Spn* was successful in reducing the targeting effect of *Syd-1* on overexpressed *Nrx-1*^{GFP} (see above). It will be interesting to see whether this interaction can be differentially regulated, for example, by (de)phosphorylation.

It is worth noting that apart from *Syd-1* and *Spn*, several other proteins containing PDZ domains, including CASK, Mint1/X11, CIPP and Syntenin^{13,36,56–59}, were found to bind to the *Nrxs* C-termini (also see Fig. 5e,f). CASK was previously shown to interact genetically with *Nrx-1*, controlling endocytic function at *Drosophila* NMJs³⁶. However, when we tested for an influence of CASK on *Nrx-1*^{GFP} motility using FRAP, genetic ablation of CASK had no effect (Supplementary Fig. 6). Thus, CASK function seemingly resembles neither *Syd-1* nor *Spn*. Clearly, future work will have to address and integrate the role of other synaptic regulators converging on the *Nrx-1* C-term. In particular, CASK (which displays a kinase function that phosphorylates certain motifs within the *Nrx-1* C-term) might alternately control *Spn*- and *Syd-1*-dependent functions³⁷. Presynaptic *Nrx-1*, through binding to postsynaptic *Nlg1* at developing *Drosophila* NMJ terminals, is important for the proper assembly of new synaptic sites^{11,13,15,36}. It is of note, however, that while mammalian *Nrxs* display robust synaptogenetic activity in cellular *in vitro* systems, direct genetic evidence for synaptogenetic activity of *Nrxs* in the mammalian CNS remained rather scarce. Triple knockout mice lacking all α -*Nrxs* display no gross synaptic defects at the ultrastructural level^{60,61}. Future analysis will have to investigate whether differences here might be explained by specific compensation mechanisms in mammals; for example, by β -*Nrxs*, or other parallel trans-synaptic communication modules. Genuine functional deficits in neurotransmitter release were also observed after the elimination of presynaptic *Spn*. Elimination of ligand binding to the PDZ domain rendered the protein completely nonfunctional, without affecting its synaptic targeting. Thus, the *Spn* functional defects are likely to be mediated via a lack of *Nrx-1* binding. Notably, ample evidence connects *Nrx-1* function with both the functional and structural maturation of *Drosophila* presynaptic AZs^{8,16,41,62,63}. Our work now promotes the possibility that binding of *Spn* to *Nrx-1* is important for establishing correct release probability, independent of absolute AZ scaffold size (Fig. 7). It is noteworthy that *Nrx-1* function was previously shown to be important for proper Ca²⁺ channel function and, as a result, properly evoked SV release⁶⁰. Thus, it will be interesting to investigate whether the specific functional contributions of *Spn* are mediated via deficits in the AZ organization of voltage-gated Ca²⁺ channels or Ca²⁺ sensors, such as synaptotagmin^{64–66}. Taken together, we found an unexpected function for *Spn* in addition of AZs at *Drosophila* glutamatergic terminals, through the integration of signals from both the pre- and postsynaptic compartment. Given that we find the *Spn*/*Nrx-1* interaction to be conserved from *Drosophila* to rodents, addressing similar roles of presynaptic *Spn* in mammalian brain physiology and pathophysiology might be informative.

Methods

Genetics and molecular cloning. Fly strains were reared under standard laboratory conditions⁶⁷. Both male and female larvae were used for analysis in all experiments (except electrophysiological recordings, see below). The structure of the *spn*^{A3.1} allele eliminating the complete *Spn* locus, CG16758 (and partially deleting the CG45186 loci) was validated by genomic PCR²³. The combination of *spn*^{A3.1} in trans with the deficiency chromosome *dfBSc116* (*Spn* deficiency; *Df*) resulted in animals deficient in the *Spn* locus. Lethality in *Spn* was completely

rescued by returning one copy of the genomic region of *Spn* in this mutant background. It is of note that another mutant allele of *Spn* was reported previously and was shown to be 'semi-lethal'⁶⁸; however, no functional analysis was performed in this study. *w¹¹¹⁸* served as a genetic background for all experiments. Recombinations were verified using PCR or complementation analysis. The following recombination lines were used: for *Syd-1* (*dsyd-1^{ex3.4}/+*, *spn*^{A3.1}/*SpnDf*), *Nrx-1* (*Nrx-1²⁴¹/+*, *spn*^{A3.1}/*SpnDf*) and *Nlg1* (*Nlg1^{ex2.3}/+*, *spn*^{A3.1}/*SpnDf*). Flies carrying UAS-green fluorescent protein (GFP)-tagged *Nrx-1* (ref. 15), UAS-GFP or mStraw-tagged *Syd-1* were described previously¹³. UAS-untagged or GFP-tagged *Spn* were obtained by recombining pUAS-attb-rfa and pUAS-attb-GFP-rfa with pENTR-*Spn* FL, respectively. The full-length *Spn* cDNA was cloned into pENTR from BDGP clone LD45234, via *Spe*I and *Kpn*I restriction sites, using primers 5'-ATGGATAGCGAAAAGGTGGCCAAAC-3' and 5'-CTTCTTTTGGCCGCTTCTCTC-3'.

A rabbit polyclonal antibody was raised against a 6 × His-tagged fusion protein of *Spn* N-term region (Fig. 1a, green bar). The corresponding expression construct was cloned after PCR with 5'-CACCAGCGTTCTCATCCAGTC-3' and 5'-TTACACAATGTCCACGGCTTCA-3' primers, and TOPO cloned into pENTR D-TOPO.

The point-mutated PDZ domain of *Spn* cDNA (^{PDZ'}*Spn* cDNA) was constructed by circular PCR using primers: 5'-GTGGAATTGATGGCGGGTCC TGAGGGTGGCGGTCTCAGTATAATTG-3' and 5'-CAATTATACTGAGACCC GCACC CTCAGGACCCGCCATCAA TTCCAC-3'.

Clonings for crystal trials, ITC and GST pull-down assays. The constructs comprising the PDZ domains of *dmSpn* (residue 1,258–1,347), *dmSyd-1* (residue 155–242) and *mSpn* (residue 493–583) were amplified by PCR and cloned into the pET-MBP vector using *Nco*I and *Sal*I restriction sites with primers: *dmSpn*_fwd: 5'-TATACCATGGCGCATGTCTTCCCCGTGG-3', *dmSpn*_rev: 5'-TATA CCATGGTGGCGCTTCGG-3', *dmSyd-1*_fwd: 5'-TATACCATGGCGCAGGCGGTCTG ATGC-3', *dmSyd-1*_rev: 5'-TATACCATGGCGCACCGTTCAACTGTTCG-3', *mSpn*_fwd: 5'-TATACCATGGAGCTGTTTCTGTGGAG-3' and *mSpn*_rev: 5'-ATATGTGCGACCTACTCCCGCCAATCATC-3'.

The resulting constructs contained an N-terminal His6-MBP-tag followed by a tobacco etch virus cleavage site and the respective PDZ domain. The constructs comprising the last 10 C-terminal amino acids of *dmNrx-1* (residue 1,831–1,840) and *mNrx-1* (residue 1,498–1,507) were amplified by PCR and cloned into the pGEX-6-P1 vector by a SLIC reaction using overlapping primers: *dmNrx-1*_ct_fwd: 5'-GACTCCAAGGACGTCAAGGAGTGGTATG TGTAATGACGATCTGCG CTGC-3', *dmNrx-1*_ct_rev: 5'-TTACACATACCCTCTTGCAGTC CTGG AGTC GTCACGATGCGGCC-3', *mNrx-1*_ct_fwd: 5'-AAGAAGAACAAGACAA AGAGTATTACGTCTAGCTG ACGATCTGCGCTCG-3', *mNrx-1*_ct_rev: 5'-CTAG ACGTAATACCTTTGTCTTTGTCTTCTTGTGCAC GA TGCGGCC-3'.

The resulting constructs comprised an N-terminal GST-tag followed by a PreScission cleavage site and the respective 10 C-terminal amino acids of *Nrx-1*. Detailed version of methods for Protein expression and purification, ITC assays and crystallization are presented in Supplementary Methods.

Generation of *Spn* genomic constructs. *Pac* (*Spn*¹) was created from P[acman] BAC clone CH321-01N11 (genomic region 2499270 to 2581398; CHORI-321 library of the BACPAC Resource Centre), which was subjected to transgenesis using the Phi31 system (P[acman] strain 24872, M[vas-int.Dm]ZH-2A, PBac[y+]-attP-3B[VK00037]). Similarly, *Pac*(*Spn*²) was obtained by injecting the P[acman] BAC clone CH321-67O06 (genomic region 2469714 to 2556468). *Pac*(*Spn*^{*}) corresponds to P[acman] BAC clone CH321-67O06, but lacks the whole *Spn* open reading frame, and was cloned according to the Counter Selection BAC Modification kit obtained from Gene Bridges GmbH. rpsL-neomycin (neo) template DNA was used to generate selectable cassettes. Primers contained a 50-bp homology region and a sequence for amplification of the rpsL-neo counter selection cassette. Selectable cassettes were generated by PCR using Vent Polymerase (New England Biolabs, Inc.) and the following primer pairs. *Spn*-rpsL-fwd: 5'-GGCCCCAATTCAAGCTAAACGGACGCGTTTTCTGTCGCGAGTTTA ACC CGCGCTGGTATGATGGCGGGATCG-3', *Spn*-rpsL-rev: 5'-ATTTCAG AGTATATTTATTAGCACTGATTTTGTGAGATTTATT ATTTCCATTCAGAAG AACTCGTCAAGAAGGCG-3'.

Yeast-2-hybrid clones. Yeast-2-hybrid analysis was carried out using the LexA system (pB27 bait vector; pP6 bait vector). The cytoplasmic C terminus of *Nrx-1* was cloned into pB27 using primers: 5'-GATGGAATTC-AATGGCGATCGTG GCT-3' and 5'-GTCTATACTAGT-TTACACATACCCTCTTGCAGTCCT-3'.

The *Spn* and *Syd-1* fragments depicted in Fig. 6 were cloned into pP6 using: F1-fwd: 5'-CAATCCATGGC-CATGGAGAAACCGATGCATCAT-3', F1-rev: 5'-CAACCTCGAGTTA-ATA GC CGACGTCCACGTA-3', F2-fwd: 5'-CAAAAC ATGGCC-GTTCGCAAAATCTGTGGACG-3', F2-rev: 5'-CTTGGATCCTT-ACT CGTGCAGTATTCCCC-3', F3-fwd: 5'-GATCCATGGCC-CGTGAAGAGCTG GAAAAC-3', F3-rev: 5'-GTTGGATCCTTA-CGTCCTACGCATCATCTG-3', F4-fwd: 5'-GATCCcatggccGAGGAGCGCTTGAAGCCGCAA-3', F4-rev: 5'-CTGG GATCCTTGTGCACCTTGGGATA-3', F5-fwd: 5'-GATC CCATGGCCAACT GCATCTGCTGGCCAAAGTG-3', F5-rev: 5'-GGAATCCTCGAG-CTTCTTTTTG

GCCGCTTCTCT-3', Syd-1 F1-fwd: 5'-GTCTATGAATTC ATGACG GTGC AACCGCTGAA-3', Syd-1 F1-rev: 5'-GTCTATACT-AGTT CCCGTT GACA TTC TTCTCG-3'.

Immunostaining and imaging. Larval filets were dissected and stained as described previously^{13,21}. Primary antibodies used were: rabbit (Rb) SPN^{N2.2} (1:3,000), RbGluRIID (1:500), RbDSyd-1 (1:500), RbNlg1 (1:500), RbDRBP (1:500) and guinea pig Nrx-1 (1:500) (generously provided by M. Bhat). We used MNc82 (1:100) and MCSP (1:500) (Developmental Studies Hybridoma Bank (DSHB), the University of Iowa, Iowa City, IA), MFasII (1D4; DSHB), mouse monoclonal antibody 3E6 (to stain GFP) (1:500) (Invitrogen) and rabbit anti-dsRed (1:500) (Clontech). Secondary antibodies were generally diluted 1:500. Secondary antibodies for STED were used in the following concentrations: goat anti-mouse Atto590 1:100 and goat anti-rabbit star635 1:100. The dyes Atto590 (ATTO-TEC) and Star635 (Abberior) were coupled to the stated IgGs (Dianova). Imaging larvae were mounted in Mowiol (Sigma-Aldrich) for STED.

The sizes and surface densities of AZ cluster (visualized using BRP^{nc82}, RimBP and Cac^{GFP}) were quantified from maximal projections of confocal NMJ stacks. A Cy5-HRP antibody (23-175-021, Jackson ImmunoResearch, 1:250) was used to outline the shape of the NMJ. Control and mutant larvae were stained in the same vial. All images for synapse quantification from fixed samples were acquired using the same microscope settings (with $\times 63$ magnification and numerical aperture 1.4 oil objective, Leica). AZ cluster analysis was done as described previously⁶⁹; AZ densities were obtained by normalizing the total number of particles analysed to the total synaptic area (pixel units) measured via HRP. Similarly, the absolute intensities of synaptic proteins per NMJ were normalized to the absolute intensity of synaptic HRP of the corresponding NMJ.

In vivo imaging and FRAP analysis. All UAS constructs were driven in motoneurons using OK6-Gal4⁷⁵. Intravital live imaging was performed as described previously^{13,21}.

STED and EM. STED microscopy was performed as described previously³⁰. BRP ring diameter measurements were performed on deconvolved images. Line profiles were placed across the middle of planer-oriented BRP rings and the longest peak-to-peak distance measured. Five to seven images obtained from four to five third instar larvae per genotype were processed and analysed.

Head fractionation, co-immunoprecipitation and Y2H assay. We followed a new protocol using *Drosophila* head fractionation, to obtain protein extracts used in co-immunoprecipitation experiments. Extracts were run on 6% Tris-HCl gels. Proteins were then transferred onto a nitrocellulose membrane and blocked with 5% milk in 1 \times PBS supplemented with 0.1% Tween-20 (PBS-T). Membranes were probed with guinea pig anti-Nrx-1 (1:5,000; a custom polyclonal directed against the last 100 amino acids of Nrx-1) and rabbit anti-Spn^{N2.2} (1:10,000) diluted in PBS-T. After washing, secondary anti-guinea pig or anti-rabbit HRP-conjugated antibodies were used for detection (Dianova) in conjunction with an enhanced chemoluminescence (GE Healthcare ECL Prime; product number RPN 2232) detection system with Hyperfilm ECL (GE Healthcare). Films were scanned in transmission mode (Epson V770). Images were imported to Photoshop (Adobe), and brightness and contrast were adjusted. The liquid Y2H β -galactosidase assay was performed as reported previously⁷⁰.

Co-immunoprecipitation from mouse brain. Brains were homogenized in 25 ml per g tissue in homogenization buffer (50 mM Tris-HCl, pH7.4, 150 mM NaCl, 10% glycerol, 2 mM CaCl₂ + EDTA free protease and phosphatase inhibitor mixes) using glass homogenizer. After homogenization samples were sonicated with 3 \times 10 pulses, Triton-X100 was added to the final concentration of 1% and homogenate was incubated for 10 min at 4 °C with rotation. Sample was sonicated again with 10 pulses. Samples were spun down at 20,000 \times g for 30 min. About 10 μ l per ml homogenate of protein A/G magnetic beads were added following 30 min incubation and separation of magnetic beads from the homogenate. Homogenate was aliquoted in 2 ml tubes (1.6 ml per tube) and 0.8 μ g affinity-purified anti-pan-NRX or rabbit IgG was added to each aliquot. Samples were incubated overnight with rotation at 4 °C. About 8 μ l protein-A magnetic beads (Dyna beads) were added and samples were incubated for additional 2 h. Samples were washed 3 \times with homogenization buffer + 0.1% Triton-X100 and once with homogenization buffer without detergent. Bound proteins were eluted with 30 μ l 2% sodium deoxycholate. Eluted proteins were separated on 8% PAA gel and probed with anti-spinophilin (1:1,000, Cell Signaling, E1E7R) and anti-pan-Nrx (40 μ g ml⁻¹, homemade, affinity purified).

Two-electrode voltage clamp recordings. TEVC recordings were performed on larval NMJs of third instar males (muscle 6 and segments A2 and A3), essentially as described⁶. The composition of the extracellular hemolymph-like saline (HL-3) was (in mM) NaCl 70, KCl 5, MgCl₂ 20, NaHCO₃ 10, trehalose 5, sucrose 115, HEPES 5 and CaCl₂ 1.5, pH adjusted to 7.2. Recordings were made from cells with an initial membrane potential (*V*_m) between -50 and -70 mV and input resistances

of ≥ 4 M Ω , using intracellular electrodes with resistances of 8–20 M Ω and filled with 3 M KCl. eEJCs, which reflect the compound excitatory junctional current of both the motoneurons innervating muscle 6 (voltage clamp at -60 mV) and mEJCs (voltage clamp at -80 mV) were low pass filtered at 1 kHz. The 0.2-Hz stimulation protocols included 20 traces per cell. Paired-pulse recordings consisted of 10 traces per interval per cell in which a 4-s rest was left between paired pulses. For determination of the base line of the second pulse at the 10-ms interpulse interval, the decay of the first pulse was extrapolated. Recordings were analysed with pClamp 10 (Molecular Devices). Stimulation artifacts in eEJC recordings were removed for clarity.

GCaMP5 imaging; assaying spontaneous and evoked release by Ca²⁺ imaging. Optical analysis of spontaneous and evoked transmitter release was performed similarly as described³ by imaging postsynaptic GCaMP5 fluorescence signals in flies expressing UAS-myrGCaMP5. Local activity patterns were aligned to confocal images of a post-fixed staining against GFP and BRP to identify single AZs. See Supplementary Methods for full details of Ca²⁺ imaging, image alignment and signal processing.

Statistics. Data were analysed using Prism (GraphPad Software). Nonparametric Mann-Whitney *U*-tests were used to compare two groups for all data sets. Nonparametric Kruskal-Wallis tests were used for comparison of more than two groups, followed by a Dunn's multiple comparison test. *P* values, *n* values and *U* or *K* statistics are given in the figure legends or main text. Similarly, the electrophysiological data are reported as mean \pm s.e.m. and *P* value denotes the significance according to one-way analysis of variance with Tukey's multiple comparison post-test.

References

- Sudhof, T. C. The presynaptic active zone. *Neuron* **75**, 11–25 (2012).
- Peled, E. S. & Isacoff, E. Y. Optical quantal analysis of synaptic transmission in wild-type and rab3-mutant *Drosophila* motor axons. *Nat. Neurosci.* **14**, 519–526 (2011).
- Melom, J. E., Akbergenova, Y., Gavornik, J. P. & Littleton, J. T. Spontaneous and evoked release are independently regulated at individual active zones. *J. Neurosci.* **33**, 17253–17263 (2013).
- Holderith, N. *et al.* Release probability of hippocampal glutamatergic terminals scales with the size of the active zone. *Nat. Neurosci.* **15**, 988–997 (2012).
- Dai, Y. *et al.* SYD-2 Liprin-alpha organizes presynaptic active zone formation through ELKS. *Nat. Neurosci.* **9**, 1479–1487 (2006).
- Kittel, R. J. *et al.* Bruchpilot promotes active zone assembly, Ca²⁺ channel clustering, and vesicle release. *Science* **312**, 1051–1054 (2006).
- Spangler, S. A. & Hoogenraad, C. C. Liprin- α proteins: scaffold molecules for synapse maturation. *Biochem. Soc. Trans.* **35**, 1278–1282 (2007).
- Dean, C. *et al.* Neurexin mediates the assembly of presynaptic terminals. *Nat. Neurosci.* **6**, 708–716 (2003).
- Scheiffele, P., Fan, J., Choeh, J., Fetter, R. & Serafini, T. Neuroligin expressed in nonneuronal cells triggers presynaptic development in contacting axons. *Cell* **101**, 657–669 (2000).
- Hu, Z. *et al.* Neurexin and neuroligin mediate retrograde synaptic inhibition in C. elegans. *Science* **337**, 980–984 (2012).
- Banovic, D. *et al.* *Drosophila* neuroligin 1 promotes growth and postsynaptic differentiation at glutamatergic neuromuscular junctions. *Neuron* **66**, 724–738 (2010).
- Knight, D., Xie, W. & Boulianne, G. L. Neurexins and neuroligins: recent insights from invertebrates. *Mol. Neurobiol.* **44**, 426–440 (2011).
- Owald, D. *et al.* Cooperation of Syd-1 with Neurexin synchronizes pre- with postsynaptic assembly. *Nat. Neurosci.* **15**, 1219–1226 (2012).
- Chen, Y. C. *et al.* *Drosophila* neuroligin 2 is required presynaptically and postsynaptically for proper synaptic differentiation and synaptic transmission. *J. Neurosci.* **32**, 16018–16030 (2012).
- Li, J., Ashley, J., Budnik, V. & Bhat, M. A. Crucial role of *Drosophila* neurexin in proper active zone apposition to postsynaptic densities, synaptic growth, and synaptic transmission. *Neuron* **55**, 741–755 (2007).
- Zeng, X. *et al.* Neurexin-1 is required for synapse formation and larvae associative learning in *Drosophila*. *FEBS Lett.* **581**, 2509–2516 (2007).
- Owald, D. *et al.* A Syd-1 homologue regulates pre- and postsynaptic maturation in *Drosophila*. *J. Cell Biol.* **188**, 565–579 (2010).
- Wentzel, C. *et al.* mSYD1A, a mammalian synapse-defective-1 protein, regulates synaptogenic signalling and vesicle docking. *Neuron* **78**, 1012–1023 (2013).
- Collins, C. A. & DiAntonio, A. Synaptic development: insights from *Drosophila*. *Curr. Opin. Neurobiol.* **17**, 35–42 (2007).
- Owald, D. & Sigrist, S. J. Assembling the presynaptic active zone. *Curr. Opin. Neurobiol.* **19**, 311–318 (2009).
- Fouquet, W. *et al.* Maturation of active zone assembly by *Drosophila* Bruchpilot. *J. Cell Biol.* **186**, 129–145 (2009).

22. Depner, H., Lutzkendorf, J., Babkir, H. A., Sigrist, S. J. & Holt, M. G. Differential centrifugation-based biochemical fractionation of the *Drosophila* adult CNS. *Nat. Protoc.* **9**, 2796–2808 (2014).
23. Parks, A. L. *et al.* Systematic generation of high-resolution deletion coverage of the *Drosophila melanogaster* genome. *Nat. Genet.* **36**, 288–292 (2004).
24. Allen, P. B., Ouime, C. C. & Greengard, P. Spinophilin, a novel protein phosphatase 1 binding protein localized to dendritic spines. *Proc. Natl Acad. Sci. USA* **94**, 9956–9961 (1997).
25. Nakanishi, H. *et al.* Neurabin a novel neural tissue-specific actin filament-binding protein involved in neurite formation. *J. Cell Biol.* **139**, 951–961 (1997).
26. Muly, E. C. *et al.* Subcellular distribution of neurabin immunolabelling in primate prefrontal cortex: comparison with spinophilin. *Cereb. Cortex* **14**, 1398–1407 (2004).
27. Muly, E. C., Smith, Y., Allen, P. & Greengard, P. Subcellular distribution of spinophilin immunolabelling in primate prefrontal cortex: localization to and within dendritic spines. *J. Comp. Neurol.* **469**, 185–197 (2004).
28. Qin, G. *et al.* Four different subunits are essential for expressing the synaptic glutamate receptor at neuromuscular junctions of *Drosophila*. *J. Neurosci.* **25**, 3209–3218 (2005).
29. Venken, K. J., He, Y., Hoskins, R. A. & Bellen, H. J. P[acman]: a BAC transgenic platform for targeted insertion of large DNA fragments in *D. melanogaster*. *Science* **314**, 1747–1751 (2006).
30. Liu, K. S. *et al.* RIM-binding protein, a central part of the active zone, is essential for neurotransmitter release. *Science* **334**, 1565–1569 (2011).
31. Gottfert, F. *et al.* Coaligned dual-channel STED nanoscopy and molecular diffusion analysis at 20 nm resolution. *Biophys. J.* **105**, L01–L03 (2013).
32. Gustafsson, M. G. *et al.* Three-dimensional resolution doubling in wide-field fluorescence microscopy by structured illumination. *Biophys. J.* **94**, 4957–4970 (2008).
33. Schmid, A. *et al.* Activity-dependent site-specific changes of glutamate receptor composition *in vivo*. *Nat. Neurosci.* **11**, 659–666 (2008).
34. Schuster, C. M., Davis, G. W., Fetter, R. D. & Goodman, C. S. Genetic dissection of structural and functional components of synaptic plasticity. I. Fasciclin II controls synaptic stabilization and growth. *Neuron* **17**, 641–654 (1996).
35. Kwon, H. B. *et al.* Neuroigin-1-dependent competition regulates cortical synaptogenesis and synapse number. *Nat. Neurosci.* **15**, 1667–1674 (2012).
36. Sun, M. *et al.* Genetic interaction between Neurexin and CAKI/CMG is important for synaptic function in *Drosophila* neuromuscular junction. *Neurosci. Res.* **64**, 362–371 (2009).
37. Mukherjee, K. *et al.* CASK Functions as a Mg²⁺-independent neurexin kinase. *Cell* **133**, 328–339 (2008).
38. Ataman, B. *et al.* Nuclear trafficking of *Drosophila* Frizzled-2 during synapse development requires the PDZ protein dGRIP. *Proc. Natl Acad. Sci. USA* **103**, 7841–7846 (2006).
39. Doyle, D. A. *et al.* Crystal structures of a complexed and peptide-free membrane protein-binding domain: molecular basis of peptide recognition by PDZ. *Cell* **85**, 1067–1076 (1996).
40. Peled, E. S., Newman, Z. L. & Isacoff, E. Y. Evoked and spontaneous transmission favored by distinct sets of synapses. *Curr. Biol.* **24**, 484–493 (2014).
41. Missler, M., Sudhof, T. C. & Biederer, T. Synaptic cell adhesion. *Cold Spring Harb. Perspect. Biol.* **4**, a005694 (2012).
42. Sudhof, T. C. Neuroigins and neurexins link synaptic function to cognitive disease. *Nature* **455**, 903–911 (2008).
43. Feng, J. *et al.* Spinophilin regulates the formation and function of dendritic spines. *Proc. Natl Acad. Sci. USA* **97**, 9287–9292 (2000).
44. Terry-Lorenzo, R. T. *et al.* Neurabin/protein phosphatase-1 complex regulates dendritic spine morphogenesis and maturation. *Mol. Biol. Cell.* **16**, 2349–2362 (2005).
45. Allen, P. B. *et al.* Distinct roles for spinophilin and neurabin in dopamine-mediated plasticity. *Neuroscience* **140**, 897–911 (2006).
46. Sarrouilhe, D., di Tommaso, A., Metaye, T. & Ladeveze, V. Spinophilin: from partners to functions. *Biochimie* **88**, 1099–1113 (2006).
47. Patel, M. R. *et al.* Hierarchical assembly of presynaptic components in defined *C. elegans* synapses. *Nat. Neurosci.* **9**, 1488–1498 (2006).
48. Taru, H. & Jin, Y. The Liprin homology domain is essential for the homomeric interaction of SYD-2/Liprin-alpha protein in presynaptic assembly. *J. Neurosci.* **31**, 16261–16268 (2011).
49. Chia, P. H., Li, P. & Shen, K. Cell biology in neuroscience: cellular and molecular mechanisms underlying presynapse formation. *J. Cell Biol.* **203**, 11–22 (2013).
50. Ou, C. Y. & Shen, K. Setting up presynaptic structures at specific positions. *Curr. Opin. Neurobiol.* **20**, 489–493 (2010).
51. Dai, S., Hall, D. D. & Hell, J. W. Supramolecular assemblies and localized regulation of voltage-gated ion channels. *Physiol. Rev.* **89**, 411–452 (2009).
52. Chia, P. H., Patel, M. R. & Shen, K. NAB-1 instructs synapse assembly by linking adhesion molecules and F-actin to active zone proteins. *Nat. Neurosci.* **15**, 234–242 (2012).
53. Penzes, P. *et al.* The neuronal Rho-GEF kalirin-7 interacts with PDZ domain-containing proteins and regulates dendritic morphogenesis. *Neuron* **29**, 229–242 (2001).
54. Sarrouilhe, D. & Ladeveze, V. The tumour suppressor function of the scaffolding protein spinophilin. *Atlas Genet. Cytogenet. Oncol. Haematol.* **18**, 691–700 (2014).
55. Buchsbaum, R. J., Connolly, B. A. & Feig, L. A. Regulation of p70 S6 kinase by complex formation between the Rac guanine nucleotide exchange factor (Rac-GEF) Tiam1 and the scaffold spinophilin. *J. Biol. Chem.* **278**, 18833–18841 (2003).
56. Hata, Y., Buts, S. & Sudhof, T. C. CASK: a novel dlg/PSD95 homolog with an N-terminal calmodulin-dependent protein kinase domain identified by interaction with neurexins. *J. Neurosci.* **16**, 2488–2494 (1996).
57. Biederer, T. & Sudhof, T. C. Mints as adaptors. Direct binding to neurexins and recruitment of munc18. *J. Biol. Chem.* **275**, 39803–39806 (2000).
58. Grootjans, J. J., Reekmans, G., Ceulemans, H. & David, G. Syntenin-syndecan binding requires syndecan-syntenin and the co-operation of both PDZ domains of syntenin. *J. Biol. Chem.* **275**, 19933–19941 (2000).
59. Kurschner, C., Mermelstein, P. G., Holdena, W. T. & Surmeier, D. J. CIPP, a novel multivalent PDZ domain protein, selectively interacts with Kir4.0 family members, NMDA Receptor subunits, neurexins, and neuroligins. *Mol. Cell. Neurosci.* **11**, 161–172 (1998).
60. Missler, M. *et al.* Alpha-neurexins couple Ca²⁺ channels to synaptic vesicle exocytosis. *Nature* **10**, 939–948 (2003).
61. Dudanova, I., Tabuchi, K., Rohlmann, A., Sudhof, T. C. & Missler, M. Deletion of alpha-neurexins does not cause a major impairment of axonal pathfinding or synapse formation. *J. Comp. Neurol.* **502**, 261–274 (2007).
62. Craig, A. M. & Kang, Y. Neurexin-neuroigin signalling in synapse development. *Curr. Opin. Neurobiol.* **17**, 43–52 (2007).
63. Varoqueaux, F. *et al.* Neuroigins determine synapse maturation and function. *Neuron* **51**, 741–754 (2006).
64. O'Connor, V. M., Shamotienko, O., Grishin, E. & Betz, H. On the structure of the 'synaptosecretosome' Evidence for a neurexin/syntaxin/Ca²⁺ channel complex. *FEBS Lett.* **326**, 255–260 (1993).
65. Zhang, W. *et al.* Extracellular domains of alpha-neurexins participate in regulating synaptic transmission by selectively affecting N- and P/Q-type Ca²⁺ channels. *J. Neurosci.* **25**, 4330–4342 (2005).
66. Dudanova, I. *et al.* Important contribution of alpha-neurexins to Ca²⁺-triggered exocytosis of secretory granules. *J. Neurosci.* **26**, 10599–10613 (2006).
67. Sigrist, S. J., Reiff, D. F., Thiel, P. R., Steinert, J. R. & Schuster, C. M. Experience-dependent strengthening of *Drosophila* neuromuscular junctions. *J. Neurosci.* **23**, 6546–6556 (2003).
68. Keegan, J., Schmeurer, M., Ring, B. & Garza, D. The 62E early-late puff of *Drosophila* contains D-spinophilin, an ecdysone-inducible PDZ-domain protein dynamically expressed during metamorphosis. *Genet. Res.* **77**, 27–39 (2001).
69. Andlauer, T. F. & Sigrist, S. J. Quantitative analysis of *Drosophila* larval neuromuscular junction morphology. *Cold Spring Harb. Protoc.* **2012**, 490–493 (2012).
70. Mockli, N. & Auerbach, D. Quantitative beta-galactosidase assay suitable for high-throughput applications in the yeast two-hybrid system. *Biotechniques* **36**, 872–876 (2004).

Acknowledgements

We would like to thank A. Stawrakakis and N. Holton for technical assistance; H. Aberle and U. Thomas for critically reading the manuscript; and M. Bhat (the University of North Carolina) for generously sharing reagents. The project was supported by grants from the Deutsche Forschungsgemeinschaft Grant (SFB958/A3 and A6). We thank Chris Weise SFB958/Z3 for mass spectrometric analysis. We accessed beamlines of the BESSY II (Berliner Elektronenspeicherring-Gesellschaft für Synchrotronstrahlung II) storage ring (Berlin, Germany) via the Joint Berlin MX Laboratory sponsored by the Helmholtz Zentrum Berlin für Materialien und Energie, the Freie Universität Berlin, the Humboldt-Universität zu Berlin, the Max-Delbrück Centrum and the Leibniz-Institut für Molekulare Pharmakologie. M.H. is funded by a European Research Council Starting Grant (Astrofunc). P.S. is funded by the Swiss National Science Foundation, EU-AIMS which receives support from the /InnovativeMedicines Initiative/ Joint Undertaking of the EU FP7, and the Kanton Basel-Stadt.

Author contributions

K.M., S.R.-A., A.M.W. and S.J.S. designed the research. K.M., S.R.-A., J.H.D., D.S., U.R., M.A.B., C.H., N.R., H.D., J.L., T.M., D.D.B., J.S. and A.M.W. performed the experiments. K.M., S.R.-A., U.R., C.H. and A.M.W. analysed the data. F.G., M.H., M.C.W., S.W.H., P.S. and B.L. shared the protocols, reagents and advice. K.M., S.R.-A. and S.J.S. wrote the paper with inputs from M.H. and A.M.W.

Additional information

Author Information. The structure factors and atomic coordinates of the Spn-PDZ domain are deposited in the Protein Data Bank with accession number 4XHV.

Supplementary Information accompanies this paper at <http://www.nature.com/naturecommunications>

Competing financial interests: The authors declare no competing financial interests.

Reprints and permission information is available online at <http://npg.nature.com/reprintsandpermissions/>

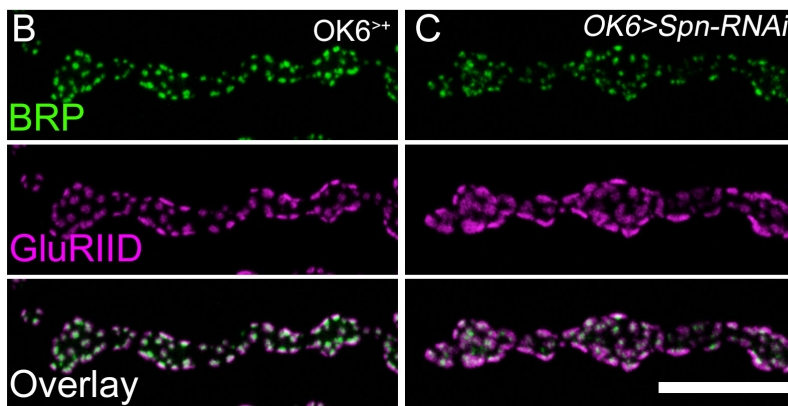
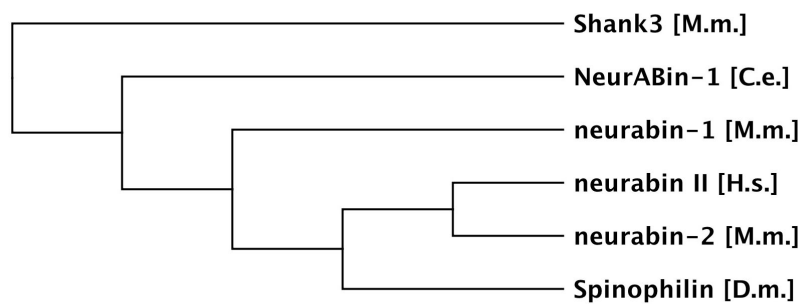
How to cite this article: Muhammad, K. G. H. *et al.* Presynaptic spinophilin tunes neurexin signalling to control active zone architecture and function. *Nat. Commun.* 6:8362 doi: 10.1038/ncomms9362 (2015).



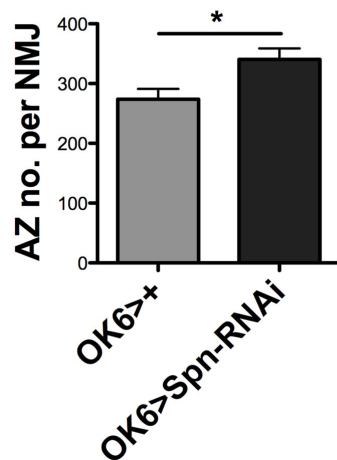
This work is licensed under a Creative Commons Attribution 4.0 International License. The images or other third party material in this article are included in the article's Creative Commons license, unless indicated otherwise in the credit line; if the material is not included under the Creative Commons license, users will need to obtain permission from the license holder to reproduce the material. To view a copy of this license, visit <http://creativecommons.org/licenses/by/4.0/>

Supplementary Figure 1

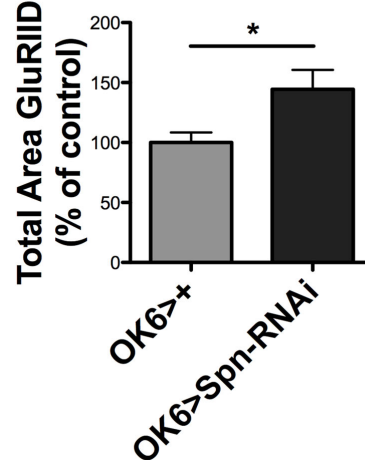
A



D

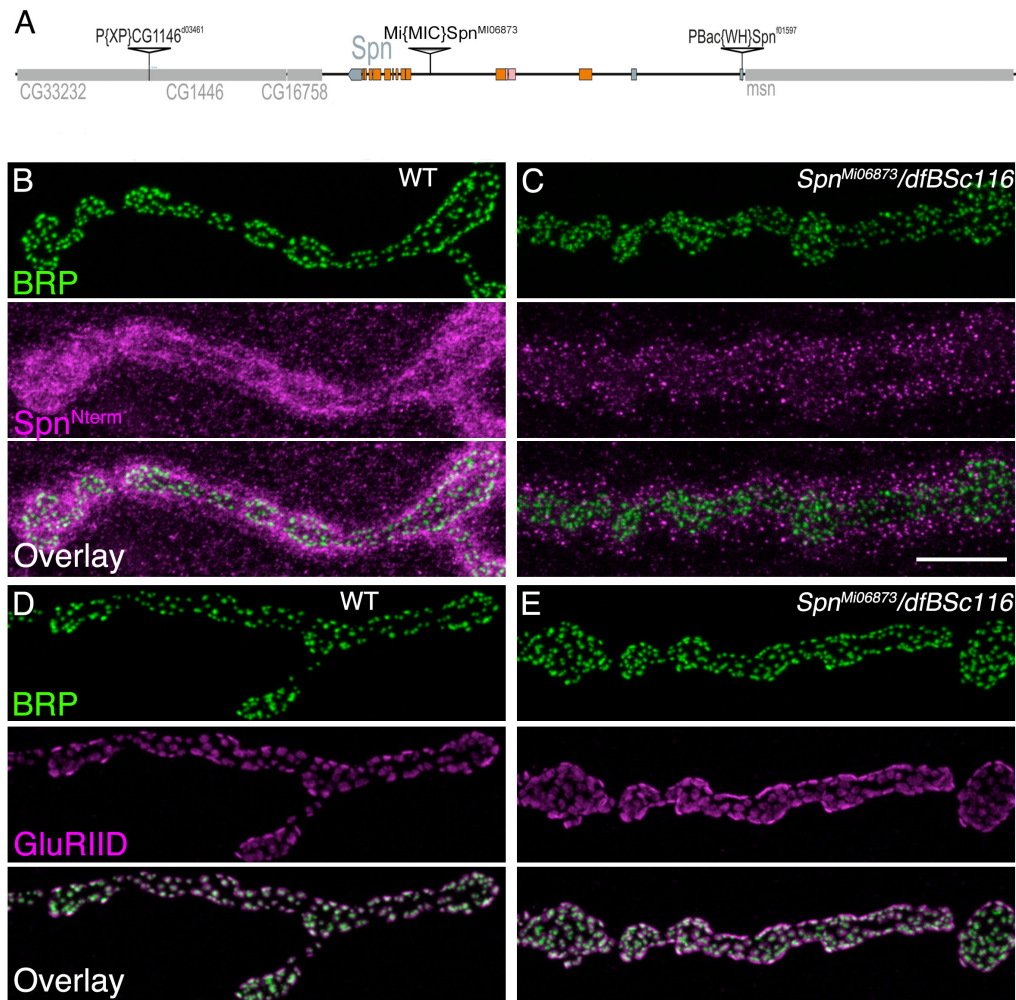


E



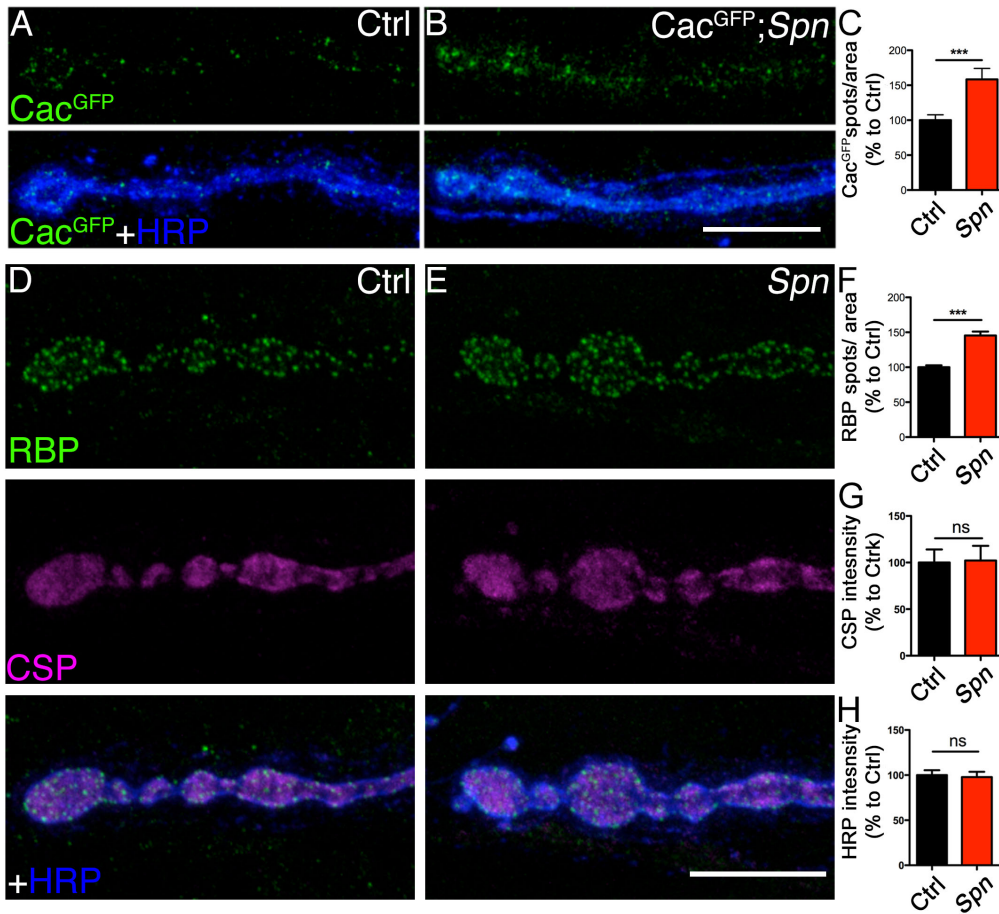
Supplementary Figure 1 related to figure 1: (A) Dendrogram analysis comparing Neurabin family of proteins together with that of Drosophila Spn. Shank3 has been used as an out-group. (B-C) RNAi mediated knockdown of presynaptic Spn results in more AZ scaffolds and enlarged glutamate receptor field size. (D-E) Quantifications of total BRP spots and Glutamate receptor field sizes in motoneuron derived Spn-RNAi, BRP spots: in ctrl : 274 ± 17.4, $n = 9$; *Spn*: 340 ± 18.1, $n = 10$; ctrl versus *Spn* $P < 0.05$; Mann-Whitney *U*-test ($U = 15$). Total GluRIID area: in ctrl: 77.8 ± 6.5, $n = 9$; *Spn*: 113.6 ± 11.2, $n = 10$; ctrl versus *Spn* $P < 0.05$; Mann-Whitney *U*-test ($U = 17$). Scale bar 10µm.

Supplementary Figure 2



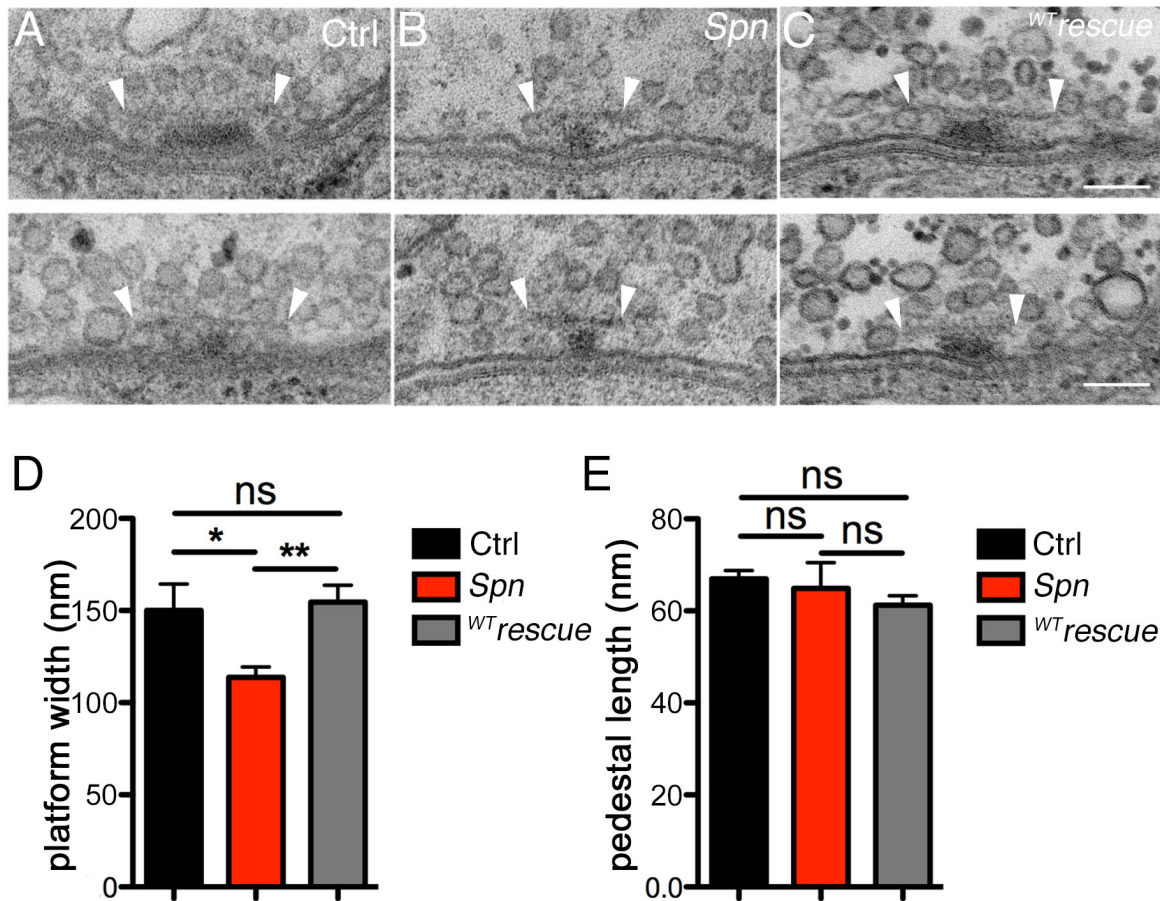
Supplementary Figure 2 related to Figures 1&2. Additional allele of *spn* locus, MiMic-*Spn*^{Mi06873} shows similar phenotypes of *Spn* larvae. **(A)** Genomic locus of transposon element integration. **(B-C)** Reduced anti-*Spn* staining at the NMJ of *Spn*^{Mi06873} allele with concomitant increase of BRP spot density. **(D-E)** Enlarged GluRIID field size in MiMic-*Spn*^{Mi06873} hypomorphic allele. Scale bar 10 μ m.

Supplementary Figure 3



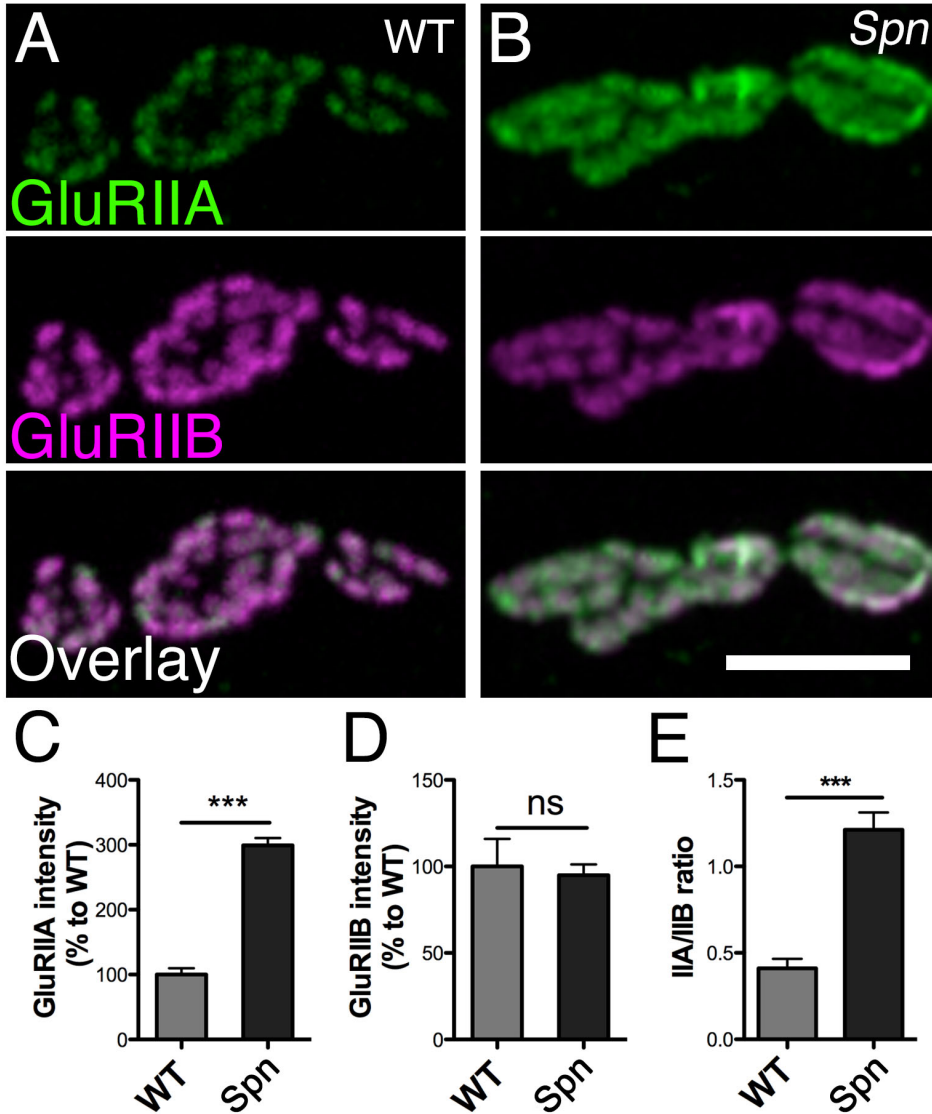
Supplementary Figure 3 related to Figures 2 and 3. RBP and Cac^{GFP} spot density increased at *Spn* NMJs. **(A)** UAS-Cac^{GFP} expression in Ctrl compared to **(B)** *Spn* show significant increase of total amount of Ca²⁺ channels at *Spn* NMJs. **(D-E)** RBP spot density is similarly increased in *Spn* NMJ while synaptic vesicle marker CSP does not alter. **(C, F-H)** Cac^{GFP} in Ctrl: 100 ± 7.6, *n* = 9; Cac^{GFP} in *Spn*: 158 ± 15.67 *n* = 8; Ctrl versus *Spn* P<0.001 Mann-Whitney U-test (U = 4), (RBP in Ctrl: 100 ± 2.7, 771 *n* = 10; RBP in *Spn*: 145.5 ± 5.6 *n* = 10; Ctrl versus *Spn* P<0.001 Mann-Whitney U-test (U = 1), (CSP in Ctrl: 100 ± 14, *n* = 10; CSP in *Spn*: 102 ± 15.64 *n* = 10; Ctrl versus *Spn* P>0.05 Mann-Whitney U-test (U = 47), (HRP integrated intensity in Ctrl: 100±5.4, *n*=10; HRP in *Spn*: 97.8±5.9, *n*=10; Ctrl versus *Spn* P>0.05 Mann-Whitney U-test (U = 41). Error bars indicate SEM. *, P < 0.05; **, P < 0.01; ***, P < 0.005; ns, P > 0.05. Scale bar: 10μm.

Supplementary Figure 4



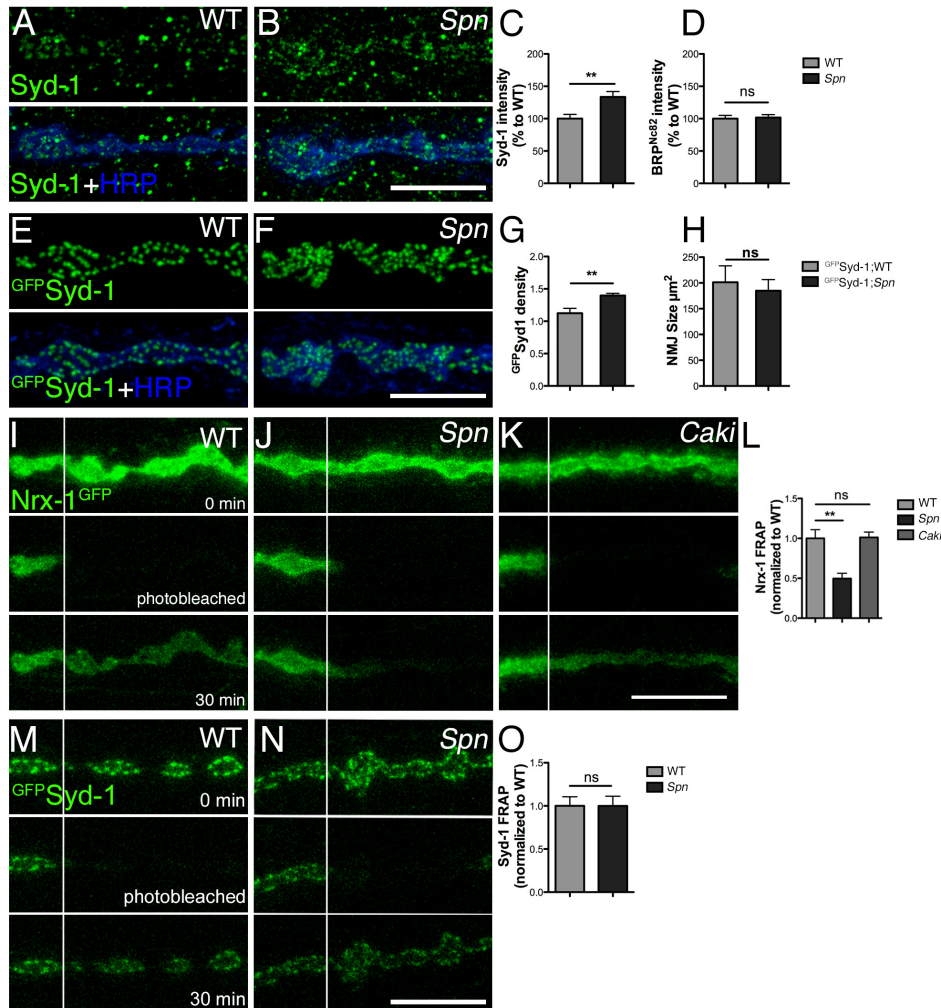
Supplementary Figure 4 related to Fig.3. Electron dense projection analyses in *Spn* NMJs. Two independent examples of dense projection (T-bars) are shown per indicated genotypes of Ctrl (**A**), *Spn* (**B**) and ^{WT}*Spn* rescue(**C**). (**D**)T-bar platform's width (electron-dense materials parallel to double membrane) were significantly shorter in *Spn* compared with Ctrl and ^{WT}*Spn* rescue (Ctrl: 150±14.3 nm, n=12; *Spn*: 113.8 ± 5.6 nm, P<0.05, n=21; ^{WT}*Spn*-rescue: 154± 9 nm, P<0.01 n=19; one-way ANOVA Tukey's posttest). (**E**) The T-bar height (pedestal plus platform perpendicular to double membrane) was unaffected in *Spn* compared to controls (Ctrl: 66.9±1.7 nm, n=1; *Spn*: 64.8±5.6 nm, P>0.05, n=21; ^{WT}*Spn*-rescue: 61.3±2.08 nm, P> 0.05, n=19; one-way ANOVA Tukey's posttest). All panels show mean values and errors bars representing SEMs. *, P ≤ 0.05; n.s., P > 0.05. Scale bar: 100 nm.

Supplementary Figure 5



Supplementary Figure 5 related to Fig.4. *Spn* controls postsynaptic GluR field size and composition. **(A-B)** Co-labelling of DGluRIIA and DGluRIIB for wild type **(A)**, *Spn* **(B)**, NMJs. **(C)** Integrated GluRIIA signal (wild type: 100±9.9, n=7; *Spn*: 299.3±11.15, n=8; WT versus *Spn* $P < 0.001$; Mann-Whitney U -test ($U = 0.0$)). **(D)** Integrated GluRIIB signal (wild type: 100±15.9, n=7; *Spn*: 94.95±6.2, n=8; WT versus *Spn* $P: 0.8$; Mann-Whitney U -test ($U = 26$)). **(E)** Increased incorporation of GluRIIA compared to GluRIIB (wild type: 0.41±0.05, n=7; *Spn*: 1.2±0.1, n=8; wild type versus *Spn* $P < 0.001$; Mann-Whitney U -test ($U = 1$)). Scale bar 5 μ m.

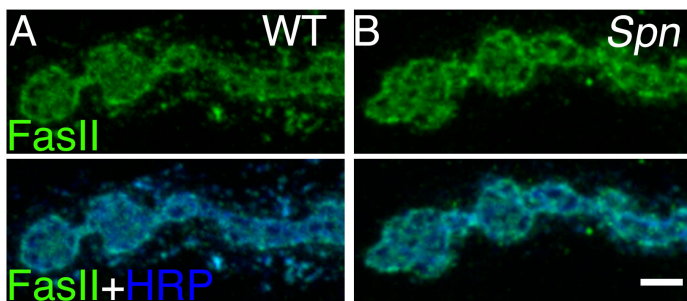
Supplementary Figure 6



Supplementary Figure 6 related to Fig.4. Elevated levels of endogenous Syd-1 in *Spn* NMJs. **(A)** co-labelling of Syd1 and HRP in WT and **(B)** in *Spn* NMJs. **(C)** Total amount of Syd-1 is increased in *Spn*, Wild type: 100 ± 6 , $n = 14$; *Spn*: 133.5 ± 8.4 , $n = 19$; wild type versus *Spn* $P < 0.01$; Mann-Whitney U -test ($U = 55$). **(D)** while amount of BRP is unaffected, Wild type: 100 ± 5 , $n = 14$; *Spn*: 101.8 ± 4.5 , $n = 19$; wild type versus *Spn* $P > 0.05$; Mann-Whitney U -test ($U = 123$). The NMJ size (chart not depicted), measured via HRP staining, is not changed in *Spn*, Wild type: 228 ± 11 , $n = 14$; *Spn*: 206 ± 7.7 , $n = 19$; wild type versus *Spn* $P > 0.05$; Mann-Whitney U -test ($U =$ **(E-H)** Similarly, ^{GFP}Syd-1 over-expression in *Spn* **(F)** shows more but smaller ^{GFP}Syd1 spots compared to controls **(E)**. Quantifications of ^{GFP}Syd-1 spot

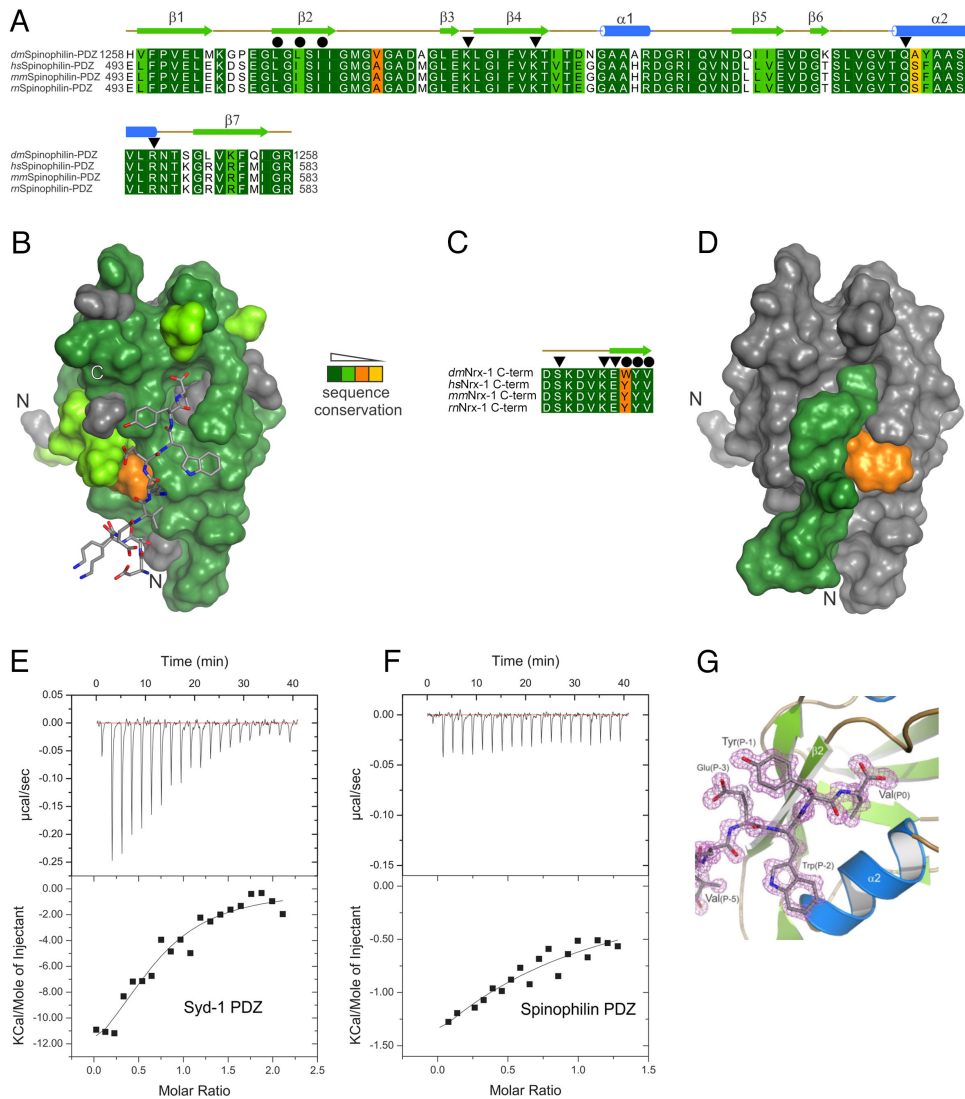
density **(G)** and NMJ size **(H)** in control and *Spn* animals, ^{GFP}Syd-1 spots: Wild type: 1.12 ± 0.07 , $n = 7$; *Spn*: 1.39 ± 0.03 , $n = 6$; wild type versus *Spn* $P < 0.01$; Mann-Whitney *U*-test ($U = 2$). NMJ size: wild type: 201.4 ± 31.8 , $n = 7$; *Spn*: $184.8 \pm 21.6 \mu\text{m}^2$; wild type versus *Spn* $P > 0.05$; Mann-Whitney *U*-test ($U = 18$). **(I-L)** FRAP of Nr_x-1^{GFP} expressed in motor neurons of wild type, *Spn* and *Caki* larvae. The middle (photobleached) rows were taken 2 min after the top row. **(L)** Quantifications of the Nr_x-1^{GFP} recovery signal in respected genotypes were normalized to its recovery in wild type larvae. Nr_x-1^{GFP} in wild type: 1.0 ± 0.1 , $n = 47$; Nr_x-1^{GFP} in *Spn*: 0.49 ± 0.06 , $n = 14$; Nr_x-1^{GFP} in *Caki*: 1.01 ± 0.06 , $n = 27$. Nr_x-1^{GFP} recovery in wild type versus *Spn*, $P < 0.001$ Mann-Whitney *U*-test ($U = 138$), Nr_x-1^{GFP} recovery in wild type versus *Caki*, $P > 0.05$ Mann-Whitney *U*-test ($U = 518$). **(M-O)** FRAP of ^{GFP}Syd-1 expressed in motor neurons of wild type and *Spn* larvae. The middle (photobleached) row taken 2 min after the top row. **(O)** Quantifications of ^{GFP}Syd-1 recovery signal normalized to wild type. ^{GFP}Syd-1 in wild type: 1.0 ± 0.1 , $n = 9$; ^{GFP}Syd-1 in *Spn*: 1.0 ± 0.1 , $n = 6$; ^{GFP}Syd-1 in wild type versus *Spn* background, $P > 0.05$; Mann-Whitney *U*-test ($U = 27$). Scale bars $10 \mu\text{m}$.

Supplementary Figure 7



Supplementary Figure 7 related to figure 4 Synaptic cell adhesion molecule Fasciclin II staining in *Spn* NMJs. Co-labelling of FasII staining with HRP marker in **(A)** wild type and **(B)** *Spn* NMJs, show no changes upon lack of *Spn*. Scale bar $2.5 \mu\text{m}$.

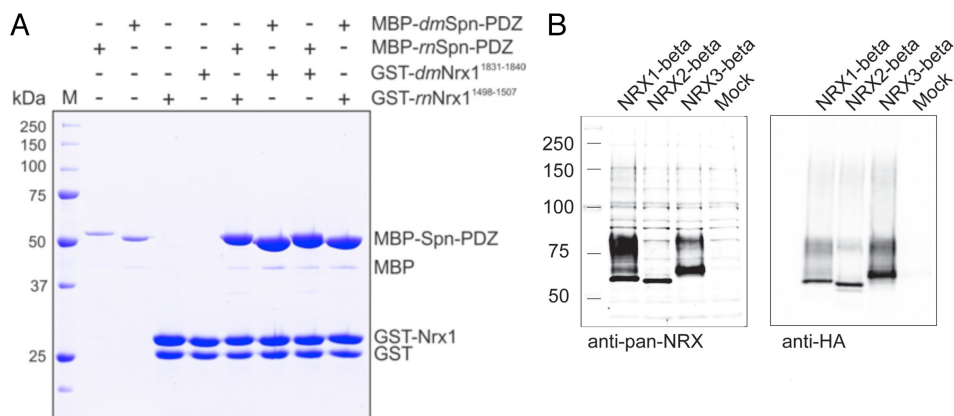
Supplementary Figure 8



Supplementary Figure 8 related to figure 5. Similarity between Nrx-1 C-termini and PDZ domains of fly and rodent animal models. **(A)** Alignment of PDZ domains from *dmSpinophilin*, *Homo sapiens* Spinophilin (*hsSpinophilin*), *Mus musculus* Spinophilin (*mmSpinophilin*), and *Rattus norvegicus* Spinophilin (*rnSpinophilin*). Secondary structure elements are indicated on top of the sequences. Filled circles indicate residues involved in *dmSpinophilin* protein backbone to peptide backbone interactions and triangles describe residues involved in side chain interactions. **(B)** Sequence conservation is mapped on the surface of the crystal structure of *dmSpinophilin*-PDZ. The bound *dmNeurexin* peptide is shown in stick representation. Secondary structure elements are indicated on top of the sequences. Filled circles indicate residues involved in *dmSpinophilin* protein backbone to peptide backbone interactions and triangles describe residues involved in side chain interactions. **(C)** Alignment of the last ten C-terminal amino acid residues of *dmNeurexin*, *Homo sapiens* Neurexin (*hsNeurexin*), *Mus musculus* Neurexin (*mmNeurexin*), and *Rattus norvegicus* Neurexin (*rnNeurexin*). **(D)** Sequence conservation is mapped on the surface of the bound *dmNeurexin* peptide. *dmSpinophilin*-PDZ is

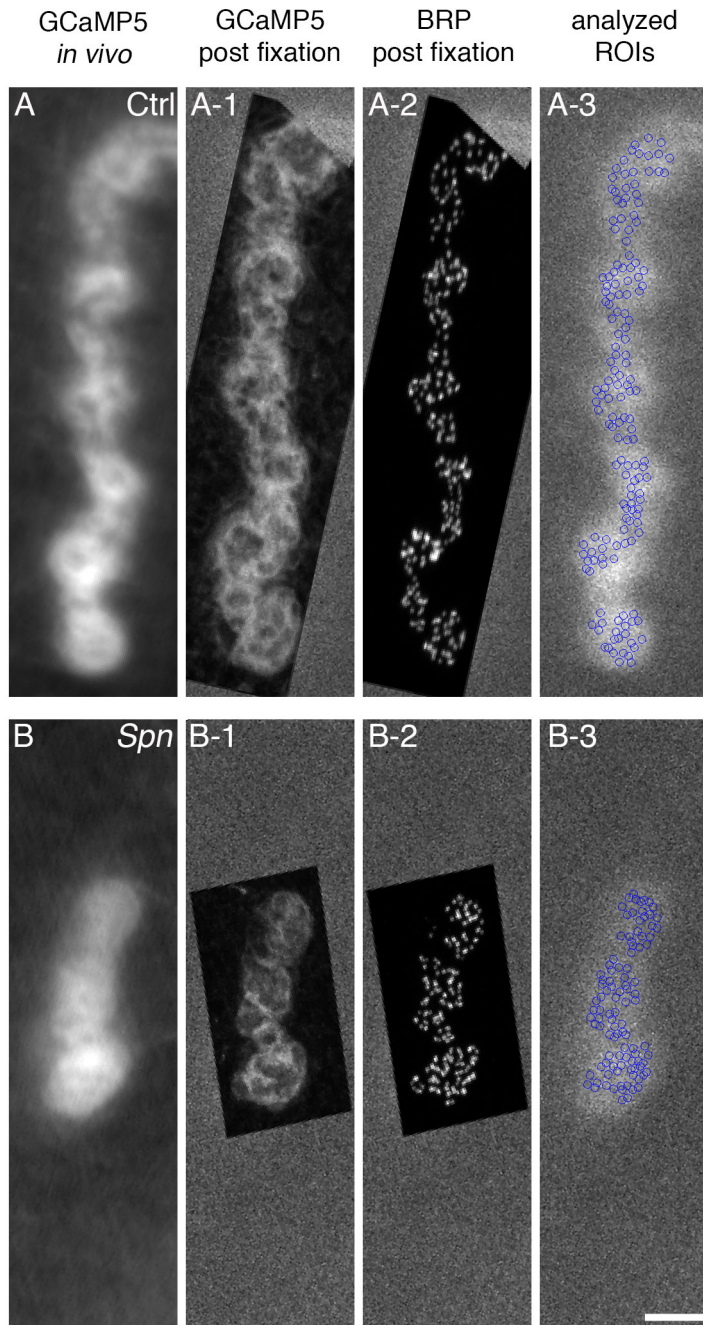
shown as gray surface. **(E,F)** Quantification of protein-peptide interactions by ITC. Both the raw data and the integrated data are shown. Data were fitted based on the “One Set of Sites” model. **(E)** Titration of MBP-*dm*Syd-1 PDZ and the *dm*Neurexin peptide. In a control experiment with MBP, we could not detect any binding of the *dm*Neurexin peptide. **(F)** Titration of *dm*Spinophilin-PDZ and the *dm*Neurexin peptide. **(G)** mFoDFc simulated annealing omit map shown as violet mesh contoured at 3.0 σ around the bound peptide. For calculation of the electron density map the *dm*Neurexin peptide had been omitted. The peptide is shown in gray stick representation and *dm*Spinophilin-PDZ in cartoon representation.

Supplementary Figure 9



Supplementary Figure 9 related to Fig. 5 **(A)** MBP-*dm*Spinophilin (MBP-*dm*Spn PDZ) and MBP-*m*Spinophilin (MBP-*m*Spn PDZ) pull-down assays in the presence of GST- *dm*Neurexin1 (GST-*dm*Nrx1¹⁸³¹⁻¹⁸⁴⁰) and GST-*m*Neurexin 1 (GST-*m*Nrx1¹⁴⁹⁸⁻¹⁵⁰⁷) peptides and the indicated proteins. **(B)** Immunoprecipitation of Nr-x1 complex from mouse brain homogenate.

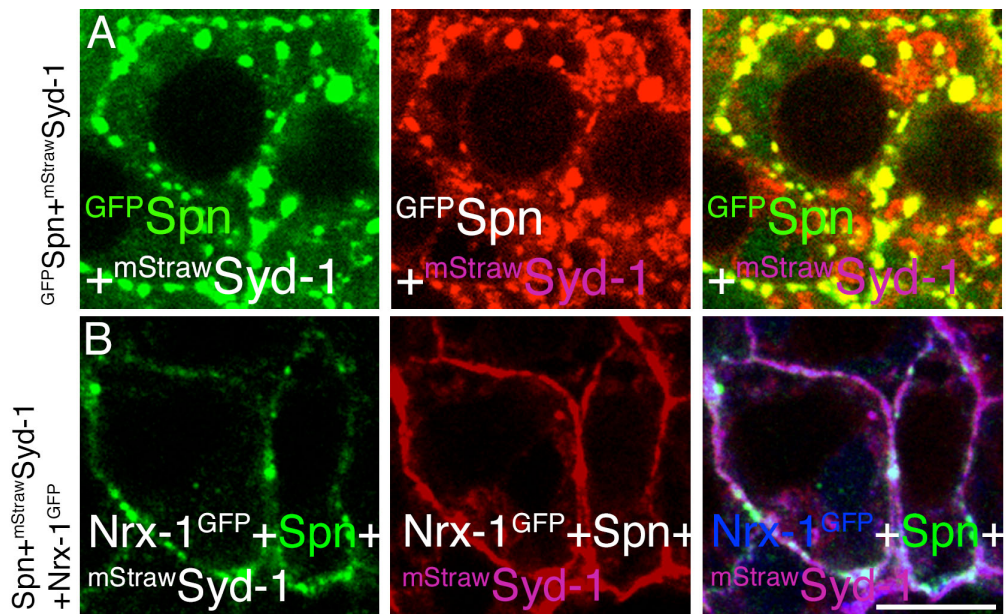
Supplementary Figure 10



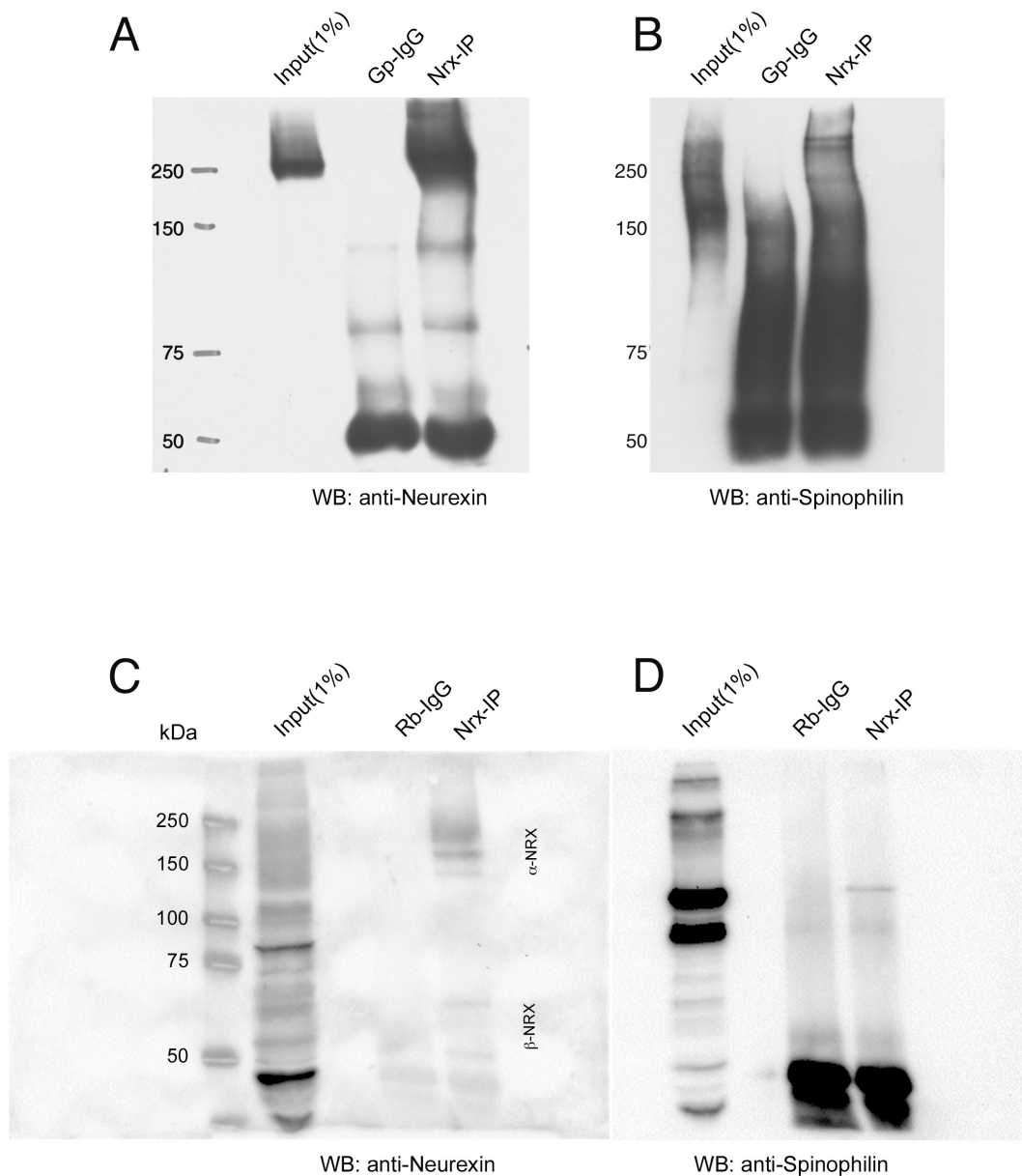
Supplementary Figure 10 related to figure 7 Assignment of single active zones identified by post-hoc staining against Bruchpilot (BRP) to GCaMP5 events at control and *Spn* NMJs. **(A, B)** *In vivo* GCaMP5 signal, produced from live movies by an average projection of 2000 frames acquired during spontaneous activity. **(A1, B1)** GCaMP5 signal after fixation, shown is a Z-projection of confocal light microscopic scans. Individual areas of the confocal image were registered to the first frame of the *in vivo* GCaMP5 signal (see Methods). A2, B2) The same registration transformation as for the confocal GCaMP5 images (A1, B2) was used to align individual active zones identified in confocal scans by staining against the presynaptic active zone marker BRP. **(A3, B3)** BRP

staining was used to place uniformly sized regions of interest (ROIs) to read out GCaMP5 fluorescence over time. Images A1, A2, A3 and B1, B2, B3 are placed on top of the first frame acquired in the live Ca^{2+} -imaging experiment (exposure time 0.05s). Scale bar $5\mu\text{m}$.

Supplementary Figure 11



Supplementary Figure 11 In-vivo complex formation between GFP^{Spn} , mStrawSyd-1 and $\text{Nrnx-1}^{\text{GFP}}$. **(A)** co-expression of GFP^{Spn} and mStrawSyd-1 leads to co-aggregation of both proteins at the membrane but also in cytoplasm of salivary gland cells. **(B)** Addition of $\text{Nrnx-1}^{\text{GFP}}$ to **(A)**, triple expression, leads to diffused localization of both Spn and Syd-1 at the membrane. Scale bar $25\mu\text{m}$.



Supplementary Figure 12 Conserved interaction between Spn and Nrxx-1 as shown in Fig.5. **(A-B)** Immunoblot (un-cropped) of fly Nrxx-1 immunoprecipitate (IP) from *Drosophila* head fractionation sample enriched for AZ proteins (see Methods). **(A)** Enrichment of Nrxx-1 in genuine pig anti-Nrxx-1 Co-IP sample. **(B)** Spn bands of expected size can be detected in Nrxx-1 Co-IP sample, but is absent in control immunoglobulin G is used (IgG). **(C-D)** Similarly this interaction could be detected in rodent brain homogenates. **(C)** Western-blot analysis of a pan-Nrxx antibody IP. **(D)** Co-IP complex with anti-Spn antibody.

Supplementary Table 1 Data collection and refinement statistics for *dmSpinophilin*-PDZ bound to a *dmNeurexin* derived peptide.

Data collection	
PDB entry	4XHV
Space group	$P4_32_12$
Wavelength [Å]	0.91841
Unit cell a; b; c [Å]	45.3; 45.3; 94.5
α ; β ; γ [°]	90.0; 90.0; 90.0
Resolution [Å] ^a	45.30-1.23 (1.30-1.23)
Unique reflections	29395 (4571)
Completeness ^a	99.7 (98.5)
$\langle I/\sigma(I) \rangle$ ^a	21.6 (2.4)
R_{meas} ^{a, b}	0.060 (0.699)
$CC_{1/2}$ ^a	100.0 (75.8)
Redundancy ^a	6.1 (3.8)
Refinement	
Non-hydrogen atoms	
R_{work} ^{a, c}	0.138 (0.207)
R_{free} ^{a, d}	0.162 (0.210)
Average B-factor [Å ²]	14.6
Protein residues	94 / 13.5
Peptide residues	10 / 14.1
Water molecules	176 / 25.0
Buffer molecules	3 / 18.3
r.m.s.d. ^e bond length [Å]	0.016
bond angles [°]	1.628
Ramachandran outliers [%]	0
Ramachandran favored [%]	99.1

^a values in parentheses refer to the highest resolution shell.

^b $R_{\text{meas}} = \sum_h [n/(n-1)]^{1/2} \sum_i |I_h - I_{h,i}| / \sum_h \sum_i I_{h,i}$, where I_h is the mean intensity of symmetry-equivalent reflections and n is the redundancy.

^c $R_{\text{work}} = \sum_h |F_o - F_c| / \sum F_o$ (working set, no σ cut-off applied).

^d R_{free} is the same as R_{work} , but calculated on 5% of the data excluded from refinement.

^e Root-mean-square deviation (r.m.s.d.) from target geometries.

Supplementary Table 2 Peptide interactions with a distance cut-off of ≤ 3.3 Å.

<i>dmSpinophlin-</i> PDZ	<i>dmNeurexin</i>	distance	Peptide	Peptide	distance
Leu1271 ^N	Val1840 ^O	2.7			
Leu1273 ^N	Val1840 ^{OXT}	3.3			
Leu1273 ^O	Val1840 ^N	2.9			
Arg1335 ^{NE}	Thr1839 ^O	3.0			
Arg1335 ^{NH}	Thr1839 ^O	2.9			
			Tyr1839 ^{OH}	Glu1837 ^{OE2}	2.6
Ile1275 ^N	Trp1838 ^O	2.9			
Ile1275 ^O	Glu1837 ^N	2.9			
Lys1294 ^{NZ}	Glu1837 ^{OE1}	3.0			
Gln1327 ^{NE2}	Lys1836 ^O	3.1			
			Asp1834 ^N	Ser1832 ^O	3.1
			Asp1834 ^{OD1}	Asp1831 ^O	2.9
			Asp1834 ^{OD1}	Asp1831 ^{OD1}	2.8
Lys1288 ^{NZ}	Ser1832 ^{OG}	3.1			
			Asp1831 ^O	Asp1831 ^{OD1}	2.9

Supplementary Methods

Protein expression and purification

Protein expression was performed using BL21-T1^R cells. Cells were grown in auto-induction ZY-medium (Studier, 2005) with Kanamycin for 4 h at 37 °C. Afterwards, the temperature was decreased to 18 °C and cells were grown overnight. Harvested cells were resuspended in extraction buffer (40 mM Tris/HCl (pH 7.5) 400 mM NaCl, 1 mM DTT, 10 mg/l lysozyme and 5 mg/l DNase I) at room temperature and subsequently lysed by sonification. Lysates were centrifuged at 56,000 x g for 45 min to pellet the cell debris. Supernatants were subjected to affinity chromatography using amylose resin (NEB). Two washing steps were performed using washing buffer (20 mM Tris/HCl (pH 7.5) 200 mM NaCl, 1 mM DTT) at room temperature. Amylose resin was incubated twice with washing buffer supplemented with 10 mM maltose for 15 min for protein elution. The MBP-tag of the PDZ domains was cleaved off using TEV protease (1 mg/ml). Protease was added to the eluted protein in a molar ratio of 1:30 and the reaction incubated at 4 °C overnight. TEV protease and cleaved His₆-MBP-tag was removed using Ni-NTA resin. TEV-cleaved constructs were purified using a Superdex 75 26/60 column (GE Healthcare), where fractions containing protein were pooled and concentrated using a Centricon (MWCO 3,000) (Millipore). Protein concentrations were determined by UV-absorption.

Isothermal titration calorimetry

Isothermal titration calorimetry experiments were performed at 25°C on an iTC200 microcalorimeter (Malvern Instruments Ltd.). A peptide with the sequence ¹⁸³¹DSKDVKEWYV¹⁸⁴⁰ was synthesized by JPT – Innovative Peptide Solutions company. Lyophilized peptide was resuspended in the same buffer as the proteins. Spn-PDZ was injected in steps of 30 µM equivalent concentration against 182 µM of peptide; MBP-Syd-1-PDZ was injected in steps of 18 or 19 µM equivalent concentration against 160 or 174 µM of peptide. In a control experiment, MBP with injected (22 µM equivalents) against 174 µM peptide. All measurements were performed with 20 injections of 2.0 µl volume at intervals of 2 min. The heat released was obtained by integrating the calorimetric output curves. Binding

parameters were calculated with Origin5 software using the “One Set of Sites” curve-fitting model provided by the software.

Thermofluor

A thermofluor analysis was performed for buffer optimization using a Mx3005P qPCR system (Agilent). Buffers containing zinc salts in different concentrations gave a thermal shift of at least 12 °C.

Crystallization and crystal cooling

For crystallization, Spn-PDZ was purified as described, with 100 µM zinc chloride present in all buffers. The protein was concentrated to 60 mg/ml. The unsolubilized peptide (DSKDVKEWYV) was mixed in a three-fold molar excess with the protein and incubated for 2 h on ice. Insoluble peptide was removed by centrifugation (16,000 g for 1 min) prior to the crystallization experiments. The initial crystals were obtained by the sitting-drop vapor-diffusion method at 18 °C with a reservoir solution composed of 0.1 M Tris-HCl (pH 8.5 at RT), 0.01 M nickel chloride and 20 % (w/v) PEG 2000 MME. Crystals were cryo-protected using 20 % (v/v) ethylene glycol, which was added to the reservoir solution.

X-ray data collection, structure determination and refinement

Synchrotron diffraction data were collected at beamline 14.2 of the Joint Berlin MX Laboratory at BESSY (Berlin, Germany). X-ray data collection was performed at 100 K. Diffraction data were processed with XDS¹. The structure of Spn-PDZ in space group $P4_32_12$ was solved by molecular replacement using Phaser-MR², in which the shortened structure of the Spn PDZ domain from *Rattus norvegicus* (PDB entry 3EGG³) was used as a search model. A randomly generated set of 5 % of reflections was excluded from the refinement for the calculation of the free R-factor. The structure was initially refined by applying a simulated annealing protocol and, in later refinement cycles, by maximum-likelihood restrained refinement using PHENIX^{4, 5}. Model building and water picking was performed with COOT⁶. Model quality was evaluated with MolProbity^{4, 7}. Figures were prepared using PyMOL⁸.

Detailed methods for GCaMP5 imaging; assaying spontaneous and evoked release by Ca²⁺ imaging.

Third instar larvae of both sexes expressing UAS-myrGCaMP5⁹ in the muscle were dissected in Ca²⁺ free, ice-cold HL3 saline containing (in mM): NaCl 70, KCl 5, MgCl₂ 20, NaHCO₃ 10, trehalose 5, sucrose 115, Hepes 5 (pH 7.2) at room temperature). The motoneuron nerves were cut below the ventral nerve cord and the CNS was removed. The preparation was allowed to rest for 5-10 min in HL3 containing 1.5 mM CaCl₂ at RT. During this time, the motor nerve of the respective segment was sucked into a stimulation pipette filled with HL3 for later NMJ stimulation. Image sequences (spontaneous and evoked release) were acquired at 20 Hz with an Olympus BX51WI epifluorescence microscope with a 40x (NA 0.8) water immersion objective (Olympus), equipped with a Lambda DG-4 light source (Sutter Instruments, Novato, CA, USA) and a Hamamatsu Orca-Flash 4.0 V2 camera (exposure time 0.05 s). The camera was operated in stream mode using HoKaWo software (vers. 2.9, Hamamatsu Germany). First, spontaneous activity in muscle 4 in segments A2 or A3 was recorded for 100 s. Then evoked release was stimulated 35 times by depolarizing the afferent motor nerve using voltage steps to 10 V. Each step lasted 300 μs and was applied at a frequency of 0.2 Hz with an S48 Stimulator (Grass Technologies, Warwick, RI, USA). The stimulator and camera were triggered using a Digidata 1440A (Axon CNS, Molecular Devices, Sunnyvale, CA, USA), running Clampex software (vers. 10.4, Molecular Devices, UK). The larval fillet was fixed immediately in PBS containing 4 % PFA immediately after the final stimulation was applied. Fillets were then stained for BRP(see above).

Ca²⁺ imaging and data analysis.

Image sequences were processed using ImageJ (version 1.48t and 1.48q). Slight drift between images was corrected with the “TurboReg” plugin (<http://bigwww.epfl.ch/thevenaz/turboreg/>), which uses the “Rigid Body” transformation¹⁰ to register all images to the first frame of the spontaneous recording. Additionally, maximal z-projections of post-hoc confocal images of the GCaMP5 fluorescence were aligned to this target frame using the

“affine” transformation. The same transformation was also applied to the other channel with the BRP staining (Supplementary Fig.10). Single AZs were automatically identified through their intensity maxima and equally-sized regions of interest (ROIs, 0.65 μm diameter) were placed around each maximum (Supplementary Fig.10). Integrated fluorescence intensity values from each ROI were read out from each frame to capture the temporal change in GCaMP5 fluorescence at a particular AZ. Each ROIs was then moved to a region outside of the GCaMP5 signal to obtain a background intensity value, which was subtracted from the signal. Data were transferred to Matlab (Mathworks, vers. R2011a) for further analysis. Spikes were detected by analyzing the background corrected GCaMP5 intensity profiles using a custom-written script. Traces were filtered using a running average filter implemented in the Matlab function “filter” with a box size of four frames. Spikes were identified by detecting signals that exceeded the standard deviation of the signal by a factor of 4 for at least three consecutive frames. The following criteria were applied to prevent the same signal being counted several times at adjacent AZs: only the largest signal in recordings of spontaneous activity was considered if several AZs had simultaneous fluorescence peaks. Signals were only considered for the analysis of evoked episodes if they were temporally locked to the stimulation, with peak values occurring within 1 s after the stimulus. Spikes that coincided at different AZs were only considered if they were at least 2.5 μm apart, otherwise only the largest signal was considered. All signals matching these criteria were evaluated by visual inspection and peaks that showed atypical rise and decay kinetics were rejected. A section of the local GCaMP5 fluorescence signal (2 s prior and 2s after the maximal spike value) was selected to obtain the average GCaMP5 response (Fig. 7c and d) and the baseline corrected by subtracting a line that was fitted to the fluorescence signal during the first and last second of this 4 s window. Traces were then averaged over all events from all AZs in one animal and, finally, averaged over all animals. The total number of spontaneous events per NMJ was divided by the number of analyzed AZs and the acquisition time in order to calculate the frequency of spontaneous events per AZ. The total number of AZs that showed activity at least once

was divided by the total AZ number to obtain the fraction of active AZs. The release probability per AZ was calculated by dividing the total number of stimulus-locked, evoked events per NMJ by the number of AZs and stimuli. All values were then averaged over all animals. The BRP intensities per AZ were measured from confocal maximal projection images using the same ROIs that were used for reading out the GCaMP5 fluorescence. The BRP intensities were then binned in ascending order in five bins containing the same number of AZs and the average BRP intensity as well as the average number of evoked events calculated per AZ. Binned data were then averaged over all animals of one group. Linear fits were performed in OriginPro 6G (vers. 8.0773) taking vertical and horizontal error bars into account. The function “Compare Datasets” was used to test whether the two datasets were significantly different from one another.

Supplementary References

1. Kabsch W. Xds. *Acta Crystallogr D Biol Crystallogr* **66**, 125-132 (2010).
2. McCoy AJ, Grosse-Kunstleve RW, Adams PD, Winn MD, Storoni LC, Read RJ. Phaser crystallographic software. *J Appl Crystallogr* **40**, 658-674 (2007).
3. Ragusa MJ, Dancheck B, Critton DA, Nairn AC, Page R, Peti W. Spinophilin directs protein phosphatase 1 specificity by blocking substrate binding sites. *Nat Struct Mol Biol* **17**, 459-464 (2010).
4. Adams PD, *et al.* PHENIX: a comprehensive Python-based system for macromolecular structure solution. *Acta Crystallogr D Biol Crystallogr* **66**, 213-221 (2010).
5. Afonine PV, *et al.* Towards automated crystallographic structure refinement with phenix.refine. *Acta Crystallogr D Biol Crystallogr* **68**, 352-367 (2012).
6. Emsley P, Lohkamp B, Scott WG, Cowtan K. Features and development of Coot. *Acta Crystallogr D Biol Crystallogr* **66**, 486-501 (2010).
7. Laskowski RA, Macarthur MW, Moss DS, Thornton JM. Procheck - a Program to Check the Stereochemical Quality of Protein Structures. *Journal of Applied Crystallography* **26**, 283-291 (1993).
8. DeLano WL. The PyMOL Molecular Graphics System (2002).
9. Melom JE, Akbergenova Y, Gavornik JP, Littleton JT. Spontaneous and evoked release are independently regulated at individual active zones. *J Neurosci* **33**, 17253-17263 (2013).

10. Thevenaz PT, Ruttimann UE, Unser M. A Pyramid Approach to Subpixel Registration Based on Intensity. *IEEE TRANSACTIONS ON IMAGE PROCESSING* 7, (1998).

Publication IV

Bohme, M. A., C. Beis, S. Reddy-Alla, E. Reynolds, M. M. Mampell, A. T. Grasskamp, J. Lutzkendorf, D. D. Bergeron, J. H. Driller, H. Babikir, F. Gottfert, I. M. Robinson, C. J. O'Kane, S. W. Hell, M. C. Wahl, U. Stelzl, B. Loll, A. M. Walter and S. J. Sigrist (2016). "Active zone scaffolds differentially accumulate Unc13 isoforms to tune Ca(2+) channel-vesicle coupling" Nat Neurosci 19(10): 1311-1320.

1 **Title:**

2 **Active zone scaffolds differentially accumulate Unc13 isoforms to tune Ca²⁺ channel-**
3 **synaptic vesicle coupling**

4

5 Mathias A. Böhme^{1,2,9}, Christina Beis^{1,9}, Suneel Reddy-Alla^{1,9}, Eric Reynolds^{1,9}, Malou M.
6 Mampell¹, Andreas T. Grasskamp^{2,3}, Janine Lützkendorf¹, Dominique Dufour Bergeron¹, Jan
7 H. Driller⁴, Husam Babikir¹, Fabian Göttfert⁵, Iain M. Robinson⁶, Cahir J. O’Kane⁷, Stefan W.
8 Hell⁵, Markus C. Wahl⁴, Ulrich Stelzl⁸, Bernhard Loll⁴, Alexander M. Walter^{3,10,11}, Stephan J.
9 Sigrist^{1,2,10,11}

10 1 Institute for Biology/Genetics, Freie Universität Berlin, Berlin, Germany

11 2 NeuroCure, Cluster of Excellence, Charité Universitätsmedizin, Berlin, Germany

12 3 Molecular and Theoretical Neuroscience, Leibniz-Institut für Molekulare Pharmakologie,
13 Berlin, Germany

14 4 Institute of Chemistry and Biochemistry/Structural Biochemistry, Freie Universität Berlin,
15 Berlin, Germany

16 5 Department of Nanobiophotonics, Max Planck Institute for Biophysical Chemistry,
17 Göttingen, Germany

18 6 Peninsula College of Medicine and Dentistry, Universities of Exeter and Plymouth,
19 Plymouth, United Kingdom

20 7 Department of Genetics, University of Cambridge, Cambridge, United Kingdom

21 8 Institute of Pharmaceutical Sciences, Pharmaceutical Chemistry, University of Graz, Graz,
22 Austria

23

24 9 equal contribution

25 10 equal senior author contribution

26 11 correspondence: stephan.sigrist@fu-berlin.de

27 awalter@fmp-berlin.de

28

29 Editorial correspondence to:

30 stephan.sigrist@fu-berlin.de

31 Prof. Dr. Stephan Sigrist

32 Institut für Biologie / Genetik

33 Takustraße 6

34 14195 Berlin, Germany

35 Tel.: +49 (0)30-838-56940 (FU, Dahlem)

36 Fax: +49 (0)30-838-56938

37 and

38 awalter@fmp-berlin.de

39 Dr. Alexander M. Walter

40 Molecular and Theoretical Neuroscience

41 Leibniz Institute for Molecular Pharmacology

42 Charité Campus Mitte, Charitéplatz 1, 10117 Berlin Germany

43 Tel.: +49 (0)30-450-639-026

44 **ABSTRACT**

45 Brain function relies on fast and precisely timed synaptic vesicle (SV) release at active zones
46 (AZs). SV release efficacy depends on SV-Ca²⁺ channel distances, but molecular
47 mechanisms controlling this are unknown. Here we show that distances can be defined by
48 targeting two Unc13 isoforms to presynaptic AZ sub-domains. Super-resolution and intravital
49 imaging of developing *Drosophila* glutamatergic synapses revealed that the Unc13B isoform
50 was recruited to nascent AZs by the scaffolding proteins Syd-1/Liprin-α, while Unc13A was
51 positioned by Bruchpilot/Rim-binding protein complexes at maturing AZs. Unc13B localized
52 120 nm away from Ca²⁺ channels, while Unc13A localized only 70 nm away, and was
53 responsible for docking SVs at this distance. *Unc13A*^{Null} mutants suffered from inefficient,
54 delayed and EGTA supersensitive release. Mathematical modelling suggests that synapses
55 normally operate via two independent release pathways differentially positioned by either
56 isoform. We identify isoform-specific Unc13/AZ scaffold interactions regulating SV-Ca²⁺
57 channel topology whose developmental tightening optimizes synaptic transmission.

58

59 INTRO

60 Synaptic communication relies on the timed fusion of synaptic vesicles (SV) to release
61 neurotransmitter from the presynapse in response to action potentials (APs). To gain release
62 competence, prior reactions need to take place. Docking, the targeted SV localization to the
63 AZ plasma membrane, and priming, the maturation of SVs into a readily releasable pool
64 (RRP), were shown to require the neuronal SNAREs Syntaxin, SNAP25, and VAMP2¹⁻³. A
65 conformational change from closed to open Syntaxin required to engage all 3 neuronal
66 SNAREs, is thought to be catalyzed by the essential priming factor (M)Unc13, thus
67 establishing an RRP and enhancing SV replenishment following exocytosis^{2, 4-7}. To couple
68 SV release to electrical stimulation by APs, Ca²⁺ ions entering the cell through voltage-gated
69 Ca²⁺ channels activate the Ca²⁺ sensor Synaptotagmin on the SV to trigger fusion¹. The
70 efficacy of synaptic transmission largely depends on the distance between SVs and voltage-
71 gated Ca²⁺ channels. Close proximity is required for immediate responses, which may
72 require active localization of RRP SVs, a process referred to as positional priming⁸⁻¹⁰.

73 At AZs, an evolutionarily conserved set of large proteins is implicated in the spatial
74 organization of synapse topology including RIM, (M)Unc13, Rim-binding protein (RBP),
75 Liprin- α , and ELKS/Bruchpilot (BRP) proteins¹¹. Among these, ELKS/BRP-family proteins,
76 RIMs and RBPs are required to ensure proper Ca²⁺ channel-SV topology, Ca²⁺ channel
77 density and their levels predict release at single AZs¹²⁻¹⁷. Furthermore, Liprin- α organizes AZ
78 composition¹⁸⁻²⁰. Intravital imaging of the AZ assembly-trajectory of the *Drosophila*
79 neuromuscular junction (NMJ) showed that an early Syd-1/Liprin- α scaffold protein complex
80 initiates AZ-assembly. This protein complex precedes a second one containing BRP and
81 RBP by hours^{18, 21}.

82 Here we show that two scaffold protein complexes define the spatio-temporal
83 organization of two Unc13 isoforms during AZ maturation. Unc13B appeared together with
84 the “early” Liprin- α /Syd-1 scaffold and its AZ accumulation was specifically dependent on this
85 scaffold. At matured AZs, Unc13B remained clustered at larger distances from Ca²⁺ channels
86 (>100 nm). Later during the assembly process, Unc13A was positioned and stabilized in

87 discrete clusters via the ELKS/BRP/RBP scaffold close to presynaptic Ca^{2+} channels (<100
88 nm). In line with a function in both molecular priming and vesicle positioning, we find that
89 Unc13A dominates release not only by enhancing the number of docked and primed
90 vesicles, but also by regulating the probability of release, its latency and sensitivity to Ca^{2+}
91 buffers. Our results are in line with two coexisting functional exocytosis pathways with
92 identical Ca^{2+} sensing and fusion mechanisms at mature AZs, differentially positioned by the
93 two Unc13 isoforms whose precise spatio-temporal placement determines AZ maturation
94 and function.

95

96 RESULTS

97 We previously analyzed the developmental assembly and maturation of glutamatergic
98 synapses in *Drosophila* and discovered that the central AZ protein scaffold, consisting of
99 BRP and RBP, is incorporated at an advanced stage of a maturation process lasting many
100 hours¹⁸. Elimination of either BRP or RBP leads to severe SV release deficits, at least partly
101 caused by reduced coupling of Ca²⁺ channels to the SV fusion machinery^{14, 15}. As neither
102 RBP nor BRP are *per se* proteins with established direct function in SV exocytosis, we
103 wondered whether additional effectors among release machinery proteins might be
104 organized via the scaffolding function of the RBP/BRP complexes.

105

106 **Unc13A and B are important for efficient AZ formation**

107 In order to identify novel RBP interaction partners which might be relevant in this context, we
108 performed a pair-wise yeast two-hybrid (Y2H) matrix screen using a construct consisting of
109 the 2nd and 3rd SH3 domains of *Drosophila* RBP as bait. The screen recovered a direct binary
110 interaction with an N-terminal proline-rich (PxxP) motif-containing region of *Drosophila*
111 Unc13A (Figure 1a), one of the two Unc13 isoforms transcribed from a single *Drosophila*
112 *Unc13* locus (www.flybase.org). An arrangement in which two promoters of the same locus
113 produce different isoforms was noted before for the AZ-protein BRP²². Similar to the BRP
114 isoforms, the two Unc13 isoforms differ within their N-terminal region, but are identical at
115 their C-terminal region which includes the so-called C1, C₂B, MUN and C₂C domains²³
116 (Figure 1a,b). Binding of diacylglycerol (DAG) to the C1 domain was shown to induce the
117 translocation of (M)Unc13s to the plasma membrane and to influence vesicular release
118 probability, linking C1 domain activation to a lowering of the energy barrier for SV fusion^{24, 25}.
119 The central C₂B domain is involved in Ca²⁺-dependent phospholipid binding and modulates
120 presynaptic plasticity²⁶. Furthermore, both isoforms harbor the MUN domain, the minimal
121 domain required for molecular priming^{27, 28}. Unlike Unc13B, Unc13A also harbors a central

122 Ca²⁺-dependent Calmodulin (CAM) binding domain that is required for Ca²⁺-dependent
123 acceleration of RRP replenishment at mammalian synapses⁷.

124 To investigate the isoform-specific localization of Unc13A and -B at the *Drosophila*
125 NMJ, we raised antibodies (ABs) against their N-terminal regions (epitopes see Figure 1a,b)
126 which detected both proteins at Wild type NMJ terminals (Figure 1c,d). Unc13A showed a
127 somewhat higher degree of colocalization with the AZ-specific BRP signal than Unc13B
128 (Figure 1c,d; arrows in 1d indicate Unc13B spots devoid of BRP; Pearson's correlation
129 coefficient: BRP/Unc13A (n=21 NMJs from 6 larvae): 0.535 ± 0.021; BRP/Unc13B (n=11
130 NMJs from 4 larvae): 0.458 ± 0.02; p=0.0124 (U=52), Mann-Whitney U-test). To ensure the
131 specificity of staining and to investigate the functionality of both isoforms, we generated
132 isoform-specific mutant alleles. For this, we performed chemical (ethane methyl sulfonate;
133 EMS) mutagenesis, screened for chromosomes that were lethal over a 4th chromosomal
134 *Unc13^{Null}* allele (*P84200*²³) and isolated two alleles harbouring premature STOP codons
135 which specifically affect Unc13A translation (*EMS7.5* (from now on called *Unc13A^{Null}*);
136 *EMS7.96*; see Figure 1a). When these alleles were placed in *trans* to the *Unc13^{Null}* allele, few
137 positive larvae were observed. These were hardly able to move and only occasionally
138 developed to weak adult flies. However, by incorporating a genomic clone (pacman
139 technology²⁹) encoding the complete *Unc13* locus (from now on 'Ctrl' if not specified
140 otherwise) in the *Unc13^{Null}* allele background, adult vitality was restored, proving that the
141 deficits of the *Unc13A* specific alleles in fact map to the *Unc13* locus. In these flies, staining
142 for Unc13A and B was restored (Figure 1e,f) while NMJs of larvae carrying the *Unc13A^{Null}*
143 mutation specifically lost the Unc13A-, but not the Unc13B-signal (Figure 1g,h). Notably, no
144 Unc13B-specific mutations could be isolated when screening for lethality over the *Unc13^{Null}*
145 situation, possibly because *Unc13B* specific mutants are viable. To nonetheless create
146 specific *Unc13B* mutants, we deleted the first 1000 base pairs of the *Unc13B* specific N-
147 terminal exon on the basis of a large genomic clone and re-inserted this transgene into an
148 *Unc13^{Null}* mutant background (*Unc13B^{Null}*; see Figure 1b for deleted region). The *Unc13B*
149 deficient flies were viable to adulthood and fertile. At *Unc13B^{Null}* mutant NMJs, Unc13B

150 staining was lost while Unc13A staining was normal (Figure 1i,j). Furthermore, we produced
151 C-terminally GFP-labeled versions of both isoforms, which, when expressed in motoneurons,
152 effectively reached NMJ terminals and occupied typical positions (compare Figure 1k with 1c
153 and Figure 1l with 1d).

154 Previous analyses showed that *Drosophila Unc13^{Null}* mutant alleles are embryonically
155 lethal²³. Given that both isoform-specific mutants reached larval stages, we concluded that
156 both isoforms must be functionally relevant, and started to comparatively analyze their
157 importance for the AZ-maturation at larval NMJs. AZ-densities were significantly reduced in
158 terminals lacking either Unc13A or Unc13B (Figure 1m-p) and NMJs had a tendency to be
159 smaller in both genotypes (not shown). Despite these similarities, we also identified major
160 differences. At *Unc13A^{Null}* mutant NMJ terminals, individual AZs often showed larger BRP-
161 labeled AZs (arrows in Figure 1m), while *Unc13B^{Null}* AZs appeared normal (Figure 1n).

162

163 **Unc13B precedes Unc13A at nascent AZs**

164 Developing AZs at NMJ terminals undergo a stereotypical but desynchronized maturation
165 process where new synapses are “born” in-between preexisting ones. Unlike Unc13A, which
166 showed a somewhat higher degree of overlap with BRP (compare Figure 1c,k with 1d,l),
167 Unc13B had a tendency to be prominent at inter-bouton sites (Figure 1l; arrows), where new
168 AZs often form (Böhme and Sigrist, unpublished observation). To analyze the accumulation
169 of Unc13A and Unc13B along the AZ “maturation trajectory”, we comparatively analyzed AZ-
170 accumulation of both isoforms in relation to the early arriving scaffold protein Liprin-α by
171 intravital imaging of developing NMJ terminals. Early third instar larval NMJs were imaged
172 once (=time point zero) and the same NMJs were re-imaged 6 hours later to reconstruct the
173 temporal sequence of protein arrival (Figure 2a). At AZs of larvae co-expressing Unc13A^{C-}
174 ^{term-GFP} with Liprin-α (motoneuronally expressed Liprin-α^{Strawberry}), we frequently observed
175 single Liprin-α spots that did not contain Unc13A^{C-term-GFP} at time point zero (Figure 2b,
176 arrows), but never observed single Unc13A^{C-term-GFP} spots without Liprin-α labelling.

177 Interestingly, Unc13B^{C-term-GFP} and Liprin- α colocalized almost entirely at any investigated time
178 point (Figure 2c). When tracking the temporal sequence of protein arrival at maturing AZs,
179 individual Liprin- α spots were often also positive for Unc13A^{C-term-GFP} at the second imaging
180 time point (compare Figure 2d with 2e). In contrast, nearly all newly forming AZs were
181 positive for both Unc13B^{C-term-GFP} and Liprin- α (compare Figure 2f with 2g). We conclude that
182 Unc13B arrives at a similar time point as Liprin- α and thus in an early phase of the AZ
183 maturation^{18, 21, 30}, while Unc13A arrives later.

184

185 **Unc13A/B clustering depends on different scaffolding proteins**

186 Apart from Liprin- α , Syd-1, another major scaffolding protein, also arrives early at nascent
187 AZs. We therefore investigated whether Unc13B clustering depended on these proteins.
188 While Unc13A and BRP levels were only slightly reduced in *Liprin- α ^{Null}* and *Syd-1^{Null}* mutants
189 (Figure 3a,c; Supplementary Figure 1a-f), Unc13B was almost completely lost at AZs of
190 *Liprin- α ^{Null}* mutants (Figure 3b,d; Supplementary Figure 1i,j). Similar (albeit somewhat
191 weaker) effects were observed in *Syd-1^{Null}* mutants (Supplementary Figure 1g-j). To
192 investigate whether Liprin- α and Syd-1 interact physically with Unc13B, suitably sized
193 domains of Liprin- α and Syd-1 were tested against the Unc13B N-terminus in a Y2H
194 approach (Supplementary Figure 2a for domain structures and Y2H constructs) and indeed
195 revealed several interactions. Specifically, the central N-terminal Unc13B fragment (fragment
196 2; Supplementary Figure 2a) interacted with an N-terminal fragment of Liprin- α . This
197 fragment, along with fragment 1, also interacted with a stretch of Syd-1 between the N-
198 terminal PDZ and the central C₂ domain (Supplementary Figure 2a).

199 As previously mentioned, we found a direct interaction of an N-terminal Unc13A
200 sequence with RBP in a pair-wise Y2H matrix screening, and Unc13A immunoreactivity
201 largely overlapped with BRP at the confocal level (Figure 1c,k). Thus, we tested for a
202 dependence of Unc13A and -B on the “late scaffold” components. Unc13A (and, similarly,
203 BRP) levels were severely reduced at NMJs following *Brp* knock-down (via RNAi;

204 Supplementary Figure 3a,b,d-f) and in *Rbp*^{Null} mutants (Supplementary Figure 3a,c,d-f).
205 Moreover, hardly any Unc13A or BRP spots could be detected upon *Brp* knockdown in
206 *Rbp*^{Null} (Figure 3e,g; Supplementary Figure 3d-f; double-homozygous combinations of null
207 alleles of *Rbp* and *Brp* hardly survived into larval stages). With regard to Unc13B levels,
208 neither *Brp* knock-down (Supplementary Figure 3g,h,j,k), nor *Rbp* deletion (Supplementary
209 Figure 3g,i,j,k), nor the combined knockdown of *Brp* in the *Rbp*^{Null} background significantly
210 affected Unc13B levels (Figure 3f,h; Supplementary Figure 3j,k).

211 To address the molecular basis of the redundancy between BRP and RBP in Unc13A
212 accumulation, we tested for interactions of the Unc13A N-terminal region with various BRP
213 and RBP fragments (Supplementary Figure 2b). The Y2H screen recovered that solely the
214 very N-terminal fragment of Unc13A, including the PxxP motif (Fragment 1; Supplementary
215 Figure 2b), bound to C-terminal fragments of RBP. This fragment also interacted with an N-
216 terminal fragment of BRP (Supplementary Figure S2b). These results make it likely that
217 direct N-terminal interactions of Unc13A with BRP and RBP accumulate Unc13A at the AZ in
218 a partially redundant fashion. To independently test the differential role of the BRP/RBP
219 scaffold in clustering Unc13A, but not Unc13B, we made use of the *Rab3* mutant phenotype
220 in which BRP is concentrated in only about half of all available AZs, leaving the other half
221 (which are still positive for postsynaptic glutamate receptors) devoid of this key presynaptic
222 release component³¹. In this situation of more extreme local patterning, we found that RBP
223 also exclusively concentrated at BRP positive sites (not shown), indicating that RBP and
224 BRP tightly co-operate and invariably co-cluster within NMJ AZs. Notably, at *Rab3*^{Null} NMJs,
225 Unc13A strictly “followed” the BRP scaffold and appeared to scale with the local amounts of
226 BRP (Figure 3i). In contrast, Unc13B also segregated towards BRP/RBP negative sites
227 (Figure 3j; arrows indicate Unc13B positive, but BRP negative positions, while arrowheads
228 indicate sites positive for both Unc13B and BRP). In conclusion, we find a remarkable
229 specificity concerning the scaffold accumulation of the two Unc13 isoforms: whereas Unc13A
230 is recruited by the “late” BRP/RBP scaffold, Unc13B is recruited via the “early” Liprin- α /Syd-1
231 scaffold.

232 **Unc13A dominates evoked SV release at larval NMJs**

233 As both Unc13 isoforms localized to NMJ AZs via different scaffold complexes, we went on
234 investigating their functional roles in AP-evoked and spontaneous SV release performing
235 two-electrode voltage clamp recordings (TEVC) at 3rd instar larval NMJs of both *Unc13*
236 isoform specific mutants (Figure 4). Recordings of *Unc13B^{Null}* mutant animals uncovered a
237 rather moderate but significant reduction of evoked excitatory NMJ currents (eEJCs; Figure
238 4a,c) without changes in their kinetics (Figures 4b,d; Supplementary Figure 4a,b). The
239 amplitudes of spontaneous release events were unchanged, while frequencies were slightly
240 but non-significantly reduced (Figure 4e-g). We found no differences in miniature excitatory
241 NMJ current (mEJC) rise times but significantly longer decay times in *Unc13B^{Null}* cells
242 (Supplementary Figure 4e,f). Strikingly, mutants of *Unc13A* showed drastically reduced
243 eEJCs, less than 10 % of control values, and increased eEJC 10%-90% rise times (Figure
244 4h-k). Loss of Unc13A also increased the time-to-peak (ttp) while the decay was unchanged
245 (Supplementary Figure 4c,d). In the *Unc13A^{Null}* mutants we discovered a higher frequency of
246 spontaneous events which may have been a consequence of their increased amplitude (thus
247 resulting in an increased signal-to-noise ratio, facilitating their detection; Figure 4l-n) but
248 mEJCs kinetics were unchanged (Supplementary Figure 4g,h). Thus, compound recordings
249 at 3rd instar NMJ terminals demonstrated a fundamental role of Unc13A for evoked release,
250 which cannot be substituted by Unc13B.

251

252 **Distinct sub-active zone patterning of Unc13A versus Unc13B**

253 At the confocal level we had noticed that the endogenous Unc13A signal showed a stronger
254 overlap with the AZ-specific BRP label than Unc13B (Figure 1c,d). To analyze the sub-AZ
255 distribution of both isoforms in detail, we performed dual-color super-resolution STED
256 microscopy (with 35 nanometer lateral resolution for both channels) which confirmed this
257 impression with Unc13A being localized closer to the BRP positive signals (Figure 5a). At
258 single AZs, Unc13A localized to discrete clusters facing the inner margin of antibody staining

259 against BRP in top view (Figure 5b). Unc13A signals appeared interspersed with the RBP
260 signal which we previously showed to form a ring-like array of clusters in the AZ center¹⁵
261 (Figure 5c). In striking contrast, Unc13B clusters were often attached to the outer edge of the
262 BRP signal but sometimes also localized at BRP-negative positions (Figure 5d, arrows). At
263 single BRP-labeled AZs, Unc13B was located further away from the AZ center (Figure 5e) in
264 some distance to the RBP signal (Figure 5f). Our previous analysis showed that Syd-1/Liprin-
265 α co-cluster and localize at the outer edge of matured AZs^{18, 21}. In fact, Syd-1 clusters closely
266 matched the positions of Unc13B (compare Figure 5e with 5g) and co-labelling of
267 motoneuronally overexpressed Syd-1^{GFP} and endogenous Unc13B revealed their close
268 apposition (Figure 5h). We also investigated the differential localization of BRP and Unc13B
269 in the *Rab3^{Null}* mutant background with STED resolution. In *Rab3^{Null}*, BRP ring-like structures
270 clustered together and Unc13B still localized at the outer edge of this scaffold (Figure 5i;
271 clustered AZs magnified in 5j; arrowheads point to Unc13B immunoreactivity at the edge of
272 clustered BRP rings). In addition, Unc13B immunoreactivity was also observed at BRP/RBP
273 negative positions (Figure 5i; arrows). Thus, early and late AZ scaffold complexes not only
274 control the temporal, but also the spatial patterning of Unc13 isoforms at single AZs.

275

276 **Unc13A mediates SV docking at the AZ center**

277 Previous work showed that the voltage operated N/P/Q-type Ca²⁺ channel $\alpha 1$ subunit
278 Cacophony (Cac) is exclusively responsible for evoked release at NMJ AZs and clusters in
279 the center of the BRP labeled AZ^{15, 18, 32}. To map the topology of Unc13 isoforms with respect
280 to the Ca²⁺ channels, we investigated AZs immunostained for Cac^{GFP} and Unc13A and -B,
281 respectively, using STED microscopy (Figure 6a,b). We found that Unc13A localized close to
282 Cac^{GFP}, while Unc13B was found at larger distances, in line with the distribution of the two
283 isoforms with respect to BRP (Figure 5b,e). To obtain a quantitative measure of the local
284 isoform distribution at single AZs, we calculated the average intensity profiles of the two
285 isoforms from the center of the BRP scaffold (see methods for details; Figure 6c). The

286 maximum of the average (and normalized) intensity profile was found around 70 nm away
287 from the AZ center in the case of Unc13A, and around 120 nm away for Unc13B (Figure 6c).
288 Unc13 proteins have established functions in vesicle docking^{2, 33}. Since Unc13A localized
289 close to Ca²⁺ channels and dominated release, we wondered whether Unc13A specifically
290 targeted SVs close to the Ca²⁺ channels in the AZ center to facilitate their release. SV
291 distributions are ideally captured with high-pressure freeze (HPF) electron microscopy, which
292 preserves AZ-morphology without fixation artefacts². We determined lateral distances of
293 docked SVs (with no discernible distance to the plasma membrane) to the center of the
294 electron dense *Drosophila* cytomatrix (T-bar), which is assembled from the BRP/RBP
295 scaffold and overlays the position of the AZ-centered Ca²⁺ channels^{14, 15, 18}. At Wild type AZs,
296 SVs were often docked in close proximity to the T-bar (Figure 6d; black circles; quantification
297 in f). In contrast, in *Unc13A^{Null}*s, the number of docked SVs was reduced (Figure 6e,g), but
298 neither total nor T-bar tethered SV-numbers were changed (data not shown and Figure 6h).
299 Loss of SV-docking was specific to positions close to the AZ (T-bar) center (Figure 6e; black
300 circles; quantification in f), resulting in increased average distances from the AZ center from
301 87 nm to 147 nm (Figure 6i). Subtracting the average vesicle distribution at *Unc13A^{Null}* AZs
302 from the one in the Wild type controls revealed Unc13A-specific docking positions, which
303 peaked around 50 nm (Figure 6f, grey dotted line), in close agreement with the position of
304 maximal Unc13A immunoreactivity from the AZ center seen by STED microscopy (70 nm;
305 compare Figure 6f with 6c). We did not detect any difference in SV diameters between
306 *Unc13A^{Null}* and Wild type animals (*Unc13A^{Null}* (n=16 AZs from 2 larvae): 27.44 ± 0.38 nm;
307 Wild type (n=10 AZs from 5 larvae): 27.40 ± 0.65 nm; p = 0.7102 (U=72.5), Mann-Whitney U-
308 test) suggesting that an increase in neurotransmitter content is unlikely to cause the
309 observed increased mEJC amplitudes (Figure 4m). Together, our data suggest that both
310 isoforms differ dramatically in their sub-AZ localization, with Unc13A mediating SV-docking
311 close to Ca²⁺ channels.

312

313

314 **Unc13A controls vesicular release probability**

315 Previous analyses in several systems have identified Unc13 proteins as essential exocytosis
316 factors with established functions in SV docking and priming^{2, 5, 6, 34}. In line with this, fewer
317 (~50%) SVs were docked in *Unc13A^{Null}*s (Figure 6g). Recently it was suggested that docking
318 and priming are morphological and physiological correlates of the same molecular process².
319 However, the (~90 %) reduction of release at *Unc13A^{Null}* NMJs (Figure 4j) was much larger
320 than the (~50 %) reduction of docked vesicles. Our data therefore argue that not only
321 docking and priming are reduced but that the remaining vesicles in *Unc13A^{Null}*s further suffer
322 from reduced release probability (pVr) in response to single APs. Changes in pVr can be
323 detected by a shift in the apparent Ca²⁺ sensitivity of release which can be probed by
324 monitoring evoked transmission while titrating extracellular Ca²⁺ concentrations³⁵. When
325 performing such experiments, we found that absolute eEJC amplitudes increased with
326 extracellular Ca²⁺ concentrations in both genotypes, as expected from increased AP-induced
327 Ca²⁺ currents. However at *Unc13A^{Null}* NMJs, exocytosis was highly significantly reduced at all
328 investigated extracellular Ca²⁺ concentrations (Figure 7a,b; Supplementary Table 1).
329 Importantly, we observed a major shift in the dependence of neurotransmitter release on
330 extracellular Ca²⁺, reflected in a rightward shift of the dependence of normalized release,
331 without detectable changes in the slope (Figures 7c; Supplementary Figure 5a-c). This
332 demonstrates that Unc13A-loss reduced the sensitivity of SV release on extracellular Ca²⁺,
333 but not its cooperativity. To probe for an altered pVr at *Unc13A^{Null}* NMJs by an independent
334 means, we investigated short-term plasticity in response to paired AP stimuli given at short
335 (10 ms) intervals. The paired pulse ratio (PPR=eEJC₂/eEJC₁; second eEJC amplitude
336 divided by the first) was investigated at all extracellular Ca²⁺ concentrations (except for the
337 0.75 mM data point in *Unc13A^{Null}* where calculation was not reliable because eEJC₁
338 amplitudes were generally close to zero). In line with reduced pVr, we found that *Unc13A^{Null}*
339 synapses displayed stronger facilitation at all extracellular Ca²⁺ concentrations (Figure 7d,e;
340 Supplementary Table 1). This effect was specific to the A isoform because loss of Unc13B

341 neither altered the apparent Ca^{2+} -dependence of release nor the PPRs (Supplementary
342 Figure 5d-h; Supplementary Table 1).

343 Coupling distances between Ca^{2+} channels and SVs can greatly influence pVr^{9, 10, 36}
344 and since deletion of *Unc13A* resulted in loss of SV-docking close to the AZ center (and
345 therefore to the Ca^{2+} channels; Figure 6e,f,i) we tested whether *Unc13A*^{Null} AZs suffered from
346 looser Ca^{2+} channel-SV coupling by studying the effects of the slow exogenous Ca^{2+} buffer
347 EGTA. A competition between this buffer and the SV release machinery for Ca^{2+} leads to an
348 inhibition of SV release, which largely depends on the distances Ca^{2+} ions need to diffuse
349 from the channel to the SV: the larger the distance, the stronger the inhibition by EGTA^{8, 37}.
350 To investigate genotype-specific changes in EGTA sensitivity, APs were elicited at low
351 frequencies (0.1 Hz) and after 5 baseline stimulations, EGTA-AM (an esterified membrane-
352 permeable version of EGTA, final concentration 200 μM) was added to the bath and eEJCs
353 were monitored for 30 min. Consistent with looser Ca^{2+} channel-SV coupling, we found that
354 at *Unc13A*^{Null} mutant synapses, relative amplitudes declined much faster (Figures 7f,g;
355 Supplementary Figure 5i-k), reached lower asymptotic values (Supplementary Figure 5k) and
356 were reduced at all investigated time points (Figures 7g; Supplementary Figure 5i). We could
357 exclude that this was due to differential loading of AM-esters, because incubation with the
358 fast Ca^{2+} buffer Bapta-AM (which also affects vesicles close to the Ca^{2+} source) led to
359 indistinguishable reductions of eEJC amplitudes regardless of the genotype (Supplementary
360 Figure 5l-o). Together, our data establish that *Unc13A* is required to maintain proper pVr and
361 its loss results in an increased EGTA sensitivity, consistent with a function in tight coupling of
362 SVs and Ca^{2+} channels.

363

364 **Co-existence of nano- and microdomain coupling at single AZs**

365 Given the differential positioning of the two *Unc13* isoforms, we next wanted to investigate
366 whether SV release from Wild type AZs may occur from two differentially placed pathways
367 (A- and B-pathway; Figure 7i) and whether the *Unc13A*^{Null} release phenotype may reflect loss
368 of the closely coupled one. We hypothesized that the two pathways merely differed in

15

369 positioning, but were independent and had identical fusion and Ca^{2+} sensing mechanisms.
370 To quantitatively test this hypothesis against our data, we turned to mathematical modelling
371 to describe SV release from both pathways in the Wild type and from the B-pathway only in
372 the *Unc13A^{Null}* situation (Figure 7i). A necessary assumption of our model was that Ca^{2+}
373 channels were localized in the AZ center in both genotypes, which was confirmed in STED
374 analyses (data not shown). However, *Unc13A^{Null}* AZs had larger BRP ring diameters
375 (Supplementary Figure 6a-d) and increased Cac^{GFP} spot sizes (Supplementary Figure 6e-g),
376 suggestive of an increased Ca^{2+} channel number per AZ, which we accounted for in our
377 model (see methods for details).

378 AP-induced Ca^{2+} influx was described from a point source in the AZ-center and Ca^{2+}
379 dynamics were simulated in space and time (Figure 7h). Due to an increased distance, Ca^{2+}
380 transients reached lower peak amplitudes and were delayed at the B pathway (Figure 7i). SV
381 release was driven by the same Ca^{2+} sensing mechanism at both pathways (allosteric five-
382 site binding model³⁸; see Supplementary Table 2 for all parameter values) and eEJCs were
383 calculated by convolving vesicle release rates with genotype-specific mEJCs (Figure 7j, see
384 methods for details). To calculate the parameters of our model, especially the distances of
385 the two pathways from the AZ center, we simultaneously fit the output of the model to all
386 experimental data of both genotypes (see Supplementary Table 1 for simulated values,
387 Supplementary Table 2 for parameter values, and methods for more details). The best fit
388 resulted in a very satisfactory agreement of simulation and experimental data (data are
389 points, model predictions lines in Figure 7b,c,e,g), demonstrating that a parallel arrangement
390 of micro- and nanodomain coupled release pathways can explain the observed phenotype. In
391 fact, loss of pathway A in this model was sufficient to account for all phenotypes of the
392 *Unc13A^{Null}*: reduced exocytosis (Figure 7b,j), delayed release (calculated eEJCs had a
393 difference in time-to-peak (ttp) of $\Delta\text{ttp} = 1.2$ ms; Supplementary Figure 4c and Figure 7j),
394 rightward shift in the dependence on extracellular Ca^{2+} (Figure 7c), paired pulse facilitation
395 (Figure 7e,j) and increased sensitivity to EGTA (Figure 7g). Finally, though not constrained in
396 any way, distances of the two release pathways to the Ca^{2+} channels in the model were

397 calculated to 76.75 nm and 144.7 nm respectively, in close agreement with the distance of
398 Unc13A and -B proteins from the AZ center quantified by STED microscopy (70 nm and
399 120 nm, Figure 6c). Together, our collective data and theoretical calculations favor a
400 scenario in which two SV release pathways, whose positions are determined by the priming
401 factors Unc13A and/or B, operate in parallel via the same Ca^{2+} sensing mechanism.

402

403

404 **DISCUSSION**

405 All presynaptic AZs accumulate scaffold proteins from a canonical set of few protein families,
406 which are characterized by extended coiled-coil stretches, intrinsically unstructured regions
407 and a few classical interaction domains, particularly PDZ- and SH3-domains. These multi-
408 domain proteins collectively form a compact “cytomatrix” often observable by electron dense
409 structures covering the AZ membrane which were found to physically contact SVs, and thus
410 suggested to promote SV docking and priming, as well as to recruit Ca²⁺ channels¹²⁻¹⁵. Still,
411 how the structural scaffold components (ELKS, RBP, RIM, Liprin-α) tune the functionality of
412 the SV release machinery remains largely enigmatic. Liprin-α is crucial for the AZ assembly
413 process and at *Drosophila* NMJ AZs, Liprin-α/Syd-1 cluster formation initializes the assembly
414 of an “early” scaffold complex, which subsequently guides the accumulation of a “late”
415 RBP/BRP scaffold complex^{18-20, 39}. Here we provide evidence that these scaffold complexes
416 together operate as “molecular rulers” which confer a remarkable degree of order, patterning
417 AZ composition and function in space and time: the “early” Liprin-α/Syd-1 clusters recruit
418 Unc13B and this scaffold serves as a template to accumulate the “late” BRP/RBP scaffold
419 which recruits Unc13A (Supplementary Figure 7). Spatially, Unc13 isoforms are precisely
420 organized in the 10s of nanometers range which our data suggest to be instrumental to
421 control SV release probability and SV-Ca²⁺ channel coupling (see below). As a molecular
422 basis of this patterning and recruitment, we identified a multitude of molecular contacts
423 between the Unc13 N-termini and the respective scaffold components using systematic Y2H
424 analysis. As one out of several interactions, we identified a cognate PxxP motif within the N-
425 terminus of Unc13A to interact with the 2nd and 3rd SH3 domain of RBP (Supplementary
426 Figure 2b). Point mutants within the PxxP motif interfered with the binding of the RBP-SH3
427 domains II and III on the Y2H level, however, were without major impact on Unc13A
428 localization and function when introduced into an *Unc13* genomic transgene (data not
429 shown). Nonetheless, elimination of the scaffold components BRP and RBP on the one-or
430 Liprin-α on the other hand, drastically impaired the accumulation of Unc13A or -B. We
431 suggest that these results are explained by a multitude of parallel interactions which provide

432 the avidity needed to enrich the respective Unc13 isoforms in their specific “niches” and may
433 cause a functional redundancy among interaction motifs, as we likely observed in the case of
434 the Unc13A PxxP motif. Future analysis will also have to investigate these interaction
435 surfaces in greater detail, and address how exactly “early” and “late” scaffolds coordinate AZ
436 assembly.

437 Unc13 proteins have well-established functions in SV docking and priming^{2, 23, 33, 34}.
438 Accordingly, we observed that loss of Unc13A resulted in overall reduced SV-docking without
439 affecting T-bar-tethered SVs (Figure 6g,h), which is qualitatively opposite to a function of
440 BRP in SV-localization, whose C-terminal amino acids function in T-bar-tethering, but not
441 docking. Mutants lacking these residues suffer from increased synaptic depression⁴⁰,
442 suggesting a role in SV replenishment. Therefore, in addition to its role in localizing Unc13A
443 to the AZ reported here, BRP may also cooperate functionally with Unc13A by facilitating SV
444 delivery to docking sites.

445 Synapses are highly adapted to their specific features, varying widely concerning their
446 release efficacy and short-term plasticity. These features impact on information transfer and
447 may provide neurons with the ability to detect input coherence, maintain stability, and
448 promote synchronization. Differences in the “biochemical milieu of SVs” can tune priming
449 efficacy and release probability, which largely affects short-term plasticity⁴¹. In our
450 experiments, we could show that Unc13A-loss resulted in dramatically (~90%) reduced
451 synaptic transmission which exceeded the (~50%) reduction in SV-docking, pointing to an
452 additional function in enhancing release efficacy. These changes were paralleled by
453 drastically increased short-term facilitation as well as EGTA super-sensitivity and could be
454 due to decreased Ca²⁺ sensitivity of the molecular release machinery, e.g. mediated by
455 different Synaptotagmin-type Ca²⁺ sensors, or different numbers of SNARE complexes^{12, 42},
456 ⁴³. However, while we observed a rightward shift of the dependence of normalized release
457 amplitudes on extracellular Ca²⁺ concentration at Unc13A deficient synapses, its slope and
458 thus Ca²⁺-cooperativity was unaltered, arguing against fundamentally different Ca²⁺-sensing
459 mechanisms (Figures 7c; Supplementary Figure 5a-c). Instead we favor a scenario in which

460 SV Ca^{2+} -sensing is conserved, but local Ca^{2+} signals at SV positions are attenuated because
461 of their larger distances to Ca^{2+} channels upon Unc13A-loss. Both Unc13 isoforms were
462 clearly segregated physically with different distances to the Ca^{2+} channel cluster and loss of
463 Unc13A selectively reduced the number of docked SVs in the AZ center. These findings are
464 easiest explained by Unc13A promoting the docking and priming of SVs closer to Ca^{2+}
465 channels than Unc13B. In fact, mathematical modelling reproduced our data by merely
466 assuming release from two independent pathways with identical Ca^{2+} sensing and fusion
467 mechanisms which only differed in their physical distance to the Ca^{2+} source in the AZ
468 center. The distances estimated by the model were in very good agreement with the
469 positions of the two Unc13 isoforms defined by STED microscopy. Thus, our data suggest
470 that differences in the distance of SVs in the 10's of nm range to the Ca^{2+} channels mediated
471 by the two Unc13 isoforms likely contribute profoundly to the observed phenotypes. We imply
472 that the role of the N-terminus is to differentially target the isoforms into specific zones of the
473 AZ, while the conserved C-terminus confers identical docking and priming functions at both
474 locations. Notably, recent work in *C. elegans* also characterized two Unc13 isoforms, with
475 fast release being mediated by UNC-13L, whereas slow release required both UNC-13L and
476 -S⁴⁴. The proximity of the UNC-13L isoform to Ca^{2+} entry sites was mediated by the protein's
477 N-terminal C₂A-domain (not present in *Drosophila*) and was critical for accelerating
478 neurotransmitter release, and for increasing/maintaining the probability of evoked release
479 assayed by the fraction of AP- to sucrose-induced release⁴⁵. In contrast, the slow SV release
480 form dominantly localized outside AZ regions⁴⁴. Thus it would be interesting to investigate the
481 sub-AZ distribution of *C. elegans* Unc-13 isoforms and test whether the same scaffold
482 complexes as in *Drosophila* mediate the localization of the different Unc-13 isoforms.

483 Striking differences in short-term plasticity have been reported for mammalian Unc13
484 isoforms⁴⁶. The mammalian genome harbours five Munc13 genes¹¹. Of those, Munc13-1, -2
485 and -3 are expressed in the brain and function in SV release¹¹, and differential expression of
486 Munc13 isoforms at individual synapses may represent a mechanism to control short-term
487 plasticity⁴⁶. Thus, it might be warranted to analyze whether differences in the sub-active zone

488 distribution of Munc13 isoforms contribute to these aspects of synapse diversity in the rodent
489 brain.

490 Fast and slow phases of release have recently been attributed to parallel release
491 pathways operating in the Calyx of Held of young rodents (56 nm and 135 nm)⁴⁷ qualitatively
492 matching the co-existence of two differentially positioned release pathways described here.
493 Our finding of discretely localized release pathways with distances larger than 60 nm is
494 further in line with the recent suggestion that SVs need to be positioned outside an
495 “exclusion zone” from the Ca²⁺ source (~50 nm distance to the center of the SV for the Calyx
496 of Held)⁴⁸. At mammalian synapses, developmental changes in the coupling of SVs and Ca²⁺
497 channels were described^{47, 49, 50}, which qualitatively matches the sequential arrival of loosely
498 and tightly coupled Unc13B and -A isoforms during synaptogenesis described here. Thus,
499 our work suggests that differential positioning of Unc13 isoforms couples functional and
500 structural maturation of AZs. To what degree modulation of this process contributes to the
501 functional diversification of synapses should be an interesting subject of future analysis.

502

503 **ACKNOWLEDGEMENT**

504 This work was supported by grants from the Deutsche Forschungsgemeinschaft to S.J.
505 Sigrist (Exc 257, TP A3 and A6 SFB 958, TP B9/SFB665; TP09/SFB740) and J.H. Driller,
506 M.C. Wahl, B. Loll (TP A6/SFB958). A.M. Walter was supported by a DFG Emmy Noether
507 grant. M.A. Böhme was supported by a Ph.D. fellowship from the graduate school GRK 1123
508 funded by the DFG and by the SFB 740. A.T. Grasskamp was supported by a NeuroCure
509 Ph.D. fellowship within the International Graduate Program Medical Neurosciences funded
510 by the DFG (Exc257). We would like to thank Madeleine Brünner and Anastasia Stawrakakis
511 for excellent technical assistance. We are grateful to Sean Sweeney for help with the EMS
512 screen and to Tanja Matkovic for help with cloning.

513

514 **AUTHOR CONTRIBUTIONS**

515 M.A.B, S.R-A, A.M.W and S.J.S conceived the project. M.A.B and M.M.M performed all
516 confocal and in vivo imaging experiments and analysed the data. M.A.B performed STED
517 experiments and analysed the data. C.B., S.R-A and E.R. performed all electrophysiological
518 experiments and C.B. and E.R. analysed the data. J.L., U.S. and J.H.D. performed and
519 analysed Y2H experiments. M.C.W and B.L. contributed to the Y2H experiments and
520 analysis. C.B. and D.D.B. performed HPF experiments and C.B. analyzed the data. A.T.G
521 and A.M.W. performed modelling and simulation. H.B. and M.M. created antibodies and
522 isoform specific mutants. I.M.R. and C.J.O performed the EMS screen. F.G. and S.W.H.
523 developed and built the STED microscope. M.A.B., A.M.W. and S.J.S wrote the paper with
524 input from all co-authors.

525

526 **COMPETING INTERESTS**

527 All authors declare no conflicting financial and non-financial interest.

- 529 1. Jahn, R. & Fasshauer, D. Molecular machines governing exocytosis of synaptic
530 vesicles. *Nature* **490**, 201-207 (2012).
- 531 2. Imig, C., *et al.* The morphological and molecular nature of synaptic vesicle priming at
532 presynaptic active zones. *Neuron* **84**, 416-431 (2014).
- 533 3. Walter, A.M., Wiederhold, K., Bruns, D., Fasshauer, D. & Sorensen, J.B.
534 Synaptobrevin N-terminally bound to syntaxin-SNAP-25 defines the primed vesicle
535 state in regulated exocytosis. *J. Cell Biol.* **188**, 401-413 (2010).
- 536 4. Ma, C., Li, W., Xu, Y. & Rizo, J. Munc13 mediates the transition from the closed
537 syntaxin-Munc18 complex to the SNARE complex. *Nat. Struct. Mol. Biol.* **18**, 542-549
538 (2011).
- 539 5. Man, K.M., *et al.* Identification of a Munc13-sensitive step in chromaffin cell large
540 dense-core vesicle exocytosis. *eLife* **4** (2015).
- 541 6. Varoqueaux, F., *et al.* Total arrest of spontaneous and evoked synaptic transmission
542 but normal synaptogenesis in the absence of Munc13-mediated vesicle priming. *Proc.*
543 *Natl. Acad. Sci. U. S. A.* **99**, 9037-9042 (2002).
- 544 7. Lipstein, N., *et al.* Dynamic control of synaptic vesicle replenishment and short-term
545 plasticity by Ca(2+)-calmodulin-Munc13-1 signaling. *Neuron* **79**, 82-96 (2013).
- 546 8. Eggermann, E., Bucurenciu, I., Goswami, S.P. & Jonas, P. Nanodomain coupling
547 between Ca(2)(+) channels and sensors of exocytosis at fast mammalian synapses.
548 *Nat. Rev. Neurosci.* **13**, 7-21 (2012).
- 549 9. Wadel, K., Neher, E. & Sakaba, T. The coupling between synaptic vesicles and Ca2+
550 channels determines fast neurotransmitter release. *Neuron* **53**, 563-575 (2007).
- 551 10. Young, S.M., Jr. & Neher, E. Synaptotagmin has an essential function in synaptic
552 vesicle positioning for synchronous release in addition to its role as a calcium sensor.
553 *Neuron* **63**, 482-496 (2009).
- 554 11. Sudhof, T.C. The presynaptic active zone. *Neuron* **75**, 11-25 (2012).
- 555 12. Acuna, C., Liu, X., Gonzalez, A. & Sudhof, T.C. RIM-BPs Mediate Tight Coupling of
556 Action Potentials to Ca(2+)-Triggered Neurotransmitter Release. *Neuron* **87**, 1234-
557 1247 (2015).
- 558 13. Kaeser, P.S., *et al.* RIM proteins tether Ca2+ channels to presynaptic active zones
559 via a direct PDZ-domain interaction. *Cell* **144**, 282-295 (2011).
- 560 14. Kittel, R.J., *et al.* Bruchpilot promotes active zone assembly, Ca2+ channel clustering,
561 and vesicle release. *Science* **312**, 1051-1054 (2006).
- 562 15. Liu, K.S., *et al.* RIM-binding protein, a central part of the active zone, is essential for
563 neurotransmitter release. *Science* **334**, 1565-1569 (2011).
- 564 16. Matz, J., Gilyan, A., Kolar, A., McCarvill, T. & Krueger, S.R. Rapid structural
565 alterations of the active zone lead to sustained changes in neurotransmitter release.
566 *Proc. Natl. Acad. Sci. U. S. A.* **107**, 8836-8841 (2010).
- 567 17. Han, Y., Kaeser, P.S., Sudhof, T.C. & Schneggenburger, R. RIM determines Ca(2)+
568 channel density and vesicle docking at the presynaptic active zone. *Neuron* **69**, 304-
569 316 (2011).
- 570 18. Fouquet, W., *et al.* Maturation of active zone assembly by Drosophila Bruchpilot. *J.*
571 *Cell Biol.* **186**, 129-145 (2009).
- 572 19. Spangler, S.A., *et al.* Liprin-alpha2 promotes the presynaptic recruitment and turnover
573 of RIM1/CASK to facilitate synaptic transmission. *J. Cell Biol.* **201**, 915-928 (2013).
- 574 20. Zhen, M. & Jin, Y. The liprin protein SYD-2 regulates the differentiation of presynaptic
575 termini in *C. elegans*. *Nature* **401**, 371-375 (1999).
- 576 21. Oswald, D., *et al.* A Syd-1 homologue regulates pre- and postsynaptic maturation in
577 Drosophila. *J. Cell Biol.* **188**, 565-579 (2010).
- 578 22. Matkovic, T., *et al.* The Bruchpilot cytomatrix determines the size of the readily
579 releasable pool of synaptic vesicles. *J. Cell Biol.* **202**, 667-683 (2013).
- 580 23. Aravamudan, B., Fergestad, T., Davis, W.S., Rodesch, C.K. & Broadie, K. Drosophila
581 UNC-13 is essential for synaptic transmission. *Nat. Neurosci.* **2**, 965-971 (1999).

- 582 24. Basu, J., Betz, A., Brose, N. & Rosenmund, C. Munc13-1 C1 domain activation
583 lowers the energy barrier for synaptic vesicle fusion. *J. Neurosci.* **27**, 1200-1210
584 (2007).
- 585 25. Schotten, S., *et al.* Additive effects on the energy barrier for synaptic vesicle fusion
586 cause supralinear effects on the vesicle fusion rate. *eLife* **4**, e05531 (2015).
- 587 26. Shin, O.H., *et al.* Munc13 C2B domain is an activity-dependent Ca²⁺ regulator of
588 synaptic exocytosis. *Nat. Struct. Mol. Biol.* **17**, 280-288 (2010).
- 589 27. Basu, J., *et al.* A minimal domain responsible for Munc13 activity. *Nat. Struct. Mol.*
590 *Biol.* **12**, 1017-1018 (2005).
- 591 28. Stevens, D.R., *et al.* Identification of the minimal protein domain required for priming
592 activity of Munc13-1. *Curr. Biol.* **15**, 2243-2248 (2005).
- 593 29. Venken, K.J., He, Y., Hoskins, R.A. & Bellen, H.J. P[acman]: a BAC transgenic
594 platform for targeted insertion of large DNA fragments in *D. melanogaster*. *Science*
595 **314**, 1747-1751 (2006).
- 596 30. Oswald, D., *et al.* Cooperation of Syd-1 with Neurexin synchronizes pre- with
597 postsynaptic assembly. *Nat. Neurosci.* **15**, 1219-1226 (2012).
- 598 31. Graf, E.R., Daniels, R.W., Burgess, R.W., Schwarz, T.L. & DiAntonio, A. Rab3
599 dynamically controls protein composition at active zones. *Neuron* **64**, 663-677 (2009).
- 600 32. Kawasaki, F., Zou, B., Xu, X. & Ordway, R.W. Active zone localization of presynaptic
601 calcium channels encoded by the cacophony locus of *Drosophila*. *J. Neurosci.* **24**,
602 282-285 (2004).
- 603 33. Weimer, R.M., *et al.* UNC-13 and UNC-10/rim localize synaptic vesicles to specific
604 membrane domains. *J. Neurosci.* **26**, 8040-8047 (2006).
- 605 34. Augustin, I., Rosenmund, C., Sudhof, T.C. & Brose, N. Munc13-1 is essential for
606 fusion competence of glutamatergic synaptic vesicles. *Nature* **400**, 457-461 (1999).
- 607 35. Fernandez-Chacon, R., *et al.* Synaptotagmin I functions as a calcium regulator of
608 release probability. *Nature* **410**, 41-49 (2001).
- 609 36. Meinrenken, C.J., Borst, J.G. & Sakmann, B. Calcium secretion coupling at calyx of
610 Held governed by nonuniform channel-vesicle topography. *J. Neurosci.* **22**, 1648-
611 1667 (2002).
- 612 37. Naraghi, M. & Neher, E. Linearized buffered Ca²⁺ diffusion in microdomains and its
613 implications for calculation of [Ca²⁺] at the mouth of a calcium channel. *J. Neurosci.*
614 **17**, 6961-6973 (1997).
- 615 38. Lou, X., Scheuss, V. & Schneggenburger, R. Allosteric modulation of the presynaptic
616 Ca²⁺ sensor for vesicle fusion. *Nature* **435**, 497-501 (2005).
- 617 39. Kaufmann, N., DeProto, J., Ranjan, R., Wan, H. & Van Vactor, D. *Drosophila* liprin-
618 alpha and the receptor phosphatase Dlar control synapse morphogenesis. *Neuron*
619 **34**, 27-38 (2002).
- 620 40. Hallermann, S., *et al.* Naked dense bodies provoke depression. *J. Neurosci.* **30**,
621 14340-14345 (2010).
- 622 41. Regehr, W.G. Short-term presynaptic plasticity. *Cold Spring Harb. Perspect. Biol.* **4**,
623 a005702 (2012).
- 624 42. Sugita, S., Shin, O.H., Han, W., Lao, Y. & Sudhof, T.C. Synaptotagmins form a
625 hierarchy of exocytotic Ca(2+) sensors with distinct Ca(2+) affinities. *EMBO J.* **21**,
626 270-280 (2002).
- 627 43. Mohrmann, R., *et al.* Synaptotagmin interaction with SNAP-25 governs vesicle
628 docking, priming, and fusion triggering. *J. Neurosci.* **33**, 14417-14430 (2013).
- 629 44. Hu, Z., Tong, X.J. & Kaplan, J.M. UNC-13L, UNC-13S, and Tomosyn form a protein
630 code for fast and slow neurotransmitter release in *Caenorhabditis elegans*. *eLife* **2**,
631 e00967 (2013).
- 632 45. Zhou, K., Stawicki, T.M., Goncharov, A. & Jin, Y. Position of UNC-13 in the active
633 zone regulates synaptic vesicle release probability and release kinetics. *eLife* **2**,
634 e01180 (2013).
- 635 46. Rosenmund, C., *et al.* Differential control of vesicle priming and short-term plasticity
636 by Munc13 isoforms. *Neuron* **33**, 411-424 (2002).

- 637 47. Chen, Z., Das, B., Nakamura, Y., DiGregorio, D.A. & Young, S.M., Jr. Ca²⁺ channel
638 to synaptic vesicle distance accounts for the readily releasable pool kinetics at a
639 functionally mature auditory synapse. *J. Neurosci.* **35**, 2083-2100 (2015).
- 640 48. Keller, D., *et al.* An Exclusion Zone for Ca²⁺ Channels around Docked Vesicles
641 Explains Release Control by Multiple Channels at a CNS Synapse. *PLoS Comput.*
642 *Biol.* **11**, e1004253 (2015).
- 643 49. Nakamura, Y., *et al.* Nanoscale distribution of presynaptic Ca(2+) channels and its
644 impact on vesicular release during development. *Neuron* **85**, 145-158 (2015).
- 645 50. Wang, L.Y., Neher, E. & Taschenberger, H. Synaptic vesicles in mature calyx of Held
646 synapses sense higher nanodomain calcium concentrations during action potential-
647 evoked glutamate release. *J. Neurosci.* **28**, 14450-14458 (2008).
- 648

649

650 **FIGURE LEGENDS**

651 **Figure 1: Generating isoform-specific mutants of Unc13A and Unc13B**

652 **(a,b)** Schematic representation of Unc13A/B gene loci and domain structures: Calmodulin
653 (CAM), C1, C₂B, MUN and C₂C domain. Both isoforms differ exclusively in their N-terminal
654 region (purple for Unc13A including the RBP-binding PxxP motif (a), orange for Unc13B (b)).
655 Epitope positions of N-terminal isoform-specific antibodies (ABs) are indicated (Unc13A
656 epitope/Unc13B epitope). Positions of Unc13A isoform-specific EMS point mutations
657 (*EMS7.5 (Unc13A^{Null})* and *7.96*) as well as the position of the deleted fragment giving rise to
658 the *Unc13B^{Null}* pacman construct (*Unc13B^{Null}*) are also shown. **(c-l)** Muscle 4 NMJs of
659 segments A2-A4 from 3rd instar larvae of the displayed genotypes labelled with the ABs
660 indicated. **(c)** Immunostaining with an Unc13A-specific antibody (magenta) revealed a high
661 degree of overlap with the AZ-protein BRP (green) at Wild type NMJs. **(d)** Immunostaining
662 with an Unc13B-specific antibody (magenta) labelled Wild type NMJs but showed only partial
663 overlap with BRP (green) and exhibited Unc13B-positive signals devoid of BRP (arrows).
664 **(e,f)** Unc13A and -B specific immunoreactivity was restored in Ctrl. **(g)** Unc13A-specific
665 immunoreactivity was lost in *Unc13A^{Null}* and BRP spots appeared enlarged. **(h)** Unc13B-
666 specific immunoreactivity was present at *Unc13A^{Null}* NMJs. **(i)** Unc13A-specific
667 immunoreactivity was present in *Unc13B^{Null}*. **(j)** Unc13B-specific immunoreactivity was
668 completely lost in *Unc13B^{Null}*. **(k)** Motoneuronally overexpressed *Unc13A^{C-term-GFP}*
669 immunoreactivity showed an almost complete overlap with BRP, similar to the endogenous
670 Unc13A immunoreactivity (Figure 1c). **(l)** Motoneuronally overexpressed *Unc13B^{C-term-GFP}*
671 immunoreactivity only showed partial overlap with BRP similar to the endogenous Unc13B
672 immunoreactivity (Figure 1d). Single Unc13B spots lacking BRP often localized in-between
673 synaptic boutons, exhibiting sites thought to be positions of new AZ formation (arrows). **(m,n)**
674 Muscle 4 NMJs of segments A2-A4 from 3rd instar larvae of the displayed genotypes labelled
675 with indicated ABs. Arrows point to enlarged BRP spots in *Unc13A^{Null}*. **(o,p)** BRP density is
676 reduced in *Unc13A^{Null}* and *Unc13B^{Null}* in comparison to their respective controls (Wild type

677 (n=19 NMJs) vs. *Unc13A^{Null}* (n=23 NMJs), p=0.0002 (U=69); Ctrl (n=28 NMJs) vs. *Unc13B^{Null}*
678 (n=35 NMJs), p=0.0337 (U=336)). For each genotype 5 larvae were used. Number and p
679 values are listed in Supplementary Table 1 as well. Statistics: Mann-Whitney U-test. All
680 panels show mean \pm SEM; *, p \leq 0.05; **, p \leq 0.01; ***, p \leq 0.001; ns, not significant, p >0.05.
681 For all representative images experiments were repeated with at least 4 larvae and 3
682 different NMJs per larva. Scale bars: 5 μ m.

683

684

685

686

687

688

689

690

691

692

693

694

695

696

697

698

699 **Figure 2: In vivo analysis of Unc13A and -B accumulation**

700 (a) *In vivo* imaging procedure at *Drosophila* larval NMJs. Early 3rd instar larval NMJs were
701 imaged once (=time point zero) and the same NMJs were reimaged after 6h. The
702 incorporation of new AZs was tracked. (b,c) Muscle 26/27 NMJs of segments A2-A4 from 3rd
703 instar larvae of the displayed genotypes labelled with the fluorophores indicated. (b) *In vivo*-
704 imaged larval NMJ boutons from motoneurons overexpressing Unc13A^{C-term-GFP} and Liprin-
705 α^{Straw} . Liprin- α^{Straw} often showed single positive spots at t=0h (arrows). Box shows magnified
706 example from d and e. (c) Unc13B^{C-term-GFP} and Liprin- α^{Straw} showed an almost complete
707 overlap at t=0h. Box shows magnified example in f and g. (d,e) Single AZs overexpressing
708 Unc13A^{C-term-GFP} and Liprin- α^{Straw} reimaged after 6h. Single AZs with Liprin- α^{Straw} being single
709 positive at t=0h (d, arrows) also obtained Unc13A^{C-term-GFP} 6h later (e, arrows). (f,g) Single
710 AZs overexpressing Unc13B^{C-term-GFP} and Liprin- α^{Straw} reimaged after 6h. Single AZs devoid of
711 Unc13B^{C-term-GFP} and Liprin- α^{Straw} at t=0h (f, arrow) obtained both proteins 6h later (g, arrow).
712 Experiments were repeated with 3 larvae and 6 NMJs for Unc13A^{C-term-GFP} and Liprin- α^{Straw}
713 and with 5 larvae and 13 NMJs for Unc13B^{C-term-GFP} and Liprin- α^{Straw} . Scale bars: (b,c) 5 μm ;
714 (d-g) 500 nm.

715 **Figure 3: Two different scaffold complexes organize the AZ localization of Unc13**
716 **isoforms**

717 **(a,b,e,f,i,j)** Muscle 4 NMJs of segments A2-A4 from 3rd instar larvae of the displayed
718 genotypes labelled with indicated ABs. **(a,c)** Unc13A intensity was unaffected in *Liprin- α ^{Null}*
719 (Wild type (n=13 NMJs from 4 larvae) vs. *Liprin- α ^{Null}* (n=12 NMJs from 4 larvae), p=0.1495
720 (U=51)). **(b,d)** Unc13B intensity was severely decreased in *Liprin- α ^{Null}* (Wild type (n=11 NMJs
721 from 5 larvae) vs. *Liprin- α ^{Null}* (n=15 NMJs from 5 larvae), p=0.0002 (U=9)). **(e,g)** Unc13A
722 intensity was severely decreased in *Brp, Rbp* double mutants (Ctrl (n=14 NMJs from 5
723 larvae) vs. *Brp^{RNAi};Rbp^{Null}* (n=15 NMJs from 5 larvae), p <0.0001 (U=0)). **(f,h)** Unc13B
724 intensity was unaffected in *Brp, Rbp* double mutants (Ctrl (n=12 NMJs from 5 larvae) vs.
725 *Brp^{RNAi};Rbp^{Null}* (n=10 NMJs from 5 larvae), p=0.339 (U=45)). **(i)** Unc13A strictly “followed”
726 BRP in *Rab3^{Null}* mutants. **(j)** Unc13B was unaffected by BRP-redistribution in *Rab3^{Null}*
727 mutants. Arrows show Unc13B signals devoid of BRP signal while arrowheads show
728 BRP/Unc13B double-positive labels. Number and p values are listed in Supplementary Table
729 1. Statistics for c,d,g,h: Mann-Whitney U-test. All panels show mean \pm SEM; *, p \leq 0.05; **, p
730 \leq 0.01; ***, p \leq 0.001; ns, not significant, p >0.05. For representative images i,j experiments
731 were repeated with at least 3 larvae and 3 different NMJs per larva. Scale bars: 5 μ m.

732

733 **Figure 4: Unc13A is essential for fast, efficient synaptic transmission**

734 (a) Representative eEJC traces for Ctrl (black) and *Unc13B^{Null}* (blue). (b) Normalized
735 amplitudes for Ctrl and *Unc13B^{Null}* revealed similar kinetics for both genotypes. (c) eEJC
736 amplitudes for Ctrl and *Unc13B^{Null}* differ significantly with reduced amplitudes in *Unc13B^{Null}*
737 (Ctrl (n=12 NMJs) vs *Unc13B^{Null}* (n=12 NMJs), p=0.0260 (t(22)=2.388)). For both genotypes
738 12 larvae were used. (d) The eEJC (10% to 90%) rise time is unaltered in *Unc13B^{Null}* (blue)
739 in comparison to the Ctrl (black) (Ctrl (n=12 NMJs from 12 larvae) vs *Unc13B^{Null}* (n=11 NMJs
740 from 11 larvae), p=0.7671 (t(21)=0.2998)). (e) Representative mEJC traces for Ctrl (black)
741 and *Unc13B^{Null}* (blue). (f,g) mEJC amplitudes and frequencies are similar in Ctrl and
742 *Unc13B^{Null}* (mEJC amplitudes: Ctrl (n=14 NMJs from 10 larvae) vs *Unc13B^{Null}* (n=7 NMJs
743 from 5 larvae), p=0.6425 (t(19)=0.4717); mEJC frequencies: Ctrl (n=14 NMJs from 10 larvae)
744 vs *Unc13B^{Null}* (n=7 NMJs from 5 larvae), p=0.1783 (t(19)=1.398)). (h) Representative eEJC
745 traces for Wild type (black) and *Unc13A^{Null}* (red). (i) Normalized amplitudes for Wild type and
746 *Unc13A^{Null}* revealed delayed synaptic transmission in *Unc13A^{Null}* in comparison to Wild type.
747 (j) eEJC amplitudes are dramatically decreased in *Unc13A^{Null}* compared to Wild type (Wild
748 type (n=12 NMJs from 12 larvae) vs *Unc13A^{Null}* (n=12 NMJs from 12 larvae), p <0.0001
749 (t(22)=10.37)). (k) The eEJC (10% to 90%) rise time is dramatically increased in *Unc13A^{Null}*
750 (red) relative to Wild type (black) (Wild type (n=12 NMJs from 12 larvae) vs *Unc13A^{Null}* (n=9
751 NMJs from 9 larvae), p=0.003 (U=13.50)). (l) Representative mEJC traces for Wild type
752 (black) and *Unc13A^{Null}* (red). (m) *Unc13A^{Null}* exhibit significantly larger mEJC amplitudes
753 compared to Wild type (Wild type (n=12 NMJs from 6 larvae) vs *Unc13A^{Null}* (n=11 NMJs from
754 6 larvae), p=0.0004 (t(21)=4.248)). (n) The mEJC frequency is increased in *Unc13A^{Null}* (Wild
755 type (n=12 NMJs from 6 larvae) vs *Unc13A^{Null}* (n=11 NMJs from 6 larvae), p=0.043
756 (t(21)=2.154)). Recordings were performed in the presence of 1.5 mM extracellular Ca²⁺.
757 Number and p values are listed in Supplementary Table 1. Statistics: Student's t-test besides
758 panel k where a Mann-Whitney U-test was performed. All panels show mean ± SEM; *, p
759 ≤0.05; **, p ≤0.01; ***, p ≤0.001; ns, not significant, p >0.05.

760 **Figure 5: Two-color STED analysis of Unc13A and Unc13B organization at *Drosophila***
761 **NMJ synapses.**

762 (a-j) Two-color STED images of synaptic boutons (a,d,i) or individual planar AZs (b,c,e-h,j)
763 from 3rd instar larvae of the displayed genotypes labelled with the indicated ABs. (a) Unc13A
764 localized almost exclusively to the BRP-positive signal. (b,c) Unc13A immunoreactivity
765 localized to the inside or partly overlapped with the BRP signal (b) and in close proximity to
766 the RBP signal, surrounding or overlapping with it (c). (d) Unc13B localized to the BRP-
767 positive signal but also showed immunoreactivity devoid of BRP (d; arrows). (e,f) Unc13B
768 immunoreactivity localized to the outer edge of the BRP signal (e) and further away from the
769 RBP signal, not contacting it (f). (g) Motoneuronal Syd-1^{GFP} showed a similar localization as
770 Unc13B outside at the edge of the BRP ring-like structure (compare 5g with 5e). (h) Co-
771 labelling of motoneuronally overexpressed Syd-1^{GFP} and endogenous Unc13B revealed a
772 close apposition of both proteins to another. (i) BRP ring-like structures clustered together at
773 *Rab3^{Null}* mutant NMJs. Unc13B still localized to the edge of the BRP scaffold (arrow heads,
774 also magnification in j) but also showed immunoreactivity devoid of BRP following a pattern
775 that was very reminiscent of the shape of the bouton even without the presence of the
776 BRP/RBP scaffold (arrows). (j) Magnification of single AZs clustered together in *Rab3^{Null}*.
777 Unc13B localized to a similar position as at Wild type AZs (arrow heads; compare 5j with 5e).
778 For representative images experiments were repeated with at least 2 larvae and 3 NMJs.
779 Scale bars: (a,d,i) 1.5 μ m; (b,c,e-h) 50 nm; (j) 250 nm.

780

781 **Figure 6: Unc13A and -B localize in distinct distances from the presynaptic Ca²⁺**
782 **channels**

783 (a,b) Two-color STED images of individual planar AZs from 3rd instar larvae of the displayed
784 genotypes labelled with the indicated ABs. Unc13A localized in close proximity to
785 motoneuronally overexpressed Cac^{GFP}, surrounding it (a) while Unc13B localized in a larger
786 distance (b). (c) Mean intensity profile of Unc13A/-B immunoreactivity plotted from the center
787 of the AZ (the reference center being that of the BRP signal). The intensity maximum of the
788 average fluorescence profile was found 70 nm from the AZ center for Unc13A and at 120 nm
789 for Unc13B. (d,e) High-pressure-freeze (HPF) images of T-bar cross section from Wild
790 type (d) and *Unc13A^{Null}* (e) NMJs. In *Unc13A^{Null}* T-bars appeared larger, and SVs docked
791 (black circles) in close proximity to the T-bar center were lost. (f) Docked SVs were binned
792 with regard to their distance from the T-bar center, and the average number of docked SVs
793 per bin was plotted. The number of docked SVs in close proximity to the T-bar center where
794 Ca²⁺-channels are located is reduced in *Unc13A^{Null}* (red) compared to Wild type (black).
795 Subtracting the average vesicle distribution at *Unc13A^{Null}* AZs from Wild type controls
796 revealed Unc13A-specific docking positions, which peaked around 50 nm (grey dotted line).
797 (g) The average number of docked SVs is significantly reduced at *Unc13A^{Null}* (red) NMJs in
798 comparison to Wild type (black) (Wild type (n=11 AZs from 5 larvae) vs *Unc13A^{Null}* (n=16 AZs
799 from 2 larvae), p=0.0015 (U=22)). (h) The average number of T-bar tethered SVs is similar in
800 Wild type and *Unc13A^{Null}* (Wild type (n=11 AZs from 5 larvae) vs *Unc13A^{Null}* (n=16 AZs from 2
801 larvae), p=0.7275 (U=80.5)). (i) The average distance of docked SVs to the T-bar center is
802 significantly increased in *Unc13A^{Null}* compared to Wild type (Wild type (n=11 AZs from 5
803 larvae) vs *Unc13A^{Null}* (n=16 AZs from 2 larvae), p=0.0035 (U=169.5)). Statistics for g-
804 i: Mann-Whitney U-test. All panels show mean ± SEM; *, p ≤0.05; **, p ≤0.01; ***, p ≤0.001;
805 ns, not significant, p >0.05. For representative images a and b experiments were repeated
806 with at least 2 larvae and 6 NMJs. Scale bars: (a,b,d,e) 50 nm.

807

808 **Figure 7: *Unc13A* increases extracellular Ca^{2+} sensitivity, release probability and**
809 **mediates tight SV to Ca^{2+} channel coupling**

810 (a) Extracellular Ca^{2+} was varied (in mM: 0.75, 1.5, 3, 6, 10), and single eEJCs and paired-
811 pulse stimulations with 10 ms inter-stimulus interval (ISI) recorded. Representative eEJC-
812 traces for Wild type (black) and *Unc13A^{Null}* (red) at various $[\text{Ca}^{2+}]_{\text{ext}}$ reveal severely impaired
813 release in *Unc13A^{Null}* synapses, at all extracellular Ca^{2+} concentrations. (b) The mean eEJC-
814 amplitude in *Unc13A^{Null}* is significantly lower than in Wild type animals at all tested $[\text{Ca}^{2+}]_{\text{ext}}$
815 (n=12 NMJs from 12 larvae per Ca^{2+} concentration and genotype; p<0.0001 for all tested
816 Ca^{2+} concentrations; 0.75 mM Ca^{2+} : t(22)=4.961; 1.5 mM Ca^{2+} : t(22)=10.37; 3 mM Ca^{2+} :
817 t(22)=16.05; 6 mM Ca^{2+} : t(22)=15.89; 10 mM Ca^{2+} : t(22)=12.54). Experimental data is
818 indicated as dots, model predictions are shown as lines. (c) Analysing the Ca^{2+} -dependence
819 of release revealed a rightward shift in the sensitivity of release to extracellular Ca^{2+}
820 concentrations in *Unc13A^{Null}* mutant synapses (see also Figure S5a-c for analyses using the
821 hill equation). Dots represent experimental data, lines represent model predictions (Wild type
822 (n=12 NMJs from 12 larvae per Ca^{2+} concentration) vs *Unc13A^{Null}* (n=10 NMJs from 10
823 larvae per Ca^{2+} concentration): 0.75 mM Ca^{2+} : p=0.0092 (U=20); 1.5 mM Ca^{2+} : p<0.0001
824 (U=0); 3 mM Ca^{2+} : p=0.0005 (U=7); 6 mM Ca^{2+} : p=0.0272 (U=26); 10 mM Ca^{2+} : p=0.0062
825 (U=18)). (d) Representative, normalized paired-pulse eEJC traces with 10 ms ISI for Wild
826 type (black) and *Unc13A^{Null}* (red) at various $[\text{Ca}^{2+}]_{\text{ext}}$. (e) The paired-pulse ratios were
827 significantly increased in *Unc13A^{Null}* at 10 ms ISI for all $[\text{Ca}^{2+}]_{\text{ext}}$ (Wild type (n=12 NMJs from
828 12 larvae per Ca^{2+} concentration) vs *Unc13A^{Null}* (n=10 NMJs from 10 larvae per Ca^{2+}
829 concentration): 1.5 mM Ca^{2+} : p=0.0001 (t(20)=4.579); 3 mM Ca^{2+} : p<0.0001 (t(20)=5.028); 6
830 mM Ca^{2+} : p<0.0001 (t(20)=6.222); 10 mM Ca^{2+} : p=0.0002 (t(20)=4.534)). Dots represent
831 experimental data, lines represent model predictions. (f) Effect of 200 μM EGTA-AM/DMSO
832 6 min after addition to the extracellular-solution. Representative normalized eEJC traces for
833 Wild type (black with DMSO, blue with EGTA-AM/DMSO) and *Unc13A^{Null}* (gold with DMSO,
834 red with EGTA-AM/DMSO). *Unc13A^{Null}* animals showed a stronger reduction of eEJCs.
835 Recordings were performed in the presence of 2.5 mM extracellular Ca^{2+} . (g) Time course of

836 the effects of 200 μM EGTA-AM addition in both genotypes. Normalized amplitudes declined
837 much faster and reached lower values in *Unc13A^{Null}* mutant synapses than in Wild type
838 synapses. Dots represent experimental data, lines represent model predictions (Wild type
839 (n=10 NMJs from 10 larvae) vs *Unc13A^{Null}* (n=10 NMJs from 10 larvae): 3 min: p=0.0004
840 (t(18)=4.387); 6 min: p=0.0115 (t(18)=2.812); 9 min: p=0.025 (t(18)=2.446); 12 min:
841 p=0.0063 (t(18)=3.090)). (h) 3D plots of simulated Ca^{2+} -transients at 1.5 mM $[\text{Ca}^{2+}]_{\text{ext}}$ in 0.1
842 ms intervals, starting with the peak of Ca^{2+} -influx (set to t=0.0 ms). $[\text{Ca}^{2+}]_{\text{int}}$ shows rapid
843 spatial and temporal decrease. Ca^{2+} influx was assumed to occur from a point source at the
844 base of the simulation volume (AZ) located in the center. (i) Illustration of the exocytosis
845 model containing two independent SV release pathways (A and B), both driven by identical
846 Ca^{2+} sensing and fusion mechanisms, but differentially positioned with respect to the Ca^{2+} -
847 source (Cac, blue). Ca^{2+} -transients in the Wild type were smaller at the B position (grey line)
848 than at the A position (black line). Release in the *Unc13A^{Null}* was assumed to occur from the
849 B position only, with the only difference to the Wild type situation being a slightly increased
850 Ca^{2+} -current to account for the observed increase in Ca^{2+} channels in this mutant
851 (Supplementary Table 2, Supplementary Figure 6e,f). The background color indicates the
852 spatial heterogeneity in free Ca^{2+} at the peak of the AP-induced Ca^{2+} transient. Ca^{2+}
853 concentrations are only shown in the relevant range between 0 and 150 μM for better
854 visualization, while actual peak concentration at the simulated source reached $\sim 887 \mu\text{M}$ (see
855 panel h). (j) Simulated single eEJCs at 1.5 mM extracellular Ca^{2+} are shown for the Wild type
856 and the *Unc13A^{Null}* model. The normalized simulated eEJC traces reveal a similar delay in
857 the *Unc13A^{Null}* model as observed experimentally (Figures 4i,k and Supplementary Figure
858 4c). Simulations of paired pulse responses (10 ms interval) for 1.5 mM $[\text{Ca}^{2+}]_{\text{ext}}$ are also
859 shown. Number and p values are listed in Supplementary Table 1. Statistics: Student's t-test
860 except for panel (c) where a Mann-Whitney U-test was used. All panels show mean \pm SEM;
861 *, p \leq 0.05; **, p \leq 0.01; ***, p \leq 0.001; ns, not significant, p > 0.05.

862

863 **ONLINE METHODS**

864 **MATERIAL AND METHODS**

865

866 **Genetics**

867 Fly strains were reared under standard laboratory conditions⁵¹ and raised at 25°C on semi-
868 defined medium (Bloomington recipe). For most experiments both male and female larvae
869 were used. For electrophysiological analysis only male larvae were used. The following
870 genotypes were used: Wild type: +/+ (*w1118*). *Unc13A^{Null}*: *EMS7.5/P84200*. *Unc13B^{Null}*:
871 *Del100BPacman/+;P84200/P84200*. Ctrl: *Unc13Pacman/+;P84200/P84200*. Motoneuronal
872 driven *UAS-Unc13A^{C-term-GFP}* (Figure 1): *Ok6-GAL4/+; UAS-Unc13A^{C-term-GFP}/+*. Motoneuronal
873 driven *UAS-Unc13B^{C-term-GFP}* (Figure 1): *Ok6-GAL4/+; UAS-Unc13B^{C-term-GFP}/+*. Genotypes
874 used for in vivo imaging were: *Unc13B* and *Liprin-α*: *Ok6-GAL4/+; UAS-Unc13B^{C-term-}*
875 *GFP/UAS-Liprin-α^{Straw}*. *Unc13A* and *Liprin-α*: *Ok6-GAL4/+; UAS-Unc13A^{C-term-GFP}/ UAS-Liprin-*
876 *α^{Straw}*. Genotypes used for scaffold dependence (Figure 3 and Supplementary Figures 1,3):
877 *Syd-1^{Null}*. *Syd-1^{1.2}/Syd-1^{3.4}*. *Liprin-α^{Null}*. *Liprin-α^{F3ex15}/Liprin-α^{R60}*. Ctrl: *Ok6-GAL4,Dicer/+*. *Brp-*
878 *RNAi*: *Ok6-GAL4,Dicer/+; UAS-Brp-RNAi-B3,C8/+*. *Rbp^{Null}*. *Ok6-GAL4,Dicer/+; Rbp^{Stop1}/*
879 *Df(3R)S201*. *Brp-RNAi;Rbp^{Null}*. *Ok6-GAL4,Dicer/+; Rbp^{Stop1}/Df(3R)S201, UAS-Brp-RNAi-*
880 *B3,C8*. *Rab3^{Null}*. *Rab3^{rup}/Rab3^{rup}*. Motoneuronal driven *Syd-1^{GFP}* (Figure 5): *Ok6-GAL4/UAS-*
881 *Syd-1^{GFP}*. Motoneuronal driven *Cac^{GFP}* (Figure 6): *Ok6-GAL4/UAS-Cac^{GFP}*. Genotypes used
882 for *Cac^{GFP}* in *Unc13A^{Null}* (Supplementary Figure 6): Ctrl: *genomic CacGFP/+*. *Unc13A^{Null}*:
883 *genomic CacGFP/+; EMS7.5/P84200*. *Unc13B^{Null}*: *Del100BPacman/ genomic CacGFP;*
884 *P84200/P84200*.

885 Stocks were obtained from: *Ok6-Gal4⁵²*; *UAS-Brp-RNAi-B3,C8⁵³*; *genomic CacGFP²²*; *UAS-*
886 *Cac^{GFP15}*; *Rbp^{Stop1}*; *Df(3R)S201¹⁵*; *Syd-1^{1.2}*; *Syd-1^{3.4 21}*; *Liprin-α^{F3ex15}*; *Liprin-α^{R60 39}*; *Rab3^{rup31}*;
887 *UAS-Syd-1^{GFP21}*; *UAS-Liprin^{Straw30}*. *P84200* was provided by the *Drosophila Genetic*
888 *Resource Center (DGRC)*.

889

890 **Generation of *Unc13A^{Null}* by chemical mutagenesis**

891 The EMS screen was performed according to standard protocols. In brief, isogenic *w1118*
892 males were mutagenized with 25 mM EMS solution and crossed to virgins carrying a fourth
893 chromosomal balancer. For initial mapping, male F1 offspring were crossed with *P84200*
894 virgins, and candidate flies were tested for adult lethality. Genomic DNA was extracted from
895 positive candidate flies, and PCR amplicons containing *Unc13* exon clusters were double-
896 strand sequenced to identify the mutations.

897

898 **Generation of *Unc13B^{Null}* and Ctrl**

899 *Unc13* genomic transgenes were generated by Red/ET Recombineering. For this purpose,
900 the *Unc13* P[acman] BAC CH321-60O10 clone containing the *Drosophila unc13* gene was
901 obtained from the BACPAC Resources Center, CA, USA used as a template for all cloning
902 strategies. Based on the P[acman] technology²⁹ and using Red/ET Recombineering in *E.coli*
903 for modifying large DNA vector constructs (*GeneBridges Protocol*: Counter-Selection BAC
904 Modification Kit, Version 3.2, January 2012), a genomic rescue construct encompassing the
905 whole *Drosophila Unc13* locus including putative promoter regions was generated giving
906 raise to 'Ctrl'. Based on this wild type construct, an *Unc13* isoform B specific deletion
907 construct (*Unc13B^{Null}*) was generated by removing the first 1000 bp of the *Unc13B* DNA
908 sequence, causing a shift of the reading frame, which interrupts the translation of *Unc13B* by

909 generating an early stop-codon. The cloning strategy was performed according to the
910 Counter-Selection BAC Modification Kit by Red®/ET® Recombination (Gene Bridges
911 Protocol, No. K002, Version 3.2, January 2012). For the Generation of transgenic flies both
912 constructs were sent for DNA micro-injection in embryos to Rainbow Transgenic Flies, Inc,
913 CA, USA(service type: B/D2, injected fly strain: Strain 24862; y[1] M{vas-int.Dm}vZH-2A w[*];
914 PBac{y[+]-attP-9A}VK00005) on LB agar.

915

916 **Generation of UAS-Unc13A^{GFP} and UAS-Unc13B^{GFP}**

917 UAS-Unc13A^{GFP}

918 To generate the cDNA of Unc13A, the C-term of Unc13 (1647- 2871 aa) was cloned from
919 cDNA clone LD28927 (obtained from DGRC) into pENTR/D-Topo (Invitrogen) using the
920 following primers:

921 Unc13-Cterm-FW 5'- CACCATGCATCCCGGTGACAATCCATTC - 3'

922 Unc13-Cterm-Rev 5'- TGTACCCATGGTTGGCTCCT- 3'

923 The N-term of Unc13A is available at DGRC as cDNA with clone number LD15472. The
924 Unc13A C-term fragment was ligated to the Unc13A N-term. The obtained construct is
925 lacking 1859 bp in the N-terminal region of Unc13A, which were cloned into pENTR/D-Topo
926 vector using the following primers:

927 Unc13-1859 FW 5'- CACCATGCGCACTACGTGAGGC - 3'

928 Unc13-1859 REV 5'- AGGCTTCAGATACTCAGATATG- 3'

929 In a final step both fragments were fused to the Unc13A cDNA in pENTR/D-Topo vector.
930 Through Gateway reaction, the construct was shuttled into GAL4/UAS vector containing a
931 GFP tag.

932

933 UAS-Unc13B^{GFP}

934 Unc13B N-term was generated from the Pacman clone CH321-74A09 (obtained from
935 BACPAC Resource Center BPRC, California, USA) and cloned into pENTR/D-Topo using
936 the following primers:

937 Unc13-N-term/IsoB FW 5'-CACCATGATGAACACATCTCAGCT- 3'

938 Unc13-N-term/IsoB REV 5'--CTTGTCCCTGTCCTTTATCAT- 3'

939 The N-terminal part (exon 1) of Unc13B was fused to exons 2,3 and 4 by elongase PCR
940 using a Unc13B Y2H construct (containing the last 1000 bp of exon 1) and Unc13A cDNA as
941 templates. The primers used for amplification are:

942 HB-dunc13RB-prey4 FW 5'-CACCATGGCTGCACATTCTGACGACGATG- 3'

943 Unc-13 PCR2 REV 5'-CGGCGCTGCAGGCAGTCCGCATTCAGAAGG- 3'

944 The amplified fragment was cloned to pENTR/D-Topo vector and ligated to the C-terminal
945 part of Unc13A cDNA resulting in the final Unc13B cDNA entry clone. Through Gateway
946 reaction, the construct was shuttled into GAL4/UAS vectors containing a GFP tag.

947

948 **Generation of Unc13A and Unc13B specific antibodies**

949 Unc13A specific antibody:

950 The poly clonal antibody was raised in Guinea pig. The immunization of the animals was
951 performed using a GST tagged fusion protein. The coding sequence corresponding to 384-
952 494aa of Unc13A:

953 SVTSFPSSAVTAITKTRKLPKVLPTPLCKSSRHPITIATDALSSSYTSDPLPEKSHRPAAKQLP

954 KLPISLPQSNDRASLNSNWATPPAPDALPFNSFDHKSASSPTPTTTITK

955 The PCR was performed using the following primers:

956 Unc13A N-term FW 5 CA AATTCA C TCACAA TTTCCC
957 Unc13A N-term REV 5 TACTC A TCATTTT TTATT TT TTTT
958 The PCR product was ligated to pGEX-6p1 (GST tag vector). The expression and purification
959 of the target protein were conducted as mentioned above. After injection into guinea pig
960 animals, several attempts to produce a 6×His tagged fusion protein of the same protein
961 construct were not successful. Therefore, the GST tag of the GST tagged fusion protein was
962 cleaved and the pure protein was used for the affinity purification of the AB containing serum
963 which obtained from Selbaq.

964

965 Unc13B specific antibody:

966 A rabbit poly clonal antibody was raised against the N-terminus of Unc13B with the following
967 peptide sequence (941-1602 AA):

968 SNFHSFPLSHEQAQTTNQTEFVILEENLNYYIELSKNLPICSAYENKSIFDMKYEICDSNEIGK
969 FSTVDEMLEWDQLNEPDKQNFSGKRLNSNLMPDLLTAQIPNSISKHNKNTSVNIEYVRQKE
970 NKGMDRRSIIIEPNYNGKSEDQICRPCLTDKLVFYPSSNSITDHNSSHDFNCLSQQDQTRIIK
971 EFGSAHLNQDPTNYLDYTSGTYSKAPPEVLTHETNSSHLEFNHESESLFNSPNTSSYCKQK
972 FVPGTSPAKPSKVWKRNLNTILADNLKLRVSKFNRSLSLPGDVQSQGLQRQPRGQAGSCPF
973 IHKRSNLAGSPVQLSKRIQKLPPIRFIGRAKGVFVRRSSSPDSAVSLDSAADKRFSSSEKGLKK
974 KTISSKMSGLMQAKTYKRHSFVLRRCNMSDSELEMPDFVSSGNDNSSISTREILLNQSIE
975 VEDEQEDFNKYKNCDSKSVLGGSEIKLNGNLNLFPIVGDLLKIQSPLPLAVLTEIPSYKDE
976 YSNKSDSIKNSPIEMPKILLETACNQELNLAHSDDDVDKNILANSAKDYNAPTFSILKTVEDA
977 SEPTMTPLHTTTTTNSSLNVTSALWVTQQCLDLPNYPGWGSREDDDNRSQHSARTLSSSR
978 RQSTEDSIDTDEYFYELRQLEEQEKQRAHNSAIPSCER

979 The coding sequence was cloned from Pacman clone CH321-74A09 (BACPAC Resource
980 Center BPRC, CA, USA) into pENTR/D-Topo (Invitrogen, CA, USA). The following primers
981 were used:

982 Unc13B FW 5'-CACCATGGCTTCGAACCTTTCACAGTTTCCC-3'

983 Unc13B REV 5'-AGTACTAGTTTATCGTTCACAAGATGGAATTGC-3'

984 Through Gateway reaction, the construct was shuttled into the bacterial expression vectors
985 pDEST17(N-terminal 6xHis--tag) and expressed as corresponding fusion proteins. Rabbit
986 antisera, obtained from Selbaq, were affinity purified with the same fusion protein.

987

988 **Generation of RBP^{SH3-II+III} antibody**

989 A guinea-pig poly clonal antibody was generated against a GST tagged fusion protein of
990 RBP with the following sequence:

991 YFVAMFDYDPSTMSPNPDGCDEELPFQEGDTIKVFGDKDADGFYWGELRGRRGYVPHNM
992 VSEVEDTTASMTAGGQMPGQMPGQMGQQGQVGVGGTAQVMPGQAGAPQQSMRNVS RD
993 RWGDIYANMPVKRMIALYDYDPQELSPNVDAEQVELCFKTEIILVYGDMDDEDGFYMGELD
994 GVRGLVPSNFLAD

995 The fragment of expression was amplified from RBPcDNA clone AT04807 (Drosophila
996 Genomics Resource Centre) using the following primers:

997 FW 5'-CAGAATTCCGCTATTTTGTGGCCATGTTTC-3'

998 REV 5'-TACTCGAGTCAGTCCGCCAGGAAGTTAGA-3'

999 Following the PCR, the fragment was cloned into the pGEX-6p1 GST vector. The expression
1000 and purification of the target protein were performed in *Escherichia coli* under native
1001 conditions. For affinity purification of the AB containing serum (obtained from Selbaq), a
1002 6×His tagged fusion protein was used with the same amino acid sequence of the GST
1003 construct used for immunization.

1004

1005 Immunostaining

1006 Larval filets were dissected and stained as described previously²¹. The following primary
1007 antibodies were used: guinea-pig Unc13A (1:500; this study); rabbit Unc13B (1:1000; this
1008 study); rabbit BRP^{C-term} (1:500;¹⁵) guinea-pig BRP^{SH3-II+III} (1:500; this study); mouse GFP (3E6;
1009 1:500, Life Technologies A-11120), rabbit GFP (1:500, Life Technologies A11122), mouse
1010 Nc82 = anti-BRP^{C-term} (1:100, Developmental Studies Hybridoma Bank, University of Iowa,
1011 Iowa City, IA, USA); rabbit BRP^{Last200} (1:1000;⁵⁴). Except for staining against Cac^{GFP} and
1012 Unc13A, where larvae were fixed for 5 min with ice-cold methanol, all fixations were
1013 performed for 10 min with 4 % paraformaldehyde (PFA) in 0.1 mM phosphate buffered saline
1014 (PBS). Secondary antibodies for standard immunostainings were used in the following
1015 concentrations: goat anti-HRP-Cy5 (1:250, Jackson ImmunoResearch, PA, USA); goat anti-
1016 rabbit-Cy3 (1:500, Jackson ImmunoResearch 111-165-144, PA, USA); goat anti-mouse-Cy3
1017 (1:500, Jackson ImmunoResearch 115-165-146); goat anti-mouse or anti guinea pig Alexa-
1018 Fluor-488 (1:500, Life Technologies A11001/A11073, CA, USA). Larvae were mounted in
1019 vectashield (Vector labs, CA, USA). Secondary antibodies for STED were used in the
1020 following concentrations: goat anti-mouse Atto590 (1:100); goat anti-rabbit Atto590 (1:100);
1021 goat anti-guinea pig star635 (1:100); goat anti-rabbit star635 (1:100); Atto590 (ATTO-TEC
1022 AD 590-31) and star635 (Abberior 1-0101002-1) coupled to respective IgGs (Dianova). For
1023 STED imaging larvae were mounted in Mowiol (Max-Planck Institut for Biophysical
1024 Chemistry, Group of Stefan Hell).

1025

1026 Image Acquisition, Processing and Analysis

1027 Confocal microscopy was performed with a Leica SP8 microscope (Leica Microsystems,
1028 Germany). STED microscopy was performed with a custom-built STED-microscope (see
1029 below). Images of fixed and live samples were acquired at room temperature. Confocal
1030 imaging of NMJs was done using a z step of 0.25 μm . The following objective was used:
1031 63 \times 1.4 NA oil immersion for NMJ confocal imaging. All confocal images were acquired using
1032 the LCS AF software (Leica Microsystems, Germany). Images from fixed samples were
1033 taken from 3rd instar larval NMJs (segments A2-A4). Images for figures were processed with
1034 ImageJ software to enhance brightness using the brightness/contrast function. If necessary
1035 images were smoothed (0.5 pixel Sigma radius) using the Gauss blur function. Confocal
1036 stacks were processed with ImageJ software (<http://rsbweb.nih.gov/ij/>). Quantifications of AZ
1037 spot number, density and size (scored via BRP) were performed following an adjusted
1038 manual⁵⁵, briefly as follows. The signal of a HRP-Cy5 antibody was used as template for a
1039 mask, restricting the quantified area to the shape of the NMJ. The original confocal stacks
1040 were converted to maximal projections and after background subtraction, a mask of the
1041 synaptic area was created by applying a certain threshold to remove the irrelevant lower
1042 intensity pixels. The segmentation of single spots was done semi-automatically via the
1043 command "Find Maxima" embedded in the ImageJ software and by hand with the pencil tool
1044 and a line thickness of 1 pixel. To remove high frequency noise a Gaussian blur filter (0.5
1045 pixel Sigma radius) was applied. The processed picture was then transformed into a binary
1046 mask using the same lower threshold value as in the first step. This binary mask was then
1047 projected onto the original unmodified image using the "min" operation from the ImageJ
1048 image calculator. The synapses of the resulting images were counted with the help of the
1049 "analyze particle" function with the threshold set to 1. The spot density was obtained by
1050 normalizing the total number of analyzed particles to the NMJ area measured via HRP. The
1051 mean intensity of synaptic proteins per NMJ was measured using the command "measure"
1052 giving the mean gray pixel value within the HRP mask. For colocalization analysis (Manders
1053 or Pearson correlation) the ImageJ plugin "JACOP"
1054 (<http://rsb.info.nih.gov/ij/plugins/track/jacop2.html>) was used.

1055

1056 **STED Microscopy**

1057 Two-colour STED images were recorded on a custom-built STED-microscope⁵⁶, which
1058 combines two pairs of excitation laser beams of 595 nm and 640 nm wavelength with one
1059 STED fiber laser beam at 775 nm. All STED images were acquired using Inspector Software
1060 (Max Planck Innovation GmbH, Germany). STED images were processed using a linear
1061 deconvolution function integrated into Inspector Software (Max Planck Innovation GmbH,
1062 Germany). Regularization parameters ranged from $1e^{-09}$ to $1e^{-10}$. The point spread function
1063 (PSF) for deconvolution was generated by using a 2D Lorentz function with its half-width and
1064 half-length fitted to the half-width and half-length of each individual image. Images for figures
1065 were processed with ImageJ software to remove obvious background, enhance
1066 brightness/contrast and smoothed (1 pixel Sigma radius) using the Gauss blur function.
1067 The average aligned intensity profiles depicted in Figure 6C were generated from STED
1068 images obtained by co-staining BRP together with either Unc13A or -B. The BRP signal was
1069 used to align the local fluorescence signal in the following way: first, several sub-images
1070 (size 51 x 51 pixel, pixel size 10 nm) containing BRP rings were placed per STED images.
1071 The sub-images were cut out in both channels (BRP and either Unc13A or Unc13B) and
1072 centered according to the BRP signal. This was achieved by finding individual BRP peaks
1073 with the ImageJ (version 1.48q) function “find maxima”, and shifting the image such that the
1074 center of gravity of the peaks was in the center of the sub-image. Only sub-images with at
1075 least two maxima were considered. To generate average fluorescence profiles, intensity line
1076 profiles were read out across a horizontal line in the middle of the image (pixels 1 to 51 in x
1077 at pixel position y=26). The image was then successively rotated 35 times in 10° steps while
1078 reading out intensity profiles in the same manner. Intensity profiles of all rotations were
1079 averaged. This procedure was performed for all images in all channels (no. of sub-images for
1080 BRP/Unc13A: n=132; no. of sub-images for BRP/Unc13B: n=117). Intensity profiles
1081 generated this way contained a local minimum at the center of the sub-images in all
1082 channels, demonstrating the proper alignment of the BRP signal and a stereotypical
1083 distribution of Unc13 fluorescence. Intensity profiles were then plotted from the center
1084 outwards and the midline pixel position (x=26) was set to zero (no information is lost by this
1085 because intensity profiles were symmetric due to the averaging across full rotations of the
1086 individual images). To plot the mean fluorescence distribution across the plot area, mean
1087 absolute fluorescent values were normalized. For this, the traces were integrated over the full
1088 range (0 to 250 nm) and the individual values divided by this number in a genotype specific
1089 manner.

1090 The measurements of BRP ring diameters (as depicted in Supplementary Figure 6)
1091 were performed on deconvolved images. A line profile was laid across the middle of planar
1092 oriented BRP rings and the peak-to-peak distance measured. Subsequently the line was
1093 rotated 90 degrees, a second line profile was created and the peak-to-peak distance
1094 measured again. The average of both peak-to-peak distances gave the ring diameter.

1095

1096 ***In vivo* live imaging and analysis**

1097 For temporal analysis of synapse assembly imaging of intact *Drosophila* larvae was
1098 performed as previously described^{57, 58}. Briefly, third instar larvae were put into a drop of
1099 Voltalef H10S oil (Arkema, Inc., France) within an airtight imaging chamber. Before imaging,
1100 the larvae were anaesthetized with 20 short pulses of a desflurane (Baxter,IL, UAS) air
1101 mixture until the heartbeat completely stopped. Selected NMJs were exclusively located in
1102 abdominal segments A2, A3 and A4 on muscles 26 and 27. Confocal stacks of NMJs were
1103 recorded using a z step size of 0.25 μ m. After image acquisition, single larvae were kept
1104 separately for 6h on normal food at 25°C to capture the whole maturation process.
1105 Subsequently, the very same NMJs were subjected to live imaging again.

1106

1107 Electrophysiology

1108 Recordings were performed essentially as previously described⁵⁹. All experiments were
1109 performed on male, 3rd instar, larvae raised on semi-defined medium (Bloomington recipe) at
1110 25°C. The eEJCs were low-pass filtered at 5 kHz and sampled at 10 kHz. The stimulation
1111 artifact of eEJCs was removed for clarity. TEVC recordings were performed at room
1112 temperature on third-instar larval NMJs (muscle 6 of abdominal segments A2/A3). Larvae
1113 were dissected in ice cold Ca²⁺-free hemolymph-like solution (HL3;⁶⁰; Composition (in mM):
1114 NaCl 70, KCl 5, MgCl₂ 20, NaHCO₃ 10, trehalose 5, sucrose 115, HEPES 5, pH adjusted to
1115 7.2). The CaCl₂ concentration used for experiments is noted in the corresponding figures.
1116 Recordings were made only from cells with an initial V_m between -50 and -70mV and input
1117 resistances of ≥4 MΩ, using intracellular electrodes with resistances of 8-15 MΩ, filled with
1118 3M KCl. eEJCs were recorded at a voltage clamp of -60 mV and mEJCs were recorded at a
1119 voltage clamp of -80 mV.

1120 Ca²⁺ titration experiments were performed from an initial Ca²⁺ concentration of 0.75
1121 mM. The concentration was subsequently increased to 1.5, 3.0, 6.0, and 10 mM. At each
1122 Ca²⁺ concentration, a single eEJC was recorded. Following the 10 seconds rest, one paired
1123 pulse trace was recorded (10 ms ISI). Paired pulse ratios were calculated by dividing the
1124 amplitude after the second stimulus by the amplitude after first stimulus. The bath solution
1125 was then exchanged five times via pipetting and the process was repeated at the next
1126 Ca²⁺ concentration. Calcium-dependence of release data in individual cells were fit with a
1127 standard site-specific Hill equation ($I = I_{max} * [Ca^{2+}]_{ex}^h / (K_D^h + [Ca^{2+}]_{ex}^h)$), where [Ca²⁺]_{ex} is the
1128 concentration of extracellular Ca²⁺, I is current, I_{max} is the asymptotic current, h is the hill
1129 slope, and K_D is the extracellular Ca²⁺ concentration at which I=0.5*I_{max}. To obtain the plots in
1130 Figure 7c and Supplementary Figure 5a,d, amplitudes (I) were divided by I_{max} in each cell,
1131 then averaged. Quantifications of the K_D and the hill coefficient h (slope) were obtained from
1132 individual cell fits with a site-specific Hill equation (Graphpad Prism, vers. 5). Cells were
1133 excluded if the Hill equation could not be properly fit to the data (affected only 2 cells in
1134 *Unc13A^{Null}*). The data are reported as mean ± s.e.m., n indicates the number of cells
1135 examined.

1136

1137 Ca²⁺ buffering with EGTA-AM and Bapta-AM (TEVC)

1138 In an EGTA-AM wash-in experiment, initial amplitudes were recorded for 1 min before
1139 0.2 mM EGTA-AM (in DMSO) and Pluronic F-127 (same volume like EGTA-AM, ratio 1:1)
1140 was added to the extracellular solution containing 2.5 mM Ca²⁺. For control, the same
1141 volume (final concentration 0.4%DMSO (v/v) and Pluronic F-127 (ratio 1:1, stock solution
1142 20% (w/v) in DMSO) was added to the extracellular solution. The cell was clamped at -60mV
1143 and recordings lasted for a total of 3000s. Nerve stimulation was applied throughout at 0.1
1144 Hz. The baseline amplitude was obtained by averaging the initial five amplitudes. The decay
1145 of the amplitudes upon addition of EGTA-AM was fitted in the range between wash-in and
1146 1000 s with a single exponential fit in Igor Pro with the following formula:

1147

$$1148 f(x) = y_0 + (1 - y_0) * \exp(-(x - x_0) / \text{Tau})$$

1149

1150 where x is time, f(x) are normalized amplitudes, which start at 1 and decay in a
1151 monoexponential fashion once EGTA-AM concentrations rise in the presynaptic terminal.
1152 The function features a delay (x₀) to account for variable delay times between experiments.
1153 Tau is the time constant of the inhibition and y₀ represents the asymptotic plateau value at
1154 full inhibition at steady state.

1155 In an incubation experiment, Bapta-AM (Abcam, 100 mM stock solution in DMSO)
1156 was dissolved in Ca²⁺-free HL3 to a final concentration of 0.1 mM. The same volume of
1157 Pluronic F-127 (Molecular Probes, OR, UAS, 20% (w/v) in DMSO) was added. For control an
1158 equal amount of DMSO (final concentration v/v: 0.2%) and Pluronic F-127 was dissolved in

1159 Ca²⁺-free HL3. The dissected larva was incubated exactly 30 minutes at room temperature,
1160 then it was rinsed three times with HL3 containing 2.5 mM Ca²⁺ to remove residual Bapta-AM
1161 from the fillet before the recording was started. In TEVC at -60mV 100 APs of a 60Hz train
1162 were measured in HL3 in the presence of 2.5 mM extracellular Ca²⁺. Data was analyzed
1163 using pClamp 10 (Molecular Devices, CA, USA) and a custom-written MATLAB (MathWorks,
1164 MA, USA, R2010b) script. Changes in the first amplitude of the train upon Bapta-AM
1165 incubation were compared by dividing the amplitude with Bapta/DMSO (with Pluronic F-127)
1166 treatment by the amplitude with DMSO (with Pluronic F-127) treatment to reveal potential
1167 genotype-specific changes in Bapta sensitivity.

1168

1169 **Electron Microscopy/HPF**

1170 HPF embedding was performed as described previously²². In brief, about three to five
1171 *Drosophila* late second/early third instar larvae were placed in an aluminum specimen carrier
1172 of 200- μ m depth (type A; Leica, Germany), filled with yeast paste, and covered with a lid
1173 (specimen carrier typeB, Leica, Germany). Samples were frozen immediately in an HPF
1174 machine (HPM100; Leica). Cryosubstitution was performed in an AFS (Leica, Germany) in
1175 anhydrous acetone with 1% EMD Millipore water, 1% glutaraldehyde, and 1%
1176 osmiumtetroxide. From -90°C for 10 h the temperature was slowly (5°C/h) increased to -
1177 20°C, the samples incubated for additional 12 h before being warmed (10°C/h) to 20°C. The
1178 samples were washed with acetone and incubated with 0.1% uranylacetate dissolved in
1179 anhydrous acetone for 1 h at RT. After washing, the samples were infiltrated with the plastic
1180 resin Epon in increasing concentrations. The first incubation step in 30% Epon/70% acetone
1181 for 4 h was followed by 70% Epon/30%acetone overnight. The samples were incubated twice
1182 in 100% Epon for 2 h before being embedded. 60–65 nm sections were cut using an
1183 ultramicrotome (RMC Power Tome XL; Reichert Ultracut S). Sections were collected on
1184 Formvar-coated 100 mesh grids. Sections were post stained with 2% uranylacetate for 30
1185 min and lead citrate for 3 min. Micrographs were acquired on an electron microscope
1186 (Tecnai Spirit; FEI or Zeiss 900). The analysis of the EM micrographs was done with ImageJ
1187 (<http://imagej.nih.gov/ij>). The micrographs were rotated (linear extrapolation) till the AZ
1188 membrane was horizontal. The plasma membrane, the electron-dense T-bar and SV in a 300
1189 nm radius from the T-bar center were detected by eye and labeled manually. The nearest
1190 distance of the outer leaflet of SVs to the inner leaflet of the plasma membrane at the T-bar
1191 pedestal center was measured. Only SVs with direct contact to the plasma membrane were
1192 categorized as "docked". SVs with contact to the T-bar were classified to be "tethered". The
1193 SV distances to the T-bar pedestal center were binned in 30 nm bins and the number of SVs
1194 in a respective bin was counted and plotted.

1195

1196 **Yeast two-Hybrid Interaction Mating**

1197 To create a prey matrix for interaction mating, the MAT α yeast strain L40cca⁶¹ was
1198 individually transformed with plasmids pACT4-DM and pGAD426-D3 (coding Gal4 activation
1199 domain fusions at the N-terminus) encoding prey proteins (Unc13A Frag I;II;III and Unc13B
1200 Frag I;II;III;). The resulting yeast colonies were arrayed in 384-well microtiter plates. cDNA
1201 fragments encoding the bait protein fragments (BRP; RBP; Syd1; Liprin- α Fragments) were
1202 subcloned into two gateway compatible yeast expression vectors: pBTM116-D9 and
1203 pBTMcc24-DM (identical to pBTM116-D9 except that the lexA DNA-binding protein is fused
1204 at the C-terminus of the ORF⁶¹). The resulting plasmids were transformed into the MAT α
1205 yeast strain L40ccua and assembled in 96-well plates. For the Y2H matrix approach⁶²,
1206 autoactivating strains starting the transcription of the reporter genes HIS3, URA3 were
1207 excluded from the set of bait strains (e.g. all Unc13 constructs). The matrix-format Y2H
1208 protein-protein interaction screening was designed and run as described in⁶². For interaction
1209 mating, 25 ml fresh overnight cultures of the bait strains (-Trp/+His +Ade +Ura +Leu) were

1210 distributed into a 384-well MTPs (40µl each well) using a pipetting robot (Biomek FX,
1211 Beckman Coulter, Germany). The freshly grown prey yeast colonies (- L/+His +Ade +Ura +
1212 Trp) were individually scratched off the agar and resuspended each into a well of the 40µl bait
1213 strains containing MTPs. The pair-wise combinations of bait and prey strains were mixed and
1214 transferred immediately onto YPD agar plates in a grid pattern using a spotting robot
1215 (KBiosystems, Great Britain) and incubated for 36 hr at 30°C. For detection of protein-protein
1216 interactions, diploid yeasts carrying both -baits and preys- were spotted from YPD agar onto
1217 selective SDIV (-Leu-Trp-Ura-His) agar plates. Interacting bait-prey pairs were identified by
1218 growth on selective agar plates (Leu-Trp-Ura- His) after 5–6 days of incubation at 30°C. Non
1219 autoactivating baits (L40ccU MATa yeast strains) were mated with prey strains at least four
1220 times using independently transformed bait and prey yeast colonies (384 array format). Only
1221 bait-prey pairs that showed growth and therefore a protein-protein-interaction at least twice
1222 were considered as a “+”. All others were considered as non-interacting and therefore signed
1223 with a “-”.

1224

1225 **Primer sequences of the prey fragments of Unc13A N-term**

1226 **Unc13A N-term Fragment 1 (length: 1-606 AA)**

1227 **Primer:**

1228 **Unc13A N-term FW1:**

1229 GGGGACAAGTTTGTACAAAAAAGCAGGCTCCATGACGCACTACGTGAGGCAT

1230 **Unc13A N-term RV1:**

1231 GGGGACCACTTTGTACAAGAAAGCTGGGTGCCCGCTATATGGATCGGCTAA

1232 **Giving rise to the following protein sequence:**

1233 MTHYVRHDYFHNTQNGALSSDTSRISYSQISYETQPSREYFSESYALSNQGPEECRSRVSHL
1234 NSDTVLTTVDNSNNSYGYDYLECYGANIQCDPEEDSVDNWNENTS VVADQYGLGHNNLNC
1235 TSSKLLPKLPNIENGRGSSNACAPQMDVKFNTKGMCIKIDHSYGVCMAKAHDFVGR LSPSD
1236 YQNILGNLNGYAGCAYSSTFLDNAMSSAPLRVLPQSPRCSSYLGRNIIGFNADAAQRDGR
1237 GFDTDQTDAMGSESSTYEVYEKMRPYTSMPLDYSYQEGCYNTDNLSTYSSTPPSNNT
1238 QLKRMQRKISLMMAMTTASVIASGEIRVPVHSHKQSKKSTEIQTDSIIGNTISTNAAARDLDR
1239 CLATESCEVIVDTRDSGSVTSFPSSAVTAITKTRKLPKVLPTPLCKSSRHPITATDALSSSYT
1240 SDPLPEKSHRPKQLPKLPISLPQSNDRASLNSNWATPPAPDALPFNSFDHKSASSPTPTTTI
1241 TKDTETTSYLVETDFIGARHNALYQYDSKEPNIVFSDKSVEAEHSPTWTPLSPIQSKQSPCP
1242 PVALPSNIMQNVSLTCHLPEIEATRSDIEREPESSSIEPILEIEKLADPYSG
1243

1244 **Unc13A N-term Fragment 2 (length: 494 -1111 AA)**

1245 **Primer:**

1246 **Unc13A N-term FW2:**

1247 GGGGACAAGTTTGTACAAAAAAGCAGGCTCAAAGATACGGAAACCACCTCA

1248 **Unc13A N-term RV2:**

1249 GGGGACCACTTTGTACAAGAAAGCTGGGTGATTTCTGACTAAGGTCTGA

1250 **Giving rise to the following sequence:**

1251 KDTETTSYLVETDFIGARHNALYQYDSKEPNIVFSDKSVEAEHSPTWTPLSPIQSKQSPCPP
1252 VALPSNIMQNVSLTCHLPEIEATRSDIEREPESSSIEPILEIEKLADPYSGPGSALFNISEYLKP
1253 YTLNKPILSEEKKNHIANAASTSTTTPLNITSDDEFSSYSNKWTSTCVNFQPLDVESLNISLK
1254 VNAGTNQAE LLMTPLKSSTPLFISSNGTSDNFNLKSSPPDSAFTTTVNVNSFETVLVSGSQ
1255 TASPSPSNLKSPPSIAPLLSYSDYMKQFELPELPQPI MDLSENDTATQSDSFNVINNTLTNAD
1256 NLNSYNQMDVESKSSLQLPSYSSESFDPCSVPFSIKNKEYKIVEKLDLSNVESVESPKTL
1257 VSPVNPLNCSKLLPGTESIVSNDVAFDDTFYDSFNVDIKELTAFVDHVAPEDGLYNFPNDKT
1258 SVEFSFDKTEDTIDMNQNLSSGECGYKPSQAQKASVVASAASSVLDGISKGLKGGLDGV
1259 FSGVSSTVDVTQSNPSSKRGFSFNLASKIVPSVGLLTSTSTSIKQTGSETNPTLILISPENV
1260 SSRNSNYIPTTSPSCTQKNGEENLYSATVHNKSTKSNSYYNEVGEISSTLVRN
1261

1262 **Unc13A N-term Fragment 3 (length: 1000-1632 AA)**
1263 **Primer:**
1264 **Unc13A N-term FW3:**
1265 GGGGACAAGTTTGTACAAAAAAGCAGGCTCCTCAACAGTTGATGTCACTCAA
1266 **Unc13A N-term RV3:**
1267 GGGGACCACTTTGTACAAGAAAGCTGGGTGATTAAGCTGCATGATTATTTT
1268 **Giving rise to the following sequence:**
1269 STVDVTQSNPSSKRGFSFNLASKIVPSVGGLLTSTSSTSIKQTGSETNPTLILISPENVSSRNS
1270 NYIPTTSPSCTQKNGEENLYSATVHNKSTKSNSYYNEVGEISSTLVRNVCDSYDNSYDEMIL
1271 TNEMVNIGMLDSESEFGLIENSYSYQVPDNEQIDSVNSYNNKTQNVNTNNGIEKANTKNKPVP
1272 LHDPTTKASTVGMFGSILGAAAAVQSATQAVNQSASSVASVAQKPTIVPRTNNVLLSS
1273 VCSPNEIKRNSSSVEFDSEYGYQMPDVESLSSHYANTGGDYDNSNMKIHEFGTYADDRPY
1274 ADYHTNGNQSQFKEEAVIPGEPEVINTNILPIGPQATGKKLPTVNGKSALLIKQMPTEVYDDE
1275 SDTDEL DVSPSTGKVPSYSIYSEQEDYYMDLQQTTPSIQPNGFYEQVNNGYDYREDYFNEE
1276 DEYKYLEQQREQEEHNQPKNKYLKQAKISKIQQPSLDFIDVGGDDDFIYDNYHSEDDSGNY
1277 LEGSSSGSVGPIEGSIKVDNSNIEASFASLNKKSDFSFTPTNDSLQKHDTVIGESTTKLTRLRTE
1278 KMCPDVDEEDENLSDHVS DLTDL SKLISQKKKTLRGETEEVVGGMQVLRQTEITARQRW
1279 HWAYNKIIMQLN
1280

1281 **Primer sequences of the bait and prey fragments of Unc13B N-term**

1282 **Unc13B N-term Fragment 1 (length: 1-711 AA)**

1283 **Primer:**

1284 **Unc13B N-term FW1:**

1285 GGGGACAAGTTTGTACAAAAAAGCAGGCTCCATGATGAACACATCTCAGCTG

1286 **Unc13B N-term RV1:**

1287 GGGGACCACTTTGTACAAGAAAGCTGGGTGTGAGCTGCCAACTAATTTTTT

1288 **Giving rise to the following sequence:**

1289 MMNTSQLQVTGDTEKKSQLLKELKINTQEKLIFAENALKSQIKIKEQLRLQQSTIYASSLLS
1290 SSAAGSVRAPLLSQGHLNSIQHNMDFLAKAQIPEMQPPMSKSPNGLDFSYSYPSINTNES
1291 MISIKSEQQLCQSYNSEQHSDYIISDYMDKIATRISLLETTELKFAWRALDLLSTEYGKIWIRLEK
1292 LENISIEQQSVGNLVDLIGASKKELQKVDIERMKVPLYQDEDQLLPLEMEDTLDIDIQSSNRD
1293 FDKNLTFENHEKTFVTKHTQATKSEDLMNSAYAIDSHPNFENIDFNGKNLDIGIIFGFYKGY
1294 EPKQKGNQSDFEAYKESRTKLYSDSDLMLYERQQFLANSARAELMKEFLNGRRVLNEISAS
1295 SGALSKSSEKDKNLVKPRELLSEIDDTYVRRSTCELVSPSSNFFQIAASKTGECCGQVLP
1296 EDTGGTESPANINEVDES FYKNLNEAYRDNELSSEIFKVDALLHQSEATHDHISFIRNQSTSS
1297 PVLNNQRVNAITGTQPLQTAKACLVTENQHLNKEPRKHKRKKKHTNEMDMINKLKCILAQA
1298 QSTEIIRKRDIEELGSKLSDACVKQTETENKSDNHISTSYLKDDIRKMLNINVITLLGEINKIKGL
1299 QLSATQLSQLQNAVWSEERFFQKISLVDKLLTLLLNPLTVTEELQRLCISNTNEKFVLVIKK
1300 LKKNIDTLKKL VGSS
1301

1302 **Unc13B N-term Fragment 2 (length: 600-1322 AA)**

1303 **Primer:**

1304 **Unc13B N-term FW2:**

1305 GGGGACAAGTTTGTACAAAAAAGCAGGCTCCAACCATATTAGTACCAGTTAT

1306 **Unc13B N-termRV2:**

1307 GGGGACCACTTTGTACAAGAAAGCTGGGTGACCACTCATCTTGGACGAAAT

1308 **Giving rise to the following sequence:**

1309 NHISTSYLKDDIRKMLNINVITLLGEINKIKGLQLSATQLSQLQNAVWSEERFFQKISLVDK
1310 L TLLLNPLTVTEELQRLCISNTNEKFVLVIKKLKNIDTLKKL VGSSLDDFKIDNSHANMTTFH
1311 SLNPSHNSNDSSFSALLRNNSNLDEQLKILETQEIEIHRKKKIDEIVSGLSEETYTFNPDM
1312 KSQHSCNTSDNIIIGFSKNIYNEDEYIKSLRKSRLERHNSMIFLLHLQNPEKHKVLADIN
1313 DSNRASLSPPPPAPTDTVYLNDAINQITYQQRNGKSDSGLSSMSGWSANSQVSVGLQNYD
1314 PACNNILENCSERLQTYHSFPLAENS NFHSFPLSHEQAQTTNQTEFVILEENLN YIELSKNL
1315 PICSAYENKSIFDMKYEICDSNEIGKFSTVDEMLEWDQLNEPDKQNFSGKRLNSNLMPDLLT

1316 AQIPNSISKHNKNTSVNIEYVRQKENKGMDDRRSIIIEPNINYNGKSEDQICRPCLTDKLVFYPSS
1317 NSITDHNSSSHDFNCLSQDQTRIIKEFGSAHLNQDPTNYLDYTSYKAPPEVLTHETNSS
1318 HLEFNHESESLFNSPNTSSYCKQKFVPGTSPAKPSKVWKRLNTILADNLKLRVSKFNRSLS
1319 LPGDVQSQGLQRQPRGQAGSCPFIIHKRSNLAGSPVQLSKRIQKLPPIRFIGRAKGVVFPVRRS
1320 SSPDSAVSLDSAADKRFSSSEKGLKKKTISSKMSG
1321

1322 **Unc13B N-term Fragment 3 (length: 1200-1944 AA)**

1323 **Primer**

1324 **Unc13B N-term FW3:**

1325 GGGGACAAGTTTGTACAAAAAAGCAGGCTCCTCAAAGGTATGGAAGAGGCTA

1326 **Unc13B N-term RV3:**

1327 GGGGACCACTTTGTACAAGAAAGCTGGGTGCTTGCCCTGTCCTTTATCAT

1328 **Giving rise to the following sequence:**

1329 SKVWKRLNTILADNLKLRVSKFNRSLSLPGDVQSQGLQRQPRGQAGSCPFIIHKRSNLAGS
1330 PVQLSKRIQKLPPIRFIGRAKGVVFPVRRSSSPDSAVSLDSAADKRFSSSEKGLKKKTISSKMSG
1331 MQKAKTYKRHSFVLRGRCNMSDSELEMPDFVSSGNDNSSISTREILLNQSIEVEDEQEDFN
1332 YKNRCDKSVLGGSEIKLNGNLTNLFPIVGDLLKIQSPLPLAVLTEIPSYKDEYSNKSDSIKN
1333 SPIEMPKILLETACNQELNLAHSDDDVDKNILANSADYVNAPTFSILKTVEDASEPTMTPLHT
1334 TTTTNSLNVTSALWVTQQCLDLPNYPGWGSREDDNRSQHSARTLSSRRQSTEDSIDT
1335 DDEYFYELRQLEEQEKQRAHNSAIPSCERQNDNDVLFSSQIGQLLQNDVNGGDGFRHSNG
1336 CNDGEDAIIIFSPSESVKLRMSEVFKELKSVVSLNPSVNNDATFEGVPIVKPTYEKLETVSDLH
1337 SAWQDVNGDLQIAASDIDSNEDLVGNKGRETPTYNKQRKLRRLKKKTRDRKINISKNTSSS
1338 SSCHSENECNTPLGQCTQKSVAEKDNDISNKSEASSETS GPDTPAELSDVDISETENGLR
1339 ADDGQNIDNMRGNSGSLKVNRYLLQFDVDHSLINQPLETSQYNTHMLENITSASIPSQNR
1340 QIDSKTLMSSHADGSQAVGNETAVGLSSSKWLLKTLKERKIEEKNNQDKIKEDEMIKDR
1341 DK
1342

1343 **Liprin α isoform A fragment 1 (length: 1-550 AA)**

1344 **Primer**

1345 **Lip1F:**

1346 GGGGACAAGTTTGTACAAAAAAGCAGGCTCCATGTGGAACATGATGTGCG

1347 **Lip550R:**

1348 GGGGACCACTTTGTACAAGAAAGCTGGGTGACTGGGGTCCACTACG

1349 **Giving rise to the following sequence:**

1350 MWNMMCDVMPPTISEDSSISQRSSQFSGEDANFEQLMVSMLEDERDKLMDSLREAQERLNETE
1351 NKLRDVEKERDSLQRQINANLPQEFATLTKELTQARETLLERDEEIGELKAERNNTRLLLEHL
1352 ECLVSRHERSLRMTVVKRQAAAQSGVSSEVEVLKALKSLFEHHKALDEKVRERLRLSIEKNN
1353 MMEEEELSSAKEELAQYKAGVVPAGVSGSGAGSAATTAGGGGAENGLKEKMAVGSGSG
1354 GVNGEANELNDYAAKTHELQTIIEKQTSSELSQWQRRVSDLNKNKISELEENMSRVQKEHCKA
1355 QDQCAKLQRDLRENVAQKEDQEERITTLKRYLNAQRESTSLHDLNEKLEQELRHKEAQLK
1356 LHEEKIGAIIEEKLELSEQKLAQHAKLQPDMEQLKARMEALTKAQERHGS AEDRIRGLETNL
1357 DEKTNEVVRLNQRLKMNEEHNRLSSTVDKLLSESNERLQVHLKERMHALDEKNALTQELE
1358 KARKVAEELHHEKSEIMKELSKTRLEIENFKRQLLQEQEIAYNIIQQTEALTRSLSPSSVVDPS
1359

1360 **Liprin- α isoform A fragment 2 (length: 250-550 AA)**

1361 **Primer**

1362 **Lip250F:**

1363 GGGGACAAGTTTGTACAAAAAAGCAGGCTCCATGGAGCTGAACGACTACGC

1364 **Lip550R:**

1365 GGGGACCACTTTGTACAAGAAAGCTGGGTGACTGGGGTCCACTACG

1366 **Giving rise to the following sequence:**

1367 NELNDYAAKTHELQTIIEKQTSSELSQWQRRVSDLNKNKISELEENMSRVQKEHCKA QDQCAK
1368 LQRDLRENVAQKEDQEERITTLKRYLNAQRESTSLHDLNEKLEQELRHKEAQLKLHEEKIG

1369 AIEEKLELSEKLAQHAKLQPDMEELKARMEALTKAQRHGS AEDRIRGLETNLDEKTNEV
1370 VRLNQR LKMNEEHNLR LSS TVDKLL SESNERLQVHLKERMHALDEKNALTQELEKARKVAE
1371 ELHHEKSEIMKELSKTRLEIENFKRQLLQQEIAYNIQQTEALTRSLSPSSVVDPS
1372

1373 **Liprin α isoform A fragment 3 (length: 526-946 AA)**

1374 **Primer**

1375 **Lip526F:**

1376 GGGGACAAGTTTGTACAAAAAAGCAGGCTCCATGGAGATCGCCTACAACATCC

1377 **Lip946R:**

1378 GGGGACCACTTTGTACAAGAAAGCTGGGTGATTCCACAGGGCAAACG

1379 **Giving rise to the following sequence:**

1380 EIAYNIQQTEALTRSLSPSSVVDPSGAFSRNSHASFETHSLRRQSKQRLSEENALVRSMAE
1381 QEWEKLQAAHAQQQAYELASAADCDDSDVLYAAATDMMSPSGHTDAQTLAMMLQEQLD
1382 AINNEIRLIQEEKQSTEARAEELSRVGSLEHVNLLARGRSMRQSPPMGRSTPNSPQRD
1383 FMQKYHTLNLPVLSSDASREELHGGMSTTGDSSSGGAASPLTARSMRLERVAQALAHSQE
1384 ELRRRSIGLNPNASVAPNHTGGHMPLSSHSYGLSPLSSRYGSQESLRHYNTMGSMMLQT
1385 PTSGVSREAAAAAVQKKKGKSSLRFFSKKEKVKGVKDTLPDGSPSMMSIGNLSIGLSEVD
1386 SNYDAMSMTGGMMPRIASSQGSKISSVDYGRQKKEHDYRNDLLGEAMKAGTPFALWN
1387

1388 **Syd-1 fragment 1 ORF 1²¹; length: 1-242AA; synthetic gene)**

1389 **Primer**

1390 **Syd1F:**

1391 GGGGACAAGTTTGTACAAAAAAGCAGGCTCCATGACTGTTCAACCTGCTG

1392 **Syd242R:**

1393 GGGGACCACTTTGTACAAGAAAGCTGGGTGACGCTGACGTATGGCC

1394 **Giving rise to the following sequence:**

1395 MTVQPAEMAENGRSVPDVTASPGRAPPGLPANQMPAMGNQQHHGNQQHHGNQQQHH
1396 GNQHSNHRGQSGSLSNAAGVKDPVMLQGDFRQVSGISSEIFRQIEAVENDHDPNTAAALEA
1397 VERRGEMIVRVLEPRCMGSKQAVDAAHKLMNKADARHTVQLVEIVKRPQGTLGLYIREGNG
1398 ADRTDGVFISRIALES AVYNSGCLRVGDEILAVNLVDVTHMSLDDVVIIMSIPRRLVLAIRQR
1399

1400 **Syd-1 fragment 2 ORF 1²¹; length:1-777 AA; Synthetic gene)**

1401 **Primer**

1402 **Syd1F:**

1403 GGGGACAAGTTTGTACAAAAAAGCAGGCTCCATGACTGTTCAACCTGCTG

1404 **Syd777R:**

1405 GGGGACCACTTTGTACAAGAAAGCTGGGTGTCCGGAGATGCCGC

1406 **Giving rise to the following sequence:**

1407 MTVQPAEMAENGRSVPDVTASPGRAPPGLPANQMPAMGNQQHHGNQQHHGNQQQHH
1408 GNQHSNHRGQSGSLSNAAGVKDPVMLQGDFRQVSGISSEIFRQIEAVENDHDPNTAAALEA
1409 VERRGEMIVRVLEPRCMGSKQAVDAAHKLMNKADARHTVQLVEIVKRPQGTLGLYIREGNG
1410 ADRTDGVFISRIALES AVYNSGCLRVGDEILAVNLVDVTHMSLDDVVIIMSIPRRLVLAIRQRR
1411 GNRGTGSPGPPTLSRPEQKPPPVVVIKRDRLDEDLDETDRMPPRPRSSRDGEMTESRSRL
1412 GLGLNNYSPQSEQLDMYYNTRGGGGGAMGEPNWWGYKPPPPPSSVITEQPTKAHAFAPS
1413 HAYYQNAAGTLES LAEKVHAFYPGQPGGPPVGPSRRMSTGTGNVGLAQQHARFPRSGSDQ
1414 HLP RVEYSDYSNSLGRHSLLRSSLKPGTTGGAPMQVGVGGTLGRYGRYDQQRAGVSKYG
1415 PPSGGAQSLTRRSRPNLDYSSDTEATIGPRPSYYYYNRPAIGSMSRSGGGAGGGVGAAS
1416 AALLAGAADLNKFNLSLPRERPGTRLQGIRSRMGDRLVDENDGNTSAPEFDVRRGRDLRQRI
1417 TASPSIFTADEYRAWLRRAPSSSAIAEQMRMTRDMFAQPRAQRFSCSAENIHDALRNTESIY
1418 SSRNHILGTGTLDRNMGLTRPISALPVRSMSSQHIGGAGSIRSPSIRRMRLLELSAGPASP
1419 SGSILSTGGHQSPAPTPSATLPRPHRQIDINPAEFAKYKLDKPIVDIGGISG
1420

1421 **Syd-1 fragment 3 ORF 1²¹; 155-1120aa; Synthetic gene)**
1422 **Primer**
1423 **Syd155F:**
1424 GGGGACAAGTTTGTACAAAAAAGCAGGCTCCATGCACACGGTTCAACTTGTCTG
1425 **Syd1120R:**
1426 GGGGACCACTTTGTACAAGAAAGCTGGGTGGGGCCAAATCTGGAGAAG
1427 **Giving rise to the following sequence:**
1428 HTVQLVEIVKRPGQTLGLYIREGNGADRTDGVFISRIALESVYNSGCLRVGDEILAVNLVDV
1429 THMSLDDVVIIMSIPRRLVLAIRQRRGNRGTGSPGPPTLSRPEQKPPPVVVVKRDLRDEDLDE
1430 TDRMPRPRSSRDGREMTESRSRLGLGLNNYSPQSEQLDMYYNTRGGGGGAMGEPNNG
1431 YKPPPPSSVITEQPTKAHAFAPSHAYYQNAGTLES LAEKVHAFYPGQPGGPPVGPSRRMS
1432 TGTGNVGLAQQHARFPRSGSDQHLPRVEYSDYSNSLGRHSLLRSSLKPGTTGGAPMQVG
1433 VGGTLGRYGRYDQQRAGVSKYGPPSGGAQSLTRRSRPNLDYSSDTEATIGPRPSYYYYNR
1434 PAIGSMSRSGSGGAGGGVGAASTAALLAGAADLNKFNLSLPRERPRTLQGIRSRMGDRLVD
1435 ENDGNTSAPEFDVRRGRDLRQRITASPSIFTADEYRAWLRRAPSSSAIAEQMRMTRDMFAQ
1436 PRAQRFSCSAENIHDALRNTE SIYSSRNHILGTGTLDRNMGLTRPISALPVRSMSSQHIGGA
1437 GSIRSPSIRRMQRQLELSAGPASPSGSILSTGGHQSPAPTPSATLPRPHRQIDINPAEFAKYK
1438 LDKPIVDIGGISGMLWIHLLAGRGLRTAPEGAAGTATQGQTRDLYCVIECDRVHKARTVVR
1439 GDLQFDWDESFELDLVGNKQLDVLVYSWDPQHRHKL CYRGAISLSSILRQSPLHQLALKVE
1440 PRGTIYIRMRHTDPLALYKRRGLPSLRAGYPTLFGADLETVNRRESKNAPGSAPVPIVLRRC
1441 VEEVERRGLDIIGLYRLCGSATKKRLLREAFERNSRAVELTPEHVPDINVITGVLKDYLRPE
1442 PLFTRCLFQMTVDALAVCLPDDPEGNAKLMLSILDCLPRANRATLVFLLDHLSLVVSNERN
1443 KMSAQALATVMGPPLMLHSASAQPGADIDHAQPIAVLKYLLQIWP
1444

1445 **Syd-1 fragment 4 ORF 1²¹; 243-777aa; Synthetic gene)**
1446 **Primer**
1447 **Syd243F:**
1448 GGGGACAAGTTTGTACAAAAAAGCAGGCTCCATGCGTGGCAACCGTGG
1449 **Syd777R:**
1450 GGGGACCACTTTGTACAAGAAAGCTGGGTGTCCGGAGATGCCGC
1451 **Giving rise to the following sequence:**
1452 RGNRGTGSPGPPTLSRPEQKPPPVVVVKRDLRDEDLDETDRMPRPRSSRDGREMTESRSR
1453 LGLGLNNYSPQSEQLDMYYNTRGGGGGAMGEPNNGYKPPPPSSVITEQPTKAHAFAP
1454 SHAYYQNAGTLES LAEKVHAFYPGQPGGPPVGPSRRMSTGTGNVGLAQQHARFPRSGSD
1455 QHLPRVEYSDYSNSLGRHSLLRSSLKPGTTGGAPMQVG VGGTLGRYGRYDQQRAGVSKY
1456 GPPSGGAQSLTRRSRPNLDYSSDTEATIGPRPSYYYYNRPAIGSMSRSGSGGAGGGVGAAS
1457 TAALLAGAADLNKFNLSLPRERPRTLQGIRSRMGDRLVDENDGNTSAPEFDVRRGRDLRQ
1458 RITASPSIFTADEYRAWLRRAPSSSAIAEQMRMTRDMFAQPRAQRFSCSAENIHDALRNTE
1459 SIYSSRNHILGTGTLDRNMGLTRPISALPVRSMSSQHIGGAGSIRSPSIRRMQRQLELSAGPAS
1460 PSGSILSTGGHQSPAPTPSATLPRPHRQIDINPAEFAKYKLDKPIVDIGGISG
1461

1462 **Syd-1 fragment 5 ORF 1²¹; 778-1500aa; Synthetic gene)**
1463 **Primer**
1464 **Syd778F:**
1465 GGGGACAAGTTTGTACAAAAAAGCAGGCTCCATGCTGTGGATTACCTG
1466 **Syd1500R:**
1467 GGGGACCACTTTGTACAAGAAAGCTGGGTGCGACTCAGGCGACTTG
1468 **Giving rise to the following sequence:**
1469 MLWIHLLAGRGLRTAPEGAAGTATQGQTRDLYCVIECDRVHKARTVVRSGDLQFDWDESF
1470 ELDLVGNKQLDVLVYSWDPQHRHKL CYRGAISLSSILRQSPLHQLALKVEPRGTIYIRMRHT
1471 DPLALYKRRGLPSLRAGYPTLFGADLETVNRRESKNAPGSAPVPIVLRRCVEEVERGLDIIG
1472 LYRLCGSATKKRLLREAFERNSRAVELTPEHVPDINVITGVLKDYLRPEPLFTRCLFQMTV
1473 DALAVCLPDDPEGNAKLMLSILDCLPRANRATLVFLLDHLSLVVSNERNKMSAQALATVMG
1474 PPLMLHSASAQPGADIDHAQPIAVLKYLLQIWPQQAQHQMAQHMGAAGAMMGLVTA

1475 GSMSNMAGVASGNTGRRGESTGQRGSKVSALPADRQQLLQQQAQLMAAGNLLRSSTSV
1476 TNILSQGHPQLSATANNHLYQSVVGQLAQSHRALQQAVQQPYQLGGSVGS AIPDPSPLPLP
1477 GTPSPGSSSASTGSGSGSGKSTDTIKRGASPVSVKQVKIVDQPSSPYSIVMKKPPLQKDAP
1478 VEITPTTQADTESTLGCKESNGTASRRGNVDFYDTHKTQAKSVVNEESSYSSKYTGSETK
1479 KIIPGNSSYTPSKANASGLSGGEDYKAMRNKSSATSSSSSSSQATVLSAGSTATSAPTTSSDD
1480 SDDLVSYSKSSASTNALLAQSQAMTTSQLMSKYLKREPRVQFTPIKSPES
1481

1482 **Syd-1 fragment 6 ORF 1²¹; 921-1844aa; Synthetic gene)**

1483 **Primer**

1484 **Syd921F:**

1485 GGGGACAAGTTTGTACAAAAAAGCAGGCTCCATGTTTGGTGCTGATCTCGAAAC

1486 **Syd1844R:**

1487 GGGGACCACTTTGTACAAGAAAGCTGGGTGTTTAATGTCATCGTACTCGTCAG

1488 **Giving rise to the following sequence:**

1489 FGADLETVVNRESKNAPGSAPVPIVLRRCVVEEVERRGLDIIGLYRLCGSATKKRLLREAFER
1490 NSRAVELTPEHVPDINVITGVLDYLRELPEPLFTRCLFQMTVDALAVCLPDDPEGNAKLMLS
1491 ILDCLPRANRATLVFLLDHLSLVVSNERNKMSAQALATVMGPPLMLHSASAQPGADIDHAQ
1492 PIAVLKYLQIWPQPQAQHQQMAQHMGGAAGAMMGLVTAGSMSNMAGVASGNTGRRG
1493 ESTGQRGSKVSALPADRQQLLQQQAQLMAAGNLLRSSTSVTNILSQGHPQLSATANNHLY
1494 QSVVGQLAQSHRALQQAVQQPYQLGGSVGS AIPDPSPLPLPGTPSPGSSSASTGSGSGSG
1495 KSTDTIKRGASPVSVKQVKIVDQPSSPYSIVMKKPPLQKDAPVEITPTTQADTESTLGCKES
1496 NGTASRRGNVDFYDTHKTQAKSVVNEESSYSSKYTGSETKKIIPGNSSYTPSKANASGLSG
1497 GEDYKAMRNKSSATSSSSSSSQATVLSAGSTATSAPTTSSDDSDDLVSYSKSSASTNALLAQS
1498 QAMTTSQLMSKYLKREPRVQFTPIKSPESPPPGSGDGLPKGTYQLVTPISGSSSKPGATT
1499 GAISKYTTGSVESSINANSQKLSSPSRLCNSKDSNSRTGTASSTTPATSMVSTGRRLFDLSLA
1500 SSSSSETETKTYIGGTTAASGAIITTIYNTDKNSGSSSSKSGIGGGSGTGLGAVSGASSETR
1501 SFGSTLFGSSGLGNGNGSSHNHSSASPSPFTTTNGNGNHNTMHLYGTLPKNGTSTGAALF
1502 GGSANSSSYHSSASGSGAGTASSSGVSSMTGSTNSYDFYTSTSSTVSSSRPFANGGNNYH
1503 TLGTYRAQYAATNPFLDAFDEKPGSNGGNAHGEEKLGADKGGHRAAVMAFQSSGDSKNG
1504 SDEYDDIK
1505

1506 **Syd-1 fragment 7 ORF 1²¹; 1-1844aa; Synthetic gene)**

1507 **Primer**

1508 **Syd1F:**

1509 GGGGACAAGTTTGTACAAAAAAGCAGGCTCCATGACTGTTCAACCTGCTG

1510 **Syd1844R:**

1511 GGGGACCACTTTGTACAAGAAAGCTGGGTGTTTAATGTCATCGTACTCGTCAG

1512 **Giving rise to the following sequence:**

1513 MTVQPAEMAENGRSVPDVTASPGRAPPGLPANQMPAMGNQQHHGNQQHHGNQQHH
1514 GNQHSNHRGQSGSLSNAAGVKDPVMLQGDFRQVSGISSEIFRQIEAVENDHDPNTAAALEA
1515 VERRGEMIVRVLEPRCMGSKQAVDAAHKLMNKADARHTVQLVEIVKRPQGTLGLYIRENG
1516 ADRTDGVFISRIALESVYNSGCLRVGDEILAVNLVDVTHMSLDDVVIIMSIPRRLVLAIRQRR
1517 GNRGTGSPGPPTLSRPEQKPPPVVVIKRDRLDEDLDETRMPRPRSSRDGREMTESRRL
1518 GLGLNNYSPQSEQLDMYYNTRGGGGGAMGEPNWWGYKPPPPSSVITEQPTKAHAFAPS
1519 HAYYQNAGTLES LAEKVHAFYPGQPGPPVGPSRRMSTGTGNVGLAQQHARFPRSGSDQ
1520 HLPVEYSYDYSNSLGRHSLLRSSLKPGTTGGAPMQVGVGGTLGRYGRYDQQRAGVSKYG
1521 PPSGGAQSLTRRSRPNLDYSSDTEATIGPRPSYYYYNRPAIGSMSRSGGAGGGVGAAS
1522 AALLAGAADLNKFNLSLPRERPGTRLQGIRSRMGDRLVDENDGNTSAPEFDVRRGRDLRQRI
1523 TASPSIFTADEYRAWLRRAPSSSAIAEQMRMTRDMFAQPRAQRFSCSAENIHDALRNTESIY
1524 SSRNHILGTGTLDRNMGLTRPISALPVRSMSSQHIGGAGSIRSPSIRRMRLLELSAGPASP
1525 SGSILSTGGHQSPAPTPSATLPRPHRQIDINPAEFAKYKLDKPIVDIGGISGMLWIHLLAGRGL
1526 RTAPEGAAGTATQGGQTRDLYCVIECDRVHKARTVVRSGDLQFDWDESFELDLVGNKQLDV
1527 LVYSWDPQHRHKLQCYRGAILSSILRQSPLHQLALKVEPRGTIYIRMRHTDPLALYKRRGLPS
1528 LRAGYPTLFGADLETVVNRESKNAPGSAPVPIVLRRCVVEEVERRGLDIIGLYRLCGSATKKRL

1529 LREAFERNSRAVELTPEHVPDINVITGVLKDYRELPEPLFTRCLFQMTVDALAVCLPDDPEG
1530 NAKLMLSILDCLPRANRATLVFLLDHLSLVVSNERNKMSAQALATVMGPPLMLHSASAQPG
1531 ADIDHAQPIAVLKYLQIWPQPQAQHQMAQHMGGAAGAMMGLVTAGSMSNMAGVASG
1532 NTGRRGESTGQRGSKVSALPADRQQLLQQAQLMAAGNLLRSSTSVTNILSQGHPQLSA
1533 TANNHLYQSVVGQLAQSHRALQAVQQPYQLGGSVGS AIPDPSPLPLPGTSPGSSSAST
1534 GSGSGSGKSTDTIKRGASPVSVKQVKIVDQPSSPYSIVMKKPPLQKDAPVEITPTTQADTE
1535 STLGCKESNGTASRRGNVDFYDTHKTQAKSVVNEESSYSSKYTGSETKKIIPGNSSYTPSKA
1536 NASGLSGGEDYKAMRNKSSATSSSSSSQATVLSAGSTATSAPTTSSDDSDDLVSYKSSAST
1537 NALLAQSQAMTTSQLMSKYLKREPRVQFTPIKSPESPSPPGSGDGLPKGTYQLVTPISGSSS
1538 KPGATTGAISKYTTGSVESSINANSQKLSSPRLCNSKDSNSRTGTASSTTPATSMVSTGRR
1539 LFDLASSSSSETEKTYIGGTTAASGAITTTIYNDTKNSGSSSSKSGIGGSGTGGLGAVSG
1540 ASSETRFSGSTLFGSSGLGNGNGSSHNSASPSPTTTNGNGNHNTMHLYGTLPKNGTS
1541 TGAALFGGSANSSSYHSSASGSGAGTASSSGVSSMTGSTNSYDFYTSTSSTVSSSRPFAN
1542 GGNNYHTLGTYRAQYAATNPFLDAFDEKPGSNGGNAHGEEKLGADKGHHRAAVMAFQSS
1543 GDSKNGSDEYDDIK
1544

1545 **BRP isoform G fragment 1 (length: 1-650 AA; Synthetic gene)**

1546 **Primer**

1547 **BRP1F:**

1548 GGGGACAAGTTTGTACAAAAAAGCAGGCTCCATGTCTCGTGATGACTATAATCCC

1549 **BRP650R:**

1550 GGGGACCACTTTGTACAAGAAAGCTGGGTGTTGGGTTCTTCTCAGCTC

1551 **Giving rise to the following sequence:**

1552 MSRDDYNPVTSSGVRSPGRVRRQLQELPTVDRSPSRDYGAPRGSPLAMGSPYYRDMDEPT
1553 SPAGAGHHRSRASRPPMAHAMDYPRTRYQSLDRGGLVDPHDREFIPIREPRDRSRDRSL
1554 ERGLYLEDELYGRSARQSPSAMGGYNTGMGPTSDRAYLGD LQHQN TD LQRELGNL KREL
1555 ELTNQKLGSSMHSIKTFWSPELKKERALRKEESAKYSLINDQLKLLSTENQKQAMLVRQLEE
1556 ELRLRMRQP NLEMQQQMEAIYAENDHLQREISILRETIKDLECRVETQKQTLIARDESIIKLE
1557 MLQAKGMGKEEERQMFQQMQAMAQKQLDEFRLIQRRDQEILAMAAMKMTLEE QHQDYQ
1558 RHIAVLKESLCAKEEHYNMLQTDVEEMRARLEEKNRLIEKKTQGT LQTVQERNRLTSELTEL
1559 KDHMDIKDRKISVLQRKIENLEDLLKEKDNQVDMARARLSAMQAHHSSEGALTSLEEAIGD
1560 KEKQMAQLRDQRDRAEHEKQEERDLHEREVADYKIKLRAAESEVEKLQTRLERAVTERERL
1561 EIKLEASQSELGKSKAELEKATCEMGRSSADWESTKQRIARLELENERLKHDLERSQNVQK
1562 LMFETGKISTTFGR TMTTSQELDRAQERADKASAE LRRTQ
1563

1564 **BRP isoform G fragment 2 (100-650aa; Synthetic gene)**

1565 **Primer**

1566 **BRP100F:**

1567 GGGGACAAGTTTGTACAAAAAAGCAGGCTCCATGCATGATAGAGAATTTATCCCAATCC

1568 **BRP650R:**

1569 GGGGACCACTTTGTACAAGAAAGCTGGGTGTTGGGTTCTTCTCAGCTC

1570 **Giving rise to the following sequence:**

1571 HDREFIPIREPRDRSRDRSLERGLYLEDELYGRSARQSPSAMGGYNTGMGPTSDRAYLGD
1572 LQHQN TD LQRELGNL KRELEL TNQKLGSSMHSIKTFWSPELKKERALRKEESAKYSLINDQL
1573 KLLSTENQKQAMLVRQLEEELRLRMRQP NLEMQQQMEAIYAENDHLQREISILRETIKDLEC
1574 RVETQKQTLIARDESIIKLEMLQAKGMGKEEERQMFQQMQAMAQKQLDEFRLIQRRDQ
1575 EILAMAAMKMTLEE QHQDYQRHIAVLKESLCAKEEHYNMLQTDVEEMRARLEEKNRLIEKKT
1576 QGT LQTVQERNRLTSELTELKD HMDIKDRKISVLQRKIENLEDLLKEKDNQVDMARARLSAM
1577 QAHHSSSEGALTSLEEAIGDKEKQMAQLRDQRDRAEHEKQEERDLHEREVADYKIKLRAAE
1578 SEVEKLQTRLERAVTERERLEIKLEASQSELGKSKAELEKATCEMGRSSADWESTKQRIARL
1579 ELENERLKHDLERSQNVQKLMFETGKISTTFGR TMTTSQELDRAQERADKASAE LRRTQ
1580

1581 **BRP isoform G fragment 3 (length: 100-850 AA; Synthetic gene)**

1582 **Primer**
1583 **BRP100F:**
1584 GGGGACAAGTTTGTACAAAAAAGCAGGCTCCATGCATGATAGAGAATTTATCCCAATCC
1585 **BRP850R:**
1586 GGGGACCACTTTGTACAAGAAAGCTGGGTGCTCGCTGCGTTCCTTG
1587 **Giving rise to the following sequence:**
1588 HDREFIPIREPRDRSRDRSLERGLYLEDELYGRSARQSPSAMGGYNTGMGPTSDRAYLGD
1589 LQHQNLDLQRELGNLKRELELTNQKLGSSMHSIKTFWSPELKKERALRKEESAKYSLINDQL
1590 KLLSTENQKQAMLVRQLEEEELRLMRQP NLEMQQQMEAIYAENDHLQREISILRETIKDLEC
1591 RVETQKQTLIARDESIIKLLLEMLQAKGMGKEEERQMFQQMQAMAQKQLDEFRLIQRRDQ
1592 EILAMAAKMKTLEE QHQDYQRHIAVLKESLCAKEEHYNMLQTDVEEMRARLEEKNRLIEKKT
1593 QGTLQTVQERNRLTSELTELKDHMDIKDRKISVLQRKIENLEDLLKEKDNQVDMARARLSAM
1594 QAHHSSSEGALTSLEEAIGDKEKQMAQLRDQRDRAEHEKQEERDLHEREVADYKIKLRAAE
1595 SEVEKLQTRLERAVTERERLEIKLEASQSELGKSKAELEKATCEMGRSSADWESTKQRIARL
1596 ELENERLKHDLERSQNVQKLMFETGKISTTFGRTTMTTSQELDRAQERADKASAE LRRTQA
1597 ELRVTQSDAERAREEAAALQE KLEKSQGEVYRLKAKLENAQGEQESLRQELEKAQSGVSRI
1598 HADRDRAFSEVEKIKEEMERTQATLGKSQ LQHEKLQNSLDKAQNEVDHLQDKLDKACTEN
1599 RRLVLEKEKLT YDYNLQSQLDKALGQAARMQKERETLSLDTDRIREKLEKTQVQLGRIQKE
1600 RDQFSDELETLKERSE
1601

1602 **BRP isoform G fragment 4 (length: 790-1786 AA; Synthetic gene)**

1603 **Primer**
1604 **BRP790F:**
1605 GGGGACAAGTTTGTACAAAAAAGCAGGCTCCATGCAATCCCAGTTGGACAAGG
1606 **BRP1786R:**
1607 GGGGACCACTTTGTACAAGAAAGCTGGGTGGAAGAAGGATTTGAGGAAACCG
1608 **Giving rise to the following sequence:**
1609 QSQLDKALGQAARMQKERETLSLDTDRIREKLEKTQVQLGRIQKERDQFSDELETLKERSE
1610 SAQTLMLKAARDREAMQTDLEVLKERYEKSHAIQQKLQMERDDAVTEVEILKEKLDKALYAS
1611 QKLIDEKDTSNKEFEKMLEKYDRAQNEIYRLQSRCDTAEADRARLEVEAERSGLAASKARE
1612 DLRKLQDESTRLQEACDRAALQLSRAKECEDNARSELEHSRDRFDKLTDIRRAQGEKEHF
1613 QSELERVTYELERAHAAQTKASASVEAAKEEAAHYAVELEKMRDRYEKSQVELRKLQD TDT
1614 FGRETRRLKEENERLREKLDKTLMELETIRGKSQYSESEFEKYKDKYEKIEME VQNMESKLH
1615 ETSLQLELSKGEVAKMLANQEKQRSELERAHIEREKARDKHEKLLKEVDRLRLQQSSVSPG
1616 DPVRASTSSSSALSAGERQEIDRLRDRLEKALQSRDATELEAGRLAKELEKAQMHLAKQQE
1617 NTESTRIEFERMGAELGRLHDRLEKAEAREALRQANRSGGAGAAPHQLEKHVQKLESD
1618 VKQLAMEREQLVLQLEKSQEILMNFQKELQNAEAE LQKTREENRKLNRNGHQVPPVAAPPAG
1619 PSPAEFQAMQKEIQTLQQKLQESERALQAAGPQQAQAAAAAGASREEIEQWRKVIEQEKS
1620 RADMADKAAQEMHKRIQLMDQHDKDQHAQM QKMQQQMQQQQQAQQAVQQAQQQQS
1621 AAGAGGADPKELEKVRGELQAAC TERDRFQQQLELLVTELEKSKMSNQEQAKQLQTAQQQ
1622 VQQLQQQVQQLQQQMQLQQAASAGAGATDVQRQQLEQQQKQLEEV RKQIDNQAKATE
1623 GERKIIDEQRKQIDAKRKDIEEKEKKMAEFDVQLRKRKEQMDQLEKSLQTQGGGAAAAGEL
1624 NKKLMDTQRQLEACVKELQNTKEEHKKAATETERLLQLVQMSQEEQNAKEKTIMDLQQALK
1625 IAQAKVKQAQTQQQQQQDAGPAGFLKSFF
1626

1726 **Statistics**

1727 Data were analyzed using Prism (Version 5, GraphPad Software, CA, USA). To compare two
1728 groups, two-tailed t-test or Mann-Whitney U-test was used for all data sets. Data distribution
1729 was assumed to be normal but this was not formally tested. For comparison of more than two
1730 groups, nonparametric one-way analysis of variance (ANOVA) tests were used, followed by
1731 a Turkey's multiple comparison test. No statistical methods were used to pre-determine
1732 sample sizes but our sample sizes are similar to those generally employed in the field. Data
1733 collection and analyses were not performed blind to the conditions of the experiments, nor
1734 was data collection randomized. For immunostainings, all genotypes were prepped in one
1735 session, stained in one cup and analyzed in an unbiased manner. For electrophysiological
1736 recordings, genotypes were measured in an alternating fashion on the same day and strictly
1737 analyzed in an unbiased manner. P values and n values are given in the figure legends,
1738 reporting checklist or main text. Means are annotated \pm SEM. Asterisks are used to denote
1739 significance: *, $p < 0.05$; **, $p < 0.01$; ***, $p < 0.001$; n.s. (not significant), $p > 0.05$. For further
1740 information a supplementary methods checklist is available with the manuscript.

1741

1742 **Mathematical Modelling**

1743 We wanted to investigate whether synaptic transmission at the NMJ may rely on two
1744 independently operating release pathways with identical Ca^{2+} sensing and vesicle fusion
1745 mechanisms that are located at different distances from the Ca^{2+} channels. We were
1746 especially interested in understanding whether loss of the close pathway may underlie the
1747 *Unc13A^{Null}* phenotype. To test this, we developed a mathematical model (see Figure 7) to
1748 simulate vesicle release and postsynaptic responses. The model assumes two independent
1749 release pathways controlled by identical Ca^{2+} sensitivity and identical fusion rate constants
1750 which only differ in their distances from the Ca^{2+} source.

1751 Calculation of local Ca^{2+} signals at distinct distances from the Ca^{2+} source

1752 To calculate Ca^{2+} transients occurring upon opening of voltage-gated channels in the
1753 presynapse, we used the tool 'Calc' (v6.8.5 x64) developed and maintained by Victor
1754 Matveev⁶³ which allows the simulation of Ca^{2+} concentrations in four dimensions (spatial and
1755 temporal). It permits the definition of the position of the Ca^{2+} source, Ca^{2+} currents, the
1756 reaction volume, and endogenous and exogenous Ca^{2+} . To reproduce conditions similar to
1757 those at AZs of the *Drosophila* NMJ, Ca^{2+} influx was simulated from a point source placed in
1758 the bottom center of a reaction box (depth x width x height: $0.54 \times 0.54 \times 0.4 \mu\text{M}$, volume:
1759 $116.64 \mu\text{m}^3$). We assumed these currents to be Gaussian with a full-width at half maximum
1760 of $460 \mu\text{s}$, which was previously shown to be in reasonable agreement with Ca^{2+} transients at
1761 sufficient distances ($>30 \text{ nm}$) from Ca^{2+} channel clusters, even if channels gated
1762 stochastically³⁶. The simulated reaction volume dimensions were chosen to match
1763 experimentally determined inter-AZ distances of 540 nm (observation from STED
1764 experiments; data not shown) and the height was taken from Meinrenken et al.³⁶. Like in
1765 previous simulations of local Ca^{2+} diffusion at single active zones^{36, 49}, boundaries were
1766 assumed to be reflective, which intrinsically accounts for exchange of Ca^{2+} ions across AZs
1767 and thus allows consideration of all AZs and their interactions while only simulating one. To
1768 obtain the local free $[\text{Ca}^{2+}]$ at the positions of the two independent release pathways
1769 assumed in our model, the temporal changes in Ca^{2+} upon AP-stimulation at two distinct
1770 distances from the AZ center (Ca^{2+} source) were calculated. This assumes radial symmetry
1771 between Ca^{2+} channel clusters and vesicles, a premise that is in line with a recently
1772 proposed "perimeter release model" found at the Calyx of Held synapse⁴⁹. For our purposes,
1773 Calc was iteratively called from a custom-written MATLAB (2015b, Mathworks Inc., MA,
1774 USA) script, where one or several of the free parameters (explained below) were written into
1775 the parameter-file with each iteration, and used in the calculations. Basal Ca^{2+} concentrations
1776 were assumed to be 50 nM , the diffusion coefficient was set to $0.223 \mu\text{m}^2/\text{ms}$ ⁶⁴, and Ca^{2+}

1777 extrusion rate was 0.4 ms^{-1} ⁶⁵. To mimic physiological Ca^{2+} buffering, we incorporated ATP
 1778 (diffusion coefficient = $0.22 \text{ } \mu\text{m}^2/\text{ms}$, $K_D = 200 \text{ } \mu\text{M}$, $k_{\text{off}} = 100 \text{ ms}^{-1}$, $[\text{ATP}] = 650 \text{ } \mu\text{M}$ ^{37, 49}) and a
 1779 fixed endogenous Ca^{2+} buffer (diffusion coefficient = $0.001 \text{ } \mu\text{m}^2/\text{ms}$, $K_D = 100 \text{ } \mu\text{M}$, $k_{\text{on}} = 0.1$
 1780 $\text{ } \mu\text{M}^{-1}\text{ms}^{-1}$, concentration = 4 mM ^{65, 66}). To simulate the EGTA-AM wash-in experiment (Figure
 1781 7g), we included another buffer representing EGTA in increasing concentrations (diffusion
 1782 coefficient = $0.22 \text{ } \mu\text{m}^2/\text{ms}$, $K_D = 0.07 \text{ } \mu\text{M}$, $k_{\text{on}} = 0.0105 \text{ } \mu\text{M}^{-1}\text{ms}^{-1}$)⁶⁷. EGTA concentrations
 1783 within the AZ at different time points ([3 6 9 12] min) were calculated assuming the following
 1784 exponential growth function:

$$1785 \quad (1.1) \quad [\text{EGTA}](t) = [\text{EGTA}]_{\infty}(1 - e^{-\frac{t}{\tau}})$$

1786 where $[\text{EGTA}]_{\infty}$ is the asymptotic EGTA concentration at $t=\infty$ and τ is the time constant. Both
 1787 were set as free parameters in our simulations (see below). To simulate synaptic responses
 1788 at varying extracellular Ca^{2+} concentrations ($[\text{Ca}^{2+}]_{\text{ext}}$, [0.75 1.5 3 6 10] mM), we assumed a
 1789 Michaelis-Menten-like relationship for calculating the electrical charge of Ca^{2+} influx
 1790 (equation(1.2))⁶⁸.

$$1791 \quad (1.2) \quad Q_{\text{Ca}^{2+}} = Q_{\text{max}} \cdot \frac{[\text{Ca}^{2+}]_{\text{ext}}}{[\text{Ca}^{2+}]_{\text{ext}} + K_M}$$

1792 Exocytosis model

1793 Ca^{2+} -driven exocytosis from distinct RRP_s at both locations was described by the so-called
 1794 “allosteric model” developed by Lou et al.³⁸ where single vesicles bind up to five Ca^{2+} ions,
 1795 which maximizes their exocytosis rate. There is slower release from states with fewer Ca^{2+}
 1796 ions associated, and even in the absence of Ca^{2+} , release rates are non-zero. We did not
 1797 explicitly describe endocytosis and vesicle replenishment reactions, but assumed constant
 1798 refilling of the RRP_s (R) from upstream (infinite) depots. All reactions are comprised in the
 1799 chemical equation depicted in Supplementary Figure 8 (all considerations identical for
 1800 pathways 1 and 2).

1801

1802 The temporal changes of all states are given by the following kinetic equations, which are
 1803 ordinary differential equations (R – releasable vesicle, C_{ref} - refill constant, F – fused vesicle):

$$1804 \quad (1.3) \quad \frac{d[R]}{dt} = -(5[\text{Ca}^{2+}]k_3 + L^+)[R] + k_{-3}[RCa] + C_{\text{ref}}$$

$$1805 \quad (1.4) \quad \frac{d[RCa]}{dt} = 5[\text{Ca}^{2+}]k_3[R] - (k_{-3} + 4[\text{Ca}^{2+}]k_3 + L^+f)[RCa] + 2k_{-3}b[RCa_2]$$

$$1806 \quad (1.5) \quad \frac{d[RCa_2]}{dt} = 4[\text{Ca}^{2+}]k_3[RCa] - (2k_{-3}b + 3[\text{Ca}^{2+}]k_3 + L^+f^2)[RCa_2] + 3k_{-3}b^2[RCa_3]$$

$$1807 \quad (1.6) \quad \frac{d[RCa_3]}{dt} = 3[\text{Ca}^{2+}]k_3[RCa_2] - (3k_{-3}b^2 + 2[\text{Ca}^{2+}]k_3 + L^+f^3)[RCa_3] + 4k_{-3}b^3[RCa_4]$$

$$1808 \quad (1.7) \quad \frac{d[RCa_4]}{dt} = 2[\text{Ca}^{2+}]k_3[RCa_3] - (4k_{-3}b^3 + [\text{Ca}^{2+}]k_3 + L^+f^4)[RCa_4] + 5k_{-3}b^4[RCa_5]$$

$$1809 \quad (1.8) \quad \frac{d[RCa_5]}{dt} = [\text{Ca}^{2+}]k_3[RCa_4] - (5k_{-3}b^4 + k_4)[RCa_5]$$

$$1810 \quad (1.9) \quad \frac{d[F]}{dt} = L^+([R] + f[RCa] + f^2[RCa_2] + f^3[RCa_3] + f^4[RCa_4]) + k_4[RCa_5]$$

1811 where:

$$1812 \quad (1.10) \quad f = \sqrt[5]{\frac{k_4}{L^+}}$$

1813 To find the starting point of the simulations, steady state populations of the vesicle states at
 1814 50 nM resting $[Ca^{2+}]_0$ were calculated and C_{ref} determined by forcing mass conservation of
 1815 vesicles (i.e. constant pool sizes). This was achieved by assuming a replenishment of
 1816 vesicles equal to the number of vesicles fused at steady state, as seen in equation (1.11):

1817

$$1818 \quad (1.11) \quad C_{ref} = L^+([R]_0 + f[RCa]_0 + f^2[RCa_2]_0 + f^3[RCa_3]_0 + f^4[RCa_4]_0) + k_4[RCa_5]_0$$

1819 with the index „0“ denoting steady state values. Steady state values were calculated with the
 1820 function *fsolve* in MATLAB from equations (1.3)-(1.7) and mass conservation. Exocytosis
 1821 was driven by the temporal changes in Ca^{2+} at the vesicle position (pathway A or B) and the
 1822 temporal development of all vesicle states was calculated by integrating the kinetic equations
 1823 (1.3)-(1.10) using the *ode15s* function in MATLAB, yielding a time vector and a
 1824 corresponding vector giving the population of all vesicle states at each time point.

1825 In our simulations, Wild type synapses had release from both pathways (Figure 7i,
 1826 distance values see Supplementary Table 2), so that the total transmitter release (NT) was
 1827 summed over those (NT(WT) = F(pathway 1)+F(pathway 2)). *Unc13A^{Null}* mutants were
 1828 assumed to only have release from pathway 2 (NT(*Unc13A^{Null}*)=F(pathway 2)), but at the
 1829 same time we corrected for increased Ca^{2+} channel numbers observed in *Unc13A^{Null}* in the
 1830 model (described below).

1831 To generate eEJCs that could be compared to the experimentally determined
 1832 postsynaptic responses, the temporal change of the released vesicles (NT) was interpolated
 1833 over a resampled time vector using the MATLAB function *interp1* (sampling rate: $10^6 s^{-1}$). For
 1834 quantization to single vesicle transitions, the resulting vector was rounded (using the
 1835 MATLAB function *round*), and then differentiated (with the MATLAB function *diff*) to give
 1836 differences between successive elements along the vector. The result is a vector that - at
 1837 these sufficiently high sampling rates - only contained the values 0 and 1, where 1 demarks
 1838 the timing of a single vesicle fusion event. To calculate evoked excitatory junctional currents
 1839 (eEJCs) corresponding to these events, this vector was convolved with genotype-specific
 1840 mEJCs (using the MATLAB function *conv*) derived from fitting individual experimentally
 1841 acquired mEJCs with the following function modified from Equation A2 by Neher & Sakaba⁶⁹
 1842 (1.12):

$$1843 \quad (1.12) \quad mEPSC(i) = amp \cdot \left[e^{-\frac{t(i)-t_{start}}{\tau_{decay}}} - e^{-\frac{t(i)-t_{start}}{\tau_{rise}}} \right] + corr$$

1844 where *amp* is the maximal glutamate release which is liberated with a time constant τ_{rise}
 1845 resulting in the mEPSC rise. The effect of the transmitter dissipates with a time constant
 1846 τ_{decay} , resulting in the mEPSC decay. Both processes begin with the liberation of the
 1847 transmitter at the time t_{start} . *corr* is a constant baseline offset. This function was fit to all
 1848 individual mEPSCs (using the MATLAB function *fminsearch*) and the average of all
 1849 parameters was used to generate representative, genotype specific mEJCs. These had
 1850 amplitudes of -503 pA (Wild type) and -614 pA (*Unc13A^{Null}*). The convolution led to simulated
 1851 compound eEJCs as depicted in Figure 7j.

1852

1853 **Comparison of simulation and experimental values, and parameter optimization**

1854 In order to compare our simulation output with the experimentally determined values, we
 1855 calculated first and second eEJC amplitudes and their time-to-peak (ttp) from our simulated
 1856 traces. Just as in the analysis of experimentally recorded currents, the first amplitudes were
 1857 calculated as the difference between baseline and first minimum, and paired-pulse ratios
 1858 were calculated as the difference between second peak and maximum value between both
 1859 peaks (\triangleq starting point of second response) divided by the first amplitude. To calculate I/I_{max}

1860 values, I_{max} was determined by fitting a hill curve to the first amplitudes at all $[Ca^{2+}]_{ext}$ values,
 1861 as was done for experimental data, shown in equation (1.13):

1862 (1.13)
$$I = I_{max} \frac{[Ca^{2+}]_{ext}^h}{K_D^h + [Ca^{2+}]_{ext}^h}$$

1863

1864 where h is the hill slope. In this instance I_{max} , K_D , and h were determined by the least square
 1865 MATLAB curve fitting function *lsqcurvefit*.

1866 All parameters of our model were either taken from the literature, experimentally
 1867 determined, or optimized to match experimental data. We identified a minimal set of 9 free
 1868 parameters as input for our optimization algorithm: (1) The distance of pathway A to the Ca^{2+}
 1869 channels and (2) the size of the RRP of pathway A; (3) the distance of pathway B to the Ca^{2+}
 1870 channels and (4) the size of the RRP of pathway B; (5 and 6) the asymptotic values of the
 1871 electrical charge over the Ca^{2+} channel cluster in the Wild type and *Unc13A^{Null}* mutants. We
 1872 assumed genotype specific differences here because of the observation that *Cac^{GFP}* spots
 1873 visualized with IHC were ~1.6-fold larger in the *Unc13A^{Null}* situation (Figure S6f). Another free
 1874 parameter - which we assumed to be identical in both genotypes - was the (7) Michaelis-
 1875 Menten constant that described the dependence of the synaptic Ca^{2+} charge as a function of
 1876 $[Ca^{2+}]_{ext}$ (see equation (1.2)). Finally, application of EGTA-AM was assumed to lead to
 1877 identical increases in synaptic EGTA levels regardless of the genotype and was described by
 1878 the (8) asymptotic $[EGTA]_{\infty}$ and (9) the time constant τ of EGTA accumulation in the cell to
 1879 calculate $[EGTA](t)$ at $t = [3\ 6\ 9\ 12]$ minutes (see equation (1.1)).

1880 To quantify the deviation between model simulation and data, cost values indicating the
 1881 quality of the fit were calculated as follows: differences between experimental (exp) and
 1882 simulated (sim) values were calculated and normalized once to the experimental and to the
 1883 simulated values. The mean of these values was squared (Chi-squared cumulative cost
 1884 function, see equation (1.14)). To account for the different number of data points in each
 1885 experiment, a weight factor was introduced. The model was fit to the following datasets: 9 (5
 1886 wt, 4 mutant) PPR values recorded at various $[Ca^{2+}]_{ext}$ (Figure 7E), 8 EGTA values (two at
 1887 each time point, see Figure 7G), 1 shift in the time-to-peak (ttp) value (the shift between Wild
 1888 type and *Unc13A^{Null}* ttps, see Figure S4c), but 10 values in each 1st amplitude and I/I_{max}
 1889 values (Figure 7B+C). The weighting factors were hence:

1890
$$weight = \left[\frac{5}{5} (PPR\ wt); \frac{5}{4} (PPR\ mutant); \frac{5}{4} (EGTA\ wt); \frac{5}{4} (EGTA\ mutant); \frac{10}{1} (ttp); \right.$$

1891
$$\left. \frac{5}{5} (1st\ amp\ wt); \frac{5}{5} (1st\ amp\ mutant); \frac{5}{5} \left(\frac{1}{I_{max}}\ wt \right); \frac{5}{5} \left(\frac{1}{I_{max}}\ mutant \right) \right]$$

1892 (1.14)

$$cumulative\ cost = \sum_{i=1}^n weight(n) \cdot \left\{ \frac{\left[\frac{exp(i) - sim(i)}{sim(i)} \right] + \left[\frac{exp(i) - sim(i)}{exp(i)} \right]}{2} \right\}^2$$

1893 where n is the number of simulated experiments and $weight(n)$ the respective weighting
 1894 factor. The weighted cumulative costs for each $[Ca^{2+}]_{ext}$ were then summed to give the final
 1895 cost value. Best fit parameters were found by minimizing cost values with the MATLAB
 1896 function *fminsearch*. The best fit parameters can be found in Supplementary Table 2
 1897 (highlighted in red). The choice of *fminsearch* as a solver posed the risk of our results
 1898 representing a local minimum of the objective function (the cumulative cost). Therefore, we
 1899 performed a separate global optimization using a genetic algorithm (MATLAB function *ga*,
 1900 implemented in the global optimization toolbox) with loose constraints and a small population
 1901 size of 30 individuals in each generation, but otherwise with all routines identical to the ones
 1902 described above. Constraints and a small population size were necessary for feasibility, as
 1903 calculations were very time-consuming even with highly efficient parallel execution of CalC

1904 (MATLAB function *parfor*). As expected from a global minimum at the parameter values
1905 found by *fminsearch*, this routine identified similar parameter values (data not shown).

1906

1907 **Data and code availability**

1908 The data that support the findings of this study are available from the corresponding author
1909 upon request. Furthermore all custom-written code files are available upon request.

1910

1911

1912 **METHODS-ONLY REFERENCES**

1913 51. Sigrist, S.J., Reiff, D.F., Thiel, P.R., Steinert, J.R. & Schuster, C.M. Experience-
1914 dependent strengthening of Drosophila neuromuscular junctions. *J. Neurosci.* **23**,
1915 6546-6556 (2003).

1916 52. Aberle, H., *et al.* wishful thinking encodes a BMP type II receptor that regulates
1917 synaptic growth in Drosophila. *Neuron* **33**, 545-558 (2002).

1918 53. Wagh, D.A., *et al.* Bruchpilot, a protein with homology to ELKS/CAST, is required for
1919 structural integrity and function of synaptic active zones in Drosophila. *Neuron* **49**,
1920 833-844 (2006).

1921 54. Ullrich, A., *et al.* Dynamical Organization of Syntaxin-1A at the Presynaptic Active
1922 Zone. *PLoS Comput. Biol.* **11**, e1004407 (2015).

1923 55. Andlauer, T.F. & Sigrist, S.J. Quantitative analysis of Drosophila larval neuromuscular
1924 junction morphology. *Cold Spring Harb Protoc* **2012**, 490-493 (2012).

1925 56. Gottfert, F., *et al.* Coaligned dual-channel STED nanoscopy and molecular diffusion
1926 analysis at 20 nm resolution. *Biophys. J.* **105**, L01-03 (2013).

1927 57. Fuger, P., Behrends, L.B., Mertel, S., Sigrist, S.J. & Rasse, T.M. Live imaging of
1928 synapse development and measuring protein dynamics using two-color fluorescence
1929 recovery after photo-bleaching at Drosophila synapses. *Nat. Protoc.* **2**, 3285-3298
1930 (2007).

1931 58. Rasse, T.M., *et al.* Glutamate receptor dynamics organizing synapse formation in
1932 vivo. *Nat. Neurosci.* **8**, 898-905 (2005).

1933 59. Qin, G., *et al.* Four different subunits are essential for expressing the synaptic
1934 glutamate receptor at neuromuscular junctions of Drosophila. *J. Neurosci.* **25**, 3209-
1935 3218 (2005).

1936 60. Stewart, B.A., Atwood, H.L., Renger, J.J., Wang, J. & Wu, C.F. Improved stability of
1937 Drosophila larval neuromuscular preparations in haemolymph-like physiological
1938 solutions. *J. Comp. Physiol. A* **175**, 179-191 (1994).

1939 61. Worsack, J.M., Grossmann, A., Weimann, M., Hegele, A. & Stelzl, U. A stringent
1940 yeast two-hybrid matrix screening approach for protein-protein interaction discovery.
1941 *Methods Mol. Biol.* **812**, 63-87 (2012).

1942 62. Hegele, A., *et al.* Dynamic protein-protein interaction wiring of the human
1943 spliceosome. *Mol. Cell* **45**, 567-580 (2012).

1944 63. Matveev, V., Sherman, A. & Zucker, R.S. New and corrected simulations of synaptic
1945 facilitation. *Biophys. J.* **83**, 1368-1373 (2002).

1946 64. Allbritton, N.L., Meyer, T. & Stryer, L. Range of messenger action of calcium ion and
1947 inositol 1,4,5-trisphosphate. *Science* **258**, 1812-1815 (1992).

1948 65. Helmchen, F., Borst, J.G. & Sakmann, B. Calcium dynamics associated with a single
1949 action potential in a CNS presynaptic terminal. *Biophys. J.* **72**, 1458-1471 (1997).

1950 66. Xu, T., Naraghi, M., Kang, H. & Neher, E. Kinetic studies of Ca²⁺ binding and Ca²⁺
1951 clearance in the cytosol of adrenal chromaffin cells. *Biophys. J.* **73**, 532-545 (1997).

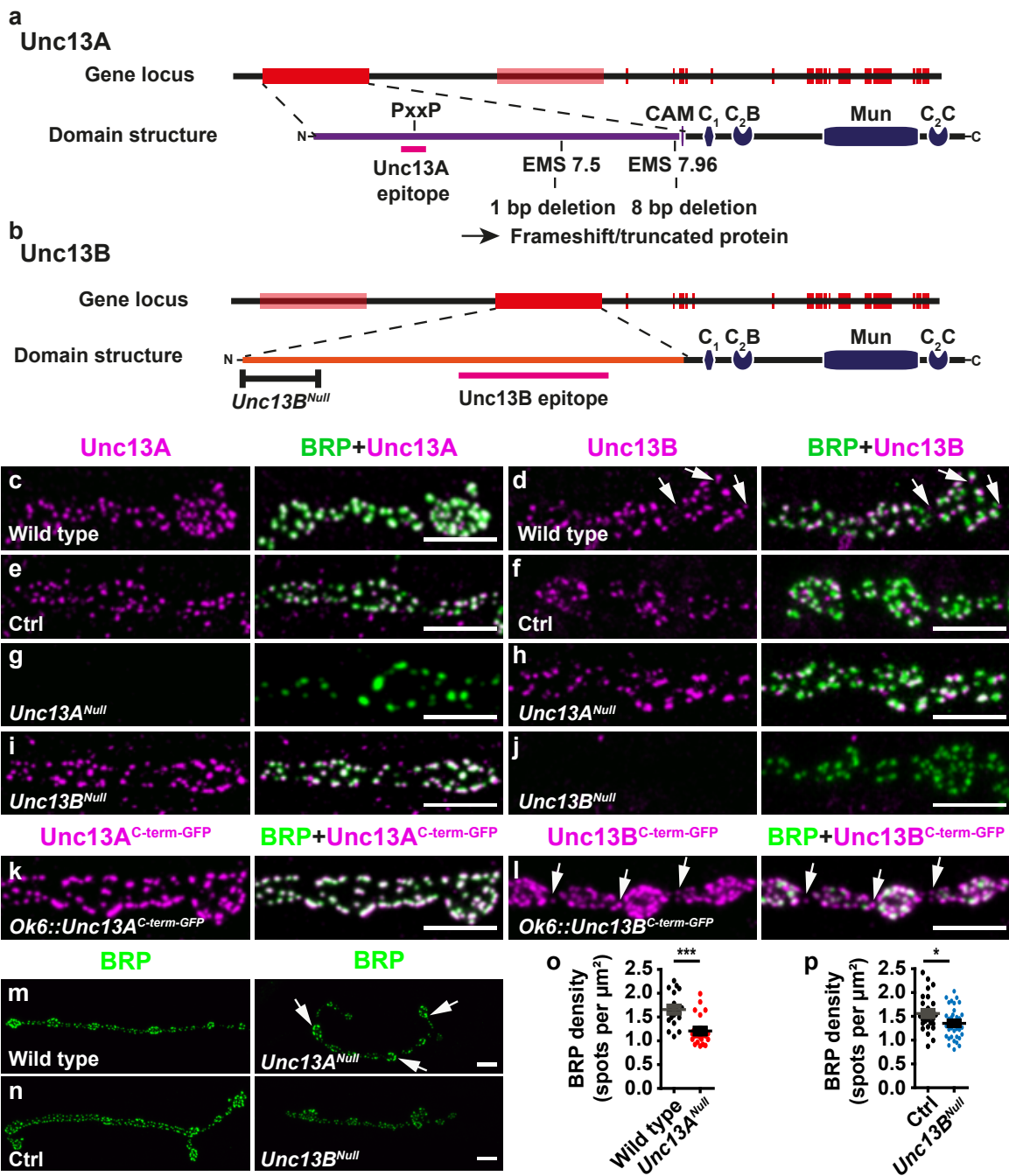
1952 67. Nagerl, U.V., Novo, D., Mody, I. & Vergara, J.L. Binding kinetics of calbindin-D(28k)
1953 determined by flash photolysis of caged Ca(2+). *Biophys. J.* **79**, 3009-3018 (2000).

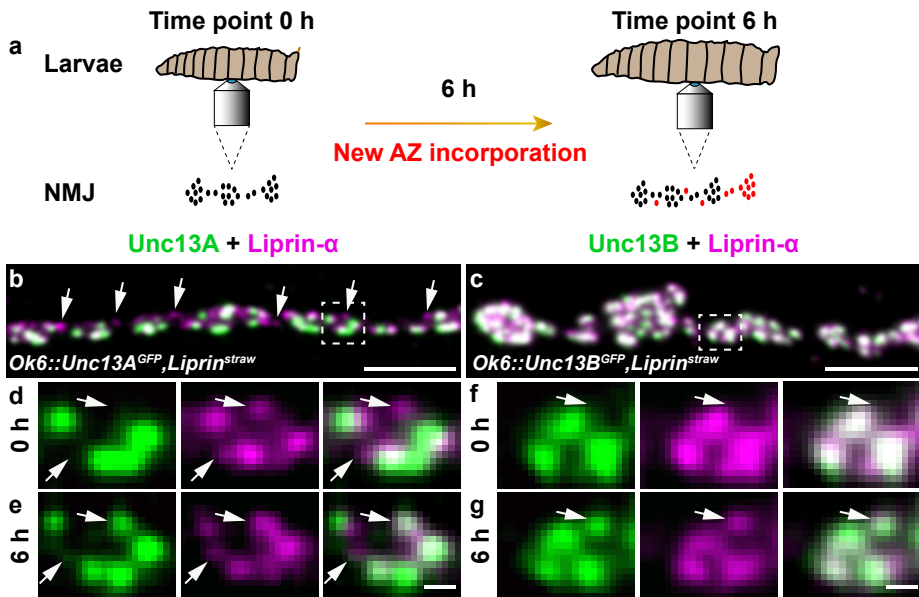
1954 68. Klingauf, J. & Neher, E. Modeling buffered Ca²⁺ diffusion near the membrane:
1955 implications for secretion in neuroendocrine cells. *Biophys. J.* **72**, 674-690 (1997).

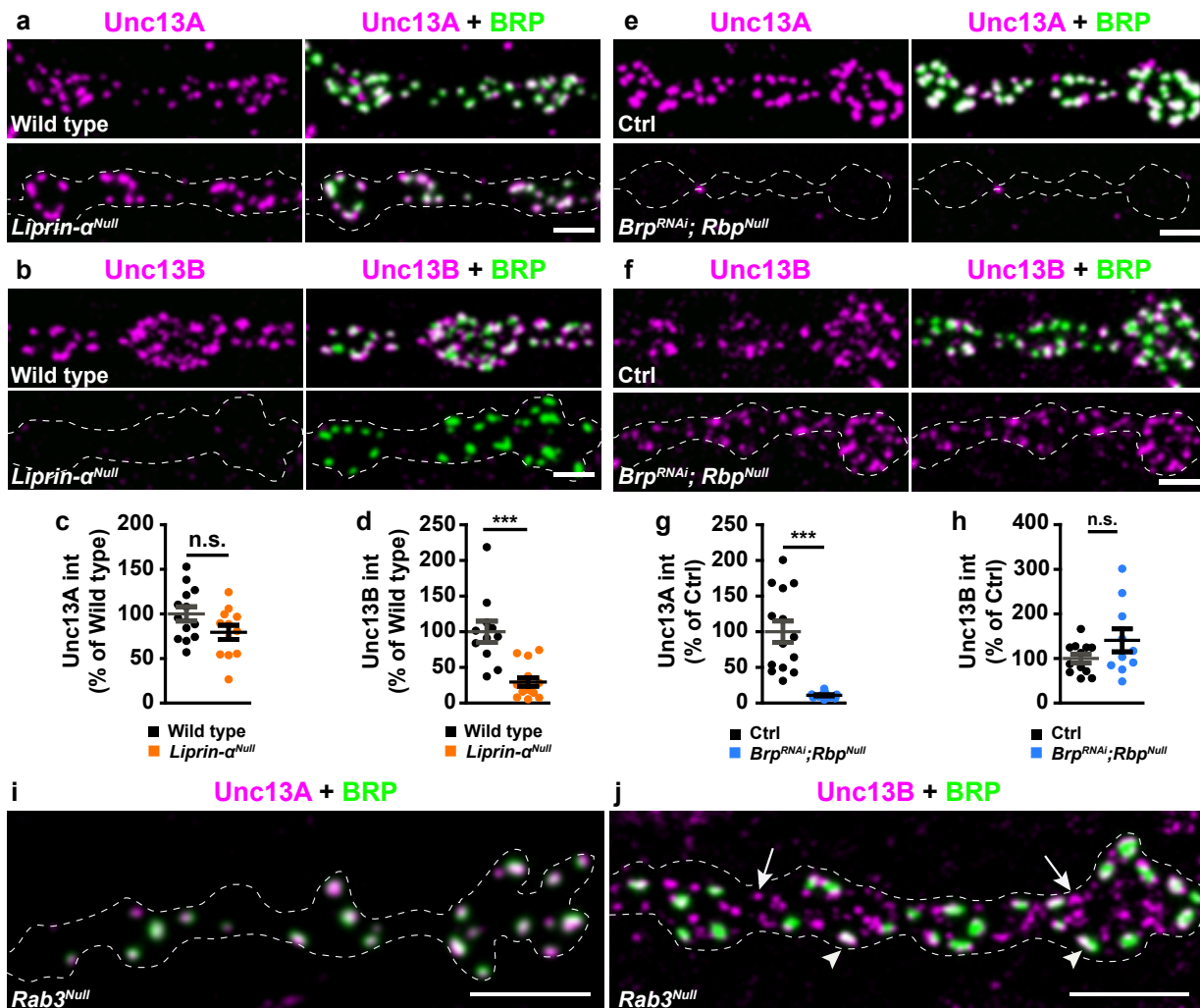
1956 69. Neher, E. & Sakaba, T. Combining deconvolution and noise analysis for the
1957 estimation of transmitter release rates at the calyx of held. *J. Neurosci.* **21**, 444-461
1958 (2001).

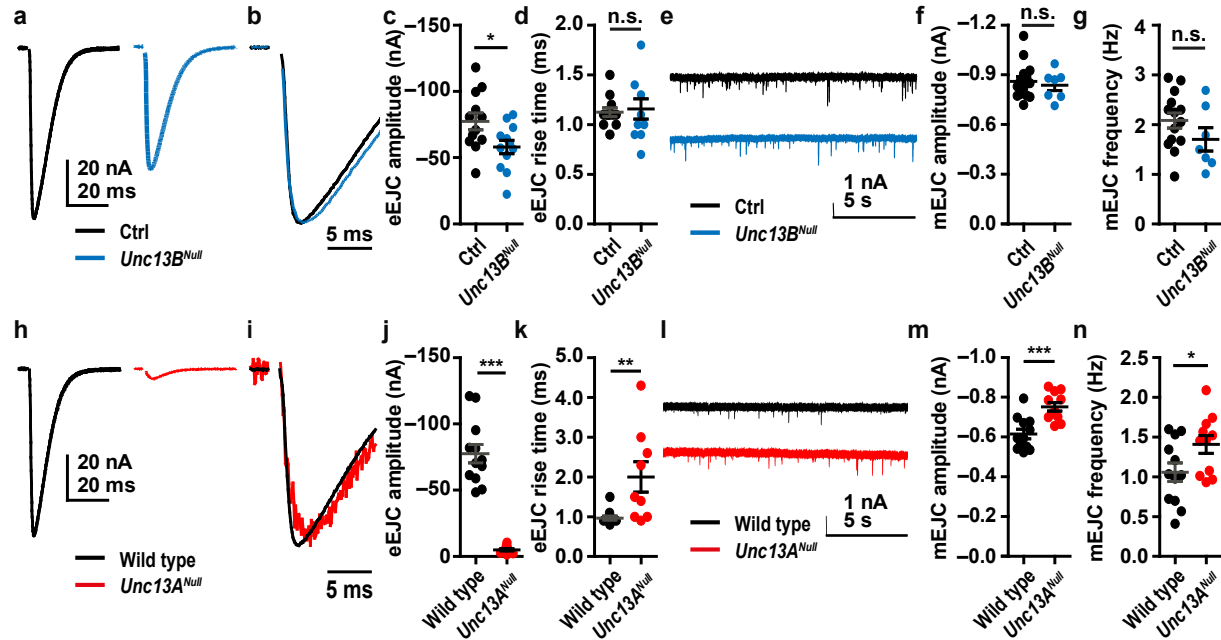
1959

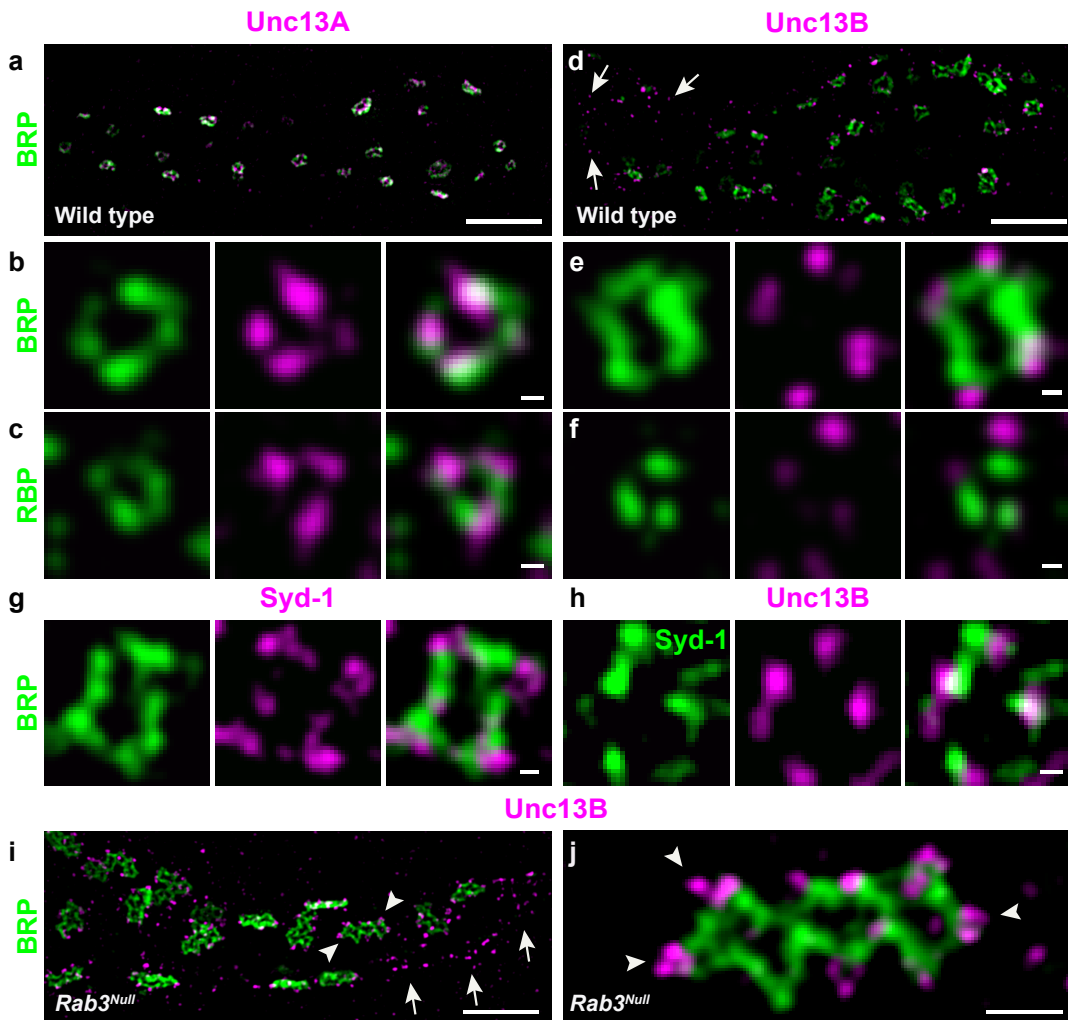
1960

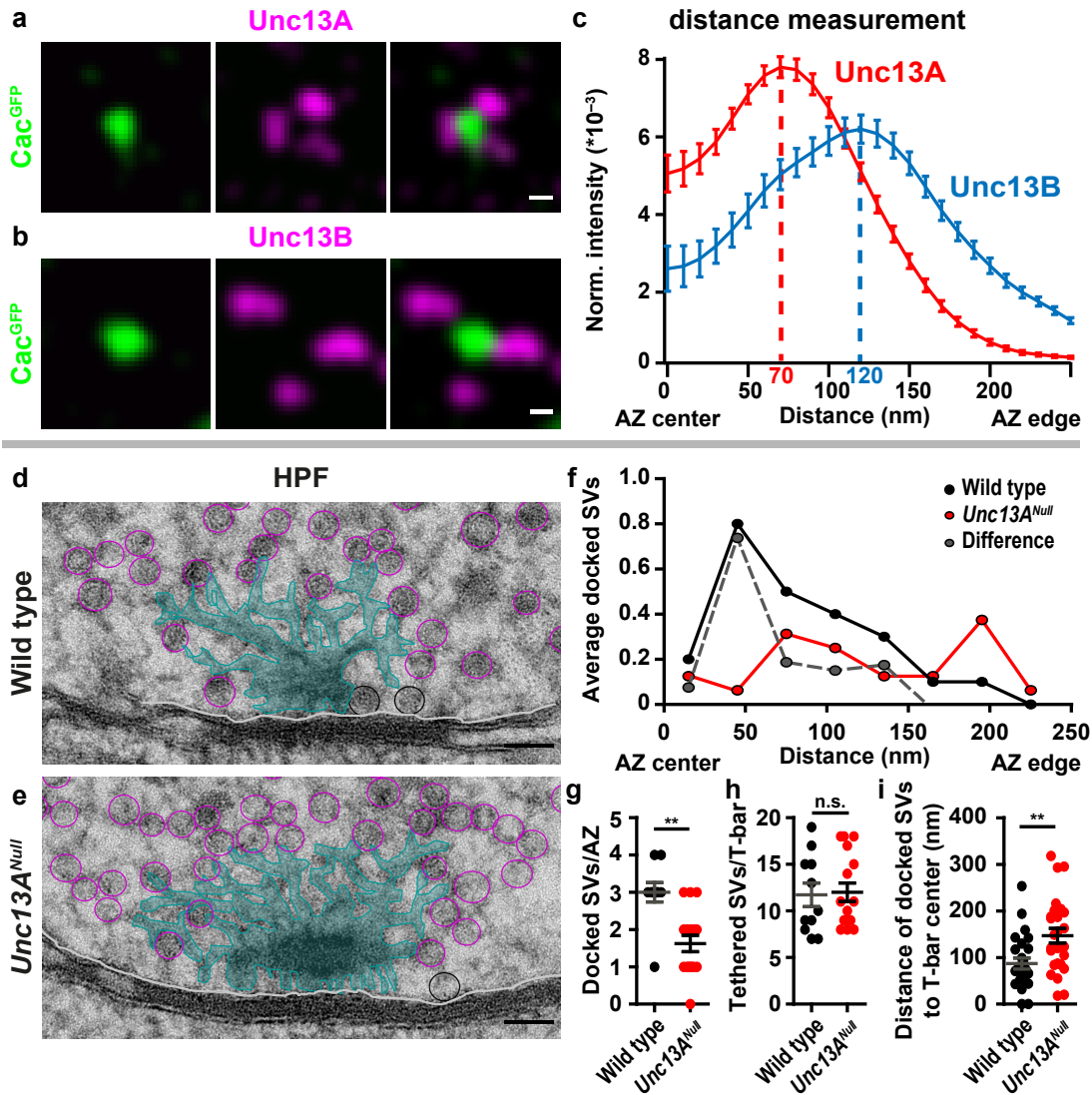


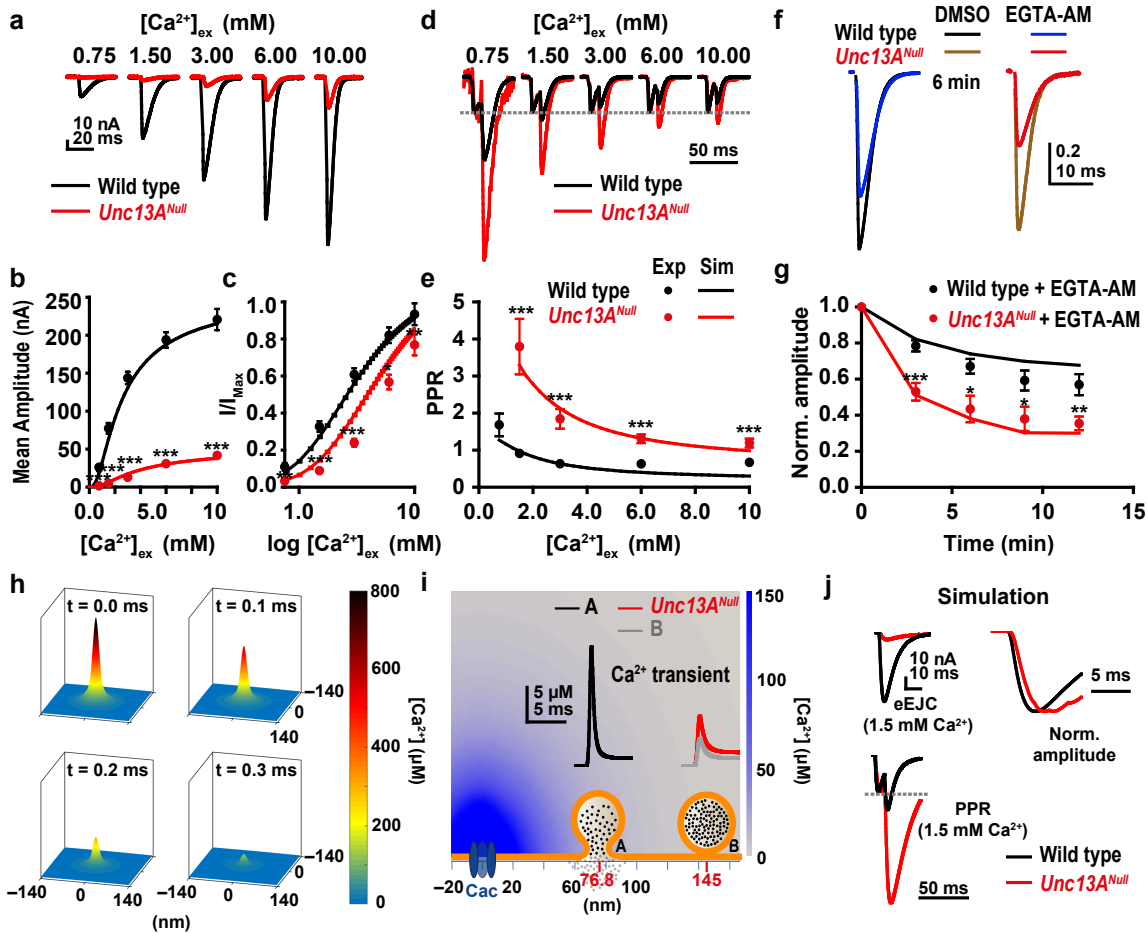


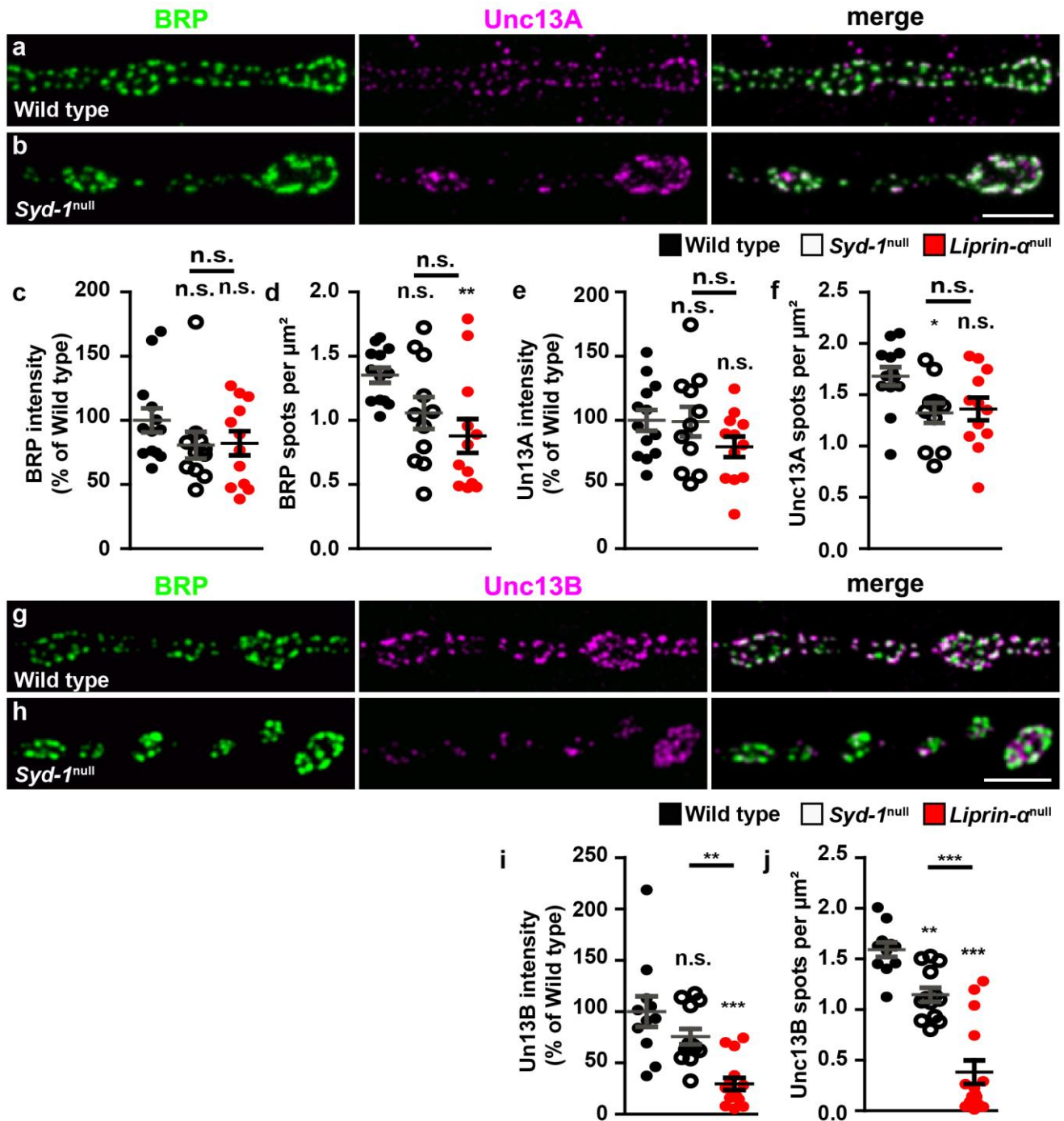










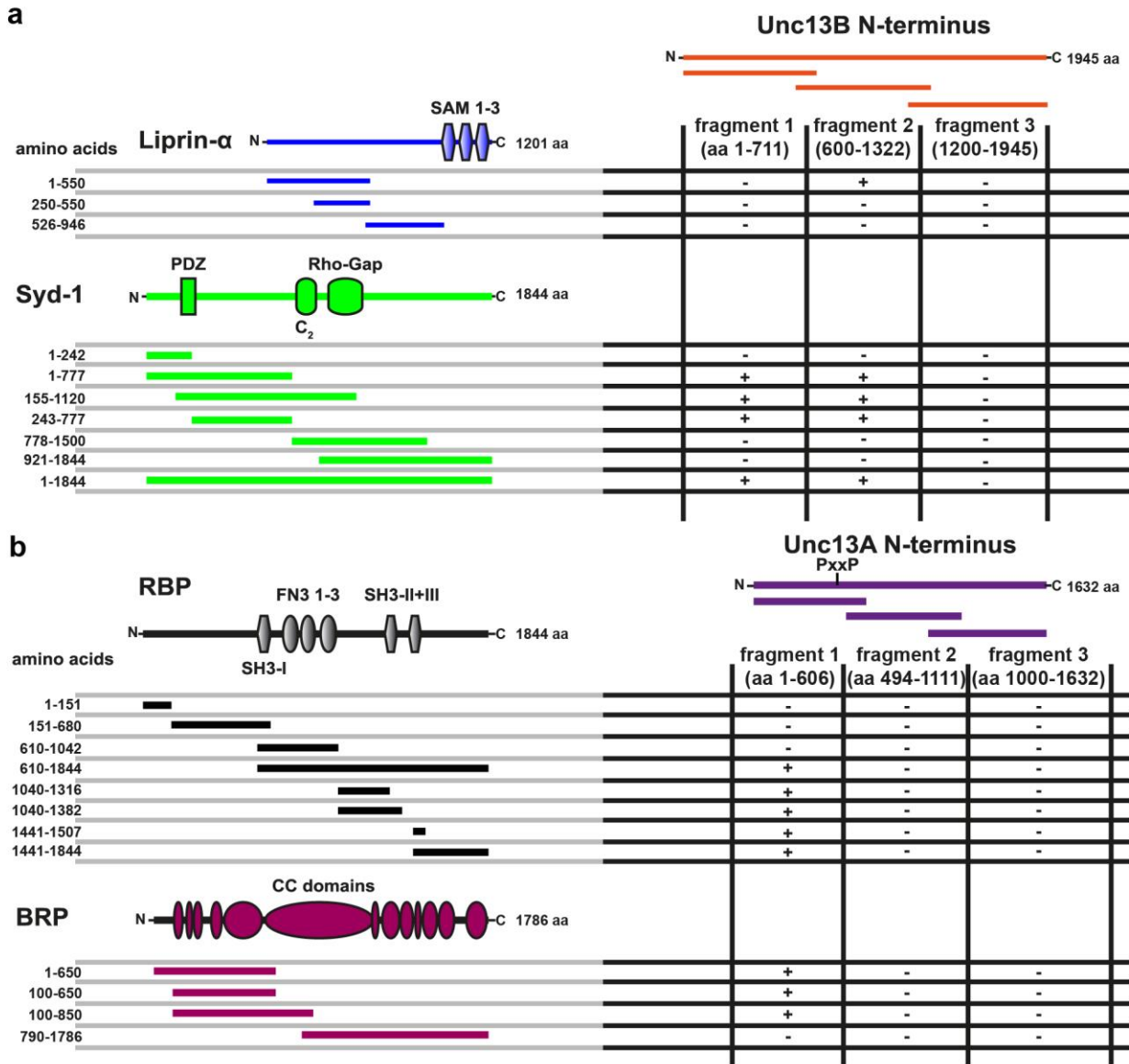


Supplementary Figure 1

Liprin- α /Syd-1 scaffold complexes organize the AZ localization of Unc13B

(a,b) Muscle 4 NMJs of segments A2-A4 from 3rd instar larvae of the displayed genotypes labelled with the antibodies (ABs) indicated. (c) Mean BRP intensity measured over the whole NMJ was unchanged in *Syd-1*^{null} and *Liprin- α* ^{null} in comparison to the Wild type (Wild type (n=13 NMJs from 4 larvae) vs. *Syd-1*^{null} (n=11 NMJs from 4 larvae) vs. *Liprin- α* ^{null} (n=12 NMJs from 4 larvae): $p > 0.05$ for Wild type vs *Syd-1*^{null}, $p > 0.05$ for Wild type vs. *Liprin- α* ^{null}, $p > 0.05$ for *Syd-1*^{null} vs. *Liprin- α* ^{null}; $p = 0.2883$ ($F(2,33) = 1.29$)). (d) BRP spots per μm^2 NMJ were slightly reduced in *Syd-1*^{null} and significantly reduced in *Liprin- α* ^{null} in comparison to the Wild type (Wild type (n=13 NMJs from 4 larvae) vs. *Syd-1*^{null} (n=11 NMJs from 4 larvae) vs. *Liprin- α* ^{null} (n=12 NMJs from 4 larvae): $p > 0.05$ for Wild type vs *Syd-1*^{null}, $p \leq 0.01$ for Wild type vs. *Liprin- α* ^{null}, $p > 0.05$ for *Syd-1*^{null} vs. *Liprin- α* ^{null}; $p = 0.0108$ ($F(2,33) = 5.207$)). (e) Mean Unc13A intensity measured

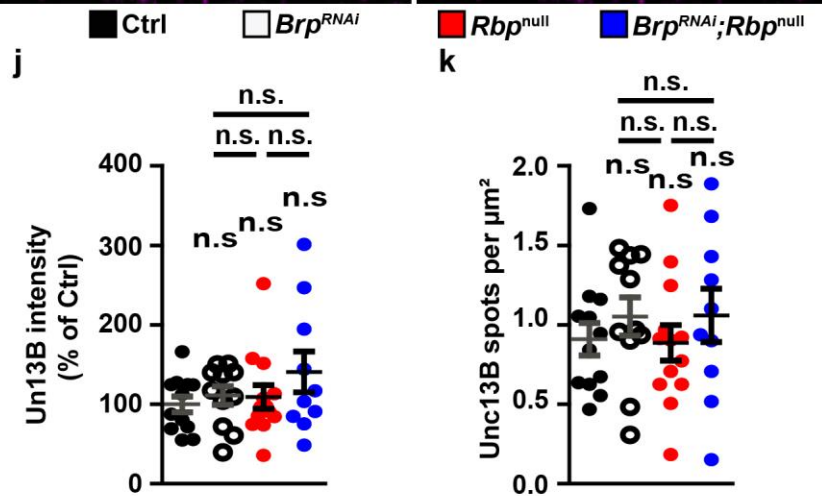
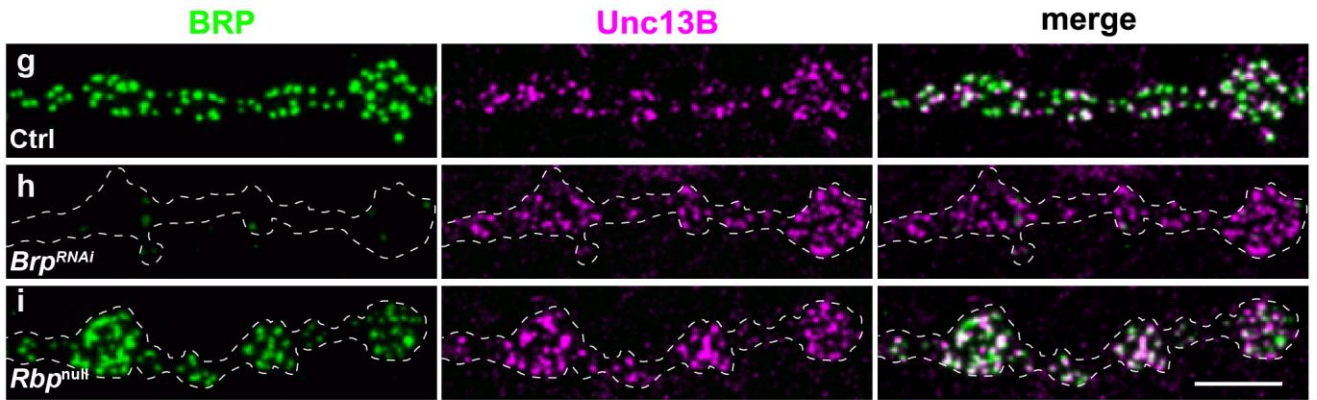
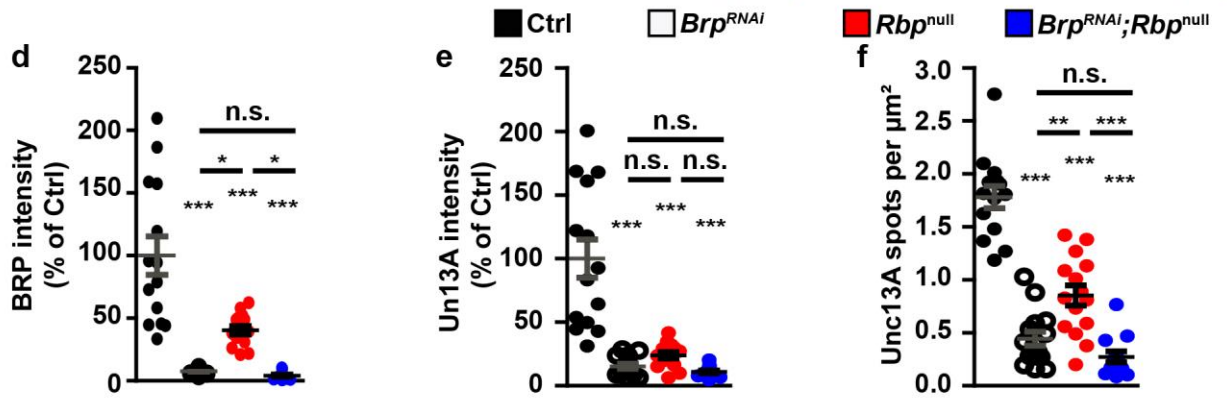
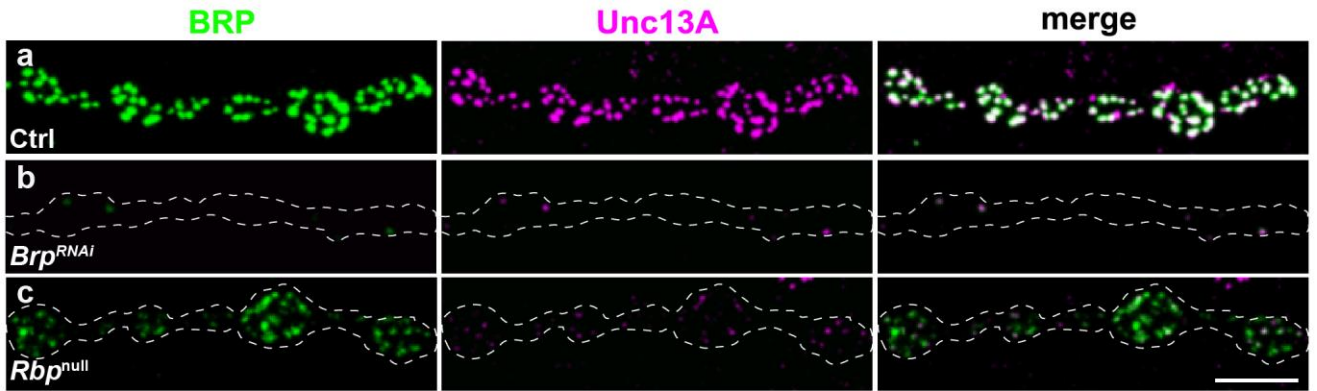
over the whole NMJ was unchanged in *Syd-1^{null}* and *Liprin- α ^{null}* in comparison to the Wild type (Wild type (n=13 NMJs from 4 larvae) vs. *Syd-1^{null}* (n=11 NMJs from 4 larvae) vs. *Liprin- α ^{null}* (n=12 NMJs from 4 larvae): p >0.05 for Wild type vs *Syd-1^{null}*; p >0.05 for Wild type vs. *Liprin- α ^{null}*; p >0.05 for *Syd-1^{null}* vs. *Liprin- α ^{null}*; p=0.2105 (F(2,33)=1.63)). (f) Unc13A spots per μm^2 NMJ were slightly reduced in *Syd-1^{null}* and *Liprin- α ^{null}* in comparison to the Wild type (Wild type (n=13 NMJs from 4 larvae) vs. *Syd-1^{null}* (n=11 NMJs from 4 larvae) vs. *Liprin- α ^{null}* (n=12 NMJs from 4 larvae): p \leq 0.05 for Wild type vs *Syd-1^{null}*; p >0.05 for Wild type vs. *Liprin- α ^{null}*; p >0.05 for *Syd-1^{null}* vs. *Liprin- α ^{null}*; p=0.0278 (F(2,33)=4.00)). (g,h) Muscle 4 NMJs of segments A2-A4 from 3rd instar larvae of the displayed genotypes labelled with the ABs indicated. (i) Mean Unc13B intensity measured over the whole NMJ was slightly reduced in *Syd-1^{null}* but severely reduced in *Liprin- α ^{null}* in comparison to the Wild type (Wild type (n=13 NMJs from 5 larvae) vs. *Syd-1^{null}* (n=11 NMJs from 5 larvae) vs. *Liprin- α ^{null}* (n=15 NMJs from 5 larvae): p >0.05 for Wild type vs *Syd-1^{null}*; p \leq 0.001 for Wild type vs. *Liprin- α ^{null}*; p \leq 0.01 for *Syd-1^{null}* vs. *Liprin- α ^{null}*; p <0.0001 (F(2,36)=15.13)). (j) Unc13B spots per μm^2 NMJ were significantly reduced in *Syd-1^{null}* but severely reduced in *Liprin- α ^{null}* in comparison to the Wild type (Wild type (n=13 NMJs from 5 larvae) vs. *Syd-1^{null}* (n=11 NMJs from 5 larvae) vs. *Liprin- α ^{null}* (n=15 NMJs from 5 larvae): p \leq 0.01 for Wild type vs *Syd-1^{null}*; p \leq 0.001 for Wild type vs. *Liprin- α ^{null}*; p \leq 0.001 for *Syd-1^{null}* vs. *Liprin- α ^{null}*; p <0.0001 (F(2,36)=42.93)). Number and p values are listed in Supplementary Table 1. Statistics for c-f, i, j: nonparametric one-way analysis of variance (ANOVA) test, followed by a Turkey's multiple comparison test. All panels show mean \pm SEM; *, p \leq 0.05; **, p \leq 0.01; ***, p \leq 0.001; ns, not significant, p >0.05. Scale bars: 5 μm .



Supplementary Figure 2

Unc13B interacts with Syd-1/Liprin- α ; Unc13A interacts with BRP/RBP

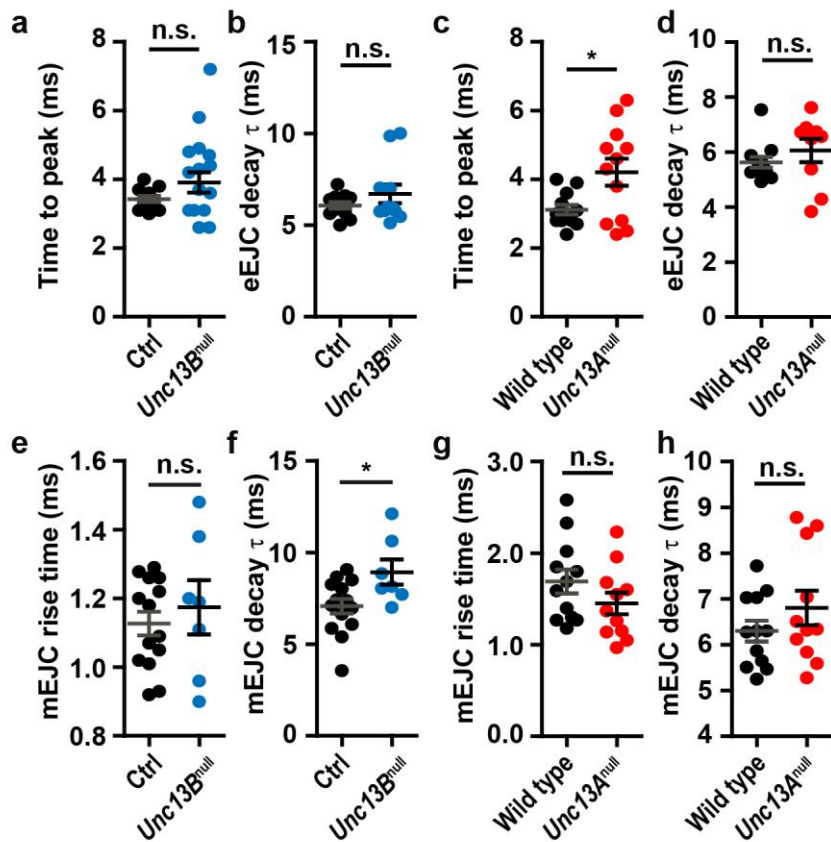
(a) Schematic representation of Unc13B N-terminus including three fragments (1-3) that were used in the Y2H screen; Liprin- α domain structure containing three C-terminal SAM domains (I-III from the N terminus); Syd-1 domain structure containing an N-terminal PDZ domain, a C₂ and a Rho-GAP domain. The corresponding fragments of each protein used in the Y2H screen are indicated. A central N-terminal fragment of Unc13B interacted with an N-terminal part of Liprin- α . Both very N-terminal fragments of Unc13B interacted with a central stretch of Syd-1 located in-between PDZ- and C₂-domain. (b) Schematic representation of Unc13A N-terminus including three fragments (1-3) that were used in the Y2H screen. The RBP-binding PxxP motif is indicated; RBP domain structure containing three SH3 domains (I-III from the N terminus) and three Fibronectin 3 (FN3) domains; BRP domain structure containing several coiled-coil (CC) domains. The corresponding fragments of each protein used in the Y2H screen are indicated. The most N-terminal fragment of Unc13A (including the RBP binding PxxP motif) interacted with both C-terminal fragments of RBP including the SH3-domains II and III, and with an N-terminal part of BRP.



Supplementary Figure 3

BRP/RBP scaffold complexes organize the AZ-localization of Unc13A

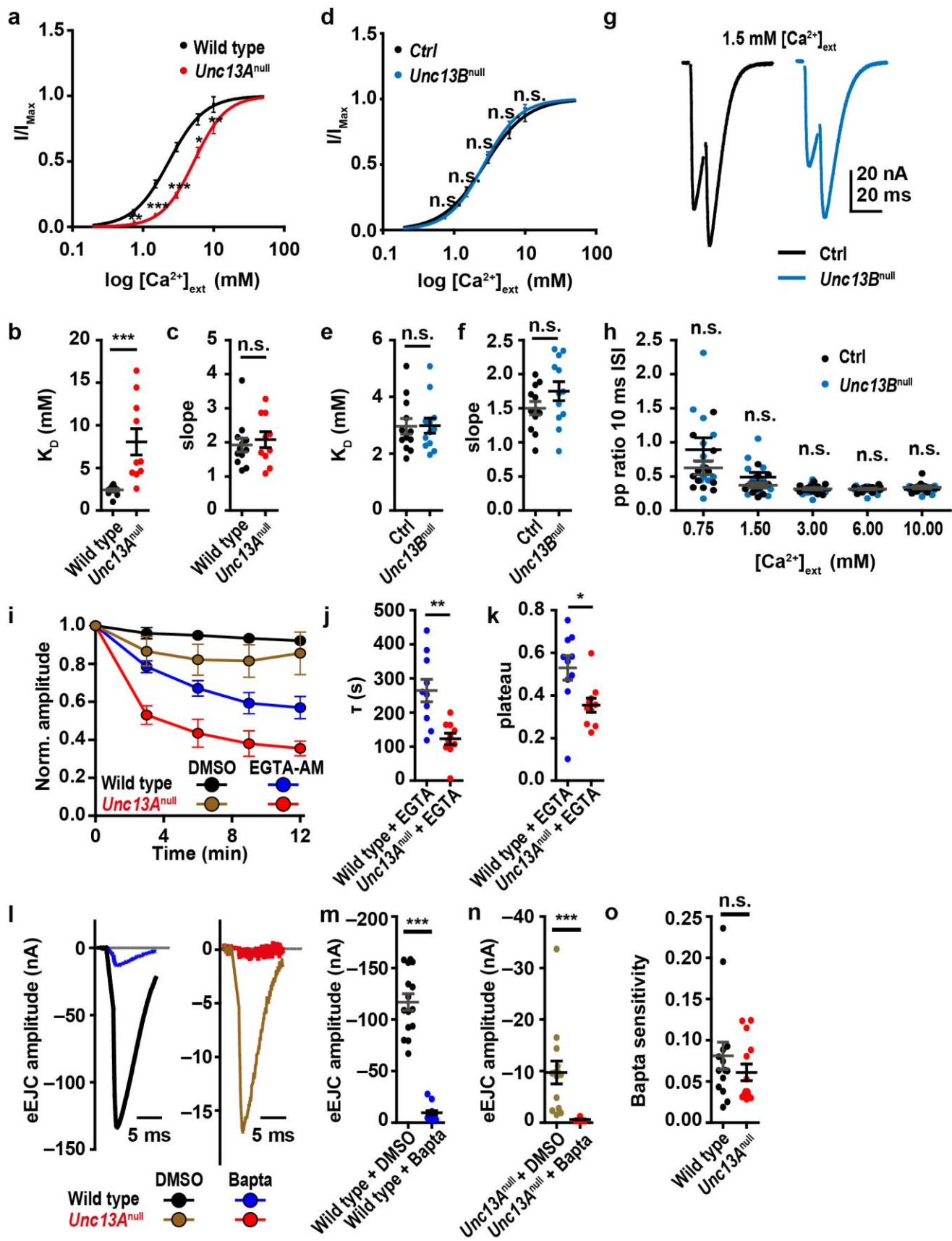
(a-c) Muscle 4 NMJs of segments A2-A4 from 3rd instar larvae of the displayed genotypes labelled with the ABs indicated. BRP as well as Unc13A were severely decreased upon motoneuronal downregulation of BRP or in *Rbp*^{null} mutants. (d,e) BRP as well as Unc13A intensity were severely decreased upon motoneuronal downregulation of BRP or in *Rbp*^{null} mutants with the strongest downregulation upon *Brp* knockdown in *Rbp*^{null} (BRP intensity: Ctrl (n=14 NMJs from 5 larvae) vs. *Brp*^{RNAi} (n=15 NMJs from 5 larvae) vs. *Rbp*^{null} (n=15 NMJs from 5 larvae) vs. *Brp*^{RNAi};*RBP*^{null} (n=13 NMJs from 5 larvae): p ≤0.001 for Ctrl vs *Brp*^{RNAi}; p ≤0.001 for Ctrl vs. *Rbp*^{null}; p ≤0.001 for Ctrl vs. *Brp*^{RNAi};*RBP*^{null}; p ≤0.05 for *Brp*^{RNAi} vs. *Rbp*^{null}; p >0.05 for *Brp*^{RNAi} vs. *Brp*^{RNAi};*RBP*^{null}; p ≤0.05 for *Rbp*^{null} vs. *Brp*^{RNAi};*RBP*^{null}; p <0.0001 (F(3,53)=31.96)); Unc13A intensity: Ctrl (n=14 NMJs from 5 larvae) vs. *Brp*^{RNAi} (n=15 NMJs from 5 larvae) vs. *Rbp*^{null} (n=15 NMJs from 5 larvae) vs. *Brp*^{RNAi};*RBP*^{null} (n=13 NMJs from 5 larvae): p ≤0.001 for Ctrl vs *Brp*^{RNAi}; p ≤0.001 for Ctrl vs. *Rbp*^{null}; p ≤0.001 for Ctrl vs. *Brp*^{RNAi};*RBP*^{null}; p >0.05 for *Brp*^{RNAi} vs. *Rbp*^{null}; p >0.05 for *Brp*^{RNAi} vs. *Brp*^{RNAi};*RBP*^{null}; p >0.05 for *Rbp*^{null} vs. *Brp*^{RNAi};*RBP*^{null}; p <0.0001 (F(3,53)=30.07)). (f) Unc13A spots per μm² NMJ were decreased upon motoneuronal downregulation of BRP or in *Rbp*^{null} mutants with the strongest downregulation upon *Brp* knockdown in *Rbp*^{null} (Ctrl (n=14 NMJs from 5 larvae) vs. *Brp*^{RNAi} (n=15 NMJs from 5 larvae) vs. *Rbp*^{null} (n=15 NMJs from 5 larvae) vs. *Brp*^{RNAi};*RBP*^{null} (n=13 NMJs from 5 larvae): p ≤0.001 for Ctrl vs *Brp*^{RNAi}; p ≤0.001 for Ctrl vs. *Rbp*^{null}; p ≤0.001 for Ctrl vs. *Brp*^{RNAi};*RBP*^{null}; p ≤0.01 for *Brp*^{RNAi} vs. *Rbp*^{null}; p >0.05 for *Brp*^{RNAi} vs. *Brp*^{RNAi};*RBP*^{null}; p ≤0.001 for *Rbp*^{null} vs. *Brp*^{RNAi};*RBP*^{null}; p <0.0001 (F(3,53)=63.28)). (g-i) Muscle 4 NMJs of segments A2-A4 from 3rd instar larvae of the genotypes indicated labelled with the ABs indicated. BRP but not Unc13B were severely decreased upon motoneuronal downregulation of BRP as well as in *Rbp*^{null} mutants. (j) Mean Unc13B intensity measured over the whole NMJ was not affected upon downregulation of BRP or in *Rbp*^{null} mutants or even upon *Brp* knockdown in *Rbp*^{null} (Ctrl (n=12 NMJs from 5 larvae) vs. *Brp*^{RNAi} (n=11 NMJs from 5 larvae) vs. *Rbp*^{null} (n=13 NMJs from 5 larvae) vs. *Brp*^{RNAi};*RBP*^{null} (n=10 NMJs from 5 larvae): p >0.05 for Ctrl vs *Brp*^{RNAi}; p >0.05 for Ctrl vs. *Rbp*^{null}; p >0.05 for Ctrl vs. *Brp*^{RNAi};*RBP*^{null}; p >0.05 for *Brp*^{RNAi} vs. *Rbp*^{null}; p >0.05 for *Brp*^{RNAi} vs. *Brp*^{RNAi};*RBP*^{null}; p >0.05 for *Rbp*^{null} vs. *Brp*^{RNAi};*RBP*^{null}; p=0.3491 (F(3,42)=1.127)). (k) Unc13B spots per μm² NMJ were unchanged upon downregulation of BRP or in *Rbp*^{null} mutants or even upon *Brp* knockdown in *Rbp*^{null} (Ctrl (n=12 NMJs from 5 larvae) vs. *Brp*^{RNAi} (n=11 NMJs from 5 larvae) vs. *Rbp*^{null} (n=13 NMJs from 5 larvae) vs. *Brp*^{RNAi};*RBP*^{null} (n=10 NMJs from 5 larvae): p >0.05 for Ctrl vs *Brp*^{RNAi}; p >0.05 for Ctrl vs. *Rbp*^{null}; p >0.05 for Ctrl vs. *Brp*^{RNAi};*RBP*^{null}; p >0.05 for *Brp*^{RNAi} vs. *Rbp*^{null}; p >0.05 for *Brp*^{RNAi} vs. *Brp*^{RNAi};*RBP*^{null}; p >0.05 for *Rbp*^{null} vs. *Brp*^{RNAi};*RBP*^{null}; p=0.6570 (F(3,42)=0.5408)). Number and p values are listed in Supplementary Table 1. Statistics for d-f, j,k: nonparametric one-way analysis of variance (ANOVA) test, followed by a Turkey's multiple comparison test. All panels show mean ± SEM; *, p ≤0.05; **, p ≤0.01; ***, p ≤0.001; ns, not significant, p >0.05. Scale bars: 5 μm.



Supplementary Figure 4

TEVC analysis of *Unc13A* and *Unc13B* mutant terminals

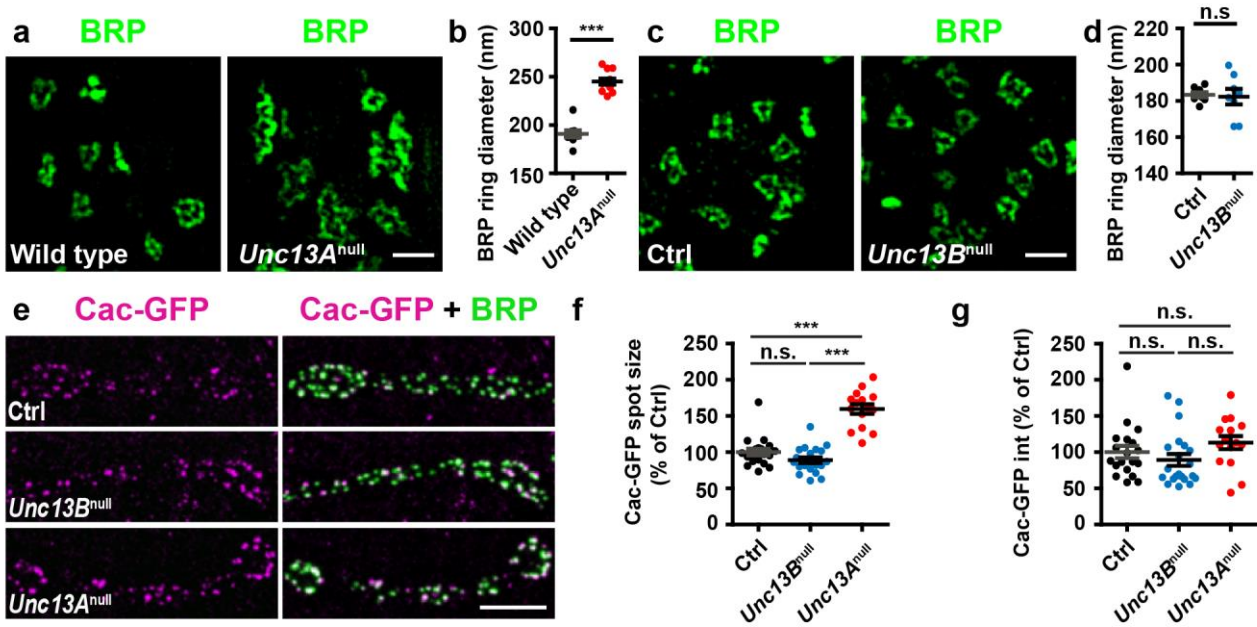
(a,b) The time-to-peak (time difference between stimulation pulse to the afferent nerve and the eEJC minimum) and eEJC decay, which is the time constant τ resulting from a single exponential fit in the range from 60% of the eEJC amplitude back to baseline, both are similar in Ctrl (black) and *Unc13B^{null}* (blue) (time to peak: Ctrl (n=12 NMJs from 12 larvae) vs *Unc13B^{null}* (n=12 NMJs from 12 larvae), $p=0.1333$ ($t(22)=1.559$); eEJC decay: Ctrl (n=12 NMJs from 12 larvae) vs *Unc13B^{null}* (n=11 NMJs from 11 larvae), $p=0.2413$ ($t(21)=1.206$)). (c) The time to peak is significantly prolonged in *Unc13A^{null}* mutant synapses (Wild type (n=12 NMJs from 12 larvae) vs *Unc13A^{null}* (n=12 NMJs from 12 larvae), $p=0.0162$ ($t(22)=2.605$)). (d) The eEJC decay is similar in Wild type and *Unc13A^{null}* (Wild type (n=12 NMJs from 12 larvae) vs *Unc13A^{null}* (n=9 NMJs from 9 larvae), $p=0.2136$ (U=36)). (e) The mEJC rise time is unaltered in *Unc13B^{null}* mutant synapses compared to Ctrl (Ctrl (n=14 NMJs from 10 larvae) vs *Unc13B^{null}* (n=7 NMJs from 5 larvae), $p=0.7652$ (U=44.5)). (f) In *Unc13B^{null}* the mEJC decay is significantly increased compared to Ctrl (Ctrl (n=14 NMJs from 10 larvae) vs *Unc13B^{null}* (n=7 NMJs from 5 larvae), $p=0.0480$ (U=22.00)). (g,h) mEJC kinetics do not differ between Wild type and *Unc13A^{null}* (mEJC rise time: Wild type (n=12 NMJs from 6 larvae) vs *Unc13A^{null}* (n=11 NMJs from 6 larvae), $p=0.1914$ ($t(21)=1.350$); mEJC decay: Wild type (n=12 NMJs from 6 larvae) vs *Unc13A^{null}* (n=11 NMJs from 6 larvae), $p=0.2546$ ($t(21)=1.171$)). All recordings were performed in the presence of 1.5 mM extracellular Ca^{2+} . Number and p values are listed in Supplementary Table 1. Statistics: Student's t-test besides panels d,e,f where a Mann Whitney U-test was performed. All panels show mean \pm SEM; *, $p \leq 0.05$; **, $p \leq 0.01$; ***, $p \leq 0.001$; ns, not significant, $p > 0.05$.



Supplementary Figure 5

Ca²⁺ sensitivity and release probability is altered upon loss of Unc13A but not -B

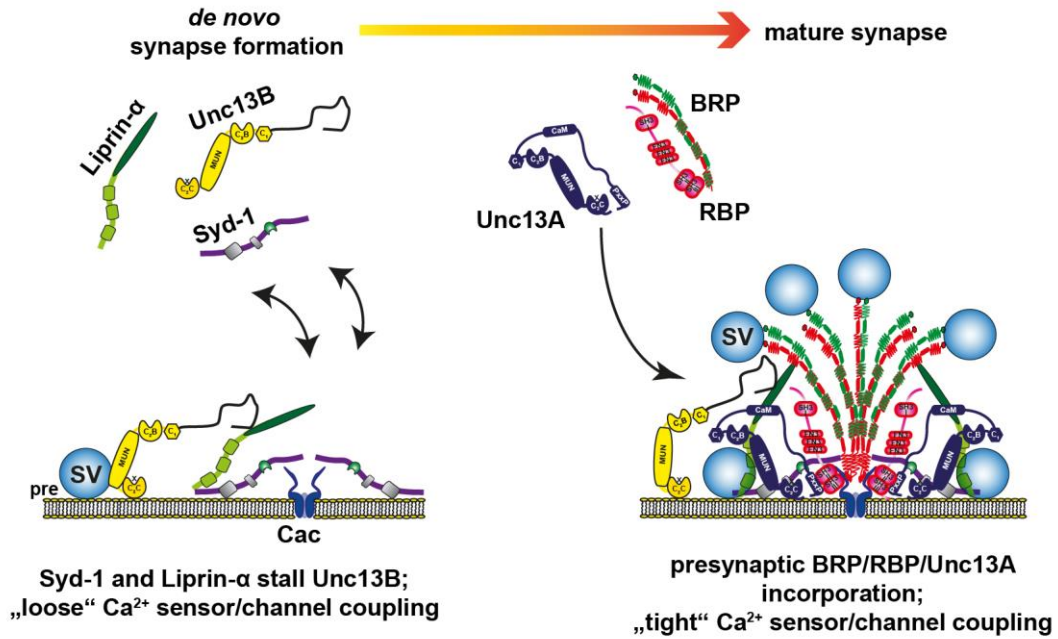
(a-f) Plot of eEJC amplitude as a function of extracellular Ca²⁺ concentrations [Ca²⁺]_{ext} fitted with Hill equations to determine the values for slope and K_D. A clear shift can be observed in (a) *Unc13A*^{null} mutant synapses (red) compared to Wild type (black), whereas in (d) there is no change upon loss of *Unc13B*^{null} (blue) compared to Ctrl (black) (a: Wild type (n=12 NMJs from 12 larvae per Ca²⁺ concentration) vs *Unc13A*^{null} (n=10 NMJs from 10 larvae per Ca²⁺ concentration): 0.75 mM [Ca²⁺]_{ext}: p=0.0092 (U=20); 1.5 mM [Ca²⁺]_{ext}: p<0.0001 (U=0); 3 mM [Ca²⁺]_{ext}: p=0.0005 (U=7); 6 mM [Ca²⁺]_{ext}: p=0.0272 (U=26); 10 mM [Ca²⁺]_{ext}: p=0.0062 (U=18)); d: Ctrl (n=12 NMJs from 12 larvae per Ca²⁺ concentration) vs *Unc13B*^{null} (n=12 NMJs from 12 larvae per Ca²⁺ concentration): 0.75 mM [Ca²⁺]_{ext}: p=0.1971 (t(22)=1.330); 1.5 mM [Ca²⁺]_{ext}: p=0.2652 (t(22)=1.143); 3 mM [Ca²⁺]_{ext}: p=0.9269 (t(22)=0.09278); 6 mM [Ca²⁺]_{ext}: p=0.5181 (t(22)=0.6569); 10 mM [Ca²⁺]_{ext}: p=0.6284 (t(22)=0.4908)). The values for I/I_{max} can be found in Supplementary Table 1. (b) Ca²⁺-dependence of release analysis revealed an increased Ca²⁺ requirement (K_D, obtained from fitting with the Hill function) in *Unc13A*^{null} mutant synapses (Wild type (n=12 NMJs from 12 larvae) vs *Unc13A*^{null} (n=10 NMJs from 10 larvae), p=0.0004 (U=6)). (c) The apparent Ca²⁺ cooperativity of release (slope, obtained from fitting with the Hill function) is not different in *Unc13A*^{null} relative to Wild type (Wild type (n=12 NMJs from 12 larvae) vs *Unc13A*^{null} (n=10 NMJs from 10 larvae), p=0.6682 (U=53)). (e,f) The Ca²⁺-dependence and Ca²⁺-cooperativity of release are both unaltered upon loss of *Unc13B* (K_D: Ctrl (n=12 NMJs from 12 larvae) vs *Unc13B*^{null} (n=12 NMJs from 12 larvae), p=0.9566 (t(22)=0.05502); slope: Ctrl (n=12 NMJs from 12 larvae) vs *Unc13B*^{null} (n=12 NMJs from 12 larvae), p=0.1574 (t(22)=1.464)). (g) Sample traces of paired pulse stimulation for Ctrl (black) and *Unc13B*^{null} (blue) at 10 ms ISI show no differences between genotypes. (h) The paired pulse ratios were not significantly changed in *Unc13B*^{null} at 10 ms ISI, in all Ca²⁺ concentrations (Ctrl (n=12 NMJs from 12 larvae per Ca²⁺ concentration) vs *Unc13B*^{null} (n=12 NMJs from 12 larvae per Ca²⁺ concentration): 0.75 mM [Ca²⁺]_{ext}: p=0.1971 (t(22)=1.33); 1.5 mM [Ca²⁺]_{ext}: p=0.1678 (t(22)=1.426); 3 mM [Ca²⁺]_{ext}: p=0.474 (t(22)=0.7284); 6 mM [Ca²⁺]_{ext}: p=0.3726 (t(22)=0.9102); 10 mM [Ca²⁺]_{ext}: p=0.2602 (t(22)=1.156)). Values can be found in Supplementary Table 1. (i) *Unc13A*^{null} (gold: control with DMSO, red: with EGTA-AM/DMSO) shows faster and stronger inhibition of eEJC amplitudes after addition of 200 μM EGTA-AM to the extra-cellular solution compared to Wild type (black: control with DMSO, blue: with EGTA-AM/DMSO). Amplitudes are normalized to average eEJC amplitudes obtained during 1 min of baseline recording prior to the addition of EGTA-AM/DMSO or DMSO, each with Pluronic F-127. Synaptic transmission was stimulated by single action potentials every 10 s. Experiments were performed in the presence of 2.5 mM extracellular Ca²⁺. Values can be found in Supplementary Table 1. (j) The time constant of the inhibition caused by EGTA-AM application was determined by fitting a single exponential decay function to 100 peak amplitude values after addition of EGTA-AM in individual cells. This revealed a significantly faster inhibition in *Unc13A*^{null} compared to Wild type animals (Wild type + EGTA (n=10 NMJs from 10 larvae) vs *Unc13A*^{null} + EGTA (n=10 NMJs from 10 larvae), p=0.0012 (t(18)=3.835)). (k) The asymptotic inhibition is captured in the exponential fit as the plateau value which was significantly decreased in *Unc13A*^{null} in comparison to Wild type (Wild type + EGTA (n=10 NMJs from 10 larvae) vs *Unc13A*^{null} + EGTA (n=10 NMJs from 10 larvae), p=0.016 (t(18)=2.6508)). (l) 30 min incubation with the fast Ca²⁺-buffer Bapta-AM reduced eEJC amplitudes in both genotypes to a similar extent. Sample traces for Wild type (black with DMSO, blue with Bapta-AM/DMSO) and *Unc13A*^{null} (gold with DMSO, red with Bapta-AM/DMSO) exhibit similar Bapta-sensitivity for both genotypes. For clarity, the stimulation artefact was removed and replaced by a straight line. (m,n) The significant reduction of the eEJC amplitude after 30 min Bapta-AM incubation is similar in Wild type (m) and *Unc13A*^{null} (n) compared to DMSO incubated cells (m: Wild type + DMSO (n=15 NMJs from 9 larvae) vs Wild type + Bapta (n=14 NMJs from 9 larvae), p<0.0001 (t(27)=12.59); n: *Unc13A*^{null} + DMSO (n=14 NMJs from 10 larvae) vs *Unc13A*^{null} + Bapta (n=14 NMJs from 8 larvae), p=0.0004 (t(26)=4.095)). Values can be found in Supplementary Table 1. (o) The Bapta sensitivity is calculated as the ratio of eEJC amplitude size in the presence of Bapta-AM/DMSO to the eEJC amplitude size in the presence of DMSO. The Bapta-sensitivity does not differ between Wild type and *Unc13A*^{null} (Bapta sensitivity: Wild type (n=14 NMJs from 9 larvae) vs *Unc13A*^{null} (n=14 NMJs from 8 larvae), p=0.304 (t(26)=1.049)). Values can be found in Supplementary Table 1. Statistics: Student's t-test except for panels (a-c) where a Mann-Whitney U-test was performed. All panels show mean ± SEM; *, p ≤ 0.05; **, p ≤ 0.01; ***, p ≤ 0.001; ns, not significant, p > 0.05.



Supplementary Figure 6

Increased Ca²⁺ channel abundance at *Unc13A^{null}* mutant AZs

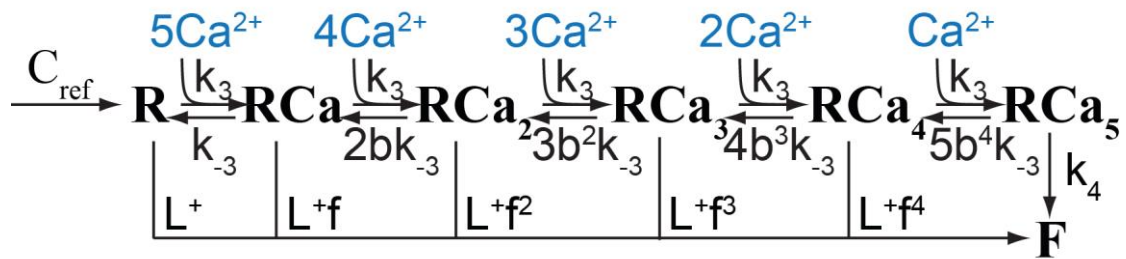
(a) Two-color STED images of multiple AZs from 3rd instar larvae of the displayed genotypes labelled with the indicated ABs. BRP rings were larger in *Unc13A^{null}*. (b) BRP ring diameters were increased in *Unc13A^{null}* in comparison to the Wild type (Wild type (n=9 NMJs from 3 larvae) vs *Unc13A^{null}* (n=12 NMJs from 3 larvae), p=0.0001 (U=0)). (c) Two-color STED images of multiple AZs from 3rd instar larvae of the displayed genotypes labelled with the indicated ABs. BRP ring structure appeared normal in *Unc13B^{null}*. (d) BRP ring diameters were unchanged in *Unc13B^{null}* in comparison to Ctrl (Ctrl (n=8 NMJs from 3 larvae) vs *Unc13B^{null}* (n=8 NMJs from 3 larvae), p=0.9591 (U=31)). (e) Muscle 4 NMJs of segments A2-A4 from 3rd instar larvae of the displayed genotypes labelled with the ABs indicated. (f) Cac-GFP spot sizes were increased in *Unc13A^{null}* but not *Unc13B^{null}* in comparison to Ctrl (Ctrl (n=19 NMJs from 5 larvae) vs. *Unc13A^{null}* (n=15 NMJs from 5 larvae) vs. *Unc13B^{null}* (n=21 NMJs from 5 larvae): p >0.05 for Ctrl vs *Unc13B^{null}*; p ≤0.001 for Ctrl vs. *Unc13A^{null}*; p ≤0.001 for *Unc13B^{null}* vs. *Unc13A^{null}*; p <0.0001 (F(2,52)=54.12)). (g) Mean Cac-GFP intensity measured over the whole NMJ was similar in *Unc13A^{null}*, *Unc13B^{null}* and Ctrl (Ctrl (n=19 NMJs from 5 larvae) vs. *Unc13A^{null}* (n=15 NMJs from 5 larvae) vs. *Unc13B^{null}* (n=21 NMJs from 5 larvae): p >0.05 for Ctrl vs *Unc13B^{null}*; p >0.05 for Ctrl vs. *Unc13A^{null}*; p >0.05 for *Unc13B^{null}* vs. *Unc13A^{null}*; p=0.166 (F(2,52)=1.855)). Number and p values are listed in Supplementary Table 1. Statistics: Mann-Whitney U-test, except for f and g where a nonparametric one-way analysis of variance (ANOVA) test, followed by a Turkey's multiple comparison test was performed. All panels show mean ± SEM; *, p ≤0.05; **, p ≤0.01; ***, p ≤0.001; ns, not significant, p >0.05. Scale bar: (a,c) 500 nm; (e) 5 μm.



Supplementary Figure 7

Sketch of *de novo* synapse formation

During the process of AZ assembly, clusters of Syd-1 and Liprin- α undergo rounds of assembly and disassembly at the presynaptic membrane. Unc13B localizes to sites of *de novo* synapse formation via the Syd-1/Liprin- α scaffold. At nascent synapses, this induces a loose SV-Ca²⁺ channel coupling. Later during the AZ maturation process, Unc13A localizes to more mature synapses via a second, central RBP/BRP scaffold that concentrates Unc13A at the center of the AZ. Unc13A facilitates a close localization of SVs to the presynaptic Ca²⁺ channels and therefore maintains a tight stimulus/secretion coupling.



Supplementary Figure 8

Allosteric five-site binding model of Ca^{2+} -driven exocytosis

Reaction scheme (derived from the 'allosteric model'; Lou et al., 2005. Nature. 435:497-501) depicts the sequential binding of up to five Ca^{2+} ions to a single vesicle (RCa_{0-5}).

Supplementary Table 1

Summary of all obtained parameters in this study

Light microscopy: CLSM (Fig. 1, 3; Fig. S1, S2, S5)		mean ± SEM			
Parameter (Figure)	Description	control (n)	mutant (n)	P	(test)
AZ density (Fig. 1)	BRP spots/ μm^2				
<i>Unc13A</i> ^{null} (Fig.1o)		1.658 ± 0.079 (19)	1.207 ± 0.063 (23)	≤0.001***	(Mann-Whitney U-test)
<i>Unc13B</i> ^{null} (Fig.1p)		1.559 ± 0.070 (28)	1.354 ± 0.055 (35)	≤0.05*	(Mann-Whitney U-test)
mean BRP intensity (Fig. S1c; S3d)	measured over the whole NMJ (% of Wild type)				
in <i>Syd-1</i> ^{null} (Fig. S1c)		100.0 ± 9.269 (13)	80.62 ± 10.390 (11)	n.s.	(ANOVA test, followed by a Turkey's multiple comparison test)
in <i>Liprin-α</i> ^{null} (Fig. S1c)			82.13 ± 9.353 (12)	n.s.	
in <i>Brp</i> ^{RNAi} (Fig. S3d)		100.0 ± 15.41 (14)	7.639 ± 0.498 (15)	≤0.001***	(ANOVA test, followed by a Turkey's multiple comparison test)
in <i>Rbp</i> ^{null} (Fig. S3d)			40.29 ± 3.292 (15)	≤0.001***	
in <i>Brp</i> ^{RNAi} ; <i>Rbp</i> ^{null} (Fig. S3d)			4.135 ± 0.843 (13)	≤0.001***	
AZ density (Fig. S1d)	BRP spots/ μm^2				
in <i>Syd-1</i> ^{null} (Fig. S1d)		1.352 ± 0.058 (13)	1.057 ± 0.124 (11)	n.s.	(ANOVA test, followed by a Turkey's multiple comparison test)
in <i>Liprin-α</i> ^{null} (Fig. S1d)			0.878 ± 0.132 (12)	≤0.01**	
mean Unc13A intensity (Fig. 3c, g; S1e; S3e)	measured over the whole NMJ (% of Wild type)				
in <i>Syd-1</i> ^{null} (Fig. S1e)		100.0 ± 8.084 (13)	99.04 ± 11.50 (11)	n.s.	(ANOVA test, followed by a Turkey's multiple comparison test)
in <i>Liprin-α</i> ^{null} (Fig. 3c, S1e)			79.36 ± 7.923 (12)	n.s.	
in <i>Brp</i> ^{RNAi} (Fig. S3e)		100.0 ± 15.060 (14)	15.24 ± 1.916 (15)	≤0.001***	(ANOVA test, followed by a Turkey's multiple comparison test)
in <i>Rbp</i> ^{null} (Fig. S3e)			23.88 ± 2.478 (15)	≤0.001***	
in <i>Brp</i> ^{RNAi} ; <i>Rbp</i> ^{null} (Fig. 3g, Fig. S3e)			10.88 ± 1.117 (13)	≤0.001***	
Unc13A density (Fig. S1f; S3f)	Unc13A spots/ μm^2				
in <i>Syd-1</i> ^{null} (Fig. S1f)		1.679 ± 0.088 (13)	1.322 ± 0.098 (11)	≤0.05*	(ANOVA test, followed by a Turkey's multiple comparison test)
in <i>Liprin-α</i> ^{null} (Fig. S1f)			1.361 ± 0.110 (12)	n.s.	

in <i>Brp</i> ^{RNAi} (Fig. S3f)	1.781 ± 0.106 (14)	0.442 ± 0.065 (15)	≤0.001***	(ANOVA test, followed by a Turkey's multiple comparison test)
in <i>Rbp</i> ^{null} (Fig. S3f)		0.851 ± 0.094 (15)	≤0.001***	
in <i>Brp</i> ^{RNAi} ; <i>Rbp</i> ^{null} (Fig. S3f)		0.271 ± 0.052 (13)	≤0.001***	
mean Unc13B intensity (Fig. 3d, h; S1i; S3j)	measured over the whole NMJ (% of Wild type)			
in <i>Syd-1</i> ^{null} (Fig. S1i)	100.0 ± 14.770 (11)	75.58 ± 7.521 (13)	n.s.	(ANOVA test, followed by a Turkey's multiple comparison test)
in <i>Liprin-α</i> ^{null} (Fig. 3d, Fig. S1i)		29.52 ± 5.936 (15)	≤0.001***	
in <i>Brp</i> ^{RNAi} (Fig. S3j)	100.0 ± 10.07 (12)	111.20 ± 11.60 (11)	n.s.	(ANOVA test, followed by a Turkey's multiple comparison test)
in <i>Rbp</i> ^{null} (Fig. S3j)		109.20 ± 14.80 (13)	n.s.	
in <i>Brp</i> ^{RNAi} ; <i>Rbp</i> ^{null} (Fig. 3h, S3j)		140.7 ± 25.88 (10)	n.s.	
Unc13B density (Fig. S1j; S3k)	Unc13B spots/μm ²			
in <i>Syd-1</i> ^{null} (Fig. S1j)	1.592 ± 0.072 (11)	1.145 ± 0.069 (13)	≤0.01**	(ANOVA test, followed by a Turkey's multiple comparison test)
in <i>Liprin-α</i> ^{null} (Fig. S1j)		0.382 ± 0.115 (15)	≤0.001***	
in <i>Brp</i> ^{RNAi} (Fig. S3k)	0.910 ± 0.102 (12)	1.053 ± 0.119 (11)	n.s.	(ANOVA test, followed by a Turkey's multiple comparison test)
in <i>Rbp</i> ^{null} (Fig. S3k)		0.886 ± 0.112 (13)	n.s.	
in <i>Brp</i> ^{RNAi} ; <i>Rbp</i> ^{null} (Fig. S3k)		1.060 ± 0.168 (10)	n.s.	
BRP ring diameter (Fig. S6b,d)	measured with STED microscopy (nm)			
in <i>Unc13A</i> ^{null} (Fig. S6b)	191.0 ± 3.721 (9)	244.9 ± 3.045 (12)	≤0.001***	(Mann-Whitney U-test)
in <i>Unc13B</i> ^{null} (Fig. S6d)	183.4.0 ± 1.421 (8)	182.3 ± 4.262 (8)	n.s.	(Mann-Whitney U-test)
mean Cac spot size (Fig. S6f)	% of control			
in <i>Unc13A</i> ^{null}	100.0 ± 4.70 (19)	159.5 ± 6.65 (15)	≤0.001***	(Mann-Whitney U-test)
in <i>Unc13B</i> ^{null}		88.84 ± 3.819 (21)	n.s.	(Mann-Whitney U-test)
mean Cac intensity (Fig. S6g)	% of control			
in <i>Unc13A</i> ^{null}	100.0 ± 8.543 (19)	113.1 ± 9.082 (15)	n.s.	(Mann-Whitney U-test)
in <i>Unc13B</i> ^{null}		89.17 ± 8.146 (21)	n.s.	(Mann-Whitney U-test)

TEVC recordings (Fig. 4, 7; Fig. S4, S5)

Parameter (Figure)	Description	mean ± SEM		P	(test)
		control (n)	mutant (n)		
eEJC amplitude [nA] in <i>Unc13A</i>^{null}					
(Fig. 4j; 7a, b)					
[Ca ²⁺] _{ex} = 0.75 mM	measured (n) (simulated with mathematical modeling)	-26.10 ± 4.89 (12) (-18.34)	-1.82 ± 0.17 (12) (-1.589)	≤0.001***	(t- test)
[Ca ²⁺] _{ex} = 1.5 mM		-77.46 ± 6.95 (12) (-63.58)	-4.88 ± 0.77 (12) (-6.471)	≤0.001***	(t- test)
[Ca ²⁺] _{ex} = 3 mM		-143.90 ± 8.07 (12) (-130.8)	-13.07 ± 1.13 (12) (-17.35)	≤0.001***	(t- test)
[Ca ²⁺] _{ex} = 6 mM		-193.96 ± 10.04 (12) (-187.6)	-30.86 ± 2.12 (12) (-30.20)	≤0.001***	(t- test)
[Ca ²⁺] _{ex} = 10 mM		-220.72 ± 13.94 (12) (-215.3)	-41.78 ± 3.09 (12) (-37.99)	≤0.001***	(t- test)
eEJC amplitude [nA] in <i>Unc13B</i>^{null}					
(Fig. 4c)					
[Ca ²⁺] _{ex} = 0.75 mM		-30.64 ± 3.643 (12)	-20.17 ± 3.176 (12)	≤0.05*	(t- test)
[Ca ²⁺] _{ex} = 1.5 mM		-77.33 ± 6.383 (12)	-57.93 ± 5.026 (12)	≤0.05*	(t- test)
[Ca ²⁺] _{ex} = 3 mM		-138.3 ± 8.208 (12)	-117.3 ± 7.375 (12)	n.s.	(t- test)
[Ca ²⁺] _{ex} = 6 mM		-189.4 ± 11.54 (12)	-164.8 ± 8.270 (12)	n.s.	(t- test)
[Ca ²⁺] _{ex} = 10 mM		-224.1 ± 13.14 (12)	-190.9 ± 8.751 (12)	≤0.05*	(t- test)
time to peak [ms] in <i>Unc13A</i>^{null}					
(Fig. S4c)					
[Ca ²⁺] _{ex} = 0.75 mM		3.892 ± 0.309 (12)	4.900 ± 0.760 (12)	n.s.	(t- test)
[Ca ²⁺] _{ex} = 1.5 mM		3.117 ± 0.142 (12)	4.208 ± 0.394 (12)	≤0.05*	(t- test)
[Ca ²⁺] _{ex} = 3 mM		2.350 ± 0.120 (12)	3.017 ± 0.263 (12)	≤0.05*	(t- test)
[Ca ²⁺] _{ex} = 6 mM		1.925 ± 0.0913 (12)	2.600 ± 0.140 (12)	≤0.001***	(t- test)
[Ca ²⁺] _{ex} = 10 mM		1.883 ± 0.0694 (12)	2.275 ± 0.143 (12)	≤0.05*	(t- test)
time to peak [ms] in <i>Unc13B</i>^{null}					
(Fig. S4a)					
[Ca ²⁺] _{ex} = 0.75 mM		4.225 ± 0.240 (12)	4.275 ± 0.332 (12)	n.s.	(t- test)
[Ca ²⁺] _{ex} = 1.5 mM		3.425 ± 0.0888 (12)	3.908 ± 0.297 (12)	n.s.	(t- test)
[Ca ²⁺] _{ex} = 3 mM		2.542 ± 0.0528 (12)	2.592 ± 0.119 (12)	n.s.	(t- test)

[Ca ²⁺] _{ex} =6 mM	2.175 ± 0.0664 (12)	2.108 ± 0.114 (12)	n.s.	(t- test)
[Ca ²⁺] _{ex} =10 mM	2.042 ± 0.106 (12)	1.950 ± 0.116 (12)	n.s.	(t- test)
mEJC analysis in <i>Unc13A</i>^{null}				
(Fig. 4m, n; S4g,h)				
Amplitude (nA)	-0.614 ± 0.02 (12)	-0.751 ± 0.02 (11)	≤0.001***	(t- test)
Frequency (Hz)	1.06 ± 0.12 (12)	1.41 ± 0.11 (11)	≤0.05*	(t- test)
Rise time (ms)	1.690 ± 0.129 (12)	1.451 ± 0.119 (11)	n.s.	(t- test)
Decay (ms)	6.299 ± 0.228 (12)	6.805 ± 0.376 (11)	n.s.	(t- test)
mEJC analysis [nA] in <i>Unc13B</i>^{null}				
(Fig. 4f, g; S4e,f)				
Amplitude (nA)	-0.859 ± 0.03 (14)	-0.837 ± 0.03 (7)	n.s.	(t- test)
Frequency (Hz)	2.08 ± 0.15 (14)	1.70 ± 0.23 (7)	n.s.	(t- test)
Rise time (ms)	1.127 ± 0.034 (14)	1.174 ± 0.078 (7)	n.s.	(Mann-Whitney U-test)
Decay (ms)	7.075 ± 0.398 (14)	8.931 ± 0.683 (7)	≤0.05*	(Mann-Whitney U-test)
eEJC analysis in <i>Unc13A</i>^{null}				
(Fig. 4k; S4d)				
Rise time (ms)	0.966 ± 0.052 (12)	2.0 ± 0.383 (9)	≤0.01**	(Mann-Whitney U-test)
Decay (ms)	5.627 ± 0.196 (12)	6.058 ± 0.425 (9)	n.s.	(Mann-Whitney U-test)
eEJC analysis [nA] in <i>Unc13B</i>^{null}				
(Fig. 4d; S4b)				
Rise time (ms)	1.125 ± 0.044 (12)	1.158 ± 0.101 (11)	n.s.	(t- test)
Decay (ms)	6.074 ± 0.181 (12)	6.706 ± 0.511 (11)	n.s.	(t- test)
<hr/>				
paired pulse ratio in <i>Unc13A</i>^{null}				
(Fig. 7e)				
	measured (n)	(simulated with mathematical modeling)		
[Ca ²⁺] _{ex} = 0.75 mM	1.683 ± 0.308 (12) (1.273)	--	--	--
[Ca ²⁺] _{ex} = 1.5 mM	0.904 ± 0.065 (12) (0.973)	3.796 ± 0.748 (10) (3.297)	≤0.001***	(t- test)
[Ca ²⁺] _{ex} =3 mM	0.633 ± 0.021 (12) (0.635)	1.846 ± 0.264 (10) (2.128)	≤0.001***	(t- test)
[Ca ²⁺] _{ex} =6 mM	0.631 ± 0.023 (12) (0.402)	1.309 ± 0.116 (10) (1.324)	≤0.001***	(t- test)
[Ca ²⁺] _{ex} =10 mM	0.674 ± 0.035 (12) (0.304)	1.192 ± 0.111 (10) (0.986)	≤0.001***	(t- test)
paired pulse ratio in <i>Unc13B</i>^{null}				
(Fig. S5h)				
[Ca ²⁺] _{ex} = 0.75 mM	1.255 ± 0.201 (12)	1.787 ± 0.245 (12)	n.s.	(t- test)

[Ca ²⁺] _{ex} = 1.5 mM	0.741 ± 0.079 (12)	0.974 ± 0.143 (12)	n.s.	(t- test)
[Ca ²⁺] _{ex} = 3 mM	0.637 ± 0.034 (12)	0.596 ± 0.044 (12)	n.s.	(t- test)
[Ca ²⁺] _{ex} = 6 mM	0.503 ± 0.117 (12)	0.614 ± 0.0316 (12)	n.s.	(t- test)
[Ca ²⁺] _{ex} = 10 mM	0.680 ± 0.043 (12)	0.619 ± 0.029 (12)	n.s.	(t- test)
I_{Max} in <i>Unc13A</i>^{null} (Fig. 7c; S5a)	measured (n)			
[Ca ²⁺] _{ex} = 0.75 mM	0.110 ± 0.020 (12) (0.079)	0.033 ± 0.003 (10) (0.036)	≤0.01**	(t- test)
[Ca ²⁺] _{ex} = 1.5 mM	0.327 ± 0.029 (12) (0.274)	0.089 ± 0.014 (10) (0.146)	≤0.001***	(t- test)
[Ca ²⁺] _{ex} = 3 mM	0.608 ± 0.034 (12) (0.563)	0.240 ± 0.020 (10) (0.390)	≤0.001***	(t- test)
[Ca ²⁺] _{ex} = 6 mM	0.820 ± 0.042 (12) (0.808)	0.560 ± 0.039 (10) (0.679)	≤0.05*	(t- test)
[Ca ²⁺] _{ex} = 10 mM	0.934 ± 0.058 (12) (0.927)	0.768 ± 0.056 (10) (0.854)	≤0.01**	(t- test)
I_{Max} in <i>Unc13B</i>^{null} (Fig. S5d)				
[Ca ²⁺] _{ex} = 0.75 mM	0.096 ± 0.015 (12)	0.120 ± 0.014 (12)	n.s.	(t- test)
[Ca ²⁺] _{ex} = 1.5 mM	0.277 ± 0.024 (12)	0.303 ± 0.025 (12)	n.s.	(t- test)
[Ca ²⁺] _{ex} = 3 mM	0.562 ± 0.035 (12)	0.542 ± 0.032 (12)	n.s.	(t- test)
[Ca ²⁺] _{ex} = 6 mM	0.790 ± 0.039 (12)	0.743 ± 0.045 (12)	n.s.	(t- test)
[Ca ²⁺] _{ex} = 10 mM	0.915 ± 0.041 (12)	0.879 ± 0.053 (12)	n.s.	(t- test)
K_D and slope in <i>Unc13A</i>^{null} (Fig. S5b,c)	values of fitted Hill coefficients			
K _D (mM)	2.048 ± 0.160 (12)	8.063 ± 1.537 (10)	≤0.001***	(Mann-Whitney U-test)
slope	1.922 ± 0.2003 (12)	2.079 ± 0.232 (10)	n.s.	(Mann-Whitney U-test)
K_D and slope in <i>Unc13B</i>^{null} (Fig. S5e, f)	values of fitted Hill coefficients			
K _D (mM)	2.966 ± 0.273 (12)	2.987 ± 0.265 (12)	n.s.	(Mann-Whitney U-test)
slope	1.501 ± 0.096 (12)	1.751 ± 0.140 (12)	n.s.	(Mann-Whitney U-test)
normalized residual amplitude in <i>Unc13A</i>^{null} (Fig. 7g; S5i)	with 200μM EGTA-AM/DMSO in the extracellular solution; measured (n) (simulated with mathematical modeling)			
after 3 min	0.784 ± 0.031 (10) (0.821)	0.530 ± 0.048 (10) (0.512)	≤0.001***	(t- test)
after 6 min	0.671 ± 0.040 (10) (0.741)	0.434 ± 0.073 (10) (0.382)	≤0.05*	(t- test)

after 9 min		0.592 ± 0.055 (10) (0.699)	0.379 ± 0.066 (10) (0.303)	≤0.05*	(t- test)
after 12 min		0.569 ± 0.058 (10) (0.677)	0.354 ± 0.038 (10) (0.300)	≤0.01**	(t- test)
normalized residual eEJC amplitude in <i>Unc13A</i>^{null} (Fig. S5i)	with DMSO in the extracellular solution (control)				
after 3 min		0.960 ± 0.029 (10)	0.8660 ± 0.077 (10)	n.s.	(t- test)
after 6 min		0.949 ± 0.015 (10)	0.8216 ± 0.081 (10)	n.s.	(t- test)
after 9 min		0.934 ± 0.012 (10)	0.8145 ± 0.085 (10)	n.s.	(t- test)
after 12 min		0.921 ± 0.014 (10)	0.8554 ± 0.111 (10)	n.s.	(t- test)
Decay and plateau in <i>Unc13A</i>^{null} (Fig. S5j, k)	values of single exponential fit to amplitude (normalized) decay upon 200 μm EGTA-AM/DMSO application				
tau (s)		264.5 ± 32.94 (10)	122.8 ± 16.73 (10)	≤0.01**	(t- test)
plateau		0.530 ± 0.057 (10)	0.354 ± 0.033 (10)	≤0.05*	(t- test)
total residual eEJC amplitude in <i>Unc13A</i>^{null} (Fig. S5m, n, o)	upon incubation with 100μM Bapta-AM/DSMO				
DMSO (Ctrl): amplitude (nA)	after 30 min	-116.9 ± 8.033 (15)	9.707 ± 2.224 (14)	≤0.001***	(t- test)
Bapta-AM: amplitude (nA)	after 30 min	-9.481 ± 1.921 (14)	-0.591±0.096 (14)	≤0.001***	(t- test)
Bapta sensitivity		0.081 ± 0.016 (14)	0.060 ± 0.009 (14)	n.s.	(t- test)

Supplementary Table 2: Model values (dual pathway model)				
Parameter name	Value	Unit	Description	Source
$dist_1$	76.8	nm	Pathway 1: Distance from Ca^{2+} source and RRP size	best fit
ROA	670	vesicles		
$dist_2$	145	nm	Pathway 2: Distance from Ca^{2+} source and RRP size	
ROB	196	vesicles		
Q_{max} (Wild type)	2.57	fC	max Ca^{2+} channel charge in Wild type AZs (see equation (2))	
Q_{max} ($Unc13A^{null}$)	4.41	fC	max Ca^{2+} channel charge in $Unc13A^{null}$ AZs (see equation (2))	
K_M	1.74	mM	Michaelis-Menten constant to calculate dependence of synaptic Ca^{2+} current on extracellular $[Ca^{2+}]$ (see equation (2))	
$[EGTA]_{max}$	3925	μM	asymptotic value and time constant of exponential $[EGTA]_{int}$ increase (see equation (1))	
τ_{EGTA}	5.12	min		
Further Parameters				
Parameter name	Value	Unit	Description	Source
L^+	$3.5 \cdot 10^{-4}$	s^{-1}	basal fusion rate constant of [R]	Kochubey&Schneppenburger, 2011. Neuron. 69:736-748.
k_3	$1.4 \cdot 10^8$	$M^{-1} \cdot s^{-1}$	rate constants of Ca^{2+} binding/release	
k_3	4000	s^{-1}		Wolfel et al., 2007. J. Neurosci. 27:3198-3210.
k_4	6000	s^{-1}	fusion rate constant of $[RCa_5]$	Lou et al., 2005. Nature. 435:497-501.
b	0.5	-	cooperativity factor	

Publication V

Driller, J. H., Lützkendorf, J., Depner, H., Siebert, M., Kuropka, B., Weise, C., Petzoldt, A. G.,
Lehmann, M., Stelzl, U., Zahedi, R., Sickmann, A., Freund, C., Sigrist, S. J., Wahl, M. C.
“Phosphorylation of the Bruchpilot N-terminus by SRPK79D controls axonal transport of
active zone building blocks” *J. Cell Sci.*, *in revision*

1 **Phosphorylation of the Bruchpilot N-terminus unlocks axonal transport**
2 **of active zone building blocks**

3

4 **Running title: SRPK79D mediated BRP transport**

5

6 Jan H. Driller^{1,†}, Janine Lützkendorf^{2,†}, Harald Depner², Matthias Siebert², Benno Kuroopka³,
7 Christoph Weise³, Chengji Piao², Astrid G. Petzoldt^{2,6}, Martin Lehmann⁴, Ulrich Stelzl⁵, René
8 Zahedi⁸, Albert Sickmann⁸, Christian Freund³, Stephan J. Sigrist^{2,6,*}, Markus C. Wahl^{1,7,*}

9

10 ¹ Freie Universität Berlin, Institute of Chemistry and Biochemistry, Laboratory of Structural
11 Biochemistry, Takustraße 6, D-14195 Berlin, Germany

12 ² Freie Universität Berlin, Institute of Biology, Laboratory of Genetics, Takustraße 6, D-14195
13 Berlin, Germany

14 ³ Freie Universität Berlin, Institute of Chemistry and Biochemistry, Laboratory of Protein
15 Biochemistry, Thielallee 63, D-14195 Berlin, Germany

16 ⁴ Leibniz-Forschungsinstitut für Molekulare Pharmakologie, Cellular Imaging, Robert-Roessle-
17 Straße 10, D-13125 Berlin, Germany

18 ⁵ University of Graz, Institute of Pharmaceutical Sciences, Pharmaceutical Chemistry,
19 Universitätsplatz 1/I, A-8010 Graz, Austria

20 ⁶ NeuroCure Cluster of Excellence, Charité - Universitätsmedizin Berlin, Charitéplatz 1, 10117
21 Berlin, Germany

22 ⁷ Helmholtz-Zentrum Berlin für Materialien und Energie, Macromolecular Crystallography,
23 Albert-Einstein-Straße 15, D-12489 Berlin, Germany

24 ⁸ Leibniz-Institut für Analytische Wissenschaften -ISAS- e.V., Bunsen-Kirchhoff-Straße 11, D-
25 44139 Dortmund, Germany

26

27 † These authors contributed equally to this work.

28 * Correspondence to: stephan.sigrist@fu-berlin.de; markus.wahl@fu-berlin.de

29

30 **Summary statement**

31 Our results indicate that reversible SRPK79D-mediated phosphorylation of a conserved N-
32 terminal region in BRP/ELKS operates as a switch that ensures safe axonal transport of active
33 zone precursor building blocks.

34

35 **Abstract**

36 Protein scaffolds at presynaptic active zone membranes control information transfer at
37 synapses. For scaffold biogenesis and maintenance, scaffold components must be safely
38 transported along axons. A spectrum of kinases was suggested to control transport of scaffold
39 components, but direct kinase/substrate relationships and operational principles steering
40 phosphorylation-dependent active zone protein transport are presently unknown. Here we show
41 that extensive phosphorylation of a 150-residue unstructured region at the N-terminus of the highly
42 elongated BRP/ELKS active zone proteins *in vivo* is crucial for ordered active zone precursor
43 transport. Point mutations that block SRPK79D-kinase-mediated phosphorylation of the
44 BRP/ELKS N-terminus interfered with axonal transport *in vivo*, leading to BRP/ELKS-positive
45 axonal aggregates that also contain additional active zone scaffold proteins. Axonal aggregates
46 only formed in the presence of non-phosphorylatable BRP/ELKS isoforms containing the
47 SRPK79D-targeted N-terminal stretch. Our results suggest that specific active zone proteins are
48 pre-assembled and co-transported as functional scaffold building blocks, and that transient post-
49 translational modification of a discrete unstructured domain of one master scaffold component
50 blocks precocious oligomerization of such building blocks during their long-range transport.

51

52 **Keywords**

53 Active zone/Axonal transport/Bruchpilot/ELKS/SRPK79D/phosphorylation

54

55 Introduction

56 Functionality of the nervous system is based on rapid communication between neurons and
57 their target cells through specialized cell-cell contacts generically termed synapses. Appropriate
58 synaptic function is essential for all types of cognitive processes, including memory formation and
59 learning. Chemical synapses are asymmetrically organized with a presynaptic active zone (AZ)
60 capable of neurotransmitter release upon action potential arrival and a postsynaptic compartment
61 able to receive and further process this signal. The presynaptic compartment regulates the
62 docking, priming, exocytic fusion and endocytic recovery of synaptic vesicles (SVs) at the plasma
63 membrane of chemical synapses and usually accumulates large numbers of SVs (Südhof, 2012,
64 Walter, Bohme et al., 2018). To support these functions, AZs comprise specialized membrane-
65 associated protein scaffolds, *i.e.* electron dense structures essential for synapse tenacity,
66 localization of SV fusion and positioning of voltage-dependent calcium channels (Haucke, Neher
67 et al., 2011).

68 The cytoplasm of the presynaptic bouton is populated with several hundred protein species,
69 whose copy numbers cover several orders of magnitude (Wilhelm, Mandad et al., 2014). However,
70 AZ scaffolds *per se* are composed of members of only a few protein families: ELKS/CAST family,
71 RIM-superfamily, including the mammalian Piccolo and Bassoon, RIM-binding protein (RIM-BP),
72 (M)UNC-13, Liprin- α and SYD-1 (Gundelfinger, Reissner et al., 2015, Petzoldt & Sigrist, 2014,
73 Südhof, 2012, Walter, Haucke et al., 2014). AZ scaffold composition is evolutionarily conserved;
74 for example, AZ scaffolds at *Drosophila* neuromuscular junctions (NMJs) form T-bar-shaped
75 structures, also referred to as cytomatrices at the AZ (CAZs), that are organized around the central
76 ELKS/CAST scaffolding protein Bruchpilot (BRP) and RIM-BP (Kittel, Wichmann et al., 2006, Liu,
77 Siebert et al., 2011, Van Vactor & Sigrist, 2017). The use of electron tomography and super-
78 resolution light microscopy revealed underlying macromolecular architectures within presynaptic
79 scaffolds (Ackermann, Waites et al., 2015, Kittel et al., 2006, Kittelmann, Liewald et al., 2013,
80 Maglione & Sigrist, 2013).

81 New AZ scaffolds have to be assembled during the development of synaptic circuits and most
82 likely are dynamic structures, in which components are turned over. Work on mammalian and
83 *Drosophila* synapses provided evidence for a tight link between AZ size and complexity and the
84 resulting functional synaptic output (Ackermann et al., 2015). Modulation of the size and possibly
85 the composition of AZ scaffolds might serve as a mechanism, by which the SV release function
86 could be adapted to activity-related or homeostatic demands. These programs seem to span vast
87 time scales, ranging from minutes to days (Van Vactor & Sigrist, 2017). Consistent with these
88 notions, scaffold assembly is based on dynamically regulated protein-protein interactions that rely
89 on a conserved set of interaction surfaces, including both intra- and intermolecular coiled-coil,
90 SAM and PDZ domain interactions (Südhof, 2012).

91 Current efforts seek to characterize the routes and kinetics of proteins to and from the AZ
92 scaffolds and to define the different pools of AZ proteins contributing to scaffold dynamics.
93 However, our current understanding of the mechanisms that regulate assembly of new AZ
94 scaffolds and of the dynamics of already established ones remains very fragmentary. *De novo*
95 assembly and turnover of AZ scaffolds presumably involve synthesis of AZ scaffold components
96 in the cytoplasm of the neuronal cell body and transport over large distances along axons to
97 synaptic terminals (Johnson, Fetter et al., 2009, Nieratschker, Schubert et al., 2009, Siebert,
98 Bohme et al., 2015). Electron and light microscopic analyses of AZ scaffolds provided some
99 evidence for AZ scaffold formation from discrete building blocks (Ehmann, Sauer et al., 2015,
100 Kittelmann et al., 2013, Matkovic, Siebert et al., 2013, Shapira, Zhai et al., 2003). Thus, a logical
101 principle underlying AZ assembly mechanisms and dynamics could be the provision of pre-formed
102 AZ building blocks *via* axonal transport. Indeed, presynaptic material has been suggested to travel
103 along the axon as pre-assembled protein clusters on different types of transport vesicles (Bury &
104 Sabo, 2016, Maeder, San-Miguel et al., 2014). However, direct demonstration of the existence of
105 such scaffold building blocks has been notoriously difficult, potentially reflecting low steady state
106 numbers of scaffold protein copies per unit. Thus, to date it still remains unclear which proteins

107 travel together and on what kind of organelle. Moreover, it is presently unclear how premature
108 aggregation of the scaffold components beyond the level of individual building blocks during
109 transport would be prevented.

110 Previous work on the mechanisms underlying transport of AZ components through axons
111 implicated serine/arginine-rich protein (SR protein)-specific kinase at cytological position 79D
112 (SRPK79D) in this process: Knockout of SRPK79D or inactivation of its kinase activity led to the
113 formation of interconnected, electron-dense, axonal aggregates that contained BRP and that
114 resembled over-sized T-bars (Johnson et al., 2009, Nieratschker et al., 2009). Given that SRPKs
115 are known to phosphorylate serine residues in serine/arginine dipeptide-rich regions (RS domains)
116 of SR proteins, a family of regulatory factors involved in alternative pre-mRNA splicing and other
117 gene regulatory processes (Lin & Fu, 2007, Zhou & Fu, 2013), the functional implication of
118 SRPK79D in the transport of AZ scaffold components is surprising. Furthermore, as known AZ
119 scaffold components do not contain canonical RS domains or extended RS dipeptide repeats and
120 as direct phosphorylation of these proteins by SRPK79D has not yet been demonstrated, it is
121 presently unclear how SRPK79D might mechanistically intersect with the transport of AZ proteins.

122 Here, we delineated *in vivo* phosphorylation sites in BRP and found that BRP variants bearing
123 a phosphorylation-defective N-terminus led to axonal T-bar-like assemblies that closely resembled
124 aggregates elicited by SRPK79D mutants. The assemblies not only contained the major AZ
125 components BRP and RIM-BP, but also comprised the critical release factor Unc13A, suggesting
126 co-transport of the three proteins as a pre-formed AZ scaffold building block. Systematic yeast
127 two-hybrid (Y2H) screening, *in vitro* interaction studies and mass spectrometric analyses showed
128 that SRPK79D specifically binds at the N-terminus of BRP and phosphorylates specific sites within
129 this predicted unstructured region, including sites that upon mutation led to axonal aggregation.
130 The homologous region of mammalian ELKS/CAST was phosphorylated by members of the SRPK
131 family as well. Genetic analyses showed that phosphorylation of the N-terminal BRP stretch keeps
132 transporting AZ building blocks in solution. Reversible phosphorylation of N-terminal regions in AZ

133 scaffold proteins of the ELKS/CAST family by SRPKs thus might constitute an evolutionarily
134 conserved master switch to stabilize the transport of a major AZ building block.
135

136 **Results**

137 **The unstructured N-terminus of BRP undergoes extensive phosphorylation *in vivo***

138 We hypothesized that reversible phosphorylation of AZ core components may prevent their
139 precocious oligomerization, which poses a potential problem during their axonal transport. An N-
140 terminal region of about 300 residues in BRP appears to be largely intrinsically unstructured, while
141 the remaining portions of BRP are predicted to adopt α -helical conformations, giving rise to an
142 extended coiled-coil structure of the protein that shapes the T-bar AZ scaffold in its ultrastructural
143 extensions (Fig 1A) (Fouquet, Oswald et al., 2009). Bioinformatics analyses using the NetPhos 3.1
144 server (Blom, Gammeltoft et al., 1999) predicted many phosphorylation sites clustered in the
145 presumably unstructured N-termini of BRP/ELKS-family AZ proteins (Fig 1A).

146 To experimentally determine sites at which BRP is phosphorylated *in vivo*, synaptosomes were
147 isolated from adult *Drosophila* fly head protein extracts as previously described by us (Depner,
148 Lützkendorf et al., 2014). Monoclonal antibody NC82 was used to immunoprecipitate BRP. The
149 precipitate was fractionated by SDS-PAGE, the prominent 190 kDa band was excised and
150 subjected to tandem mass spectrometry (MS)-based peptide sequencing. This analysis revealed
151 27 phosphorylation sites in the long BRP-190 isoform (Fig 1A). Notably, 13 of these phosphosites
152 fall within an N-terminal 140-residue portion that precedes the extended coiled-coil regions of BRP
153 (Fig 1 A, B). The five phosphosites found within the coiled-coil regions predominantly reside in
154 stretches that interrupt the predicted coiled-coil structures. Interestingly, several phosphorylation
155 sites detected in *Drosophila* BRP are conserved in mammalian homologue ELKS proteins and
156 have been partially experimental validated (Dephoure, Zhou et al., 2008, Hornbeck, Zhang et al.,
157 2015, Parker, Yang et al., 2015, Sacco, Humphrey et al., 2016, Sharma, D'Souza et al., 2014).

158

159 **Phosphorylation of the BRP N-terminus ensures safe transport of active zone building**
160 **blocks**

161 To delineate functional roles of BRP phosphorylation, we generated large, genomic p[acman]
162 *brp* constructs, in which identified phosphorylation sites were abrogated by alanine mutations. We
163 had previously shown that wild type (wt) p[acman] *brp* constructs (*brp*^{rescue}) completely rescued
164 *brp*^{null} (*brp*^{Δ6.1}/*brp*^{DF(2R)69}) alleles (*per se* pupal lethals) to full viability and fertility and are thus
165 equivalent to the endogenous locus (Matkovic et al., 2013). We started by simultaneously
166 exchanging S16, S32, S43, T59, Y130, S137, S629, S1216 of BRP-190 for non-phosphorylatable
167 alanines (*brp*^{multiAla}). The majority of the corresponding residues are not strongly conserved in the
168 BRP/ELKS family (Fig 1A). Similar to *brp*^{rescue}, expression of *brp*^{multiAla} elicited a complete rescue
169 of *brp*^{null} alleles, indicating no essential function for phosphorylation at the altered sites.

170 Next, we generated a genomic p[acman] *brp* construct, in which S71, S73 and S90 that are
171 highly conserved throughout the BRP/ELKS family in mammalian (Mochida, Hida et al., 2016,
172 Parker et al., 2015) were jointly exchanged for alanines and introduced it into a *brp*^{null} background
173 in comparison to a non-mutated control construct (F). Determination of hatching rates revealed
174 robust differences between the control and the phosphorylation-defective *brp*^{SSS71/73/90AAA} mutant.
175 The Mendelian ratio within the F1 generation of *brp*^{SSS71/73/90AAA} flies was only about 12 %, as
176 compared to about 27 % for the non-mutated control (formally expected rate 33 %). These
177 observations suggest that the *brp*^{SSS71/73/90AAA} mutant is functionally compromised as compared to
178 the rescue control.

179 Strikingly, confocal microscopy revealed numerous BRP-positive (0.13 spots per μm² individual
180 axon area) and RIM-BP-positive (0.15 spots per μm² individual axon area) aggregates within
181 motoneuron axons of third instar larvae upon disruption of BRP N-terminal phosphorylation sites
182 at positions 71, 73 and 90 (Fig 2D), suggesting disturbed axonal transport of AZ scaffold proteins.
183 Most aggregates were positive for both BRP and RIM-BP. In contrast, *brp*^{rescue} axons exhibited
184 significantly less BRP-positive (0.005 spots per μm² individual axon area) and RIM-BP-positive

185 (0.04 spots per μm^2 individual axon area) punctae. Furthermore, in *brp*^{SSS71/73/90AAA} mutant animals,
186 the BRP (0.14 μm^2) and RIM-BP (0.12 μm^2) spots had a similar size and were significantly larger
187 and abnormally formed compared to those found in control nerves (BRP 0.05 μm^2 ; RIM-BP 0.06
188 μm^2).

189 The *brp*^{SSS71/73/90AAA}-dependent axonal aggregates were reminiscent of previously reported
190 BRP-positive and RIM-BP-positive axonal super T-bar structures that emerged upon loss of
191 function of SRPK79D (Fig 1C) (Nieratschker et al., 2009, Siebert et al., 2015). In *srpk79D*^{VN}
192 mutants (*srpk79D*^{VN} deletes a large part of the *srpk79D* gene, generating a *srpk79D* null mutant
193 (Johnson et al., 2009, Nieratschker et al., 2009)), we found the average sizes of BRP-positive (0.3
194 μm^2) and RIM-BP-positive (0.25 μm^2) punctae further enlarged compared to corresponding
195 punctae in *brp*^{SSS71/73/90AAA} mutants (Fig 2E). In electron microscopy (EM) analyses, electron-dense
196 aggregates were readily found in motoneuron axons of *brp*^{SSS71/73/90AAA} mutants, whose
197 appearance and distribution closely resembled the aggregates forming in *srpk79D*^{VN} mutants (Fig
198 3A, B). Likewise, stimulated emission depletion light microscopy at a resolution of about 50 nm
199 (Hell, 2007) showed a “stoichiometric patterning” of BRP and RIM-BP epitopes within the
200 *brp*^{SSS71/73/90AAA} aggregates, very similar to the previously reported, STED-visualized patterning of
201 *srpk79D* mutant axonal aggregates (Fig 3C, D) (Siebert et al., 2015).

202 Recent work by our group has shown that at AZs, the BRP/RIM-BP scaffold is crucial to properly
203 cluster and position the critical release factor Unc13A (Böhme, Beis et al., 2016). Like for RIM-
204 BP, staining with anti-Unc13A antibody revealed close and stoichiometric association of BRP and
205 Unc13A in the floating axonal aggregates of both *brp*^{SSS71/73/90AAA} and *srpk79D*^{VN} mutants (Fig 3E,
206 F). In fact, the STED-resolved relative distribution of RIM-BP vs. BRP^{C-term} as well as of Unc13A
207 vs. BRP^{C-term} were reminiscent of the organization of these epitopes within the scaffolds of synaptic
208 AZs (Böhme et al., 2016, Liu et al., 2011).

209

210 **Formation of axonal aggregates depends on an N-terminal region unique to the long of the**
211 **two BRP isoforms**

212 The above morphological and compositional analyses strongly suggest that axonal T-bar-like
213 aggregates forming in *srpk79D*-deficient and *brp*^{SSS71/73/90AAA} mutants are equivalent in nature. To
214 further characterize which AZ protein(s) cause(s) these axonal T-bar-like aggregates, we
215 eliminated several AZ proteins in the background of the *srpk79D* gene. The *brp* locus gives rise
216 to at least two prominent BRP isoforms, originating from alternative promoters, which contain
217 (BRP-190) or lack (BRP-170) an N-terminal stretch of about 320 amino acid residues (Fig 1A).
218 Previous analyses have shown that AZ scaffolds comprise a circular arrangement of alternating
219 BRP-190 and BRP-170 clusters (Matkovic et al., 2013). To test if both isoforms were needed for
220 the formation of the axonal T-bar-like aggregates, isoform-specific *brp* mutants were generated
221 and tested in a *srpk79D*^{atc} background (*srpk79D*^{atc} leads to the production of a non-functional,
222 truncated form of SRPK79D, (Johnson et al., 2009). No axonal aggregates were formed when
223 both BRP isoforms or BRP-190 alone were knocked out in a *brp* null background (Fig 4A-E). In
224 contrast, axonal aggregates were still observed when only BRP-170 was removed (Fig 4F, G).
225 Likewise, *rim-bp* and *srpk79D* double knockouts still displayed BRP-positive aggregates,
226 indicating that RIM-BP is not essential for axonal aggregate formation (Fig 4H-J). These results
227 suggest that BRP-190 might be the only AZ scaffold component that is essential for the formation
228 of axonal T-bar-like aggregates upon knockout/mutation of SRPK79D or, most likely, in
229 *brp*^{SSS71/73/90AAA} mutants. Notably, the N-terminal about 320 residues that discriminate BRP-190
230 from BRP-170 seem to play an important and specific role in the formation of BRP-positive axonal
231 aggregates. Thus, our observations suggest a functional relationship between SRPK79D and the
232 N-terminal region of BRP-190 in preventing axonal aggregation of AZ components during their
233 axonal transport to synapses.

234

235 **The BRP N-terminal region comprises several docking sites for SRPK79D**

236 As the *brp*^{SSS71/73/90AAA} mutant pheno-copies the *srpk79D*^{VN} mutant, axonal aggregates seen in
237 these mutants likely originate due to the same mechanistic principle. The most facile explanation
238 for the similar effect of these mutants would be that SRPK79D phosphorylates BRP to facilitate
239 axonal transport, although BRP does not contain a typical RS-domain. This hypothesis is
240 supported by the observation that SRPK79D and BRP co-localize *in vivo* (Johnson et al., 2009).
241 We directly tested this idea by conducting *in vitro* binding and phosphorylation studies using
242 recombinant SRPK79D and BRP fragments.

243 While SRPKs encompass the canonical N- and C-terminal lobes of Ser/Thr protein kinases, a
244 region of about 200 residues that is predicted to be intrinsically disordered intervenes between the
245 lobes in this protein kinase family (Ghosh & Adams, 2011). In addition, a shorter region of
246 predicted intrinsic disorder precedes the N-terminal lobe of these kinases. Moreover, some SRPKs
247 have been shown to engage their substrates *via* a docking groove on the C-lobe (Ngo, Chakrabarti
248 et al., 2005). SRPK79D contains a split kinase domain typical of the SRPK family and appears to
249 encompass a docking groove but harbors a significantly longer region of predicted intrinsic
250 disorder preceding the N-terminal lobe compared to mammalian SRPK1/2 (Fig 5A). The
251 SRPK79D unstructured N-terminus, which is required for its localization with BRP *in vivo* (Johnson
252 et al., 2009), and its putative docking groove on the C-lobe represent possible regions, through
253 which the enzyme might transiently engage substrate proteins at sites that are distinct from or
254 overlapping with the phosphorylated regions; alternatively, SRPK79D might use these regions to
255 dock to other proteins that in turn are associated with substrate proteins. We therefore employed
256 the Y2H system (Worseck, Grossmann et al., 2012) to uncover potential, direct interactions
257 between SRPK79D and the proteins found in the axonal aggregates. Apart from the full-length
258 proteins, we tested Y2H interactions among fragments of the proteins that covered known
259 functional regions, predicted or known folded domains or regions of predicted intrinsic disorder.

260 A robust Y2H interaction was detected between full-length SRPK79D (SRPK79D^{FL}) as well as
261 all SRPK79D constructs containing the two lobes of the kinase core (SRPK79D^{Core},
262 SRPK79D^{CoreΔlinker1}, SRPK79D^{CoreΔlinker2}) and a region comprising the N-terminal 152 residues of
263 the BRP-190 isoform (BRP-190¹⁻¹⁵²; Table 1). Neither the intrinsically disordered SRPK79D N-
264 terminal region (SRPK79D¹⁻³⁴⁰) nor the linker region between the N- and C-lobes (omitted in
265 constructs SRPK79D^{CoreΔlinker1} and SRPK79D^{CoreΔlinker2}) were required for Y2H interactions with
266 BRP-190¹⁻¹⁵². The SRPK79D N-terminus alone interacted with diverse, putatively unstructured or
267 coiled-coil regions of tested AZ proteins, among these BRP and RIM-BP. These results indicate
268 that BRP-190 might directly interact with SRPK79D, possibly *via* its N-terminal region inserting
269 into the docking groove of the kinase.

270 To test whether the observed Y2H interactions of SRPK79D and BRP-190¹⁻¹⁵² originated from
271 direct contacts between these proteins, we recombinantly produced the corresponding protein
272 fragments (Fig 5A) and tested their interactions by analytical size exclusion chromatography
273 (SEC). To test for the role of the docking groove in the interaction, we generated a SRPK79D
274 variant bearing a disrupted docking groove (SRPK79D^{CoreΔDock}) (Lukasiewicz et al., 2007).
275 SRPK79D^{Core} and BRP-190¹⁻¹⁵² co-migrated during SEC and together eluted earlier than the
276 isolated proteins (Fig 5B). Consistent with the Y2H results, truncation of the inter-lobe linker region
277 of SRPK79D (SRPK79D^{CoreΔlinker1}) had no effect on BRP-190¹⁻¹⁵² binding. In line with the idea that
278 BRP-190¹⁻¹⁵² binds to the docking groove of SRPK79D, the SRPK79D^{CoreΔDock} variant did not co-
279 elute with BRP-190¹⁻¹⁵² in SEC (Fig 5C).

280 To further narrow down the SRPK79D binding site(s) on BRP-190¹⁻¹⁵², we conducted peptide
281 SPOT analyses. SPOT membranes contained overlapping 25-residue peptides covering the BRP-
282 190 N-terminal region with a seven-residue offset (Table S2). The SRPK79D kinase domain
283 construct (SRPK79D^{Core}) bound to peptides representing three BRP regions (15-RSPGRVRR-22;
284 66-HHRSRSASR-74; 113-RSRDRSLER-121; Fig 5E), suggesting that it can attach to several
285 sites on BRP-190. Notably, the sequences of these three putative docking sites somewhat

286 resemble proposed binding motifs recognized by SRPK1, which consist of three basic residues
287 (underlined) separated by two to three positions (Lukasiewicz et al., 2007). Together, these data
288 suggest that direct binding of SRPK79D within the N-terminal about 150 residues of BRP-190
289 might underlie the functional SRPK79D-BRP interplay in preventing axonal T-bar-like aggregates.

290

291 **SRPK79D phosphorylates specific sites in the BRP N-terminus *in vitro***

292 SRPKs can employ different modes of operation depending on the nature of the substrate
293 proteins. Substrates comprising extended RS repeats can be phosphorylated *via* a processive
294 mechanism that involves an initial engagement of the substrate at a docking groove on the C-
295 terminal lobe of the kinase (Lukasiewicz et al., 2007). Subsequently, phosphorylation sites are
296 continuously funneled into the active center in a C-to-N-terminal direction. Continued
297 phosphorylation eventually reduces target affinity, most likely by electrostatic repulsion between
298 the phosphates and the acidic docking groove (Ghosh & Adams, 2011). For targets with only short
299 RS repeats, docking groove binding can be dispensable and such targets can be phosphorylated
300 *via* a distributive mechanism or in a dual-track mode that encompasses processive and distributive
301 phases (Aubol, Plocinik et al., 2013, Lukasiewicz et al., 2007).

302 To test if the observed interaction of SRPK79D with the N-terminal region of BRP-190 forms
303 the basis for SRPK79D-mediated BRP phosphorylation, we conducted *in vitro* phosphorylation
304 assays using recombinant proteins. Upon incubation with γ -[³²P]-ATP, SRPK79D^{Core}
305 phosphorylated full-length BRP-190, BRP-190¹⁻¹⁵² as well as itself, but strikingly failed to
306 phosphorylate a large BRP-190 fragment (BRP190 ^{Δ 1-152}) that lacked the N-terminal 152 residues
307 (Fig 5F). Identical preparations of catalytically inactive SRPK79D^{Core-dead}, bearing a K376M
308 exchange that disrupts ATP binding (Johnson et al., 2009), did not exhibit similar kinase activity
309 (Fig 5F), indicating that the observed phosphoryl-transfer activity originates from recombinant
310 SRPK79D^{Core}. In contrast, the SRPK79D^{Core Δ Dock} variant that exhibits a disrupted docking groove
311 phosphorylated the same BRP variants as SRPK79D^{Core} (Fig 5F). These results are consistent

312 with the idea that SRPK79D specifically targets the BRP N-terminal region, and that the enzyme
313 can act through a distributive mechanism, as previously described for SRPK1 (Aubol et al., 2013).

314 As ongoing phosphorylation of target sites reduces the affinity of substrate proteins to SRPK1
315 (Ghosh & Adams, 2011), phosphorylated BRP-190 might likewise exhibit reduced affinity to
316 SRPK79D. To test this prediction, we monitored interaction of SRPK79D^{Core} with BRP-190¹⁻¹⁵²
317 after prior phosphorylation by analytical SEC. In contrast to non-phosphorylated BRP-190¹⁻¹⁵² (Fig
318 5B), BRP-190¹⁻¹⁵² no longer co-migrated with SRPK79D^{Core} in SEC after prior incubation in the
319 presence of ATP (Fig 5B). Bands representing BRP-190¹⁻¹⁵² were shifted to slightly higher
320 apparent molecular mass on the SDS polyacrylamide gels after incubation with SRPK79D^{Core} and
321 ATP (Fig 5B), consistent with SRPK79D^{Core}-mediated phosphorylation. While the catalytically
322 inactive SRPK79D^{Core-dead} variant also bound to non-phosphorylated BRP-190¹⁻¹⁵² (Fig 5D), as
323 expected if initial binding occurs through its intact docking groove, it did not release the substrate
324 after incubation with ATP (Fig 5D).

325

326 **Identification of phosphorylation sites within the BRP N-terminus**

327 To determine the sites of SRPK79D^{Core}-mediated phosphorylation, we analyzed non-
328 phosphorylated and *in vitro* phosphorylated BRP-190¹⁻¹⁵² by matrix-assisted laser
329 desorption/ionization time-of-flight mass spectrometry (MALDI-TOF-MS). After one hour of
330 incubation with SRPK79D^{Core} or SRPK79D^{CoreΔDock} and ATP, BRP-190¹⁻¹⁵² showed an increase in
331 molecular mass of 556 Da, suggesting seven added phosphate groups (each contributing ~ 80
332 Da), with a smaller portion of the protein carrying an eight-phosphate group (Fig 6A). Time course
333 experiments monitoring BRP-190¹⁻¹⁵² phosphorylation by SRPK79D^{Core} and SRPK79D^{CoreΔDock}
334 revealed faster phosphorylation with an intact SRPK docking groove (Fig S1). Independent of the
335 docking groove, the same phosphorylation state was reached after one hour (Fig S1 and Fig S2A).
336 These findings indicate that an intact docking groove increases phosphorylation kinetics but does
337 not alter phosphorylation specificity.

338 To map the exact phosphorylation sites in BRP-190¹⁻¹⁵², we performed tryptic in-gel digestion
339 followed by mass spectrometry. By using a combination of liquid chromatography electrospray
340 ionization mass spectrometry (LC-ESI-MS) and MALDI-TOF-MS, we confirmed almost complete
341 phosphorylation of residues S16, S32, S34, S71, S73, S90 and S118 after one hour of incubation
342 (Fig 6B, C). Except for S90, all these residues reside within one of the SRPK79D docking sites on
343 BRP-190¹⁻¹⁵² and are part of RS or SR dipeptides.

344 Analyzing the time course of SRPK79D^{Core}-mediated BRP-190¹⁻¹⁵² phosphorylation by LC-ESI-
345 MS, showed that S90 and S118 are phosphorylated first, with over 90 % (S90) or over 80 % (S118)
346 of these residues phosphorylated within 30 seconds. S71/S73, S32/S34 and S16 were
347 phosphorylated at progressively lower rates (Fig 6B). The exact order of phosphorylation of the
348 closely-spaced residues could not be resolved, as S71/S73 on the one hand and S34/S32 on the
349 other were part of the same tryptic peptides.

350 Our MS analyses reliably covered over 90 % of the BRP-190¹⁻¹⁵² sequence and almost all of
351 its potential 7 to 8 phosphorylation sites observed by analysis of the intact BRP-190¹⁻¹⁵² by MALDI-
352 TOF-MS (Fig 6B, C). However, we did not observe peptides containing S114, which resides within
353 one of the binding motifs in an RSR motif, possibly due to several arginine residues in the
354 immediate vicinity giving rise to very small tryptic peptides. To confirm phosphorylation sites that
355 were not covered by detectable tryptic peptides, we used recombinantly expressed sub-fragments
356 of BRP-190¹⁻¹⁵², incubated them with SRPK79D^{Core} or SRPK79D^{CoreΔDock} and ATP and performed
357 total mass analyses by MALDI-TOF-MS, indicating an almost full phosphorylation at S114 and
358 partial phosphorylation at S16 (Fig S2).

359 The above findings show that SRPK79D predominantly phosphorylates sites in BRP-190¹⁻¹⁵²
360 that reside within or in direct vicinity of the kinase docking sites. The SRPK79D-mediated
361 phosphorylation seems to preferentially start at the C-terminal region of BRP-190¹⁻¹⁵², around S90
362 and S118. The directional C-to-N-terminal phosphorylation together with faster phosphorylation
363 with an intact docking groove hints at the possibility that SRPK79D might also be able to work

364 processively for faster phosphorylation of several sites but can still work in a distributive manner
365 (docking groove mutant), as previously seen for SRPK1 and SRSF1 (Aubol, Chakrabarti et al.,
366 2003). Reduced affinity of the substrate upon its phosphorylation additionally supports
367 mechanistic commonalities to SRPK1. Notably, all the identified *in vitro* phosphorylation sites,
368 except S114 and S118, correspond to sites that were also found phosphorylated *in vivo*; in
369 particular, they encompass S71, S73 and S90, which upon alanine mutation led to axonal
370 BRP/RIM-BP/Unc13A aggregates (see above). None of the additional, potentially
371 phosphorylatable seven serines and five threonines within the first 152 residues of BRP were
372 phosphorylated by SRPK79D significantly *in vitro*, suggesting that the recombinant SRPK79D
373 constructs largely retain the substrate specificity of endogenous SRPK79D. Seven *in vivo* sites at
374 the BRP-190 N-terminus (S43, T59, S60, Y130, S133, S137 and S139) were not found to be
375 phosphorylated by SRPK79D *in vitro* and may thus be targeted by other kinases (Fig 6C).

376

377 **Phosphorylation of ELKS family members by SRPKs is evolutionarily conserved**

378 To test if mammalian SRPKs can phosphorylate the N-termini of mammalian BRP orthologues
379 CAST1/2, we conducted *in vitro* binding studies and kinase assays, using recombinant SRPK1,
380 SRPK2 and CAST1/2 constructs. Two fragments comprising N-terminal regions of Cast2 (Cast2¹⁻
381 ¹⁶³ and Cast2¹⁻³⁵³) co-migrated with SRPK1^{CoreΔlinker} (equivalent to SRPK1^{NS3} in and SRPK2^{Core})
382 eluting earlier from the column as the individual proteins (Fig 6D, E). Moreover, both fragments as
383 well as the related BRP-190¹⁻¹⁵² were phosphorylated by the kinases upon incubation with γ -[³²P]-
384 ATP (Fig 6F). These data are consistent with the idea that SRPK-mediated phosphorylation of the
385 N-termini of ELKS family proteins is an evolutionarily conserved regulatory principle that may be
386 involved in controlling axonal transport of AZ scaffold components in neurons across the animal
387 kingdom.

388

389 Discussion

390 The molecular mechanisms underlying ordered axonal transport of AZ scaffold proteins are
391 presently poorly understood. In particular, it is unclear whether, and if so which, AZ scaffold
392 components are co-transported as functional building blocks and how neurons avoid pre-mature
393 higher-order aggregation of AZ scaffold proteins during transport. Several lines of evidence
394 indirectly implicate reversible protein phosphorylation as an important regulatory principle for
395 axonal transport of AZ scaffold proteins. Interestingly, several kinases, such as Protein kinase A,
396 Ca²⁺/calmodulin-dependent protein kinase (CaMKII) and Glycogen synthase kinase 3 (GSK3),
397 seem to negatively regulate transport of AZ and SV material, as their knockout was shown to
398 promote transport (Guillaud, Wong et al., 2008, Hall & Hedgecock, 1991, Morfini, Szebenyi et al.,
399 2002, Sato-Yoshitake, Yorifuji et al., 1992, Waikar, Toda et al., 2009). In contrast, functional
400 impairment of SRPK79D in *Drosophila* causes ectopic accumulation of scaffold proteins within the
401 axoplasm (Johnson et al., 2009, Nieratschker et al., 2009), indicating that SRPK79D is a positive
402 regulator of axonal transport. However, how SRPK79D supports transport of AZ scaffold proteins
403 has so far remained elusive.

404 Here, we show that SRPK79D mediates its “transport-stabilization” function by phosphorylating
405 a specific, only about 150-residue stretch at the very N-terminus of the extended coiled-coil
406 domain protein BRP. SRPK79D can bind at three arginine-rich motifs and phosphorylates at least
407 seven sites within or in close vicinity of these motifs. When interfering with SRPK79D-mediated
408 phosphorylation of BRP by serine to non-phosphorylatable alanine exchanges in the *brp* genomic
409 context, axonal aggregates formed. These mimicked in ultrastructural detail and molecular
410 composition the *srpk79D^{VN}* aggregates: large, extended, multiple T-bars containing BRP, RIM-BP
411 and Unc13A. Importantly, these aggregates no longer formed when the *brp*-190 isoform
412 exclusively containing this sequence stretch was genetically eliminated. Thus, obviously a key
413 function of SRPK79D is to tonically keep the N-terminal stretch of BRP phosphorylated during
414 axonal transport. It thereby protects the transported BRP-190 isoform from undergoing a pseudo-

415 AZ-like assembly process within the axoplasm, which co-aggregates, but does not depend on,
416 RIM-BP and Unc13A. As the size of the BRP/RIM-BP/Unc13A aggregates in the *brp*^{SSS71,73,90AAA}
417 mutant was somewhat reduced compared to the qualitatively very similar aggregates in *sprk79D*
418 mutants, it is possible that the sites not included in our triple mutant but found to be phosphorylated
419 by SRPK79D *in vitro* (S16, S32, S34, S114, S118) contribute as well to a the *sprk79D* mutant
420 phenotype.

421 Further expanding on our previous analyses (Siebert et al., 2015), results reported here
422 document that *brp*^{SSS71,73,90AAA}- and *sprk79D*^{null}-induced aggregates accumulate only a specific
423 sub-spectrum of AZ proteins, namely BRP, RIM-BP and Unc13A. These three proteins exactly
424 constitute SV release sites within the central AZ scaffold (Reddy-Alla, Böhme et al., 2017). They
425 incorporate into assembling AZ scaffolds only after other scaffold proteins, Syd-1 and Liprin- α ,
426 have initialized the actual assembly process (Böhme et al., 2016). We did not find the “early
427 seeding factors” Syd-1 and Liprin- α either within the *sprk79D* mutant nor in the *brp*^{SSS71,73,90AAA}
428 mutant aggregates. Thus, BRP phosphorylation by SRPK79D seems to block the premature
429 oligomerization of a specific scaffold “building block” (BRP/RIM-BP/Unc13A) from forming pre-
430 assembled units in a kinase activity-dependent fashion. We previously showed that RIM-BP is
431 directly transported *via* a high-affinity interaction between its SH3 domains II and III and a proline-
432 rich stretch of the JIP-1 homologue Aplip1, which in turn binds to the kinesin 1A type motor
433 Unc104/Imac (Siebert et al., 2015). Thus, the RIM-BP constituent might actually provide a key
434 connection of the transported building block to the transport machinery.

435 To the best of our knowledge, our work for the first time documents direct phosphorylation and
436 consequent regulation of a synaptic protein by a SRPK-type kinase. SRPK family members have
437 so far been predominantly implicated in the phosphorylation and thus regulation of SR proteins
438 that act as regulators of various gene regulatory processes (Lin, Chen et al., 2007, Zhou & Fu,
439 2013). Our mechanistic results imply a similar mode of action of SRPK79D on BRP as previously
440 described for SRPKs acting on RS domain-containing substrates. Depending on the nature of its

441 substrate, SRPK1 can phosphorylate them *via* a semi-processive, directional or distributive
442 mechanism (Aubol et al., 2013). Although the docking groove seems to be dispensable for the
443 overall phosphorylation state of the BRP N-terminus, our data show faster phosphorylation with
444 an SRPK79D variant bearing an intact docking groove. Thus, while SRPK79D can obviously
445 phosphorylate the BRP-190 N-terminus by employing a distributive mechanism, an intact docking
446 groove ensures faster phosphorylation of specific sites. SRPK79D with an intact docking groove
447 also shows a tendency to phosphorylate the more C-terminal region of BRP-190¹⁻¹⁵² first, indicated
448 by the faster phosphorylation rate of S90 and S118 compared to the more N-terminally located
449 sites. SRPK79D may thus act at least to some extent processively and in a C-to-N direction on
450 BRP-190 *in vivo*.

451 Consistent with our results, it has been shown that the non-conserved, putatively unstructured
452 N-terminus of SRPK79D is important for its localization with BRP (Johnson et al., 2009). Our Y2H
453 studies further show that this SRPK79D N-terminal portion engages in several weak and rather
454 unspecific interactions with AZ proteins in unstructured or coiled-coil regions, notably also in the
455 co-transported proteins BPR and RIM-BP. We suggest that these weaker interactions do not
456 directly impact on the SRPK79D mechanism of action but might rather ensure a high local
457 concentration of SRPK79D at the transported protein complex.

458 The question arises of how the phosphorylation status of a confined, likely intrinsically
459 disordered stretch at the BRP N-terminus might influence the aggregation status of a "whole
460 transport package" that, apart from BRP, contains RIM-BP and Unc13A. We speculate that the
461 high charge density at the BRP N-terminus introduced through multiple phosphate moieties might
462 trigger an extensive, cooperative conformational switch in the protein, rendering it less
463 aggregation-prone. Consistent with this notion, conformational changes can be propagated over
464 long distances through coiled-coil arrangements in proteins, as illustrated for example by ATP
465 binding-hydrolysis-ADP/Pi release cycles in motor proteins (Carter, Diamant et al., 2016). As an
466 alternative mechanism, EEA1 has recently been shown to undergo a massive extended-to-

467 collapsed conformational change that is initiated by upon binding to Rab5:GTP and is propagated
468 over the entire length of this 1400-residue protein (Murray, Jahnel et al., 2016).

469 Ultimately, the BRP/RIM-BP/Unc13A building block transported down the axon must be
470 integrated into the AZ scaffold. It appears likely that local de-phosphorylation of BRP might be part
471 of the integration process. Thus, one might expect localized phosphatase activity to promote
472 scaffold assembly. In fact, in previous synaptic AZ assembly studies at *Drosophila* NMJ synapses,
473 protein phosphatase 2A (PP2A) was found to regulate presynaptic assembly. In absence of the
474 phosphatase, assembling postsynaptic glutamate receptor fields often lacked presynaptic AZ
475 scaffolds (Viquez, Fuger et al., 2009), a finding that is at least consistent with PP2A supporting
476 developmental scaffold assembly *via* BRP de-phosphorylation. PP2A activity and assembly
477 function seemingly are tuned by activities of the serine-threonine kinase GSK-3beta (Viquez et al.,
478 2009) and Unc-51 (Atg1) (Wairkar et al., 2009).

479 We also show that mammalian BRP homologues are equally phosphorylated by SRPKs at their
480 conserved N-terminal stretches. Notably, SRPKs have been implicated in various
481 neurodegenerative diseases (Chan & Ye, 2013, Jang, Liu et al., 2009). Furthermore, mammalian
482 SRPK2 has already been shown to play a role in neuronal function by phosphorylating tau at a
483 specific position to inhibit axonal elongation in neurons (Hong, Chan et al., 2012). Our results,
484 therefore, might be of importance for AZ assembly and plasticity, and consequently developmental
485 circuit formation, learning and memory processes, in the human brain as well. In addition, they
486 further underscore that future studies investigating the molecular principles underlying SRPK-
487 related neuronal diseases (Chan & Ye, 2013) should take into account not only well-documented
488 functions of SRPKs in regulating gene expression but also roles, by which these enzymes might
489 more directly influence the functions of neuronal proteins.

490

491 **Materials and methods**

492 **Cloning and mutagenesis**

493 DNA fragments encoding SRPK79D constructs were cloned into pGEX 6P1 vector from a
494 codon-optimized gene (Centic Biotec) using BamHI and NotI. A DNA fragment encoding
495 SRPK2^{Core} was cloned into pETM11 vector (EMBL, Heidelberg) from a mSRPK2 plasmid
496 (provided by S. Schoch-McGovern, Universität Bonn), using NcoI and Sall. SRPK1 expression
497 constructs were provided by G. Ghosh, University of California, San Diego. DNA fragments
498 encoding BRP N-terminal constructs were cloned into pETM11 vector from a codon-optimized
499 gene (Centic Biotec) using NcoI and Sall. DNA fragments encoding BRP-190 and BRP-190^{Δ1-152}
500 were cloned from a codon-optimized gene into a modified pFL vector (EMBL, Grenoble) that
501 directed production of protein bearing an N-terminal His₁₀-tag followed by a TEV cleavage site and
502 a C-terminal Strep-tag, using EcoRI and Sall. A DNA fragment encoding Cast1 was cloned from
503 cDNA into a modified pFL vector that directed production of protein bearing an N-terminal His₁₀-
504 tag followed by a TEV cleavage site, using EcoRI and Sall. DNA fragments encoding Cast2 N-
505 terminal fragments were cloned from cDNA into pETM11 vector, using NcoI and Sall. A DNA
506 fragment encoding BRP-190^{1-152,6SD} was obtained as a synthetic gene (GeneArt, ThermoFischer)
507 in a pET151/D-TOPO expression vector. All other mutations were incorporated by QuikChange
508 mutagenesis (Agilent). All constructs were verified by DNA sequencing.

509

510 **Protein production and purification**

511 Protein constructs used here are listed in Table S1. Production of SRPK79D constructs was
512 done in *Escherichia coli* BL21 Rosetta 2 cells in ZYM auto-induction media (Studier, 2005). Cells
513 were grown for 4 h at 37° C and subsequently incubated at 18° C overnight. Cells were harvested
514 by centrifugation (9000 x g, 7 min) and resuspended in lysis buffer (400 mM NaCl, 40 mM Tris/HCl,
515 pH 7.5, 5 % (v/v) glycerol, 1 mM DTT) supplemented with DNase. The cells were lysed by
516 sonication (Sonopuls HD 3100, Bandelin) and lysate was cleared by centrifugation (55,000 g, 1 h,

517 4° C). Cleared lysate was incubated for 1 h with Glutathione-Sepharose 4B resin (GE Healthcare),
518 washed with lysis buffer and protein was eluted in steps by adding 10 mM reduced glutathione to
519 the lysis buffer. Tags were cleaved by adding 1:20 Prescission protease and dialyzing against
520 SEC buffer (200 mM NaCl, 20 mM Tris/HCl, pH 7.5, 1 mM DTT) overnight. Depending on the size
521 of the protein construct, the GST-tag was removed by recycling over Glutathione-Sepharose or in
522 a final SEC step (Superdex 75 16/60, GE Healthcare). Proteins were concentrated and flash
523 frozen in liquid nitrogen at concentrations of 10-20 mg/ml.

524 Constructs of the BRP N-terminus and the Cast2 N-terminus were produced and cells were
525 lysed as described above, with addition of 20 mM imidazole to the lysis buffer. Affinity
526 chromatography was carried out using Ni²⁺-NTA agarose (Macherey Nagel). Prior to protein
527 loading, the resin was equilibrated with lysis buffer and the protein was eluted by addition of 300
528 mM imidazole to the lysis buffer. His-tags were cleaved by adding 1:20 TEV protease overnight.
529 Further purification was performed by ion-exchange chromatography on MonoS and MonoQ
530 columns (GE Healthcare). Proteins were eluted by applying a linear salt gradient to 200 mM NaCl.
531 Purified proteins were concentrated to 1-2 mg/ml and flash frozen in liquid nitrogen.

532 SRPK1 and SRPK2 constructs were expressed and purified by Ni²⁺-NTA affinity
533 chromatography as described above. His-tags were not cleaved, and final purification was done
534 by SEC on Superdex S200 16/60 or 10/300 increase columns (GE Healthcare). Purified proteins
535 were concentrated to 5-20 mg/ml and flash frozen in liquid nitrogen.

536 For production of BRP and Cast1 variants *via* recombinant baculoviruses in insect cells, *E. coli*
537 DH10MultiBac cells were used to generate bacmids. SF9 cells were transfected with the purified
538 bacmids for each construct and a first virus generation (V_0) was harvested after 72 h. V_0 virus was
539 used to generate a virus with a higher titer (V_1) in SF9 cells, which was then used for large-scale
540 production in High Five cells. Cells were harvested when viability dropped below 90 % or when
541 the eYFP signal reached a plateau. Harvested cells were either flash frozen in liquid nitrogen and
542 stored at -80° C or directly used for purification.

543 Cell pellets of BRP-190 and BRP-190^{Δ1-152} expressions were resuspended in 400 mM NaCl,
544 40 mM Tris/HCl, pH 8.5, 5 % (v/v) glycerol, 1 mM DTT supplemented with protease inhibitors
545 (Roche) and lysed by sonication. Lysates were cleared by centrifugation and proteins were
546 captured on Strep-Tactin resin (IBA). After washing, proteins were eluted by addition of 2.5 mM
547 desthiobiotin in 400 mM NaCl, 40 mM Tris/HCl, pH 8.5, 5 % (v/v) glycerol, 1 mM DTT and flash
548 frozen in liquid nitrogen.

549 Cast1 was purified *via* Ni²⁺-NTA affinity chromatography, MonoQ ion exchange
550 chromatography (elution in a linear salt gradient to 500 mM NaCl). Final SEC was carried out on
551 a Superdex S200 10/300 column in 200 mM NaCl, 20 mM Tris/HCl, pH 7.5, 1 mM DTT. Purified
552 protein was concentrated to 0.8 mg/ml and flash frozen in liquid nitrogen.

553

554 **Animal rearing and fly strains**

555 Fly strains were reared under standard laboratory conditions (Sigrist, Reiff et al., 2003) at 25°
556 C, 65 % – 70 % humidity and constant 12/12 hr light/dark cycle in incubators. Both male and
557 female larvae were used for analysis in all experiments. The following genotypes were used: WT:
558 +/+ (*w11118*). *srpk79D^{VN}*: *srpk79D^{VN} / srpk79D^{VN}*. *srpk79D^{atc}*: *srpk79D^{atc} / srpk79D^{atc}*. *brp^{Df/+}*;
559 *srpk79D^{atc}: Df(2R)BSC29/+*; *srpk79D^{atc} / srpk79D^{atc}*. *brp^{null/brp^{Df}}*; *srpk79D^{atc}: brp⁶⁹/Df(2R)BSC29*;
560 *srpk79D^{atc}/srpk79D^{atc}*. *rim-bp^{Df/+}*; *srpk79D^{atc}: Df S2.01/+*; *srpk79D^{atc} / srpk79D^{atc}*. *rim-bp^{null/rim-}*
561 *bp^{Df}*; *srpk79D^{atc}: rim-bp^{STOP1}/Df S201*; *srpk79D^{atc} / srpk79D^{atc}*. Genomic *brp^{p[acman]^{WT}}* was crossed
562 to *brp^{null Δ6.1/brp^{Df69}}* and genomic phosphorylation mutant *brp^{SSS71/73/90AAA}* was crossed to *brp^{null}*
563 *Δ6.1/brp^{Df69}*. Stocks were obtained from: *brp⁶⁹* (Kittel et al., 2006); *Df2.01* and *rim-bp^{STOP1}* (Liu et al.,
564 2011); *srpk79D^{atc}*; *srpk79D^{vn}* (Nieratschker et al., 2009); genomic *brp^{p[acman]^{WT}}* (Matkovic et al.,
565 2013).

566

567 **Generation of modified P[acman]-BRP construct**

568 The attB-P[acman] BAC clone containing the genomic region of BRP was obtained from
569 (Matkovic et al., 2013). Mutations were incorporated according to the Counter Selection BAC
570 Modification Kit (Gene Bridges GmbH) by using the following primers: Amplification of the rpsL
571 cassette: 5'-
572 CGACATGGATGAGCCAACCAGTCCGGCCGGAGCGGGTCACCATCGCAGCCGGGGCCTGG
573 TGATGATGGCGGG-3' (forward); 5'-
574 GAATGGGTATGAACTCGCGATCATGGGGATCCACGAGTCCACCGCGATCCAGTCAGAAGA
575 ACTCGTCAAGAAG-3' (reverse); mutagenesis 5'-
576 ACATGGATGAGCCAACCAGTCCGGCCGGAGGGGTCACCATCGCAGCCGGGGCCGCCCA
577 GACCACCGATGGCCCATGCC-3' (forward); 5'-
578 ATGGGTATGAACTCGCGATCATGGGGATCCACGAGTCCACCGCGATCCAGCGCTTGGTAG
579 CGGGTTC-3' (reverse). After sequencing, the construct was injected into an attP site-containing
580 fly strain (y[1] w[1118]; P_{Bac}{y[+]-attP-9A}VK00005; Bloomington *Drosophila* Stock Center line
581 #9725) using the services of BestGene Inc.

582

583 **BRP immunoprecipitation of fly heads**

584 For the identification of BRP residues phosphorylated *in vivo*, protein extractions from wild type
585 *Drosophila* heads in the presence of phosphatase inhibitors (PhosStop, Roche) combined with
586 immunoprecipitations and mass-spectrometry based analyses were done as previously described
587 (Owald, Fouquet et al., 2010). Briefly, synaptosome membranes were enriched by differential
588 centrifugation (Depner et al., 2014) 10 µg - 20 µg of Ms-anti-NC82 antibody and IgG control were
589 coupled to protein A beads (Bio-Rad). Antibody-coupled resin was incubated with solubilized and
590 precleared synaptosome membrane preparations (LP1; 1 mg protein at 2 µg/µl) in IP buffer (20
591 mM HEPES pH 7.4, 200 mM KCl, 2 mM MgCl₂, 1% Triton X-100) for 10 h at 4° C. After washing
592 four times with IP buffer, Ab-Ag-complexes were eluted with 60 µl 2x sample buffer (containing

593 1M Tris-HCl pH 6,8; 10% SDS; glycerol; β -mercaptoethanol; 1% Bromphenol blue). Samples were
594 analyzed by Western blot and subjected to liquid chromatography-tandem mass spectrometry
595 (LC-MS/MS) analysis. MS data were searched against the flybase.org database using the
596 MASCOT search algorithm.

597

598 **Yeast two-hybrid analyses**

599 Y2H analyses were performed as described in (Böhme et al., 2016). Briefly, DNA fragments
600 encoding various regions of SRPK79D, BRP and RIM-BP were each cloned into two bait and two
601 prey vectors. Diploid yeasts, carrying each a unique bait/prey vector pair, were generated by
602 mating yeast carrying individual bait and prey vectors. Putative protein-protein interactions (PPIs)
603 were identified by yeast growth on selective media (Worseck et al., 2012). Bait and prey constructs
604 that led to auto-activation were removed from the analysis. Only bait vector/prey vector
605 combinations that showed growth at least in four independent replicas were considered as putative
606 PPIs. Y2H interactions are listed in Table 1.

607

608 **Analytical size exclusion chromatography**

609 Analytical SEC was performed on an 3.2/300 Superdex 200 increase column (GE Healthcare)
610 at 4° C in 200 mM NaCl, 20 mM Tris/HCl, pH 7.5, 2 mM MgCl₂, 1 mM DTT. 50 – 100 μ g of SRPK
611 variant was mixed with a 1.2-fold molar excess of BRP or ELKS family constructs. Samples were
612 incubated for 15 min on ice before loading onto the column. For runs involving prior
613 phosphorylation, 1 mM ATP was added to the protein mixtures and samples were incubated for
614 30 min on ice. Fractions were collected and analyzed by SDS-PAGE.

615

616 **Radioactive *in vitro* phosphorylation assays**

617 50 pmol of SRPKs were mixed with 50 pmol of a phosphorylation target in 20 μ l reaction buffer
618 (200 mM NaCl, 20 mM Hepes/NaOH, pH 7.5, 2 mM MgCl₂, 1 mM DTT). Reactions were started

619 by addition of 1 μ l of a 5 mM ATP solution in reaction buffer supplemented with γ -[³²P]-ATP (9.25
620 MBq, 250 μ Ci). Samples were incubated for 1 h at room temperature and reactions were stopped
621 by addition of SDS sample buffer and subsequent heating of the samples to 95° C for 5 min.
622 Samples were analyzed *via* SDS-PAGE. Gels were scanned on a Storm PhosphorImager (GE
623 Healthcare).

624

625 ***In vitro* phosphorylation for mass spectrometry**

626 Time course experiments were performed to analyze the SRPK97D-dependent
627 phosphorylation of the BRP N-terminus. 3 μ g (180 pmol) of BRP-190¹⁻¹⁵² were incubated *in vitro*
628 with equal amounts of SRPK79D^{Core} or SRPK79D^{Core Δ Dock} in 200 mM NaCl, 40 mM HEPES, pH
629 7.5, 2 mM MgCl₂ on ice. The reactions were started by addition of 1 mM ATP. Samples were
630 collected at time points of 30 s, 5 min and 1 h and stopped by addition of SDS sample buffer and
631 boiling for 10 min at 95° C.

632

633 **Liquid chromatography-mass spectrometry**

634 Samples were separated by SDS-PAGE and proteins were stained by Coomassie Brilliant
635 Blue. Gel bands corresponding to BRP-190¹⁻¹⁵² were excised, washed with 50 % (v/v) acetonitrile
636 in 50 mM ammonium bicarbonate, shrunk by dehydration in acetonitrile and dried in a vacuum
637 centrifuge. The dried gel pieces were incubated with 50 ng trypsin (sequencing grade modified,
638 Promega) in 25 μ l of 50 mM ammonium bicarbonate at 37° C overnight. To extract the peptides,
639 25 μ l of 0.5 % (v/v) trifluoroacetic acid (TFA) in acetonitrile was added and the extract was dried
640 under vacuum.

641

642 **Liquid chromatography-tandem mass spectrometry**

643 Peptides were transferred to 10 μ l of 0.1 % (v/v) TFA, 5 % (v/v) acetonitrile and 2 μ l were
644 analyzed on a reversed-phase capillary nano liquid chromatography system (Ultimate 3000,

645 Thermo Scientific) connected to an Orbitrap Velos mass spectrometer (Thermo Scientific).
646 Samples were desalted on a trap column (PepMap100 C18, 3 μm , 100 \AA , 75 μm i.d. \times 2 cm;
647 Thermo Scientific) using a mobile phase of 0.05 % TFA, 2 % acetonitrile in water. After switching
648 the trap column inline, LC separations were performed on a capillary column (Acclaim PepMap100
649 C18, 2 μm , 100 \AA , 75 μm i.d. \times 25 cm, Thermo Scientific) at an eluent flow rate of 300 nl/min.
650 Mobile phase A contained 0.1 % formic acid in water, mobile phase B contained 0.1 % formic acid
651 in acetonitrile. The column was pre-equilibrated with 3 % mobile phase B followed by an increase
652 to 50 % mobile phase B in 50 min. Mass spectra were acquired in a data-dependent mode, utilizing
653 a single MS survey scan (m/z 350-1500) with a resolution of 60,000 in the Orbitrap, and MS/MS
654 scans of the 20 most intense precursor ions in the linear trap quadrupole.

655

656 **Data processing and phosphorylation analysis**

657 Identification of proteins was performed using the Mascot Daemon and Mascot Server version
658 2.5.0 (Matrix Science). Raw data were searched against an in-house custom protein sequence
659 database including the sequence of BRP-190¹⁻¹⁵². A maximum of two missed cleavages was
660 allowed and the mass tolerance of precursor and sequence ions was set to 10 ppm and 0.35 Da,
661 respectively. Oxidation (M), propionamide (C), acetylation (protein N-terminus) and
662 phosphorylation (STY) were used as variable modifications. A significance threshold of 0.05 was
663 used based on decoy database searches and a peptide ion score cut-off of 20 was applied. In
664 addition, tandem mass spectra of phosphopeptides were manually verified. Phosphorylation
665 degrees for each residue were estimated by manually comparing relative MS peak intensities in
666 the extracted ion chromatograms of the corresponding peptide/phosphopeptide pairs as described
667 (Boehm, Seidler et al., 2012, Seidler, Adal et al., 2009).

668

669 **Intact protein mass determination by MALDI-TOF mass spectrometry**

670 Protein masses were analyzed by matrix-assisted laser desorption/ionization-time of flight
671 mass spectrometry (MALDI-TOF-MS) using an Ultraflex-II TOF/TOF instrument (Bruker Daltonics,
672 Bremen, Germany) equipped with a 200 Hz solid-state Smart beam™ laser. The mass
673 spectrometer was operated in the positive linear mode. MS spectra were acquired over an m/z
674 range of 3,000 - 20,000 and data were analyzed using FlexAnalysis 2.4. software provided with
675 the instrument.

676 Sinapinic acid was used as the matrix (saturated solution in acetonitrile:0.1% trifluoroacetic
677 acid 1:2) and samples were spotted undiluted using the dried-droplet technique. Where necessary,
678 samples were diluted in TA₃₃ (33 % acetonitrile, 0.1 % trifluoroacetic acid in water). External
679 calibration was performed using the Bruker Protein Calibration Standard I (Bruker Daltonics,
680 Bremen, Germany).

681

682 **Peptide SPOT analysis**

683 Membranes with the spotted peptides (Table S2) were washed once with 100 % ethanol for 10
684 min and three times with PBS/1 mM DTT. The membranes were blocked with 5 % BSA in PBS/1
685 mM DTT for 3 h. After three additional washing steps, the membranes were incubated overnight
686 with GST-SRPK79D (20 µg/ml) and GST (6 µg/ml) in PBS/1 mM DTT plus 5 % BSA. The
687 membranes were then washed three times with PBST/1 mM DTT and subsequently incubated for
688 1 h with 1:1000 α-GST-Z5 in PBS plus 5 % BSA. After incubation, the membranes were washed
689 again three times with PBS/1 mM DTT and were then incubated with 1:5000 horseradish
690 peroxidase (HRP)-coupled αRabbit antibody for 1 h. Final detection was done by adding
691 electrochemiluminescence solution (PJK GmbH) after three more washing steps with PBS/1 mM
692 DTT. Luminescence was detected by sequential scanning using an Intas Advanced Fluorescence
693 Imager.

694

695 **Immunohistochemistry, image acquisition and analysis**

696 Immunohistochemistry was performed according to our standard protocol (Andlauer, Scholz-
697 Kornehl et al., 2014). Conventional confocal and STED images were acquired with TCS SP8 and
698 TCS SP8 gSTED 3× microscopes (Leica Microsystems), respectively. Images of fixed samples
699 were acquired at room temperature. NMJ z-stacks had a step size of 0.3 μm between single optical
700 slices. Images were acquired from 3rd instar larval axons. All images were acquired using the LCS
701 AF software (Leica Microsystems, Wetzlar, Germany). For previous descriptions see (Fouquet et
702 al., 2009).

703

704 **Immunostainings of larval and embryonic NMJs**

705 Dissections were performed in HL3 by opening the larvae/embryo dorsally along the midline
706 and removing the innards to grant visual access to the larval CNS axons. Dissections were fixated
707 with 4 % paraformaldehyde in PBS (pH 7.2) for 10 min. After fixation, the filets were washed with
708 PBS plus 0.05 % Triton-X 100 (PBT) and blocked for 60 min in 5 % normal goat serum (NGS).
709 For immunostainings, the larvae were incubated with primary antibodies at 4° C overnight and
710 subsequently washed in a 0.05 % PBT solution for 12 h at room temperature. Larvae were then
711 incubated overnight with secondary antibodies at 4° C. Washing procedures were repeated.
712 Immunocytochemistry was equal for both conventional confocal and STED microscopy. Larvae
713 were finally mounted either in Vectashield (Vector Laboratories) or Mowiol. Antibody dilutions
714 were: 1:100 – 1:200 M-α-Nc82; 1:500 Rb-α-RIM-BP; 1:500 GP-α-Unc13A (Böhme et al., 2016)
715 and HRP-Cy5 1:250 (Dianova). All confocal secondary antibodies were diluted 1:500. Secondary
716 antibodies used for STED images (Goat-α-M-STAR635p (Abberior); Goat-α-Rb-Atto594
717 (Invitrogen); and Goat-α-Gp-Atto594 (Invitrogen)) were diluted 1:200.

718

719 **Statistics**

720 Unless otherwise stated, data were analyzed with GraphPad Prism 5 software using the
721 ANOVA Tukey's post test. Asterisks are used to indicate statistical significance of the results (* =
722 $p < 0.05$; ** = $p < 0.01$; *** = $p < 0.005$; ns = $p > 0.05$). Briefly, the signal of an HRP-Cy5 Ab was
723 used as template for a mask, restricting the quantified area to the shape of the axon/nerve bundle.
724 The original confocal stacks were converted to maximal projections. After background subtraction,
725 a mask of the axonal area was created by applying a threshold to remove spurious low-intensity
726 pixels. The segmentation of single spots was done semi-automatically *via* the "Find Maxima"
727 routine and by hand with the pencil tool and a line thickness of 1 pixel. To remove high-frequency
728 noise, a Gaussian blur filter (0.5-pixel Sigma radius) was applied. The processed picture was then
729 transformed into a binary mask using the same lower threshold value as in the first step. This
730 binary mask was then projected onto the original unmodified image using the "min" operation from
731 the ImageJ image calculator. The axonal spots of the resulting images were counted with the help
732 of the "analyze particle" function with a lower threshold set to 1. The spot density was obtained by
733 normalizing the total number of analyzed particles to the axonal area measured *via* HRP.

734

735 **Electron-microscopy**

736 Conventional embedding was performed as described previously (Fouquet et al., 2009).

737

738 **Acknowledgements**

739 We thank Christine Quentin for excellent technical assistance, Susanne Schoch-McGovern,
740 Universität Bonn, for providing a mSRPK2 plasmid, and Gourisankar Ghosh, University of
741 California, San Diego, for providing SRPK1 and SRPK1^{CoreΔlinker} (SRPK1^{NS3}) expression
742 constructs. We acknowledge access to the Core Facility BioSupraMol supported by the Deutsche
743 Forschungsgemeinschaft.

744

745 **Funding**

Funder	Grant reference number	Author
Deutsche Forschungsgemeinschaft	SFB958-A6	Markus Wahl, Stephan Sigrist
Deutsche Forschungsgemeinschaft	SFB958-Z03	Christoph Weise, Christian Freund

746

747 **Author contributions**

748 Jan H Driller, Experimental Design, Experiments, Data Interpretation, Writing – original draft

749 Janine Lützkendorf, Experimental Design, Experiments, Data Interpretation, Writing – original
750 draft

751 Harald Depner, Experiments

752 Matthias Siebert, Experiments

753 Benno Kuropka, Experimental Design, Experiments, Data Interpretation, Writing – review and
754 editing

755 Christoph Weise, Experimental Design, Experiments, Data Interpretation, Writing – review and
756 editing

757 Astrid G Petzold, Experimental Design

758 Martin Lehmann, Experimental Design

759 Ulrich Stelzl, Experimental Design, Data Interpretation

760 René Zahedi, Experimental Design, Experiments, Data Interpretation

761 Albert Sickmann, Data Interpretation

762 Christian Freund, Conceptualization, Supervision, Funding acquisition, Project administration

763 Stephan J. Sigrist, Conceptualization, Supervision, Funding acquisition, Project administration,
764 Writing – review and editing

765 Markus C. Wahl, Conceptualization, Supervision, Funding acquisition, Project administration,
766 Writing – review and editing

767

768 **Conflict of interest**

769 The authors declare that no conflict of interest exist.

770

771

772

773

774 **Author ORCIDs**

775 Markus Wahl <https://orcid.org/0000-0002-2811-5307>

776 Jan Driller <https://orcid.org/0000-0001-7561-964X>

777 Chris Weise <http://orcid.org/0000-0002-5507-4694>

778 Janine Lützkendorf <https://orcid.org/0000-0001-5051-6281>

779

780 **References**

- 781 Ackermann F, Waites CL, Garner CC (2015) Presynaptic active zones in invertebrates and
782 vertebrates. *EMBO Rep* 16: 923-38
- 783 Andlauer TF, Scholz-Kornehl S, Tian R, Kirchner M, Babikir HA, Depner H, Loll B, Quentin C,
784 Gupta VK, Holt MG, Dipt S, Cressy M, Wahl MC, Fiala A, Selbach M, Schwarzel M, Sigrist SJ
785 (2014) Drep-2 is a novel synaptic protein important for learning and memory. *Elife* 3
- 786 Aubol BE, Chakrabarti S, Ngo J, Shaffer J, Nolen B, Fu XD, Ghosh G, Adams JA (2003)
787 Processive phosphorylation of alternative splicing factor/splicing factor 2. *Proc Natl Acad Sci*
788 *U S A* 100: 12601-6
- 789 Aubol BE, Plocinik RM, Hagopian JC, Ma CT, McGlone ML, Bandyopadhyay R, Fu XD, Adams
790 JA (2013) Partitioning RS domain phosphorylation in an SR protein through the CLK and
791 SRPK protein kinases. *J Mol Biol* 425: 2894-909
- 792 Blom N, Gammeltoft S, Brunak S (1999) Sequence and structure-based prediction of eukaryotic
793 protein phosphorylation sites. *J Mol Biol* 294: 1351-62
- 794 Boehm ME, Seidler J, Hahn B, Lehmann WD (2012) Site-specific degree of phosphorylation in
795 proteins measured by liquid chromatography-electrospray mass spectrometry. *Proteomics*
796 12: 2167-78
- 797 Böhme MA, Beis C, Reddy-Alla S, Reynolds E, Mampell MM, Grasskamp AT, Lutzkendorf J,
798 Bergeron DD, Driller JH, Babikir H, Gottfert F, Robinson IM, O'Kane CJ, Hell SW, Wahl MC,
799 Stelzl U, Loll B, Walter AM, Sigrist SJ (2016) Active zone scaffolds differentially accumulate
800 Unc13 isoforms to tune Ca²⁺ channel-vesicle coupling. *Nature neuroscience*
- 801 Bury LA, Sabo SL (2016) Building a Terminal: Mechanisms of Presynaptic Development in the
802 CNS. *Neuroscientist* 22: 372-91
- 803 Carter AP, Diamant AG, Urnavicius L (2016) How dynein and dynactin transport cargos: a
804 structural perspective. *Curr Opin Struct Biol* 37: 62-70
- 805 Chan CB, Ye K (2013) Serine-arginine protein kinases: new players in neurodegenerative
806 diseases? *Rev Neurosci* 24: 401-13
- 807 Chen C, Huang H, Wu CH (2017) Protein Bioinformatics Databases and Resources. *Methods Mol*
808 *Biol* 1558: 3-39
- 809 Dephoure N, Zhou C, Villen J, Beausoleil SA, Bakalarski CE, Elledge SJ, Gygi SP (2008) A
810 quantitative atlas of mitotic phosphorylation. *Proc Natl Acad Sci U S A* 105: 10762-7
- 811 Depner H, Lützkendorf J, Babkir HA, Sigrist SJ, Holt MG (2014) Differential centrifugation-based
812 biochemical fractionation of the *Drosophila* adult CNS. *Nat Protoc* 9: 2796-808
- 813 Dinkel H, Chica C, Via A, Gould CM, Jensen LJ, Gibson TJ, Diella F (2011) Phospho.ELM: a
814 database of phosphorylation sites--update 2011. *Nucleic Acids Res* 39: D261-7
- 815 Ehmann N, Sauer M, Kittel RJ (2015) Super-resolution microscopy of the synaptic active zone.
816 *Frontiers in cellular neuroscience* 9: 7
- 817 Fouquet W, Oswald D, Wichmann C, Mertel S, Depner H, Dyba M, Hallermann S, Kittel RJ, Eimer
818 S, Sigrist SJ (2009) Maturation of active zone assembly by *Drosophila* Bruchpilot. *The Journal*
819 *of cell biology* 186: 129-45
- 820 Ghosh G, Adams JA (2011) Phosphorylation mechanism and structure of serine-arginine protein
821 kinases. *FEBS J* 278: 587-97
- 822 Guillaud L, Wong R, Hirokawa N (2008) Disruption of KIF17-Mint1 interaction by CaMKII-
823 dependent phosphorylation: a molecular model of kinesin-cargo release. *Nat Cell Biol* 10: 19-
824 29

825 Gundelfinger ED, Reissner C, Garner CC (2015) Role of Bassoon and Piccolo in Assembly and
826 Molecular Organization of the Active Zone. *Front Synaptic Neurosci* 7: 19

827 Hall DH, Hedgecock EM (1991) Kinesin-related gene *unc-104* is required for axonal transport of
828 synaptic vesicles in *C. elegans*. *Cell* 65: 837-47

829 Haucke V, Neher E, Sigrist SJ (2011) Protein scaffolds in the coupling of synaptic exocytosis and
830 endocytosis. *Nat Rev Neurosci* 12: 127-138

831 Hell SW (2007) Far-field optical nanoscopy. *Science* 316: 1153-8

832 Hong Y, Chan CB, Kwon IS, Li X, Song M, Lee HP, Liu X, Sompol P, Jin P, Lee HG, Yu SP, Ye K
833 (2012) SRPK2 phosphorylates tau and mediates the cognitive defects in Alzheimer's disease.
834 *The Journal of neuroscience : the official journal of the Society for Neuroscience* 32: 17262-
835 72

836 Hornbeck PV, Zhang B, Murray B, Kornhauser JM, Latham V, Skrzypek E (2015)
837 PhosphoSitePlus, 2014: mutations, PTMs and recalibrations. *Nucleic Acids Res* 43: D512-20

838 Jang SW, Liu X, Fu H, Rees H, Yepes M, Levey A, Ye K (2009) Interaction of Akt-phosphorylated
839 SRPK2 with 14-3-3 mediates cell cycle and cell death in neurons. *J Biol Chem* 284: 24512-
840 25

841 Johnson EL, 3rd, Fetter RD, Davis GW (2009) Negative regulation of active zone assembly by a
842 newly identified SR protein kinase. *PLoS Biol* 7: e1000193

843 Kittel RJ, Wichmann C, Rasse TM, Fouquet W, Schmidt M, Schmid A, Wagh DA, Pawlu C, Kellner
844 RR, Willig KI, Hell SW, Buchner E, Heckmann M, Sigrist SJ (2006) Bruchpilot promotes active
845 zone assembly, Ca²⁺ channel clustering, and vesicle release. *Science* 312: 1051-4

846 Kittelmann M, Liewald JF, Hegemann J, Schultheis C, Brauner M, Steuer Costa W, Wabnig S,
847 Eimer S, Gottschalk A (2013) In vivo synaptic recovery following optogenetic
848 hyperstimulation. *Proc Natl Acad Sci U S A* 110: E3007-16

849 Lin CW, Chen LJ, Lee PL, Lee CI, Lin JC, Chiu JJ (2007) The inhibition of TNF-alpha-induced E-
850 selectin expression in endothelial cells via the JNK/NF-kappaB pathways by highly N-
851 acetylated chitooligosaccharides. *Biomaterials* 28: 1355-66

852 Lin S, Fu XD (2007) SR proteins and related factors in alternative splicing. *Adv Exp Med Biol* 623:
853 107-22

854 Liu KS, Siebert M, Mertel S, Knoche E, Wegener S, Wichmann C, Matkovic T, Muhammad K,
855 Depner H, Mettke C, Buckers J, Hell SW, Muller M, Davis GW, Schmitz D, Sigrist SJ (2011)
856 RIM-binding protein, a central part of the active zone, is essential for neurotransmitter release.
857 *Science* 334: 1565-9

858 Lukasiewicz R, Velazquez-Dones A, Huynh N, Hagopian J, Fu XD, Adams J, Ghosh G (2007)
859 Structurally unique yeast and mammalian serine-arginine protein kinases catalyze
860 evolutionarily conserved phosphorylation reactions. *J Biol Chem* 282: 23036-43

861 Maeder CI, San-Miguel A, Wu EY, Lu H, Shen K (2014) In vivo neuron-wide analysis of synaptic
862 vesicle precursor trafficking. *Traffic* 15: 273-91

863 Maglione M, Sigrist SJ (2013) Seeing the forest tree by tree: super-resolution light microscopy
864 meets the neurosciences. *Nature neuroscience* 16: 790-797

865 Matkovic T, Siebert M, Knoche E, Depner H, Mertel S, Oswald D, Schmidt M, Thomas U, Sickmann
866 A, Kamin D, Hell SW, Burger J, Hollmann C, Mielke T, Wichmann C, Sigrist SJ (2013) The
867 Bruchpilot cytomatrix determines the size of the readily releasable pool of synaptic vesicles.
868 *The Journal of cell biology* 202: 667-83

869 Mochida S, Hida Y, Tanifuji S, Hagiwara A, Hamada S, Abe M, Ma H, Yasumura M, Kitajima I,
870 Sakimura K, Ohtsuka T (2016) SAD-B Phosphorylation of CAST Controls Active Zone Vesicle
871 Recycling for Synaptic Depression. *Cell Rep* 16: 2901-2913

872 Morfini G, Szebenyi G, Elluru R, Ratner N, Brady ST (2002) Glycogen synthase kinase 3
873 phosphorylates kinesin light chains and negatively regulates kinesin-based motility. *EMBO J*
874 21: 281-93

875 Murray DH, Janel M, Lauer J, Avellaneda MJ, Brouilly N, Cezanne A, Morales-Navarrete H,
876 Perini ED, Ferguson C, Lupas AN, Kalaidzidis Y, Parton RG, Grill SW, Zerial M (2016) An
877 endosomal tether undergoes an entropic collapse to bring vesicles together. *Nature* 537: 107-
878 111

879 Ngo JC, Chakrabarti S, Ding JH, Velazquez-Dones A, Nolen B, Aubol BE, Adams JA, Fu XD,
880 Ghosh G (2005) Interplay between SRPK and Clk/Sty kinases in phosphorylation of the
881 splicing factor ASF/SF2 is regulated by a docking motif in ASF/SF2. *Mol Cell* 20: 77-89

882 Nieratschker V, Schubert A, Jauch M, Bock N, Bucher D, Dippacher S, Krohne G, Asan E, Buchner
883 S, Buchner E (2009) Bruchpilot in ribbon-like axonal agglomerates, behavioral defects, and
884 early death in SRPK79D kinase mutants of *Drosophila*. *PLoS Genet* 5: e1000700

885 Oswald D, Fouquet W, Schmidt M, Wichmann C, Mertel S, Depner H, Christiansen F, Zube C,
886 Quentin C, Korner J, Urlaub H, Mechtler K, Sigrist SJ (2010) A Syd-1 homologue regulates
887 pre- and postsynaptic maturation in *Drosophila*. *The Journal of cell biology* 188: 565-79

888 Parker BL, Yang G, Humphrey SJ, Chaudhuri R, Ma X, Peterman S, James DE (2015) Targeted
889 phosphoproteomics of insulin signaling using data-independent acquisition mass
890 spectrometry. *Sci Signal* 8: rs6

891 Petzoldt AG, Sigrist SJ (2014) Synaptogenesis. *Curr Biol* 24: R1076-80

892 Reddy-Alla S, Böhme MA, Reynolds E, Beis C, Grasskamp AT, Mampell MM, Maglione M,
893 Jusyte M, Rey U, Babikir H, McCarthy AW, Quentin C, Matkovic T, Bergeron DD, Mushtaq
894 Z, Göttfert F, Oswald D, Mielke T, Hell SW, Sigrist SJ et al. (2017) Stable positioning of Unc13
895 restricts synaptic vesicle fusion to defined release sites for synchronization of
896 neurotransmission *In*

897 Sacco F, Humphrey SJ, Cox J, Mischnik M, Schulte A, Klabunde T, Schafer M, Mann M (2016)
898 Glucose-regulated and drug-perturbed phosphoproteome reveals molecular mechanisms
899 controlling insulin secretion. *Nat Commun* 7: 13250

900 Sato-Yoshitake R, Yorifuji H, Inagaki M, Hirokawa N (1992) The phosphorylation of kinesin
901 regulates its binding to synaptic vesicles. *J Biol Chem* 267: 23930-6

902 Seidler J, Adal M, Kubler D, Bossemeyer D, Lehmann WD (2009) Analysis of autophosphorylation
903 sites in the recombinant catalytic subunit alpha of cAMP-dependent kinase by nano-UPLC-
904 ESI-MS/MS. *Anal Bioanal Chem* 395: 1713-20

905 Shapira M, Zhai RG, Dresbach T, Bresler T, Torres VI, Gundelfinger ED, Ziv NE, Garner CC
906 (2003) Unitary assembly of presynaptic active zones from Piccolo-Bassoon transport
907 vesicles. *Neuron* 38: 237-52

908 Sharma K, D'Souza RC, Tyanova S, Schaab C, Wisniewski JR, Cox J, Mann M (2014) Ultradeep
909 human phosphoproteome reveals a distinct regulatory nature of Tyr and Ser/Thr-based
910 signaling. *Cell Rep* 8: 1583-94

911 Siebert M, Bohme MA, Driller JH, Babikir H, Mampell MM, Rey U, Ramesh N, Matkovic T, Holton
912 N, Reddy-Alla S, Göttfert F, Kamin D, Quentin C, Klinedinst S, Andlauer TF, Hell SW, Collins
913 CA, Wahl MC, Loll B, Sigrist SJ (2015) A high affinity RIM-binding protein/Aplip1 interaction
914 prevents the formation of ectopic axonal active zones. *Elife* 4

915 Sigrist SJ, Reiff DF, Thiel PR, Steinert JR, Schuster CM (2003) Experience-dependent
916 strengthening of *Drosophila* neuromuscular junctions. *The Journal of neuroscience : the*
917 *official journal of the Society for Neuroscience* 23: 6546-56

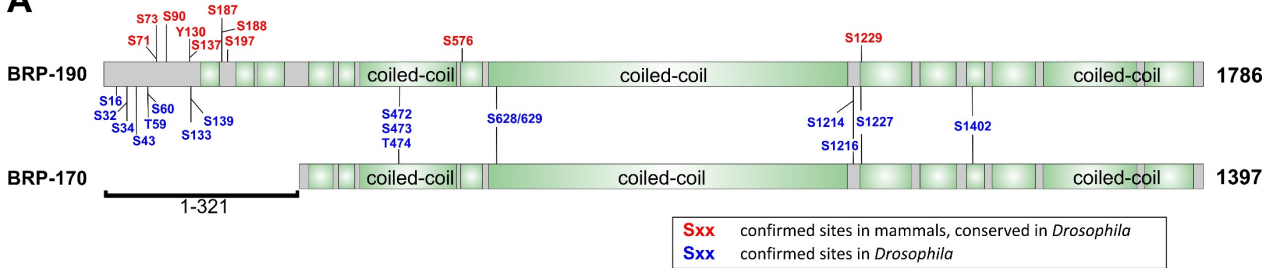
918 Studier FW (2005) Protein production by auto-induction in high density shaking cultures. *Protein*
919 *Expr Purif* 41: 207-34

- 920 Südhof TC (2012) The presynaptic active zone. *Neuron* 75: 11-25
- 921 Van Vactor D, Sigrist SJ (2017) Presynaptic morphogenesis, active zone organization and
922 structural plasticity in *Drosophila*. *Current opinion in neurobiology* 43: 119-129
- 923 Viquez NM, Fuger P, Valakh V, Daniels RW, Rasse TM, DiAntonio A (2009) PP2A and GSK-3beta
924 act antagonistically to regulate active zone development. *The Journal of neuroscience : the
925 official journal of the Society for Neuroscience* 29: 11484-94
- 926 Wairkar YP, Toda H, Mochizuki H, Furukubo-Tokunaga K, Tomoda T, DiAntonio A (2009) Unc-51
927 controls active zone density and protein composition by downregulating ERK signaling. *The
928 Journal of neuroscience : the official journal of the Society for Neuroscience* 29: 517-28
- 929 Walter AM, Bohme MA, Sigrist SJ (2018) Vesicle release site organization at synaptic active
930 zones. *Neurosci Res* 127: 3-13
- 931 Walter AM, Haucke V, Sigrist SJ (2014) Neurotransmission: spontaneous and evoked release
932 filing for divorce. *Curr Biol* 24: R192-4
- 933 Wilhelm BG, Mandad S, Truckenbrodt S, Krohnert K, Schafer C, Rammner B, Koo SJ, Classen
934 GA, Krauss M, Haucke V, Urlaub H, Rizzoli SO (2014) Composition of isolated synaptic
935 boutons reveals the amounts of vesicle trafficking proteins. *Science* 344: 1023-8
- 936 Worseck JM, Grossmann A, Weimann M, Hegele A, Stelzl U (2012) A stringent yeast two-hybrid
937 matrix screening approach for protein-protein interaction discovery. *Methods Mol Biol* 812:
938 63-87
- 939 Zhou Z, Fu XD (2013) Regulation of splicing by SR proteins and SR protein-specific kinases.
940 *Chromosoma* 122: 191-207
- 941

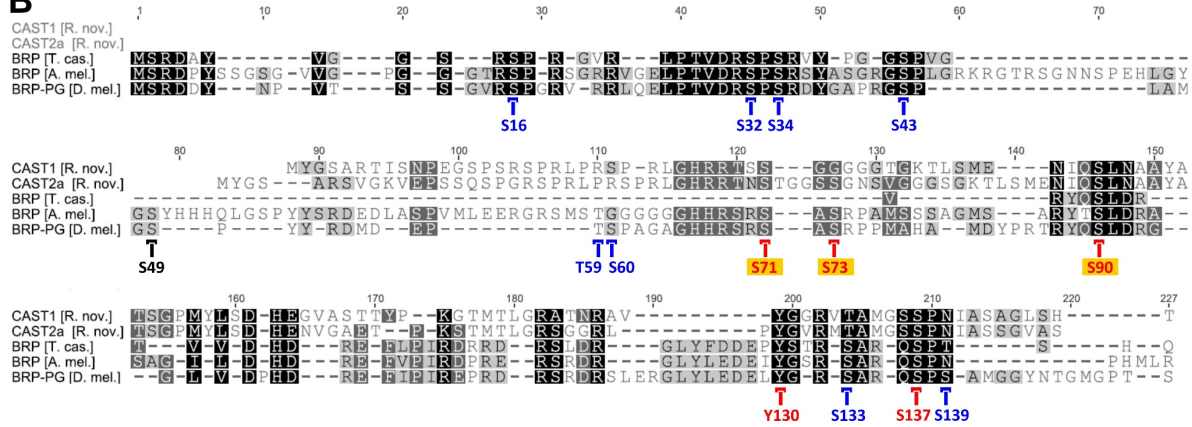
942 **Figures and figure legends**

943

A



B



944

945

946 **Figure 1. Extensive phosphorylation at the BRP/ELKS N-terminus**

947 **(A)** Overview of the domain architectures and phosphosites in BRP-190 and BRP-170 isoforms.

948 Indicated phosphosites were predicted by the NetPhos 3.1 server (Blom et al., 1999) and

949 confirmed experimentally. BRP isoforms are predicted to be rich in α -helices and to contain large

950 stretches of coiled-coil (green). Phosphorylation sites found in mammalian ELKS proteins and are

951 conserved in *Drosophila* BRP proteins are colored in red, while phosphorylation sites only

952 identified in *Drosophila* are shown in blue. **(B)** Multiple sequence alignment of the N-terminal

953 region (residues 1-152) of *D. melanogaster* BRP isoform G with homologues from *Apis mellifera*

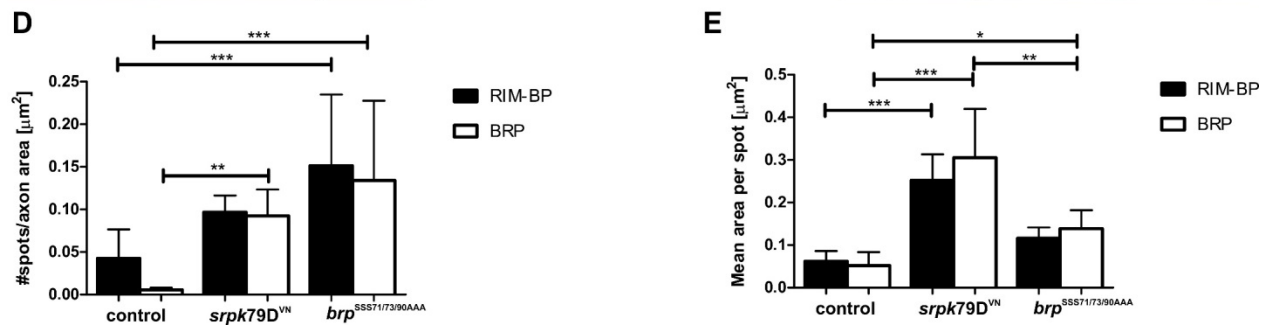
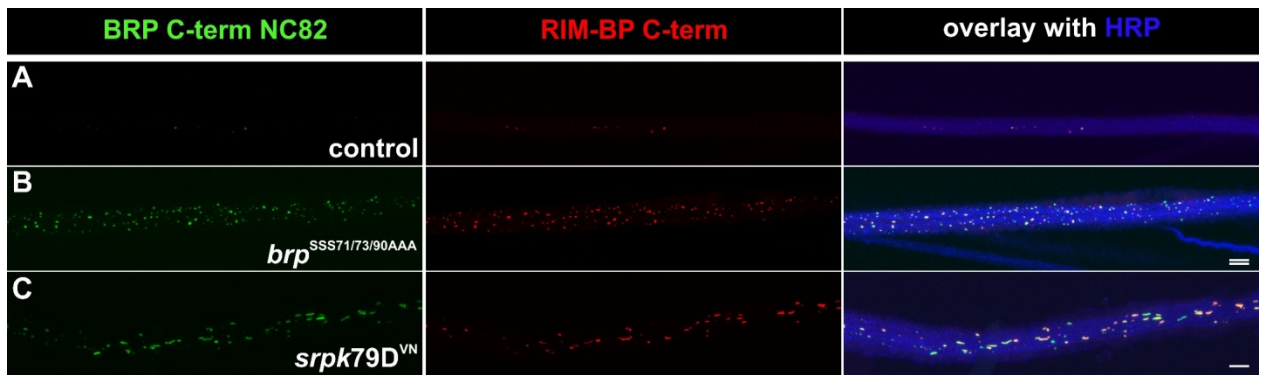
954 (honey bee), *Tribolium castaneum* (red flour beetle) and *Mus musculus* (mouse) prepared with

955 Geneious version 8.1.9 software. Darker shading indicates higher conservation of residues.

956 Phosphorylatable residues are highly evolutionarily conserved at positions corresponding to BRP

957 residues S71, S73, S90, Y130, S133 and S137. Colors were used as above phosphorylation sites

958 with yellow background were subjected to further functional characterization.



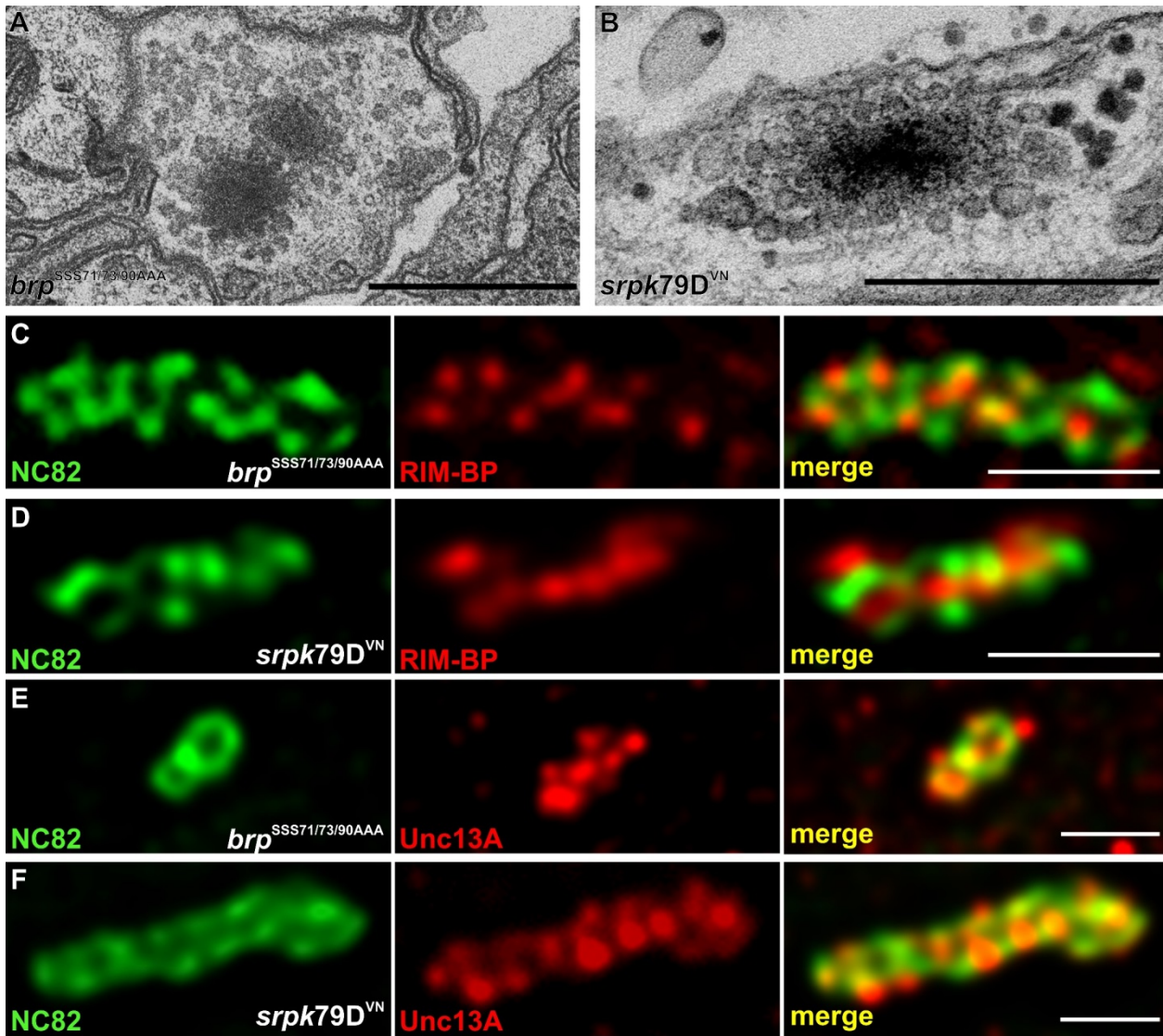
959

960

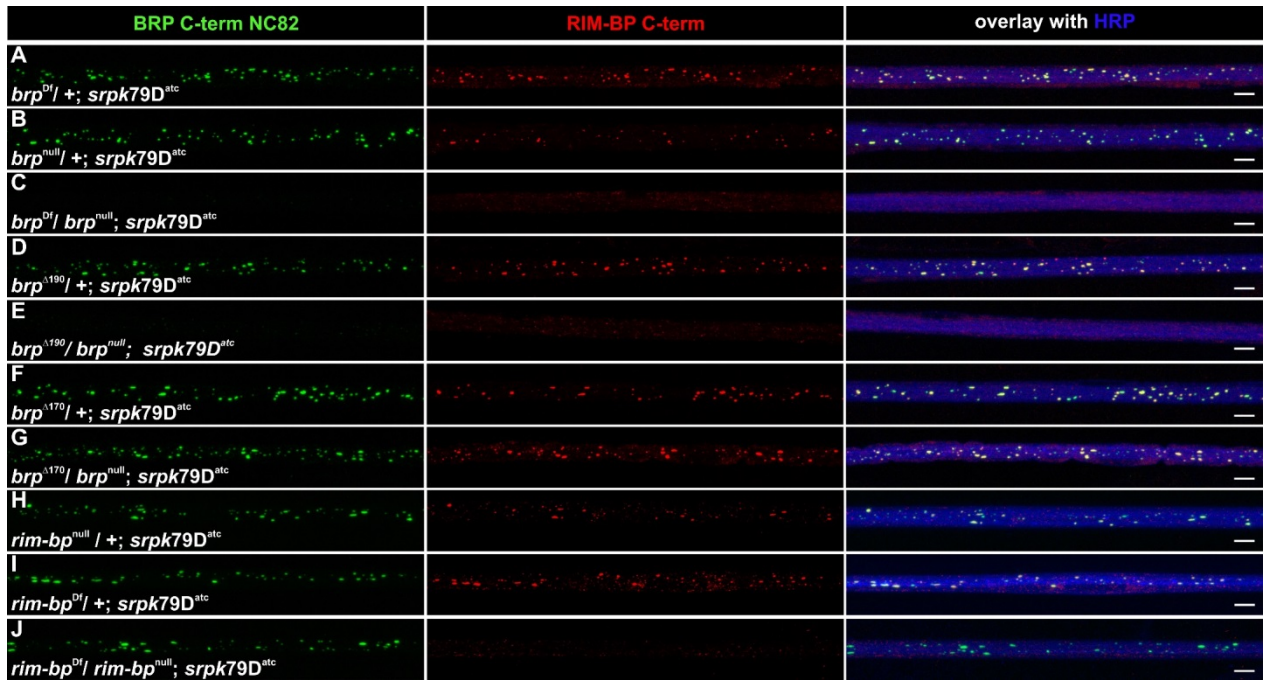
961 **Figure 2. BRP phosphorylation mutant phenocopies *srpk79D* deletion.**

962 Immunofluorescence images of the indicated genotypes. (A) The control (*brp*^{rescue}) shows only
 963 few, isolated and small BRP and RIM-BP spots per individual axon area, compared to BRP and
 964 RIM-BP of a *brp*^{SSS71/73/90AAA} phospho-destructive mutant (B) and *srpk79D*^{VN} mutant (C) and in a
 965 *brp*^{null} mutant (*brp* ^{$\Delta 6.1$} /*brp*^{Df(2R)69}) background. (D) Quantification of measured spot numbers per
 966 individual axon area. *brp*^{rescue}: 0.04258 \pm 0.01073 RIM-BP punctae/ μm^2 axon area and 0.00551 \pm
 967 0.0007957 BRP punctae/ μm^2 axon area (n = 12 NMJs; n = 6 animals); *brp*^{SSS71/73/90AAA}: 0.1514 \pm
 968 0.02410 RIM-BP punctae/ μm^2 axon area and 0.134 \pm 0.02702 BRP punctae/ μm^2 axon area (n =
 969 12 NMJs; n = 6 animals); *srpk79D*^{VN} mutant: 0.0967 \pm 0.005668 RIM-BP punctae/ μm^2 axon area
 970 and 0.09243 \pm 0.008974 BRP punctae/ μm^2 axon area (n = 10 NMJs; n = 5 animals). (E)
 971 Quantification of averaged aggregate sizes. *brp*^{rescue}: mean area for RIM-BP punctae 0.0620 \pm
 972 0.007572 μm^2 ; mean area for BRP punctae 0.052 \pm 0.009978 μm^2 (n = 12 NMJs; n = 6 animals).
 973 *brp*^{SSS71/73/90AAA} phosphorylation mutant: mean area for RIM-BP punctae 0.1158 \pm 0.007432 μm^2 ;
 974 mean area for BRP punctae 0.1383 \pm 0.01260 μm^2 (n = 12 NMJs; n = 6 animals). *srpk79D*^{VN}

975 mutant: mean area for RIM-BP punctae $0,2525 \pm 0,0175 \mu\text{m}^2$ and mean area for BRP punctae
976 $0,3050 \pm 0,03318 \mu\text{m}^2$ (n = 10 NMJs; n = 5 animals). Quantification was done using ANOVA
977 Tukey's post test. Scale bars – 500 nm.
978



979
 980 **Figure 3. Ectopic assembly of electron-dense cytomatrices in *srpk79D* and *brp*^{SSS71/73/90AAA}**
 981 **mutant axons.**
 982 **(A, B)** Electron micrographs showing a large, electron-dense, ectopic super-assembly of AZ
 983 structures in axons of *srpk79D* mutants **(A)** and *brp*^{SSS71/73/90AAA} mutants **(B)**. Scale bars – 500 nm.
 984 **(C, D)** Immunofluorescence images of nerve bundles of the indicated genotypes with the indicated
 985 antibodies. In the *srpk79D*^{VN} mutant **(C, E)** and the *brp*^{SSS71/73/90AAA} phosphorylation mutant **(D, F)**
 986 in a *brp*^{null} mutant (*brp*^{Δ6.1/brp}^{Df(2R)69}) background, both active zone components RIM-BP **(C, D)** and
 987 Unc13A **(E, F)** co-localize with BRP in axonal aggregates. Scale bars – 500 nm.



988

989

990 **Figure 4. BRP-190 is required for axonal aggregate formation in *srpk79D* mutants**

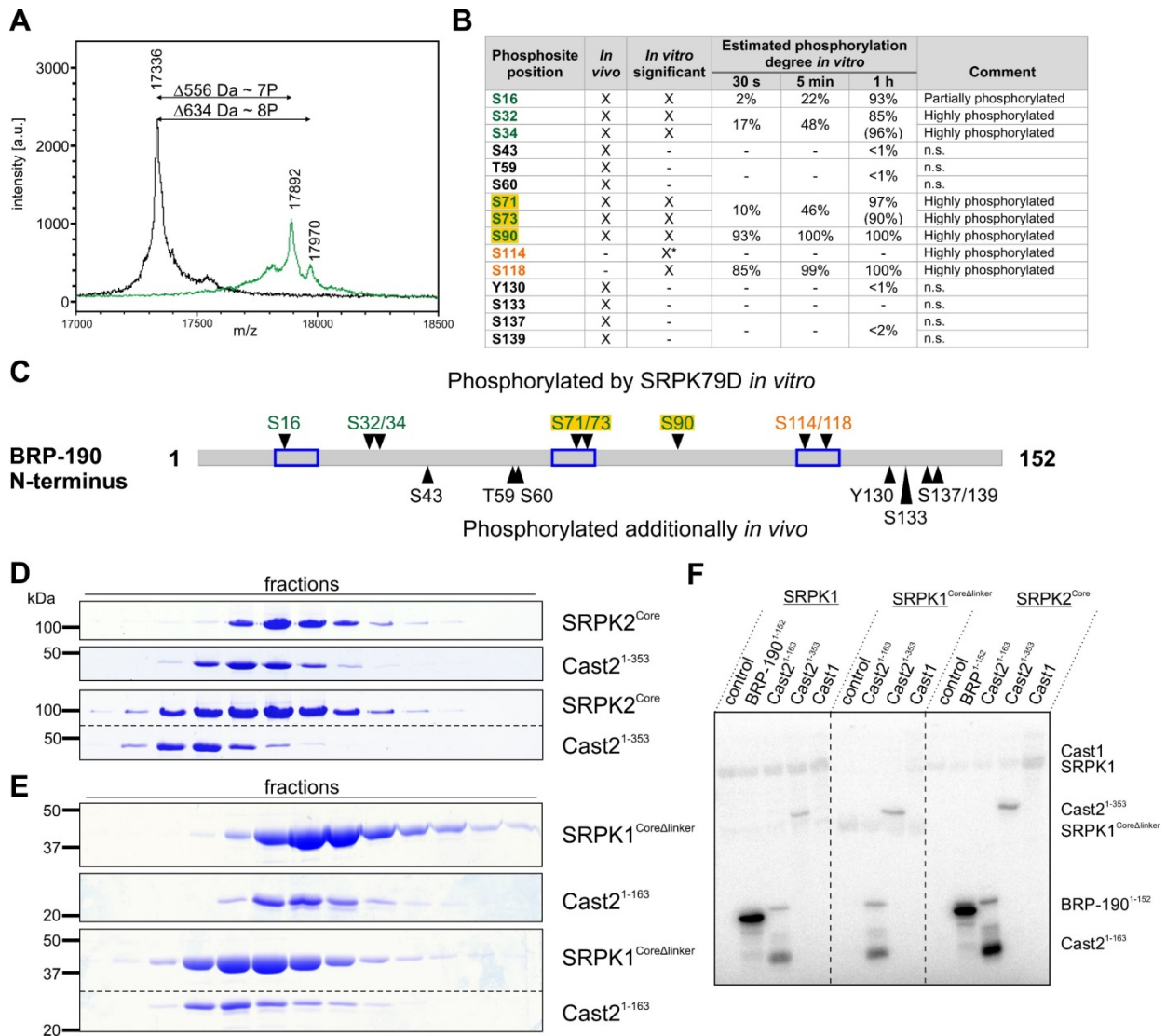
991 Nerve endings of the indicated genotypes were co-stained with antibodies against the BRP C-
992 terminus (NC82) and RIM-BP. **(A, B)** Positive controls (*srpk79D* homozygous null mutant in trans
993 to heterozygous *brp^{Df}* or *brp^{null}*). **(C)** Axonal aggregate formation requires BRP. No axonal
994 aggregates are formed in *brp^{Df} / brp^{null}; srpk79D^{atc}* double mutants. **(D, E)** The BRP-190 isoform is
995 sufficient to form axonal aggregates (*brp¹⁹⁰ / brp^{null}; srpk79D^{atc}*). Nomenclature of genotypes:
996 *brp^{null}* = *brp⁶⁹*, *brp^{Df}* = Df(2R)BSC29. **(F, G)** Axonal aggregate formation requires BRP-190,
997 removal of only the BRP-170 isoform in a double mutant background (*brp¹⁷⁰ / brp^{null}; srpk79D^{atc}*)
998 has no effect on axonal aggregate formation. **(H, I)** Positive controls for *srpk79D* mutant in double
999 heterozygous mutant combination for RIM-BP: *rim-bp^{null}* or *rim-bp^{Df}*; *srpk79D* crossed against +;
1000 *srpk79D*. **(J)** Axonal aggregation formation does not depend on RIM-BP. Double mutant
1001 combination (*rim-bp^{null}; srpk79D* crossed against *rim-bp^{Df}; srpk79D*) still show BRP-positive axonal
1002 agglomerates. Nomenclature of genotypes: *rim-bp^{null}* = *rim-bp^{STOP1}*, *rim-bp^{Df}* = *rim-bp^{S2.01}* (Liu et
1003 al., 2011) HRP – horseradish peroxidase. Scale bars – 500 nm.

1004

1015 Peptide SPOT analysis of overlapping BRP-190¹⁻¹⁵² peptides with GST (control) and GST-tagged
1016 SRPK79D^{Core}. Numbers at the beginning and the end of each line indicate the starting and the end
1017 residues of the peptides spotted, respectively. **(F)** Radioactive phosphorylation assay using
1018 SRPK79D^{Core}, SRPK79D^{CoreΔDock} SRPK79D^{Core-dead}, γ -[³²P]-ATP and BRP-190 fragments. Only
1019 BRP constructs that contain the N-terminal 152 residues of BRP-190 are phosphorylated.
1020 SRPK79D^{Core} and SRPK79D^{CoreΔDock} show similar activities, while SRPK79D^{Core-dead} shows no
1021 activity. Control – SRPK79D^{Core}, SRPK79D^{CoreΔDock} or SRPK79D^{Core-dead} alone. Gel slices
1022 separated by gaps are from separate gels. Gel regions between relevant lanes were removed for
1023 clarity (dashed line).

1024

1025



1026

1027

1028 **Figure 6. Identification of evolutionarily conserved phosphorylation sites in the BRP N-**
 1029 **terminus.**

1030 **(A)** MALDI-TOF analysis of untreated BRP-190¹⁻¹⁵² and BRP-190¹⁻¹⁵² phosphorylated by
 1031 SRPK79D^{Core} (green) indicates 7-8 phosphorylation sites. BRP-190¹⁻¹⁵² M_{theoretical} = 17340 Da. **(B)**
 1032 *In vitro* and *in vivo* phosphorylation sites within the BRP-190 N-terminus identified by mass
 1033 spectrometric analysis. Sites only found *in vivo* – black; sites only found *in vitro* – orange; sites
 1034 found *in vivo* and *in vitro* – green. Phosphorylation sites on yellow background were found to
 1035 pheno-copy *srpk79D* mutants *in vivo*. The degree of phosphorylation was estimated from

1036 comparing MS peak intensities of unphosphorylated and phosphorylated peptides, in brackets
1037 indicated the estimation for the double phosphorylated peptide. Phosphosites with an estimated
1038 degree of less than 5% were considered as not significant (n.s.) *in vitro*. **(C)** Schematic view on
1039 the BRP-190 N-terminus with all identified phosphorylation sites *in vitro* and *in vivo*. Colors as
1040 used in the table, blue rectangles indicate the regions bound in our peptide SPOT analysis (Fig.
1041 5E). **(D, E)** Analytical SEC shows binding of SRPK2^{Core} to Cast2¹⁻³⁵³ **(D)** and SRPK1^{CoreΔlinker} to
1042 Cast2¹⁻¹⁶³ **(E)**. Portions of the gels between the regions, to which SRPK1/2 and Cast2 constructs
1043 migrated, were removed (dashed lines). **(F)** *In vitro* phosphorylation of BRP-190¹⁻¹⁵² and Cast1/2
1044 fragments by SRPK1, SRPK1^{CoreΔlinker} and SRPK2^{Core} using γ -[³²P]-ATP.
1045

1046 **Tables**

1047 **Table 1. Yeast two-hybrid interactions of SRPK79D and BRP constructs***

	BRP-190¹⁻¹⁵²	BRP-190¹⁰⁰⁻³⁶⁰	BRP-190³⁰⁰⁻⁸⁵⁰	BRP-190⁵⁰⁰⁻¹³⁵⁰	BRP-190¹²⁰¹⁻¹⁷⁸⁶
SRPK79D	+	-	-	-	-
SRPK79D^{Core}	+	-	-	-	-
SRPK79D^{CoreΔlinker1}	++	-	-	-	-
SRPK79D^{CoreΔlinker2}	++	-	-	-	-

1048

1049 * Y2H interactions were regarded as reproducible if unique bait vector/prey vector combination
 1050 grew at least in four independent replicas. + – Y2H interactions that were reproducible with one
 1051 bait vector/prey vector combination; ++ – interactions that were reproducible with two bait
 1052 vector/prey vector combinations.

1053

1054 **Supplementary information**

1055 **Phosphorylation of the Bruchpilot N-terminus unlocks axonal transport**
1056 **of active zone building blocks**

1057

1058 Jan H. Driller^{1,†}, Janine Lützkendorf^{2,†}, Harald Depner², Matthias Siebert², Benno Kuroopka³,
1059 Christoph Weise³, Chengji Piao², Astrid G. Petzoldt^{2,6}, Martin Lehmann⁴, Ulrich Stelzl⁵, René
1060 Zahedi⁸, Albert Sickmann⁸, Christian Freund³, Stephan J. Sigrist^{2,6,*}, Markus C. Wahl^{1,7,*}

1061

1062 ¹ Freie Universität Berlin, Institute of Chemistry and Biochemistry, Laboratory of Structural
1063 Biochemistry, Takustraße 6, D-14195 Berlin, Germany

1064 ² Freie Universität Berlin, Institute of Biology, Laboratory of Genetics, Takustraße 6, D-14195
1065 Berlin, Germany

1066 ³ Freie Universität Berlin, Institute of Chemistry and Biochemistry, Laboratory of Protein
1067 Biochemistry, Thielallee 63, D-14195 Berlin, Germany

1068 ⁴ Leibniz-Forschungsinstitut für Molekulare Pharmakologie, Cellular Imaging, Robert-Roessle-
1069 Straße 10, D-13125 Berlin, Germany

1070 ⁵ University of Graz, Institute of Pharmaceutical Sciences, Pharmaceutical Chemistry,
1071 Universitätsplatz 1/I, A-8010 Graz, Austria

1072 ⁶ NeuroCure Cluster of Excellence, Charité - Universitätsmedizin Berlin, Charitéplatz 1, 10117
1073 Berlin, Germany

1074 ⁷ Helmholtz-Zentrum Berlin für Materialien und Energie, Macromolecular Crystallography,
1075 Albert-Einstein-Straße 15, D-12489 Berlin, Germany

1076 ⁸ Leibniz-Institut für Analytische Wissenschaften -ISAS- e.V., Bunsen-Kirchhoff-Straße 11, D-
1077 44139 Dortmund, Germany

1078

1079 † These authors contributed equally to this work.

1080 * Correspondence to: stephan.sigrist@fu-berlin.de; markus.wahl@fu-berlin.de

1081

1082 **Supplementary tables**1083 **Table S1. Overview of *in vitro* constructs**

Construct	Organism	Protein	Residues	Residue exchanges/ deletions
SRPK79D	<i>D. melanogaster</i>	SRPK79D isoform F	1-869	
SRPK79D ^{Core}	<i>D. melanogaster</i>	SRPK79D isoform F	327-869	
SRPK79D ^{CoreΔDock}	<i>D. melanogaster</i>	SRPK79D isoform F	327-869	D758A, D774A, E781A, K825A
SRPK79D ^{Core-dead}	<i>D. melanogaster</i>	SRPK79D isoform F	327-869	K376M
SRPK79D ^{CoreΔlinker1}	<i>D. melanogaster</i>	SRPK79D isoform F	327-869	Δ570-696
SRPK79D ^{CoreΔlinker2}	<i>D. melanogaster</i>	SRPK79D isoform F	327-869	Δ492-696
SRPK79D ¹⁻³⁴⁰	<i>D. melanogaster</i>	SRPK79D isoform F	1-340	
BRP-170	<i>D. melanogaster</i>	Bruchpilot isoform I	1-1397	
BRP-190	<i>D. melanogaster</i>	Bruchpilot isoform G	1-1786	
BRP-190 ^{Δ1-152}	<i>D. melanogaster</i>	Bruchpilot isoform G	153-1786	
BRP-190 ¹⁻¹⁵²	<i>D. melanogaster</i>	Bruchpilot isoform G	1-152	
BRP-190 ³⁶⁻¹⁵²	<i>D. melanogaster</i>	Bruchpilot isoform G	36-152	
BRP-190 ^{1-(Δ107-122)152}	<i>D. melanogaster</i>	Bruchpilot isoform G	1-152	Δ107-122
BRP-190 ^{1-152,6SD}	<i>D. melanogaster</i>	Bruchpilot isoform G	1-152	S32D, S34D, S71D, S73D, S90D, S118D
SRPK1	<i>Homo sapiens</i>	SRSF protein kinase 1	1-655	
SRPK1 ^{CoreΔlinker}	<i>H. sapiens</i>	SRSF protein kinase 1	58-655	Δ256-473
SRPK2 ^{Core}	<i>Mus musculus</i>	SRSF protein kinase 2 isoform c	49-682	
Cast2 ¹⁻¹⁶³	<i>Rattus norvegicus</i>	Cast2a	1-163	
Cast2 ¹⁻³⁵³	<i>R. norvegicus</i>	Cast2a	1-353	
Cast1	<i>R. norvegicus</i>	Cast1	1-957	

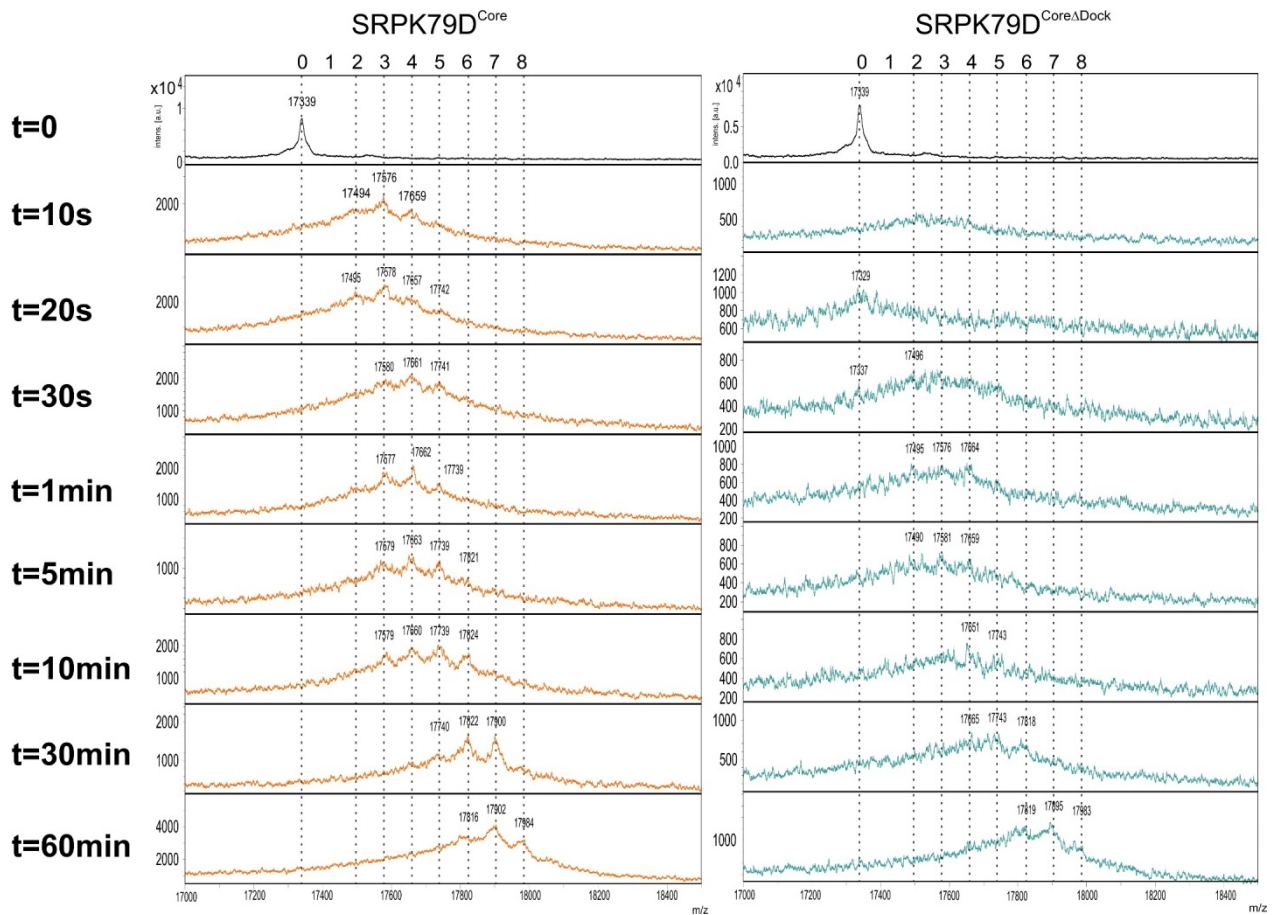
1084

1085 **Table S2. Peptide sequences of the BRP-190¹⁻¹⁵² SPOT membrane**

No.	Peptide	Length	Position
1	MSRDDYNPVTSSGVRSPGRVRRRLQE	25	1-25
2	PVTSSGVRSPGRVRRRLQELPTVDRS	25	8-32
3	RSPGRVRRRLQELPTVDRSPSRDYGA	25	15-39
4	RLQELPTVDRSPSRDYGAPRGSPLA	25	22-46
5	VDRSPSRDYGAPRGSPLAMGSPYYR	25	29-53
6	DYGAPRGSPLAMGSPYYRDMDEPTS	25	36-60
7	SPLAMGSPYYRDMDEPTSPAGAGHH	25	43-67
8	PYYRDMDEPTSPAGAGHHRSRASR	25	50-74
9	EPTSPAGAGHHRSRASRPPMAHAM	25	57-81
10	AGHHRSRASRPPMAHAMDYPRTYR	25	64-88
11	SASRPPMAHAMDYPRTYRQSLDRGG	25	71-95
12	AHAMDYPRTYRQSLDRGGLVDPHDR	25	78-102
13	RTRYQSLDRGGLVDPHDREFIPIRE	25	85-109
14	DRGGLVDPHDREFIPIREPRDRSRD	25	92-116
15	PHDREFIPIREPRDRSRDRSLERGL	25	99-123
16	PIREPRDRSRDRSLERGLYLEDELY	25	106-130
17	RSRDRSLERGLYLEDELYGRSARQS	25	113-137
18	ERGLYLEDELYGRSARQSPSAMGGY	25	120-144
19	DELYGRSARQSPSAMGGYNTGMGPT	25	127-151
20	ARQSPSAMGGYNTGMGPTS	19	134-152

1086

1087 **Supplementary figures**



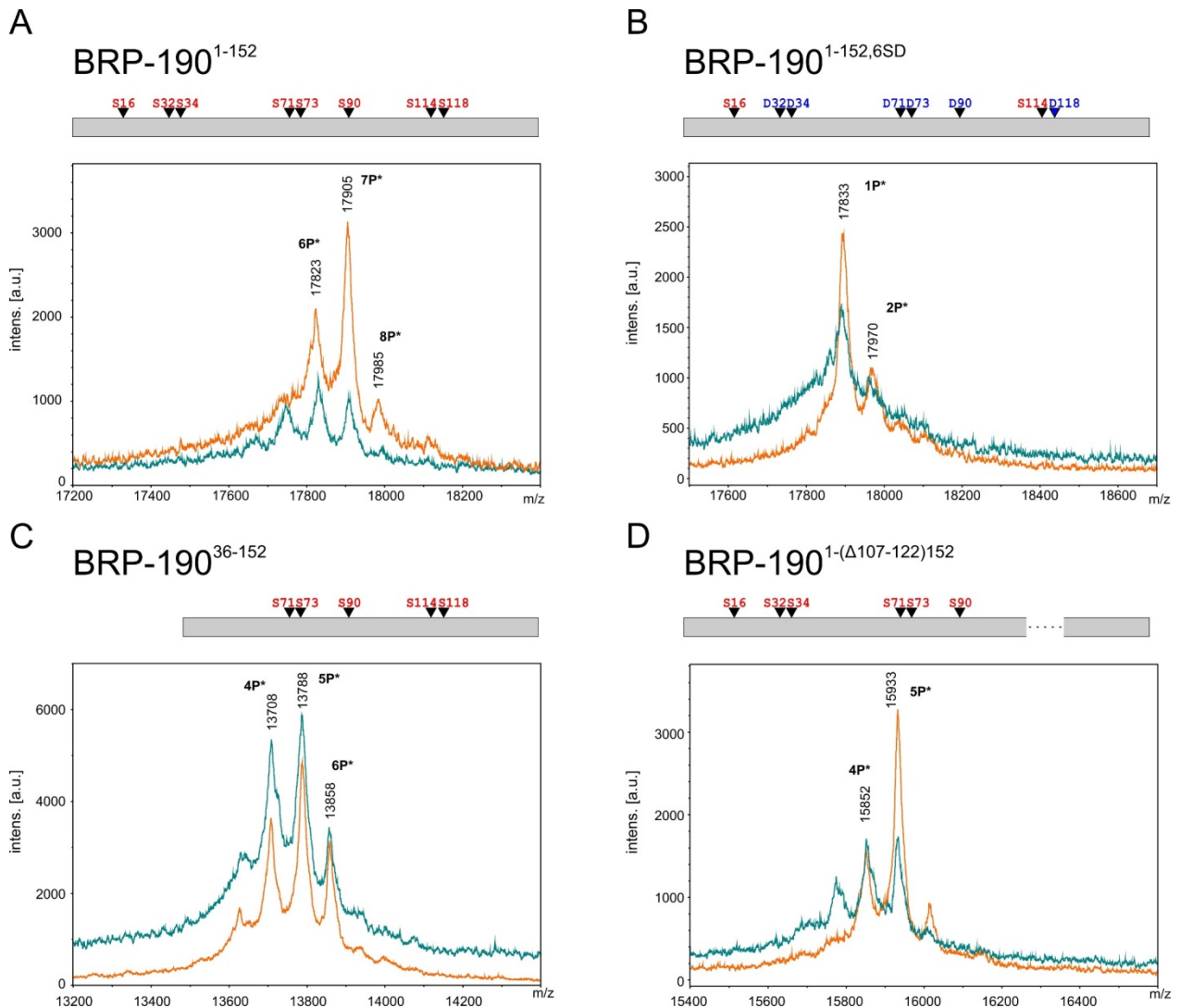
1088

1089

1090 **Figure S1. Intact protein mass analysis of phosphorylated BRP-190¹⁻¹⁵² in a time course**
 1091 **experiment**

1092 BRP-190¹⁻¹⁵² (unphosphorylated, black) was phosphorylated by SRPK79D^{Core} (orange) and
 1093 SRPK79D^{CoreΔDock} (teal). Reactions were stopped by adding SDS sample buffer at certain time
 1094 points and analyzed by MALDI-TOF-MS. Dashed lines in the spectra indicate the number of
 1095 phosphorylation sites. SRPK79D^{Core} phosphorylates BRP-190¹⁻¹⁵² faster than SRPK79D^{CoreΔDock},
 1096 as indicated by higher intensity peaks representing phosphorylated protein at all time points. After
 1097 one hour, both kinase constructs had added at least seven phosphates to BRP-190¹⁻¹⁵².

1098



1099

1100

1101 **Figure S2. Mass analysis of phosphorylated BRP-190 fragments**

1102 **(A-D)** Phosphorylation was carried out by SRPK79D^{Core} (orange) and SRPK79D^{CoreΔDock} (teal). **(A)**

1103 Both kinases added roughly seven phosphates to BRP-190¹⁻¹⁵² **(B)** BRP-190^{1-152,6SD} (phospho-

1104 mimetic aspartate residues at positions 32, 34, 71, 73, 90 and 118) was phosphorylated at mainly

1105 one site by both kinase constructs. **(C)** Phosphorylation of BRP-190³⁶⁻¹⁵², which yielded on

1106 average five attached phosphates (mass shift of 402 Da), indicated that in the region of residues

1107 1-35 only two predominant sites are located, probably S32 and S34. **(D)** Phosphorylation of BRP-

1108 190^{1-(Δ107-122)152} (deletion of one SRPK binding motif found by our peptide SPOT analysis; Fig 5E)

1109 resulted in a total mass shift of 403 Da, indicating five attached phosphates. In summary, these
1110 results indicate a more complete phosphorylation of S114 compared to S16.
1111
1112